LASER AND ELECTRON BEAM MATERIAL PROCESSING

HANDBOOK

MIR PUBLISHERS MOSCOW

N.N. Rykalin, Member of the USSR Academy of Sciences, D.Sc. (Tech.), author of 10 monographs and over 400 papers. He headed the laboratory at the Baikov Institute of Metallurgy (of the USSR Academy of Sciences) until his death in 1985.

A.A. Uglov, D. Sc. (Tech.), now head of the laboratory at the Baikov Institute of Metallurgy, has penned 9 monographs and over 500 papers.

I.V. Zuev, D.Sc. (Tech.), head of the chair at the Moscow Power Engineering Institute, has 3 monographs and more than 200 papers to his credit.

A.N. Kokora, Cand. Sc. (Tech.), head of the laboratory of the Scientific Center of Industrial Lasers at the USSR Academy of Sciences, author of 5 monographs and more than 150 papers.

LASER AND ELECTRON BEAM MATERIAL PROCESSING

Handbook

ЛАЗЕРНАЯ И ЭЛЕКТРОННО-ЛУЧЕВАЯ ОБРАБОТКА МАТЕРИАЛОВ

Справочник

Москва
«Машиностроение»

LASER AND ELECTRON BEAM MATERIAL PROCESSING

HANDBOOK

N. RYKALIN, A. UGLOV,
I. ZUEV, A. KOKORA

MIR PUBLISHERS MOSCOW

First published 1988
Revised from the 1985 Russian edition

Translated from the Russian by
P. S. Ivanov

На английском языке

Printed in the Union of Soviet Socialist Republics

ISBN 5-03-0000-23-2

© Издательство «Машиностроение», 1985
© English translation, Mir Publishers, 1988

CONTENTS

Preface 8

Part 1. LASER RADIATION AND ELECTRON BEAMS AS HEAT SOURCES 9

Chapter 1. LASERS AND LASER RADIATION 9
1.1. Physical Principles of Laser Action 9
1.2. Materials for Solid-State Lasers 15
1.3. Materials for Liquid Lasers 24
1.4. Mediums for Gas Lasers 31
1.5. Molecular Lasers 35
1.6. Electroionization CO_2 Lasers 41
1.7. Gas-Dynamic Lasers 43
1.8. Chemical Lasers 48
1.9. Properties and Characteristics of Laser Radiation . . . 51
1.10. Focusing of Laser Radiation 55
1.11. Optical Materials for CO_2 Lasers 67
References 73

Chapter 2. ELECTRON BEAM PARAMETERS AND MEASUREMENTS 74
2.1. CW and Pulsed Electron Beam Parameters 74
2.2. Rotating-Probe Measurement Method 76
2.3. Current Density Distribution over EB Cross Section . . 77
2.4. Other Measurement Methods 90
References 96

Chapter 3. THERMAL PROCESSES IN INTERACTION ZONES 98
3.1. CEF-Produced Heat Sources 98
3.2. Statement of Heat Source Problems. Linear Heat-Transfer Problems and Stationary Sources 115
3.3. Moving Heat Sources. Critical Heat Power Densities 134
3.4. Nonlinear Problems of LR and EB Interaction 145
References 166

Chapter 4. HYDRODYNAMIC PROCESSES IN INTERACTION REGIONS 168
4.1. Melt Formation 169
4.2. Deformation of the Melt Surface Under Reactive Pressure 178
4.3. Keyholing 184
4.4. Thermocapillary Effects in the Liquid Phase 189
References 193

Chapter 5. VAPORIZATION OF MATERIALS 194
5.1. Models of Surface Vaporization 194
5.2. Volumetric Vaporization 198
5.3. Vapor Expansion in Vacuum 205
5.4. Interaction of Radiation with Blowoff Products 209
5.5. Effects of Laser-Induced Plasma on Thermal Processes in the Interaction Region 217
References 231

Chapter 6. LASER-INDUCED PLASMA EFFECTS AND THERMOCHEMICAL PROCESSES 233
6.1. Laser-Material Interaction at High Ambient Pressure 234
6.2. The Mechanisms of Optical Breakdown in High-Pressure Gas at the Target Surface 244
6.3. Plasma Dynamics Near a Solid Surface at High Nitrogen Pressure 252
6.4. Reduction of Metals and Synthesis of Inorganic Materials 260
6.5. Laser-Induced Thermochemical Processes 269
References 274

Part 2. LASER MATERIAL PROCESSING 277

Chapter 7. HEAT TREATMENT 277
7.1. Physical Principles of Material Hardening 279
7.2. Changes in the Structures and Properties of Materials in the Zones of Pulsed Laser Interaction 286
7.3. CW Laser-Iron Alloy Interaction 297
7.4. Surface Alloying 306
7.5. Cladding 314
7.6. Shock Wave Effects 316
7.7. Amorphization 320
7.8. On Some Features of Laser Heat Treatment 324
7.9. Mass Transfer Processes 339
7.10. Laser Surface Hardening in Nitrogen 343
7.11. Laser-Assisted Machining 347
7.12. Examples of Laser Heat Treating 350
References 354

Chapter 8. LASER WELDING 358
8.1. Thermal Processes 358
8.2. Laser Welding Technology 370
8.3. Continuous Laser Cutting 386
8.4. Seam Welding with Multikilowatt CW Lasers 402
8.5. Welding at Low Environmental Pressures 416
References 417

Chapter 9. LASER DRILLING 419
9.1. Laser-Induced Material Removal 419
9.2. Melt Flushing Mechanism 424
9.3. Effect of the Pulse Length and Energy on Hole Parameters 428
9.4. Surface Finish of Holes Drilled by Normal Pulses. . . . 434
9.5. Factors Affecting the Hole Quality 435
9.6. Multiple Shot Drilling 438
9.7. Use of a Conical Lens to Produce Large Diameter Holes 443
9.8. Ways of Improving the Reproducibility of Holes 447
9.9. An Example of Hole Drilling with Split Pulses 449
References 450

Part 3. ELECTRON BEAM MATERIAL PROCESSING 451

Chapter 10. ELECTRON BEAM-SOLID INTERACTIONS 451
10.1. Mechanisms of Hole Formation 451
10.2. Examples of EB Material Processing 461
References 468

Chapter 11. ELECTRON BEAM WELDING 469
11.1. Effect of the Gun-to-Part Distance on the Fusion Zone Geometry 469
11.2. Relation between EB and Weld Parameters 472
11.3. Calculation of the Weld Depth and Width 475
11.4. Effect of Beam Voltage on the Penetration Depth 484
11.5. Positions of Welding 487
References 488

Chapter 12. THERMAL PROCESSES 489
12.1. EB-Plasma Interaction 489
12.2. Kinetics of Cavity Formation 490
12.3. Free Oscillation 496
References 500

Chapter 13. ELECTRON BEAM APPLICATIONS IN MICROELECTRONICS 501
13.1. Vacuum Film Deposition 501
13.2. Integrated Circuit Packaging 503
References 514

Chapter 14. CONTROL OF ELECTRON BEAM-MATERIAL INTERACTION 515
14.1. Electron Emission 515
14.2. Weld Penetration Control 521
14.3. Control of EB Heating Stages 523
14.4. Weld Penetration Control by the Ion Current Ripple Frequency 530
References 532

Part 4. LASER AND ELECTRON BEAM EQUIPMENT 533

Chapter 15. LASER AND ELECTRON BEAM SETUPS 533
15.1. Laser Setups 533
15.2. Electron Beam Setups 573
References 582

Index 583

PREFACE

Concentrated energy fluxes (CEFs), such as ion and electron beams, laser beams, and plasma clouds, are finding ever increasing application in research and industry because of the versatile control and easy optimization of their parameters. The use of CEFs offers the possibility of a relatively simple automation and programming of a wide variety of industrial processes.

The last few years have seen a still greater progress in the field of material processing with lasers operating at various wavelengths and with electron beams using accelerating voltages in the "industrial" range, from 10 to 150 kV. The main advantage of a CEF is that it can deliver a very high power per unit area to localized regions on a target surface. This opens up many potential applications and has led to the emergence of a number of industrial techniques, namely, laser and electron beam welding, heat treatment, cutting, annealing, alloying, and hole piercing.

Over the past few years, both in the USSR and other countries, a number of books and articles have been published on the problems of interaction of CEFs with materials. These publications cover the achievements in this domain of science and describe the ways of application of laser and electron beams to various industrial processes.

The knowledge gained in this dynamic field of science enables scientists to obtain a better insight into seemingly "indisputable" facts and to clear up "intersecting" aspects in different technologies. There are many such intersections in laser and electron beam processes because their energy-related parameters are rather similar from the technical point of view. For this reason, a common "energetic" approach has been used on treatment of the main physical phenomena specific to CEFs.

This book is of a specific kind. Since the laser and electron beam technologies continue to advance with huge strides, the idea of writing the handbook on the subject seems futile in itself. That is why we have made an attempt to select and describe only the basic processes and phenomena, the concepts of which, in our opinion, may be subject only to corrections, but not drastic alterations.

In designing the book, we have tried to present the material in a definite sequence relying on our own experience and in the order scientists in other countries have adopted.

Authors

Part 1
LASER RADIATION AND ELECTRON BEAMS AS HEAT SOURCES

Chapter 1
LASERS AND LASER RADIATION

1.1. PHYSICAL PRINCIPLES OF LASER ACTION

Laser radiation (LR) is the stimulated monochromatic emission of light in the wide range of wavelengths from several nanometers to tens and hundreds of micrometers. Fig. 1.1 illustrates the main regions of the electromagnetic wave spectrum.

The frequencies of extreme regions differ by a factor of about 10^{16}. The boundaries between the wave bands of the electromagnetic

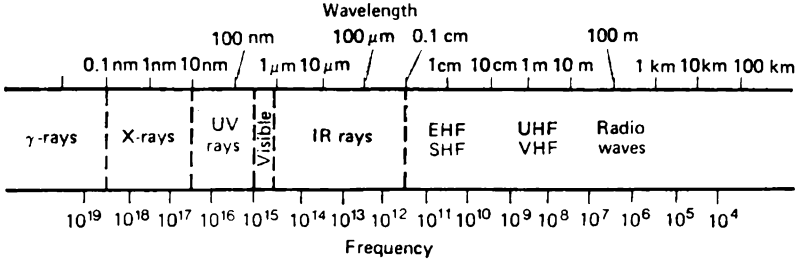

Fig. 1.1. Electromagnetic wave spectrum illustrating main frequency (wavelength) ranges: EHF, extremely high frequency band (0.1-1 cm); SHF, superhigh frequency band (1-10 cm); UHF, ultrahigh frequency band (0.1-1 m); VHF, very high-frequency band (1-10 m)

spectrum are defined rather conditionally, according to the character of interaction of radiation with substances. Modern physics accepts the concept of the dual nature of radiation: it has the wave-like properties but at the same time occurs as a sequence of discrete energy bursts or packets called quanta or photons. The energy of a photon is

$$E = h\nu = hc/\lambda \tag{1.1}$$

where $h = 6.6 \times 10^{-34}$ J s is Planck's constant, ν the frequency of an electromagnetic radiation, λ the radiation wavelength, and c the velocity of propagation of the electromagnetic radiation (velocity of light).

Thus, in the phenomena of diffraction and interference, the wave nature of light prevails; in other phenomena associated with absorption of radiation by atomic or molecular systems, for example, in the photoelectric effect, the quantum (corpuscular) nature of light is predominant.

The energy of a photon can be used to characterize a radiation (Table 1.1).

TABLE 1.1. Relationships Among Various Radiation Units

Unit	Wavelength, μm	Frequency, Hz	Unit	Wave number, cm^{-1}	Photon energy, eV
μm	1	3.33×10^{-15}	μm	1×10^{-4}	0.81
Hz	3×10^{14}	1	Hz	3.33×10^{-11}	4.14×10^{15}
cm^{-1}	1×10^{4}	3.0×10^{10}	cm^{-1}	1	1.24×10^{-4}
eV	1.23	2.42×10^{-14}	eV	8.07×10^{3}	1

In Fig. 1.2 are given the wavelengths of radiation of the most popular lasers [1]. Laser radiation covers the wavelength range of 10^{-5} to 10^{-2} cm, which extends from the near ultraviolet (UV) into the infrared (IR), overlapping the visible region. The total wavelength range of laser radiation is approximately 0.1 to 1 000 μm, although only experimental lasers operate in the extreme regions of wavelengths. Commercial lasers give outputs at wavelengths between 0.3 and 10.6 μm:

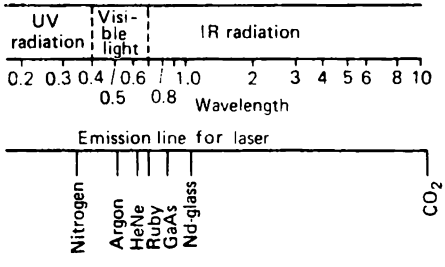

Fig. 1.2. Emission wavelengths for most popular lasers

— the nitrogen (UV) laser emits at $\lambda = 0.3371$ μm;
— the argon laser emits at a few wavelengths in the blue-green region of the visible spectrum;
— the helium-neon laser emits at $\lambda = 0.6328$ μm;
— the gallium arsenide laser emits in the near IR at $\lambda = 0.85$ to 0.9 μm;
— the ruby laser emits at $\lambda = 0.6943$ μm;
— the Nd-glass laser emits in the near IR at $\lambda = 1.06$ μm;
— the CO_2 laser emits in the far IR at $\lambda = 10.6$ μm.

Energy levels. The principle of laser action is inseparable from the notion of an energy level (energy state) — the value of energy of an atom, molecule, or any other quantum system that

consists of electrons, nuclei, and atoms and obeys the quantum laws specific to the microcosm.

The most important property of a quantum system composed of bound particles such as atoms, nuclei, and electrons is that the internal energy E of the system, which does not involve the motion of the microparticle as a whole, can take on only definite discrete values $E_0, E_1, \ldots, E_n$ $(E_0 < E_1 < E_2 \ldots)$. For each of these allowed energy values there correspond one or a few stable states of motion of a particle in the system, i.e. the system can have only definite discrete orbits of motion of particles such as electrons and nuclei.

Any change in the energy E leads to an abrupt transition of the system from one stable state to another, or from one energy level to another.

In gases, liquids, and solids, the atoms or molecules interact with one another, so that their energy levels vary — the denser the substance, the greater the energy level variations. The energy levels of individual atoms can expand to form an almost continuous energy band, for example, a valence band and a conduction band in semiconductor materials.

In many transition metals, which include vanadium, chromium, manganese, iron, and rare-earth metallic elements such as neodymium, samarium, and europium, the energy levels on the uncompleted inner electron orbits remain narrow because the outermost electron orbit shields the electric field. This feature is of substantial importance for the operation of lasers [1, 2]. A molecule, just like an atom, also represents a quantum system, but its energy spectrum is more complex. Along with the motion of electrons about the nucleus, other types of motion are possible in a molecule namely, the vibrational motion of atoms with respect to one another and rotational motion of the molecule itself. The total energy of a molecule is

$$E = E_e + E_v + E_r \tag{1.2}$$

where E_e is the electron energy, E_v is the vibrational energy, and E_r is the rotational energy, with $E_e \gg E_v \gg E_r$. The pattern of energy levels of a molecule is then the set of electron energy levels far distant from each other, vibrational energy levels spaced closer to each other, and rotational energy levels disposed still more closely together.

Thus, in a CO_2 molecule, the carbon atom lies along the same line between the two oxygen atoms. Here the vibrational energy levels correspond to the motion of oxygen atoms relative to the carbon atom. The rotational motion of the asymmetric molecule gives rise to the rotational energy levels, etc.

The structure of an energy spectrum, i.e. the number and the

distribution pattern of energy levels, is different for various quantum systems and depends on the character of interaction of the microparticles in the structure, or on the potential energy of the system.

Interaction of radiations with a substance arises from an abrupt transition of the quantum system such as an atom or a molecule from one energy level to another. When it moves from a higher energy level E_i to a lower energy level E_k, the system gives up part of its energy, equal to $E_i - E_k$. When it executes the reverse transition, the system absorbs this energy. The absorbed energy is

$$h_\nu = E_i - E_k \tag{1.3}$$

The known processes of interaction of radiation with substances include fluorescence, absorption, resonance emission, and stimulated (induced) emission of radiation, which are fully consistent with the notion of energy levels and expression (1.3).

Fluorescence arises from the spontaneous transition of an excited atom from the upper to the lower energy level, followed by the emission of energy, equal to the energy difference between the two levels, in the form of a photon of frequency ν. The energy of the system constituting an atom or a molecule thus decreases, while the energy of the field grows by ΔE_{ik}.

The number of spontaneous transitions in the system for the time dt [3] is given by

$$dW_{21} = A_{21} N_2 \, dt = dN_2 \tag{1.4}$$

where A_{21} is Einstein's A coefficient which expresses the probability per unit time that the atom will fall from the level 2 (state 2) into level 1 (state 1). Then,

$$N_2 = N_{20} \exp(-A_{21} t) \tag{1.5}$$

where N_{20} is the initial number of atoms in the level 2 at $t = 0$.

The power of spontaneous radiation is

$$P_s = h\nu A_{21} N_{20} \exp(-A_{21} t) \tag{1.6}$$

The mean lifetime τ of an atom in the excited state is inversely proportional to the transition probability, i.e. $\tau = 1/A_{21}$, and reaches about 10^{-8} s. Hence,

$$P_s = h\nu A_{21} N_{20} \exp(-t/\tau) = P_{s0} \exp(-t/\tau) \tag{1.7}$$

As follows from (1.6), the mean lifetime of an excited atom is equal to the decay time of spontaneous radiation and can be determined experimentally.

Since the individual acts of spontaneous radiation occur independent of each other in time, the spontaneous emission is incoherent, i.e. the spatial and time correlations of the electromagnetic oscillations in frequency and in phase do not exist.

In the case of resonance absorption, the probability of absorption of a photon in time dt at an average power density q_0 is

$$dW_{12} = q_\nu B_{12} N_1 \, dt = dN_1 \tag{1.8}$$

where B_{12} is Einstein's B coefficient which defines the probability that an individual atom will make a transition from level 1 to level 2.

If the frequency ν does not satisfy formula (1.3) for any pair of energy levels, absorption does not occur. Nevertheless, the material will absorb the given radiation because a large number of closely spaced allowed energy levels commonly exist for this radiation and the required combination of energy levels will be available for practically any frequency.

In the case of stimulated radiation, the excited atom falls from the upper energy level to the lower level and emits excess energy. This process underlies the operation of lasers. A. Einstein was the first to predict that there is a possibility of initiating light emission by an external photon whose energy corresponds to the energy difference between the excited state and the initial state of a lower electron energy. The interaction of this photon with an atom leads to the simultaneous emission of two photons of the same frequency, which propagate in the same direction.

Since stimulated transitions occur simultaneously and the frequency of the emitted radiation corresponds to the frequency of the absorbed photon, the stimulated radiation is coherent.

The total probability dW_{21} that an atomic system will make a transition from level 2 to level 1 is the sum of probabilities dW_s and dW_{st} for the spontaneous transition and stimulated transition respectively:

$$dW_{21} = dW_s + dW_{st} \tag{1.9}$$

where $dW_s = A_{21} N_2 \, dt$, and $dW_{st} = q_\nu B_{21} N_2 \, dt$. Then,

$$dW_{21} = (A_{21} + q_\nu B_{21}) \, N_2 \, dt = dN_2$$

Here A_{21} and B_{21} are the Einstein coefficients for the spontaneous radiation and spontaneous absorption respectively.

Thus, on exposure to the external electromagnetic field the system generates the total radiation which consists of the spontaneous component and stimulated component, the latter being coherent. The relation between the stimulated and the spontaneous radiation in the total radiation is proportional to the Einstein probabilistic coefficients and is an important quantitative characteristic of radiation.

Two relations of the Einstein coefficients are known. The first relation is

$$g_1 B_{12} = g_2 B_{21} \tag{1.10}$$

where g_1 and g_2 are the degrees of level degeneracy for the system with energies E_1 and E_2 respectively, and B_{12} and B_{21} the Einstein coefficients for absorption and stimulated emission respectively, which characterize the probability of absorption and stimulated emission and are equal to the number of photons the system absorbs and emits under the action, on the average, of one initiating particle in 1 s at radiant density $q_\nu = 1$.

The second relation is

$$A_{21} = 8\Pi h\nu^3 B_{21}/c^3 \qquad (1.11)$$

Expression (1.11) for A_{21} is only valid for a medium with a refractive index n equal to 1. Since for most solids $n \neq 1$, the vacuum light velocity c in (1.11) should be replaced by the light velocity in the medium under consideration, $v = c/n$. The coefficient $8\Pi h\nu^3/c^3$ represents the number of possible modes of oscillation in a unit volume.

Formulas (1.10) and (1.11) give the quantitative characteristic of radiation and can be considered to form the basis of the theory of lasers.

Materials for lasers. The materials used in the production of lasers must exhibit definite properties.

Laser action takes place, in accordance with expression (1.3), in the region of those wavelengths (or frequencies), where a material emits a fluorescent radiation.

Materials for lasers are studied by spectroscopic methods [2]. From the spectroscopic viewpoint, laser materials display enhanced fluoresence and narrow spectral fluorescent lines. The fluorescent line uscd in lasing has a finite width, and the frequency distribution of the emitted light within the line determines its shape, Lorentzian lineshaepe or Gaussian lineshape [2].

The Lorentzian lineshape distribution function conditioned by the finite lifetime of an excited atom takes on the form $[(\nu - \nu_0)^2 + (\Delta\nu)^2]^{-1}$, where ν is the frequency, ν_0 is the central line frequency, and $\Delta\nu$ is the frequency at the halfwidth of the line.

The Gaussian lineshape distribution function determined by the Doppler shift due to the motion of molecules in a gas has the form $\exp\{-(\ln 2)[(\nu - \nu_0)/\Delta\nu]^2\}$ [1]. The intensity of a fluorescent line is defined by the above distribution functions depending on the value of frequency.

Fluorescent lines can be homogeneous and inhomogeneous. As regards the homogeneous line, every atom of a substance can emit electromagnetic energy within the entire linewidth; in the case of the inhomogeneous line, atoms can emit in a narrow region of the linewidth. This means that in a material displaying the homogeneous line, every atom can contribute to lasing within the fluorescent linewidth, while in a material with the inhomogeneous line only

a small amount of atoms contribute to laser action and thus to the laser output [1]. Lorentzian lines are always homogeneous and Gaussian lines are inhomogeneous; ruby displays homogeneous lines at room temperature and inhomogeneous lines at low temperatures.

1.2. MATERIALS FOR SOLID-STATE LASERS

These materials can be crystalline and noncrystalline in structure.

A crystal consists of a base — matrix — which is a working host material and an active material called an activator or a lasant, which is an impurity properly distributed in the host material. The atoms (ions) of a lasant that substitute for the base, or host, atoms must uniformly occupy crystal lattice sites. For this the atomic radii of the lasant and the host must be equal. The host is a dielectric material, in which the band gap exceeds 2 eV. Lasant atoms give rise to energy levels which lie within the band gap between the energy bands of the crystal. The number of these energy levels and their width depend on the energy spectrum of the lasant and the character of its bonding with the base atoms. The materials used as lasants include actinoids, rare-earth elements, and transition metals. Radiative transitions in the atoms of these impurities occur between the energy levels of electrons arranged on incomplete inner electron shells.

What should be considered to be the direct effect of the activator is that the activated matrix displays selective absorption regions, often in the visible, and spontaneous luminescence (color centers).

Thus, the difference between the spectra of the isolated atoms of the lasant and the activated crystal results from the interaction of the lasant atoms with the electromagnetic field of the crystal lattice.

Since the actual structure of a crystal always has defects, the position of the lasant atoms in the crystal are different, the crystal field exerts different effects on the atoms and leads to the shift of levels with respect to one another. This causes an additional broadening of the lines. Thermal lattice vibrations also broaden the spectral lines.

The magnetic interaction of the energy levels of a lasant atom can also change the levels of the atom [3].

The main requirements placed on a base material (matrix) are the following:

— low energy loss due to intrinsic and impurity absorptions at the pump and laser frequencies;

— high thermal conductivity;

— absence of optical and other inhomogeneities and also local mechanical stresses;

— high mechanical strength and adequate thermal and chemical stability;
— stability to the UV radiation flux from the pump tube.

A lasant must comply with the following requirements:
— the radiation pattern must conform to the requirements of the three- or four-level quantum system and must not exhibit secondary absorption lines;
— the metastable level must feature a long lifetime and very narrow luminescence line, not over a few cm^{-1};
— the absorption band must be as wide as possible;
— the pump frequency must not appreciably exceed the laser frequency.

Crystalline laser materials can be classified by the spectroscopic properties of lasant ions and by the crystal-chemical structure of the host. The latter approach is more convenient since the structure of the host material serves as the most representative basis for the unification and distinction of materials by optical, thermal, electrical, and chemical properties and also by production-process features [3]. The classification presented below relies on the second approach.

Crystalline laser materials fall into two large groups, oxidates and fluorides.

Oxidates include the oxides of Group III elements, oxides of rare-earth elements, and oxides of V and VI elements.

Oxides of Group III elements. Ruby α-$Al_2O_3(Cr^{+3})$ consists of an α-corundum, which is the α-Al_2O_3 crystalline matrix, and a

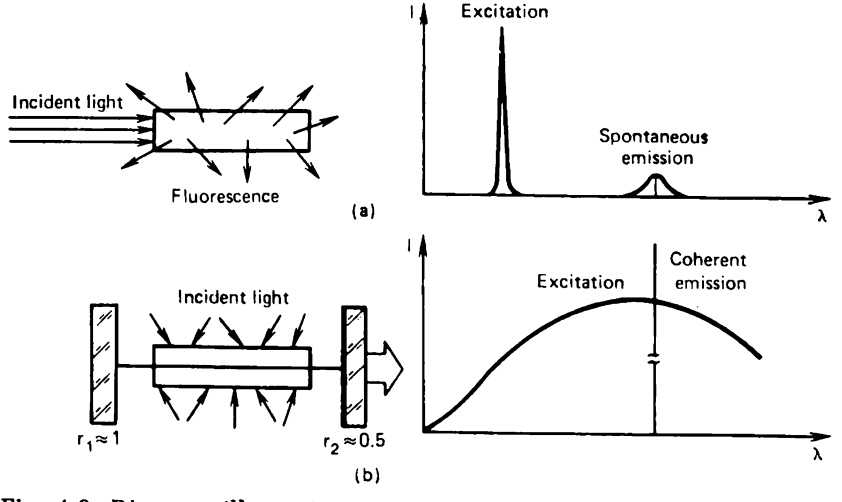

Fig. 1.3. Diagrams illustrating spontaneous fluorescence emission (*a*) of ruby and coherent emission (*b*) of laser radiation

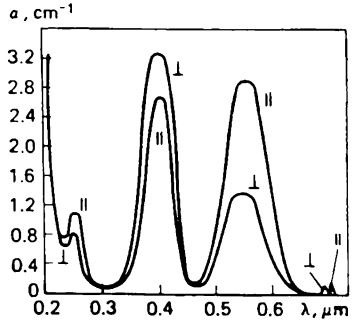

Fig. 1.4. Absorption by ruby as a function of light wavelength and orientation of ruby optic axis with respect to incident light flux: ∥, absorption parallel to optic axis; ⊥, absorption normal to optic axis

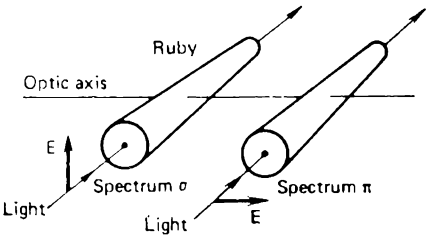

Fig. 1.5. Methods of obtaining absorption spectra of σ and π types in ruby

small amount of Cr^{+3} ions that occupy some lattice sites in the matrix. With 0.05% chromium dissolved in Al_2O_3, 1 cm^3 of the ruby crystal contains 1.6×10^{19} ions of this impurity. The ruby crystal has a rhombohedral (R) lattice, the space group being D_{3d}^6. An aluminum ion is surrounded by six O^{-2} ions to form an octahedron. An oxygen ion is surrounded by four aluminum ions. The radius of chromium ions (0.65×10^{-4} μm) is fairly close in value to the radius of aluminum ions (0.57×10^{-4} μm), for which reason the impurity atom insignificantly distorts the crystal lattice as it substitutes for a matrix atom. Ruby displays a high chemical stability and appreciable thermal conductivity. The thermal conductivity of ruby is slightly higher than that of copper at the temperature of liquid nitrogen, but decreases with increasing temperature and at 293 K it drops to about half the value at 40 K.

In Fig. 1.3 are shown the spontaneous (fluorescent) emission and stimulated emission of ruby during lasing [2]. A sufficiently long ruby crystal, about a few centimeters, illuminated by a strictly monochromatic directional beam, for example, of the green light, will totally absorb the light and will emit the fluorescent radiation that does not exhibit directionality, nor chromaticity (see Fig. 1.3*a*).

Optical pumping even by white light can rather effectively excite ruby, which is evident from the spectrophotometric curves of ruby crystal absorption plotted versus wavelengths of the incident light (Fig. 1.4). The figure displays two wide absorption bands near 0.4 μm and 0.55 μm (about 2 500 cm^{-1} and 18 000 cm^{-1} respectively). The total width of the two bands is about 0.3 μm. Characteristic of ruby is a substantial dependence of absorption on the angle between the electric field vector of the light wave and the optic axis of

the crystal. The best known absorption spectra are σ and π spectra, as illustrated in Fig. 1.5.

Soviet industry produces synthetic ruby rods whose specifications and dimensions are given in branch standards 3-24-70 and 3-25-70 [4]. In accordance with these standards, ruby and neodymium doped rods have the shapes such as illustrated in Table 1.2.

TABLE 1.2. **Types of Ruby and Neodymium-Doped Glass Rods**

Type	Element	Type	Element
R		RLOL1B	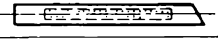
RL		RLOL2B	
RL1B	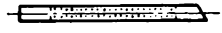	ENTs-90	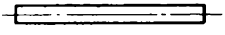
RL2B	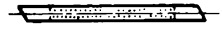	ENTs-φ	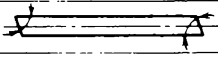
RLS		ENTs-5	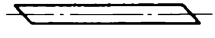
RLO		ENP-90	
RLOL		ENP-φ	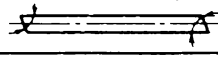

The designation of each element given in transliterated Russian letters denotes its type and size. For example, the RL1B (10 × 120) rod is 10 mm in diameter and 120 mm long. Ruby rods are available in diameters from 3.5 to 16 mm and in lengths from 45 to 240 mm, with angles of inclination of end faces ranging from 60 to 90° [4]. The rod surface is ground and mechanically polished.

It should be noted that the ends of R, RL, and RL2B ruby elements are parallel to within 10″. Table 1.3 lists three categories of ruby rods specified by the chromium mass concentration, refractive index variation, number of defects (poor fusion sites and bubbles), and fringe count (nonplaneness of ends).

The advantages of ruby are its ability to operate at 293 K, high mechanical strength, and increased damage threshold. A disadvantage is an appreciable optical inhomogeneity due to crystal lattice defects such as dislocations, clusters, slip planes, foreign impurities, and nonuniform distribution of chromium ions in the matrix. Lattice imperfections give rise to internal stresses. The nonuniform distribution of Cr^{+3} ions is responsible for an appreciable variation in the refractive index and causes lattice deformation which results in abnormal birefringence.

TABLE 1.3. Categories of Rudy Rods [4]

Category	Diameter, mm	Mean Cr^{+3} mass concentration, %	Change in refractive index $\Delta n \times 10^5$	Number of poor fusion sites and bubbles, not over		Fringe count
				0.2 mm	0.3 mm	
1	8	0.013-0.017	0.6	9	—	0.3
2	8	0.018-0.025	0.9	16	—	0.5
3	8	0.026-0.036	2.7	—	—	—
1	—	—	0.7	15	—	0.3
2	10	0.20-0.028	1.1	25	—	0.5
3	10	0.25-0.040	4.0	—	—	—
1		—	1.2	—	20	0.3
2	16	0.024-0.037	1.6	—	30	0.5
3		—	9.0	—	—	—

The angular divergence and wave-front deformation heavily depend on mechanical stresses and the degree of nonuniform distribution of chromium over the cross section of the element.

The refractive index n of a ruby rod is larger in the central portion than near its periphery because the available technology of ruby crystal growth does not afford a uniform distribution of chromium over the crystal bulk. Besides, stresses appear in the crystal during its growth. The above factors render the element with mutually parallel ends equivalent to a diverging lens as regards its optical properties [4]. The plane wave passing through the active medium with a varying refractive index on the radius gets heavily distorted, so that the laser beam divergence increases and results in a nonuniform energy distribution within the beam. Internal stresses in the rod most heavily affect the beam divergence, mode selection, and beam distribution.

Of substantial importance for improving the energy parameters of a ruby laser is the radiation stability of ruby, i.e. the resistance to attack by powerful radiant fluxes which destroy the ends of the rod and its body when the flux density exceeds the threshold value. As a rule, the end faces of the rod begin to disintegrate first. The destruction arises when local surface defects such as microcracks and boundaries between clusters absorb the radiation and heat up to temperatures at which the surface irreversibly changes, for example, melts and cracks. The surface damage threshold of ruby depends on the light pulse length, surface defects, and structure of the rod end faces.

Ruby specimens with single-crystal surface layers stand up to much higher powers of radiation than specimens with the amorph-

ous surface structure. The finer the polish given to the rod ends, the higher the surface radiation resistance.

Garnets are compounds having the general formula $A_3B_5O_{12}$ or $A_3B_2(BO_4)_3$ [4, 5], where A denotes yttrium ions or ions of lanthanides, and B denotes aluminum, gallium, iron, indium, chromium, etc. Of all garnets used for lasers, the most popular type is the neodymium- or chromium-doped yttrium-aluminum-garnet, known as YAG, of the formula $Y_3Al_5O_{12}$-(Cr^{+3}, Nd^{+3}) [5].

Neodymium and chromium introduced in the yttrium matrix serve as substitution ions. The concentration of neodymium is 1.3 to 1.5% and that of chromium is 1%. The emission wavelength for Nd is 1.065 μm. The thermal conductivity is up to 30% lower than that for ruby.

Technical characteristics of garnet crystals [3]

Number of active centers in yttrium per cm^3	1.36×10^{22}
Melting point, K	1.488
Thermal conductivity, W m^{-1} K^{-1}	11
Linear expansion coefficient, K^{-1}	7.7×10^{-6}
Absorption coefficient (for $\lambda = 0.6328$ μm), cm^{-1}	1.83
Absorption band in the ultraviolet, μm	0.24
Absorption band in the infrared, μm	5.6
Lattice cell size, μm	0.0012
Crystal structure	perfect

The YAG crystal effectively absorbs radiation in a band from 0.5 to 0.8 μm. The lifetime of an ion at the metastable laser level is 240 μs and fluorescence quantum yield is close to unity. The Nd ^{3}-YAG crystal exhibits good mechanical properties, high thermal conductivity, and has a perfect crystal structure.

Oxides of rare-earth elements [2, 3, 6]. In practical use are the oxides of neodymium-doped lanthanum, $La_2O_3(Nd^{+3})$, Nd^{+3}-doped gadolinium, $Ga_2O_3(Nd^{+3})$, and erbium, $Er_2O_2(Ho^{+3}, Tm^{+3})$. The lanthana crystallizes in the hexagonal system, while most of other oxides have a cubic lattice of the Mn_2O_3 type.

The yttria has the formula $Y_2O_3(Nd^{+3}, Eu^{+3})$. The crystal lattice is cubic. The Nd^{+3} concentration is about 1%.

Materials based on oxides of Group V elements. These materials include vanadates $Ca_3(VO_4)_2$, YVO_4, $GdVO_4$, $LaVO_4$, $Th_2Ln(VO_4)_3$ doped with impurity ions Nd, Eu, Tb, Dy, Er, and also other oxides.

Calcium niobates $Ca(NbO_3)_2$ doped with Nd^{+3}, Ho^{+3}, Pr^{+3}, Tm^{+3} and lithium niobates $LiNbO_3(Nd^{+3})$ show rather good characteristics of stimulated emission in the wavelength region 1.04-2.047 μm. Niobates of transition metals and binary niobates of the $Ba_2NaNb_3O_{15}$ type display good electrooptic nonlinear properties and serve as inactive materials for frequency modulation and multiplication.

Calcium fluorophosphate $Ca_5(PO_4)_3F(Nd^{+3})$ employed in pulsed operation gives 4 times the gain of the garnet doped with neodymium. The fundamental wavelength is 1.0029 μm with a line-width of (4-5) $\times$ 10^{-4} μm.

Materials based on oxides of Group VI elements. These are tungstates and molybdates. The matrixes of tungstates are $CaWO_4$, $SrWO_4$, and $Na_{0.5}Gd_{0.5}WO_4$ doped with appropriate elements Pr^{+3}, Tm^{+3}, Ho^{+3}, Er^{+3}, Dy^{+3}, and Nd^{+3}. Of these, $CaWO_4$ is the most widely used system which requires a low excitation threshold and can lase in the continuous wave (CW) mode at 300 K. Another distinguishing feature of this tungstate is its high chemical stability. Tungstate crystals have the structure of scheelite (calcium tungstate) with a tetragonal lattice [5].

Molybdates include $CaMoO_4$, $SrMoO_4$, $CdMoO_4$, $PbMoO_4$, $NaLa(MoO_4)$, $NaNd(MoO_4)_2$, and $Gd_2(MoO_4)_3$. The matrixes change their structure when doped with neodymium: $CaMoO_4(Nd^{+3})$, etc. The Nd content does not exceed 1-1.5%. Molybdates typically have the scheelite structure. The emission wavelength for calcium molybdate is 1.067 μm with an emission linewidth of 5 $\times$ 10^{-4} μm; for strontium molybdate the wavelength is 1.065 μm at 300 K. The threshold excitation energy is 1 J.

Fluorides. These are fluorides of alkali earth metals, such as CaF_2, SrF_2, MgF_2, and BaF_2 using the following lasants: U^{+3} uranium ions, lanthanides, as Dy^{+2}, Tm^{+2}, and Sm^{+2}, and also other elements, as Nd^{+3}, Ni^{+2}, and Co^{+2}. These crystals display the cubic structure similar to that of fluorite (fluorspar CaF_2). Thus, CaF_2 doped with Nd^{+3} makes a four-level material for laser emission with a threshold pump energy of 3.28 J at 77 K and up to 1 200 J at 300 K. The absorption bands lie in the ultraviolet and the visible regions of the spectrum, and also in the near infrared.

Calcium fluoride doped with bivalent ions of lanthanides features wide absorption bands in the near infrared and the infrared, which ensure efficient pumping. Dysprosium-doped CaF_2 has a low level of pump threshold, near 1 J at 77 K and near 0.1 J at 4.2 K. The luminescent linewidth is 4 cm^{-1} at 200 K and 0.024 cm^{-1} at 4.2 K.

For Ni^{+2}-doped magnesium fluoride, the emission wavelength is 1.62 μm and emission linewidth 6 cm^{-1}. Manganese fluoride MnF_2 doped with Ni^{+2} emits continuously and in pulses at wavelengths of 1.929 and 1.939 μm.

Amorphous laser materials. These are glasses, which are inorganic thermoplastic materials based on the covalent-bonded network of polyhedrons of anions $(SiO_4)^{-4}$, $(BO_3)^{-4}$, $(BO_3)^{-3}$, and $(PO_4)^{-3}$.

Glasses are classified by the glass former (base, or glass-forming anion) and by the content of a modifier which is an oxide as is the glass former. Thus, for example, silica, borax, and lead glasses

receive their names from respective glass formers: silica SiO_2, borax $N_2B_4O_7$, and lead oxide. Laser technology utilizes alkali-free glasses with a very low content of alkali oxides.

Lasant ions dissolved in the glass former are the components of glass. What adversely affects the spectral characteristics of the laser glass is the absence of the long-range order of the structure. The random distribution of neighbor atoms surrounding lasant ions broadens emission lines, shortens the lifetime of the excited state, and decreases the quantum yield [3, 6].

Glasses offer a number of advantages over crystals: appreciable lasant concentrations in the glass former, low cost of base materials, ease of reproducibility of rods of any size and shape, high optical homogeneity, and low radiation loss.

Neodymium-doped glasses are most popular. The basic components of these glasses are the oxides of silicon, barium, and potassium. Using these glasses, it is always possible to form a four-level system of lasing.

In the USSR, various grades of Nd-doped glasses are available. The types and sizes of Nd-glass rods and their technical characteristics are set up in branch standards Nos. 3-31-70 and 3-30-70 [4].

Table 1.2 illustrates the designations of Nd-glass rod types proceeding from the rod cross section and the angle of inclination of end faces to the generating line. In the designation of each rod, the transliterated Russian letters identify the name of the rod type and the numbers enclosed in brackets (not shown in Table 1.2) denote its size in mm, for example, ENTs-90 (8 × 100). Soviet industry produces Nd-glass rods 5 to 60 mm in diameter and 8 to 1 200 mm in length.

Given below are the Soviet grades of glasses characterized by the absorption coefficient n_λ at wavelength $\lambda = 0.586$ μm.

Glass grade	n_λ
GLS-1	0.190
GLS-1P	0.190
GLS-2	0.185
GLS-3	0.47
GLS-4	0.41
GLS-4P	0.41

As a rule, the surface of a rod, with the exception of the belts for rod fastening, is etched in the mixture of hydrofluoric and sulfuric acids and then coated with a protective layer in the course of acid-wax treatment [4]. The error in the perpendicularity of end faces with respect to the rod axis must not exceed 10″ and the error in other angles must not be over 2″. The methods used to assess the quality of glass activated by neodymium rely on the estimation of the intensity of inactive absorption (at $\lambda = 1.06$ μm), the number

and size of bubbles, and the number and size of solid nonmetallic inclusions. These factors determine the category of glass (Table 1.4).

TABLE 1.4 Glass Categories Defined by the Absorption Coefficient at $\lambda = 1.06\mu m$ and the Type, Size, and Number of Defects

Category	Absorption coefficient, cm^{-1}	Maximum bubble diameter, cm	Mean number of bubbles not over 0.01 cm in size per kg of glass	Number of particles and crystals 0.006 to 0.5 mm in size per kg of glass
1	0.002	—	—	Impermissible
2	0.004	—	—	10
3	0.006	0.02	—	—
4	—	0.03	—	—
5	—	0.05	—	—
6	—	0.07	—	—
7	—	0.10	—	—
A	—	—	10	—
B	—	—	30	—
C	—	—	100	—

The time-dependent luminescent emission intensity for glasses with different concentrations of neodymium and also the absorption spectra are given in the literature on the subject [5].

Nd-doped glasses have low values of thermal stability and thermal conductivity. When the laser emits pulses with an insignificant pulse separation, the Nd-glass laser materials develops stresses which can break the glass. The inactive absorption of pump energy leads to an appreciable evolution of heat which deforms the rod and impairs its properties, thereby affecting the parameters of laser radiation.

Nonuniform pumping gives rise to the temperature gradient along the rod and the nonuniform distribution of population inversion over the rod section. This changes the optical path length and initiates birefringence [4] which heavily affects the intensity distribution over the beam cross section and laser polarization. The rod configuration is responsible for the effect of thermal deformation. It is advisable that the rods should have a rectangular shape to minimize the effect of induced birefringence.

In Nd-doped glasses, optical pumping and self-emission cause spalling of the outer surface [4]. Because of a rather intensive absorption of UV radiation, the surface glass layer 20 to 60 μm thick attenuates the radiation by one half in the UV region at $\lambda \leqslant 330$ μm, which accounts for 10% of the total light energy delivered by the flash lamp [4].

Nd-doped glasses are also inherently unstable in the quantum-chemical respect. In the laser material, the UV radiation reduces

ferric iron to ferrous iron which absorbs radiation at $\lambda = 1.06$ μm. The glass thus gradually loses its lasing ability until it stops lasing at all [4].

It is good practice to use filter solutions or special glass filters that absorb the "harmful" range of the spectrum at $\lambda < 400$ μm [4]. This approach can appreciably reduce the adverse effect of UV radiation on the glass characteristics [4]. Fig. 1.6 illustrates how filters employed in the optical pump system change the laser efficiency [4]. As seen, the use of filters (curves *a* and *b*) appreciably increases the efficiency as against that of the laser without filters (curve *c*).

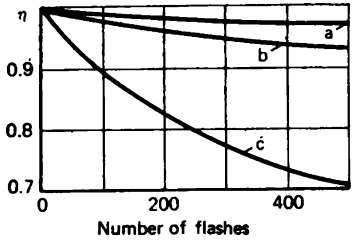

Fig. 1.6. Laser efficiency η obtained with filtering pump energy (curves *a* and *b*) and without filtering (curve *c*)

The self-absorption by trace impurities in the bulk of the glass and on its surface and self-focusing effects limit the emitting power [4]. Thus, the microparticles of platinum diffusing into the bulk of glass in the course of its melting become the centers of intensive laser radiation absorption, which rapidly heat up the material at local points, give rise to thermoelastic deformation, and cause rod cracking. The threshold energy that causes the bulk disintegration of a glass rod due to microparticle impurities depends on the orientation and size of microparticles and also on the pump energy and laser pulse length. At a pulse length of about 50 ns, the threshold density of energy that causes bulk disintegration ranges from 4 to 6 J/cm^2. The radiation resistance of glass substantially grows in the absence of microparticles and its damage threshold then only depends on the effect of self-focusing. The laser power density that results from the effect of self-focusing is equal to 3×10^{12} W/cm^2. This value is enough to destroy a homogeneous glass.

1.3. MATERIALS FOR LIQUID LASERS

Lasing in plastic materials and liquids was obtained after the creation of solid-state (crystalline and glass), gas, and other types of lasers.

Stimulated emission can be readily achieved by irradiating the solution of naphthalene (0.02%) in benzophenone (diphenyl ketone) by a mercury-vapor lamp at $\lambda = 0.365$ μm owing to an effective transfer of energy from the triplet state T of benzophenone to the triplet state T of naphthalene (Fig. 1.7). The stimulated emission wavelength is $\lambda = 0.470$ μm. Stimulated emission occurs in

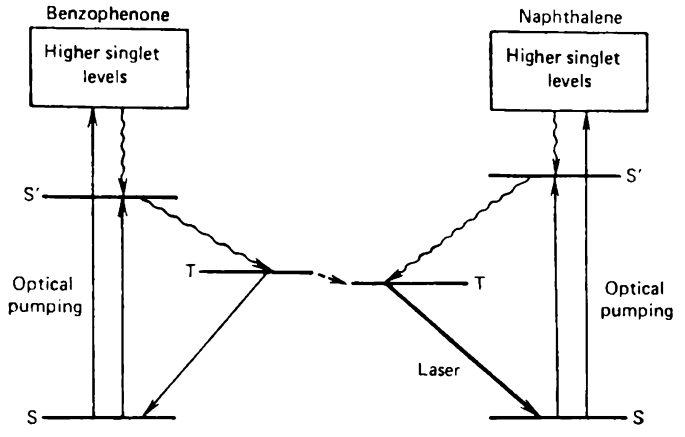

Fig. 1.7. Diagrams of energy levels for naphthalene and benzophenone; straight and wavy lines denote radiative and nonradiative transitions respectively

chelates of rare-earth elements such as europium and samarium and also in free ion systems, as trioxide neodymium dissolved in an appropriate acid.

In general, a minimum population inversion in the quantum system is necessary to initiate lasing:

$$(\Delta N)_{\min} = k\Delta\lambda\tau/t \tag{1.12}$$

where k is a constant; $\Delta\lambda$ the spontaneous emission linewidth, τ the lifetime of the transition in question; and t the characteristic time of decay of energy in the optical cavity, determined by the quality factor (Q) of the cavity. It is possible to reduce the energy loss in the cavity to a minimum and thus sufficiently increase the time t. The substances used for lasers should be chosen such that they display a high luminescent quantum yield, narrow emission linewidth, sufficient optical homogeneity, and wide absorption band to provide efficient optical pumping and thus to obtain the inverse population at the corresponding energy levels. Fluorescence arises as a result of optical transitions from the metastable triplet state to the ground singlet state [2].

The vibrational nature of the ground state S determines a number of fluorescence bands with the most typical time of fluorescence ranging into a few microseconds (for solids this time can run into a few hours and even a few days). A rather large emission linewidth (1×10^{-3} to 2×10^{-2} μm) involves substantial difficulties in producing the inverse population in accordance with formula (1.12). Besides, the quantum system suffers an enhanced total loss due to

the radiation absorption during transitions from the lower triplet state to the upper triplet state.

Fluorescence results from allowed transitions between the excited singlet state and the ground state; the lifetime of fluorescence ($\tau \approx 10^{-8}$ s) is much lower than that for phosphorescence, although $\Delta\lambda$ remains as wide as that for phosphorescence.

The maximum population inversion ΔN_{max}, taking into consideration the transitions from the excited singlet level to the lower lying triplet level, is given by the expression

$$\Delta N_{max} = n_0/(1 + \mu) \tag{1.13}$$

Here n_0 is the concentration of lasant molecules in the system and μ is [2]

$$\mu = v_i/v_r$$

where v_i is the rate of intercombination transitions, and v_r the rate of relaxation of the triplet state.

Under intercombination transition is understood the transition of singlet-triplet type. The constant μ reaches about 10^5; at this value of μ, a peculiar capture of excited electrons at the singlet level by the triplet state may inhibit the inversion. Therefore, it is well to select those laser liquids which have a low value of μ or to pump for a short time so that the probability of singlet-triplet transitions can be negligible.

Liquids for lasers have a number of advantages over solids. A liquid can be made homogeneous, generally irrespective of its volume, which factor allows one to appreciably increase the laser threshold energy. Liquids exhibit stable optical characteristics and are isotropic. They are cheap and any volume of the spent liquid can be readily replaced when necessary. It is possible to circulate the liquid in the cell and thus noticeably improve the heat removal. An important advantage of laser liquids is that they afford the possibility of continual tuning in a relatively wide range.

Liquids for lasers fall into three groups [2, 3]: solutions of diketones of rare-earth elements (europium or terbium) in organic solvents; solutions of fluorescent organic dyes; and solutions of inorganic compounds of rare-earth elements.

Solution of diketones of rare-earth elements in organic solvents. S. G. Rautian and I. I. Sobelman [3] were the first to reveal the way of using chelates of rare-earth elements as laser materials. The first practical chelate laser based on the alcohol solution of europium benzoylacetonate was devised by A. Lempitski and G. Samelson [2]. The chelate is an organometallic complex where a rare-earth ion is in the environment of coordinate-bonded oxygen atoms belonging to the ligand or chelate groups.

Of the greatest interest for producing laser oscillation are the complexes of europium ions with β-diketones because they display an intensive line fluorescence of the Eu^{+3} ion in the red region of the spectrum. Absorption occurs in wide bands specific to organic radicals of the molecule. The absorption bandwidth for europium benzoylacetonate reaches 0.06 μm at a maximum absorption coefficient of 850 cm^{-1} and europium ion concentration of about 10^{18} cm^{-3}. But emission occurs in narrow lines of the rare-earth ions.

In distinction from the systems containing rare-earth ions in inorganic compounds, chelates heavily absorb the pump light [2, 3]. The light absorbed at a maximum rate excites only very thin layers of the medium, so that the pump emission intensity decays by a factor of *e* at a depth of about 0.02 mm. If the size of the cell appreciably exceeds the depth of light penetration into the liquid, the intensive absorption in the medium region of the pump band will make it impossible to excite deep layers of the liquid. Pumping will proceed at the boundaries of the absorption band where the absorption intensity drops off sharply. At the same time, the strongly heated surface layer of the liquid will tend to produce inhomogeneities in the liquid and thus impair the Q of the optical cavity. That is why, to make the best of the laser pump system, it is expedient to decrease the layer thickness of the working medium, i.e. to use small-diameter cells. Thus, the laser developed by A. Lempitski and G. Samelson included a 4-mm diameter 50-mm long quartz cell with approximately confocal mirrors. On cooling the europium benzoylacetonate (EuBA) solution in the mixture of ethanol and methanol to a temperature of 123 K, the oscillation threshold reached 1 920 J (the ruby crystal in the same reflector has a 940-J threshold at room temperature). In the temperature range 153-103 K, emission from EuBA largely consisted of two lines of 0.131-μm and 0.615-μm wavelengths with a beam intensity ratio of 1.0 : 0.82 at line halfwidth of 8×10^{-4} and 2×10^{-3} μm respectively; the respective fluorescence yield was 25 and 50% of the entire fluorescence, which resulted from the electric dipole transitions between $^5D_0$ and $^7F_2$ levels, the latter level being located 900-1 000 cm^{-1} above the ground level [2, 3]. The fluorescent lifetime was 5×10^{-4} s.

By and large, the properties of emission obtained from liquid systems based on rare-earth chelates are very similar to those of solid-state laser emission. The investigated chelates employed in lasers do not display optimal properties required of oscillators. Because of an extremely high absorption coefficient, an appreciable amount of pump energy is lost in thin layers of the medium. This prevents generation of large output powers. The output energy of EuBA lasers with 5.0-cm cells 0.1 cm in diameter reaches 1 MJ.

Solutions of inorganic compounds of rare-earth elements. Inorganic solutions of the salts of rare-earth elements, which serve

as laser medium, combine the advantages of substances utilized in solid-state and liquid lasers. Unlike many organic liquids, these solutions are typically ionic systems. The solvent plays the role of the matrix that insignificantly affects the pattern of the electronic levels of the ionic system. In distinction from the organometallic complex where the role of the ligand in the transfer of energy to an ion is important, in the solution containing free ions, optical pumping proceeds solely through the intrinsic absorption band of the

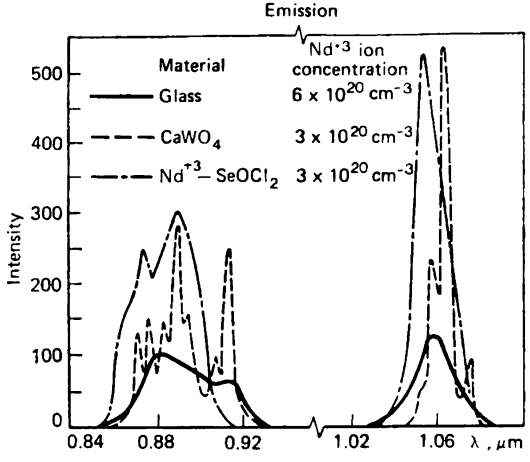

Fig. 1.8. Emission spectra of Nd^{+3} ions in glass, crystal, and liquid hosts

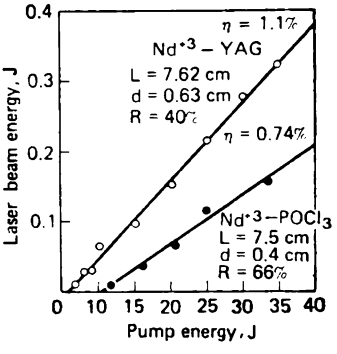

Fig. 1.9. Efficiency of liquid laser and solid-state Nd^{+3}-YAG laser: 4-mm diameter cell with working liquid is 7.5 cm long; R is reflectivity of output mirror

ion. To ensure a high pumping efficiency, it is advisable to select a neodymium ion which exhibits a rather broad absorption band.

In Fig. 1.8 are shown the emission spectra of Nd^{+3} ions, the concentration of which in three different host materials is approximately the same. As seen, the emission spectrum for Nd^{+3} ions in the liquid is closer to the emission spectrum in the crystal than to that in the glass.

Table 1.5 lists the effective absorption cross sections and typical lifetimes of fluorescence in three host materials: YAG, liquid solvent $SeOCl_2$, and glass [2]. Fig. 1.9 illustrates the efficiency of a liquid laser and a Nd^{+3}-YAG laser [2].

If the product of reflection factors for mirrors is small, self-modulation of laser radiation is possible.

Experiments showed that instead of irregular spikes about a few hundred microseconds long, liquid lasers generated giant pulses each of a duration of 50-100 ns and power close to 1 MW. The

TABLE 1.5. Effective Absorption Cross Sections and Typical Lifetimes of Fluorescence of Nd^{+3} Ions in Three Host Materials

Host material	$\sigma \times 10^{20}$, cm^2	τ, ms
YAG	27-29	0.24
Liquid solvent $SeOCl_2$	6-8	0.25-0.4
Glass	0.3-3	0.1-1.0

$POCl_3 : ZrCl_4$-Nd^{+3} laser generated 76-J pulses at a frequency up to 5 Hz. With a pump energy of 4 000 J, the laser efficiency amounted to 2%. In the system with a two-stage amplifier which operated with the same solution as that used in the master oscillator, the pulse power was as high as 500 MW. The inorganic-liquid laser also has the advantages of a highly uniform distribution of the radiation field in the near and the far region and high values of output parameters.

Organic dye solutions considerably extended the range of available laser materials after the development of first dye lasers [2].

Dyes are complex organic compounds which heavily absorb the visible light and consist of benzene rings C_6H_6, pyridine rings C_5H_5N, nitrogen rings $C_4H_4N_2$, etc. Most of the dyes in solutions show an ionic character, the sign of the ion being determined by the solution acidity: it is positive in the acidic medium and negative in the basic medium. The absorption ability is mainly governed by CH_3 or C_2H_5, radicals. The optical properties of a dye show up completely only in solid and liquid solutions; if the dye has a crystal form, the absorption gets weaker or totally vanishes, and the liquid solutions most often exhibit short-time luminescence [2]. In solid solutions long-time luminescence appears in addition. The lifetime of the excited state of a molecule is 10^{-9} s. The use of various organic dyes substantially extended the range of laser radiation frequencies, to 0.35-1.1 μm.

The absorption or emission spectrum of dyes consists of a main band 150 MHz wide in the visible and an additional band in the UV region. Luminescence of most of the dyes does not depend on the wavelength of exciting radiation. For example, the dye rodamine B can emit over the entire luminescence spectrum if we excite it by the radiation within the yellow line of sodium ($\lambda = 0.589$ μm) or by UV light ($\lambda = 0.2537$ μm) despite the fact that in the last case the absorption results from the transfer of molecules to upper singlet states. Consequently, a molecule very rapidly returns to a lower excited singlet state from which the process of luminescence commences.

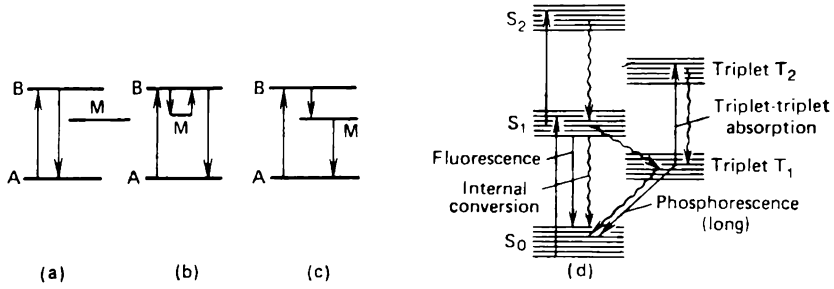

Fig. 1.10. Simplified diagrams (*a*), (*b*) and (*c*) and detailed diagram (*d*) of energy levels illustrative of short-time and long-time luminescence: A, B, and M are ground, excitation, and metastable levels respectively

Dye lasers can generate giant pulses in a wide spectrum and in a narrow spectrum of almost monochromatic light. They can be made to lase in both the pulse and the CW operation with mode locking. Dyes are cheap and feature a high efficiency of pump energy conversion into radiation: the efficiency of some dyes reaches 50%.

Figure 1.10 illustrates the simplified and the detailed diagrams of energy levels of a typical dye molecule, which elucidate both long-time and short-time luminescence [2]. The technical characteristics of dye lasers are given below.

Technical data on dye lasers

Wavelength, with laser or flashlamp pumping, μm	0.34-1.175
Tuning range, μm	$\leqslant 0.04$
Emission spectrum, μm, using:	
broad-band mirrors	1.5×10^{-3}-1.5×10^{-2}
diffraction grating	5×10^{-5}
Fabry-Perot interferometer inside cavity	1×10^{-6}
Beam divergence, mrad	2-5
Efficiency, %:	
with laser pumping	to 25
with flashlamp pumping	0.4
Output energy, J	
maximum	2
typical	0.1
Power, MW:	
with laser pumping	2
with flashlamp pumping	0.75-2.0
Pulse repetition rate, Hz:	
with laser pumping	to 200
with flashlamp pumping	20-50
Pulse length:	
with laser pumping, ns	20
with flashlamp pumping, μs	0.5-150

1.4. MEDIUMS FOR GAS LASERS

The main distinction of the working medium of a gas laser from that of a solid-state laser lies in its low density, for which reason the energy spectrum of active particles such as neutral atoms, ions, and molecules is not prone to distortion by the fields of other atoms, and so the energy level width remains narrow. Gas lasers, unlike high-power solid state (ruby or glass) lasers, are free from the danger of medium disintegration under laser radiation. It is easy to secure heat removal in gas lasers by enabling the hot gas to flow from the region of interaction.

A high optical homogeneity of the medium stems from a relatively low density of gases, which do not practically scatter the beam. This feature largely accounts for a high chromaticity of the radiation and a narrow radiation pattern of gas lasers. On the other hand, a low density of the gaseous medium does not allow producing large output powers [3].

The excitation of gases involves various processes: elastic and inelastic collisions, ionization, recombination, dissociation, chemical reactions, etc. [3]. This explains why there are a variety of methods for obtaining the inverse population in gaseous laser mediums. Three groups of the methods of laser medium excitation are most popular, which rely on an electric discharge, optical pumping, and chemical reactions [3]. The mechanisms by which inverse population is built up are the following: collisions of the first kind, collisions of the second kind, dissociation of molecules from predissociating states, optical excitation, photodissociation, chemical reactions, and creation of the relaxation time difference between vibrational and rotational states, for example, during adiabatic expansion of the molecular gas in a gas-dynamic laser.

Atomic gas lasers rely on first-kind elastic collisions of electrons with both neutral atoms of gases (Ne, Ar, Cr, Xe) and atoms in the vapors of metals (Cu, Pb, Mn) and also on second-kind collisions in the process of energy transfer from an excited atom of one element (as He) to an excited atom of another element (as Ne) [3, 6]. In the mixture of two gases, such as He and Ne, where the metastable states of atoms of the first gas coincide with the excited states of atoms of the second gas, an effective transfer of energy occurs from one atom to the next with the transition of atoms of the first gas to the ground state, the process being referred to as the inelastic collision of the second kind [2]. An important condition for the implementation of this process is the equality of energies of the lasant level and the excited level of other atoms.

The classical gas laser which operates on this principle is a helium-neon (He-Ne) laser.

Figure 1.11 demonstrates the diagram of some energy levels of neon and two levels of helium that coincide with the first levels and also illustrates three important transitions [2]. The lasers emitting at a wavelength of 0.6328 μm are most common. The population of the upper level in these lasers mainly occurs via $^1S_0$ collisions of the second kind with the metastable atoms of helium.

The He-Ne laser operates in a mixture of He and Ne with optimal proportions of 7 : 1 to 5 : 1. The beam divergence in this laser is very small, near 2×10^{-4} rad, and approaches the diffraction limited value. It features the highest frequency stability, near 10^{-14}. Despite a low output power (up to tens of milliwatts at a gain of 4-10% per meter length and an efficiency of about 10^{-3}-10^{-2}%), the He-Ne laser enjoys wide uses owing to a high stability of laser frequency, small beam divergence, simple construction, and rather long lifetime, up to 10 000 h.

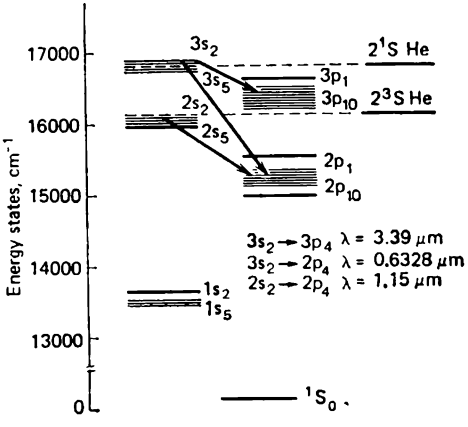

Fig. 1.11. Diagrams of some energy levels of neon and two energy levels of helium, which are coincident with former levels

Ion gas lasers operating in the continuous mode on the ionized gaseous medium can give much higher outputs, tens of watts.

Laser radiation is now available in more than 200 lines emitted from many elements: inert gases (helium, neon, argon, krypton), chlorine, bromine, mercury, iodine, oxygen, nitrogen, silicon, sulfur, phosphorus, zinc, cadmium, etc. The most popular and typical representatives of gas-discharge lasers are argon ion lasers which give the highest outputs at wavelengths of 0.488, 0.5145, and 0.4965 μm. The CW laser output power reaches tens of watts at a maximum efficiency up to 0.2% [2].

Ionization of argon atoms occurs in the arc discharge at a low pressure of 39.9-53.2 Pa. The discharge plasma must be highly ionized. For this, ion lasers utilize a powerful arc discharge noted for an enhanced level of ionization. The working current in ion lasers reaches a few tens of amperes and the current density can amount to 1 000 A/cm² and over [2, 3].

Figure 1.12 displays the output power plotted versus discharge current and relative power as a function of the argon pressure and the strength H of the axial magnetic field concentrating electrons

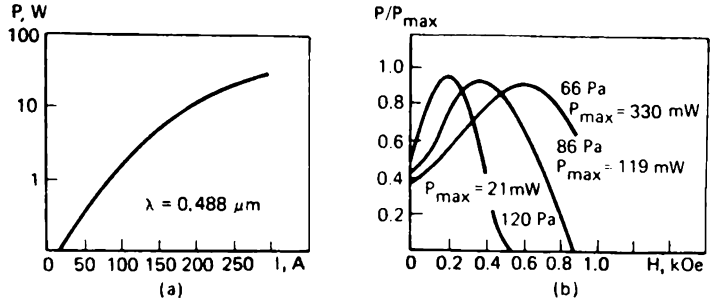

Fig. 1.12. Output power of argon laser at 0.4880 μm versus discharge current (*a*) and relative power versus argon pressure and axial magnetic field strength *H* (*b*)

and, to a lesser degree, ions near the tube axis in order to increase the number of collisions [3] and to reduce the erosion of the discharge tube walls; the tube is 28 cm long and 4 mm in diameter. The discharge current is 30 A.

High values of discharge current place stringent constraints on the design of discharge tubes. The early models of water-cooled discharge tubes were made from quartz which is a thermostable material. The lifetime of such a tube did not exceed 100 h. Later models began to use more stable materials such as ceramics, alundum, beryllium oxide BeO, and graphite [3]. A BeO-based tube, for example, can serve for about 1 000 h.

Ion lasers can also operate on other gases apart from argon: krypton, xenon, helium, neon, chlorine, and nitrogen. They can use the vapors of such metals as Cd, Sn, Zn, Se, Pb, Hg, Cu, Tl, Au, and Mn.

In pulsed ion lasers the population inversion mainly occurs via the transitions of atoms colliding with electrons from the ground state to upper excited levels [2]. In CW ion lasers the population inversion is brought about in the course of a two-step or a multistep process: first, the ionization takes place to yield an ion in the metastable state and then the subsequent collisions excite the ion to higher energy levels from which it moves to the corresponding laser level [2, 3].

In 1960 investigations revealed stimulated emission in the vapors of metallic cadmium from a singly ionized laser medium. The power in the beam reached 200 and 20 mW at 0.4416- and 0.325-μm wavelengths respectively. Later, a large number of works on ion lasers using vapors of various metals appeared [2].

The excitation of active ions to higher laser levels largely proceeds with the aid of the buffer gas helium, whose pressure in the discharge tube reaches a few hundred pascals. The metal vapor pressure is much lower, merely a few tens of pascals. As reported

in work [2], a He-Cd laser produced a 10-mW beam at 0.4416 μm and also gave 2.5 mW of power in the beam at 0.325 μm in the ultraviolet.

In Table 1.6 are given the technical characteristics of metal vapor lasers.

TABLE 1.6. **Technical Characteristics of Metal Vapor Lasers**

Metal vapor	Emission wavelength, μm	Gain per meter tube length, %	Optimum He pressure	Optimum vapor pressure	Working temperature, K
			Pa		
Cd II	0.4416	~ 10	400	0.4	513
Cd II	0.325	3-4	400	0.4	513
Sn II	0.6453	3-4	1064	0.2	1373
Sn II	0.6844		1064	0.2	1373
Zn II	0.7479	2	532	0.53	593
Zn II	0·7588	—	67-532	0.266-13.3	533-673
Se II	0.4604	—	—	—	—
Se II	6.4845	2.3	798-1064	0.67	—
Se II	0.4976	3.3	798-1064	0.67	—
	0.4993	3.3	798-1064	0.67	—
	0.5069	3.3	798-1064	0.67	—
	0.5176	4.6	798-1064	0.67	—
	0.5228	5.4	798-1064	0.67	—
	0.5305	2.6	798-1064	0.67	—
	0.6056	1.3	798-1064	0.67	—

An appreciable output power of ion lasers makes them suitable tools for use in the laser processing of materials — cutting, welding, etc.

In the general case, the inverse population in a gas is easier to obtain using a pulsed discharge rather than a continuous discharge. Pulsed laser emission in gases was obtained at a few hundred wavelengths covering the range from UV waves ($\lambda \approx 0.1$ μm) to submillimetric waves ($\lambda \approx 0.08$ cm). A number of lasers can operate on a pulsed basis. These are neutral atom lasers and also ion and molecular lasers. The gain in the discharge tubes of modern pulsed gas lasers amounts to 600 dB/m, with peak powers ranging into several megawatts [2].

Pulsed lasers are similar in design to CW lasers. What distinguishes the pulsed laser is that it incorporates a pulsed power unit which provides a discharge current in the pulse of up to a few kiloamperes at voltages up to hundreds of kilovolts. Also, the elements of the radiator, namely, the discharge tube and its accessories, feature an enhanced dielectric strength and employ a more powerful cathode than that used for the steady glow discharge.

One of the features of pulsed operation lies in the fact that it allows an easier way of producing high discharge currents and thus makes it possible to raise the pump system power by a few orders of magnitude, which is favorable for some gaseous mediums, for example, those used in ion lasers, where the population inversion required for lasing is built up only at increased discharge currents.

One more feature of pulsed operation is that it affords higher excited states. A pulsed laser can thus use the spectrum of excited states of multiply charged ions to ensure lasing in the ultraviolet since these ions can be effectively excited only in the pulse discharge.

In pulsed lasers the unsteady-state gas-discharge plasma can be put to use to populate excited levels when generating microsecond current pulses, i.e. to achieve lasing and population inversion essentially in the time interval when the unexcited gas converts to a stationary plasma or the stationary plasma to the unexcited gas.

The efficiency of a CW laser is given by [2]

$$\eta_{CW} = f_p h\nu_e / E_e$$

where f_p is the fraction of pump energy required to populate the laser level, $h\nu_e$ the quantum energy of the laser transition, and E_e the energy of a higher level. For a CW laser, $\eta_{CW} \approx 10^{-3}$-$10^{-4}$ [2]. The efficiency of a pulsed laser is

$$\eta_P = f_p \frac{h\nu_e}{E_e} \frac{g_g}{g_g + g_e}$$

where g_g and g_e are the statistical weights of the ground and the excited level respectively:

$$g_g/(g_g + g_e) \approx 1$$

Since $f_p \approx 0.5$ for resonance excitation, $\eta_P \approx 25\%$. It is practically rather easy to achieve a pulsed laser efficiency of about 10%.

1.5. MOLECULAR LASERS

In atomic and ion gas-discharge lasers the efficiency of the electron mechanism of pumping is low because of a considerable difference in energy between the upper and lower levels.

Assuming that the distribution of electrons in plasma is Maxwellian, the share of energy due to fast electrons capable of exciting an atom or ion is proportional to $\exp(-\Delta W/kT_e)$, where ΔW is excitation energy, and k Boltzmann's constant.

For a helium-neon laser, the excitation energy is $\Delta W \approx 20$ eV at (8-9) $\times 10^4$ K, which gives an efficiency of the electron pump mechanism of merely 5-6%. The efficiency of this type of pumping for an argon CW arc discharge-driven laser is of the same order

of magnitude as that for a pulsed argon laser, in which the pumping efficiency is even lower than the above given value.

The use of lower lying energy levels looks promising for an increase in the efficiency of gas lasers. Vibrational excited states of molecules can be considered as the levels of interest. In a molecule consisting of a few atoms, the internal energy includes not only the energy of electrons in each atom but also the energy of the vibrational motion of atoms about a certain equilibrium position.

Excited molecular gases exhibit a more complex emission spectrum than atomic and ion systems. The transitions generally

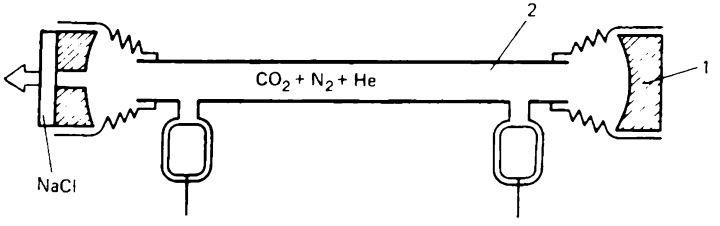

Fig. 1.13. Schematic diagram of first molecular lasers

occur between various electron, vibrational, and rotational energy levels of the molecule [3], with the result that the molecular system may emit a much larger number of lines than the atomic system. The number of laser transitions brought about by the excitation of such gases as N_2, O_2, CO, and H_2 is rather high [3]. Of the electronic-transition molecular lasers, the promising types are the lasers that give pulsed powers up to 1 MW in the ultraviolet ($\lambda = 0.337$ μm) and the hydrogen lasers emitting in the vacuum ultraviolet at $\lambda =$ $= 0.16$-0.18 μm [7].

Vibrational- and rotational-transition lasers emit in the infrared.

CO_2 lasers are the most widely used devices. In 1964, C. Patel investigated vibrational-rotational transitions in CO_2 molecules and later developed a vibration-rotation laser [2]. He obtained laser emission within 13 lines in the infrared at a wavelength of about 10 μm. The power of the CO_2 laser (about 1 mW) was substantially increased by adding He and N_2.

Figure 1.13 illustrates the schematic of the first molecular lasers. Here gilded metal mirrors *1*, for example, steel mirrors, arranged at the ends of a glass discharge tube *2* form a confocal cavity from which the emission of the laser line of $\lambda = 10.6$ μm is brought out through an aperture in the front mirror, which is sealed with a NaCl crystal that transmits infrared radiation. The front mirror can also be made from pure germanium, KCl crystals, zinc selenide, etc.

Carbon dioxide dissociates in the discharge to form oxygen and carbon monoxide: $2CO_2 \rightarrow 2CO + O_2$. This "spoils" the gas mixture and markedly decreases the output power. By circulating a gas mixture along the discharge tube, it is possible to increase the output to a large degree. Also, the laser power grows with gas flow rate. Besides, to decrease the discharge temperature and, hence, to improve the performance of the CO_2 laser, the discharge tube is usually made complete with a water-cooling system that ensures intensive heat removal.

Fast gas transport CO_2 lasers. Initially, the approach used to raise the output from molecular lasers was to increase the length of discharge tubes up to 100 m and above, in which a 1-m column of the discharge gave 50-80 W at a system efficiency of 10-20% [2, 3]. Lasers using the CO_2-N_2-He mixture have received a large development effort and found wide application. The physical processes occurring in gas-discharge CO_2 lasers are given a fairly detailed examination in a number of works [2, 3].

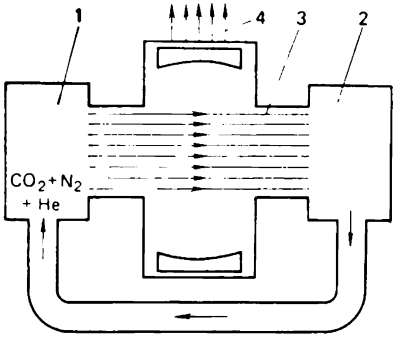

Fig. 1.14. Configuration for fast gas transport transverse-flow CO_2 laser: *1*, compressor; *2*, cooling system; *3*, discharge chamber; *4*, laser output

Despite the considerable potentialities of CO_2-N_2-He lasers with CW discharge pumping, there is a complex problem involved in increasing the CO_2 laser output. This is primarily due to the fact that the low density of the working mixture cooled via tube walls places a limit on the specific power of the CO_2 laser.

The use of longer discharge tubes to increase the CO_2 laser output presents practical difficulties in aligning cavity mirrors. In some cases this approach is unsuitable. The continuous-electric-discharge CO_2 laser that yielded a maximum output power of 8.8 kW had an optical path length of 185 m [4].

In 1969 W. B. Tiffany, R. Targ, and J. D. Foster [2] suggested the system of transverse flow of the working gas mixture with respect to the laser cavity axis instead of the axial flow configuration (Fig. 1.14). The emission of 1 kW of power was obtained from a 1-m laser. To reduce the temperature of the working mixture and to increase the inversion in the system, the blower circulated the gas mixture through a heat exchanger. The gas flow rate in this laser amounted to 300 m/s.

The transmittance of the front mirror from pure germanium

was 35%. The gas mixture consisted of CO_2 (2.7×10^2 Pa), He (8.1×10^2 Pa), and N_2 (1.6×10^3 Pa) in the ratios of 5 : 11 : 2, 5 : 7 : 3, 5 : 5 : 2, and 5 : 7 : 2 for *A*, *B*, *C*, and *D* respectively (Fig. 1.15).

In Fig. 1.15 are shown the plots of the output power of a fast flow laser versus the gas flow rate and electric discharge power. Fast flow lasers can produce CW outputs of up to 27 kW at a conversion efficiency of about 17% [2].

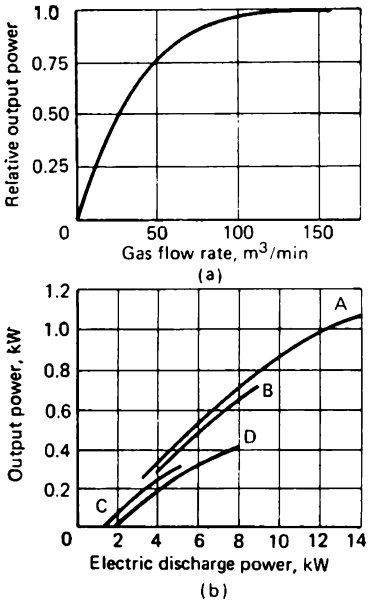

Fig. 1.15. Output power of fast flow CO_2 laser as a function of gas flow rate (*a*) and electric discharge power (*b*)

TEA CO_2 laser. In 1970, A. Beaulieu developed a molecular laser with excitation by the electric discharge applied transverse to the optical axis, which permitted operation at higher gas pressure of up to 10^5 Pa [2]. The schematic diagram of the transversely excited atmospheric pressure (TEA) CO_2 laser appears in Fig. 1.16. The 1-m long TEA laser produced about 1 MW of power in a pulse. This device operated with the electric discharge maintained between the long upper electrode (anode) and the cathode, which consisted of a set of parallel needles connected through resistors of a total value of about 1 kΩ. The discharge chamber received voltage pulses from a capacitor of about 0.02 μF, charged to 17 kV.

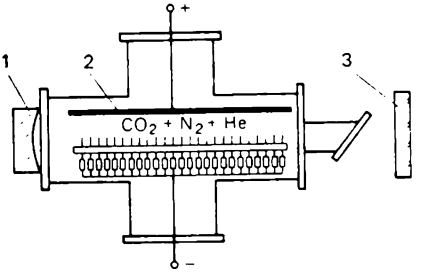

Fig. 1.16. Schematic diagram of TEA laser: *1*, *3*, spherical and flat mirrors respectively; *2*, anode

The pulse repetition rate could be varied from a few hertz to 10^3 Hz. The total pressure of the gas mixture was approximately 10^5 Pa. The volume ratio of the N_2-CO_2-He mixture was 1 : 1.2 : 10. The laser pulse duration was 300 ns, discharge pulse duration 1 μs, and pulse energy 30 mJ.

One of the mirrors from NaCl with a selenium coat had a reflectance of about 85%. The improved lasers of Beaulieu operated at an efficiency of near 17% with a pulse energy of up to 1 J and pulse repetition rate of up to 1 Hz. The average powers of such lasers are low. Consequently, it is difficult to obtain repetition rates of a few tens of hertz with these devices. The manufacture of crystals for large output windows used in such lasers is a laborious and costly process.

With the advent of pulsed gas lasers operating at an efficiency of nearly 20%, it has become possible to obtain high outputs in the range of megawatts at pulse energies of hundreds of joules in large volumes of the working gas mixture. These lasers offer a number of advantages over solid-state lasers. Unlike solid-state device, TEA lasers can produce a high average output power at an appreciable pulse repetition rate as well as generate powerful single pulses.

A TEA laser about 90 cm long provides 20 mW of power at a pulse energy of 2 J and an efficiency of nearly 17%. Powers of 100 mW and energies of 9 J in a pulse have been obtained within a discharge gap about 305 cm long. The transverse gas transport combined with transverse excitation enabled a TEA laser to produce 150 W of average power at a repetition rate of 1 kHz in a discharge gap approximately 152 cm long.

A TEA laser is available as a source of laser material processing, which generates 20-J pulses at a peak output power of 2.5 MW, repetition rate of a few hundred hertz, and efficiency in the order of 20%. The features specific to the action of TEA CO_2 lasers and also the systems of pulsed excitation of the working medium are described in work [8]. To ensure population inversion, TEA lasers utilize plasmatrons (plasma generators) which directly introduce the plasmoids in the laser medium contained in the discharge tube [8]. Ionizing radiation is used to preionize the working medium and eliminate arcing. To promote preionization and subsequently ensure uniform breakdown of large volumes of the working gas mixture, TEA lasers can be fitted with three-electrode systems which perform the function of plasma cathodes and precipitate arc discharges.

The direct injection of plasma into the laser volume by capillary plasmatrons is put forward by Yu. I. Kuklev and A. A. Uglov [8]. In the experiment described, 25 capillary plasmatrons, which replaced discrete cathodes in the interelectrode gap of the TEA system, introduced plasma jets into the optical cavity normal to its longitudinal axis. Intensive lasing took place on applying voltage to the electrodes. Lasing did not appear in the case of filling the working chamber with pure CO_2 and supplying nitrogen through the capillary plasmatrons. The laser emitted when helium was fed through the capillary tubes. This means that a factor of importance for plasma-jet excitation is the ejection of plasmoids at the instant when

no vibrationally excited nitrogen molecules escape from the capillary tubes [8]. Besides, the voltage pulses simultaneously applied to the capillary plasmatrons and to the electrodes must be in exact synchronism.

The plasmatron method of CO_2 laser excitation is suitable for work at higher pressures of the working mixture, thereby affording

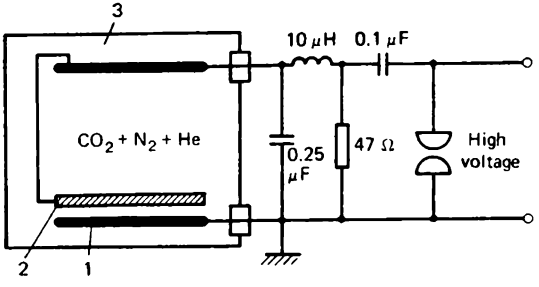

Fig. 1.17. Schematic of high-power TEA laser: *1*, comb cathode; *2*, ignitor electrode; *3*, anode

higher concentrations of particles in the laser medium. This type of excitation is analogous in many respects to the excitation employed in electron-beam controlled CO_2 lasers.

Work in the domain of TEA lasers is being carried out with the aim to obtain a high output power in a pulse and to increase the repetition rate.

The power derived from a TEA laser is proportional to the pressure squared. This is because the rate of population of the lower laser level and the number of molecules involved in laser action grow with pressure [1]. The result is the square pressure dependence of output power.

The TEA CO_2 lasers available today emit IR radiation at a power of about 1 MW and even 1 GW and at an energy of a few hundred joules in a submicrosecond pulse.

Figure 1.17 illustrates the schematic arrangement of a molecular CO_2 laser [2]. The 10-m laser cavity has 12 sections, and the total length of the active volume 4×7 cm^2 in cross section is equal to 5 m. The typical ratio of CO_2-N_2-He partial pressures in this laser is 2 : 2 : 3 and the total pressure is 40 kPa. Output pulses have durations of nearly 100 ns with energies reaching 150 J.

Other molecular lasers. Laser technology based on various active gases is capable of covering the ultraviolet, visible, and infrared regions of the spectrum: N_2 at 0.3371 μm; CO, 5 μm; N_2O, 10.5-11 μm; H_2O, 28, 78, and 118 μm; and HCN, 311 and 337 μm.

The N_2 laser emitting at $\lambda = 0.3371$ μm operates only in the pulsed mode and yields pulses of about 10 ns duration at a peak power up to 100 kW.

The CO laser generating at nearly 5 μm has a number of advantages over other molecular lasers:

— efficient conversion of electrical to vibrational energy of molecules;

— ease of reaching inverse populations of vibrational energy levels due to anharmonic vibration of molecules;

— high quantum yield;

— slow relaxation from vibrational to transition states (v-T type processes) and fast relaxation of vibrational states (v-v type processes).

The above advantages have led to the development of a CW CO laser whose efficiency reaches 47% with the conventional feed system and 65% with an electron gun used to initiate the discharge. As much as 80% of the energy of electrons in the gas discharge can convert to the vibrational energy of CO molecules on condition that the mean temperature of these electrons is held at about 2×10^4 K. This mean temperature has a substantial effect on the transfer of energy from electrons to molecules.

In the CO laser, stimulated emission can arise between arbitrary energy levels when the system maintains the population inversion. Here the finite state of one laser transition can serve as an initial state for another laser transition. An electron colliding with the CO molecule which has decayed to the finite state can again excite it, but its return to the ground state is not an obligatory condition [3, 6]. For this reason the theoretical quantum yield exceeds 90%. The performance of the CO laser improves with a decrease of its temperature (the boiling point of CO is at 83 K).

The efficiency of optical pumping can be substantially increased by adding argon or nitrogen to the CO medium in the ratio 1 : 10. The potential offered by the CO laser can be judged from an example of the laser with a volume of the laser medium of nearly 10^{-3} m^3. It can generate 100 kW of power in the quasigiant pulse mode. In the conditions of pulsed excitation, the beam energy reaches 200 J.

1.6. ELECTROIONIZATION CO_2 LASERS

In a laser, electrons of the discharge plasma have a dual purpose. As they move across the discharge region under the action of the applied electric field, electrons undergo collisions and produce new electron pairs to compensate for the loss of electrons due to recombination and diffusion onto tube walls. If the electric field is weak, the electron concentration drops off and the discharge ceases.

At the same time, these electrons must be able to excite gas molecules during collisions to promote the population of the upper energy level and to ensure the population inversion required for laser operation. Besides, a certain temperature difference is needed to maintain a steady discharge and to make lasing effective.

In electroionization (ELION) lasers, also called electron-beam (E-beam) controlled lasers, a beam of high-energy electrons impinges on the gas medium and maintains the discharge.

Preionization of the gas occurs as the electron beam of 100-200 keV initiates one of the laser discharges. The transverse electric field applied to the gas mixture then accelerates the electrons arising from ionization to enable them to excite N and CO_2 molecules.

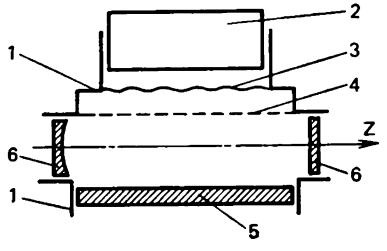

Fig. 1.18. Schematic of ELION laser

By varying the electric field strength, it is possible to adjust the electron velocity distribution so that the excitation of molecules becomes most efficient.

In work [1], an example of this type of laser is given. It uses a 130-keV electron beam injected into the discharge chamber that contains 40 liters of a 1 : 2 : 3 mixture of CO_2, N_2, and He at a pressure of 10^5 Pa. The laser can generate both pulses on the fundamental mode with energies of up to 1 200 J at a peak power of 50 MW and duration of 50 μs and multimode pulses with energies of up to 2 000 J.

The ELION CO_2 laser can operate at high pressures of the gas medium, in the order of 10^6 Pa [8]. At such pressures, the excitation methods applied in TEA lasers are unsuitable for ELION lasers, excepting the case where they use ionizing radiation from an external source of plasmatron excitation. In this respect, one can regard these lasers as a separate group of devices in the CO_2 laser family. One of the main features of the ELION laser is its tunability over a broad wavelength range combined with intensive emission of radiation.

The first experiments involved in the research on ELION lasers operating at a pressure of the working mixture above the atmospheric have been treated in work [8].

The schematic diagram of an ELION laser is shown in Fig. 1.18. Mounted in the laser casing *1* is an external source *2*, namely, an electron gun generating an intensive electron beam of high energy. The film *3* separates the vacuum volume of the gun from the discharge chamber formed by cavity mirrors *6* and filled with a working gas

mixture at high pressure. The film *3* of the mylar type, for example, is transparent to the high-energy electron beam which propagates in the direction normal to the longitudinal *z*-axis of the cavity. The spacing between a grating electrode *4* and a blind electrode *5* forms a discharge gap. The gas mixture is forced into the chamber through a hole provided in the laser casing. The principle of action consists in the following: the ionizing radiation from the external source makes the dense gas medium conductive and thus enables the current to pass through the discharge gap, with the result that the electrical energy converts to the vibrational energy of molecules. The requisite condition for producing a high-current flow in the gas is a high degree of gas ionization. The electron concentration in the gas must be above a certain threshold value that depends on the size of the discharge gap, gas pressure, and composition of the gas mixture. Experiments on the characteristics of ELION lasers operating at the pressures of CO_2-N_2-He mixture up to 5 MPa are described in work [8]. In the experiments, the electron beam with an energy of nearly 700 keV and current density of 10-20 A/cm^2 was used to provide for ionizing radiation. The external electron source generated pulses of 10^{-8} s duration. The discharge gap electrodes received voltage pulses from a low-inductance 10-20 pF capacitor charged to 50 kV. The specific power of radiation amounted to 10^6 W/cm^3 at a pulse length of 10^{-7} s. The maximum efficiency reached 25% in a 1 : 2 mixture of CO_2-N_2 gas. Studies were also made on current characteristics, threshold characteristics, gain-pressure and gain-mixture composition relations, and emission spectrum of ELION lasers. The analysis of the results revealed that the mechanism of excitation of working levels at high pressures of up to 10^6 Pa was in the main analogous to that of excitation of CO_2 levels at low pressures.

From experimental data it follows that the specific power expended in the ELION laser grows with pressure faster than the width of working levels. The gain of the active medium in this type of laser can thus be much higher than that in a gas-discharge CO_2 laser. Moreover, the gain can be varied by adjusting the degree of ionization of the working gas mixture [8].

Evidently, ELION lasers operating at high pressures are promising devices. They can be tailored to give a high specific output power at extremely high efficiencies and to afford smooth tuning of laser frequencies.

1.7. GAS-DYNAMIC LASERS

By the method of preexcitation of the vibrational levels of CO_2 molecules, the known gas-dynamic (GD) lasers can be divided into three groups: heat-pumped lasers, chemically pumped (chemically excited) lasers, and electrically excited lasers.

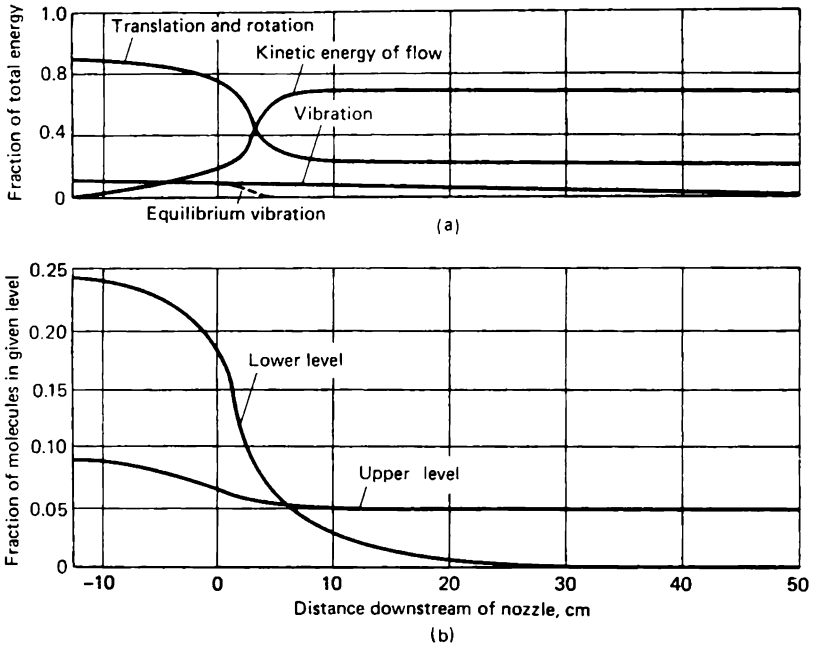

Fig. 1.19. Mechanism of initiation of population inversion in gas dynamic laser: (*a*) fraction of total energy due to various degrees of freedom as a function of distance from nozzle; (*b*) share of CO_2 molecules at lower and upper laser levels as a function of distance downstream of nozzle

Heat-pumped GD lasers. Gas-dynamic lasers rely on one of the methods of producing the population inversion, by which the preliminarily excited gas undergoes deep and fast cooling due to adiabatic expansion. It is important that the lower temperatures and pressures can be set up earlier than the vibrational relaxation of CO_2 and N_2 molecules from upper laser levels. Such lasers using the CO_2-N_2-He mixture can afford an increase in the power density by a factor of 10^3-10^5 in comparison with lasers relying on a continuous discharge.

Population inversion on the CW basis was experimentally obtained in the CO_2-N_2 mixture through its adiabatic expansion as the hot gas was passed through a supersonic nozzle.

One of the methods for producing the inverse population in gas lasers is a thermal method which calls for fast heating or fast cooling of the working medium. The requisite condition is that there must exist a definite relationship between the relaxation time for the population of levels, for example, in a three-level quantum system,

and the thermodynamically equilibrium value of the population of these levels.

To produce the inverse population by the method of fast heating, it is necessary that the time required to populate the upper level should be shorter than the time needed for the population of the lower level (Fig. 1.19). For its implementation, the method can rely on shock or detonation waves to heat the compressed mediums to enhanced temperatures and greatly accelerate them [8]. Shock tubes can rather quickly and uniformly heat up the laser gas volume to temperatures as high as 10^4 K. The shock-tube lasers operating on this principle are pulsed systems.

With the method of fast cooling used, it is necessary to reduce the system temperature at such a rate that the relaxation time for the upper level can be longer than that for the lower level. High rates of cooling can be achieved by forcing the gas through a slit or nozzle to promote its adiabatic expansion. The gas mixture heated to 1 500-3 000 K can be cooled at a rate of 10^8-10^9 K/s.

A CO_2 molecule exhibits three vibrational degrees of freedom, each being characterized by its temperature θ_1, θ_2, and θ_3 respectively. These temperatures can differ from each other and from the gas temperature T (commonly, $\theta_1 \approx \theta_2$). The condition required for maintaining the inverse population is that $\theta_3 > \theta_1$ during the radiative transition of the CO_2 molecule from level $(00\mathring{0}1)$ to level $(10\mathring{0}0)$.

By forcing through a slit or nozzle the hot gas mixture of temperature T, which displays the equilibrium distribution of CO_2 molecules over their degrees of freedom, the adiabatic expansion causes the thermal energy of chaotically moving molecules to transform into the kinetic energy of the molecules that now execute an ordered motion. The temperatures θ_1, θ_2, and θ_3 drop off at different rates. Since θ_3 decreases at a slower rate than $\theta_1 \approx \theta_2$, a difference appears between "vibrational" temperatures. This temperature difference keeps on until the pressure falls to a value at which the collisions of molecules with one another have no effect on the relaxation. At this instant the vibrational temperatures remain constant, "frozen", as it were, for a certain time until the radiative decay of vibrational levels begins (for a CO_2 molecule, this time is 10^{-2} s). The inverse population in the gas mixture that undergoes adiabatic expansion occurs by virtue of a fairly fast "freezing" of vibrational temperatures as compared to the decay time for the upper laser level of the CO_2 molecule.

The use of a nonequilibrium gas-dynamic flow is thus a rather effective way of obtaining the inverse population in the laser medium.

The jet engine can be taken as an example illustrative of the most typical design of a heat-pumped GD laser. The GD laser construction includes a combustion chamber where the gas mixture is

preheated and then allowed to force its way through a nozzle to effect lasing in the optical cavity formed by mirrors arranged parallel to each other on the walls of the exhaust chamber. Such a GD laser gives a CW output from a few kilowatts to a few hundred kilowatts. A laser setup is available, which yields 6 kW of CW output power for 10 s. The combustible C_2H_2-CO-air mixture ignited by a methane torch is burnt to form a gas mixture consisting of 7.5% CO_2, 91.3% N_2, and 1.2% H_2O that is held at a temperature of 1 400 K and pressure of 1.7×10^6 Pa. The subsequent expansion of the mixture at a rate of 4 M (where M is the Mach number) occurs as it escapes through a row of nozzles, each with a slit height of 0.08 cm, $3 \times \times 30$ cm in cross section, and with a ratio of the nozzle throat areas equal to about 14. At the outlet from the nozzle, the temperature of the flow drops off to 354 K and pressure to 8.7×10^3 Pa. The gas flow rate is 1 360 g/s. At a gas flow rate approaching 13.5 kg/s, the laser emits 60 kW of power in multimode operation.

This laser incorporates a diffuser placed adjacent to the cavity, which changes the pressure of the gas from a value of 10^4 Pa at a flow rate of 4 M to a pressure higher than the atmospheric at a flow rate lower than 4 M. As a result, the gas is directly vented to the atmosphere.

The GD laser operating with the heat-pumped CO_2-N_2-He mixture has an average efficiency of approximately 2-5%. As shown by calculations, the efficiency of conversion of thermal energy into laser radiation can be stepped up to 25% by way of thermal energy regeneration in the gas recycling system. The general heat-pumped gas recycling arrangement for a gas dynamic laser is described in [8].

The strength of optical elements puts limits on GD laser outputs. Investigations have been undertaken with the aim to work out the cavity configuration that would minimize damage to mirrors [1, 2]. The configuration with mirrors arranged in the recess 3 cm distant from the nozzle walls proved most favorable.

In the mechanism of thermal excitation of GD lasers, chemical reactions play a substantial role apart from heat effects. The best use of chemical energy can be made by selecting a fuel such that its combustion directly yields excited molecules. Because the flame strongly excites vibrational levels, this method of GD laser pumping will ensure a high specific power of emitted radiation. According to preliminary estimates cited in [4], 450 g of fuel going into the flame evolves 2×10^6 J, and the output power of the laser reaches 100 kW at 5% conversion efficiency.

The available laser systems relying on chemical explosive reactions which yield excited CO_2 molecules can produce pulses of 0.3 s duration with energies of up to 20 J on igniting the mixture of CO, O_2, N_2, and H_2 with a spark. They also use acetylene and pro-

pane as a fuel. As distinct from CW GD lasers, in this type of GD laser the explosion pumping eliminates the need for a compressor.

Chemically pumped GD lasers. When using explosive reactions for chemical pumping of gas dynamic lasers, the composition of the starting mixture should be so chosen as to ensure the optimum ratio of CO_2, N_2, and H_2O in the working gas mixture.

These GD lasers operate on the principle of conversion of chemical bond energy into stimulated radiation during purely chemical mixing of reactants. As an example of this process, one can take the chemical reaction caused by mixing DF or HF with CO_2, where a number of levels of the DF molecule coincide with the upper lasing level of the CO_2 molecule [2, 7].

The inverse population can also arise in the supersonic flow of the gas-aerosol mixture from the adsorption of anisotropic molecules of the CO_2 type on the surface of aerosol particles.

Electrically excited GD lasers. The electrical method of GD laser pumping is used in electroaerodynamic lasers [8]. As distinct from the above described type of excitation of the upper lasing level of active molecules, this type of excitation occurs not in the combustion chamber but just in the nozzle during the resonant transfer of energy from N_2 molecules preliminarily heated to high temperatures by a powerful electric discharge. At the same time, the working medium obtained from the mixing of nonequilibrium gas flows rapidly expands in the nozzle.

To produce the N_2 flow to be heated to the desired temperature, use is made of a standard electric-discharge jet pump with a power of a few kilowatts. In a large-volume chamber the preheated nitrogen is mixed with an additional flow of N_2 at 20°C to maintain the required equilibrium temperature and pressure. The heated nitrogen then undergoes a rapid expansion at a rate of 3.4 M as it flows through a two-dimensional wedge-like nozzle whose height varies from 0.1 cm in the throat to 0.6 cm at the outlet. The nozzle is 5 cm long. The N_2 molecule well retains its vibrational temperature since it exhibits a long relaxation time. At this stage the excitation of the CO_2 molecule to the upper level occurs, accompanied by the fast mixing of the nonequilibrium N_2 flow with CO_2 or N_2O molecules injected through two narrow 0.1-cm wide slits located opposite each other at right angles to the supersonic flow. The injection rate can be made to reach the sound velocity by changing the pressure in the injector.

What promotes a rather high power density in this case is an increased density of the working medium coupled with a flow velocity of the injected gases close to the supersonic velocity. The population of the upper laser level is held stable owing to a short time of transit of particles from the point of their excitation to the resonator. The depopulation of the lower level comes about by virtue of gas cooling

during fast expansion, thereby providing the conditions that enable an enhanced population inversion. However, because of appreciable aerodynamic disturbances, the homogeneous gas with the inverse population can be evolved only at the end of the flow.

At a starting nitrogen temperature of 2 600 K, the vibrational excitation of molecules accounts for 13% of the internal energy, the conversion efficiency in the infrared being equal to 12%. An electro-aerodynamic laser is available which produces 11.5 kW of CW output power.

Electrically excited GD lasers have a higher efficiency than heat-pumped counterparts. Besides, the former type excited, for example, by arc-discharge or high-frequency plasmatrons can employ a gas recycling system which substantially increases the overall efficiency.

1.8. CHEMICAL LASERS

The chemical laser operates on the population inversion produced directly or indirectly in the course of the exothermic reaction [7].

In the chemical laser developed by J. Casper and G. Pimentel [2], the reaction of the type $H + Cl_2 \rightarrow HCl^* + Cl$ was initiated by way of photolysis. At an ion pressure of 400-2 100 Pa and with a ratio of $pCl_2 : pH_2$ of approximately 1 : 2, the laser emitted pulses of around 10 μs duration with an energy of 2×10^{-2} J in a pulse. Soon, other lasers came into being, which used excited CO* and HF* molecules. In a CO_2 laser, the process of transfer of the vibrational energy from the excited HCl* molecule to the CO_2 molecule occurs by the reaction $HCl + CO_2 \rightleftarrows HCl + CO_2 + \Delta E$, where ΔE is the reaction energy. Here one quantum of the vibrational energy in the two-atom molecule yields two vibrational quanta of energy in the polyatomic molecule. The excited HCl molecules formed by the chemical reaction of $HF + Cl_2$ serve as a pump energy source. In the laser developed by R. Gross the energy exchange occurs between DF and CO_2 molecules. This laser uses the energy of the chemical reaction to excite both active molecules directly and molecules of the other gas, which then transfer energy to the active molecules.

The main difficulty involved in obtaining the inverse population arises from a high rate of relaxation processes when the system comes to the equilibrium state since this rate often exceeds the rate of the chemical reaction. In this case, an important criterion to be met in selecting the chemical system for a laser is the optimal ratio of the reaction rates which determine the energy distribution in molecules and relaxation processes. An increase in the number of molecules populating high lying energy levels, must by far exceed the growth of the population at lower levels, while the lifetime of excited molecules must not be small as against the reaction time.

The chemical reaction is initiated by an electric discharge or a flash of a powerful flashtube and, most often, by utilizing the effect of photolysis. Electron-transition lasers find quite rare uses, whereas vibrational transition lasers have gained wide favor. In the course of exciting vibrational states, collisional deexcitation should be considered to contribute the largest share to the total energy loss. As regards the excitation of electron states, large values of Einstein's A coefficient, which add to the gain, can also limit the inverse population growth on account of spontaneous emission. Chemical lasers still largely use only vibrational transitions. Chemical laser action can be understood by considering a simple chemical reaction of the type [2, 7]

$$A + BC \rightleftarrows AB^* + C + \Delta E \tag{1.14}$$

where ΔE is the reaction energy.

This reaction proceeds in three stages: (1) the A atom approaches the BC molecule; (2) the bonds between B and C get weaker; and (3) products of the reaction of AB appear and move away from one another.

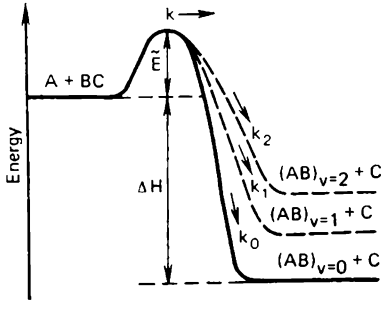

Fig. 1.20. Kinetic mechanisms of reaction in chemical laser: k_0, k_1, and k_2 are constants accounting for individual excited states of molecule subjected to different kinetic mechanisms

Energies E_1, E_2, and E_3 correspond to each of these stages. The vibrational energy of molecules commonly grows at the second stage. The heavier the A atom in comparison with B and C atoms, the greater the increment of vibrational energy against that of kinetic energy. The reaction takes place according to the curve illustrated in Fig. 1.20, which represents changes in the total energy of the chemical system. The energy released after the exothermic reaction must be equal to the sum $\Delta H + E$. Fig. 1.20 presents a constant k which can be found from the kinetic mechanism of the reaction and also constants k_1, k_2, k_3, etc. which describe various excited states of the molecule taking part in the chemical reaction. Given the temperature T of the reaction, we can calculate the populations of individual rotational levels related to the specified state of the vibrational energy of a molecule, which, in turn, allows us to estimate the gain of the laser medium as the ratio of corresponding coefficients k_1 and k_2 presented in Fig. 1.20:

$$\frac{k_2}{k_1} \approx \frac{r(2r+1)B - kT_R}{r(2r-1)B - kT_R} \exp\left(-\frac{2Br}{kT_R}\right) \tag{1.15}$$

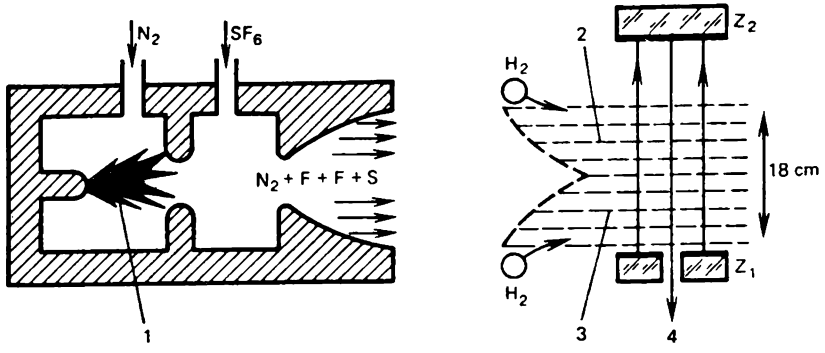

Fig. 1.21. Configurations for purely chemical laser: *1*, electric arc; *2*, optically active region; *3*, supersonic flow; *4*, laser output at 3 μm

where B is the rotational constant, T_R the temperature of the chemical reaction, and r the quantum number related to rotational motion. It is assumed here that the reaction temperature T_R is equal to the "rotational" temperature, which means that the system retains thermodynamic equilibrium during collisions of the second kind. In the case of initiating the exothermic reaction, for example, by a powerful flash of the lamp, the rotational temperature may be in excess of 293 K.

A high degree of inversion which results in an appreciable laser gain is easier to achieve in molecules having a small number of atoms and a low moment of inertia. Chemical lasers should preferably operate with linear three-atom molecules [7].

Figure 1.21 demonstrates the scheme and principle of action of a chemical laser. The mixture of the $N_2 + F + F + S$ type moves with a supersonic velocity through the tube with holes in its walls. Hydrogen added to the flow through holes maintains the reaction $H_2 + F \rightarrow HF^* + H$.

In the first chamber the electric discharge strongly heats nitrogen. In the second chamber nitrogen and CF_6 mix together to form a mixture whose temperature reaches 250 K at which a major share of CF_6 molecules dissociate. Further, the mixture expands as it flows through a rectangular 1.27×18 cm nozzle. Mirrors Z_1 and Z_2 from beryllium and bronze with gold coating form an optical cavity (resonator). The mirror Z_1 has an aperture through which the beam leaves the cavity. The aperture diameter is chosen such as to ensure a maximum power of the beam [2]. With an aperture area equal to 30% of the mirror area, the beam power at a wavelength of 3 μm was as high as 475 W. The efficiency of the laser unit reached 12% (with respect to the chemical reaction energy).

1.9. PROPERTIES AND CHARACTERISTICS OF LASER RADIATION

Laser radiation features a number of unique properties such as a high intensity of electromagnetic radiation, enhanced monochromaticity, and appreciable degree of temporal and spatial coherence. A laser differs from other sources of electromagnetic energy by the highly directional, collimated nature of the beam.

In the further discussion, we shall primarily focus on the characteristics of lasers emitting radiation in the 0.4-10.6 μm wavelength region with fairly good output parameters such as energy and pulsed or CW power, which determine the effective use of lasers in industrial applications.

One of the most important characteristics of laser radiation is its monochromaticity which defines the range of frequencies or wavelengths at which the radiation occurs, i.e. it specifies the spectral linewidth, or emission spectrum of a laser. For a certain spectral line of wavelength λ_0 or frequency ω_0, the degree of monochromaticity is

$$\mu = \Delta\lambda/\lambda_0 = \Delta\omega/\omega_0 \tag{1.16}$$

where $\Delta\lambda$ is the spectral width.

Lasers are commonly regarded as sources of monochromatic radiation because they emit within a rather narrow spectral range which can be specified by one frequency or one wavelength. For gas lasers operating in a single mode within a spectral width $\Delta\lambda$ of around 10^{-10} μm, the degree of monochromaticity is $\mu \approx 10^{-10}$. But for monochromators emitting spectral lines, this figure of merit is $\mu \leqslant 10^{-6}$. Since a major share of the radiation flux falls within a very narrow region of the emission spectrum that does not exceed hundredths of a micrometer, the spectral power density of a laser is many orders of magnitude higher than that of other known sources of radiation. For example, the emission spectrum of a ruby laser consists of a few narrow spectral lines of $\sim 10^{-8}$-10^{-7} μm.

A highly monochromatic radiation of a laser can be put to many uses, for example, in atmosphere investigations, in spectroscopic analyses, in studies of photoluminescence and photoelectric effects, for creation of reference frequency instruments, and for control of chemical reactions.

Monochromaticity is closely related to coherence, which is one of the basic properties of laser radiation. There are two manifestations of coherence, spatial and temporal. Spatial coherence refers to correlation of the characteristics of a radiation field at different points in space, but at the same time. Temporal coherence refers to correlation in phase at the same point in space but at different times. If, after wave interference, the resultant electromagnetic

radiation intensity J at point Q can take on any values from $(\sqrt{J_1} - \sqrt{J_2})^2$ to $(\sqrt{J_1} + \sqrt{J_2})^2$ depending on the phase difference, then the radiators at different points are coherent. The radiators are totally incoherent if $J = J_1 + J_2$. For the case of temporal coherence, the coherence length is

$$l_{coh} = c\tau_{coh} \tag{1.17}$$

Here the light velocity c determines the relation between the spatial and the temporal coherence of radiators, i.e. shows that if the difference between the ray lengths exceeds a definite value of l_{coh}, then the correlation between the characteristics of the electromagnetic field at different moments of time does not exist. Coherence time τ_{coh} is the time during which the difference in phase between the oscillations at various points has no time to change by a value of the same order as π. The relation between τ_{coh} and spectral width $\Delta\lambda$, or monochromaticity μ, is given by

$$\tau_{coh} \approx \Delta\lambda \approx \mu \tag{1.18}$$

For a laser, the coherence time is $\tau_{coh} = 10^{-2}$-10^{-1} s; for ordinary light sources, $\tau_{coh} = 10^{-8}$ s.

The properties of coherent radiation are commonly defined by a coherence function Γ which is the time-mean value of the product of two components of the electromagnetic field at points r_1 and r_2:

$$\Gamma(r_1, r_2, \tau) = \lim_{T\to\infty} \frac{1}{2T} \int_{-T}^{T} V(r_1, t+\tau)\, V^*(r_2, t)\, dt \tag{1.19}$$

Here,

$$V(r, t) = A(r, t) \cos[\varphi(r, t) - \bar{\omega}t] \tag{1.20}$$

where $A(r, t)$ and $\varphi(r, t)$ are the amplitude and phase of oscillations respectively, and $\bar{\omega}$ is the average frequency.

The coherence function determines the degree of correlation between the oscillations at different points of the field at the same time.

The fringe (interference) pattern present at point P gives information on the correlation of oscillations at points P_1 and P_2 at the same time ($\tau = t_2 - t_1 = 0$). The coherence that results is of the spatial type described by the function $\Gamma(r_1, r_2, 0)$.

The correlation of oscillations at one point P_1 but at different times τ is the time correlation defined by the function $\Gamma(0, 0, \tau)$.

Because of its high temporal coherence, the laser radiation makes an efficient source for use in various scientific and industrial applications involving the areas of interference, measurements of length and of linear and angular velocities, small displacement

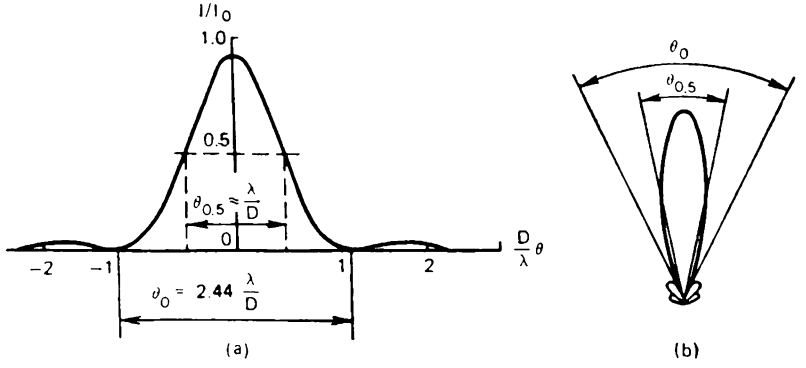

Fig. 1.22. Radiation patterns for circular emitting spot in Cartesian (*a*) and polar (*b*) coordinate systems

measurements, transmission of information at optical frequencies, etc.

Spatial coherence determines a good directionality (collimation) of the beam and enables its focusing to a small area. This figure of merit is defined by a solid angle confining a major fraction of energy carried by the beam. If the solid angle is a cone, then the parameter of radiation is the flat angle of beam divergence, or angle of spread. If the solid angle differs from a cone, the parameters commonly used to specify the beam are the two angles in the vertical and horizontal planes.

A theoretical radiation pattern for a round emitting area appears in Fig. 1.22. A major fraction of radiant energy is concentrated in the main (major) lobe of the pattern.

The maximum field intensity within the side lobes does not exceed 2% of the maximum radiant intensity J_0.

Assuming that the amplitude and phase distribution of oscillations is uniform over the cross section of the laser beam, the diffraction-limited beam divergence at half the level of power will then be equal to an angle

$$\theta_{0.5} = 1.22\ \lambda/D \qquad (1.21)$$

where D is the laser beam diameter.

For a ruby laser emitting a beam 1 cm in diameter D at λ of 0.69 μm, the divergence angle is $\theta_{0.5} \approx 0.85 \times 10^{-4}$ rad ($\approx 14''$); for a CO_2 laser producing a beam of the same diameter at $\lambda =$ $= 10.6$ μm, this figure of merit is 1.21×10^{-3} rad ($\approx 3'20''$). In actual fact the beam divergence is much higher, from units to a few tens of angular minutes. A significant increase in the beam divergence observed in practical lasers as compared with calculated values results from a nonuniform distribution of the amplitude and

phase of the radiation field within the confines of the emitting surface, multimode nature of laser light generation or, more precisely, generation of transverse modes, inhomogeneities present in the active medium, and imperfection of resonant cavity elements.

The radiating surface of a laser rod, for example, a ruby rod, is not uniform: it is a complex structure of individual luminescent points, each about 100 μm in size, which form complexes approaching 850 μm in size.

A decrease in the beam divergence can primarily be achieved through the selection of higher-order modes. Single-mode lasers operating in the dominant TEM_{00} mode have the lowest divergence angle (the term TEM stands for transverse electromagnetic). Single-mode operation is most easily realizable in gas lasers.

Single-mode operation of solid-state lasers is more difficult to attain because their active materials display a high gain, so that it is quite a problem to achieve the desired magnitudes of energy losses for higher order modes without impairing the output parameters of the laser beam.

Polarization is another important parameter of radiation. Most lasers emit plane-polarized radiation.

The type of laser material determines the kind of laser polarization. If the optic axis of a crystal such as ruby is parallel to the cavity axis, all the planes of polarization are equivalent and the laser radiation exhibits the natural kind of polarization. If the optic axis of a crystal is normal to the cavity axis, the transverse polarization of radiation results.

The parameters and properties that play the dominant role in producing any desired heat-affected zone during material processing are the following: beam energy, energy density, lasing power, power density, pulse duration, spatial and temporal coherence, spatial power (flux) density distribution in the focused spot, reflectivity of target materials, thermal and physical properties, melting temperature, etc.

The power density distribution in a focused spot depends on the angular distribution of the laser radiation intensity at various distances from a radiator. Accordingly, one distinguishes between the near-field (Fresnel) zone and far-field (Fraunhofer) zone.

The far zone where the effects of Fraunhofer diffraction occur is known as the Fraunhofer region. In this region the angular distribution is almost independent of the distance to the emitting end of the laser active element. It lies at a distance of $D^2/2\lambda$ to $2D^2/\lambda$ from a radiator.

The intermediate region in the near-field zone extending from the boundary of the far zone in the direction of the radiator to another boundary that is $(D/2)/(D/\lambda)^{1/3}$ distant from the radiator is known as the Fresnel region, or Fresnel zone.

The zone between the inner boundary of the Fresnel region and the radiator surface forms another near-field region where the description of the radiation field distribution does not allow for any approximation. The radiation fields in this region can be very complex, rapidly varying, with sharp shadow boundaries.

TABLE 1.7. **Radiation Intensity as a Function of Distance from a Radiation Source**

Zone of propagation	Distance from radiator	Phase error measured at distance L from various points on emitting surface of size D
Near-field	$L = D$	
Fresnel	$L \approx (D/2)/(D/\lambda)^{1/3}$	
Rayleigh	$L \approx D^2/2\lambda$	(parallel beam region)
Fraunhofer	$L \approx 2D^2/\lambda$	(divergent beam region)

Table 1.7 [1] shows a presentation of the radiant energy distribution for an extended diffraction-limited coherent source.

1.10. FOCUSING OF LASER RADIATION

Any optical system has an extreme lower limit of beam focusing, or a diffraction limited range, which determines a minimum size of the focal spot and, hence, a maximum attainable density of radiation power.

A simple consideration of laser beam focusing only applies to a Gaussian beam because the relative distribution of its intensity remains constant in the direction of propagation [1, 2]. Consequently, this distribution obeys the Gauss law both in the near and in the far zone. In the Gaussian beam the phase of radiation is the same at all points in the cross section, therefore this type of beam is called a single-phase beam. The Gaussian beam can be focused to a spot of a diameter in the order of one wavelength.

If the beam expands insignificantly along the optical path from the laser to a lens and its initial divergence only results from diffraction effects arising in the exit lens of the laser, then the radius r_s of the focal spot can be found from an expression used for simple estimates:

$$r_s = F\theta \tag{1.22}$$

where F is the focal lens of an aberration-free lens, and θ the beam divergence angle.

Since the Bragg angle of beam divergence is $\theta \approx \lambda/D$, where D is the diameter of the aperture through which the beam emerges, then for the case where the beam totally fills the lens aperture, the spot radius is

$$r_s \approx F\lambda/D \approx \lambda F_0 \tag{1.23}$$

where $F_0 = F/D$. Because the value of F_0 differs too much from unity, it follows from expression (1.23) that r_s can be of the same order of magnitude as λ.

The laser beam is commonly focused by means of lenses or lens systems with focal lengths ranging from 25 to 300 mm and working diameters from 10-20 mm to 60 mm and over. In use are also mirrors, reflector lenses, sets of varifocal and interchangeable lenses, and rotational lenses. Lasers operating in the visible and in the near infrared employ glass lenses, and infrared lasers use lenses from NaCl, KCl, Ge, GaAs, ZnSe, etc., which can provide power densities of around 10^6-10^{10} W/cm^2 and energy densities of 10^3-10^5 J/cm^2 and above in the focal spots of optical systems. Depending on the parameters of laser radiation and the performance of optical systems, the diameters of focused laser beams range from 10 μm to 1 mm (Table 1.8).

TABLE 1.8. **Diameters of Focused Beams Obtained from Various Lasers**

Focusing system parameter	CO_2 laser, low-power CW or pulsing, single-mode	CO_2 laser, high-power, CW, single-mode	YAG laser, low- and moderate-power, pulsing, continuously pumped, single-mode	YAG laser, pulse-pumped, single-mode	Ruby laser and Nd-glass laser, pulse-pumped, multimode
Focused beam diameter, μm	50-150	200-500	10-100	50-100	100-1 000
Lens focal length, mm	25-70	60-300	20-50	25-50	25-70

Consider the spatial profiles of laser beams, which characterize the beam cross sections.

The spatial patterns of beams of gas lasers are known as transverse electromagnetic (TEM) modes and represented in the form TEM_{mn}, where m and n are small integers.

The transverse modes arise from the conditions of resonance inside the laser cavity and represent definite configurations of the electromagnetic field that are preset by the boundary conditions in the cavity. The subscripts m and n at the notation TEM_{mn} can

be interpreted in the rectangular coordinate systems as the number of nulls in the spatial pattern in each of two orthogonal directions transverse to the direction of beam propagation [1]. Fig. 1.23*a* illustrates some examples of the spatial distribution of the light intensity in rectangular transverse-mode patterns. The integers denote the number of observed minima of intensity (the number of nulls) as one scans the cross section of the beam in the horizontal and the vertical direction respectively. Thus the TEM_{00} mode has no nulls in either the horizontal or vertical direction, whereas the TEM_{10} mode has one null in the horizontal direction and none

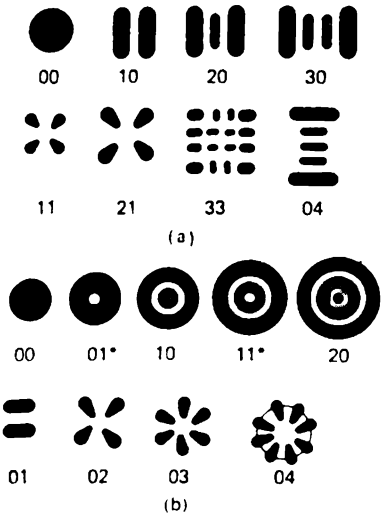

Fig. 1.23. Transverse-mode patterns in rectangular symmetry (*a*) and cylindrical symmetry (*b*)

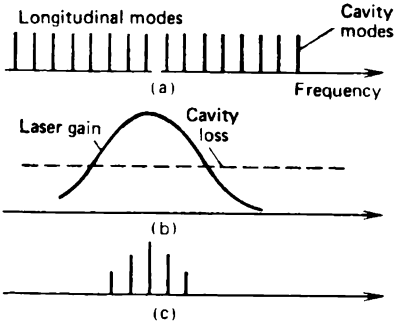

Fig. 1.24. Frequency spectrum of laser output: (*a*) longitudinal modes of laser cavity; (*b*) gain curve for fluorescent emission and cavity loss that is relatively constant with frequency; (*c*) resulting frequency spectrum covering all modes for which gain is greater than loss

in the vertical direction, the TEM_{20} has two nulls along the horizontal and none along the vertical, and the TEM_{11} has one null in both the horizontal and vertical direction.

In many cases the beam shape proves very complex because of the superposition of several modes.

In Fig. 1.23*b* are shown the examples of cylindrical TEM modes. Here, the first integer indicates the number of intensity minima (nulls) in the radial direction of the beam cross section and the second integer denotes half the number of nulls in an azimuthal direction. The mode designated as TEM^*_{01} marked with an asterisk represents a superposition of two similar modes rotated by 90° about the central axis relative to each other. The TEM^*_{01} mode is

thus a combination of TEM_{01} and TEM_{10} and is often called the doughnut mode.

Longitudinal modes are shown in Fig. 1.24. Many lasers operate simultaneously on a few longitudinal modes, so the total laser linewidth will approach the fluorescent linewidth of the active material [5].

The most common method for obtaining single-mode operation involves the use of short cavities so as to sustain gain in only one longitudinal mode. Another method uses multiple end mirrors to form two cavities of different lengths, with the laser operating at a frequency which is resonant for both the cavities [1].

For laser material processing, operation in the TEM_{00} mode called the Gaussian mode is preferable. In this case the electromagnetic field strength E and intensity q as a function of radius r are given by

$$E(r) = E_0 \exp(-r^2/w^2) \tag{1.24}$$

$$q(r) = q_0 \exp(-2r^2/10^2) = 2p/(\pi w^2)\,[\exp(-2r^2/w^2)]$$

where E_0 is the electromagnetic field strength at the center of the beam, w the Gaussian beam radius, i.e. the radius at which the intensity decreases from its central value by a factor of e^2, and q_0 the intensity of the beam at the center. As it propagates or passes through the optical system, the Gaussian beam remains invariable in shape, while higher-order modes do not retain their original spatial distribution.

The lower limit to the beam divergence angle is set by diffraction:

$$\theta = k\lambda/d \tag{1.25}$$

where λ is the wavelength of the light, d the diameter of the exit aperture, and k a numerical factor of the order of unity. For a Gaussian beam, $k = 1.22$.

The limiting aperture may be taken as the beam waist inside the laser. Inside the laser cavity the field distribution of a transverse mode is concentrated at the center of a confocal cavity, which lies near its geometric center. The beam waist is given by [2]

$$w_0 = (\lambda_c/\pi)^{1/2} \tag{1.26}$$

Here, λ_c inside the cavity is

$$\lambda_c = [2/(R_1 + R_2 - 2L)]\,[L(R_2 - L)(R_1 - L)(R_1 + R_2 - L)]^{1/2}$$

where R_1 and R_2 are the radii of curvature of mirrors spaced by distance L. In many practical cases, the beam waist is usually of the same order of magnitude as the laser aperture diameter.

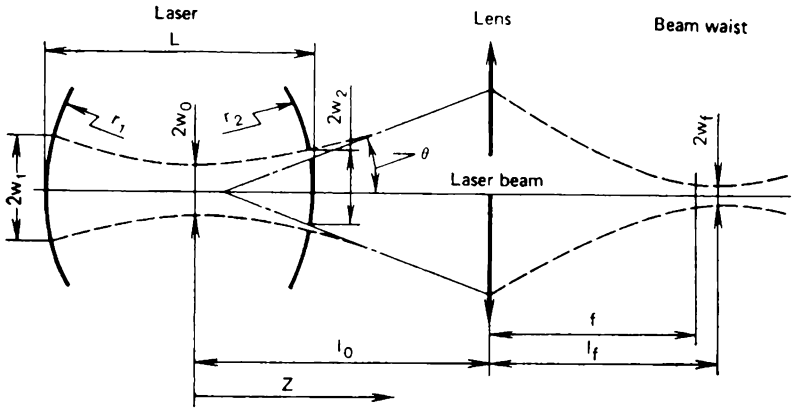

Fig. 1.25. Divergence and focusing of laser TEM_{00} beam

The beam divergence angle in mrad for most representative lasers is: 0.2-1 for He-Ne; 0.5-1 for Ar; 1-10 for CO_2; 1-10 for ruby; 0.5-10 for Ne-glass; and 2-20 for Nd-YAG lasers.

The value $2w$ is commonly taken as the diameter of the laser beam. For the TEM_{00} mode, the area of the spot of this diameter covers 86.5% of the total power in the beam, and the diameter of the TEM_{00} mode pattern on cavity mirrors is governed by the cavity geometry (Fig. 1.25). In the figure, $2w_0$ is the diameter of the beam waist inside the cavity, $2w_1$ and $2w_2$ are the diameters of beam cross sections on cavity mirrors, r_1 and r_2 are the radii of curvature of mirrors, L is the distance between mirrors; 2θ is the beam divergence angle, l_0 is the distance from the focusing lens to the beam waist, f is the lens focal length; l_f is the distance from the focus to the lens, and $2w_f$ is the beam diameter at the focus.

The radius of beam waist inside the cavity is

$$w_0 = \frac{w}{\left[1+\left(\frac{\pi w^2}{\lambda r}\right)^2\right]^{1/2}} \tag{1.27}$$

The spot sizes at mirrors of the same radius of curvature, $r_1 = r_2$, are $w_1 = w_2 = w$.

Since the TEM_{00} beam expands as it moves away from the waist w_0, the spot size at a distance z [2] becomes

$$w_z = w_0\left[1 + \left(\frac{\lambda z}{\pi w_0^2}\right)^2\right]^{1/2} \tag{1.28}$$

From this equation we can see the distinction between the near field ($z \ll \pi w_0^2/\lambda$) and the far field ($z \gg \pi w_0^2/\lambda$) [1]. In the near field, the beam diameter insignificantly exceeds the waist size. In the far

field, the divergence is defined by expression (1.26) and for the TEM_{00} mode it is given by

$$\theta = \lambda/\pi w_0 \tag{1.29}$$

The divergence of a laser beam can be reduced through its collimation in two ways: with focusing of the beam by a small-diameter lens (spatial filter) placed at the focus of the converging optical system (Fig. 1.26) and without its focusing, in which case the beam directly propagates through a Galilean telescope. The laser beam divergence will then be the inverse of the magnification of the telescope used:

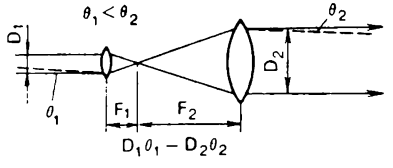

Fig. 1.26. Collimation of beam by two-lens telescope

$$\theta_i d_i = \theta_f d_f \tag{1.30}$$

where θ_i and d_i are respectively the divergence angle and the diameter of the initial beam at its entry to the telescope, and θ_f and d_f are respectively the divergence angle and the diameter of the final beam emerging from the telescope. The equation assumes that the laser beam completely fills the telescope.

The focusing of TEM_{00} beam with a lens placed a distance l_0 away from the initial beam waist w_0 (at $l_0 > f$) affords the following concentration of the beam of diameter $2w_f$ at a distance l_f:

$$1/w_f^2 = (1/w_0^2)(1 - l_0/f)^2 + 1/(f\theta)^2 \tag{1.31}$$

where f is the lens focal length, and θ the divergence of the focused beam.

By increasing the distance l_0 from the lens to the beam waist inside the cavity (an increase in the beam diameter at the lens being limited by the lens aperture) and also by reducing the lens focal length or the beam divergence, it is possible to decrease the focused spot size.

The requirement for a minimum distance from the lens to the material being worked provides a lower limit to the value of f, which is commonly equal to a few centimeters; in a Kvant-16 setup, for example, this distance is 6 cm.

The distance l_f from the waist to the focusing lens is

$$l_f = f + (l_0 - f)\frac{f^2}{(l_0 - f)^2 + (w_0/\theta)^2} \tag{1.32}$$

As a rule, l_f is larger than f, and the beam diameter in the focal plane is greater than $2w_f$. Since at low values of θ the difference between l_f and f is small, F. Kaczmarek [2] recommends the following expression for estimating the diameter of a focused TEM_{00} beam and

even that of a multimode beam:

$$w_f = f\theta \tag{1.33}$$

or

$$w_f = f\lambda/\pi w \tag{1.34}$$

For low-diverging TEM_{00} beams, the size w of the beam ahead of the focusing lens is taken as a useful parameter instead of the radius w_0 of the initial waist since it is then easy to estimate the beam diameter at the focus.

The diameter of a focused TEM_{00} beam whose intensity at the edges of the spot decreases to approximately q/e^2, i.e. to 86.5% of the total intensity, is regarded to be a minimum.

At $a \geqslant 2.8w$, where a is half the diameter of the focusing lens, the diameter of the focused diffraction-limited spot is given by

$$D_{dif} = 1.22\lambda f/2a \tag{1.35}$$

If 63% of the total radiation intensity falls within the spot, then

$$D_{dif} = \lambda f/\pi a \tag{1.36}$$

The diffraction limited size of the focused spot is only achievable in the case of aberration-free lenses and under ideal beam distribution conditions. In practice, the beams obtained are more complex in spatial profiles and mode structures. Also, insufficiently perfect focusing elements, for example, lenses with spherical aberrations, do not allow a laser to achieve diffraction limited performance. The minimum spot size of a TEM_{00} beam at the focus is not less than 50 μm for a CO_2 laser operating at the 10.6-μm wavelength and 5 μm for a YAG laser at $\lambda = 1.06$ μm.

Another important parameter characterizing the size of a focused laser beam is the depth of focus. This is the distance from the waist of the focused beam to the plane in which the intensity drops to half the maximum value achieved at the focus. For a focused Gaussian beam, the depth of focus is [2]

$$z_f = \pm\lambda f^2/\pi w_f^2 \tag{1.37}$$

where w_f is the radius of the beam incident on the focusing lens.

For practical purposes, another definition of this parameter is more convenient: the depth of focus is the distance from the focused beam waist to the plane in which the beam diameter increases to a specified value. For example, an increase in the beam diameter by 5 or 10% over the value $2w_f$ corresponds to the motion of the target plane relative to the waist along the beam axis for a distance, respectively,

$$z_f = \pm 0.32\pi w_f^2/\lambda$$

or

$$z_f = \pm 0.46\pi w_f^2/\lambda, \tag{1.38}$$

The properties of optical systems heavily suffer from lens abberations, of which spherical aberrations are most detrimental to a collimated monochromatic beam. The effect of spherical aberration shows up when the light rays that emanate from a point source and pass through the lens at different distances from its optic axis are not brought to a common point. The result is a blurring of the focal spot and increase in the spot size. Spherical aberration grows with a decrease in the lens focal length and thus places the practical lower limit to the acceptable values of f for the lens. This effect is reduced in two ways: by using aspherical lenses with specially selected surface shapes and by modifying the shapes of spherical lenses to obtain the optimal ones. Of all the practical lenses used, flat-convex (plano-convex) lenses convex toward the beam have the least spherical aberrations. For focusing of CO_2 laser radiation, J.F. Ready [1] recommends germanium meniscus (convex-concave) lenses with refractive index equal to four, which are concave away from the beam. In Fig. 1.27 are given the calculated values of the focal spot diameter as a function of the relative aperture (F-number) for the cases where either spherical aberrations or diffraction effects determine the spot diameter. In the calculations, the diameter of the lens optimized in shape was taken equal to 2.54 cm; the refractive index was 1.5 and $\lambda = 1$ μm. At large values of the relative aperture the effect of spherical aberration predominates and the diffraction limit proves unattainable since the spot size increases with the relative aperture, which is contrary to expression (1.30).

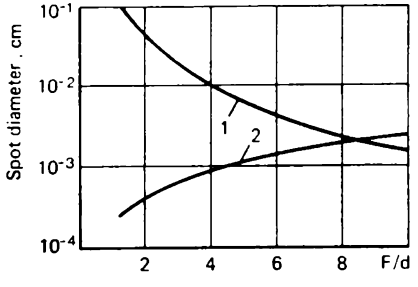

Fig. 1.27. Calculated values of focal spot diameter versus relative aperture F/d for the cases of spherical aberration *1* and diffraction effects *2*

A maximum radiation intensity (power density) at the focus center results if the lens diameter is 1.07 times the TEM_{00} beam diameter:

$$q_{f\,max} = 2.6P\,(f\lambda/a)^{-2} \tag{1.39}$$

where P is the total laser radiation power.

The diffraction can be limited by using a lens whose diameter is 2.8 times the beam diameter and the depth of focus is

$$z_f = \pm 5.56\lambda f^2/2\pi a^2 \tag{1.40}$$

A laser beam with two or more modes has a complex structure in distinction from that of the TEM_{00} beam and a large divergence angle θ, which appreciably increases the beam diameter at the focus.

For example, in a 30-W CW CO_2 laser operating in two or three modes, a lens with $f = 50$ mm focuses the beam to a spot of 135-150 μm in diameter; if the beam contains four modes, the spot size grows to 200 μm.

The radiation intensity distribution over the cross section of the focused multimode beam does not show a definite character as does the Gaussian beam because of a complex mode structure combined with the complex intensity distribution in the beam ahead of the lens. To estimate the diameter of the focused multimode beam, it is well to use expression (1.40) with consideration for an increase in the total divergence angle θ which varies directly as the mode number m. For a plane-parallel cavity,

$$\theta = \lambda m d^{-1} \tag{1.41}$$

In a Q-switched CW YAG laser, the divergence angle covering 90% of the power for the TEM_{00}, TEM_{01}, TEM_{10}, TEM_{11}, TEM_{20}, and TEM_{21} modes is equal to 1.8, 2.3, 2.8, 3.12, 3.3, and 3.36 mrad respectively.

The diameter of the beam extracted from a spherical cavity and the beam divergence angle increase with the transverse mode number in comparison with the values of these parameters for the fundamental TEM_{00} mode.

The calculated and experimental values of the focused beam diameter commonly differ to a large extent. In practice, it is advisable to determine the diameter of a focused multimode beam experimentally by measuring the diameter of the region exposed to the beam on any absorbing surface, for example, on a thin layer of metal deposited on a glass substrate.

The power density required to vaporize a thin gold layer on corundum substrate is $q = 10^8$ W/cm^2 at a pulse duration of 0.2 ms ($\lambda = 1.06$ μm). To vaporize a layer of tantalum nitride on glass, the irradiance required is 5×10^4 W/cm^2 at $\tau = 1$ to 6 ms ($\lambda = 0.69$ μm). A thin gold layer on a glass substrate moving at a rate of 1 m/min vaporizes on exposure to CW radiation ($\lambda = 10.6$ μm) of a power density of 5×10^3 W/cm^2.

In order to obtain the focused beam of requisite parameters, it is necessary to correctly select the mode structure and geometry of the beam, the focusing lens or the system of lenses and, besides, to locate most favorably the beam focus relative to the target surface.

Practical systems of lenses must be able to provide the required characteristics of the beam in the interaction region, primarily the power density and the focused beam waist. They also must absorb a small amount of radiation power, be durable and inexpensive.

Choice of the mode structure and geometry of a focused beam. The TEM_{00} beam is notable for its highest concentration of focused laser power. Fig. 1.28 illustrates some design and dimensional features of lasers, which enable these devices to operate in the fundamental TEM_{00} mode.

Obtaining the TEM_{00} beam of high energy from solid-state lasers is a rather complex task because the energy of this beam is

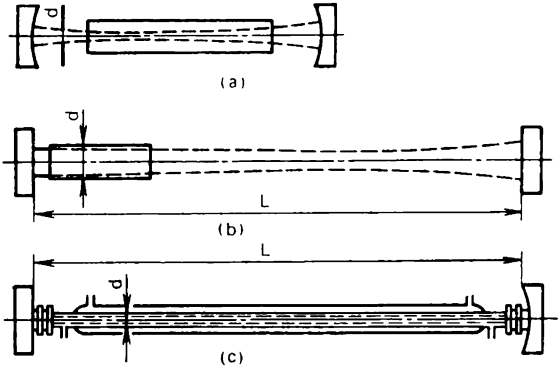

Fig. 1.28. Methods of obtaining the lowest order TEM_{00} mode: (*a*) solid-state laser with aperture $d = 1$-2 mm in optical cavity; (*b*) solid-state laser with long cavity, of length $L = 2$ m, for example; (*c*) CO_2 laser with long optical cavity which inhibits operation on higher-order modes by virtue of small inner diameter $d/2 \approx 2w$ of laser tube

a fraction of the energy of a multimode beam. This is due to large diameters of laser rods, light-induced deformations of rods, inhomogeneities in the laser material, etc.

Gas lasers are rather easily adaptable to work in the Gaussian mode; the single-mode power output they produce is not below one half the multimode output. A lens beam expander such as depicted in Fig. 1.26 can be used ahead of the final focusing lens to decrease the divergence and hence the diameter of the focused Gaussian beam [1]. The distance between the lenses is equal to the sum of their focal lengths.

Laser processing devices mostly employ Galilean telescopes since they can be made more compact [1]. These telescopes provide $2\times$ to $5\times$ magnification of the beam with an output beam diameter of 20-30 mm and also reduce the beam divergence by a factor of 10.

A disadvantage of the focused TEM_{00} beam is that its intensity distribution at the focus is nonuniform. This results in a blurring of the outer edges of the interaction region on the target surface and in a reduced accuracy of laser treatment, machining to size, for example.

Choice of focusing lenses and reflecting objectives. The use of lasers in industrial applications calls for the correct choice of focusing lenses and reflecting objectives (reflectors), which determine the operating characteristics of industrial lasers. CW CO_2 lasers harnessed to cut thick plywood sheet and other nonmetals such as leather and plastic sheet materials utilize lenses of a large focal length, up to 30 cm, to obtain the waist of the focused beam at a large distance from the lens [1, 2].

It is not advisable to use lenses of a smaller focal length in material processing applications since the disintegration products vaporizing from the target may damage the lens surface. Besides, such lenses heavily suffer from spherical aberrations. A minimum focal length f_{min} at which a simple lens proves advantageous for use is near 1 cm [1]. The value of f_{min} at which it is possible to avoid the effect of spherical aberration of a lens depends on the beam diameter, wavelength, and refractive index [1, 2].

TABLE 1.9. **Minimum Focal Length**

Beam diameter, mm	Focal length, mm, for laser		
	Ruby[1]	Nd-YAG[1]	CO_2[2]
1	3.4	3.0	0.7
2	8.6	7.5	1.7
3	14.7	12.8	2.9
4	21.6	18.8	4.3
5	29.1	25.3	5.8

[1] Glass lens with $n=1.5$.
[2] Germanium lens with $n=4$.

Table 1.9 lists the values of f_{min} of lenses for various lasers to focus the beam of the specified diameter with allowance made for lens aberrations. To obtain a small focal spot, a short-focus lens should be chosen in accordance with the data presented in Table 1.9. At a definite refractive index n, spherical aberration can be brought to a minimum by properly selecting the value of form factor g:

$$g = (r_1 + r_2)(r_1 - r_2) \tag{1.42}$$

where r_1 and r_2 are the radii of curvature of the first and the second lens respectively. At $g = 1.5$, spherical aberration drops to a minimum when $n \approx 0.71$. The plano-convex lens with $g = 1$ that is convex toward the beam should be regarded as an optimal choice for practical applications. Its spherical aberration is slightly higher than a minimum value, but this lens is easier to manufacture than the lens with $g = 0.71$ [1].

The germanium lens with $n = 4$ for CO_2 lasers shows a minimum spherical aberration at g approaching 5, which is the case for the converging meniscus lens convex toward the beam.

Large losses of CO_2 laser radiation in optical elements of transmission optics (NaCl, KCl, ZnSe, etc.), combined with a short lifetime and high cost of optic and metal-optic elements, determine

the preferential use of single-element lenses and two-mirror reflectors (Fig. 1.29).

For an ideal aberration-free reflector which ensures the same focal spot diameter d_0 as d_f for a real objective at a certain angle α_0 of focusing, the region of ideal focusing conditions is

$$\alpha < \alpha_0 = 0.44/\sqrt{AD} \tag{1.43}$$

where α is the angle of focusing, A a constant accounting for the type of objective, and D the diameter of an unfocused beam.

Figure 1.30 displays the regions of ideal conditions of focusing of radiation by optical systems illustrated in Fig. 1.29; some optical systems have additional parameters defining the position of ideal boundaries for α_0. For the lens, the additional parameter is the refractive index n; for the reflectors of Fig. 1.29*c* and *d*, this is the ratio of the free focal section l to the focal length f, $u = l/f$; for the Cassegrain reflector, this is the magnification of the telescopic system, $m = D_2/D_1$, where D_2 and D_1 are the diameters of light spots on the large and the small mirror respectively. As seen from Fig. 1.30, short-focus optical systems are realizable with the aid of asymmetric reflectors of Fig. 1.29*b* and *e*, though they need baffles to control the axial portion of the beam. NaCl and KCl lenses and also an oblique-angled reflector with one spherical mirror exhibit the poorest focusing properties. Symmetric Cassegrain systems are a reasonably good choice where there is a need to obtain beams of the highest density. For cutting and welding of thick workpieces, in which case the longitudinal dimensions of the beam waist must be comparable to

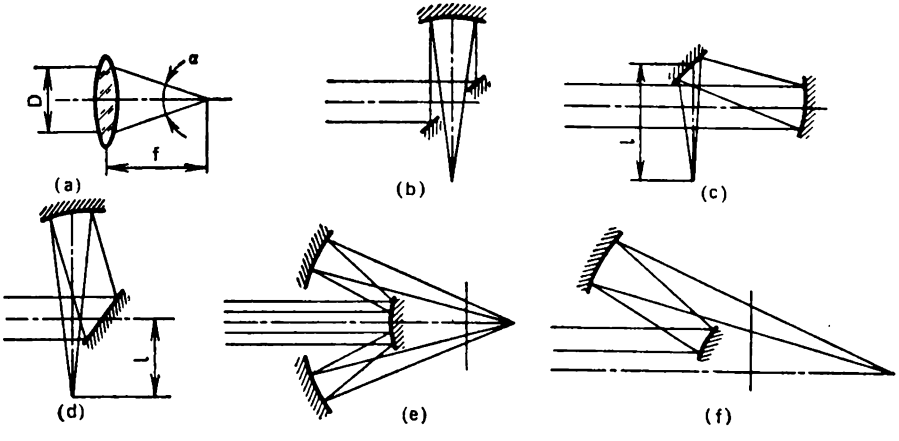

Fig. 1.29. Types of objectives used in industrial lasers: (*a*) lens; (*b*), (*c*), (*d*), reflectors, each with one spherical mirror; (*e*) center-fed Cassegrain reflector; (*f*) oblique-angled Cassegrain reflector

the metal thickness [9, 10], it is advisable to apply ZnSe lenses or Cassegrain reflectors of the type demonstrated in Fig. 1.29*f*.

The mirror arrangements of Fig. 1.29 give focused spots of large diameters, for which reason they can be put to advantageous use in welding of pieces over 2 cm thick by a high-power beam or in industrial processes which do not require the beam of enhanced intensity in the interaction zone.

The typical factors that complicate beam focusing are: (1) absorption of the laser radiation energy by lenses and mirrors, which can result in damage to these optical elements; (2) ejection of vapors, solid particles, and other disintegration products from the laser-material interaction region, which injure the lens surface, scatter and weaken the emitted radiation in the focal plane.

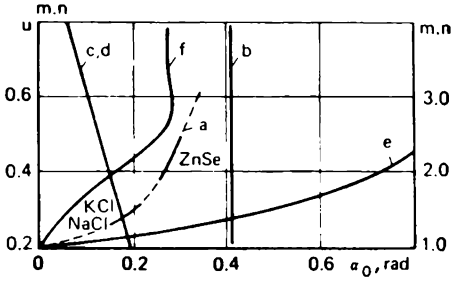

Fig. 1.30. Regions between curves and y-axis where ideal conditions exist for focusing the beam of $D = 5$ cm with objectives of Fig. 1.29 depending on parameters n, m, and u

To prolong the life of optical systems, a practical approach is to use replaceable protective shields sited ahead of lenses and mirrors or reflectors with long focal lengths, properly locate optical elements at a safe distance from the target, remove vapors and particles from the heat-effected zone with a gas jet, etc.

Choice of the site for the waist of a focused laser beam. In focusing either Gaussian or multimode beams the beam waist displaces a little beyond the focus of the focusing lens or reflector. For a highly divergent multimode beam, the waist shift reaches 2 or 3 mm. It is expedient to account for this shift in designing optical systems for industrial lasers in order to provide operation safety and also to minimize the size of the focused beam spot on the sample being worked.

1.11. OPTICAL MATERIALS FOR CO_2 LASERS

The damage threshold for optical materials limits some potential industrial applications of both pulsed and CW CO_2 lasers. The reason is that high-power CO_2 lasers impose stringent requirements on these materials, of which the main ones are:

— low absorptance β at $\lambda = 10.6$ μm;
— high limit of elasticity or high bending strength σ_b;
— high thermal conductivity;
— minimum variation in the refractive index with temperature;

— high heat capacity;
— low coefficient of thermal expansion, α_{ex};
— high critical temperatures such as the melting point and dissociation point, depending on the mechanism of destruction of the crystal in question;
— workability and nonhygroscopicity.

Table 1.10 gives the values of absorptance β, diameter D_{max}, and bending strength σ_b of ionic and semiconductor crystals used in CO_2 lasers [11].

TABLE 1.10. **Characteristics of Optical Materials**

Material	n, at λ=10.6 μm	Absorptance β at λ=10.6 μm			D_{max}, mm	$\sigma\times10^5$, Pa
		β_{exper}	theoretical			
			β_{max}	β_{min}		
		cm^{-1}				
Ionic crystals						
BaF_2	1.39	0.13-0.17	0.13	0.13	45	273
KCl	1.46	$(2\text{-}4)\times10^{-3}$	—	—	35	23
KCl, high-purity		$(1\text{-}4)\times10^{-4}$	6.6×10^{-3}	7×10^{-5}	10	
KCl, strengthened		1×10^{-3}	—	—	10	200
NaCl	1.49	$(2\text{-}4)\times10^{-3}$	—	—	35	25
NaCl, high-purity		1×10^{-3}	9×10^{-4}	1×10^{-3}	10	
NaCl, strengthened		1.5×10^{-3}	—	—	10	300
KBr	1.52	2×10^{-3}	1×10^{-5}	1×10^{-7}	30	11
CsI	1.74	2×10^{-3}	—	1×10^{-9}	30	40
AgCl	1.98	1×10^{-2}	—	—		
KRS-6	2.17	4×10^{-4}	6×10^{-5}	10^{-7}	40	320
KRS-5	2.37	6×10^{-4}	8×10^{-5}	10^{-7}	40	410
Semiconductor materials						
ZnSe	2.40	$(2\text{-}9)\times10^{-3}$	2×10^{-3}	10^{-4}	10	500
Diamond	2.41	1×10^{-2}	—	—	—	10^5
CdTe	2.67	—	2×10^{-3}	10^{-4}	—	210
CaAs	3.3	$(1\text{-}5)\times10^{-2}$	8×10^{-4}	10^{-4}	10	1400
Ge	4.00	$(4\pm2)\times10^{-2}$	—	—	20	950
Ge, pure	—	2.7×10^{-2}	—	—	65	—
Ge, high-purity	—	2.2×10^{-2}	—	2×10^{-2}	65	—
Ge, optimized	—	1.8×10^{-2}	1.3×10^{-2}	—	—	—

Table 1.11 presents technical data for many optical materials listed in Table 1.10. Figs. 1.31 and 1.32 illustrate the transmissivity and absorptivity respectively for a number of materials used in CO_2 lasers as functions of the wavelength [11].

TABLE 1.11. **Technical Data on Optical Materials for CO_2 Lasers**

Parameter	Diamond	ZnSe	CdTe	Ge	CdS	GaAs	NaCl	KCl
Refractive index at 10.6 μm	2.41	2.4	2.67	4.0	2.2	3.3	1.49	1.46
Reflectivity for uncoated surface, %	17	17	19	36	14	25	8.8	7.6
Absorptance β at 10.6 μm, % cm^{-1}	0.01	0.5	0.2	2	3	2	0.2	0.2
Resistivity, Ω cm	10^{15}	10^{12}	10^{8}	10^{2}	10^{3} (light)	10^{7}	—	—
Transmission band, μm	0.2-2 6.5 and over	0.5-20	2-28	3.23	0.5-16	1-18	0.25-16	0.3-20
Thermal conductivity, W cm^{-1} K^{-1}	20	0.21	0.07	0.6	0.27	0.46	0.1	0.1
Linear expansion coefficient, $\alpha_{ex} \times 10^{6}$, K^{-1}	1.05	8.53	4.5	6.1	—	5.7	44	36

The self-absorption in ionic crystals is low except for the very strong BaF_2 material. The calculated values of minimum losses are appreciably lower than the losses in real crystals on account of an additional absorption by defects and inclusions.

Salts of the KCl and NaCl types have an absorptance ranging into 2×10^{-3}-4×10^{-3} cm^{-1}, while for high-purity and perfect crystals the values of β are approximately a factor of 10 lower, but the latter possess a low mechanical strength, which limits their uses in powerful lasers. The available method of crystal strengthening that relies on plastic deformation by way of uniaxial compression of single crystals augments the strength by an order of magnitude

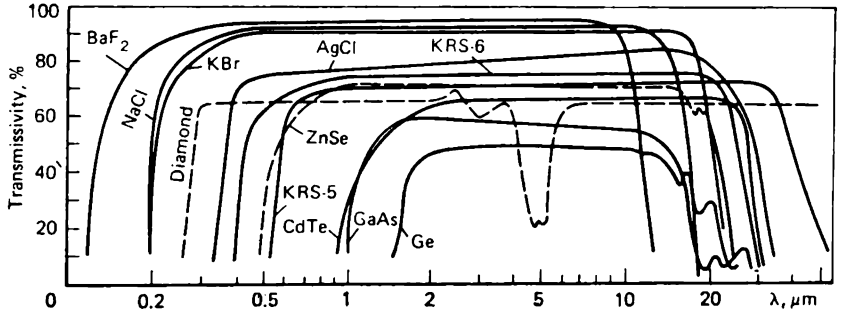

Fig. 1.31. Transmission of materials used in CO_2 lasers as a function of wavelength

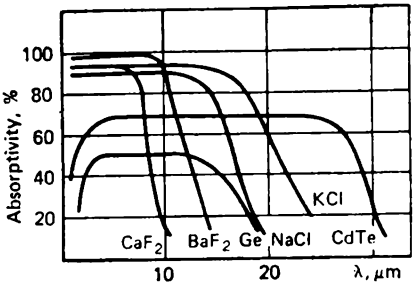

Fig. 1.32. Absorptivity of optical materials as a function of wavelength

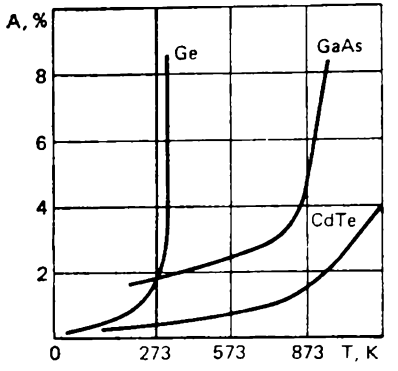

Fig. 1.33. Absorptivity A of some materials versus temperature at 10.6 μm

with an attendant increase in absorption by 1.5-2 times (in compressed KCl crystals, β is around 10^{-3} cm^{-1}).

Ionic crystals noted for better transmission as against semiconductor crystals are much inferior to the latter in strength, hygroscopicity, and thermal conductivity [11].

Insufficiently stable in properties are ZnSe and GaAs single crystals. For example, the absorption coefficient for ZnSe can vary from sample to sample by an order of magnitude depending on the starting material used and the conditions of crystal growth. In fairly narrow-gap semiconductors, powerful laser radiation leads to nonlinear absorption [11]. In germanium, the nonlinear growth of absorption begins even at 313 K, which inhibits its use in CO_2 lasers of very high power, whereas this nonlinear process affects ZnSe and GaAs only starting at 573 K. Fig. 1.33 displays the absorptivity A in percent for some materials plotted versus temperature at the 10.6-μm wavelength.

The criterion of the applicability of a given material for laser windows is the average power at which damage or excessive distortion does not yet occur [11].

The power density that initiates optical damage or optical breakdown determines the threshold of radiation resistance of a material, which is a function of a number of parameters, including the total power P_0, irradiation spot area s_0, and dwell time (time of exposure). The damage threshold for a laser window is the value of power density which the uncooled window is still able to withstand during the time it takes the steady temperature field to be set up or during the time required for the radial heat flow to reach the cooler, following which damage begins.

Mirrors for CO_2 lasers. The spectral range over which CO_2 lasers operate and high power outputs from these devices place additional requirements on the substrate materials and reflection coatings of laser mirrors. These requirements mainly relate to the thermal behaviour of mirrors and reduce to the demand to be met to obtain the maximum possible reflectivity and to create the optimum conditions for mirror cooling in an effort to increase the threshold for the laser induced damage in mirrors. In this respect, metal substrates, most often copper ones, with thin refractory-metal coatings of high reflectivity at 10.6 μm are equal to the job. The basic technical data on the most popular mirrors are given in Table 1.12.

TABLE 1.12. **Technical Data on Metal Mirrors**

Material	Reflectivity, %	Polish of surface		Damage threshold for laser	
		spherical	plane	pulsed, J cm^{-2}	CW, kW cm^{-2}
Ni-Cu	98.8, > 99 (gold coated)	λ/10-λ/20	λ/20	5 ($\tau = 0.6$ μs)	1 (cooled)
Be-Cu	98 95.5 (gold coated)	λ/20	λ/20	100	—
Mo	> 98	λ/40	λ/40	35 ($\tau \approx 0.6$ μs)	200 ($t \sim 8$ s)
Commercial	> 99	λ/20	λ/10	to 100 ($\tau \approx 0.6$ μs)	> 10 (uncooled)
Cu, superfinished	> 99	λ/40	λ/40	130 ($\tau \approx 0.6$ μs)	10 (uncooled) 200 (cooled)
Superalloy (invar)	~ 97-98	~ λ/5-λ/10	λ/5-λ/10	—	—

Ni-Cu mirrors are made from high-purity copper free of micropores and cracks. The nickel coating produced by vacuum evaporation on the copper substrate is polished accurate to within λ/20 and then checked for defects and the degree of roughness. The nickel film is then given a thin gold coat to increase the reflectance and mechanical stability of the mirror during cleaning.

Be-Cu mirrors are mainly designed for spherical resonators with convex and concave reflecting surfaces and also for other optical systems applied in pulsed lasers producing pulses with energy densities of up to 100 J cm^{-2}. Good thermal contact between Be and Cu provides a fast heat removal from the mirror surface and

prevents local overheating that can encourage damage to the mirror. This type of mirror is sometimes coated with a thin gold layer to increase the mechanical strength and reflectivity of the mirror surface.

Molybdenum mirrors are used for high-power gas dynamic CO_2 lasers. However, the high cost of this type of mirror inhibits its wider uses despite the fact that a well polished Mo surface features excellent optical and mechanical properties and does not require expensive coatings. Besides, Mo is notable for its low temperature coefficient of linear expansion and high thermal breakdown threshold, so the Mo mirror can work without additional cooling.

Commercial copper mirrors find use in high-power CO_2 laser systems. The mirrors are given thin vacuum-evaporated dielectric films to protect the polished copper surface from oxidation and to increase the strength of the reflecting layer, thereby avoiding damage to the mirror during its cleaning.

Superfinished copper mirrors can fully comply with the requirements placed on the reflecting mirrors even without thin coatings. To ensure good performance of multikilowatt CO_2 lasers, metal mirrors as a rule operate with water cooling. Dielectric coatings increase the mechanical strength of reflecting surfaces and water cooling makes it possible to reach higher values of the damage threshold for laser mirrors.

Transparent materials for infrared devices. Various materials go into the production of optical elements for CO_2 lasers operating at the 10.6 μm wavelength. Consider the parameters of the main materials.

1. Diamond has an absorption coefficient β of 0.001 cm^{-1} at 10.6 μm and high thermal conductivity equal to 1.4 W cm^{-1} K^{-1}. It can serve as the starting material for small-size windows and focusing elements of CO_2 lasers with outputs from 10 kW and above.

2. ZnSe has $\beta_{10.6}$ approaching 0.005 cm^{-1}. It is suitable for large-size windows and is nonhygroscopic, unlike KCl that has β^*_{3-5} of around 0.002 cm^{-1}.

3. CdTe has $\beta_{10.6}$ of around 0.002 cm^{-1}, low thermal conductivity, and small cost. It can replace ZnSe in low-power CO_2 lasers of up to 500 W.

4. Ge commonly goes into the production of low-power lasers, has $\beta_{10.6}$ of about 0.012 cm^{-1} and $\beta_{5.25}$ of about 0.0018 cm^{-1} at 473 K. It is cheap and makes a suitable material for many varieties of elements of optical systems.

5. Silicon is applicable for work in the 3-5 μm spectral range. Its thermal conductivity is high and $\beta_{5.25}$ is near 0.0059 cm^{-1}. A high

---

* The subscript at β stands for the wavelength in μm.

temperature coefficient of linear expansion involves difficulties in depositing adhesive films on Si substrates.

6. GaAs finds limited uses in the 3-5 μm wavelength range. Its $\beta_{10.6}$ is near 0.01 cm^{-1} and thermodynamic parameters are similar to those of Ge.

7. NaCl is hygroscopic and therefore has limited uses, mainly for windows of high-power CO_2 lasers. Its $\beta_{10.6}$ approaches 0.0013 cm^{-1}.

8. KCl is hygroscopic, but since it has an extremely low value of $\beta_{10.6}$, in the order of 10^{-4} cm^{-1}, it is more popular than NaCl.

9. CaF_2 is nonhygroscopic and has β of around 5×10^{-4} cm^{-1}. It is suitable for work in the 3-5 μm wavelength range.

10. BaF_2 is nonhygroscopic, very sensitive to temperature variations, and its β is near 3×10^{-5} cm^{-1}.

References

1. J. F. Ready. *Effects of high power laser radiation.* New York, Academic Press, 1971.
2. Franciszek Kaczmarek. *Wstep do fiziki laserów.* Warszawa, Państwowe Wydawnictwo Naukowe, 1972.
3. N. G. Ryabtsev. *Materials of quantum electronics.* Moscow, Sovetskoe Radio, 1972 (in Russian).
4. B. R. Belostotsky, Yu. V. Lyubavsky, and V. M. Ovchinnikov. *Fundamentals of laser engineering.* Moscow, Sovetskoe Radio, 1972 (in Russian).
5. R. J. Pressley (ed.). *Handbook of lasers with selected data on optical technology.* CRC Press, Cleveland, USA, 1971.
6. Yu. V. Bayborodin, L. Z. Kriksunov, and O. N. Litvinenko (eds.). *Laser engineering handbook.* Kiev, Tekhnika, 1978 (in Russian).
7. R. W. F. Gross and J. F. Bott (eds.). *Handbook of chemical lasers.* New York, London, Syndey, Toronto, John-Wiley and Sons.
8. Yu. I. Kuklev and A. A. Uglov. *Survey of high-energy IR laser sources.* Fizika i Khimiya Obrabotki Materialov, No. 2, p. 3, 1975.
9. A. I. Skripchenko and A. K. Zinchenko. *On the choice of the focusing system for CO_2 laser material processing*, in Collected articles of the seminar "Application of high-intensity energy sources in welding". Leningrad, LDNTP, p. 45, 1983.
10. A. I. Skripchenko and A. V. Surkov. *Choice of optimum light beam parameters for laser welding.* Avtomaticheskaya Svarka, No. 2, p. 11, 1983.
11. N. V. Karlov and E. V. Sisakyan. Optical materials for CO_2 lasers: Physic Series, Izvestiya AN SSSR, 44: No. 8, p. 1631, 1980.

Chapter 2

ELECTRON BEAM PARAMETERS AND MEASUREMENTS

2.1. CW AND PULSED ELECTRON BEAM PARAMETERS

The electron beam (EB) parameters essential for material processing are the beam current I, accelerating voltage V, focusing system current I_f, working path length l from the focusing system to the target surface, and linear transport speed v.

Given the beam path l, current I_f, and power input P, we can determine the beam diameter d and hence the power density which is one of the governing parameters in material processing: $q = IV/(\pi d^2/4)$.

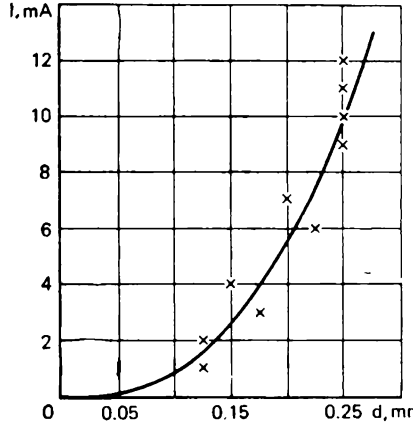

Fig. 2.1. Beam diameter versus current at constant accelerating voltage $V = 100$ kV for welding [1]

The quantity $Q = IV/v$ is not a decisive parameter because in EB welding, for example, any shape of the interaction region can be obtained at the same value of energy input per meter of weld seam depending on the power density q.

In pulsed operation, the average pulse power (W) is $P = IVf\tau$, where I is the pulse current, A; f the pulse repetition rate, Hz; and τ the pulse length, s.

The rate of processing in pulsed operation is $v = d\,(1 - K)/(\tau + \tau_w)$, where d is the diameter of the interaction region (point, or spot), K the point overlap ratio which is commonly equal to 0.5-0.9, and τ_w the pulse space width, s.

The pitch of points (center-to-center distance) is $S = v\,(\tau + \tau_w)$.

The pulse duration-to-pulse period ratio is known as the duty cycle $G = \tau/(\tau + \tau_w)$.

The beam diameter is the most essential parameter and is most difficult to determine.

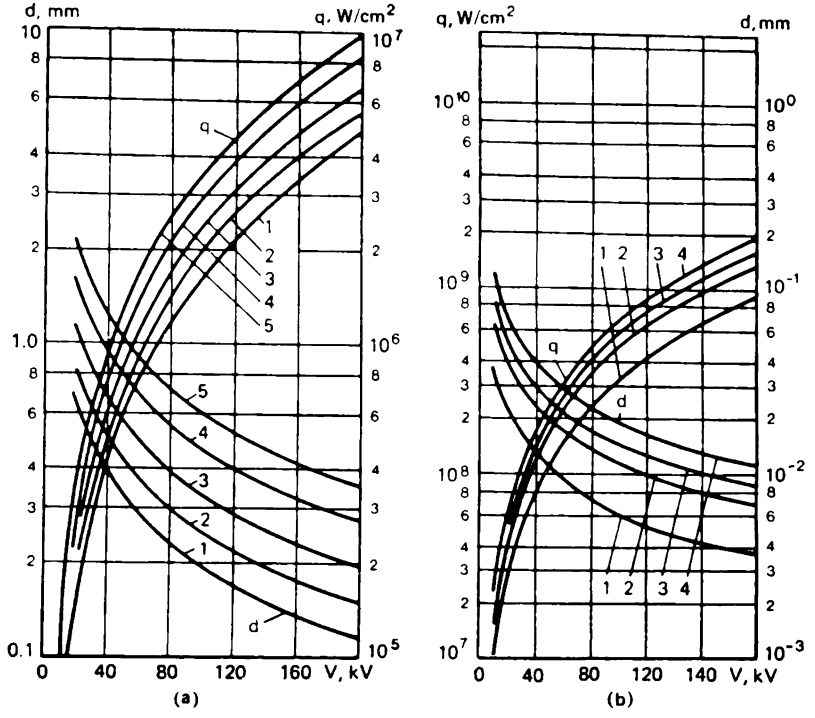

Fig. 2.2. Beam diameter d and power density q versus accelerating voltage at different values of power P [2]: (a) for welding: *1*, $P = 0.5$ kW; *2*, $P = 1$ kW; *3*, $P = 2$ kW; *4*, $P = 5$ kW; *5*, $P = 10$ kW; (b) for cutting: *1*, $P = 0.1$ kW; *2*, $P = 0.5$ kW; *3*, $P = 1$ kW; *4*, $P = 2$ kW

Given the density of the emission current from the cathode, cathode temperature, and spherical aberration of the lens system, we can estimate a minimum diameter of the focused spot of the electron beam at its maximum current [1, 2]:

$$d = s\,(I/V)^{3/8} \tag{2.1}$$

Here $s = [(4^{2/3}k/(\pi e)\,c^{2/3}f_0^{2/3}T/j]^{3/8}$ is a constant of the electron-optical system; k Boltzmann's constant, J/K; $e = 1.6 \times 10^{-19}$ C the electron charge; c a dimensionless constant for spherical aberration of the lens or lens system; f_0 the focal length, cm; T the cathode temperature, K; j the cathode emission current density, A/cm².

Considering expression (2.1), the power density is given by

$$q = \frac{1}{\pi}\left(\frac{2}{s}\right)^2 I^{1/4}V^{7/4}$$

Figures 2.1 and 2.2 illustrate the plots of the beam diameters calculated by formula (2.1) against current and accelerating voltage for welding and cutting.

2.2. ROTATING-PROBE MEASUREMENT METHOD

There are many methods for the experimental assessment of the diameter of an electron beam. A rotating-probe method is the simplest. The method relies on a thin rotating probe which cuts the electron beam normal to its axis and picks up a fraction of the beam current. From the oscilloscope trace of the probe current, we can then estimate the beam diameter: $d = 2\pi r\tau/T - \delta$, where r is the distance from the axis of rotation of the probe to the beam axis, τ the probe current pulse duration, T the period of revolution of the probe, and δ the probe diameter.

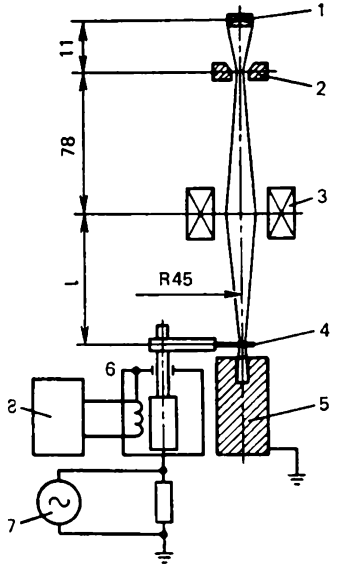

Fig. 2.3. Circuit connection of rotating probe in electron beam setup: *1*, cathode; *2*, anode; *3*, focusing system; *4*, rotating probe; *5*, collector; *6*, electric motor; *7*, oscilloscope; *8*, motor power supply

The rotating-probe method is a modification of the vibrating-probe method. Since the probe can scatter a large amount of power, this method is applicable for the analysis of high-power beams.

The circuit connection of the probe in an A.306.05 electron-beam test unit is shown in Fig. 2.3. The probe is a 0.1-mm diameter tungsten wire 5 to 7 mm long fastened to a 3-mm diameter metal rod with its coupling fitted on the shaft of a dc motor. The time of one revolution of the motor shaft, which is set by the oscilloscope, is 30 ms, and so the rotational speed is 33 rps.

The oscilloscope screen provides a means for focusing of the beam on the probe. The beam is considered to be focused optimally if the probe signal waveform has a minimum length (duration) for the given parameters of the beam.

To shield the probe from secondary electrons, the test unit is complete with a copper collector 2-3 mm distant from the plane of optimal focusing, i.e. the plane of probe rotation. The collector has a 10-mm deep hole about 3 mm in diameter to trap the beam. That is why the beam diameter measurement error from the effect of secondary electron emission is insignificant.

With the accelerating voltage V held constant at 20 kV probe responses are measured in steps at beam currents of 10, 20, 40, 60, 80, and 100 mA and at distances l from the probe to the focusing

system of 35, 45, 55, 65, 85, 105, and 125 mm. The parameters registered by the devices of the test unit of accuracy class 1 are the following: the beam current, accelerating voltage, focusing current, amplitude and length of the probe signal, and distance l accurate to 1 mm.

In the analysis of probe signals, the data obtained for the limiting values of current of 10 and 100 mA and distance l of 35 mm are left out of consideration to avoid large experimental errors. During measurements the diameter of the probe decreases on exposure to high temperatures approaching $\sim$2 700 K, which leads to an asymmetry of the probe response and a systematic error. This error is not allowed for since only the first half of the probe signal waveform is given scrutiny. The probe diameter decreases to about 70% of its value generally after 30-40 tests, following which it is changed for a new identical probe.

In the course of the data-handling procedure, a possible deflection of the probe from its axis due to a small probe diameter-to-length ratio (near 0.015) and a rather high rotational speed (33 rps) is not taken into account since it is insignificant. However, a large probe bending can lead to a distorted profile of probe current distribution and the waveform will then represent the current distributed along a certain arc rather than along the chord.

To process the data so obtained, a grid with an arbitrarily selected mesh width is laid on the photograph of the enlarged oscilloscope trace to measure the signal amplitude at different points. The probe curves so plotted point by point will give the picture of the radial distribution of the beam.

2.3. CURRENT DENSITY DISTRIBUTION OVER EB CROSS SECTION

In Fig. 2.4 are shown the probe current curves obtained experimentally from oscilloscope traces at different values of beam current and different distances l from the probe to the focusing system. Fig. 2.5 displays the radial current density distribution calculated by a numerical method from these experimental curves.

The distribution curves reveal that as the distance from the target surface to the focusing system decreases, the diameter of the electron beam decreases too, and the distribution becomes "sharper". For each specific distance from the target surface to the focusing system, the "sharpest" distribution occurs at low current values. With an increase in current, the beam diameter grows and the current density drops off.

The pattern of current density curves is approximately similar to that of curves for normal (Gaussian) distribution.

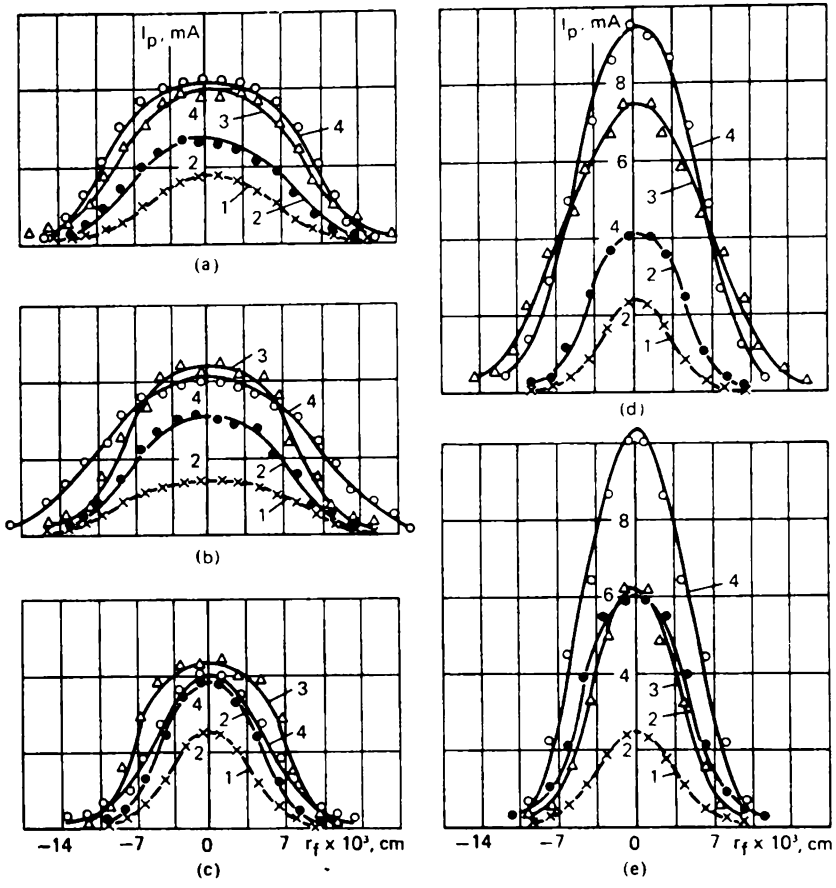

Fig. 2.4. Distribution of probe current I_p along the chord as a function of beam current and path length l from the focusing system to the target: (*a*), $l = 125$ mm; (*b*), $l = 105$ mm; (*c*), $l = 85$ mm; (*d*), $l = 65$ mm; (*e*), $l = 45$ mm; *1*, 20 mA; *2*, 40 mA; *3*, 60 mA; *4*, 80 mA; r_f is focused beam radius

Nearly half of the curves of Fig. 2.5 display minima along the current density axes; these minima shift in position with increasing current. As seen from Fig. 2.4, the probe current curves do not exhibit such minima. The character of radial current density distribution in the experimental curves, including the ones with minima, has been estimated from a few first central moments of distribution by using the method of expansion of an arbitrary function into the Chebychev-Hermite series.

The central moment μ_n of the current density distribution function $f(x)$, referred to the center line of distribution, or to the

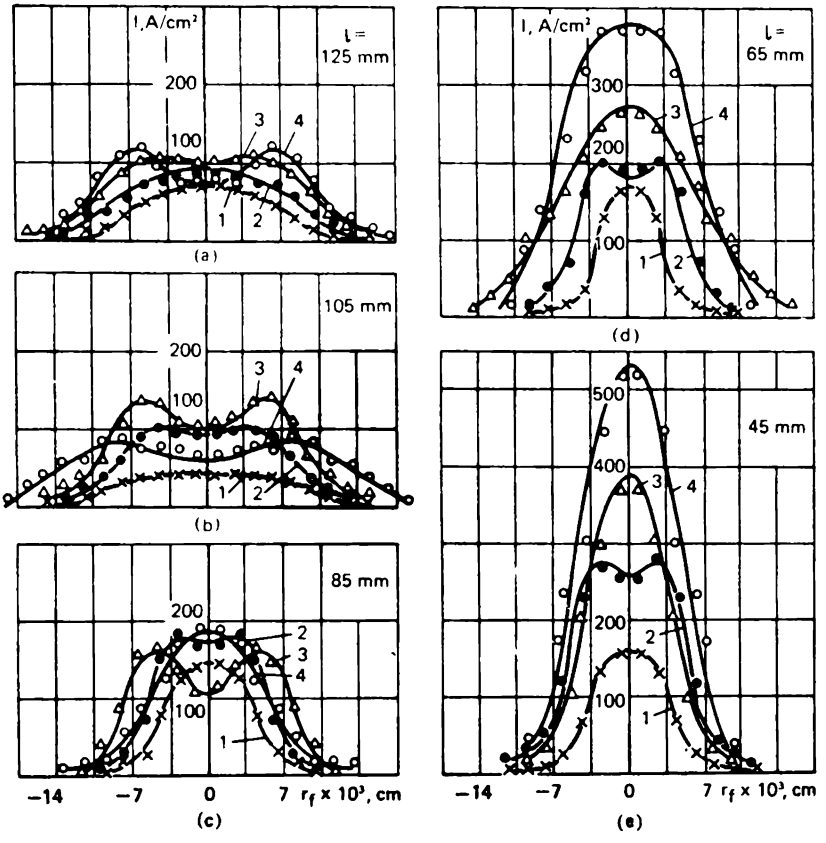

Fig. 2.5. Radial electron-beam current density distribution against beam current at different distances l from the focusing system: (*a*), $l = 125$ mm; (*b*), $l = 105$ mm; (*c*), $l = 85$ mm; (*d*), $l = 65$ mm; (*e*), $l = 45$ mm; beam current: *1*, 20 mA; *2*, 40 mA; *3*, 60 mA; *4*, 80 mA

symmetry axis, is given by

$$\mu_n = \int_{-\infty}^{+\infty} f(x)\, x_n\, dx$$

The zero term of distribution represents the area confined by the distribution curve depicted in Fig. 2.6:

$$\mu_0 = \int_{-\infty}^{+\infty} f(x)\, dx$$

For the symmetrical distribution, the first term μ_1 is always equal to zero, as is the case for all the odd terms. The ratio of the second central moment μ_2 to the zero term μ_0 represents the variance (cm^2) of distribution, $\sigma^2 = \mu_2/\mu_0$.

The standard (root-mean-square) deviation (cm) of the current density distribution from the Gaussian distribution is $\sigma = \sqrt{\mu_2/\mu_0}$.

On reducing the current density distribution to the Gaussian distribution

$$f(x) = \frac{\mu_0}{6} \sum_{n=1}^{\infty} [(-1)^n/n!] H_n^* \varphi^{(n)}(x/\sigma)$$

(where H_n^* stands for Chebychev-Hermite polynomials and $\varphi^{(n)}(x/\sigma)$ denotes the normal distribution function and its derivatives), we find that the concentration coefficient (cm^{-2}) for the current density distribution across the beam is $k = 1/2\sigma^2$ and the EB diameter (cm) at a 5% level of the amplitude $f(x)$ is $d_{0.05} = 3.46/\sqrt{k}$.

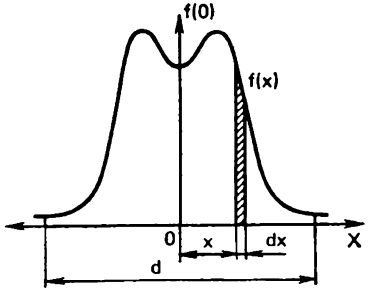

Fig. 2.6. Graph illustrating the estimation of central moments for current density distribution

The calculated parameters of current density distribution are given in Table 2.1.

In most cases the concentration coefficient k decreases with increasing current for a given distance l. This coefficient increases with decreasing beam path l at the same current. The calculated values of the beam diameter at 5% of the maximum current density are correlated to the beam diameter values obtained below at half the height of the probe current curve.

The accuracy of experiments is judged by comparing the total beam current at which the probe current curve was plotted with the volume ascribed to the current density curve obtained from the given probe current curve.

The current density at an arbitrary point is $f(r) = f(0) \times \exp(-kr^2)$, where $f(0)$ is the maximum value of current density.

The volume ascribed to the current density curve is $V = \pi f(0)/k$.

The estimates show that the difference between the total beam currents determined experimentally and by calculations reaches about 15%.

The experimental data confirm that the current density distribution in a section through an electron beam follows, to a suf-

TABLE 2.1 Current Density Distribution Parameters

Total beam current I, mA	l, mm	μ_2, A	μ_0, A/cm^2	σ^2, cm^2	k, cm^{-2}	$d_{0.05}$, mm
20	125	2.24×10^{-2}	5.8×10^{2}	3.86×10^{-5}	1.3×10^{4}	0.304
40		4.02×10^{-2}	8.8×10^{2}	4.57×10^{-5}	1.1×10^{4}	0.330
60		7.7×10^{-2}	1.3×10^{3}	5.93×10^{-5}	0.84×10^{4}	0.376
80		8.45×10^{-2}	1.33×10^{3}	6.36×10^{-5}	0.79×10^{4}	0.390
20	105	2.42×10^{-2}	4.54×10^{2}	5.32×10^{-5}	9.4×10^{3}	0.356
40		4.42×10^{-2}	1.01×10^{3}	4.37×10^{-5}	1.14×10^{4}	0.324
60		6.34×10^{-2}	1.39×10^{3}	4.57×10^{-5}	1.1×10^{4}	0.330
80		1.4×10^{-1}	1.31×10^{3}	1.066×10^{-4}	4.7×10^{3}	0.505
20	85	1.6×10^{-2}	8.32×10^{2}	1.93×10^{-5}	2.59×10^{4}	0.215
40		2.87×10^{-2}	1.25×10^{3}	2.28×10^{-5}	2.19×10^{4}	0.234
60		5.18×10^{-2}	1.4×10^{3}	3.7×10^{-5}	1.35×10^{4}	0.316
80		4.14×10^{-2}	1.32×10^{3}	3.14×10^{-5}	1.50×10^{4}	0.275
20	65	1.17×10^{-2}	7.38×10^{2}	1.58×10^{-5}	3.16×10^{4}	0.194
40		2.15×10^{-2}	1.34×10^{3}	1.61×10^{-5}	3.11×10^{4}	0.197
60		1.15×10^{-1}	2.48×10^{3}	4.62×10^{-5}	1.08×10^{4}	0.332
80		1.02×10^{-1}	3.14×10^{3}	3.25×10^{-5}	1.54×10^{4}	0.280
20	45	1.7×10^{-2}	8.32×10^{2}	2.04×10^{-5}	2.45×10^{4}	0.221
40		5.23×10^{-2}	1.98×10^{3}	2.64×10^{-5}	1.9×10^{4}	0.251
60		4.24×10^{-2}	2.12×10^{3}	2.0×10^{-5}	2.5×10^{4}	0.219
80		8.9×10^{-2}	3.46×10^{3}	2.57×10^{-5}	1.95×10^{4}	0.247

ficient degree of accuracy, the normal distribution law. From the viewpoint of electron beam technology, it is important to consider the current density minima present on the axes of some experimental distribution curves. A number of researchers [3, 4, 5, 6] plotted radial current-density distribution curves which inherently exhibited current density minima along the beam axis at large currents.

In different sections of the same beam, the current density distribution took the shape of a rectangle, a curve with a minimum on the center line, and a curve of normal distribution (Fig. 2.7).

The experimental distribution curves throw a clear light on the actual structure of the electron beam shaped by the A.306.05 setup. This setup does not stabilize either the beam current or the focusing current. This factor combined with the field distortion can lead to the "phase shift" and the appearance of a minimum on the axis

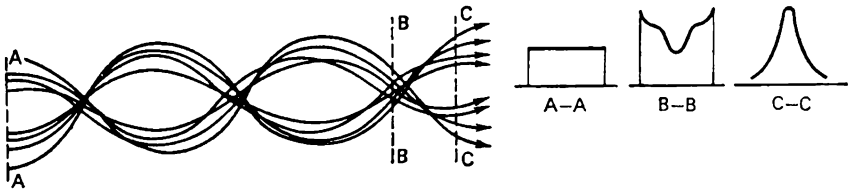

Fig. 2.7. Trajectories of electrons traveling from cathode points located at different distances from the axis [5]

of the distribution curve. Fig. 2.8 displays circular fusion zones produced in corrosion-resistant steel during 5 ms by the beam from the A.306.05 setup. That the middle area of the fusion spot struck by the beam of cross section B-B is left unmelted attests to a temporary decrease in the intensity of the beam along its axis.

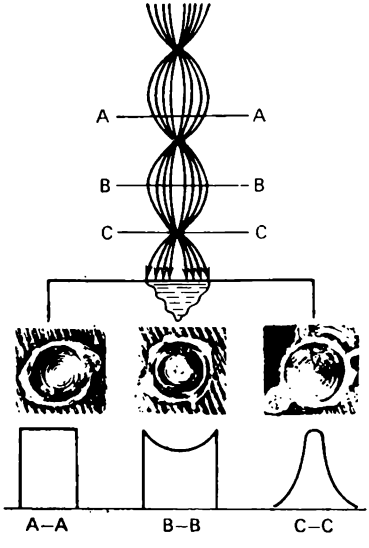

Fig. 2.8. Sketch illustrating the pulsating electron beam and top views of fusion regions corresponding to current density distributions shown at the bottom in three cross sections of the beam

Apart from the above factors that affect the temporal and spatial distribution of the intensity of the EB in its cross section, there is also a "methodical" factor. The analysis of various methods for solving the Abel equation has shown that the Pierce method gives the understated results along the axis, which may lead to a "depletion" of the beam axial intensity.

The measurements carried out by the rotating-probe method reveal the dependence of the probe current on the coordinate x coincident with the direction of motion of the probe. Of practical interest is the current density distribution on the beam radius, $I(r)$, rather than the experimentally obtained function $I(x)$.

The experimental function $I(x)$ is related to the radial current density distribution function $I(r)$ for an axisymmetrical beam by the Abel equation [7]:

$$I(x) = 2\int_{x}^{R} \frac{I(r)\, r\, dr}{(r^2 - x^2)^{1/2}} \qquad (2.2)$$

where R is the beam radius.

$I(r)$ is found from equation (2.2) by inverse transformation [4]

$$I(r) = -\frac{1}{\pi} \int_r^R \frac{I'(x)\,dx}{(x^2 - r^2)^{1/2}} \tag{2.3}$$

Since the form of $I(x)$ is known beforehand, approximation methods are used to define the function $I(r)$, which involve either the approximation of $I(x)$ by a suitable polynomial in order to solve analytically equation (2.3) or the numerical integration of this equation.

The numerical integration of equation (2.3) enables us to avoid a rather complex and awkward approximation procedure involved in the analytical solution of this equation, which must be found for each function $I(x)$ obtained in the experiment.

At present there is no as yet universal reliable method for the solution of equation (2.3) because of its ill-conditioned form [8]. The functions $I(r)$ presented by a number of workers are derived from experimental functions $I(x)$ with the aid of various recalculation methods. This causes difficulties in comparing the available data.

From the analysis of some papers it follows that the form of distribution functions $I(r)$ derived from the recalculation of the experimental function $I(x)$ depends on the numerical integration procedure used, form of the function $I(x)$, and integration step. The functions $I(r)$ obtained by numerically integrating equation (2.3) can differ rather substantially from the functions derived analytically from the same experimental data after approximating the function $I(x)$ by a polynomial. In particular, the function $I(r)$ implemented by numerical integration can have a false minimum on the symmetry axis of an electron beam.

The current density minimum on the electron beam axis may have a physical nature [5], but the distribution function $I(r)$ may assume a distorted profile on account of the incorrect application of the specific procedure of numerical integration.

A feature common to all the methods for the numerical solution of equation (2.3) is the limitation on the beam radius R, which depends on the experimental conditions, i.e. conditions of measurement of $I(x)$. Consider whether this limitation relates to a possible emergence of the false minimum on the electron beam axis of the function $I(r)$ [9].

Denoting $I(r) \equiv \varphi(r, R)$ and replacing the integration variable in equation (2.3), we can write

$$\varphi(r, R) = -\frac{1}{\pi} \int_r^R \frac{I'(x)\,dx}{(x^2 - r^2)^{1/2}}$$

$$= -\frac{2}{\pi}\int_0^{(R-r)^{1/2}} \frac{I'(r+z^2)}{(z^2+2r)}\,dz \tag{2.4}$$

$$\frac{\partial\varphi}{\partial r} = \frac{1}{\pi}\frac{I'(R)}{(R^2-r^2)^{1/2}} - \frac{2}{\pi}\int_0^{(R-r)^{1/2}} \frac{I''(r+z^2)}{(z^2+2r)}\,dz$$

$$+\frac{2}{\pi}\int_0^{(R-r)^{1/2}} \frac{I'(r+2z^2)}{(z^2+2r)^{3/2}}\,dz \tag{2.5}$$

where

$$z^2 = x - r \tag{2.6}$$

On the beam axis,

$$\left.\frac{\partial\varphi}{\partial r}\right|_{r=0} = \left|\frac{1}{\pi}\frac{I'(R)}{R} - \frac{2}{\pi}\int_0^{R^{1/2}} \frac{I''(z^2)}{z}\,dz\right.$$

$$+\frac{2}{\pi}\int_0^{R^{1/2}} \frac{I'(z^2)}{z^3}\,dz \tag{2.7}$$

In the general case, the derivative $\left.\frac{\partial\varphi}{\partial r}\right|_{r=0}$ can be either positive or negative for the monotonic function $I(x)$.

Let the derivative $\partial\varphi/\partial r$ on the beam axis be negative for an infinite R:

$$\left.\frac{\partial\varphi_\infty}{\partial r}\right|_{r=0} = \lim_{R\to\infty}\frac{\partial I}{\partial r} = -\frac{2}{\pi}\int_0^{\infty} \frac{I''(z^2)}{z}\,dz$$

$$+\frac{2}{\pi}\int_0^{\infty} \frac{I'(z^2)}{z^3}\,dz = -A < 0 \tag{2.8}$$

where $A > 0$.

If, for the same integrand, the integral (2.3) is taken at a limited value of $R = R^*$, then the derivative along the beam axis is

$$\left.\frac{\partial\varphi}{\partial r}\right|_{\substack{r=0\\R=R^*}} = \frac{1}{\pi}\frac{I'(R^*)}{R^*} - \frac{2}{\pi}\left[\int_0^{\infty} \frac{I''(z^2)}{z}\,dz - \int_{\sqrt{R^*}}^{\infty} \frac{I''(z^2)}{z}\,dz\right]$$

$$+\frac{2}{\pi}\left[\int_0^{\infty} \frac{I'(z^2)}{z^3}\,dz - \int_{\sqrt{R^*}}^{\infty} \frac{I'(z^2)}{z^3}\,dz\right] = \frac{1}{\pi}\frac{I'(R^*)}{R^*}$$

$$+\frac{2}{\pi}\int_{\sqrt{R^*}}^{\infty} \frac{I''(z^2)}{z}\,dz - \frac{2}{\pi}\int_{\sqrt{R^*}}^{\infty} \frac{I'(z^2)}{z^3}\,dz - A \tag{2.9}$$

If $\left.\frac{\partial \varphi}{\partial r}\right|_{\substack{r=0 \\ R=R^*}} > 0$, while for an infinite radius R it is $\frac{\partial \varphi_\infty}{\partial r} = -A < 0$, then the minimum $\varphi(r, R^*)$ obtained from the solution at $R = R^*$ should be considered false because the calculations have neglected the values of experimental function $I(x)$ at $R > R^*$.

The condition responsible for the appearance of a false minimum is the following:

$$\frac{1}{\pi}\frac{I'(R^*)}{R^*} + \frac{2}{\pi}\int\limits_{\sqrt{R^*}}^{\infty}\frac{I''(z^2)}{z}dz - \frac{2}{\pi}\int\limits_{\sqrt{R^*}}^{\infty}\frac{I'(z^2)}{z^3}dz - A > 0 \quad (2.10)$$

Thus, in measuring the values of $I(x)$ the limitation on R, which is dependent on the experimental conditions, may result in a false minimum on the symmetry axis of the calculated function $I(r)$.

The check on the correct choice of the boundary conditions (the value of R^*) during numerical integration of equation (2.3) can be made in the following way. If the calculations give a minimum on the axis of the function $\varphi(r, R^*)$, we must compute A by formula (2.8) and substitute it into expression (2.10). For A to be found, we should graphically differentiate the experimental function $I(x)$ and evaluate the corresponding integrals between 0 and ∞ by formula (2.8). If the calculated results correspond to the condition at which a false minimum appears, an approach to clarify the true form of the distribution function $\varphi(r, R)$ in the near-axis region is to increase R^* by changing the conditions of the experimental measurement of $I(x)$.

It is thus theoretically possible to determine whether the minimum on the axis of the calculated function $I(r)$ is false or true. But since the values of $I(x)$ depend on measurements, the computations can generally be only approximate in character. The integrals required to determine the conditions at which a false minimum of the function $I(r)$ appears can also be estimated only approximately.

In general, the task of determining the function $I(r)$ on the basis of the experimental function $I(x)$ with the aid of the Abel equation, which is a particular case of the Volterra integral equation of the first kind, is typical for ill-conditioned problems. The solution to the problem in question by traditional methods can be unstable relative to small changes in initial data. In order to solve the problems of this type, we should check the problems theoretically for the correct formulation and use special calculation methods.

The applicability of the Pierce method is given treatment in work [10]. This is one of the most popular methods of the solution of equation (2.3), the use of which can lead to the appearance of a false minimum on the symmetry axis of the function $I(r)$.

A sketch of the setup for generating probe signal waveforms appears in Fig. 2.9. The linear sensor (probe) is 0.05-mm dia. tung-

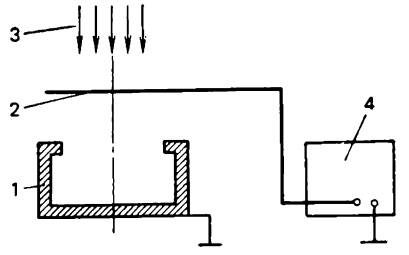

Fig. 2.9. Sketch of a setup for measuring probe current: *1*, collector; *2*, linear probe; *3*, electron beam; *4*, oscilloscope

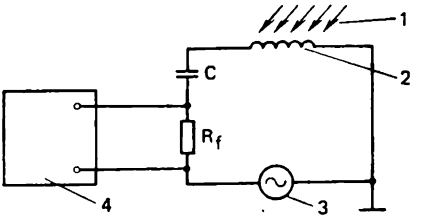

Fig. 2.10. Schematic diagram for calibrating the linear sensor (probe): *1*, beam; *2*, probe; *3*, oscillator; *4*, oscilloscope

sten wire moving normal to the EB axis at a speed of 12.5 mm/s. The free end of the wire passed over a pulley carries a weight of 10^{-2} kg fastened to it to prevent the wire from bending during measurements. Placed at a distance of 5 mm below the sensor is a grounded copper collector in the form of a cylinder with a 20-mm dia. hole 50 mm deep, which traps secondary and reflected electrons and keeps them from falling on the probe. A signal from the sensor is applied to the input of a light-beam oscilloscope to record the pattern of the signal on photographic paper which blackens instantly on exposure to the light beam.

To allow for the systematic measurement error arising from the heating of the tungsten wire as it cuts the electron beam, the device is preliminarily calibrated with the aid of an arrangement illustrated in Fig. 2.10, which includes a sinusoidal oscillator to shape a 1 kHz signal and a high-pass filter connected to the sensor (linear probe). The peak value of current i_p in the circuit is governed by the peak value of the oscillator voltage V_p: $i_p = V_p/(R_f + R_s)$, where R_f is the filter resistance, and R_s the probe resistance.

As the probe cuts the electron beam, its resistance R_s varies, causing the recorded current i_p to vary, too. The RC filter excludes the effect of the dc component, which is a function of the EB current, on i_p. This circuit arrangement thus reveals how the sensor resistance changes with the coordinate at a constant rotational speed of the sensor.

The experimental values of the probe current $I(x)$ are found at the following values of the parameters: accelerating voltage, $V =$ 60 kV; beam current, $I = 15$ mA; focusing lens current, $I_f =$ 110 mA; and distance from the electron gun to the sensor, $d =$ 300 mm. The $I(x)$ spread determined from three records of probe signals at the above values of the parameters does not exceed 5% of the average value.

The probe current curve obtained by averaging the values of $I(x)$ on the three oscilloscope records with regard to changes in the resistance of the probe as it cuts the beam is shown in Fig. 2.11. This curve is used to calculate the radial current density distribution, $I(r)$, by the Pierce method. Fig. 2.12 displays the plot of $I(r)$ calculated for ten divisions of the radius. The initial data (see the plot of Fig. 2.11) used for the calculation of $I(x)$ are the following:

$x \times 10^3$, m:	0	0.6	1.2	1.8	2.4
$I(x) \times 10^3$, A/m^2:	1.12	1.10	1.05	0.93	0.78
$x \times 10^3$, m:	3.0	3.6	4.2	4.8	5.4
$I(x) \times 10^3$, A/m^2:	0.63	0.45	0.33	0.20	0.07

As seen from Fig. 2.12, the plot of $I(r)$ obtained from the directly processed initial data by the Pierce method has a minimum on the symmetry axis.

To observe the conditions for the correct application of the Pierce method, the program of calculation of $I(r)$ involves a certain range of extrapolation of the initial data to supplement them with additional values [11]. The initial data for the program are: the experimental function $I(x)$, the limiting value of the EB radius R, the numerical integration step H, and the maximum number L of these steps.

With the calculation of the distribution function $I(r)$ performed according to the above described algorithm, the minimum on the symmetry axis of the calculated function $I(r)$ vanishes if it is false.

Figure 2.13 demonstrates how the beam diameter $d_{0.5}$ and focusing current I_f vary at half the height of the probe current curve with the distance to the target surface at a constant accelerating voltage V of 20 kV. The pattern of these variations can be revealed from the oscilloscope traces of Fig. 2.14, presented on a time scale of 50 μs/cm at an amplitude of 1.7 V/cm.

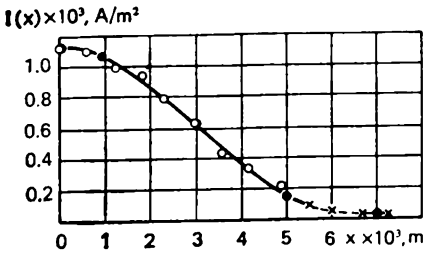

Fig. 2.11. Initial function $I(x)$ used for calculation of distribution of $I(r)$: ○, experimental points; ×, approximation points

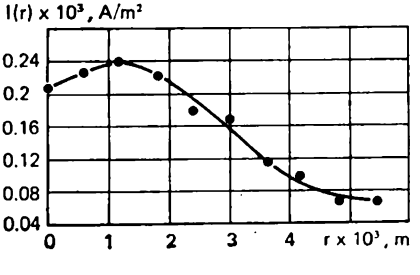

Fig. 2.12. Plot of function $I(r)$ obtained from directly processed initial data by the Pierce method

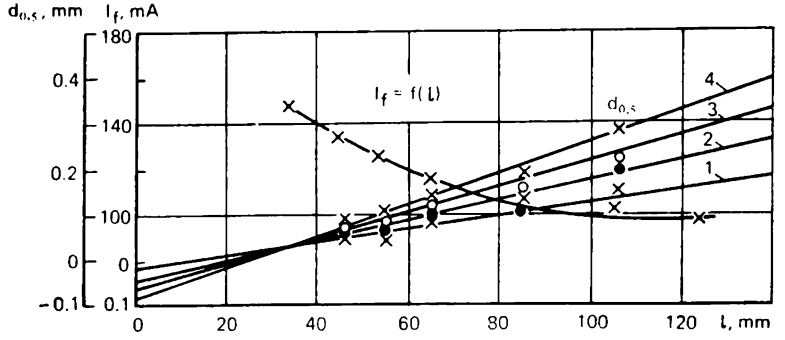

Fig. 2.13. Beam diameter $d_{0.5}$ and focusing current I_f from the A. 306.05 electron beam setup against the distance to the target at constant $V = 20$ kV: *1*, $I =$ $= 200$ mA; *2*, 40 mA; *3*, 60 mA; *4*, 80 mA

With an increase in the distance to a workpiece, the beam diameter grows linearly.

Using the equation for a straight line, the expression for the beam diameter can be written as $d = d_0 + kl$. The coefficients d_0 and k can be found by plotting the functions $d_0 = f(I)$ and $k = f(I)$ illustrated in Fig. 2.15. These plots reveal that $d_0 = -aI$

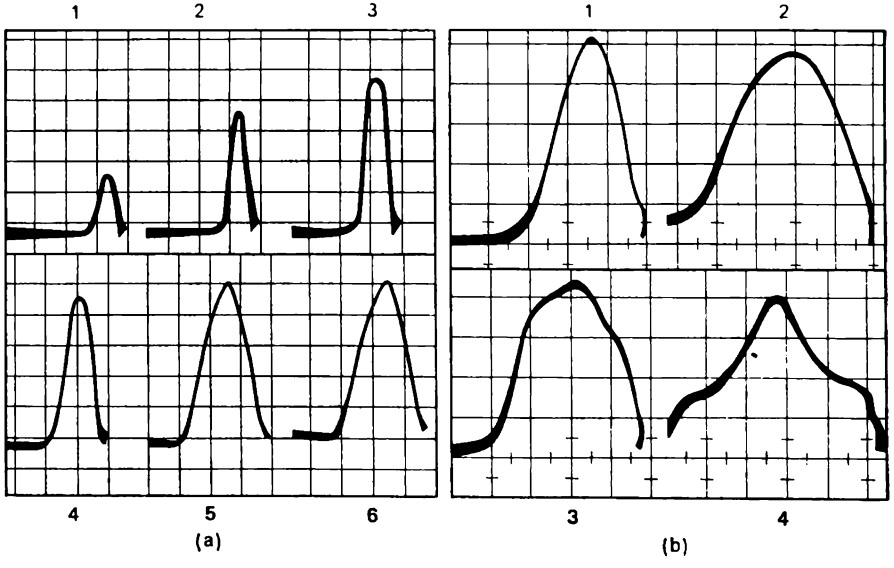

Fig. 2.14. Oscilloscope traces of probe signals: (*a*), at constant l and various beam currents I: *1*, 10 mA; *2*, 20 mA; *3*, 40 mA; *4*, 60 mA; *5*, 80 mA; *6*, 100 mA; (*b*), at constant I and various distances l: *1*, 70 mm; *2*, 75 mm; *3*, 80 mm; *4*, 85 mm

and $k = b + cI$, where a, b, and c are the coefficients experimentally determined for each type of electron beam system. For the A.306.05 setup with an A.852.04 electron beam system, $a = 8.9 \times 10^{-4}$ mm/mA, $b = 0.85 \times 10^{-3}$ and $c = 3.04 \times 10^{-5}$ mA^{-1}. The beam diameter (mm) then is $d = (b + cI)\, l - aI$, where I is the beam current, mA; and l the distance from the axis of the focusing system to the weld zone, mm.

Experimental data show that the A.852.04 system can produce a beam power density up to 1×10^7 W cm^{-2}.

Table 2.2 lists the values of the penetration depth and width (depth and width of melting) for some metals struck by the electron beam of the same parameters from the A.852.04 system at different distances l to the target surface. The experimental check on the weld penetration reveals that the melt depth decreases with increasing distance to the weld bead, but the width increases.

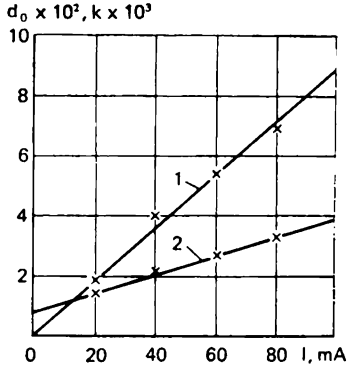

Fig. 2.15. Coefficients d_0 and k versus beam current I: 1, $d_0 = f(I)$; 2, $k = f(I)$

The current density distribution on a beam radius is found to be Gaussian: $j = j_m \times \exp(-r^2/r_e^2)$, where j_m is the maximum current density, r the beam radius of interest, and r_e the beam radius at a ratio of j_m/e (Gaussian radius).

TABLE 2.2. **Penetration Depth and Width Against Distance to the Target at $V = 20$ kV, $I = 90$ mA, and $\tau = 100$ ms**

Material	Melt depth (mm) at l, mm			Material	Melt depth (mm) at l, mm		
	35	65	125		35	65	125
Titanium	8	6.95	2.36	Titanium	2.62	4.12	4
Corrosion-resistant steel	7.2	5.9	4.08	Corrosion-resistant steel	3.87	3.25	3.53
Nickel	5.4	2.9	2	Nickel	2.25	2.67	3.13

The beam astigmatism for focal lengths of 31.2, 37.5, and 25 mm at an accelerating voltage of 10 kV and beam current of 40 mA is 0.6, 0.716, and 0.696 mm^2 respectively.

2.4. OTHER MEASUREMENT METHODS

Beam parameter measurement with a stationary probe. Assuming that an electron beam has the shape of a cone (Fig. 2.16), we can consider the current densities in the planes normal to the beam axis and establish the manner in which the concentration index varies from section to section down to the beam focus. Such a representation of the electron beam can serve as the basis for the methods of determining the beam dimensions.

The expression derived for the concentration coefficients k_r and k_{r1} in the planes A and B, respectively, of the beam of Fig. 2.16*a* takes the form

$$k_{r1} = k_r (L/l)^2 \tag{2.11}$$

As seen from the expression, if k_r for one plane of the beam is known, we can calculate the concentration coefficient for any other plane, including the focal plane. For the plane near the focusing lens, where the heat power density is low, the concentration coefficient is given by

$$k = -(\ln P_{R,\infty}/P)/R^2 \tag{2.12}$$

In expression (2.12), R and P are known and the quantity $P_{R,\infty} = VI'$, where I' is the current of the beam fraction coupled to the plate of Fig. 2.16*b*, and V the accelerating voltage.

A version of the stationary probe is a ring of tungsten wire 0.2 to 0.5 mm in diameter or a ring of a water-cooled metal tube 0.5 and 0.1 mm in diameter (Fig. 2.16*c*). The probe is set up coaxially

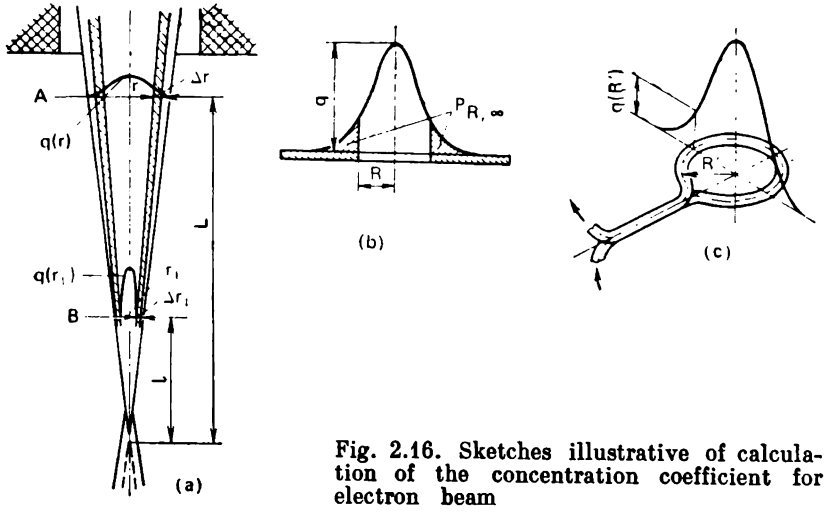

Fig. 2.16. Sketches illustrative of calculation of the concentration coefficient for electron beam

with respect to the beam. The mean heat power density on the mean probe radius R' is found from the probe current and accelerating voltage V:

$$q(R') = VI'/S = (Pk/\pi) \exp(-kR'^2) \quad (2.13)$$

where S is the area of the ring probe in plan.

From (2.13) we can define the concentration coefficient k in implicit form for any probe plane.

The procedure of testing is as follows. Before clamping the ring probe in a holder with an insulated base, a hole is burnt in the

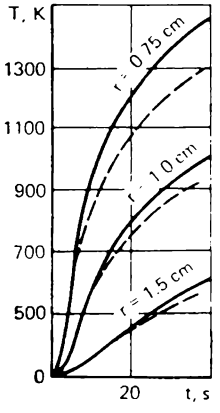

Fig. 2.17. Calculated data (solid lines) and experimental data (dash lines) on the surface temperature of semi-infinite body exposed to a stationary Gaussian beam source

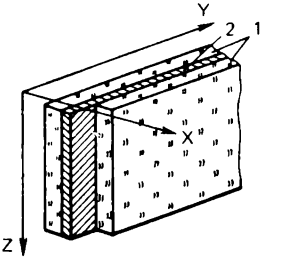

Fig. 2.18. Structure of thin-film probe: *1*, insulating plate; *2*, conducting film

foil covering the probe, which serves as the datum for the coaxial location of the probe. With the foil removed and the setup switched on, the readings are taken of the accelerating voltage, total beam current, probe current, and the distance from the probe to the center of the focusing lens. The probe current is corrected for the effect of the straight section of the probe on the current value (see Fig. 2.16*c*).

The experimental values of k are then used to compare the theoretical and experimental curves of temperature variations.

Figure 2.17 compares the calculated data (solid lines) and experimental data (dash lines) on changes in the surface temperature of an alloy interacting with a stationary Gaussian beam source. The experimental data were obtained on an electron-beam setup. Chromel-alumel thermocouples were set at distances of 0.75, 1.0, and 1.5 mm from the axis of the heat affected zone. The distance from the center

of the focusing lens to the target surface was 156 mm. The concentration coefficients determined at distances of 12 and 87 mm were equal to 11.75 and 33.0 cm^{-2} at beam diameters of 16 and 19 mm respectively. The diameters of holes in flat probes were 5.0 and 4.0 mm. The probe current was 12 and 6 mA; total beam current, 25 mA; accelerating voltage, 60 kV; and beam diameter on the target, 2.3 mm. The concentration coefficient in the interaction region, calculated from the known values of k, was 510 and 570 cm^{-2} in two planes of the beam.

As seen from Fig. 2.17, the method of determining the values of k makes it possible to define the temperature fields in the beam-material interaction region with an accuracy sufficient for practical calculations. The ring-shaped probe method gives a somewhat larger scatter in the data, which mainly depends on the accuracy of manufacture and alignment of probes. Nevertheless, the concentration coefficients of $(1.47\text{-}1.98) \times 10^4$ cm^{-2} obtained on the A.306.05 setup by the ring-probe method at $V = 20$ kV, $I = 20$ mA, a focus coil current of 70-200 mA, and a distance of 18 mm from the center of the focusing lens well agree with the experimental data presented in Table 2.1.

Measurement with a thin-film probe. The structure of a thin-film probe is shown in Fig. 2.18. It consists of a dielectric substrate, a metal film evaporated on the substrate and electrolytically grown to the required thickness, and an insulating plate bonded to the metal film, which is made of the same material as the substrate. The end face of the bonded sample is ground and polished in the X-Y plane. This plane is the working surface of the probe. The idle surfaces of the metal film are coated with a protective layer. This is a 1-μm protective film deposited on a glass ceramic substrate. In the tests carried out on higher-power beams, the films of refractory metals such as tungsten, molybdenum, and tantalum can be grown on the substrate.

The curves of current density distribution are plotted from the records of film probe signals.

The current I_x of a flat probe of thickness h with consideration for the measurement error is

$$I_x = (j_0 \pi r_e^2/2)\,[\operatorname{erf}(x + h/2)/r_e - \operatorname{erf}(x - h/2)/r_e] \tag{2.14}$$

where r_e is the Gaussian radius of the beam.

Then,

$$a(x) = \frac{I_x}{I_0} = \frac{\operatorname{erf}(x+h/2)/r_e - \operatorname{erf}(x-h/2)/r_e}{2\operatorname{erf} h/(2r_e)} \tag{2.15}$$

The calculation by expression (2.15) discloses that the distribution curve, as illustrated in Fig. 2.19, closely approximates the Gaussian curve. The departure from the Gaussian curve is due to

the measurement error which in the given case depends on the position of the probe with respect to the beam center and on the ratio of the beam radius r_e to the probe thickness h. As is clear from Fig. 2.20, the current density error δ, %, is proportional to the probe shift

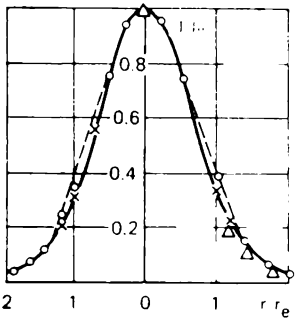

Fig. 2.19. Curves of current density distribution across the electron beam: ×, in agreement with Gauss law; ○, points found from expression (2.15); △, experimental

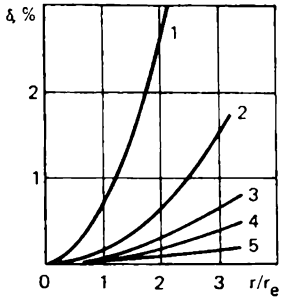

Fig. 2.20. Error δ in estimating the radial beam current density as a function of probe shift relative to beam center at different values of Gaussian beam radius r_e: *1*, 5 μm; *2*, 10 μm; *3*, 15 μm; *4*, 20 μm; *5*, 50 μm

relative to the beam center. If the ratio $r_e/h = 5$, the error at an 18% level of the probe current I_{max} does not exceed 3%. At $r_e/h = 20$, this error is 0.16%.

Figure 2.21 demonstrates the current density error δ, %, at I_{max}/e of the probe current curve against the ratio between the beam and probe dimensions. This relation can be used to determine the required probe dimensions at the preassigned error.

In Fig. 2.22 is shown the electron beam cross section at 5% of I_{max}, constructed with the aid of probe signal waveforms recorded

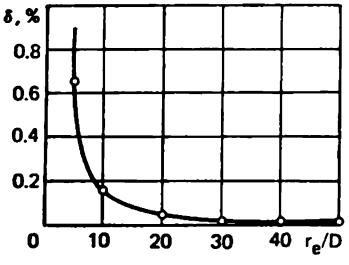

Fig. 2.21. Error δ in estimating the radial beam current density as a function of Gaussian beam and probe dimensions

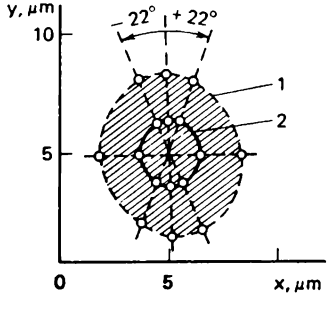

Fig. 2.22. Cross section of electron beam: *1*, at 5% of I_{max}; *2*, at I_{max}/e

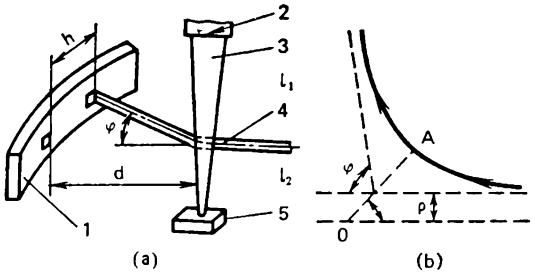

Fig. 2.23. Illustrating the method of determining the electron beam diameter with a probing beam: (*a*) schematic of measuring unit; (*b*) measured angle of deflection; *1*, sensor; *2*, end of electron gun; *3*, working beam; *4*, probing beam; *5*, workpiece

in different directions of scanning. As seen, the beam displays a slightly disturbed axial symmetry (curve *1*). The beam section has a shape of an ellipse and its location in the plane of incidence of the beam depends on the direction of electrons with respect to the probe surface.

The experimental results have revealed that the thin-film probe method provides for a rather high measurement accuracy and is free from the drawbacks inherent in other probe methods. This method is suitable for measuring the electron beams whose dimensions range between 5 and 20 μm.

Measurement with a probing electron beam. Fig. 2.23 demonstrates the method of determining the parameters of a working heat-generating electron beam by probing it with an electron beam that does not induce heat [11].

The deflection of the probing beam in the electric field of the working beam can be found from the equation describing the motion of a charged particle in a centrosymmetric field. The angle of deflection of a probing beam of energy eV_{pb} is

$$\varphi = \frac{\pi - 2\int_{r_{min}}^{d} \rho\, dr}{r^2\sqrt{1-(\rho^2/r^2)-(V/V_{pb})}}$$

where r_{min} is the root of the equation $1 - (\rho^2/r^2) - (V/V_{pd}) = 0$; d the distance from the axis of the working beam to the sensor; ρ the distance between the axes of the working and the probing beam; r the distance to which there corresponds the working-beam field potential V; and V_{pb} the accelerating voltage of the probing beam.

For $r > r_{wb}$, where r_{wb} is the radius of the working beam,

$$V = \frac{Q}{4\pi\varepsilon_0} \ln \frac{\sqrt{l_1^2+r^2}+l_1}{\sqrt{l_2^2+r^2}-l_2}$$

Here Q is the space charge per unit length of the working beam; ε_0 the permittivity of a vacuum; l_1 and l_2 the lengths of the segments of the working beam from the end face *2* of the gun to the plane of the probing beam *4* and from this plane to the target *5* respectively (see Fig. 2.23*a*):

$$Q = \frac{I_{pb}}{5.93^3 \times 10^3 \sqrt{V_{pb}}}$$

where I_{pb} is the probing beam current.

The effect of the probing beam field on the beam under analysis is vanishing because the space charge and the accelerating voltage of the probing beam are much smaller than those of the working beam, whereas $l_2/d \ll 1$, where d is the distance from the sensor to the working beam.

Given below are the results of measurements conducted on an electron-beam setup with a long-focus gun (triode) at an accelerating working beam voltage V_{wb} of 20 kV, beam current I_{wb} in a pulse of 2-15 mA, pulse length τ_p of 2-1 000 μs, pulse repetition rate of 1 000 Hz, and pressure p in a vacuum chamber of 10^{-2} Pa.

The measurements were taken at the following parameters of the probing beam: $V_{pb} = 800$ V, $I_{pb} = 10$ μA, and $r_{pb} = 3$ mm in the plane of the sensor.

The sensor consisted of two insulated Faraday cups having a common screen with two 1 × 5-mm slits spaced apart a distance $h = 10$ mm and arranged parallel to the axis of the beam under measurement, as illustrated in Fig. 2.23*a*. The electrons of the probing beam fell into the Faraday cup through these slits.

To avoid the effect of secondary emission of electrons traveling back from the workpiece, the signals from the Faraday cup were fed via grounded 50 kΩ resistors to the differential input of the oscilloscope of a sensitivity of 50 μV/cm-20 mV/cm. This arrangement can register current pulses at a sensitivity β of 1 nA; a differential-input dc voltmeter can be used to detect beams in continuous current operation.

The minimum angle of deflection, shown in Fig. 2.23*b*, is $\varphi_{min} = 1.2\beta r_{pb}/I_s d$, where I_s is the sensor current.

At $d = 300$ mm and $r_{pb} = 3$ mm, the sensitivity was $\beta = 1$ nA, $I_s = 1$ μA, and $\varphi_{min} = 1.2 \times 10^{-5}$ rad.

The probing gun and the sensor were made fast with respect to each other on the table movable relative to the working beam gun. The probing beam was aimed at one of the slits of the sensor with the aid of the deflecting system of the probing gun in such a way that the sensor current was 60% of $I_{s\,max}$ with consideration for the maximum response to the Gaussian probing beam.

To calibrate the signal sensor, use was made of a vertically suspended wire simulating the beam under measurement, which

received negative pulses of 0-10 V of the same duration and repetition rate as for the working beam. The table with the sensor and the gun was moved normal to the wire. With a change in the distance from the probing beam to the wire from 5 to 30 mm, the sensor current I_s varied by less than 10%.

Figure 2.24 displays the experimental values of the space charge ($Q \times 10^{-10}$, C/m) and potential V (V) of the working beam against

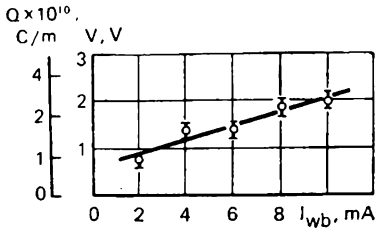

Fig. 2.24. Space charge and potential of electron beam versus beam current

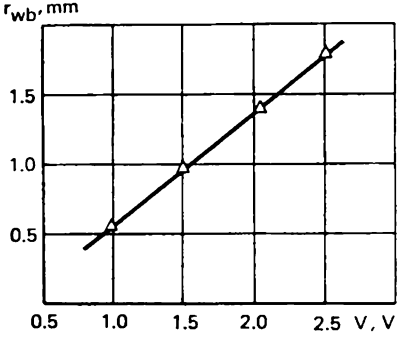

Fig. 2.25. Working beam radius r_{wb} against beam potential: $l = 300$ mm; $r_0 = 3$ mm; $V_{wb} = 20$ kV

the beam current, measured under conditions at which the beam does not vaporize the target material, nor forms the fusion region. The working beam had a potential of 1-2 V, which corresponded to a negative charge of $(1.1\text{-}2.2) \times 10^{-10}$ C/m at the following parameters: $V_{wb} = 20$ kV, $I_{wb} = 2\text{-}10$ mA, $\tau_p = 200$ μs, $f = 1$ kHz, and $r_{wb} = 0.50$ mm, the last parameter being measured by the probing-beam method at $I_{wb} = 5$ mA.

The plot of the beam radius as a function of beam potential appears in Fig. 2.25.

Thus, the observed effect of beam defocusing with an increase in the beam current at a constant accelerating voltage can be accounted for by an increase in the space charge, as follows from the obtained experimental data. The shift of the crossover for long-focus and electron-optical systems plays a much smaller part.

References

1. H. Schwartz. *Remark on power density, total power and pressure of electron beams as a welding, cutting and surfacing tool.* Review Scientific Instruments, 33: No. 6, p. 278, 1962.
2. H. Schwartz. *Power density of optimally focused spacecharge-limited electron beams.* Journal of Applied Physics, 33: No. 12, p. 252, 1962.

3. E. A. Abramyan, B. A. Alterkop, and G. D. Kuleshov. *Intensive electron beams. Physics, technology, and applications.* Moscow, Energoatomizdat, 1984 (in Russian).
4. V. A. Moskalev, G. I. Sergeev, and V. G. Shestakov. *Measurement of charge-particle beams.* Moscow, Atomizdat, 1980 (in Russian).
5. N. N. Rykalin, I. V. Zuev, and A. A. Uglov. *Basic concepts of electron-beam treatment of materials.* Moscow, Mashinostroenie, 1978 (in Russian).
6. A. A. Kharlamov (ed.). *Laboratory physics manual.* 3d edition. Moscow, Moscow State University, 1977 (in Russian).
7. M. L. Krasnov, A. I. Kiselev, and G. I. Makarenko. *Integral equations.* Guide for technical college students. 2nd edition. Moscow, Nauka, 1976 (in Russian).
8. B. R. Ryabichenko, E. I. Romanenkov, M. S. Gritsenko, et. al. *Study of numerical methods for determining the local parameters of a weld arc*, in Welding engineering handbook. 5th edition. Moscow, NIKIMT, p. 98, 1978 (in Russian).
9. V. B. Zvyagin, S. V. Selishchev, and I. V. Zuev. *On the computation of spatial characteristics of axisymmetric energy fluxes.* Fizika i Khimiya Obrabotki Materialov, No. 4, p. 27, 1982.
10. V. B. Zvyagin, I. V. Zuev, V. P. Podolskiy, et al. *Calculation and experimental estimation of the current density distribution across the electron beam.* Fizika i Khimiya Obrabotky Materialov, No. 3, p. 35, 1979.
11. V. F. Reznichenko, A. A. Uglov, and D. M. Chesakov. *On the estimation of space-time energy distribution in the electron beam*, in Electron beam welding, Moscow, MDNTP, p. 15, 1978 (in Russian).

Chapter 3
THERMAL PROCESSES IN INTERACTION ZONES

The main feature of a concentrated energy flux (CEF) such as a laser beam or electron beam is its ability to deliver high power per unit area to local regions on a workpiece and thus rapidly change the target temperature. The calculations of transient and steady-state temperatures at the local points of an interaction zone and also experimental studies confirm that the CEF can be a very useful tool in many potential applications involving surface hardening, alloying, annealing, welding, and other types of material processing.

The CEF source, whether moving or stationary, can interact with materials in a variety of ways. It can afford surface or bulk interaction, point-by-point or distributed interaction, and continuous or pulsating interaction. The choice of the kind of interaction depends on the processing unit employed, the task specified, the material worked, environmental conditions, etc.

The factors specifying the process of heating are the rate of temperature changes, temperature gradient, the time it takes the target to reach a definite temperature, etc. The character of heating varies with the properties of the material of interest, conditions of treatment, and type of energy source interacting with the material. Of importance is also the behavior of the material during the total cycle of heating and cooling.

Knowing the basic parameters of the temperature field in a material during its heating and cooling, it is possible to predict the composition of the recrystallized region, its phase state, and structure. Systematic studies on the thermal processes that occur in materials exposed to laser radiation (LR) or to an electron beam (EB) allow us to select the most efficient treatment procedures, specify the main requirements on the output parameters of LR and EB, and define the optimal interaction conditions.

3.1. CEF-PRODUCED HEAT SOURCES

As the CEF falls on a target surface, part of the energy flux is reflected and part is absorbed in a thin surface layer. The absorbed energy begins to heat the surface, causing it to melt or vaporize depending

on the process conditions. After a certain time of interaction (dwell time), the energy flux creates a local heat source definitely distributed in time and space at individual points on the surface or in the bulk of the material.

To clarify both the instant and conditions at which the notion of a heat source can be used to describe the changes in temperature of a body exposed to LR or EB, consider the process of relaxation of energy delivered to a thin surface layer of metal [1].

Let us dwell in brief on the process of energy transfer from LR to a solid. The energy of absorbed light quanta is given up to an electron gas via the triple collisions of an electron, a photon, and, for example, a lattice defect, which, as revealed by calculations, is a necessary condition for fulfilling the law of conservation of momentum. The collisions cause the electron gas temperature to grow, but the lattice temperature generally remains invariable for a definite time because of a large difference in mass between the electron and ion. Estimates disclose that the equalization of the electron gas temperature occurs for about 10^{-13}-10^{-14} s, which is much shorter than the time of energy transfer from electrons to ions. The electron-to-ion energy transfer corresponds to electron-photon interactions which tend to equalize the temperatures of the electron gas and the lattice. This process lasts around 10^{-11} s, so that the notion of a heat source for metals is valid after a dwell time of 10^{-9}-10^{-10} s.

If an LR pulse is triangular in shape, the maximum temperature difference between the electron gas and lattice can be found from the formulas [1]

$$(T_e - T_i)_{\max} = 2q/(\alpha \sqrt{\pi a \tau}) \tag{3.1}$$

where T_e is the electron gas temperature, T_i the lattice (ion) temperature, q the power (flux) density, α the electron-lattice heat-transfer coefficient, a the thermal diffusivity, and τ the light pulse length. At $q = 10^6$ W/cm^2 and $\tau = 1$ ms, the temperature difference is $(T_e - T_i)_{\max} \leqslant 1$ K; at $q = 10^9$ W/cm^2 and $\tau = 10^{-8}$ s, the difference is $(T_e - T_i)_{\max} \approx 2\,000$ K. In both cases, $\alpha = 6 \times 10^9$ W cm^3 K^{-1} and $a \approx 1$ cm^2 s^{-1}. If the power density is high and the dwell time is short, the temperature difference between the electrons and lattice is too large for it to be neglected.

In laser and electron beam processing of materials, the pulse duration τ is commonly much longer than 10^{-9} s and power density is generally lower than 10^9 W/cm^2, therefore the notion of a heat source is justifiable in most cases.

So, the practical tasks concerned with CEF material heating at pulse durations in excess of 10^{-9} s and power densities of no more than 10^9 W/cm^2 can in the main be treated on the basis of the mechanisms of common heat conduction, be it linear or nonlinear. The time

10^{-9} s can conditionally be taken as the boundary of this approximation.

In order to consider the thermal processes in the materials interacting with the LR and EB, we should know the following operating parameters of thermal sources: amount of the absorbed radiation $(1 - R)$ incident on the target; maximum power density q_0 on the target surface; pulse duration τ; laser wavelength λ; spatial power density distribution $q(r)$; conditions of focusing of the beam on the target; and depth of penetration of the beam into the material. The above parameters depend on the type and parameters of the setup used and on the properties of the target material.

For example, in the studies on laser material processing, the analysis of the effects of heat sources on opaque materials at a given laser wavelength calls for the estimation of the reflectivity R in order to determine the fraction of absorbed energy. The reflectivity R for beam power densities below 10^6 W/cm^2 can be estimated from Fresnel formulas. It heavily depends on the state of the target surface, such as the degree of roughness, type of preliminary treatment, contaminants, and oxide films. At $q_0 > 10^7$ W/cm^2, R decreases for most materials. Besides, the value of R varies with the formation and growth of oxide films due to the material treatment in an oxidizing medium, in air, for example [2, 3].

In a number of cases, it is possible to neglect the time-dependent variations in the absorptivity for LR and describe complex space-time relationships for the power density by simpler mechanisms. In particular, the calculation procedures rather often rely on the normal distribution law to describe the spatial laser beam density distribution. If the material processing occurs in the atmosphere of a neutral gas or in a vacuum, such an approximation does not introduce a rough error into the estimates of the LR energy absorbed by the workpiece. This approximation enables the researcher to carry out the thermal calculations by using to best advantage the heat source theory developed by N.N. Rykalin for welding, cutting, and other material processing applications [4]. Besides, a number of experimental results and theoretical studies allow us to conclude that the spatial power density distribution for an LR-produced heat source approaches the Gaussian distribution.

Experimental data [5] reveal that the EB power density distribution over the target surface can also be described by the normal distribution law.

Spatial-temporal characteristics of LR. The density distribution q both for a pulsed and for a CW laser beam is commonly not constant in time and, in the general case, can be written as

$$q = q(x, y, z, t) \tag{3.2}$$

where x, y, and z are space coordinates, and t is time.

The heat sources produced by some lasers display sharply varying spatial-temporal characteristics. The penetration ability of a heat source, i.e. the manner in which its characteristics vary with the z coordinate, depends on the properties of the target material and the laser wavelength. The calculations of the temperature fields in bodies are often made on the assumption that the heat source has ideal properties, which can lead to appreciable deviations of calculated data from experimental results. The solution to the problems of material heating calls for a thorough analysis of the conditions of laser operation and experimental assessment of the spatial-temporal behavior of the heat source.

In opaque materials to which belong metals and a number of dielectrics, the absorption of LR occurs in a thin surface layer; for metals, the absorption layer is a few fractions of a micrometer thick at a laser wavelength of about 1 μm. Hence, in most cases, the heat sources can be thought of as being plane ($\alpha \approx 10^4$-10^5 cm^{-1}) and distributed over the heating surface according to a definite law. Then, instead of (3.2), we have

$$q = q(x, y, t) \tag{3.3}$$

which shows that the power density distribution does not depend on the z coordinate.

For most practical case, the form of relation (3.3) is made simpler by assuming that the laser beam density can be represented as a product of the time-dependent function and the function of surface coordinates:

$$q = A\varphi(t)\, q^*(x, y) \tag{3.4}$$

where A is the absorptivity generally dependent both on the state of the target surface, namely, the degree of mechanical, chemical and other kinds of treatment, and on the surface temperature; $\varphi(t)$ the function describing the temporal behavior of the pulse; and $q^*(x, y)$ the spatial laser beam density distribution.

In the calculations of thermal processes, consideration is commonly given to two types of spatial distribution, normal (Gaussian) and uniform distribution of the power density over the focused hot spot of radius r_f. For the Gaussian density distribution, the equality below is valid:

$$q(r) = q_0 \exp(-kr^2) \tag{3.5}$$

where q_0 is the maximum power density; k the concentration coefficient, cm^{-2}, which defines the degree of "sharpness" of the spatial power distribution, so that an increase in the value of k points to a higher concentration of the heat source power per unit area near the source axis, $r = 0$; and $r = \sqrt{x^2 + y^2}$ the radial coordinate.

The expression for the uniform distribution of power density over a hot spot of radius r_f is

$$q'(r) = \begin{cases} q_0^* & r_f \geqslant r \geqslant 0 \\ 0 & r > r_f \end{cases} \tag{3.6}$$

Expression (3.5) is related to (3.6) through the concentration coefficient k for the normal distribution law:

$$r_f = B^* k^{-1/2} \tag{3.7}$$

where B^* is the factor accounting for the method of determining the spot radius r_f in the context of the normal distribution law.

If at a radial distance r_f from the spot center the laser beam density drops to $1/e$ (37%) of its value, then $B^* = 1$.

The form of the function $q(r)$ for a definite laser can be defined by a number of experimental methods. The spatial-temporal pattern of a laser pulse cannot sometimes be represented in the form of (3.4). Where this is the case, certain methods can be used to analyze the pulse profile.

As mentioned above, the absorptivity A and reflectivity R depend on the laser wavelength, laser power and power density, and surface temperature. But even at relatively low values of q, less than 10^6 W/cm^2, the values of R determined for most materials are not sufficiently accurate, particularly in the temperature range close to or in excess of the melting point. It is then assumed, where possible, that the absorptivity is independent of temperature, and the estimates are made proceeding from the mean or mean integral values of A over the temperature range of interest.

The temporal behavior of laser pulses can vary with the type of laser operation. The most typical structure of pulses consists of the train of flashes or spikes of various powers and duration of about 1 μs, which is characteristic for free-running, or normal pulse, operation. In regular spiking operation, the power of individual spikes is almost the same. In quasi-continuous operation, the spikes do not practically appear. The pulse duration τ for these types of operation is close to units of a millisecond if no measures are taken to increase or reduce τ. The technique of changing the Q-factor of a cavity, called Q-switching, or Q-spoiling, can produce high-power pulses with a duration of about 10^{-8} s. The techniques involving mode-locking make it possible to obtain ultrashort pulses with a duration in the order of 10^{-11}-10^{-12} s.

The oscilloscope trace of the output pulse of a total duration of about 1 ms, obtained from a normal pulse laser, consists of the train of spikes, called relaxation oscillations, which have a length of about 1 μs and follow each other at a duty cycle approaching 2.0 (Fig. 3.1). The amplitude of relaxation oscillations is commonly not

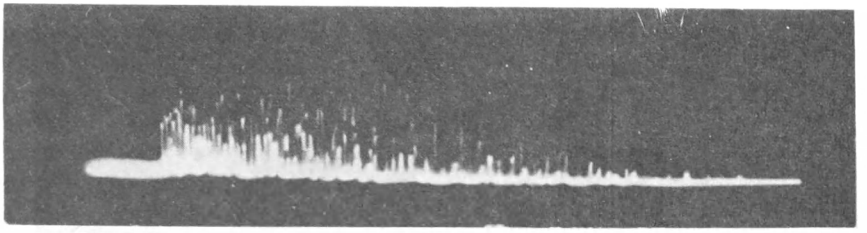

Fig. 3.1. Oscilloscope trace of free-running laser pulse

uniform, although a certain pulse envelope can be drawn. In the spiking pulse of Fig. 3.1, it is possible to discriminate the leading edge that rises at a definite rate and to reveal a certain regularity with which individual spikes decrease in amplitude at the tail of the pulse. This enables us to describe mathematically the general pulse envelope using an asymmetric bell-shaped curve. In a particular case, the pulse envelope can be defined by the product of the power function and the exponential function of time:

$$\varphi(t) = t^n \exp(-bt^m) \tag{3.8}$$

where n and m are certain numbers, either integral or fractional.

The pulse produced by a laser designed for stable spike operation is shown in Fig. 3.2. This is the train of flashes of a total duration of around 1 ms. The flashes follow each other at a duty cycle in the order of 2.0, as in the case of free-running operation. But the amplitude of flashes and space width between these flashes are almost uniform within an appreciable portion of the pulse. To a certain approximation, this regime of pulsed laser operation can be described by a periodic function of the form

$$\varphi(t) = C(t)(1 - \cos \omega t) \tag{3.9}$$

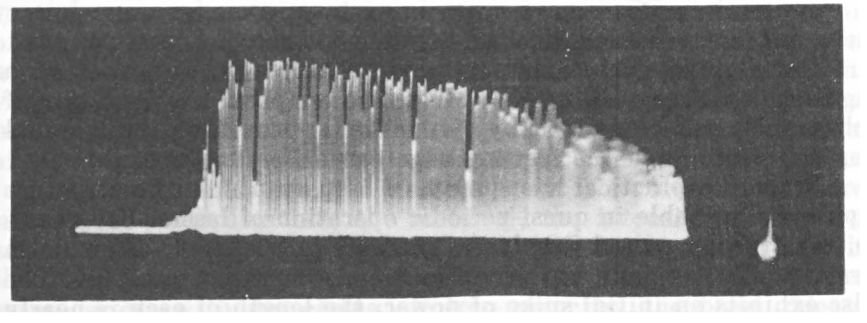

Fig. 3.2. Output from stable spiking laser

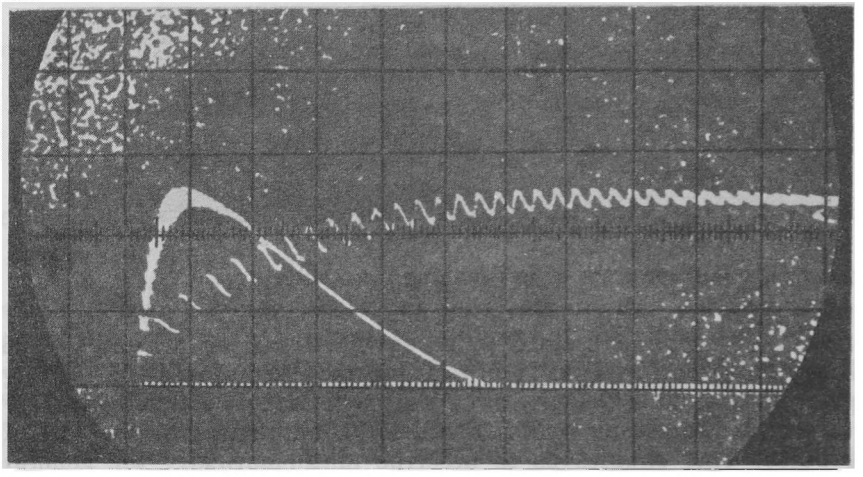

Fig. 3.3. Output from quasi-continuous laser

where $C(t)$ is a slowly varying function of time which in a first approximation is equal to 0.5 when $0 \leqslant \varphi(t) \leqslant 1$, and ω the repetition rate of flashes in the laser pulse.

The analysis of heating of a half-infinite body or plate by a heat source whose temporal behavior varies in compliance with relations (3.8) and (3.9) can be performed after solving certain thermal problems. The quasi-continuous operation of pulsed lasers does not in fact yield spikes, except for the initial portion of the pulse (Fig. 3.3). In a first approximation, the step function given below can be used to describe the temporal behavior of pulses obtained in quasi-continuous operation of lasers:

$$\varphi(t) = \begin{cases} 0 & t < 0 \\ 1 & 0 \leqslant t \leqslant \tau \\ 0 & t > \tau \end{cases} \tag{3.10}$$

where τ is the pulse length.

Q-switching enables lasers to yield single giant pulses of a length in the order of 10^{-8} s (Fig. 3.4). The temporal configuration of such a pulse can be defined by a function approaching the trigonal one; the leading and the trailing edge can differ in slope.

From the practical viewpoint, of importance is the structure of pulses obtainable in quasi-periodic operation of lasers. For example, repetitively pulsed CO_2 lasers generate pulses up to a few μs in duration. The temporal pattern of each pulse is rather complex. The pulse exhibits an initial spike of power, the length of each is nearly 1% of the total duration, which then decays in a time $\sim\tau$.

In the general case, the shaping of pulses of the desired temporal pattern is an important practical task from the viewpoint of optimal control over the processes of laser material working, for example, as regards a decrease in the consumption of laser power required to heat metals [6].

The spatial-temporal behavior exhibited by continuous CO_2 lasers can, to a first approximation, be described by the relation

$$q(r) = (1 - R)\, q_0 \exp(-kr^2) \tag{3.11}$$

where R is the reflectivity.

In equation (3.11), the absorptivity $(1 - R)$ is assumed to be equal to the mean integral value during laser-material interaction.

Fig. 3.4. Oscilloscope trace of Q-switched laser pulse

In the general case, such a description of the heat source is inexact, especially where the LR interacts with metals in an oxidizing atmosphere. The most important aspect specific to relation (3.11) is that the spatial intensity distribution for a heat source obeys the normal distribution law.

Spatial-temporal characteristics of electron beams. There are a number of experimental methods for estimating the parameters of an EB [5]. For example, the EB spot radius and current density distribution over the surface of interaction can be found by the rotating-probe method. The experimental data confirm that the spatial-temporal pattern of an electron beam can be similar to one of the types of LR pattern described above, but only if the accelerating voltage V is not too high. In metal working, for example, this voltage must not be in excess of 20 kV. The electron beam can then be thought of as a plane heat source, disregarding the mechanisms of electron energy release at a certain depth from the metal surface.

In the general case, the electron beam is a volume heat source since as it penetrates into the material, the intensity of its interaction with atoms varies because of changes in the energy lost by electrons along their path lengths. Since the cross section of interaction grows with decreasing electron velocity, the beam releases the largest share of its energy not on the surface but in the material

bulk at a certain depth depending on the accelerating voltage V and material density γ.

There are several formulas [5] for approximating in different ways the electron penetration depth δ (electron path length) over different EB energy ranges. The distribution of released electron

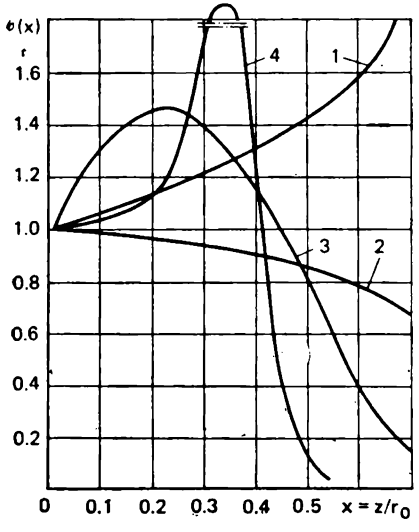

Fig. 3.5. Distribution of released electron energy according to Thomson law (curve *1*), Lenard model (curve *2*), Spenser model (curve *3*), and Archard model (curve *4*)

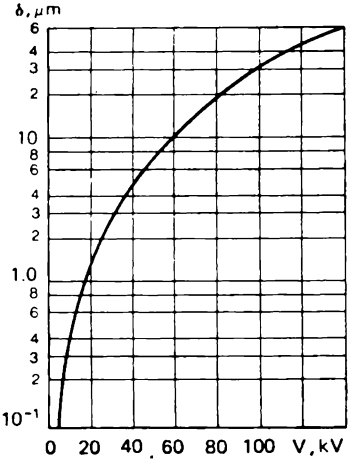

Fig. 3.6. Depth of penetration of electrons into iron as a function of accelerating field

energy E against the depth of penetration, x, of electrons into a substance is given in Fig. 3.5. The curve *1* is the plot of variations in the intensity of the energy loss

$$\varphi(x) = \frac{|dE/dx|}{|dE/dx|_0}$$

with penetration depth according to the Thomson law, when the electrons do not suffer angular scattering and release a small amount of energy in comparison with their initial energy, i.e.

$$\varphi(x) = (1 - x)^{-1/2} \tag{3.12}$$

In the formulas above, $|dE/dx|_0$ is the energy lost by electrons on the target surface; $x = z/r_0$, where z is the depth, and r_0 the total path of an electron.

As follows from expression (3.12), the highest loss of energy occurs at a depth that corresponds to the maximum electron path.

The curve *2* describes the variations in the electron current with penetration depth:

$$\varphi(x) = (1 - x)^{1.4} \tag{3.13}$$

As follows from formula (3.13), the largest fraction of released energy falls at the surface of a solid. The maximum electron penetration depth δ, cm, varies with the adopted law of absorption. For curves *1* and *2*, the depth δ is given by the Shohland formula

$$\delta = 2.35 \times 10^{-12} V^2 \gamma^{-1} \tag{3.14}$$

where V is the accelerating voltage, V; and γ the material density, g/cm^3.

The results calculated with formulas (3.14) for iron in the range of V up to 140 keV are shown in Fig. 3.6.

In other metals, the electron path as compared to that in iron (δ/δ_{Fe}) is as follows: Ni, 0.85; Cr, 1.10; Cu, 0.88; Al, 2.8; W, 0.48; Ta, 0.54; and Pb, 0.81. From the curve of Fig. 3.6 we can conclude that δ for most metals is only slightly in excess of 1 μm in the voltage range up to 20 kV, so the heat source can be regarded as a plane source.

For the range of accelerating voltages from 0.5 to 3×10^3 kV, the depth of electron penetration into metals can be found from the formula

$$\gamma\delta = 10^{-5} V^{3/2} \tag{3.15}$$

where γ is the density, g/cm^3; δ the electron path, cm; and V the accelerating voltage, kV.

The curve *3* of Fig. 3.5 represents the Spenser distribution of energy lost by electrons. According to the calculations of L.V. Spenser, the unidimensional energy loss distribution for a fast electron has a maximum whose position depends on the atomic number Z of an element and is independent of electron energy E (for aluminum, this energy is 0.02 MeV $\leqslant E \leqslant$ 2 MeV).

The curve *4* of Fig. 3.5 with the maximum at the depth of full diffusion corresponds to the Archard model. By this model, the electrons cover a certain straight path in the target, called the depth of total diffusion, and then diffusively scatter in all directions. The energy released by the electrons and the total electron path are found here from the Thomson formula. The maximum of energy release on the Archard curve is by far distant from that on the Spenser curve which represents a more accurate energy distribution. For example, the maximum x_{max} for aluminum calculated by Spenser is about 0.25, whereas the calculation made by Archard gives $x_{max} =$ 0.44. The concentration of energy distribution in terms of the Archard model is approximately twice as high as is the case for the Spenser model.

For gaseous absorbents, the EB current density obeys the Lenard equation

$$j = j_0 \exp(-\alpha \gamma_a x) \tag{3.16}$$

where j_0 is the beam current density, A/cm^2; α the absorption coefficient, cm^2/g; γ_a the gas absorbent density g/cm^3; and x the gas layer thickness. In the energy range 20-200 keV, as a first approximation, the coefficient α is taken equal to $2.4 \times 10^6 E^{-2}$ cm^2/g at $20 < E_0 < 200$ keV ($\pm 15\%$).

Consider the spatial electron energy loss distribution calculated by the Monte Carlo method. The Monte Carlo method consists of a

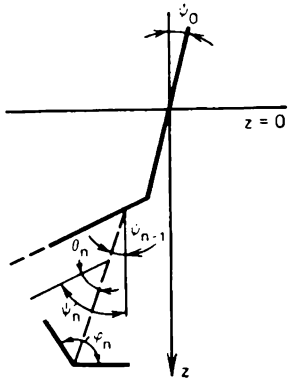

Fig. 3.7. Scheme illustrative of the calculation of electron motion in a substance by the Monte Carlo method: $\psi\psi_0$, initial angle of incidence of electrons, θ_n, angle between direction of first interaction of electron beam and φ direction of first scattering; $\varphi = \theta_n + \psi_{n-1}$

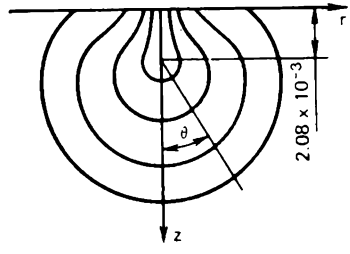

Fig. 3.8. Profiles of equal energies $|\, dE/dv \,|/|\, dE/dv \,|_0$ coupled from the electron beam to an aluminum plate; $|\, dE/dv \,|_0 = 10^6$ MeV/cm^3

direct simulation of the complex random process as a sequence of elementary events by using random numbers to determine the specific values of the parameters of scattered particles from requisite distributions (Fig. 3.7). The general procedure involved in the calculation of the interaction of emitted particles with a target material by this method includes a number of steps of simulation of the physical process called upon to reproduce the initial energy and angle of incidence from the angular distribution of source energy, the length of the electron path before the first collision from the distribution of paths, the type of process, the energy and angle of scattering from the distributions corresponding to the type of process, etc.

Using the Monte Carlo method, G.E. Gorelik has calculated the spatial distribution of energy lost in a semi-infinite aluminum specimen by 128-keV and 30-keV electron beams incident normal to the target surface at point $z = 0$, $r = 0$. Fig. 3.8 illustrates the profiles of equal energies released in a semi-infinite aluminum plate by electrons with an initial energy of 128 keV.

From the comparison of the obtained spatial electron-released energy distribution projected on the axis z/r_0 (Fig. 3.9, curve *1*) with the distribution calculated by Spenser (curve *2*), it is seen that

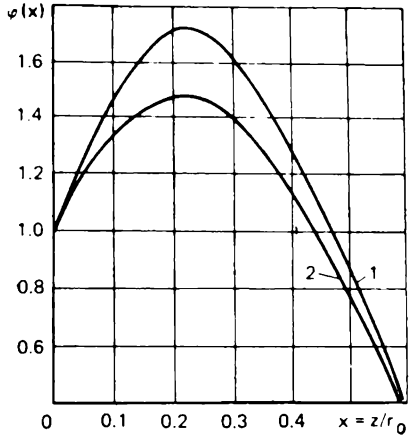

Fig. 3.9. Distribution of released electron energy: *1*, Gorelik's curve; *2*, Spenser's curve

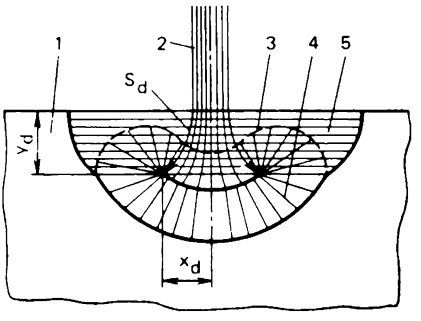

Fig. 3.10. Model of the zone of interaction of a monokinetic electron beam with a substance: *1*, target; *2*, electron beam; *3*, region of beam scattering through small angles due to collisions; *4*, region of diffusely scattered electrons; *5*, backward scattering through large angles due to collisions; subscript *d* at the symbols of parameters identifies the mean diameter

these distributions are similar since energy release maxima on both curves are found to be at a distance of about $0.25r_0$ from the surface. The gap between the two curves is due to the difference in the geometry of the structures under study. The thing is that the analysis of the distribution in a semi-infinite medium does not cover the effect of electron back-scattering, whereas in the case of the distribution in an infinite medium treated by Spenser for a monokinetic electron source this effect is taken into account: some electrons leaving the region $z > 0$ can collide with other particles and come back to the target, with the result that the pattern of distribution near the surface gets somewhat smooth.

The calculations reveal that the pattern of the spatial electron-released energy distribution, expressed in units of the total electron path, is weakly dependent on energy over a wide energy range.

The shape and size of the zone of electron beam-material interaction can be defined analytically (Figs. 3.10 and 3.11) under the following conditions: in the electron beam traveling through a medium the mean electron energy continuously varies per unit path; the number of electrons in the beam decreases due to scattering through large angles, the assumption being that the electrons undergo single scattering collisions and do not fall back into the beam; the angle of divergence of the beam in the medium increases on account of the angular spread in the directions of motion of electrons (at an angle of beam divergence equal to $\alpha > \pi/2$ the motion of electrons in a medium is thought of as being diffuse, i.e. equiprobable in all directions).

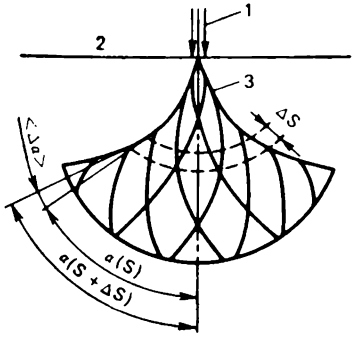

Fig. 3.11. Motion of electrons of the monokinetic beam in a substance: *1*, electron beam; *2*, substance; *3*, envelope of electron trajectories

Under these conditions, the analysis starts from the assumption that the electron energy obeys the Bethe law of continuous energy absorption. A change in the direction of motion of an electron depends on the cross section of Rutherford elastic scattering, the inelastic collisions being neglected. One more assumption is that after traveling an elementary path ΔS in a medium, the beam electrons change the initial directions of their motion by an average angle $\Delta\alpha$, which leads to an increase in the angle of beam divergence $\alpha\,(S + \Delta S)$ by the same value, i.e. $\alpha\,(S + \Delta S) - \alpha\,(S) = \Delta\alpha$.

The number of electrons dn scattered in a material within a solid angle $d\Omega$ over a path length from S to $S + dS$ is found from the Rutherford formula

$$dn = [Ze^2/4E\,(S)]\,n\,(S)\,N\,dS\,d\Omega/[\sin^4(\Phi/2)] \qquad (3.17)$$

where Z is the atomic number, e the electronic charge, and Φ the vectorial angle.

The expression for the Bethe law of continuous electron energy absorption assumes the form

$$dE/dS = [2\pi e^4 NZ/E\,(S)]\ln[2E\,(S)/I] \qquad (3.18)$$

where N is the number of atoms per cm^3, and I the mean ionization potential equal to 10.5 Z eV.

The number of beam electrons scattered back toward the sur-

face after covering an elementary path dS, which corresponds to the mean energy loss dE, is found by substituting the value of dS taken from equation (3.18) into equation (3.17) and integrating dn for the azimuthal angle φ over $0 \leqslant \varphi \leqslant 2\pi$ and for the vectorial angle Φ over $\pi/2 \leqslant \Phi \leqslant \pi$ by the expression

$$dn = \left(\frac{Z}{8}\right)[n(S)/E(S)]\,[dE/(\ln 2E/I_i)] \tag{3.19}$$

where $n(S)$ and $E(S)$ are the number and the energy of electrons, respectively, covering the path S in the substance.

The number of electrons, n, of energy E, which have traveled the path S, is estimated by integrating equation (3.19):

$$n(E) = n_0\left[\ln \frac{2E_i(S)}{I_i} \Big/ \left(\ln \frac{2E_0}{I_i}\right)\right]^{Z/8} \tag{3.20}$$

where n_0 is the number of primary electrons, and E_0 the initial electron energy.

Integrating equation (3.18) gives the relation between the electron energy $E(S)$ and S

$$\begin{aligned} S &= \frac{1}{2\pi e^4 NZ} \int_E^{E_0} \frac{E\,dE}{\ln(2E/I_i)} \\ &\approx \frac{1}{4\pi e^2 NZ}\left[\frac{E_0^2}{\ln(2E_0/I_i)} - \frac{E^2}{\ln(2E/I_i)}\right] \end{aligned} \tag{3.21}$$

The mean increment in the angle of scattering, $\Delta\alpha$, for beam electrons over the elementary path length ΔS is written as

$$\Delta\alpha = \frac{\int_S^{S+\Delta S}\int_{\Delta\Phi}^{\pi}\int_0^{2\pi} \Phi\,dn}{\int_S^{S+\Delta S}\int_{\Delta\Phi}^{\pi}\int_0^{2\pi} dn} \tag{3.22}$$

After transformations, the angle of divergence α of the electron beam of energy $E(S)$ is found from equations (3.21) and (3.22):

$$\tan^2(\alpha/4) = 7/8 \ln\left[\ln \frac{2E_0}{I_i} \Big/ \ln(2E/I_i)\right] \tag{3.23}$$

The coordinates of the envelope confining the tracks of electrons (see Fig. 3.11) that pass the distance S in the material are defined

TABLE 3.1. **Dimensions of Zones of Electron Beam-Material Interaction**

Material	I_i, eV	E_0, keV	S_0, μm	E_d, keV	s_d	x_d	y_d
					μm		
Al	136.5	10	0.985	5.650	0.632	0.266	0.421
		50	18.600	24.200	14.200	4.860	10.530
		100	67.300	44.000	52.700	16.070	40.570
Si	147	10	1.120	6.100	0.660	0.296	0.437
		50	21.200	28.000	13.900	6.272	9.165
		100	76.500	52.000	53.700	21.632	37.370
Cr-Ni steel[1]	285.6	10	0.377	7.850	0.129	0.080	0.069
		50	6.830	36.600	2.910	1.729	1.605
		100	24.400	71.400	11.250	6.576	6.285
Cu	304.5	10	0.378	8.000	0.124	0.076	0.067
		50	6.810	37.200	2.830	1.651	1.584
		100	24.400	73.000	10.800	6.359	6.000
Ta	766.5	10	0.291	9.400	0.030	0.025	0.011
		50	4.800	45.500	0.760	0.590	0.315
		100	17.100	90.000	3.000	2.309	1.257
W	777	10	0.252	9.450	0.023	0.022	0.007
		50	4.200	45.750	0.600	0.506	0.218
		100	19.700	90.500	2.400	1.980	0.905
Al_2O_3	111.3	10	0.630	4.900	0.448	0.172	0.318
		50	12.000	19.900	9.800	2.830	7.663
		100	54.000	39.600	46.080	11.210	37.617
SiO_2	116.6	10	1.140	4.900	0.824	50.30	0.594
		50	21.600	20.000	17.600	6.085	13.765
		100	78.500	35.600	67.000	1.0900	54.852
Si_3N_4	117.6	10	0.780	5.000	0.533	0.219	0.388
		50	15.000	20.500	12.100	3.680	9.310
		100	54.000	37.200	45.300	12.124	36.146
TiO_2	133	10	0.620	5.650	0.437	0.140	0.331
		50	12.000	24.500	8.820	3.222	6.387
		100	52.000	45.600	42.000	11.170	33.567
Ta_2O_5	279	10	0.460	7.800	0.170	0.097	0.097
		50	8.200	36.000	3.700	2.063	2.150
		100	29.400	70.500	13.900	7.872	7.957

[1] 20% Cr, 80% Ni.

from the expressions

$$x = d_0/2 + \int_0^S \sin[\alpha(S) + \alpha_0]\, dS$$
$$= d_0/2 + \cos\alpha_0 \int_0^S \sin\alpha(S)\, dS + \sin\alpha_0 \int_0^S \cos\alpha(S)\, dS$$
$$y = \int_0^S \cos[\alpha(S) + \alpha_0]\, dS \qquad (3.24)$$
$$= \cos\alpha_0 \int_0^S \cos\alpha(S)\, dS - \sin\alpha_0 \int_0^S \sin\alpha(S)\, dS$$

The calculated parameters of interaction of the EB with some materials are listed in Table 3.1 [5].

From Table 3.1 it follows that the current of scattered electrons in materials with low atomic numbers ($Z < 30$) is governed by elastic scattering through large angles; at $Z > 30$, the share of electrons penetrating into the material decreases because the diffusely scattered electrons come out to the surface.

The pattern of temperature distribution in the zone of interaction of the EB with a material strongly depends on the ratio of the beam diameter d to the electron penetration depth δ. The material processing that involves melting and vaporization will be effective

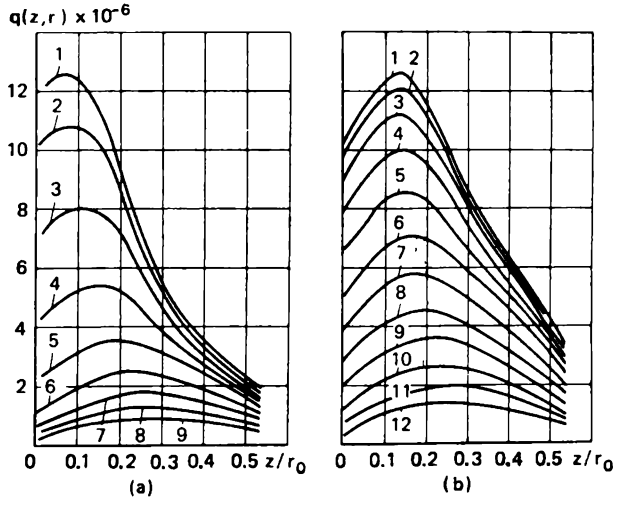

Fig. 3.12. Spatial distribution of source heat density

only at $d > 2\delta$; it is difficult to use very thin beams ($d < \delta$) for micromachining.

Figure 3.12 illustrates the plots of the spatial distribution of the heat power density $q\ (r, z)$ versus z/r_0 for heat sources of various diameters, produced in a semi-infinite aluminum plate by a monokinetic monodirectional electron beam ($D = 2a_1$, $0.25r_0$, and $0.5r_0$), whose current density varies according to the Gauss law:

$$I(r) = \frac{I}{1.44a_1^2} \exp\left(-\frac{r^2}{1.44a_1^2}\right) \tag{3.25}$$

where I is the total EB current, A; and a_1 the radius from the beam axis to the point where the current density is half of the maximum value.

The curves of Fig. 3.12 represent the heat densities produced in an aluminum target by the electron beam of energy $E = 128$ keV and current $I = 0.1$ mA. In Fig. 3.12*a*, the curves *1-9* correspond to radii $r/r_0 = 0$ to 0.4 with a pitch of 0.05 at $\bar{q}(r, z) = 1.16 \times 10^{-6} q\ (r, z)$ W cm^{-3} and beam diameter $D = 0.25r_0$. In Fig. 3.12*b*, the curves *1-12* correspond to radii $r/r_0 = 0$ to 0.55 with a pitch of 0.05 at $\bar{q}(r, z) = 3.09 \times 10^{-6} q\ (r, z)$ W cm^{-3} and $D = 0.5r_0$.

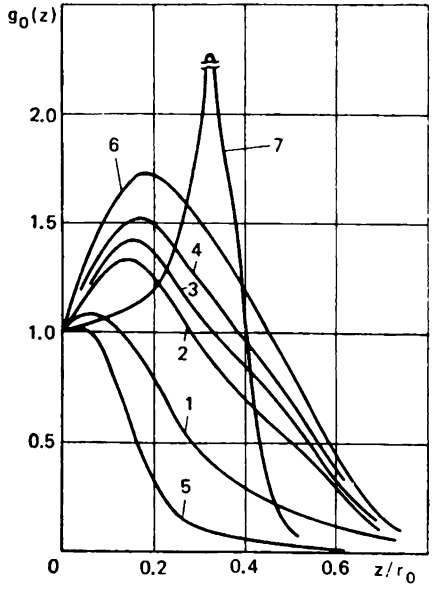

Fig. 3.13. Source heat density distribution, $g_0(z) = q\ (0, z)/q\ (0, 0)$, along axis z/r_0 $(r = 0)$

It is evident from Fig. 3.12 that as the beam diameter increases, the radial distribution "smoothes out", while the distribution in depth, particularly near the beam axis, becomes "sharper". This pattern of distribution is still more vivid in Fig. 3.13 which displays the normalized heat density distribution $g_0(z) = q\ (0, z)/q\ (0, 0)$ along the axis z/r_0 $(r = 0)$. The curves *1*, *2* and *3* correspond to beam diameters D equal to $0.25r_0$, $0.5r_0$, and $0.7r_0$ respectively. The curve *4* represents a unidimensional case for $D = \infty$. The curve *5* is the plot of the heat power density against the electron penetration depth for the EB focused to a point ($D = 0$); it corresponds to the

spatial distribution of energy lost by a single electron. The curve *6* describes a unidimensional case and curve *7* represents the Archard model. With an increase in the beam diameter, the maximum of distribution becomes more acute. It shifts from the surface into the bulk of the material and varies between the limits $z^{\delta}_{max} \leqslant z_{max} \leqslant z^{\infty}_{max}$, where z^{δ}_{max} is the position of the maximum for a δ-type electron-beam heat source, which corresponds to the spatial distribution of energy released by a single electron; and z^{∞}_{max} is the coordinate of the peak for an EB of infinite diameter, which corresponds to the unidimensional distribution.

The above result is due to the shape of the heat source with consideration for the spatial electron-released energy distribution, because the density $q(r, z)$ of energy lost by a single electron (see Fig. 3.8) as a function of r has a maximum at different depths from the surface. The depth of maximum energy release is the least at the point of impact of an electron; this depth increases with distance from the point. Therefore, at small diameters of the electron beam ($D \ll r_0$), in which case the heat distribution pattern represents the transfer of energy from a single electron, the distance from the maximum to the surface along the EB axis is at a minimum ($z_{max} \approx z^{\delta}_{max}$). As the diameter of the EB increases, the distribution of the beam along its axis tends to become unidimensional. The position of the maximum changes accordingly, which tends to z^{∞}_{max}. A similar result is impossible to obtain using the Archard model since in this model (see Fig. 3.13) the position of the energy release maximum is independent of r.

3.2. STATEMENT OF HEAT SOURCE PROBLEMS. LINEAR HEAT-TRANSFER PROBLEMS AND STATIONARY SOURCES

Proceeding from the theory of heat source [4], it is possible to reduce a variety of practical cases of heating the materials by concentrated energy flux (CEF) sources to certain generalities covering the basic features of heating processes.

The targets heated by CEF sources can be regarded as semi-infinite, finite, and multilayer bodies depending on their shape and size.

The boundary-value problems describing the heating of materials by the CEF of a power density limited to about 10^6 W/cm^2 are largely the problems of heat conduction with boundary conditions of the second kind.

The forms of the problems stated determine the choice of solution methods. It is common to use the following analytical methods

for solving linear heat-transfer problems: the source method (Green function method), Fourier analysis, finite and infinite integral transforms in space variables, Laplace transforms in time variables, theory of generalized functions, etc. [7, 8].

Let us look at the relation between the choice of a method for investigating the problem in question and the specific information to be obtained in solving the problem. For the solution to the three-dimensional problems of heating semi-infinite bodies generally for any length of time, the source method is most universal. This method in combination with the principle of local interaction [4] allows us to consider, in general terms, the basic mechanisms responsible for changes in the temperature field of material. In some cases, finite and infinite integral transforms prove effective.

In the analysis of temperature fields in composite bodies, it is convenient to employ the Laplace transform in time variables, by which one can define the solution forms valid for small heat-source dwell times and for steady temperature fields.

The finite integral transforms in space variables can be used to advantage where there is a substantial difference between the properties of materials being joined or heated, for example, in the case of butt welding of sheet materials or heating of two-layer plates limited in radial directions.

The classical Fourier method combined with integral transforms can act as an effective tool in tackling the problems of heating where the surface temperature is close to the steady-state temperature.

In a number of problems concerned with heating of metals by laser radiation (LR), allowance should be made for the temperature dependence of thermal and optical constants. The general analytic methods for the solution of these problems have not yet been evolved. The solution methods for nonlinear problems of heat conduction are systematized in works [9, 10]. The computer-aided formulation of two- or three-dimensional problems with consideration for the temperature dependence of thermal constants afford the most effective solution to these problems.

Heat-transfer equations. Boundary conditions. In the general case, the heat conduction equation written in rectangular coordinates x, y, z for a heat source in a semi-infinite body has the form

$$(\partial/\partial t)\,(c\gamma T) = \operatorname{div}\,(\lambda \operatorname{grad} T) + q_v \qquad (3.26)$$

Here, the specific heat c, density γ, and thermal conductivity λ are temperature dependent, i.e. vary with space coordinates and time. The volume source q_v in the bulk of a material is generally also temperature dependent.

Of particular interest from the practical standpoint are isotropic systems noted for the same properties in all directions and stable thermal constants. The volume heat source in such a system

is independent of temperature. For the case in hand, the equation takes the form

$$(1/a)\,(\partial T/\partial t) = \Delta T + q_v \tag{3.27}$$

where $a = \lambda/c\gamma$ is the thermal diffusivity.

When LR interacts with metals and other opaque materials, the heat source produced is plane and q_v in equation (3.27) reduces to zero. The electron beam (EB) produces a volume heat source, so its effect should be defined by equation (3.27).

Of the number of nonlinear problems involved in CEF processing of materials, the problems of heating an isotropic body whose thermal conductivity and specific heat vary with temperature are of the principal practical interest. The statement of the problem in this case can be written as

$$\lambda\,\Delta T + (\partial\lambda/\partial T)\,[(\partial T/\partial x)^2 + (\partial T/\partial y)^2 + (\partial T/\partial z)^2] - \gamma c\,(T)\,(\partial T/\partial t) + q_v = 0 \tag{3.28}$$

The boundary conditions, i.e. the set of edge and initial conditions, enable us to obtain an unambiguous solution of heat equations.

For CEF material processing, the focus of attention is on the problems with boundary conditions of the second kind:

$$-\lambda\,\partial T/\partial z = q_0|_{z=0} = A\varphi\,(t)\,q\,(r) \tag{3.29}$$

Here the power density q_0 on the target surface is generally a function of temperature as well as coordinates.

For most practical cases, the heat problem is axisymmetric, i.e. the equation and boundary conditions can be written in cylindrical coordinates.

Unidimensional models. The simplest way to clarify the basic mechanism of heating by the CEF source is to try the linear case on unidimensional models which hold at $r_f \gg (at)^{1/2}$, where r_f is the radius of the focused hot spot. This condition is not obviously met in all the cases of interaction of the heat sources with materials, but what is important is that the initial stages of heating by both pulse and continuous sources can be treated in terms of a unidimensional model. In this analysis, we shall not yet draw a distinction between the LR and EB effects on materials and assume that either of the effects shows not a qualitative but a quantitative character due to the different values of absorptivity A for different materials.

The heat-transfer equation for a unidimensional semi-infinite body and boundary conditions (3.29) must be supplemented by both the boundary conditions at infinity ($r \to \infty$, $z \to \infty$) and the initial condition.

We shall assume that the temperature has a limited value at large values of r and z:

$$T = 0|_{r,\, z\to\infty} \tag{3.30}$$

For ease of analysis, the initial temperature at all points of the body can be taken equal to zero:

$$T = 0|_{t=0} \tag{3.31}$$

Using, for example, the Laplace transform in time t, we can construct the solution of the problem in the form

$$T(z, t) = \{Aq_0/[c\gamma(\pi a)^{1/2}]\} \int_0^t \varphi(t-\xi)\, \xi^{-1/2} \exp(-z^2/4a\xi)\, d\xi \tag{3.32}$$

where q_0 is the power density, and ξ the integration variable.

Consider some specific cases of relation (3.32), which correspond to the initial stages of heating by various sources. We shall focus our attention on different types of LR temporal patterns.

In the case of stable pulse lasing, the temporal pattern of the laser pulse is defined by relation (3.9). Hence, substituting (3.9) into (3.32) yields

$$T(z, t) = q_0\lambda^{-1}\sqrt{a}\left\{\sqrt{t}\ \mathrm{ierfc}\,(z/2\sqrt{at}) - [2^{-1}\pi^{-1/2}] \int_0^t \cos[\omega(t-\xi)] \exp(-z^2/4a\xi)\, \xi^{-1/2}\, d\xi\right\} \tag{3.33}$$

where ω is the spike repetition rate, and ierfc stands for the integral of the complementary error function.

The first term in relation (3.33) describes the heating of a semi-infinite body by a steady heat source of flux density $q_0/2$; the second term defines a decrease in temperature due to the oscillatory temporal pattern of the heat source in (3.9). The estimation of the second term in (3.33) at different values of ω, z, and t can be made by numerical methods.

For the quasi-continuous operation of a pulse laser at $t < \tau$, we have

$$T(z, t) = (2q_0\sqrt{at}/\lambda)\ \mathrm{ierfc}\,[z/2\sqrt{at})] \tag{3.34}$$

The function ierfc (x) in (3.33) and (3.34), which is the integral of the probability integral function, is given by

$$\mathrm{ierfc}\,(x) = \int_x^\infty \mathrm{erfc}\,(x)\, dx = (1/\pi^{1/2})\, e^{-x^2} - x\,\mathrm{erfc}\,(x) \tag{3.35}$$

This function decays with increasing argument x more rapidly than erfc (x). The effective thickness of a heated layer is limited by the parameter

$$(z/2\sqrt{at}) \approx 1.6 \quad (\text{ierfc } 1.6 \approx 10^{-2})$$

For example, in iron ($a = 0.1$ cm^2/s) when $r_f = 5 \times 10^{-2}$ cm, at the instant t^* ($t^* \ll r_f^2/a = 2.5 \times 10^{-4}$ s) the depth of heat penetration approaches 50 μm.

Look at another limiting case of the problem of interaction of a heat source with a thin plate whose thickness δ is much smaller than its radial size. Let the heat flux of density $q(t)$ fall on a circular area of radius r_f. Since the plate is thin, we can disregard the temperature gradient over the plate thickness and assume that the temperature distribution here depends on the variable r and time t. Some researchers have solved this problem by applying the Laplace transformation with respect to t. A change in the temperature at the plate center ($r = 0$) on the time interval $0 \leqslant t \leqslant \tau$ of the heat source action is

$$T(0, t) = (q_0 t/c\delta)\,[1 - \exp(-r_f^2/4at) - (r_f^2/4at)\,Ei(-r_f^2/4at)] \tag{3.36}$$

where $Ei(-x) = \int_x^\infty \exp(-u)\,u^{-1}\,du$ at $u > 0$ is Euler's function.

Expression (3.36) is set up for the function $q(t)$ that has the form

$$q(t) = \begin{cases} q_0 & 0 \leqslant t \leqslant \tau \\ 0 & t > \tau \end{cases} \tag{3.37}$$

where τ is the pulse duration.

For any instant of time and at $t > \tau$ too, the expression below is valid:

$$T(0, t) = (q_0 t/c\delta)\,\{1 - \exp(-r_f^2/4at) - (r_f^2/4at)\,Ei(-r_f^2/4at) - \sigma_0(t-\tau)(1-\tau/t)\,[1 - \exp(-z) - zEi(-z)]\} \tag{3.38}$$

$$z = 4\,at/(1-\tau/t)\,r_f^2$$

$$\sigma_0(t-\tau) = \begin{cases} 0 & 0 \leqslant t \leqslant \tau \\ 1 & t > \tau \end{cases}$$

At $t \leqslant 0.2r_f^2/a$, instead of expression (3.36), we can form a simpler equation by asymptotically expanding the integral-exponential function $Ei(-x)$ into a series

$$T(0, t) = (q_0 t/c\delta)\,[(1 - 4at)/r_f^2 \exp(-r_f^2/4at)] \tag{3.39}$$

The problems on heating anisotropic materials, for example, two-layer bodies differing in thermal properties, are essential for

welding. We restrict our analysis to the unidimensional case which permits us to follow up the basic mechanisms of the process of heating.

The formulation of the problem on the temperature field in a semi-infinite two-layer body exposed to a heat source of constant flux density q_0, considering that the thermal contact between the layers is ideal, is given as

$$\begin{aligned} &(1/a_1)\,(\partial T_1/\partial t) = \partial^2 T_1/\partial z^2 \\ &t > 0, \quad h \geqslant z \geqslant 0 \\ &(1/a_2)\,\partial T_2/\partial t = \partial^2 T_2/\partial z_2 \\ &t > 0, \quad \infty > z \geqslant h \end{aligned} \tag{3.40}$$

The boundary conditions are

$$z = 0, \quad -\lambda_1\,\partial T_1/\partial z = q_0 \tag{3.41}$$

$$z = h, \quad \begin{cases} T_1 = T_2 \\ \lambda_1\,\partial T_1/\partial z = \lambda_2\,\partial T_2/\partial z \end{cases} \tag{3.42}$$

$$z \to \infty$$

$$z = \infty, \quad T_2 = 0 \tag{3.43}$$

$$t = 0, \quad T_1 = T_2 = 0 \tag{3.44}$$

Relation (3.42) is written for ideal thermal contact between the layers of different thermal properties.

The problem solution worked out by taking the Laplace transform in time t has the form

$$T_1(z,\ t) = \left(\frac{2q_0\sqrt{a_1 t}}{\lambda_1}\right)\left\{\operatorname{ierfc}\left(\frac{z}{2\sqrt{a_1 t}}\right) + \sum_{n=1}^{\infty}(-g)^n\left[\operatorname{ierfc}\left(\frac{2nh+z}{2\sqrt{a_1 t}}\right) + \operatorname{ierfc}\left(\frac{2ah-z}{2\sqrt{a_1 t}}\right)\right]\right\} \tag{3.45}$$

$$T_2(z,\ t) = \left(\frac{2q_0\sqrt{a_2 t}}{\lambda_1}\right)(1-g) \times \sum_{n=1}^{\infty}(-g)^n \operatorname{ierfc}\left(\frac{(2n+1)\,h + (z-h)\sqrt{a_1/a_2}}{2\sqrt{a_1 t}}\right) \tag{3.46}$$

where

$$g = \frac{\lambda_1/\sqrt{a_1} - \lambda_2/\sqrt{a_2}}{\lambda_1/\sqrt{a_1} + \lambda_2/\sqrt{a_2}} \tag{3.47}$$

Of particular interest from the practical considerations are the regularities of changes in temperature with time at points on the heating surface and at the boundary between the layers. The

relations for temperatures at corresponding points, written in a dimensionless form, are

$$\theta(0,\ t) = \frac{T_1(0,\ t)}{T^*} = 2\sqrt{\mathrm{Fo}}\left[\frac{1}{\sqrt{\pi}} + 2\sum_{n=1}^{\infty}(-g)^n \operatorname{ierfc}\left(\frac{n}{\sqrt{\mathrm{Fo}}}\right)\right] \tag{3.48}$$

$$\theta(h,\ t) = \frac{T_1(h,\ t)}{T^*} = 2\sqrt{\mathrm{Fo}}\left\{\operatorname{ierfc}\left[\frac{1}{2\sqrt{\mathrm{Fo}}}\right] + \sum_{n=1}^{\infty}(-g)^n\left[\operatorname{ierfc}\left(\frac{2n+1}{2\sqrt{\mathrm{Fo}}}\right) + \operatorname{ierfc}\left(\frac{2n-1}{2\sqrt{\mathrm{Fo}}}\right)\right]\right\} \tag{3.49}$$

where $T^* = q_0 h/\lambda_1$, and $\mathrm{Fo} = a_1 t/h^2$ is the Fourier criterion.

Figure 3.14 displays the calculated results of interest to laser welding, which are found from equations (3.48) and (3.49) for the region of changing parameters. Shown for comparison is the curve of temperature variations on the surface of a semi-infinite body heated by a source of constant power density q_0.

Using a similar unidimensional formulation of the problem but with the conditions of nonideal contact between the layers, i.e. with boundary conditions at the contact,

$$z = h\left\{\begin{array}{l} -\lambda_1\,\partial T_1/\partial z = (1/R)(T_1 - T_2) \\ \lambda_1\,\partial T_1/\partial z = \lambda_2\,\partial T_2/\partial z \end{array}\right. \tag{3.50}$$

where R is the thermal resistance at the interface of layers, we can find the solution for the problem on the temperature field, which at small times assumes the form

$$T_1(z,\ t) = q_0\left(R + \frac{h-z}{\lambda_1}\right) - \frac{2h}{\lambda_1} \times \sum_{n=1}^{\infty} \frac{[\operatorname{ctg}\mu_n \cos(1-z/h)\,\mu_n + \sin(1-z/h)\,\mu_n]\exp(-\mu_n^2 a_1 t/h^2)}{\mu_n[(1+\mu_n^2/\mathrm{Bi})\cos\mu_n + \mu_n^2]} \tag{3.51}$$

where μ_n's are the roots of the equation

$$\mu = \mathrm{Bi}\operatorname{ctg}\mu \tag{3.52}$$

and $\mathrm{Bi} = h/R\lambda_1$ is the Biot criterion.

Expression (3.51) holds for $t < t_a$, where

$$t_a \leqslant R\lambda_2^2 a_2^{-1} \times 10^{-2} \tag{3.53}$$

At $\lambda_2 = 4.2$ W cm^{-1} K^{-1} and $a_2 = 1$ cm^2 s^{-1}, the calculation by (3.53) gives $t_a = 10^{-4}/\alpha$ s. Since generally $R^{-1} \leqslant 0.4$ W cm^{-2} K^{-1}, the time t_a is about 10^{-3} s. This means that expression (3.51) is true for the entire period of action of the heat source where millisecond laser pulses are involved.

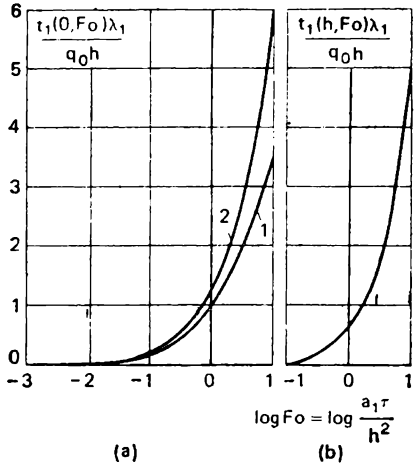

Fig. 3.14. Dimensionless temperatures as a function of Fourier's criterion: (*a*), at surfaces of semi-infinite aluminum body (curve *1*) and two-layer aluminum silicon plate (curve *2*); (*b*), at surface of contact between aluminum and silicon; $h = 0.02$ cm

Consider a unidimensional problem concerned with heating of a semi-infinite body by a volume heat source, whose flux density drops off with increasing depth z in an exponential manner (Bouguer law), in which case a change in the heat power density $q(z)$ with depth z from the body surface can be given by the expression

$$q(z) = q_0 \exp(-\alpha z) \quad (3.54)$$

where α is the absorption coefficient, cm^{-1}.

The solution to the unidimensional problem on heating a semi-infinite body by a heat source of power density defined by (3.54) takes the form

$$T(z, t) = (\alpha q_0/c\gamma)\{[\exp(-\alpha z + a\alpha^2 t)/a\alpha^2]\operatorname{erfc}[(2a\alpha t - z)/2\sqrt{at}] + [\exp(\alpha z + a\alpha^2 t)/a\alpha^2] \times \operatorname{erfc}[(2a\alpha t + z)/2\sqrt{at}] + (4\sqrt{t}/\alpha\sqrt{a}) \times \operatorname{ierfc}(z/2\sqrt{at})\} \quad (3.55)$$

We now turn to particular cases of equation (3.55). If the laser beam penetration depth, $\delta = \alpha^{-1}$, is much greater than the thickness of the layer, $h \approx (at)^{1/2}$, heated as the result of heat transfer, so that inequality $\alpha\sqrt{at} \ll 1$ is valid, then

$$T(z, t) = (\alpha q_0 t/c\gamma)\exp(-\alpha z) \quad (3.56)$$

In this case, the temperature rises linearly with time and its variation with depth depends on the direct penetration of the laser beam to a depth z.

On the surface of a body at $z = 0$,

$$T(0, t) = \alpha q_0 t/c\gamma \quad (3.57)$$

For such materials as ferrite ($\alpha = 2 \times 10^3$ cm^{-1} and $a = 5 \times 10^{-3}$ cm^2 s^{-1}), expressions (3.56) and (3.57) are valid at $t < 10^{-4}$ s. If inequality $\alpha \sqrt{at} \gg 1$ is true, the heat source can be considered plane and the temperature change with time can be given by relation (3.34). For ferrite, the above inequality holds at $\sqrt{t} \gg 10^{-4}$ s. For metals, the condition $\alpha \sqrt{at} \gg 1$ is valid in most cases, except at rather short times t.

Three-dimensional models. Stationary heat sources. Consider the problems of heating in terms of the spatial model when $r_f \approx \sqrt{at}$, i.e. the depth of penetration of heat into a body is comparable to the hot spot radius r_f.

Assume a heat source of constant power P_0 distributed by the Gauss law acts on the surface of a semi-infinite body starting at the moment $t > 0$. Applying the method of sources, we obtain the expression for temperature

$$T(r, z, t) = \frac{2P_0}{c\gamma (4\pi a)^{3/2}} \times \int_0^t \frac{d\xi \exp\{-(4a)^{-1}[z^2/\xi + r^2/(t_0+\xi)]\}}{\sqrt{\xi}(t_0+\xi)} \tag{3.58}$$

where $t_0 = (4ak)^{-1}$ is a time constant.

The integral entering into (3.58) cannot be expressed in the general form in terms of elementary functions. But it is given detailed treatment in monograph [4], so we shall not analyze in detail the behavior of this integral with changes in the parameters of the problem.

If the heat power density does not exceed the critical value $q_c^{(1)}$ (see p. 138), the process of interaction may culminate in a limiting state, in which case we can calculate the temperature at the central point in a semi-infinite body with the equation

$$T(0, 0, \infty) = (P_0/2\lambda)\sqrt{k/\pi} \tag{3.59}$$

As follows from (3.59), the growth of the concentration of the source heat leads to an increase in the limiting temperature of the source. The relation between the effective power P_0 and power density q_0 of the normal (Gaussian) heat source is given as

$$P_0 = \pi q_0/k \tag{3.60}$$

Similar relations for the calculation of the temperature field can also be written for the uniform distribution of the heat power density over the hot spot [7]. Given below are some expressions for the calculation of the temperature of a body with a heat source having a uniform distribution of the power density over the round

spot of radius r_f:

(a) along the z axis,

$$T(0,\ z,\ t) = (2q_0\sqrt{at}/\lambda\,[\mathrm{ierfc}\,(z/2\sqrt{at}) - \mathrm{ierfc}\,(\sqrt{z^2+r_f^2}/2\sqrt{at})] \tag{3.61}$$

(b) on the surface at the hot spot center,

$$T(0,\ 0,\ t) = (2q_0\sqrt{at}/\lambda)\,[1.1284 - \mathrm{ierfc}\,(r_f/2\sqrt{at})] \tag{3.62}$$

The limiting temperature at the hot spot center when $t \to \infty$ is

$$T(0,\ 0,\ \infty) = q_0 r_f/\lambda \tag{3.63}$$

The plate of finite thickness. Taking into account the finite thickness of a plate in calculating the temperature fields in CEF-heated materials is essential for welding, heat treating, and other applications. The problem of heating of a thin sheet by a Gaussian heat source with consideration for convective heat transfer at the back surface of the plate differs from the problem stated for a semi-infinite body by the boundary condition on the back side of the sheet. Instead of the limiting condition for temperature at infinity, we need to formulate the condition of heat removal from the surface where $z = h$ (h is the sheet thickness, with the origin of coordinates located on the heating surface). In the general case, the boundary condition is nonlinear since some amount of heat is lost on the heating surface. The condition of heat transfer on the surface where $z = h$ can in the simplest form be written as

$$z = h, \quad -\lambda\,\partial T/\partial z = \alpha_1 T \tag{3.64}$$

where α_1 is the heat transfer coefficient accounting for both convection and radiation heat losses.

Then, using the integral transforms in r and t, the solution can be found in the form

$$T(r,\ z,\ t) = \frac{1}{\lambda}\int_0^\infty \frac{ds\Phi(s)\,J_0(sr)\,[\lambda s\cosh(h-z)\,s + \alpha_1\sinh(h-z)\,s]}{\lambda s\sinh(hs) + \alpha_1\cosh(hs)} - \frac{2}{h}\int_0^\infty \sum_{n=1}^\infty \frac{ds\Phi(s)\,J_0(sr)\,s[\cos\mu_n(1-z/h) + \alpha_1\sin\mu_n(1-z/h)]}{(\mu_n^2/h^2+s^2)\,[(\alpha_1 h+\lambda)\sin\mu_n + \lambda\mu_n\cos\mu_n]} \times \exp[-(\mu_n^2/h^2+s^2)\,at] \tag{3.65}$$

Here μ_n denotes the roots of the transcendental equation,

$$\mu\tan\mu = \mathrm{Bi} \tag{3.66}$$

where $\mathrm{Bi} = \alpha_1/\lambda\sqrt{k} = \alpha_1 r_f/\lambda$ is the Biot criterion, and

$$\Phi(s) = (q_0/2k)\exp(-s^2/4k) \tag{3.67}$$

The calculations of temperature by equations (3.65) through (3.67) for a copper sheet have been made by N.N. Rykalin and A.A. Uglov. If the heat transfer on the back surface of the plate is not taken into account (the assumption being that the plate is heat-insulated), the equations for the temperature field assume a much simpler form.

Two-layer materials. The calculation of temperature fields in two-layer materials is particularly important for the cases where the size of the zone of laser-material interaction plays a decisive role in selecting the method of welding, for example, metals to semiconductors, which calls for a high level of local heating but does not allow for mechanical influences on account of processing conditions.

The process of laser or electron beam welding typically reduces to melting and fusion of multilayer materials whose thermal properties vary abruptly at a certain boundary, namely, in the region of contact of the layers.

Ideal thermal contact. If the dwell time τ of a heat source is short, the temperature distribution over the body volume obeys the regularities specific to the unidimensional problem of heat conduction. If the dwell time is about 10^{-3} s and over and the hot spot radius r_f is near 10^{-2} cm, the heat transfer problem must be solved in terms of the three-dimensional model since $r_f \approx \sqrt{at}$ (at $a \approx 0.1$ to 1 cm^2/s), i.e. the hot spot radius is comparable to the depth of penetration of the heat into the body.

The features typical of three-dimensional problems are the following. The spatial-temporal pattern of a heat source is defined by a time-constant pulse with a Gaussian power density distribution over the target surface. The thermal parameters of each of the materials in contact are taken to be temperature independent, with the heat transfer from the heating surface neglected. Contact at the boundary between the materials can be ideal, in which case the temperatures and thermal energies at all points of contact are the same, and nonideal. In the latter case, the temperature at the interface between the layers changes abruptly, while the heat fluxes remain equal. The problem of heating of a two-layer specimen with ideal contact at the interface is written as a set of differential equations in cylindrical coordinates:

$$(1/a_1)\,(\partial T_1/\partial t) = \Delta T_1 \tag{3.68}$$

$$\text{at } t > 0, \quad r_0 \geqslant r \geqslant 0, \quad h \geqslant z \geqslant 0$$

$$(1/a_2)\,(\partial T_2/\partial t) = \Delta T_2 \tag{3.69}$$

$$\text{at } t > 0, \quad r_0 \geqslant r \geqslant 0, \quad l \geqslant z \geqslant h$$

$$z = 0, \quad -\lambda_1\,\partial T_1/\partial z = q_0 \exp(-kr^2) \tag{3.70}$$

$$z = h, \quad \begin{cases} T_1 = T_2 \\ \lambda_1 \partial T_1/\partial z = \lambda_2 \partial T_2/\partial z \end{cases} \tag{3.71}$$

$$z = l, \quad T_2 = 0 \tag{3.72}$$

$$r = r_0, \quad t = 0, \quad T_1 = T_2 = 0 \tag{3.73}$$

If the plate radius is $r_0 \gg r_f$ and $l \gg h$, the boundary conditions at $r = r_0$ and $z = l$ exert a small influence on the temperature distribution in the regions of principal interest, namely, in the contact zone and on the surface of the body.

The calculated values of temperature for a two-layer Al-Si system are given in Fig. 3.15, which also presents the calculated

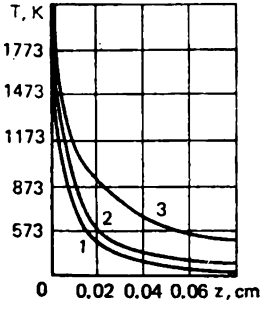

Fig. 3.15. Curves of plate temperatures along the heat source axis ($r = 0$): *1*, for Al plate at power density q_1; *2*, for two-layer Al-Si plate at $q_1 = q_2$; *3*, for Al plate at $q_1 > q_2$; $k = 3 \times 10^{-4}$ cm^2; $\tau = 8$ ms

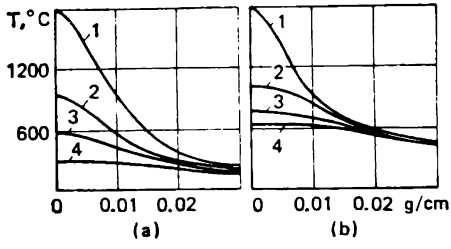

Fig. 3.16. Temperature distribution along the radial distance r for aluminum plate (*a*) and two-layer Al-Si plate (*b*): *1*, $z = 0$; *2*, $z = 10^{-3}$ cm; *3*, $z = 10^{-2}$ cm; *4*, $z = 2 \times 10^{-2}$ cm

temperatures in a single-layer Al plate for comparison. As seen, the temperature in the single-layer plate drops off faster than in the case for the two-layer plate because the thermal conductivity of aluminum is higher than that of silicon. For this reason, the isothermic lines corresponding to the melting point lie at different distance from the spot center.

Figure 3.16 presents the curves of radial temperature distribution in the spot of radius r at different values of depth z for single-layer and two-layer plates. If the hot spot diameter grows (k decreases), while the heat power density remains invariable, the melting depth (penetration depth) gets smaller in the single-layer plate, but changes little in the two-layer plate.

For a Gaussian heat source at

$$\tau < (20\ ak)^{-1} \tag{3.74}$$

it is expedient to use the approximation at short times. In this case, the temperature distribution in both a single-layer and a two-layer plate is given by the product of two cofactors: the first is the solution of the unidimensional heat problem for a continuous heat source and the second is the function describing the power density distribution along the coordinate r. This rule is also valid for volume heat sources.

For example, inequality (3.74) holds for aluminum at a pulse duration of up to 10^{-5} s and a concentration coefficient k of 10^4 cm^{-2} ($r_f = 170$ μm).

Nonideal thermal contact. In welding of workpieces, the thermal contact is commonly far from ideal if no clamp force acts on the

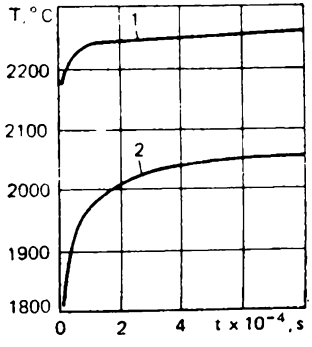

Fig. 3.17. Temperature at the surface of the upper aluminum plate at $r = 0$ versus time: *1*, $\alpha_1 = 4.2$ W cm^{-2} K^{-1}; *2*, $\alpha_1 = 42$ W cm^{-2} K^{-1}

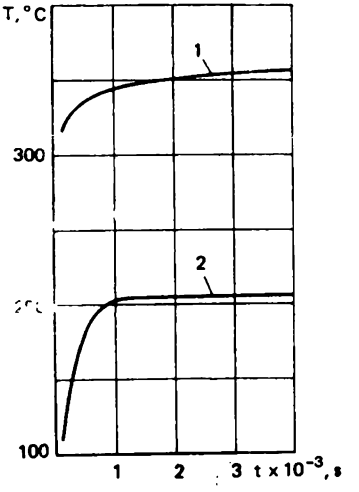

Fig. 3.18. Temperature of the upper aluminum plate in the region of contact with the lower silicon plate versus time: *1*, $\alpha_1 = 4.2$ W cm^{-2} K^{-1}; *2*, $\alpha_1 = 42$ W cm^{-2} K^{-1}

bodies to deform plastically the minute protrusions at the interface. This problem differs from the problem for the ideal case in that it necessitates a change in the boundary condition at the interface $z = h$, which takes on the form of (3.50). When the thermal resistance in the contact area is $\alpha_1^{-1} = R \to 0$, the condition of nonideal contact is replaced by the condition of ideal contact.

Figures 3.17 and 3.18 display the calculated values of temperature in a 50-μm dia. hot spot on an Al-Si specimen both at the surface of the upper 100-μm thick aluminum plate and at the inter-

face. In the region of contact, the temperature of the upper plate is not equal to that of the lower silicon plate. The estimates that are illustrative in character have been found from temperature relations at small dwell times. As follows from the calculations, the value of the heat transfer coefficient α_1 has a noticeable effect on the shape of the heat curve: as α_1 diminishes, the interface rises more quickly to its steady temperature.

The effect of α_1 on temperature in the two-layer Al-Si specimen is shown in Fig. 3.19. The laser pulse length used in the calculations corresponds to the onset of the stationary process. It is seen from the figure that at $\alpha_1 = 4.2$ W cm^{-2} K^{-1} the temperature difference at the boundary between the plates may reach 400 K. This points to the fact that if no clamp force is applied normal to the region of contact between the plates to be welded, the calculations should allow for the nonideal contact.

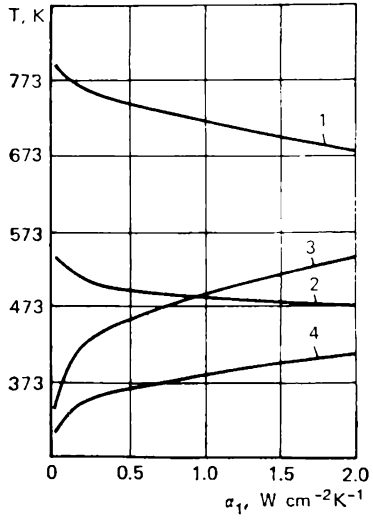

Fig. 3.19. Temperature at the surface of contact of the upper aluminum plate (curves *1* and *2*, T_1) with the silicon plate (curves *3* and *4*, T_2) as a function of heat transfer coefficient α_1: *1*, *3*, at $q = 10^6$ W cm^{-2}; *2*, *4*, at $q = 0.5 \times 10^6$ W cm^{-2}

Surface heat transfer. Consider the cases in which it is necessary to account for the heat transfer from the target surface due to radiation and convection heat losses.

In the general case, this problem is nonlinear because of the boundary condition for which the heat flow from the surface is proportional to T^4. For rough estimates to be made, it is enough to restrict the analysis to a linear approximation, assuming that the radiation component of the heat transfer coefficient is proportional to T. The boundary condition at the surface of a semi-infinite body can then be written as

$$z = 0, \quad -\lambda \partial T_1/\partial z + \alpha_1 T_1 = q_0 \exp(-kr^2)\chi(t) \tag{3.75}$$

where α_1 is the surface heat transfer coefficient, and $\chi(t)$ the function describing the temporal pattern of an LR or EB pulse.

The problem of heating a semi-infinite body by a CEF involves the zero initial condition, limiting temperature conditions at infinity when r, $z \to \infty$ and condition (3.75) for the surface when

$z = 0$. The solution of the problem takes on the form

$$T(r, z, t) = (4\lambda k \sqrt{a\pi})^{-1} \int_0^t \varphi(r, z, t, \xi)[1 - \psi(z, \xi)]\, d\xi \quad (3.76)$$

where

$$\varphi(r, z, t, \xi) = \chi(t - \xi) \exp\{-r^2/[4a(t_0 + \xi)] - z^2/4a\xi\}/[\sqrt{\xi}(t_0 + \xi)] \quad (3.77)$$

$$\psi(z, \xi) = \exp(z^2/4a\xi) \sqrt{\pi a \xi}\, (\alpha_1/\lambda) \exp(\alpha_1 z/\lambda + \alpha_1^2 a\xi/\lambda^2)^2 \operatorname{erfc}(z/2\sqrt{a\xi} + \alpha_1 \sqrt{a\xi}/\lambda) \quad (3.78)$$

At $\psi(z, \xi) = 0$, from (3.76) we obtain the solution to the problem for the CEF-induced heating of a semi-infinite body disregarding the surface heat transfer.

For the central point of the focal spot,

$$\psi(0, w) = w \sqrt{\pi} \exp w^2 \operatorname{erfc} w \quad (3.79)$$

where $w = \alpha_1 \sqrt{a\xi}/\lambda$.

Determine the conditions at which $\psi(0, w)$ will differ from zero, say, by 10%:

$$w \sqrt{\pi} \exp w^2 \operatorname{erfc} w = 0.1 \quad (3.80)$$

The solution of transcendental equation (3.80) gives $w \cong 0.061$. Knowing w, we can find the relation between α_1, λ, and r_f at the steady temperature providing that the surface heat transfer decreases the surface temperature by not more than 10%. The typical time of onset of the constant (steady) temperature on the surface of a body is $t_C \approx 10 r_f^2/a$. Then, using the relation $\lambda 0.061 = \alpha_1 \sqrt{a t_C}$, we get

$$\alpha_1 \approx 0.02\lambda/r_f \quad (3.81)$$

Equation (3.81) can be used to estimate an upper limit on the hot spot radius, above which the surface heat transfer need be taken into account. Assuming that the surface heat transfer at high temperatures is due mainly to radiation, which is valid at $T > 10^3$ K, we obtain

$$r_f = 0.02\lambda/\varepsilon\sigma_0 T_v^3 \quad (3.82)$$

where ε is the emissivity, σ_0 the Stefan-Boltzmann constant, and T_v the vaporization (boiling) temperature at the surface.

It is obvious from formula (3.82) that as the thermal conductivity of a material grows and the surface temperature diminishes, the hot spot radius, at which the heat transfer should be allowed for, increases. The minimum radius of a hot spot on the surface

heated by a laser beam in a vacuum is 140 μm for titanium, 200 μm for tungsten, 400 μm for molybdenum, and 500 μm for steel.

Models for calculating the temperature field of the weld zone in pulsed laser welding. The general models used to calculate the temperature field of the weld zone and to estimate the requisite parameters of laser radiation are the following: a semi-infinite body; single-layer plate with various boundary conditions for the back surface; and two-layer plate with the ideal and nonideal contact between the layers and with one of the conditions for the back side of the plate. The above models do not naturally replace a large variety of methods called upon to solve the same problem.

The simplest model is a pulsed or continuous point heat source on the surface of a semi-infinite solid. However, this model cannot calculate the temperature at the hot spot center, nor can it estimate the sheet thickness which can be taken to be absolute, therefore we shall not consider the point heat source in our further analysis.

The most general model is a two-layer plate subject to conditions:

at the upper boundary,

$$z = 0, \quad -\lambda_1 \partial T_1/\partial z + \alpha_1 T_1 = q\,(r,\ t) \tag{3.83}$$

at the interface,

$$z = h_1, \quad \begin{cases} \lambda_1 \partial T_1/\partial z = \lambda_2 \partial T_2/\partial z \\ -\lambda_1 \partial T_1/\partial z = \alpha_2 (T_1 - T_2) \end{cases} \tag{3.84}$$

at the lower boundary,

$$z = h, \quad -\lambda_2 \partial T_2/\partial z = \alpha_2 T_2 \tag{3.85}$$

Here $h = h_1 + h_2$ is the total thickness of the plate, where h_1 and h_2 are the thickness of the upper and the lower layer respectively.

Since the general solution to the set of differential equations for T_1 and T_2 with the zero initial condition and conditions (3.83)-(3.85) involves rather complex computations, we shall consider the calculation approaches which are the particular cases of the model with conditions (3.83)-(3.85).

1. For a semi-infinite solid, the condition is

$$z = 0, \quad -\lambda_1 \partial T_1/\partial z = q\,(r,\ t) \tag{3.86}$$

2. For a single-layer plate, this is one of the following boundary conditions on the surface where $z = h$:

$$T = 0 \tag{3.87}$$

$$\partial T/\partial z = 0 \tag{3.88}$$

$$-\lambda\, \partial T/\partial z = \alpha_3 T \tag{3.89}$$

and also condition (3.86) for the upper boundary.

3. For a two-layer plate, we shall use the condition (3.86) at the upper boundary and conditions (3.84) for the nonideal or ideal contact at the interface.

Let us estimate three specific values of time at which laser-induced heating proceeds: t_1, a small time at which the distribution of temperature over the surface occurs in the same manner as for the irradiance (laser power density); t_2, the time at which the temperature at the central point of the hot spot reaches the vaporization temperature T_v; t_3, the time at which the process of heating becomes steady at points not more than a focal spot diameter distant from the surface. The values of t_1 and t_3 depend on the thermal properties of a material and focal spot diameter; t_2 also depends on the amount of heat absorbed by the body. The time t_1 is found from the condition

$$t_1 \leqslant (20ak)^{-1} \approx 10^{-2} r_f^2/a \tag{3.90}$$

This estimate is valid for both a semi-infinite body and a single-layer plate. Where the dwell time of LR is shorter than or equal to t_1, the expression for temperature becomes the product of two functions, each being dependent only on one of the variables r or z. The time t_2 for a semi-infinite body can be defined from the condition

$$t_2 = t_0 \tan (\lambda \sqrt{\pi k}\, T_v/q_0) \tag{3.91}$$

or, if the argument of the tangent is small in value, from the condition

$$t_2 \approx t_0 \lambda \sqrt{\pi k} T_v/q_0 \tag{3.92}$$

where $t_0 = (4ak)^{-1}$. Then, from the condition

$$\lambda \sqrt{\pi k}\, T_v/q_0 \leqslant \pi/2 \tag{3.93}$$

we can determine the minimum value of the power density, called the critical power density $q_c^{(2)}$, which secures the surface temperature T_v:

$$q_{\min} \geqslant 1.128 T_v \lambda \sqrt{k} \tag{3.94}$$

For example, at $r_f = 10^{-2}$ cm, the minimum heat power density for copper is $q_{\min} = 4.5 \times 10^5$ W/cm^2 since $r_f = k^{-1/2}$.

The time t_3 is essential for the calculation of the optimal pulse duration τ in laser setups:

$$t_3 = 10 r_f^2/a \tag{3.95}$$

For copper, at $r_f = 10^{-2}$ cm, this time is 1.2 ms. Formula (3.95) is also applicable for estimating the time of onset of the stationary process when using other calculation models.

The choice of the model for calculating the material heating process depends on the laser pulse length τ. When $t \leqslant t_1$, the model of a semi-infinite body can be used if the plate thickness satisfies the condition $h \geqslant h_\infty$. The value h_∞ is found from the condition

$$T(0,\ h_\infty,\ t_1)/T(0,\ 0,\ t_1) = \exp(-u^2) - \sqrt{\pi}\ \mathrm{erfc}\ (u) = 0.05 \tag{3.96}$$

where $u = 9.6h/d_f$. Hence,

$$h_\infty = 0.12 d_f \tag{3.97}$$

At $t \geqslant t_3$, it is necessary to employ the model of a semi-infinite body if the plate thickness is $h \geqslant H_\infty$; H_∞ follows from the condition

$$T(0,\ H_\infty,\ \infty)/T(0,\ 0,\ \infty) = \exp v\ \mathrm{erfc}\ \sqrt{v} = 0.05 \tag{3.98}$$

where $v = H_\infty^2 k$. Hence,

$$H_\infty = 2.6 d_f \tag{3.99}$$

For an upper sheet whose thickness is less than H_∞, account must be taken of the heat transfer to the lower sheet. If the contact between the sheets is nearly ideal and the thickness of the upper sheet is smaller than H_∞, we must use model *3*. If the total thickness $h = h_1 + h_2$ is larger than H_∞, it is safe to assume h to be equal to H_∞. When $t > t_1$, we can single out a time interval t_4 during which the thermal properties of the second sheet do not affect the temperature of the first sheet; the temperature of the first sheet at the specified absorption coefficient is mainly a function of the thermal properties of this sheet and heat-transfer coefficient α_2.

The time t_4 can be found from the formula

$$t_4 \leqslant 0.01 \lambda_1^2/\alpha_2^2 a_1 \tag{3.100}$$

For example, this temperature for aluminum is smaller than or equal to 9×10^{-4} s. The estimate obtained with the aid of (3.100) indicates that at low values of α_2, the time t_4 is greater than t_3 at which the process becomes stationary. This means that if one sheet is in poor contact with the other the parameters of the second sheet do not practically exert an influence on the temperature of the first sheet.

Comparison between calculated and experimental data. The experimental check on the relations used to calculate heating processes is of importance since it enables us to define the regions of parameters, within which the prerequisites embodied in the calculation procedure are valid. One of the basic techniques of checking the calculation models comes to the correlation of calculated temperatures with the positions of structural transformation zones in plates exposed to LR or EB. As regards the interaction of CEF pulses with materials, recourse to this technique is made on account of appreci-

able methodical difficulties involved in the direct measurement of the temperature distribution over the zone of interaction. These difficulties arise because of a small radius of the hot spot, great rapidity with which melting begins, and sharply nonuniform distribution of temperature over the heat affected area.

From the experimental data it follows that if the heat power density does not reach the critical value $q_c^{(2)}$ but exceeds $q_c^{(1)}$, i.e. $q_c^{(1)} \leqslant q \leqslant q_c^{(2)}$, the calculated data check well with the experimental results. The experimental and calculated data on the depths of melting and hardening are listed in Table 3.2.

TABLE 3.2. **Experimental and Calculated Depths of Melting and Hardening**

Energy, J	Pulse length, ms	Spot diameter, cm	Focal length, cm	Laser	Material	Depth, μm	
						Experiment	Theory
10	0.5	0.2	5.0	Ruby	Steel ShKh 15[1]	52	52
7.5	4	0.12	5.0	Nd-glass	Steel 45[2]	300	280
4.5	8	0.025	5.0	Nd-glass	Al	80	75
1.0	1	0.01	5.0	Nd-glass	Cu	50	42
11.0	4	0.02	5.0	Nd-glass	Cu	145	132

Notes: [1]Chromium ball-bearing steel.
[2]Good-quality carbon structural steel (0.45% C).

It is seen from Table 3.2 that although the agreement between theory and experiment is on the whole satisfactory, a systematic departure of the calculated values of the melt depth from the experimental values is evident. It is to be expected considering that the calculations do not account for the extent to which the specific heat of phase transition and the temperature dependence of thermal and optical constants affect the temperature field. The thing is that during the normal pulse operation of a laser, the mean power density can differ markedly from the maximum value of power density attainable in an individual spike. This, as a rule, causes the surface of molten metal to vaporize, thereby leading to the buildup of the reactive pressure, subsequent deformation of the molten pool surface, and deeper propagation of the heat wave into the sample. Gas dynamic phenomena in laser processing are significant (see Ch. 4) and have an effect on the course of thermal processes. Deep penetration at a definite power density q_c^{IV} is possible to achieve with both pulsed and continuous lasers.

3.3. MOVING HEAT SOURCES. CRITICAL HEAT POWER DENSITIES

If a laser beam- or electron beam-produced hot spot of radius r_f travels along the surface at a constant velocity v, the material absorbs the heat and begins to melt down. After a certain dwell time which depends on the material properties, the heat affected zone (HAZ) reaches a quasistationary state, and the fusion front of constant size propagates in the direction of the moving heat source [4].

The most popular dynamic model for the calculation of the weld zone temperature is a Gaussian heat source of effective power P_0, which moves at a constant speed v in the direction of the ox axis along the surface of a plate of thickness δ or of a semi-infinite body. The concentration coefficient k and speed v of the heat source remain constant during the entire process of heating.

Plate heating. The equation for calculating the temperature at point $A\ (x,\ y)$ in the moving coordinate system, which defines the position of this point, takes the form

$$T\ (x,\ y,\ t) = \{P_0\ [\exp\ (-vx/2a + bt_0)]/2\pi\lambda\delta\} \times K_0\ (\rho_2)\ [\psi_2\ (\rho_2,\ \tau + \tau_0) + \psi_2\ (\rho_2,\ \tau_0)] \quad (3.101)$$

Here t is the time counted off from the moment when the center of the Gaussian heat source leaves the given point $A\ (x,\ y)$ lying in the plate cross section normal to the ox axis; $b = 2\alpha/c\gamma\delta$; $t_0 = 1/4ak$; K_0 is the modified Bessel function of an imaginary argument of second kind of order zero; $\rho_2 = r\sqrt{v^2/4a^2 + b/a}$ is the dimensionless criterion for distance r from the origin of moving coordinates of the point $A\ (x,\ y)$; $\psi_2\ (\rho_2,\ \tau + \tau_0)$ and $\psi_2\ (\rho_2,\ \tau_0)$ are the heat saturation coefficients for a plane heat source propagating along the surface; $\tau = (b + v^2/4a)\ t$ is the dimensionless criterion for time constant t; and $\tau_0 = (b + v/4a)\ t_0$ is the same criterion for t_0.

With an increase in the concentration coefficient k, the time constant t_0 tends to zero. In this case equation (3.101) defines the temperature of a plate heated by a continuous line source moving along the surface.

For the limiting quasi-steady state of the process when $t \to \infty$, the heat threshold coefficient is $\psi_2\ (\rho_2,\ \tau + \tau_0) = 1$ and the temperature variation at point $A\ (x,\ y)$ is written as

$$T\ (x,\ y,\ t) = \{P_0\ [\exp\ (-vx/2a + bt_0)]/2\pi\lambda\delta\} \times K_0\ (\rho_2)\ [1 - \psi_2\ (\rho_2,\ \tau_0)] \quad (3.102)$$

In the limiting case, when the speed v of a heat source grows directly with power P_0, the temperature field referred to the moving coordinates tends to a simple limiting form. A rapidly moving Gaussian heat source so quickly traverses the plate points lying

on the ox axis and beyond this axis that, without introducing a large error, we can assume it to be strip-like, i.e. totally concentrated in the direction of its travel along the ox axis. The heat of this rapidly moving source will spread only in the direction oy normal to the direction ox of source travel.

In this case the temperature balance process assumes the form

$$T(y,\ t) = \frac{P_0 \exp\{-y^2/[4a(t+t_0)] - bt\}}{v\delta \sqrt{4\pi\lambda c\gamma (t_0+t)}} \tag{3.103}$$

At $t_0 = 0$, equation (3.103) obviously describes the process of propagation of the heat from a powerful fast-moving source. At $t \gg t_0$, i.e. at longer times, the process given by (3.103) tends to become similar to the process of propagation of the heat from a line source.

Equation (3.103) is much simpler than (3.102) that describes the process for the heat source moving at an arbitrary speed.

In the plate region located behind the heat source center C and adjacent to the ox axis along which the heat source travels, the temperatures calculated from equations (3.102) and (3.103) differ little. Therefore, with the heat source traveling at an arbitrary speed, equation (3.102) for the temperatures of points close to the ox axis in the period of cooling gives rather accurate results from the practical viewpoint.

Heating of a semi-infinite body. The equation for calculating the temperature at point A (x, y) on the target heated by a Gaussian source traveling at a constant speed has the form

$$\begin{aligned} T(x,\ y,\ z,\ t) = {} & \{2P_0 \exp(-vx/a)/[c\gamma(4\pi a)]^{3/2}\} \\ & \times \int_0^t \{d\xi/[\sqrt{\xi}(t_0+\xi)]\} \exp(-z^2/4a\xi \\ & - r^2)/[4a(t_0+\xi)] - v^2(t_0+\xi)/4a \end{aligned} \tag{3.104}$$

For the calculation of the heating process in the limit $t \to \infty$, it is convenient to use the cylindrical coordinate system r, φ, z, where φ is the angle between the radius vector and the positive semiaxis ox along which the heat source moves.

In this coordinate system, the temperature for the limiting case is given by the expression

$$\begin{aligned} T(r,\ \varphi,\ z,\ \infty) = {} & T_c \exp(-2\sqrt{np}\cos\varphi)(2/\pi) \\ & \times \int_0^\infty [d\omega/(1+\omega^2)] \exp \\ & \times [-(m/\omega^2) - n/(1+\omega^2) - p(1+\omega^2)] \end{aligned} \tag{3.105}$$

where $m = kz^2$, $n = kr^2$, and $p = v^2t/4a$.

The critical temperature at the hot spot center is

$$T_c = T(0,\ 0,\ 0,\ \infty) = (P_0/2\lambda)\sqrt{k/\pi} \tag{3.106}$$

The integral of (3.105) can be expressed through a combination of elementary functions only in a certain specific case.

Let us look at some cases which follow from the analysis of relation (3.104) and attract the highest practical interest.

Temperature at the center of a stationary heat source. Setting $v = 0$ and $x = y = z = 0$ in (3.104) and finding the integral, we get

$$T(0,\ 0,\ 0,\ t) = [P_0/(2\lambda\sqrt{4\pi at_0})] \times (2/\pi)\,\mathrm{arctg}\sqrt{t/t_0} \tag{3.107}$$

At the initial stage of the process when $t \ll t_0$, $\mathrm{arctg}\sqrt{t/t_0}$ is approximately equal to $\sqrt{t/t_0}$ and the temperature grows in proportion to the square root of time. Later on, its growth slows down and the temperature rises asymptotically to T_c given by (3.106). T_c is the highest temperature attainable in a semi-infinite solid under the action of a Gaussian surface heat source of constant power and power density.

Introducing the heat saturation coefficient

$$\psi(0,\ 0,\ 0,\ t) = (2/\pi)\,\mathrm{arctg}\sqrt{t/t_0} \tag{3.108}$$

we can represent the temperature in the course of heat saturation in the form

$$T(0,\ 0,\ 0,\ t) = T_c\psi(0,\ 0,\ 0,\ t) \tag{3.109}$$

Temperature field for a limiting case. Taking $m = 0$ in equation (3.105), we obtain the temperature in the boundary plane xoy of the semi-infinite solid for the limiting case of the process:

$$T(r,\ \varphi,\ 0,\ \infty) = T_c[\exp(-2\sqrt{np}\cos\varphi)] \times (1/\pi)\,A(0,\ n,\ p) \tag{3.110}$$

where

$$A(0,\ n,\ p) = 2\int_0^\infty [d\omega/(1+\omega^2)]\exp \times [-n/(1+\omega^2) - p(1+\omega^2)] \tag{3.111}$$

The values of integral (3.111) at $p = 0.01$ to 5.0 and $n = 0$ to 10 are given in Fig. 3.20.

The temperature on the ox axis along which the center C of the Gaussian heat source moves reaches the highest values. Setting $\varphi = 0$ in (3.110) for the positive semiaxis ox and $\varphi = \pi$ for the negative semiaxis yields

$$\begin{matrix} T(r,\ 0,\ 0,\ \infty) \\ T(r,\ \pi,\ 0,\ \infty) \end{matrix} = \left\{ T_c \exp(\mp\sqrt{np})\,\frac{1}{\pi}\,A(0,\ n,\ p) \right. \tag{3.112}$$

The upper minus sign and the lower plus sign in the right side of (3.112) correspond to the temperatures at points on the positive and the negative semiaxis ox respectively.

Fast heat source. In the limiting case, as the velocity v of the heat source increases directly with its power, the temperature field referred to the moving coordinates tends to assume a simple limiting shape. The process of heat distribution for a fast Gaussian heat source is given by the equation

$$T(y,\ z,\ t) = (2P_0/vc\gamma)\ [\exp(-z/4at)/\sqrt{4\pi at}]\exp \times \{-y^2/[4a(t+t_0)]\}/\sqrt{4\pi a(t+t_0)} \qquad (3.113)$$

where t is the time counted off from the moment when the center C of the Gaussian heat source traverses the point A (y, z) on the plane normal to the direction of travel.

The highest temperature reached on the axis of the solid is

$$T(0,\ 0,\ t) = P_0/[2\pi\lambda v\sqrt{t(t+t_0)}] \qquad (3.114)$$

At the start of the process when $t_0 \gg t$, the temperature drops inversely at $\sqrt{t}$, and at the end of the process when $t_0 \ll t$, it decays as the reciprocal of t. In the middle of the time interval t, the process is transient; the temperature on the axis falls off in proportion to t^n, at which n rises from 1/2 to 1.

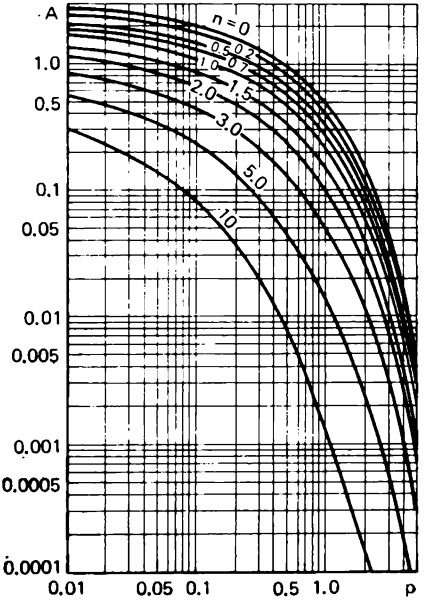

Fig. 3.20. Integral A $(0, n, p)$ versus parameters n and p

Critical heat power densities. If the temperature field in the material interacting with LR or EB is known, it is possible to determine the critical density of the heat flux required to reach a definite temperature over the given time period at a certain point on the surface or in the bulk of the material. In particular, we can estimate the density of the heat flux which disintegrates the material. By disintegration is often meant the state of a target surface which reaches the melting temperature T_m or vaporization temperature T_v at normal pressure. It should be noted that the term "disintegration" is conditional because a number of brittle materials develop fractures even after the cooling process ceases.

Using the unidimensional model of a semi-infinite body with a heat source of constant power density, we can obtain the expression for estimating $q_c^{(1)}$ required to raise the temperature of the target surface to T_m at the end of interaction of a pulse of duration τ:

$$q_c^{(1)} = 0.885 T_m \lambda / (a\tau)^{1/2} \qquad (3.115)$$

From relation (3.115) it follows that the critical density $q_c^{(1)}$ grows with the melting point of a material, its thermal conductivity, and heat capacity per unit volume, and decreases with an increase in the laser pulse length. The estimates of $q_c^{(1)}$ for steel and other metals with different thermophysical properties are listed in Table 3.3.

TABLE 3.3. **Critical Heat Power Densities for Some Metals**

Metal	λ, W cm^{-1}K^{-1}	a, cm^2 s^{-1}	T_m, K	τ, s	$q_c^{(1)}$, W cm^{-2}
Cu	3.89	1.12	1356	10^{-3}	1.1×10^4
				10^{-8}	3.5×10^7
Steel	0.51	0.15	1808	10^{-3}	3.5×10^3
				10^{-8}	1.8×10^5
Ni	0.67	0.18	1726	10^{-3}	6.5×10^3
				10^{-8}	2.0×10^5
Ti	0.15	0.06	2073	10^{-3}	3.0×10^3
				10^{-8}	1.0×10^5
Al	2.09	0.87	933	10^{-3}	4.2×10^3
				10^{-8}	1.3×10^5

Expression (3.115) can be used to estimate the critical heat power density which it is undesirable to exceed in the processes of heat treatment. Relation (3.115) is set up in terms of a unidimensional heat model, so it is valid only at $(a\tau)^{1/2} \ll r_f$. The three-dimensional analog of expression (3.115) is the formula derived, for example, from equation (3.106) and from the equation that relates the power of a Gaussian heat source to its power density q_0:

$$q_{cs}^{(1)} = 2\lambda T_m \sqrt{k} / \sqrt{\pi} = 1.128 \lambda T_m \sqrt{k} \qquad (3.116)$$

Equation (3.116) defines the heat power density required to raise the temperature to T_m in the conditions of the steady-state process, i.e. this relation is independent of the dwell time for a heat source. The estimates of $q_{cs}^{(1)}$ at different values of k for the metals of Table 3.3 are given in Table 3.4.

As seen from Tables 3.3 and 3.4, critical densities $q_c^{(1)}$ and $q_{cs}^{(1)}$ at a pulse duration of about 1 ms are close in value, i.e. the length

TABLE 3.4. Critical Steady-State Values of Heat Power Density $q_{cs}^{(1)}$ for Some Metals

Metal	$\lambda T_m \times 10^{-3}$, W cm^{-1}	k, cm^{-2}	$q_{cs}^{(1)}$, W cm^{-2}
Cu	4.2	10^2	4.2×10^4
		10^3	1.3×10^5
		10^4	4.2×10^5
Steel	0.78	10^2	7.8×10^3
		10^3	2.5×10^4
		10^4	7.8×10^4
Ni	0.97	10^2	9.7×10^3
		10^3	3.1×10^4
		10^4	9.7×10^4
Ti	0.27	10^2	2.7×10^3
		10^3	8.5×10^3
		10^4	2.7×10^4
Al	1.38	10^2	1.4×10^3
		10^3	4.3×10^3
		10^4	1.4×10^4

of time needed to reach the steady-state temperature at the center of the hot spot is of the same order of magnitude.

Using the unidimensional model of a semi-infinity solid with a source of constant heat power density, we determine the time required to reach the melting point T_m at the surface:

$$t_m = 0.79\,(\lambda T_m)^2/q_0^2 a \tag{3.117}$$

The time to bring the surface to the specified temperature increases with the melting point, thermal conductivity, and heat capacity per unit volume, and decreases with a growth of the heat power density. For copper, the time to reach melting at the surface is $t_m = 10^{-5}$ s at $q_0 = 10^6$ W/cm^2 and $t_m = 10^{-7}$ s at $q_0 = 10^7$ W/cm^2.

In accordance with (3.115) and (3.116), an equation can be written to estimate the power density at which the target surface rises to its vaporization point T_v:

$$q_c^{(2)} = 0.885 T_v \lambda/(a\tau)^{1/2} \tag{3.118}$$

As it reaches the temperature T_v, the surface begins to vaporize vigorously. For copper with $T_v = 2\,573$ K, the critical power density is $q_c^{(2)} = 2.1 \times 10^5$ W/cm^2. Accordingly, in the steady state,

$$q_{cs}^{(2)} = 1.128 \lambda T_v \sqrt{k} \tag{3.119}$$

Expression (3.118) can be used to calculate $q_c^{(2)}$ required for metal welding under conditions at which surface vaporization is undesirable during the period of a laser pulse.

The absorbed laser power density which causes an appreciable surface vaporization can be found by reasoning in the following way [1]. As LR interacts with a material, the heat wave produced propagates through the workpiece, while the substance at the surface begins to vaporize. If the absorbed power density is small, the velocity of the heat wave is substantially higher than that of the vaporization wave. With an increase in the power density, the rate of vaporization grows and becomes equal to the rate of heating at a certain value of $q_c^{(3)}$ since the velocity of the heat wave on the target surface, as regards its order of magnitude, is $v_h \sim (a/\tau)^{1/2}$ and the velocity of vaporization is $v_v \sim q_c^{(3)}/\gamma L_v$, where L_v is the specific heat of vaporization. Equating v_h and v_v gives

$$q_c^{(3)} \cong \gamma L_v (a/\tau)^{1/2} \tag{3.120}$$

It should be noted that this method of determining $q_c^{(3)}$ is not the only one. In particular, it is possible to estimate this quantity by comparing not the rates of temperature variations, but the energy fluxes removed through heat conduction and vaporization, volumes of a vaporized and molten material during the beam-material interaction, etc. [11].

A list of estimates of $q_c^{(3)}$ for some metals appears in Table 3.5.

The critical power density $q_c^{(3)}$ grows with an increase in both the specific heat of vaporization and thermal diffusivity a and

TABLE 3.5. **Critical Heat Power Densities $q_c^{(3)}$ for Some Metals**

Metal	γL_v, kJ cm^{-3}	a, cm^2 s^{-1}	τ, s	$q_c^{(3)}$, W cm^{-2}
Cu	42.88	1.12	10^{-3} 10^{-8}	1.4×10^6 4.6×10^8
Steel	54.76	0.15	10^{-3} 10^{-8}	6.7×10^5 2.1×10^8
Ni	55.3	0.18	10^{-3} 10^{-8}	7.5×10^5 2.4×10^8
Ti	44.27	0.06	10^{-3} 10^{-8}	3.4×10^5 1.1×10^8
Al	28.09	0.87	10^{-3} 10^{-8}	8.6×10^5 2.7×10^8

a decrease in pulse duration τ. The inequality $q_c^{(1)} < q_c^{(2)} < q_c^{(3)}$ holds for most materials.

Apart from the above mentioned critical densities, other critical densities can be introduced to handle the tasks of interest, for example, to analyze the process of deep penetration into metal [11, 12].

Calculation of the critical power density required for intensive vaporization [12] proceeds from the comparison of energies removed by way of heat conduction and vaporization:

$$q_{cv} \cong (6L_v\gamma a/Ar_f\sqrt{\pi}) \times \left(\ln \delta_v + \frac{1}{2} \ln \ln \delta_v\right)^{-1} \qquad (3.121)$$

The results of calculation by (3.121) are close to the results calculated from expression (3.120) which compares the speeds of vaporization and heat waves.

$$\delta_v = r_f P^*/3\gamma a \sqrt{2L_v}$$

For a volume heat source where heat distribution obeys, for example, the Bouguer law, the critical power density required to initiate material destruction, i.e. to bring the surface to the vaporization temperature T_v, can be found from the expression

$$q_c = \lambda\alpha T_v/[\exp(a\alpha^2 t)\operatorname{erfc}(\alpha\sqrt{at}) - 1 + 2\pi^{-1/2}\alpha\sqrt{at}] \qquad (3.122)$$

For example, q_c calculated by formula (3.122) for ferrite is equal to 3×10^4 W/cm^2.

Rates of heating and cooling. We shall use the expressions for the unidimensional model of a semi-infinite body heated by a source of time-constant heat density to estimate the rates of heating and cooling of materials. The rate of heating (rate of temperature changes) can be estimated by differentiating relation (3.34) with respect to t:

$$v_h = \partial T(z, t)/\partial t = (q_0/\lambda) \times [\sqrt{a/t}\operatorname{ierfc}(z/2\sqrt{at}) + (z/2t)\operatorname{erfc}(z/2\sqrt{at})] \qquad (3.123)$$

where $\operatorname{erfc}(x) = 1 - \operatorname{erf}(x) = 1 - (2/\sqrt{\pi})\int_0^x \exp(-\xi^2)\,d\xi$.

In particular, the rate of surface heating ($z = 0$) at an instant t is

$$v_h = (q_0/\lambda)\sqrt{a/\pi t} = q_0/\sqrt{\lambda c\gamma\pi t} \qquad (3.124)$$

The values of v_h are maximum at initial instants.

It is evident from equation (3.124) that the rate of heating linearly rises with heat power density, but diminishes with an increase in the thermal conductivity λ, per-unit-volume heat capacity $c\gamma$, and laser pulse dwell time.

Figure 3.21 illustrates the plots of heating rate v_h, K/s, for steel ShKh15 during the time t at different values of the absorbed power density. It is seen that the heating rate $\partial T/\partial t$ can reach large values especially at the initial period.

For the calculation of the cooling rate v_{cl}, we need to obtain the expression for the temperature field in a medium after the heat source ceases to deliver energy. The simplest way to deal with the problem is to use the notion of a heat sink [4]. Under the heat sink

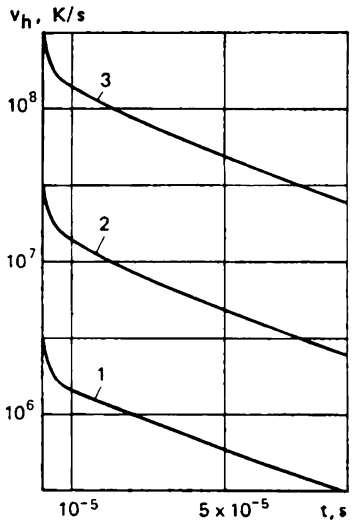

Fig. 3.21. Variations in the rate of heating, v_h, of steel ShKh 15 with time t at different power densities q_0: *1*, 10^4 W cm^{-2}; *2*, 10^5 W cm^{-2}; *3*, 10^6 W cm^{-2}

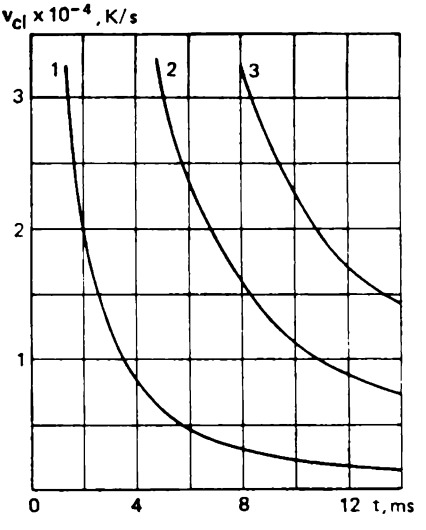

Fig. 3.22. Variations in the rate of cooling, v_{cl} of steel with time t at different values of q_0: *1*, 10^4 W cm^{-2}; *2*, 5×10^4 W cm^{-2}; *3*, 10^5 W cm^{-2}

one understands a heat source with a negative flux density. The use of the heat sink that comes into play after the pulse of duration τ decays makes it possible, without solving the problem, to write the expression for the temperature field over the time interval $t \geqslant \tau$. Then, we derive the following expression for the calculation of the temperature field in a a semi-infinite body at the stage of cooling over the time interval $t \geqslant \tau$ after the dwell time τ of the source of constant power density:

$$T(z, t) = (2q_0/\lambda)\,[\sqrt{at}\ \text{ierfc}\ (z/2\sqrt{at}) - \sqrt{a(t-\tau)}\ \text{ierfc}\ (z/2\sqrt{a(t-\tau)})] \qquad (3.125)$$

Hence, the expression for the cooling rate v_{cl} of the surface ($z = 0$) during the time $t > \tau$ takes the form

$$v_{cl} = \partial T(0,t)/\partial t|_{t>\tau} = (q_0/\sqrt{\pi\lambda c\gamma})(1/\sqrt{t} - 1/\sqrt{t-\tau}) \qquad (3.126)$$

The curves for the calculated absolute values of cooling rate v_{cl} during $t > \tau$ at different values of q_0 are shown in Fig. 3.22. The cooling rate, just like the heating rate, varies linearly with the heat power density.

The rate of heating of a semi-infinite body by a Gaussian heat source versus r, z, and t follows from expression (3.58) after differentiating it with respect to t:

$$v_h = 2q_0 \exp[-z^2/4at - r^2/(4ak + k^{-1})] \times \sqrt{a/t}/[\lambda\sqrt{\pi}(1 + 4\pi ak)] \qquad (3.127)$$

Applying the heat sink model, we write the equation for calculating the temperature field in a semi-infinite body with a Gaussian heat source that still heats the body over the time interval $t \geqslant \tau$:

$$T(r, z, t) = \frac{2P_0}{c\gamma(4\pi a)^{3/2}} \left\{ \int_0^t \frac{d\xi \exp\{-(4a)^{-1}[z^2/\xi + r^2/(t_0+\xi)]\}}{\sqrt{\xi}(t_0+\xi)} - \int_0^{t-\tau} \frac{d\xi \exp\{-(4a)^{-1}[z^2/\xi + r^2/(t_0+\xi)]\}}{\sqrt{\xi}(t_0+\xi)} \right\} \qquad (3.128)$$

Differentiating the function (3.128) with respect to t yields the equation for the cooling rate during $t \geqslant \tau$:

$$v_{cl} = \frac{q_0}{\lambda}\sqrt{\frac{a}{\pi}} \left\{ \frac{\exp[-z^2/(4at) - r^2/(4at + k^{-1})]}{\sqrt{t}(1 + 4akt)} - \frac{\exp\{-z^2/[4a(t-\tau)] - r^2/[4a(t-\tau) + k^{-1}]\}}{\sqrt{t-\tau}[1 + 4ak(t-\tau)]} \right\} \qquad (3.129)$$

Expression (3.129) uses the relation of q_0 to P_0 for Gaussian heat sources, $P_0 = \pi q_0 k^{-1}$. The heating rates and the absolute values of cooling rates calculated for a semi-infinite steel body heated and cooled over the same time intervals t are given in Fig. 3.23. It is seen that the rates of heating and cooling differ insignificantly in the order of magnitude, although the cooling rate is always lower than the heating rate [see (3.125)].

Similarly, we can formulate equations for the rates of heating and cooling of a solid heated by a circular source with its heat flux uniformly distributed over the spot of radius r_f.

The rate of heating by a uniform heat source of radius r_f can be calculated from the formula

$$v_h = [q_0 r_f \exp(-z^2/4at)/2\sqrt{\lambda c\gamma\pi t}] \times \int_0^\infty I_1(sr_f)\, I_0(sr) \exp(-s^2 at)\, ds \qquad (3.130)$$

where $I_1(u)$ and $I_0(u)$ are the Bessel functions of order one and zero, respectively, of an imaginary argument. The integral put into

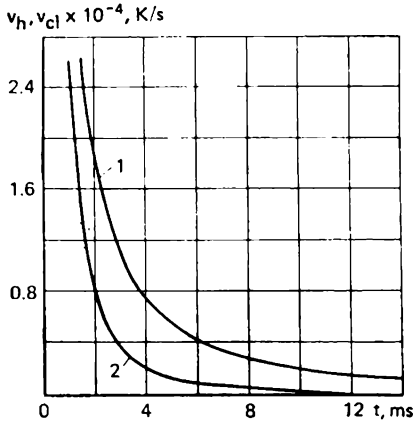

Fig. 3.23. Rates of heating (curve *1*) and absolute values of the rates of cooling (curve *2*) of the steel surface interacting with a Gaussian source of power density $q_0 = 10^4$ W cm^{-2} at $\tau = 1$ ms

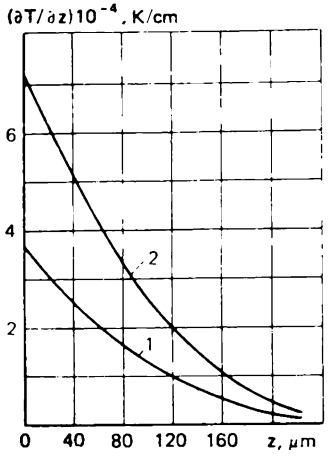

Fig. 3.24. Distribution of temperature gradient in depth through a semi-infinite steel sample at $\tau = 1$ ms: *1*, $q_0 = 10^4$ W cm^{-2}; *2*, $q_0 = 2 \times 10^4$ W cm^{-2}

equation (3.130) can be evaluated by numerical methods for various values of r_f, r, a, and t.

For $t \geqslant \tau$, the rate of cooling is

$$v_{cl} = \frac{q_0 r_f}{2\sqrt{\lambda c\gamma\pi}} \left\{ \frac{e^{-z^2/4at}}{\sqrt{t}} \int_0^\infty ds I_1(sr_f)\, I_0(sr)\, e^{-s^2 at} - \frac{e^{-z^2/4a(t-\tau)}}{\sqrt{t-\tau}} \int_0^\infty ds I_1(sr_f)\, I_0(sr)\, e^{-[s^2 a(t-\tau)]} \right\} \qquad (3.131)$$

Temperature gradient. The expression for the temperature gradient in a semi-infinite body heated by a source of constant heat power density can be set up by differentiating (3.34) with respect to z:

$$\partial T(z, t)/\partial z = (-q_0/\lambda)\, \mathrm{erfc}\,(z/2\sqrt{at}) \qquad (3.132)$$

The temperature gradient rises with the ratio q_0/λ and largely depends on the similarity variable $z/2\sqrt{at}$. If $t \to \infty$ or $z = 0$, the temperature gradient is constant:

$$\partial T(z, t)/\partial z = -q_0/\lambda \tag{3.133}$$

Figure 3.24 displays the curves of the temperature gradient distribution in depth z for steel ShKh15 at different values of q_0. The calculations reveal that the temperature gradient at the target surface can reach rather large values. Thus, the temperature gradient for copper is $\partial T(0, t)/\partial z = 3 \times 10^5$ K/cm at $q_0 = 10^6$ W/cm^2 and 3×10^6 K/cm at $q_0 = 10^7$ W/cm^2. Knowing the temperature field in a material and the temperature gradient, we can estimate the depth d of the HAZ. The relation $d \approx 4\sqrt{at}$ derived from (3.132) can be used to make qualitative estimates. For example, at $a = 0.1$ cm^2/s and $t = 10^{-3}$ s, the depth of the HAZ in steel is $d = 4 \times 10^{-2}$ cm.

3.4. NONLINEAR PROBLEMS OF LR AND EB INTERACTION

The solution found for the linear problems dealt with in the preceding sections on the interaction of LR and EB with materials are, in a certain way, a first approximation valid for handling the nonlinear problems to which belong most of the problems involved in the processing of materials by a CEF.

Nonlinear heat transfer problems are the problems in which one of the following quantities depends on temperature: the thermal conductivity λ, specific heat c, material density γ, heat transfer coefficient α, surface heat flux q, internal heat flux (heat sink), and boundaries of phase transitions [9, 10].

For brevity, the problems in which thermal constants depend on temperature are referred to as the nonlinear problems of the 1st kind; those subject to nonlinear boundary conditions as the nonlinear problems of the 2nd kind; and those concerned with the temperature-dependent heat sources as the nonlinear problems of the 3d kind.

All these problems can be met with in the processes of CEF-induced heating of materials. For the case where the flux density does not exceed $q_c^{(1)}$ required for material heating and heat treatment, the problems of the 1st and the 2nd kind prove most important. The nonlinearities of the 1st and the 2nd kind can be present simultaneously if the thermal and optical parameters markedly depend on temperature in the temperature interval of interest. If, on the other hand, the power density exceeds $q_c^{(1)}$, then, after a certain period t_c, it is necessary to allow for the nonlinearity of the 3d kind, namely, to consider the Stefan problem for the phase interface position.

The most general problem is the one in which all the three kinds of nonlinearity exist simultaneously.

Nonlinearity of the 1st kind. The basic methods for the solution of nonlinear problems involve various kinds of linearization because the methods for treating linear problems are developed much better. Use is most often made of various substitutions, or transformations, which simplify equations with nonlinear terms.

The transform given below applies where the thermal conductivity is temperature dependent, $\lambda = \lambda(T)$:

$$\lambda = \lambda_0^{-1}(T_0) \int_{T_0}^{T} \lambda(T)\, dt \tag{3.134}$$

where T_0 is the initial temperature. This substitution is called the Kirchhoff transform or, sometimes, the Varshavskiy transform [9]. It linearizes the nonlinear term in the steady-state heat-transfer equation, so that the boundary condition becomes nonlinear if it is of the 3d kind. But the boundary conditions of the 2nd kind, which are of the highest interest in the CEF treatment of materials, remain invariable. The transform (3.134) applied to nonsteady-state heat-transfer equations changes the form of these equations since they now contain nonlinear terms.

The Goodman transform

$$v = \int_{T_0}^{T} c(T)\, dT \tag{3.135}$$

or

$$v = \int_{T_0}^{T} \gamma(T)\, c(T)\, dT \tag{3.136}$$

is commonly used to account for the temperature dependence of specific heat.

As regards infinite and semi-infinite solids, the analysis sometimes relies on the Boltzmann transform

$$\xi = x/2\sqrt{t} \tag{3.137}$$

which allows us to convert from the partial differential equations to the equations involving total derivatives with respect to a variable.

The popular methods for the solution of nonlinear problems of the 1st kind are the methods based on the use of analog computer facilities. The common approaches employed here are: to simplify or

linearize the basic equation by means of Kirchhoff or Goodman transforms; to change in accordance with the functions $\lambda(T)$, $c(T)$, and $\gamma(T)$ the values of resistors, capacitors, or other parameters of devices in analog computers; and to supply the electrical model with currents which cause the same effect as that which appears when account is taken of the nonlinearities by other methods. Where consideration is given to the nonlinearities of the 1st kind, such methods of analysis are useful as the integral estimation method, iteration method, and others.

Nonlinearity of the 2nd kind. The methods used to solve nonlinear problems of the 2nd kind include the iteration, integral, finite difference methods, etc. In some cases it is advantageous to apply the method developed by V.V. Ivanov and Yu.V. Vidin [9]. This is the method of nonlinear integral transformations which reduce the original differential equation to a nonlinear equation, where the nonlinear part can be neglected if a certain number of conditions are met. Such an approach permits us to obtain an approximate solution to a definite degree of accuracy. For thermally thin sheets with $\mathrm{Bi} < 0.25$, where Bi is the Biot criterion, the problem can be reduced to an ordinary differential equation.

Nonlinearity of the 3d kind. The nonlinear problems of the 3d kind include the problems in which the power of sources in the bulk materials and at the boundaries depend on temperature. These are the Stefan problems [7, 9] solved by variational, finite difference, straight-line, substitution, and other methods.

Consider several nonlinear problems which are of interest in material processing by the CEF.

Temperature dependence of the absorptivity. We shall look into the effect resulting from the temperature dependence of the optical constants of a metal on the character of changes of temperature during LR interaction. The absorptivity A of a metal is a function of temperature (nonlinearity of the 2nd kind). In a first approximation, $A(T)$ is proportional to T, where T is the temperature of the surface absorbing LR. With consideration for the anomalous skin effect,

$$A = a_0 + bT \tag{3.138}$$

Here, $a_0 = 0.75v_0/c$, where v_0 is the velocity of a conduction electron on the Fermi surface; c the velocity of light; $b = \Omega/2\pi\sigma_0$, where Ω is the plasma frequency; and σ_0 the static electrical conductivity of metal.

Since, for most metals, A is linearly dependent on temperature, the problem under consideration is linear. Commonly, $a_0 \ll bT$, so the augend in equation (3.138) can be omitted. The statement of the problem of metal heating at a variable absorptivity for the

unidimensional case assumes the form

$$\partial T/\partial t = a\partial^2 T/\partial z^2 + Aq_0\alpha \exp(-\alpha z) \tag{3.139}$$

$$z = 0, \quad \partial T/\partial z = 0 \tag{3.140}$$

$$t = 0, \quad z = \infty, \quad T = T_0 \tag{3.141}$$

where α is the absorption coefficient, and T_0 the initial temperature of metal.

The absorption coefficient α in the same approximation is independent of temperature. The solution of the problem (3.139)-(3.141) as a function of parameter $s = 4bq_0/\alpha\lambda$ for limiting cases corresponding to small and large values of s is written as

$$T - T_0 = (A_0/b)\,[\exp(bq_0\alpha t/c_p) - 1] \tag{3.142}$$

$$T - T_0 = \left(\frac{A_0 q_0}{c_p \sqrt{a}}\right)\left\{\left(\frac{c_p\sqrt{a}}{bq_0}\right)\left[\exp\left(\frac{bq_0}{(c_p a)^2 t}\right) \times \operatorname{erfc}\left(\frac{-bq_0\sqrt{t}}{c_p a}\right) - 1\right] + \left(\frac{1}{\alpha\sqrt{a}}\right)[1 + \exp(\alpha^2 at)\operatorname{erfc}(\alpha\sqrt{at})]\right\} \tag{3.143}$$

where $A_0 = A(T_0)$ is the metal surface absorptivity at the initial temperature T_0, and c_p the thermal capacity at constant pressure.

The surface temperature and its change with time for the case where the absorptivity is time-independent can be found from equation (3.143) at $b \to 0$:

$$T - T_0 = (A_0 q_0/c_p a)\{2\sqrt{t/\pi} + (1/\alpha\sqrt{a})[\exp(\alpha^2 at)\operatorname{erfc}(\alpha\sqrt{at}) - 1]\} \tag{3.144}$$

Taking into account the temperature dependence of metal absorptivity A leads to some peculiarities of sample heating. When $s \gg 1$, the process of heating has no analog in the problem with a constant value of $A = A_0$. At $s \ll 1$, which is the most common of the realizable cases, there appear two processes of heating. If $bq_0 t/c_p\sqrt{a} \ll 1$, an increase in the surface temperature proceeds according to relation (3.144), i.e. the inclusion of the function $A(t)$ for the time intervals $t \ll c_p\sqrt{a}/bq_0$ does not result in a substantial effect. But if $t \gg c_p\sqrt{a}/bq_0$, from equation (3.143) we can obtain

$$T - T_0 = (2A_0/b)\exp[(bq_0/c_p\sqrt{a})^2 t] \tag{3.145}$$

From the comparison of equations (3.144) and (3.145) it follows that starting at the moment $t \gg c_p\sqrt{a}/bq_0$, in evidence is a substantial divergence between the cases when $A = A_0$ and $A =$

A (t). For the first case, we have $T \sim \sqrt{t}$, and for the second case,

$$T \sim \exp\left[(bq_0/c_p \sqrt{a})^2 t\right] \tag{3.146}$$

The temperature practically changes exponentially according to (3.145) starting from the moment $t \sim 2c_p^2 a/b^2 q_0^2$.

The inclusion of the effect of the absorptivity-temperature (A-T) dependence leads to changes in the heat power density required for the surface to reach the specified temperature, for example, T_m, at the end of the pulse. For silver, the heat power density $q_c^{(1)}$ is 9×10^5 W/cm^2 ($\tau = 1$ ms) and 3×10^6 W/cm^2 with and without consideration for the A-T dependence respectively.

TABLE 3.6. **Parameters Determining the A-T Dependence of Some Materials**

Material	a_0	$b \times 10^4$, K^{-1}
Tungsten	0.024	1.03
Molybdenum	0	0.99
Tantalum	0.048	0.92
Platinum	0.099	0.64
Copper	0.028	0.14
Graphite	0.890	−0.40
Alumina	0.770	−4.28
Germanium	0.747	−0.92

The three-dimensional problem of heating a semi-infinite solid with consideration for the function A (T) was treated by I.P. Dobrovolsky and A.A. Uglov. In the general case, the A-T dependence in the form of (3.138) proves valid for many substances. This conclusion follows from the analysis of experimental data: the scatter in these data is appreciable and the absorptivity A is heavily dependent on the surface states and other analogous factors which are not amenable to easy quantitative control.

The coefficients a_0 and b for some materials are listed in Table 3.6. They are taken from the experimental data by extrapolating the function A (T) in the temperature range below T_m. In nonmetals, A may decrease with increasing T.

Let the incident flux be axisymmetric and the flux density profile be Gaussian. If we disregard for now the phase transitions, surface heat loss, and temperature dependence of the thermal constants, then the problem stated will take on the form

$$\begin{aligned} &(1/a)\,\partial T/\partial t = \partial^2 T/\partial r^2 + (1/r)\,\partial T/\partial r + \partial^2 T/\partial z^2 \\ &z = 0, \quad -\lambda \partial T/\partial z = (a_0 + bT)\, q_0 \exp(-kr^2) \\ &r,\ z \to \infty, \quad t = 0, \quad T = T_0 \end{aligned} \tag{3.147}$$

The solution for this problem was found using an analytic successive approximation method which also helped in treating a number of more complex problems. Consider the solution procedure.

Introduce the dimensionless quantities

$$T = q_0 A_0 u/\lambda\sqrt{k} + T_0, \quad t = \tau/ak, \quad r = \rho/\sqrt{k}$$
$$z = \xi/\sqrt{k}, \quad \beta = q_0 b/\lambda\sqrt{k} \tag{3.148}$$

Equation (3.147) then becomes

$$\partial u/\partial\tau = (1/\rho)\,(\partial/\partial\rho)\,(\rho\,\partial u/\partial\rho) + \partial^2 u/\partial\xi^2$$
$$\xi = 0, \quad \partial u/\partial\xi + \beta u \exp(-\rho^2) = \exp(-\rho^2) \tag{3.149}$$
$$\rho \to \infty, \quad \xi \to \infty, \quad \tau = 0, \quad u = 0$$

On examination of equations (3.149) we conclude that this system of equations in the dimensionless form depends only on one parameter β proportional to the coefficient b which characterizes the degree of departure of the absorptivity from its constant value.

Introducing a new unknown function w by use of the formula for the dimensionless temperature

$$u = (1/\beta)\,[\exp(\beta w) - 1] \tag{3.150}$$

we change from system (3.149) to the system that is nonlinear with respect to w:

$$\partial w/\partial\tau = (1/\rho)\,(\partial/\partial\rho)\,(\rho\,\partial w/\partial\rho) + \partial^2 w/\partial\xi^2$$
$$+ \beta\,[(\partial w/\partial\rho)^2 + (\partial w/\partial\xi)^2] \tag{3.151}$$
$$\xi = 0, \quad \partial w/\partial\xi = -\exp(-\rho^2), \quad \tau = 0, \quad \rho \to \infty$$
$$\xi \to \infty, \quad w = 0$$

This change-over allows us to obtain a convenient approximation to the solution of the problem (3.149) at real values of β and τ. For the solution of the system of equations (3.151) we use the method of successive approximations:

$$\partial w_{n+1}/\partial\tau = (1/\rho)\,(\partial/\partial\rho)\,(\rho\partial w_{n+1}/\partial\rho)$$
$$+ \partial^2 w_{n+1}/\partial\xi^2 + \beta\,[(\partial w_n/\partial\rho)^2 + (\partial w_n/\partial\xi)^2] \tag{3.152}$$
$$\xi = 0, \quad \partial w_{n+1}/\partial\xi = -\exp(-\rho^2) \tag{3.153}$$
$$\tau = 0, \quad \rho \to \infty, \quad \xi \to \infty, \quad w_{n+1} = 0 \tag{3.154}$$

The first approximation results after solving equation (3.152) without nonlinear terms, using the conditions (3.153) and (3.154). If the parameter β does not exceed a few units in magnitude, then, as the estimate shows, the deviation of w_2 from w_1 is not more than 15%, and it decreases at lower values of β and τ. The reason is that the derivatives $\partial w/\partial\xi$ and $\partial w/\partial\rho$ are almost everywhere smaller than unity; these derivatives squared are still smaller.

The first approximate solution of the system (3.152)-(3.154) coincides with the solution found for the Gaussian heat source and has the following form at variables ρ, ξ, and τ:

$$w_1(\rho, \xi, \tau) = (2/\sqrt{\pi}) \times \int_0^{\sqrt{\tau}} \exp\{-[\rho^2/(1+4x^2) + \xi^2/4x^2]\}\, dx/(1+4x^2) \tag{3.155}$$

In the center of the hot spot,

$$w_1(0, 0, \tau) = (1/\sqrt{\pi}) \operatorname{arctg}(2\sqrt{\tau}) \tag{3.156}$$

The maximum dimensionless temperature is

$$u_{max} = \left(\frac{1}{\beta}\right) \exp\left[\left(\frac{\beta}{\sqrt{\pi}}\right) \operatorname{arctg}(2\sqrt{\tau})\right] - 1 \tag{3.157}$$

Using (3.148), we convert to denominate quantities and obtain the expression for the power density required to reach a certain temperature T_1 for time t at the center of the hot spot:

$$q_0 = \lambda \sqrt{\pi k}\,(T_1 - T_0) \times (\ln A_1 - \ln A_0)/[(A_1 - A_0) \operatorname{arctg}(2\sqrt{akt})] \tag{3.158}$$

where A_1 is the absorptivity at T_1.

When $A_1 \to A_0$, the limiting process for equation (3.158) leads to the expression for power density q_0^* corresponding to a constant A^*:

$$q_0^* = \lambda \sqrt{\pi k}\,(T_1 - T_0)/[A \operatorname{arctg}(2\sqrt{akt})] \tag{3.159}$$

From formulas (3.158) and (3.159) it is clear what the mean absorptivity $\bar{A}$ must be in order to reach the same maximum temperature as that obtainable in the case of a variable absorptivity at the same power density and for the same time. Equating q_0 and q_0^* yields the formula for the mean absorptivity

$$\bar{A} = (A_1 - A_0)/(\ln A_1 - \ln A_0) \tag{3.160}$$

For molybdenum, we get $\bar{A} = 0.112$ in the temperature range 293-2 900 K at $A_0 = 0.029$ and $A_1 = 0.284$. Expanding $\exp(\beta w_1)$ in (3.160) in a series at small values of β and restricting the analysis to the four terms of the series give

$$u \approx w_1(1 + \beta w_1/2 + \beta^2 w_1^2/6) \tag{3.161}$$

At $|\beta| < 0.2$, the A-T dependence should not be given consideration.

Compare the power density q_0 for silver calculated from (3.158) with q_0 estimated by use of a unidimensional model. At $\lambda =$

4.2 W $cm^{-1} K^{-1}$, $a = 1.74$ $cm^2 s^{-1}$, $b = 10^{-4} K^{-1}$, $A_0 = 0.03$, $T = 300$ K, $T_1 = T_m = 1\,233$ K, $t = 1$ ms, and $k = 10^4$ cm^{-2}, we have $q_0 = 7.2 \times 10^6$ W cm^{-2} ($\beta = 1.71$), whereas the unidimensional model gives $q_0 = 9 \times 10^5$ W cm^{-2}. This means that the effect of the spatial distribution of the absorbed power density is rather substantial.

From the analysis of the dependence of u_{max} on $\sqrt{\tau}$, we can draw the following conclusions. There is a qualitative disparity in the temperature changes with time between the three-dimensional and the unidimensional model when account is taken of the function $A(T)$. In the unidimensional case, the temperature at $b \geqslant 0$ rises infinitely with time, as seen from relations (3.144) and (3.145), and at $b < 0$ tends to a constant value, whereas in the three-dimensional case the quantity u_{max} always approaches a constant value at $t \to \infty$, as shown by the relation

$$u(0, 0, \infty) = (1/\beta)[\exp(\beta\sqrt{\pi}/2) - 1] \tag{3.162}$$

It should also be noted that the temperature more quickly tends to its limit at $\beta < 0$ rather than at $\beta > 0$. For example, by the moment $\tau = 1$, we have $u_{max}(\beta = 2) = 0.51\, u_{lim}$ and $u_{max}(\beta = -2) = 0.86\, u_{lim}$.

Temperature dependence of thermal constants. Consider to which extent the temperature dependence of the thermal conductivity, $\lambda(T)$, and of the specific heat per unit volume, $c_v(T) = \gamma(T)\, c(T)$, affect the temperature field in a solid heated by a stationary Gaussian heat source. This problem relates to the processes of heating of solids with EBs as well as with LR since we consider the surface absorptivity to be independent of temperature.

A semi-infinite body. Let the absorbed power density be limited to such a value that during the time interval under consideration the maximum surface temperature does not exceed the melting point. Assume that the laser pulse is rectangular in shape and the heated body is semi-infinite.

The problem stated takes the form

$$\begin{aligned} &c_v(T)\,\partial T/\partial t = (r^{-1}\partial/\partial r)[\lambda(T)(r\partial T/\partial r)] \\ &\qquad + (\partial/\partial z)[\lambda(T)(\partial T/\partial z)] \\ &z = 0, \quad \lambda(T)(\partial T/\partial z) = -q_0 \exp(-kr^2) \\ &t = 0, \quad r \to \infty, \quad z \to \infty, \quad T = T_0 \end{aligned} \tag{3.163}$$

where q_0 is the absorbed power density, and T_0 the initial temperature.

In the general case, if the functions $\lambda(T)$ and $c_v(T)$ are complex in form, it is advantageous to tackle the problem (3.163) by numerical methods. But for some materials, the functions $\lambda(T)$ and $c_v(T)$ can be approximated by linear relations over the requisite temper-

ature ranges. This makes it possible to allow for the temperature dependence of thermal constants to an accuracy sufficient for a number of applications without recourse to numerical methods. The analysis given below will cover a wide range of materials which call for a more complex approximation of functions $\lambda(T)$ and $c_v(T)$.

The algorithm for the solution of equation (3.163) can be designed in the same way as is done for the preceding problem. In handling the problem stated in terms of (3.163), we shall pass to dimensionless quantities by use of the relations

$$T - T_0 = q_0 A_0 u/(\lambda_0 \sqrt{k}), \quad r = \rho k^{-1/2}, \quad z = \xi k^{-1/2} \tag{3.164}$$
$$h = q_0\beta/(\lambda_0^2 \sqrt{k}), \quad \tau = ka_0 t, \quad g = q_0\delta/(\lambda_0 \sqrt{k} c_{v0})$$

where the subscript 0 denotes that the corresponding parameter is taken at T_0. Here, $a_0 = \lambda_0 c_{v0}^{-1}$ is the thermal diffusivity. The meaning of the parameters β and δ is clear from the following temperature relations:

$$\lambda(T) = \lambda_0 + \beta T \tag{3.165}$$
$$c_v(T) = c_{v0} + \delta T \tag{3.166}$$

This form of the temperature dependence of λ and c_v is specific to a number of steel grades over a wide temperature range, in particular, to austenitic Ni-Cr steels, molybdenum, and other metals.

Using relations (3.164)-(3.166) and performing transformations, we obtain, instead of (3.163), the relation

$$1 + hu + \Delta u + h\left[(\partial u/\partial\rho)^2 + (\partial u/\partial\xi)^2\right] = (1 + gu)\,\partial u/\partial\tau \tag{3.167}$$

where $\Delta = \partial^2/\partial\rho^2 + \rho^{-1}\partial/\partial\rho + \partial^2/\partial\xi^2$.

Let us omit the quantities $\beta T_0/\lambda_0$ and $2\delta T_0/c_{v0}$ since their values are small in comparison with those of other terms. Then, from the system of equations (3.163) we obtain

$$\rho^{-1}\partial/\partial\rho\left[(1 + hu)\,\rho\,\partial u/\partial\rho\right] + \partial/\partial\xi\left[(1 + hu)\,\partial u/\partial\xi\right] = (1 + gu)\,\partial u/\partial\tau \tag{3.168}$$
$$\xi = 0, \quad (1 + hu)\,\partial u/\partial\xi = -\exp(-\rho^2)$$
$$\tau = 0, \quad \rho \to \infty, \quad \xi \to \infty, \quad u = 0$$

Applying the Kirchhoff transform, we can reduce the system (3.168) to the form

$$v = \int_0^u (1 + hx)\,dx = u + hu^2/2 \tag{3.169}$$

It is obvious from (3.169) that there is a linear relation between v and u if $1 \gg hu/2 = \beta (T - T_0)/2\lambda$. At $(T - T_0) \approx 10^3$ K, $\beta = 4 \times 10^{-4}$ W/cm^{-1} K^{-2}, and $\lambda = 1$ W cm^{-1} K^{-1}, we have $hu/2 \approx 0.4$, and therefore the relation between u and v proves nonlinear for the typical cases of metal heating. The parameter $\varkappa = \beta (T - T_0)/\lambda_0$ to a definite degree is the criterion of the nonlinearity of the problem for the function $\lambda (T)$ because at $\varkappa \ll 1$ the problem is linear.

For the case where λ linearly varies with temperature, from formula (3.169) we obtain

$$v = [\pm(1 + 2hu)^{1/2} - 1]/h \tag{3.170}$$

The plus or minus sign ahead of the radical in (3.170) is chosen from physical considerations. With allowance made for expressions (3.169) and (3.170), the system (3.168) assumes the form

$$\Delta v = (\rho^{-1}\partial/\partial\rho)\,(\rho\,\partial v/\partial\rho) + \partial^2 v/\partial\xi^2 = W(v, h, g)\,\partial v/\partial\tau \tag{3.171}$$

$$\xi = 0, \quad \partial v/\partial\xi = -\exp(-\rho^2)$$

$$\tau = 0, \quad \rho \to \infty, \quad \xi \to \infty, \quad v = 0$$

$$W(v, h, g) = g/h + (1 - g/h)/\sqrt{1 - 2hv} \tag{3.172}$$

In the system of (3.171) and (3.172) the heat-transfer equation is nonlinear and the boundary conditions are linear. They become completely linear at $g/h = 1$ ($g/h = \delta\lambda_0/\beta c_{v0}$) in the case when β and δ are of the same sign. From (3.172) it follows that as W more closely approaches a constant value, the use of the methods of linearization for the solution of problems becomes more effective.

For the solution of the system of (3.171) and (3.172) we shall use the method of successive approximations. Let us denote the mean value of the function $W(v, h, g)$ in terms of the least squares by $\overline{W}$ within the temperature interval under consideration; in the temperature range from room temperature to the melting point, $\overline{W} = 2.169$ for molybdenum and $\overline{W} = 0.737$ for corrosion-resistant steel. We can now implement the iterative process:

$$\Delta v_n = \overline{W}\,\partial v_n/\partial\tau + [g/h + (1 - g/h) \times (1 + 2hv_{n-1})^{-1/2} - \overline{W}]\,\partial v_{n-1}/\partial\tau \tag{3.173}$$

$$\xi = 0, \quad \partial v_n/\partial\xi = -\exp(-\rho^2)$$

$$\tau = 0, \quad \rho \to \infty, \quad \xi \to \infty, \quad v_n = 0$$

where $v = 0$ is taken as a zero estimate. The first approximation v to the solution is then found from the linear system. The convergence of the iterative process to an accurate solution can be proved, for example, by the method used to solve the Volterra integral equations of the second kind [13].

For the first approximation v_1, we get

$$v_1(\rho, \xi, \tau) = (2/\sqrt{\pi}) \times \int_0^{(\tau/\overline{W})^{1/2}} \exp\{-[\rho^2/(1+4x^2) - (\xi^2/4x^2)]\}\, dx/(1+4x^2) \quad (3.174)$$

At small values of $\tau/\overline{W}$, relation (3.174) becomes simpler. If $\tau/\overline{W} \ll 1$, then, instead of (3.174), we can obtain

$$v_1(\rho, \xi, \tau) = 2\exp(-\rho^2)(\tau/\overline{W})^{1/2}\, \text{ierfc}\,(\xi/2)(\overline{W}/\tau)^{1/2} \quad (3.175)$$

Expression (3.175) represents the product of two cofactors: the function describing the radial distribution of the power density and the function describing the solution of the unidimensional problem for heating a semi-infinite body with a source of constant power density.

At large values of τ, the function $v_1(\rho, \xi, \tau)$ is independent of $\overline{W}$ in consequence of the application of the Kirchhoff transform to the original nonlinear problem. The second approximation is given in one of the works of A.A. Uglov and O.I. Isaeva.

A plate of thickness l. For the plate of thickness l, instead of the constraint at $z \to \infty$, we specify an adiabatic boundary condition on the surface ($z = l$):

$$z = l, \quad \partial T/\partial z = 0 \quad (3.176)$$

Then, introducing dimensionless variables and making transformations such as those done in the problem for a semi-infinite body, we obtain the following system of equations:

$$\begin{aligned} &\Delta v = W(v, h, g)(\partial v/\partial t) \\ &\xi = 0, \quad \partial v/\partial \xi = -\exp(-\rho^2), \quad \tau = 0, \quad \rho \to \infty, \quad v = 0 \\ &\xi = lk^{1/2}, \quad \partial v/\partial \xi = 0 \end{aligned} \quad (3.177)$$

The iterative process for the system (3.177) is run in the same way as for (3.173). The iteration procedure generates a first approximation v_1 by way of solving the linear heat-transfer equation with linear boundary conditions:

$$\begin{aligned} &\Delta v_1 = \overline{W}\, \partial v_1/\partial \tau \\ &\xi = 0, \quad \partial v_1/\partial \xi = -\exp(-\rho^2) \\ &\tau = 0, \quad \rho \to \infty, \quad v_1 = 0, \quad \xi = lk^{1/2}, \quad \partial v_1/\partial \xi = 0 \end{aligned} \quad (3.178)$$

The solution of the system (3.178) has the form

$$v_1(\rho, \xi, \tau) = [1/(2lk^{1/2})] \int_0^\infty dx \exp(-x^2/4) J_0(x\rho) \left\{ \frac{[1-\exp(-x^2\overline{W}^{-1}\tau)]}{x} + 2 \sum_{n=1}^{\infty} \frac{x\{1-\exp[-(x^2+\pi^2n^2/l^2k^2)\tau\overline{W}^{-1}]\} \cos \pi n\xi/lk^{1/2}}{x^2+\pi^2n^2/l^2k} \right\} \quad (3.179)$$

where the parameter $\overline{W}$ defines the degree of nonlinearity of the problem, and $J_0(x\rho)$ is the Bessel function of first kind of order zero.

At small values of τ and at l such that the plate cannot be thought of as the semi-infinite solid, the approximate solution of the problem (3.178) can also be given by the product of two cofactors: the first is the function of the radial power density distribution and the second is the function describing the solution of the corresponding unidimensional problem:

$$v_1 = lk^{1/2} \exp(-\rho^2) \{\tau/lk^2\overline{W} + (lk^{1/2}-\xi)^2/2l^2k - 1/6 - 2[\sum_{n=1}^{\infty} [(-1)^n \cos \pi n \times (1-\xi/lk^{1/2})/\pi^2n^2 \exp(-\pi^2n^2\tau/\overline{W}l^2k)]\} \quad (3.180)$$

The series in (3.180) converges quickly, and so for practical estimates to be made, it is enough to apply only a few terms of the series.

Expressions (3.178) and (3.179) allow us to conclude that the nonlinearity only affects the time-dependent component. At large times τ satisfying the condition $\tau \gg \overline{W}x^{-2}$, where x is a parameter in the order of unity, the problem becomes linear and the steady-state value of v_1 proves independent of $\overline{W}$, as in the problem of heating a semi-infinite body.

Figure 3.25 illustrates how the calculated values of the rates at point (0, 0) vary with time at different values of q_0, the rates being given as dimensionless variables and represented by solid curves. For comparison, dash curves *1* represent the value of $\partial u/\partial\tau$ obtained from the solution of the partially linearized problem. Curves *2* are the plots of surface temperature at point (0, 0, t) versus time at different values of q_0. Using these curves, we can readily compute the time t_m required to reach the melting temperature T_m at the given point. What is evident is an appreciable spread in the corresponding times obtained with regard to the function $\lambda(T)$ alone and with consideration for both $\lambda(T)$ and $c_v(T)$. Thus, at $q_0 = 10^5$ W/cm^2, the melting time t_m is 114 μs in the first case, but rises

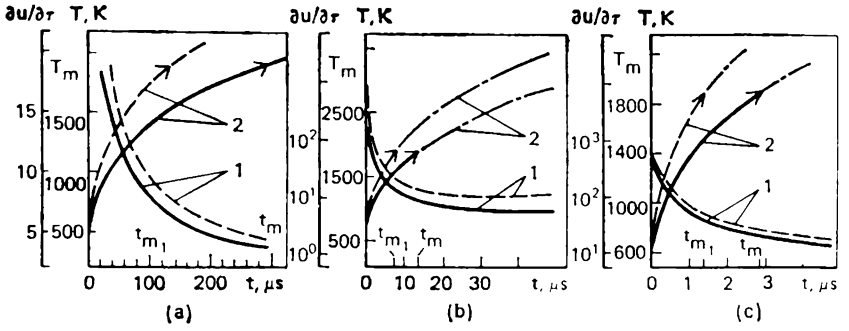

Fig. 3.25. Variations in the rate of heating (*1*) and surface temperature (*2*) with time for corrosion-resistant steel at $q_0 = 10^5$ W cm^{-2} (*a*), $q_0 = 5 \times 10^5$ W cm^{-2} (*b*), and $q_0 = 10^6$ W cm^{-2} (*c*)

up to 300 μs in the second case. The time t_m rather strongly depends on q_0: $t_m \sim q_0^{-2}$, so that t_m is near 3 μs at $q_0 = 10^6$ W/cm^2.

The results of the numerical estimates of heating rates for molybdenum are shown in Fig. 3.26. There are some features specific to the temperature variations and heating rates for this metal. The thermal conductivity of molybdenum drops off with growing temperature, while c_v rises. Therefore, $h < 0$, which means that we should place a minus sign ahead of the radical in expression (3.170) when using it to calculate the dimensionless temperature. For comparison, the figure illustrates the calculated results obtained at the values of thermal constants without any regard to their deviation due to temperature. For molybdenum, the time to reach the melting point is $t_m = 1.6$ ms at $q_0 = 10^5$ W/cm^2 and $t_m = 15.7$ μs at $q_0 = 10^6$ W/cm^2.

Temperature dependence of thermal constants in the case of a moving heat source. Consider the results of calculations on an

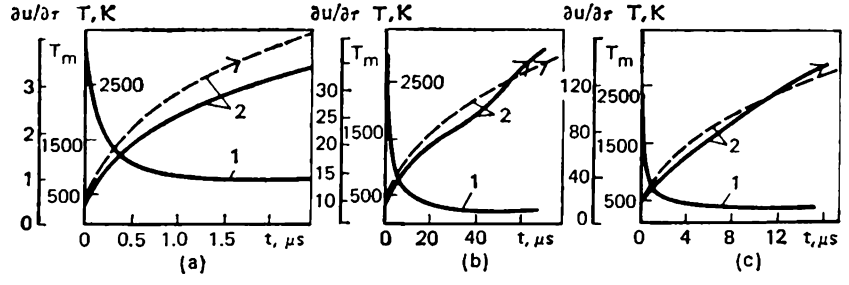

Fig. 3.26. Variations in the rate of heating (curves *1*) and surface temperature (curves *2*) with and without regard to the temperature dependence of λ and c_v (solid and dash curves *2* respectively): (*a*), at $q_0 = 10^5$ W cm^{-2}; (*b*), at $q_0 = 5 \times 10^5$ W cm^{-2}; (*c*), at $q_0 = 10^6$ W cm^{-2}

electronic computer of the temperature of metals heated by a moving heat source with consideration for the temperature dependence of their thermal constants [14]. The computations were made under two assumptions.

1. The heat source moves over the surface of a semi-infinite solid in the direction of the ox axis at a constant velocity v.

2. The boundary conditions are of the first kind, so that at the point of action of the source the temperature of the target is equal to the melting temperature T_m. The problem stated then assumes the form

$$c(T)\gamma(T)\partial T/\partial t = \lambda(T)(\partial^2 T/\partial x^2 + \partial^2 T/\partial y^2) + (\partial\lambda(T)/\partial T)[(\partial T/\partial x)^2 + (\partial T/\partial y)^2] + \gamma(T)c(T)v\,\partial T/\partial x \quad (3.181)$$

$$0 \leqslant x < \infty, \quad 0 \leqslant t < \infty, \quad t > 0$$

$$x, y = 0, \quad T = T_m \quad (3.182)$$

$$y = 0, \quad \partial T/\partial y = 0 \quad (3.183)$$

$$x, y \to \infty, \quad t = 0, \quad T = T_0 \quad (3.184)$$

Figure 3.27 displays the temperature curves plotted for copper, molybdenum, and corrosion-resistant steel assumed to be heated 3 s after the heat source started moving. The initial temperature T_0 was taken equal to 300 K, and the source speed v equal to 1 cm/s. In the calculation procedure, the dependences of thermal conductivity λ and specific heat c_v on temperature T and density γ were given by the equations of cubic parabolas and the linear temperature functions respectively. It is seen from the figure that the temperature fields markedly change in shape depending on the thermal properties of materials. The correlation of the results with the solutions of the analogous linear problem showed that allowance made for the temperature dependence of metal properties led to the refinement of the calculated data to within 3-18%. The deviation was found to be the lowest for copper and steel, and the highest for molybdenum.

Temperature dependence of thermal and optical constants. The process of heating a semi-infinite body by a stationary Gaussian source with due regard for the temperature dependence of thermal and optical constants at an invariable temperature T_0 is defined by a nonlinear heat-transfer equation with boundary conditions:

$$z = 0, \quad \lambda(T)(\partial T/\partial z) = -A(T)q_0 \exp(-kr^2) \quad (3.185)$$

$$r \to \infty, \quad z \to \infty, \quad t = 0, \quad T = T_0 \quad (3.186)$$

The solution of the equation was sought on a computer by a numerical method for certain materials [15] and by an approximate

analytic method [16]. The analytic method calls for approximation of the experimental data on functions $c_v(T)$, $\lambda(T)$, and $A(T)$. For a group of metals, it is possible to approximate $A(T)$ by a first-degree polynomial, and $\lambda(T)$ and $c_v(T)$ by a third-degree polynomial in temperature.

For the solution of the problem, an iteration method is used to account for the nonlinearity of $c_v(T)$ and $\lambda(T)$, which is similar to the above described method but more complex because it has to allow for $A(T)$. Introducing a normalized thermal conductivity [16]

$$\lambda_n = A_0(T_0)\lambda(T)/[A(T)\lambda(T_0)] \qquad (3.187)$$

we apply the Kirchhoff transformation. The surface boundary condition then becomes linear and the heat-transfer equation now contains a nonlinear component which is equivalent to a nonlinear volume heat source added to the system.

To solve the new problem, we apply the iteration method. The zero-order approximation for this method is the solution of the heat-transfer equation without the volume heat source. Calculations point to a noticeable difference between linear and nonlinear approximations due, largely, to a substantial absorptivity-temperature dependence inherent in laser heating.

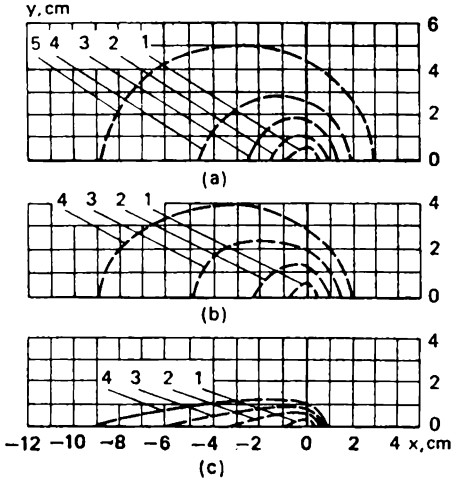

Fig. 3.27. Instantaneous distribution of temperature in a body heated by a single moving source: (*a*), copper: *1-5*, at 1 000, 800, 700, 600, and 500 K respectively; (*b*), molybdenum: *1-4*, at 2 000, 1 200, 900, and 700 K respectively; (*c*), steel: *1-4*, at 1 000, 700, 600, and 550 K respectively

Problems of ablation of materials. Ablation is the process of removal of materials, in our case, by melting and blow-off of the liquid phase. The process approaching the melting stage lends itself to a satisfactory analysis by a number of experiments. The layer of molten material on the target surface begins to form only if the absorbed power density exceeds $q_c^{(1)}$. After the time t_m, the surface rises to the melting point T_m and the melt boundary that is the interface between the liquid and the solid phase penetrates into the material bulk. This process relates to a Stefan problem with a nonlinearity of the 3d kind. The aim of the solution of the Stefan pro-

blem is to search out formulas for the temperature distribution in solid and liquid phases and the speeds of travel of the interface between the liquid and vapor phases.

Let us dwell on the main results stemming from the analysis of the problem, bearing in mind that the rigorous analytic solutions of Stefan problems only exist in a limited number of cases. Consider the unidimensional case of heating and subsequent melting of a plate of thickness l by a surface heat source under the assumption that the liquid phase is removed as soon as it is formed. Regarding the thermal constants to be independent of temperature, write down the statement of the problem in the form

$$a\partial T/\partial t = \partial^2 T/\partial z^2 \tag{3.188}$$

for $S(t) \leqslant z \leqslant l, \quad t = 0, \quad S(t) = 0$

$$t = 0, \quad T = T_0(z) \leqslant T_m \tag{3.189}$$

$$0 \leqslant z \leqslant l, \quad z = l, \quad t > 0, \quad \partial T/\partial z = 0 \tag{3.190}$$

$$z = S(t), \quad t > 0, \quad q_0(t) = -\lambda\, \partial T/\partial z + \gamma L_m\, \partial S/\partial t \tag{3.191}$$

where $S(t)$ is the position of the phase boundary, and L_m the specific heat of melting.

Equation (3.191) is referred to as the Stefan condition. In fact, it is a statement of the principle of conservation of energy at the interface. It holds both during melting and in the absence of melting if the following conditions are met on the surface being heated:

$$\begin{aligned} &\partial S/\partial t \geqslant 0, \quad T[S(t), t] = T_m \\ &\partial S/\partial t = 0, \quad T[S(t), t] < T_m \end{aligned} \tag{3.192}$$

The time t_m between the instant of heat release and the instant at which the surface reaches the temperature T_m is given by

$$t_m = (\gamma L_m \sqrt{a}\, m/q_0)^2 \tag{3.193}$$

Here $m = (\sqrt{\pi}/2)\, c\,(T_m - T_0)/L_m$, and the power density q_0 is assumed to be time-constant.

If we include new variables and cancel the moving boundary by applying a transformation

$$\xi = (l - z)/[l - S(t)] \tag{3.194}$$

we can reduce expressions (3.188)-(3.191) to the form dependent only on the parameter m. The general solution of this problem is obtained by numerical integration.

Consider some particular cases of the problems of ablation. For the steady state, the speed of melting will be written as

$$v_m = \partial S/\partial t = q_0/\{\gamma\,[L_m + c\,(T_m - T_0)]\} \tag{3.195}$$

Using relation (3.195) as a first approximation and neglecting the time it takes the surface to reach the constant rate of melting, estimate the molten layer thickness after the time t:

$$S(t) \approx v_m (t - t_m) \tag{3.196}$$

and the steady-state distribution of temperature over the body:

$$T \approx T_0 + (T_m - T_0) \exp\{-(v_m/a)[z - v(t - t_m)]\} \tag{3.197}$$

Let us look at the limiting cases of the problem for the parameter m.

The case where $m = 0$. Since the parameter m is proportional to the ratio between the enthalpy of a material when heated from T_0 to T_m and the specific melting heat L_m, the case $m = 0$ is physically unrealizable. But it is the limiting case that corresponds to a large specific heat of melting or evaporation in comparison with the enthalpy of the sample.

In terms of dimensionless variables, the temperature distribution in a solid phase, $u_0(x, y)$, has the form

$$\begin{aligned} u_0(x, y) = {} & \pi^{1/2} \operatorname{erfc}(x/2y^{1/2}) - x\pi^{-1} (\operatorname{arctg} y^{-1/2}) \\ & + [(y+1)/\pi^{1/2}] \exp\{-x^2/[4(y+1)]\} \\ & \times \operatorname{erfc}[z/2\sqrt{y(y+1)}] + 2xW(x/\sqrt{2(y+1)};\ y^{-1/2}) \end{aligned} \tag{3.198}$$

where

$$u_0(x, y) = (T - T_0)/[\sqrt{\pi}(T_m - T_0)]$$

$$x = [z - S(t)]/\sqrt{at_m}, \quad y = (t/t_m) - 1$$

$$W(\alpha, \beta) = (2\pi)^{-1} \int_0^{\alpha} \int_0^{\beta x} \exp[-(x^2 + y^2)/2]\, dy\, dx \tag{3.199}$$

The expression for the rate of melting is then written as

$$\mu_0(y) = (2/\pi) \operatorname{arctg}(y^{1/2}) \tag{3.200}$$

At the initial stages of melting when $x^{1/2}/y$ is large,

$$u_0(x, y) \approx (1+y)^{1/2} \operatorname{ierfc}[z/2(1+y)^{1/2}] \tag{3.201}$$

From the comparison between (3.201) and (3.34) it follows that when the material begins to melt ($y \ll 1$), the temperature distribution in the inner region is such as it would be during heating without melting. This conclusion made for an infinite value of the specific heat of melting shows why the temperatures and the coordinates of the melt boundary calculated by expressions of linear theory for short pulses and for finite values of the specific heat of melting are well coincident.

The case where $m = \infty$. Consider another limiting case when $L_m = 0$. For the quasisteady state, the equilibrium temperature distribution takes the form

$$u_e = \pi^{1/2} \exp(-\pi^{1/2} z/2) \tag{3.202}$$

The position of the melt boundary, expressed in dimensionless variables, for the steady state is defined by the expression

$$\omega_e = \nu_e (1 + y - \pi/4) \tag{3.203}$$

and the rate of melting is given by

$$\nu_e = \sqrt{\pi/2} \approx 1.254 \tag{3.204}$$

The relation between dimensionless parameters ω_e, μ_e, and σ assumes the form

$$\omega_e = m\sigma, \quad \sigma = \gamma L_m S/q_0 t_m$$
$$\nu_e = m\mu_e, \quad \mu_e = \gamma L_m (dS/dt)\, q_0^{-1}$$

For *the case where* $m \neq 0$, the solution was found by H. G. Landau who used numerical integration.

Along with the numerical methods of solving the problems of ablation, we can use approximate algorithms designed so as to treat the unsteady stages of ablation both in a semi-infinite solid [17] and in a plate of finite thickness [18]. Look at the problem of ablation for a plate of finite thickness keeping in mind that we should obtain fairly simple expressions.

The problem stated takes the form of expressions (3.188)-(3.191). For the solution of the problem, workers [18] used an approximate analytic technique of Biot. The temperature distribution in the plate is given as

$$T(z, t) = T_m \left[1 - \left(z - \frac{S(t)}{h(t)}\right)\right]^2 \tag{3.205}$$

where $h(t)$ is the width of the heat affected zone. So long as $S(t) + h(t) < l$, the problems of ablation for a semi-infinite body and a plate of finite thickness can be treated in the same way. At the end of time t^* when $S(t^*) + h(t^*) = l$, the finiteness of plate thickness begins to make itself felt. Starting at this moment, the solution is found to be

$$T(z, t) = [T_m - T_2(t)]\{1 - [z - S(t)]/[l - S(t)]\}^2 + T_2(t) \tag{3.206}$$

where $T_2(t)$ is the temperature of the back surface of the plate.

By applying Biot's variational formalism, we obtain the equation establishing the relation between the desired quantities:

$$[l - S(t)]\,[T_m - T_2(t)]\,(dS/dt) + 2\,[l - S(t)]^2\,[dT_2(t)/dt] = 21\,a\,[T_m - T_2(t)]/4 \qquad (3.207)$$

The second equation follows from the condition of energy balance at the phase boundary:

$$q_0(t) = \gamma\,(L_m + cT_m)\,S(t) + \gamma c \int_{S(t)}^{l} T(z,\ t)\,dz \qquad (3.208)$$

Consider the case most often met with in practice when both the temperature field and the speed of the phase boundary, v_e, have become invariable, i.e.

$$dS(t^*)/dt = v_e = q_0/[\gamma\,(L_m + cT_m)], \quad h_e = 21a/4v_e \qquad (3.209)$$

To provide an easy solution of the system (3.207)-(3.208), we change over to dimensionless quantities

$$\xi = 1 - \{[S(t) - S(t^*)]/h_e\}$$
$$y(\xi) = 1 - [(T_2(\xi) - T_0)/(T_m - T_0)] \qquad (3.210)$$

The use of the Biot method reduces the system (3.188)-(3.191) to the system of two ordinary differential equations with requisite boundary conditions:

$$v\xi\,(y + 2\xi\,dy/dt) = 2v_e y,$$
$$v\,\{1 - A\,[1 - (2/3)\,y] - (2\xi/3)\,(dy/dt)\} = v_e \qquad (3.211)$$

The boundary conditions are

$$v(\xi = 1) = v_e, \quad y(\xi = 1) = 1, \quad A = cT_m/(L_m + cT_m)$$

Omitting $v(\xi)$, we derive the equation for a definite temperature:

$$\xi\,(2\alpha\xi - y)\,(dy/dt) - y^2 + (\alpha\xi - b)\,y = 0 \qquad (3.212)$$

Here,

$$\alpha = (3/4)\,(1 + \beta)$$

where $\beta = L_m/cT_m$, $b = 3\beta/2$.

The solution of (3.211) or (3.212) involves appreciable difficulties, therefore it is expedient to employ approximation methods.

Examine the initial stage of the process when the effect of the back surface of the plate is still low, i.e. the deviations of the speed of the phase boundary and the temperature from the steady-state values are small. A change in the rate of motion of the phase transition occurs because of the reflection of the heat wave from the plate's

back surface at which the adiabatic boundary condition remains invariable. Therefore, the change in speed must be of a higher order of smallness than is the case for the change in temperature.

Try the solution of (3.211) in the form

$$\begin{aligned} &y = 1 + \varepsilon y_1(\xi) + \varepsilon^2 y_2(\xi) + \varepsilon^3 y_3(\xi) \\ &dy/dt = dy_1(\xi)/dt + \varepsilon\, dy_2(\xi)/dt + \varepsilon^2\, dy_3(\xi)/dt \\ &v = v_e[1 + \varepsilon^2 v_2(\xi)] \\ &\xi = 1 - \varepsilon(1 - \xi) \end{aligned} \tag{3.213}$$

where ε is the parameter of smallness.

Substituting (3.213) into (3.211), equating the terms with the same powers of ε, and solving the corresponding differential equations yield

$$\begin{aligned} &y = 1 - (1 - \xi)/2 - (1 - \xi)^2/2 \\ &v = v_e\{1 + [1/(1 + 3\beta)](1 - \xi)^2\} \end{aligned} \tag{3.214}$$

Consider the process of ablation for a plate of finite thickness at the final stage when the remaining portion of the plate has heated to a temperature close to T_m. In this case, the speed of the phase boundary tends to a constant value determined by the value of L_m.

Write the solution of (3.211) in the form

$$\begin{aligned} &y = \varepsilon y_1(\xi) \\ &dy/dt = \varepsilon\, dy_1(\xi)/dt, \quad v = v_0 + \varepsilon v_1(\xi) \end{aligned} \tag{3.215}$$

Substituting (3.215) into (3.211) gives

$$\begin{aligned} &y = (H/\sqrt{\xi}) \exp(-v_e/v_0\xi) \\ &v_1 = -(HBv_0/\sqrt{\xi})(1/2 + v_e/v_0\xi) \exp(-v_e/v_0\xi) \end{aligned} \tag{3.216}$$

where H is a constant of integration, $v_0 = q_0/\gamma L_m$, and $B = 2/3\beta$.

To reveal the behavior of the speed of the phase boundary and of the temperature on the back side of the plate over the entire range of changes in ξ, we join the approximate solutions (3.214) and (3.216) at a certain point ξ_0. The coordinate of the point of joining and the approximate value of the constant of integration are defined by the expressions

$$\begin{aligned} &\sqrt{z+1}\,[1/2 + v_e(z+1)/v_0] \exp(-z) + D[z/(z+1)]^2 = E \\ &H = \exp[1 - 1/(1+\beta)\xi_0] \end{aligned} \tag{3.217}$$

where $z = \xi_0^{-1} - 1$, $D = 3\beta^2/[2(1 + \beta)(1 + 3\beta)]$, $E = 3/[2(1 + \beta^{-1})]$.

In Fig. 3.28 are shown the curves of the speeds of phase boundaries plotted versus their coordinates. As is clear from (3.214) and (3.216), the speed $v(\xi)$ depends on one dimensionless parameter $\beta = L_m (cT_m)^{-1}$. The rate of motion of phase boundaries grows as β decreases. The maximum value of $v(\xi)/v_e$ is $v_c/v_e = 1 + \beta^{-1}$. This is because in the equilibrium state the steady speed v_e at decreasing β becomes largely dependent on cT_m whose effect gets weaker as the speed of the moving boundary approaches v_0.

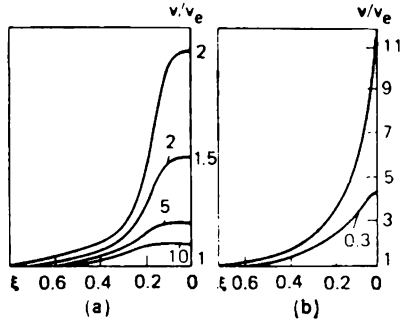

Fig. 3.28. Dimensionless speed v/v_e of the molten front against coordinate ξ: (*a*), $\beta = 1$; (*b*), $\beta = 0$

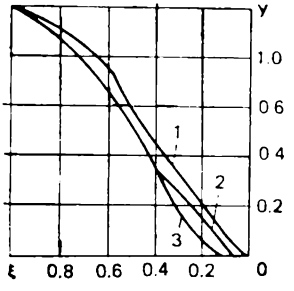

Fig. 3.29. Temperature on the back surface of a plate versus coordinate of the fusion front: *1*, $\beta = 0.1$; *2*, $\beta = 1$; *3*, $\beta = \infty$

The speed range consists of three basic regions: in the first region, the speed rises slowly since the effect of the plate's back surface is still weak; in the second, it rises exponentially to v_0; and in the third, it becomes constant and equal to v_0. In the nonstationary problem considered above, of particular interest is the second region where the phase boundary speed becomes constant. The extent of this region grows with β. In the limit, at large values of β, the speed variation pattern exhibits two regions of constant speeds, v_e and v_0, with a fairly smooth transition from one region to the other. With a decrease in β, the region $v \approx v_0$ sharply shortens and the speed changes more abruptly.

The described algorithm applies where $\beta \geqslant 1$. To describe changes in the rate of motion of the phase boundary at $\beta < 1$, we assume β to be small in comparison with unity and search for the solution of (3.211) in the form

$$y(\xi) = y_0(\xi) + \beta y_1(\xi), \quad dy(\xi)/dt + \beta\, dy_1(\xi)/dt$$
$$dS/dt = dS_0(\xi)/dt + \beta\, dS_1(\xi)/dt$$
$$v_e = v_m(1 - \beta) = q_0(1 - \beta)/\gamma cT_m \qquad (3.218)$$

After performing computations and comparative estimations of the terms in the differential equations, we obtain

$$v = (2v_m/3\xi)\,[1 - (2\beta/9\xi)\,(9\xi/2 + 5/7)]$$
$$y = 9\xi/8 + \beta\,(9\xi/8 - 9/14 + G^*\xi^7) \qquad (3.219)$$

where G^* is a constant of integration.

From the comparison of the obtained result with (3.214) and (3.216), it is seen that this solution is intermediate and, besides, at $\beta \ll 1$, it provides the basic information on the typical parameters of the process. The results of calculations appear in Fig. 3.28*b*.

The curves of the dimensionless temperature on the back surface of the plate as a function of the coordinate of the phase transition front are shown in Fig. 3.29, where it is seen that the temperature reaches T_m somewhat earlier than the speed reaches a value of v_0. Indeed, the nonstationary period for temperature must be shorter than that for speed.

The relations so obtained determine the speed of the phase boundary and the rate of change of temperature on the back surface of the plate over the entire range of changes in L_m/cT_m.

References

1. S. I. Anisimov, Ya. A. Imas, G. S. Romanov, et al. *Effect of high-power radiation on metals.* Moscow, Nauka, 1970 (in Russian).
2. A. G. Akimov, A. M. Bonch-Bruevich, A. P. Gagarin, et al. *The thickness and composition of oxide films produced on a titanium target under laser radiation in oxidizing atmosphere versus the absorption coefficient.* Izv. AN SSSR. Physics Series, 46: No. 6, p. 1186, 1982.
3. M. I. Tribelskiy. *Instability of evaporation and surface oxidation of solids under radiation.* Izv. AN SSSR. Physics Series, 46: No. 6, p. 1127, 1982.
4. N.N. Rykalin, A. A. Uglov, and A. N. Kokora. *Laser machining and welding.* Mo scow, Mir Publishers, 1978.
5. N. N. Rykalin, I. V. Zuev, and A. A. Uglov. *Fundamentals of electron-beam material processing.* Moscow, Mashinostroenie, 1978 (in Russian).
6. F. V. Bunkin, N. A. Kirichenko, and B. S. Lukyanchuk. *On problems of reducing energy required to heat metals by laser radiation.* Fizika i Khimiya Obrabotky Materialov, No. 5, p. 7, 1980.
7. H. S. Carslaw and J. C. Jaeger. *Conduction of heat in solids.* New York, Oxford University Press, 1959.
8. A. V. Lykov. *Theory of heat conduction.* Moscow, Vysshaya Shkola, 1967 (in Russian).
9. L. A. Kozdoba. *Methods of solution of nonlinear heat-transfer problems.* Moscow, Nauka, 1975 (in Russian).
10. L. A. Kozdoba. *Solution of nonlinear heat-transfer problems.* Kiev, Naukova Dumka, 1975 (in Russian).
11. M. I. Tribelskiy. *On the spatial pattern of the liquid phase in laser-induced melting of strong-absorbing media.* Kvantovaya Elektronika, 5: No. 4, p. 804, 1978.
12. F. V. Bunkin and M. I. Tribelskiy. *Nonresonant interaction of high-power optical radiation with liquids.* Uspekhi Fiz. Nauk, 130: No. 2, p. 193, 1980.

13. V. Ya. Arsenin. *Techniques of mathematical physics and special functions.* Moscow, Nauka, 1974 (in Russian).
14. A. A. Uglov, V. V. Ivanov, and A. I. Tuzhikov. *Calculation of the temperature field in a moving heat source with regard to the temperature dependence of thermal constants.* Fizika i Khimiya Obrabotki Materialov, No. 4, p. 7, 1980.
15. A. A. Uglov, V. V. Ivanov, A. I. Tuzhikov, et al. *Calculation of temperatures in the zone of interaction of concentrated energy fluxes with metals.* Promyshlennaya Teplotekhnika, No. 2, p. 68, 1980.
16. N. N. Rykalin, A. A. Uglov, and I. Yu. Smurov. *Nonlinear three-dimensional problems on laser heating of metals.* Fizika i Khimiya Obrabotki Materialov, No. 2, p. 3, 1979.
17. A. A. Uglov, I. Yu. Smurov, and S. S. Andrianov. *On calculation of the rate of unsteady ablation.* Zhurnal Tekhnich. Fiziki, 51: No. 9. p. 1787, 1981.
18. A. A. Uglov, I. Yu. Smurov, and Yu. N. Lokhov. *On calculation of the ablative process in a plate of finite thickness.* Dokl. AN SSSR, 256: No. 6, p. 1378, 1981.

Chapter 4

HYDRODYNAMIC PROCESSES IN INTERACTION REGIONS

A concentrated energy flux (CEF), i.e. a laser radiation (LR) flux or electron beam (EB), incident on a solid causes the target surface in the heat affected zone (HAZ) to melt if the power density of the heat source produced in the HAZ is in excess of $q_c^{(1)}$. The shape of the fusion zone (molten pool) continuously changes as the CEF interacts with the material. The speed of the liquid-solid interface varies with the properties of the target material and also with the spatial-temporal parameters and output parameters of the CEF. If the power density is relatively low, only a thin molten layer appears in the HAZ. At high power densities, the molten front penetrates deep into the material, so that the aspect ratio (ratio of depth to diameter) can be in the order of a few units. The process in which the energy coupled from the CEF to a target is sufficient to ensure deep penetration is often referred to as keyholing.

The CEF-induced melting is a specific process because the fusion zone reaches the highest temperature in its upper layers. If the temperature gradient determines the heat flow mainly in the direction of the gravitational force, convection in the melt is essentially brought about by the reactive back pressure due to evaporation. Since the reactive pressure distribution over the melt surface is nonuniform, the deformation of the molten pool becomes nonuniform too and is usually larger at the center than at the edges of the pool.

A change in the shape of the fusion zone mainly determines the final profile of the interaction region and exerts a substantial influence on the processes associated, for example, with the redox reactions and impurity redistribution and also on the development of defects at weld points or in weld seams. High temperatures induced in the HAZ may cause the subsurface boiling and, hence, blowoff of liquid droplets from the melt region. In some metalworking processes, for example, pulsed laser welding, this effect results in a reduced strength of the joint. Hydrodynamic processes play a substantial or, probably, decisive role in keyholing involved in the formation of narrow and deep holes or cavities. The walls of the

cavity are thin layers of molten metal held in place owing to the surface tension force, the pressure of the vapor jet forcing its way from the bottom of the cavity, and also the recoil momentum (recoil impulse) arising during material vaporization from the cavity walls. The molten metal flows back into the hole and solidifies after the beam has passed to a new area. The result is a weld seam of the desired structure and chemical composition.

In the surface layers of the molten pool the heat source initiates capillary and thermocapillary phenomena. The analysis of these phenomena permits us to get an insight into the processes in the interaction zone. This analysis is also important from the practical viewpoint since the buildup of surface states determines the absorption efficiency (ratio of absorbed power to incident power) and thermal efficiency of the processes. A thin surface layer of the melt mixed up by convective flows can effectively absorb gases from the ambient air or from a controllable gaseous atmosphere. This offers the possibility of varying the composition of the surface layer, of alloying metals, etc.

The melt ejected out on the target surface, for example, during laser hole piercing, resolidifies on the rim of the hole and thus reduces the quality of drilling. The character of mass transfer exerts various effects on the course of any process of material working. Gas pockets present in the melt and also oxide or sulfide inclusions can affect the heat distribution after the pulse ceases. Although there is a certain difference in the interactions of various CEFs, in a first approximation, it is permissible not to focus on this disparity and regard the LR or EB only as a heat source with a definite spatial-temporal pattern and preset output parameters. However, this difference shows up rather markedly in deep-penetration processes accompanied by the generation of a plasma at the target surface, which affects the parameters of heat sources.

4.1. MELT FORMATION

Let a CEF of the given output parameters fall on a target surface. For definiteness, assume that the target of interest is a metal with specified thermal and optical parameters, which occupies an area $z \geqslant 0$, i.e. a semi-space. Then, applying the notion of a critical power density q_c required to bring the target surface to the melting point, we can estimate the range of changes in q_c. For example, a pulsed laser with a pulse duration of $\tau \geqslant 1$ ms must be capable of providing a power density of 10^4 to 10^5 W/cm^2 [1] so that the surface can reach the temperature equal or close to T_m at the end of the pulse. If the power density exceeds q_c and if the time of interaction is longer than 1 ms, the surface begins to melt and the fusion front propagates into the material until the amount of heat delivered

per unit time from the molten pool to the liquid-solid interface becomes equal to the amount of heat diverted per unit time to the solid phase and expended on the phase transition. In the simplest case where, for example, the CEF interacts with a pure metal, this condition at the phase boundary, called the Stefan condition [2], has the form

$$-\lambda_s \partial T_s/\partial n = -\lambda_l \partial T_l/\partial n + \gamma L_m ds\,(t)/dt \qquad (4.1)$$

where subscripts s and l at symbols stand for the solid and the liquid phase respectively, L_m is the specific heat of melting, n the normal to each point on the liquid-solid interface, and $s\,(t)$ the coordinate of the interface (depth of melting) at an arbitrary moment of time counted off from the beginning of melting.

The shape of the molten pool formed on the target surface by the continuous heat flow, which may not necessarily be constant in time, depends on a number of factors: the absorbed power density; physical properties of the melt, including the thermal constants of the material; temperatures of melting and vaporization; viscosity, density, surface tension, and the manner in which they vary with temperature; spatial-and-temporal characteristics of the heat flow; etc.

In view of the above factors, the melt motion in the molten pool can be laminar and turbulent in character. The estimates presented in a number of works show that this motion is largely turbulent, which is borne out by experiments.

In material processing, for example, in laser or electron beam welding, it is of importance to estimate the melt volume and the shape of the liquid-solid interface at the specified heat power. It is rather difficult or probably impossible to obtain the general analytical solution to the problem on the melt motion and changes in the physical parameters of the material with changes in the temperatures of the melt and the solid phase. Therefore, we need to seek for approximate solutions that are valid over a definite range of the parameters of the problem, such as the time responses and power density, and also rely on the digital simulation of the process on a computer. From the practical viewpoint, the following limiting cases are most important: (1) the fusion zone resembles a hemisphere in shape and (2) it is similar to a keyhole. If we ignore the case of a fairly small time of action of the heat source that is only enough to melt a thin layer less than 1 μm thick, most practical cases can be regarded as intermediate ones between the 1st and the 2nd case. But the calculation of the interface position without additional assumptions of the melt motion even for the limiting cases presents rather a complex problem. The kinetic mechanism of melt formation in a semi-infinite solid with regard to the specific heat of phase transition has been dealt with in several works using the model of a stationary point heat source

which, in definite conditions, can help describe the interaction of the EB or LR with materials.

Statement of the problem. Assume a point heat source of constant power density begins to heat the surface of a semi-infinite body at an instant $t = 0$. The main assumptions are: the thermal constants of the solid and the liquid phase are temperature-independent; the time to reach a maximum melt depth is such that we can disregard the heat transfer from both phases to the environment and consider a spherically symmetric problem; and in the liquid phase the turbulent motion prevails, which determines the hydrodynamic character of heat transfer and rapidly raises the temperature to the melting point T_m throughout the volume of the interaction region. The temperature distribution over the liquid phase can then be considered invariable, and the two-phase problem under study reduces to a single-phase Stefan problem for solid phase temperature, which is subject to nonlinear boundary conditions.

The problem stated takes the form

$$(1/a)\,\partial T/\partial t = \Delta T \tag{4.2}$$

for $t > 0$, $s(t) \leqslant r < \infty$,

$$P/[2\pi s^2(t)] = -\lambda\,\partial T/\partial r + L_m\gamma\,ds(t)/dt\,|_{r=s(t)} \tag{4.3}$$

$$T[s(t),\ t] = T_m \tag{4.4}$$

$$T(\infty,\ t) = T(r,\ 0) = T_0 \tag{4.5}$$

$$s(0) = 0 \tag{4.6}$$

where $T = T(r,\ t)$ is the temperature of the solid phase, a the thermal diffusivity, P the power of the heat source, λ the thermal conductivity of the solid phase, T_m the melting temperature, $s(t)$ the molten pool radius that defines the penetration depth, and T_0 the initial temperature.

The law of motion of the phase boundary. Introduce the function $U(r,\ t) = rT(r,\ t)$, for which equation (4.2) assumes the form $a^{-1}\partial U/\partial t = \partial^2 U/\partial r^2$, and the conditions (4.3)-(4.6) can be rewritten as

$$\begin{aligned} &U[s(t),\ t] = s(t)\,T_m \\ &\partial U/\partial r = T_m + \{[\gamma L_m s(t)]/\lambda\}\,ds(t)/dt - P/[2\pi\lambda s(t)]\,|_{r=s(t)} \\ &\lim_{r\to\infty} U(r,\ t)/r = T_0 \end{aligned} \tag{4.7}$$

The solution to the problem of this type was found by B. Ya. Lyubov and D. E. Temkin. Applying this solution, we get

$$\begin{aligned} T(r,\ t) = T_m - \frac{1}{r}\sum_{n=0}^{\infty} &\frac{1}{[a^n(2n+1)!]}\,\frac{\partial^n}{\partial t^n} \\ &\times\left\{[r-s(t)]^{2n+1}\left[\frac{-L_m\gamma s(t)}{\lambda}\,\frac{ds(t)}{dt} + \frac{P}{2\pi\lambda s(t)}\right]\right\} \end{aligned} \tag{4.8}$$

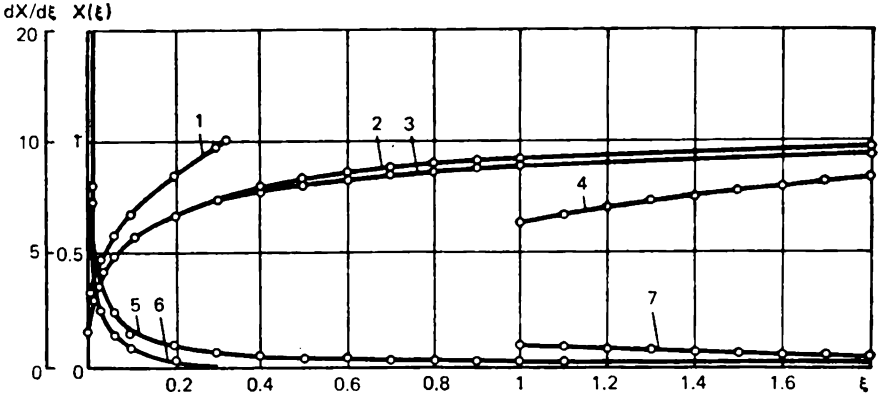

Fig. 4.1. Variations in molten pool radius $X(\xi) = s(t)\,\alpha^{-1}\beta$ and liquid-solid interface speed $dX/d\xi$ with time $\xi = t\alpha^{-2}\beta^3$

It can be shown that when $s(t) \sim t^k$, where $k < 1$, the series (4.8) converges. From (4.7) and (4.8), we obtain the equation for $s(t)$ by omitting the zero term in (4.8) and passing to the limit $r \to \infty$:

$$ds(t)/dt = \alpha/s^2(t) - \beta/s(t) \tag{4.9}$$

where $\alpha = P/2\pi L_m\gamma$, and $\beta = \lambda(T_m - T_0)/L_m\gamma$.

It is apparent from (4.9) that when $s = \alpha/\beta$, the steady state conforming to the condition $ds/dt = 0$ sets in, so that the entire power of the heat source flows to the solid phase. Hence,

$$s_m = \alpha/\beta = P/[2\pi\lambda(T_m - T_0)] \tag{4.10}$$

The function $s(t)$ has the form

$$s^2 + 2s_m s + 2s_m^2 \ln(1 - s/s_m) + 2\beta t = 0 \tag{4.11}$$

In dimensionless variables of time $\xi = \beta^3\alpha^{-2}t$ and molten pool radius $X(\xi) = s(t)\,\alpha^{-1}\beta$, expression (4.11) obtains the form

$$X^2 + 2X + 2\ln(1 - X) + 2\xi = 0 \tag{4.12}$$

Variations in the melt pool radius $X(\xi)$ and the phase boundary speed $dX/d\xi$ with time ξ are shown in Fig. 4.1. The curves *1*, *2*, *3*, and *4* identify approximations for a dimensionless melt radius of 9, 18, 17, and 19 respectively; the curves *5*, *6*, and *7* correspond to a dimensionless interface speed of 18, 9, and 19 respectively. At the start of the process, $\xi \ll 1$, $X \ll 1$, and

$$X(\xi) = (3\xi)^{1/3} - (3\xi)^{2/3}/4 \tag{4.13}$$

At the initial stage of the process, the second term in the right side of (4.13) can be omitted in view of the condition

$$L_m \gamma \, ds/dt \gg -\lambda \, \partial T/\partial r|_{r=s(t)} \tag{4.14}$$

The equalization of energy expended on the phase transition and heating of the solid phase occurs when $X = 0.5$ and $\xi \approx 0.07$. When $X(\xi) \to 1$ and $\xi > 1$, the term $\ln(1 - X)$ in (4.12) is dominant and

$$X(\xi) = 1 - \exp(-\xi) \tag{4.15}$$

As is clear from (4.15), $X(\xi)$ asymptotically tends to the steady state after a characteristic time α^2/β^3. The time required to reach the equilibrium (steady) state is

$$t_e = 4\alpha^2/\beta^3 = P^2 L_m \gamma/[\pi^2 \lambda^3 (T_m - T_0)^3] \tag{4.16}$$

Table 4.1 lists the calculated results of the maximum melt radius s_m and time t_e it takes to reach the equilibrium state at $P = 100$ W. The reflectivity at a 0.69-μm wavelength for W, Mo, and steel is 0.6 and for Al, Cu, and Ni is 0.8, 0.85, and 0.7 respectively. The experimental results are corrected to 100 W of power of the heat source.

TABLE 4.1. **Maximum Molten Pool Radius s_m and Time t_e Required to Reach the Equilibrium State**

Metal	t_e, ms	s_m, μm
Al	$10^{-2}/2 \times 10^{-4}$	21/28
Cu	$7 \times 10^{-4}/7 \times 10^{-5}$	6/4.3
Mo	$7 \times 10^{-3}/2 \times 10^{-3}$	15/8
W	$7 \times 10^{-3}/2 \times 10^{-2}$	14/-
Ni	$0.1/4 \times 10^{-2}$	42/16
Steel	40/10	410/250

Note. Theoretical data are given in the numerator, and experimental data in the denominator.

As seen from Table 4.1, the predicted values of s_m only qualitatively agree with experimental results.

The calculation of the profile of a fusion zone on the surface of a sample heated by a moving heat source has been made by A. A. Uglov and D. I. Cherednichenko [3]. For practical applications, it is of importance to obtain an insight into the process of melting of the surface heated by a linear moving heat source. Of highest interest is a quasistationary problem involved in the formation of the liquid phase by a linear heat source in the form of strip moving on the surface of a semi-infinite solid at a constant speed v. Assume a heat source of width l moves on the target surface as illustrated in Fig. 4.2, where coordinates x' and y' define the profile of the fusion zone.

The analytic solution to the problem can be found only if we idealize somewhat the process of heating. The motion of the heat source at a large velocity leads to an anisotropic heat transfer. Designating the regions of propagation of the melting wave into

the sample along the y' axis and in the direction of travel of the heat source as $\varkappa_i$ ($i = 1, 2$), where $i = 1$ relates to the x coordinate and $i = 2$ to the y coordinate, it can be shown that $\varkappa_2/\varkappa_1 = \mathrm{Pe}^{1/2}$, where $\mathrm{Pe} = vl/a$ is the Peklet number.

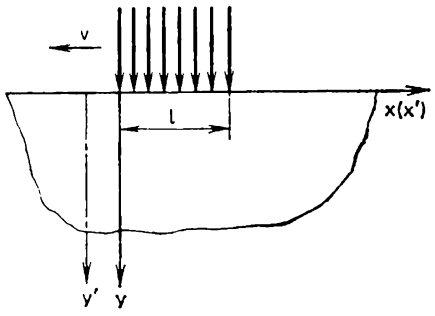

Fig. 4.2. Model for calculation of the melting process

For $\mathrm{Pe} > 1$, heating can be considered unidimensional, which corresponds to the case of a fast-moving heat source. Let us introduce new moving coordinates x and y and shift the point of reference on the y axis by $\varkappa_1$. Next, consider an imaginary heat source of width l shifted by the same value $\varkappa_1$ relative to the actual heat source.

Divide the process into three stages: the initial stage at which the material is brought to the melting point; the stage of formation of the liquid phase; and the stage of melt solidification. At the initial stage, the formulation of the problem for the temperature field is given as

$$a^{-1}v\partial T/\partial x = \partial^2 T/\partial y^2 \tag{4.17}$$

$$-\lambda\,\partial T/\partial y = q|_{y=0} \tag{4.18}$$

$$T = T_0|_{x,\,y\to\infty} \tag{4.19}$$

Assuming that the temperature field displays self-similarity, apply a new variable

$$\xi = (y/2)\,(v/ax)^{1/2} \tag{4.20}$$

Setting $d\theta/d\xi = y$ and $\theta(\xi) = T - T_0$ gives the solution in the form [3]

$$\theta(\xi) = (\alpha/\beta)\,\theta_m X^{1/2}\,\mathrm{erfc}\,\xi \tag{4.21}$$

where $\alpha = (q/L_m\gamma)\,(l/av)^{1/2}$, $\beta = \theta_m\lambda/L_m\gamma a\pi^{1/2}$, $\theta_m = T_m - T_0$, and $X = x/l$.

Knowing the temperature distribution at $\theta = \theta_m$ and $\xi = 0$, we can find the coordinate line of the onset of melting,

$$X_i = (\beta/\alpha)^2 \tag{4.22}$$

and a minimum value of the parameter α/β at which the surface begins to melt at the back edge of the heat source, $X_i = 1$. From (4.21) it follows that $\theta = \theta_m$ when $x = l$ and $y = 0$ if the condition

$\alpha/\beta = 1$ is valid. Hence, the minimum power density q_n is found to be

$$q_n = \theta_m \lambda (v/\pi a l)^{1/2} \tag{4.23}$$

The material obviously begins to melt when the power delivered per unit time by the heat source exceeds the power expended on heating the solid phase.

Consider the case where the heat power density is insufficient to initiate intensive vaporization. For this case, the inequality stated below must hold:

$$q_n \ll L_v \gamma (av/l)^{1/2} \tag{4.24}$$

where L_v is the specific heat of vaporization.

At all points of the region $x_1 \geqslant (x - l)$ there exists a two-phase zone formed by the melt and solid phase. Based on the process of self-similarity, the temperature field in this zone will be defined by the set of equations

$$\begin{aligned} &d^2\theta_1/d\xi^2 + 2\xi a a_1^{-1}\, d\theta_1/d\xi = 0 \\ &d^2\theta/d\xi^2 + 2\xi\, d\theta/d\xi = 0 \end{aligned} \tag{4.25}$$

where the subscript '1' relates to the liquid phase.

The boundary condition at the target surface ($\xi = 0$) is given by

$$-\lambda_1\, d\theta_1/d\xi = 2q\,(ax_1/v)^{1/2} \tag{4.26}$$

Other boundary conditions for the problem (4.25) are written as

$$\theta_1 = \theta = \theta_m, \quad \xi = \xi_s \tag{4.27}$$

$$\theta = 0, \quad \xi \to \infty \tag{4.28}$$

where the subscript 's' at ξ denotes the penetration depth s.

The set of equations (4.25) is related to the heat balance equation for the interface, which has the form

$$\begin{aligned} &2q\,(ax_n/v)^{1/2} + \lambda\, d\theta/d\xi - \lambda_1\, d\theta_1/d\xi = 2L_m \gamma a \xi, \\ &\xi = \xi_s \geqslant 0 \end{aligned} \tag{4.29}$$

The dimensionless parameter ξ_s is unknown. It is found from the solution of the set of equations (4.25)-(4.29) and relates to the penetration depth s by the expression

$$s = 2\xi_s\,(ax/v)^{1/2} \tag{4.30}$$

Solving equations (4.25) with boundary conditions (4.26)-(4.28), we derive the expression for the melt temperature

$$\begin{aligned} &\theta_1/\theta_m = 1 + (\alpha/\beta)\,(a_1/aX_1)^{1/2}\,(\lambda/\lambda_1) \\ &\times \{\operatorname{erf}[(a/a_1)^{1/2}\xi_s] - \operatorname{erf}[a/a_1)^{1/2}\xi]\} \end{aligned} \tag{4.31}$$

and that for the solid phase temperature

$$\theta/\theta_m = \operatorname{erfc} \xi/\operatorname{erfc} \xi_s \tag{4.32}$$

Substituting expressions (4.31) and (4.32) into heat balance equation (4.29) yields a transcendental equation in ξ_s:

$$\{(\alpha/\beta)[X_n^{1/2} + X_1^{1/2} \exp(-a\xi_s^2/a_1)] - \xi_s/\beta\} \operatorname{erfc} \xi_s \exp \xi_s^2 = 1 \tag{4.33}$$

Solving this equation, we can determine the parameter ξ_s and then the penetration depth s (x). Also, at the fixed values of s and with the parameter ξ_s determined from (4.30), we can estimate the value of α/β at which the specified penetration depth is attainable:

$$\alpha/\beta = \{[\exp(-\xi_s^2)/\operatorname{erfc} \xi_s + \xi_s/\beta - 1]^2 \exp(2a\xi_s^2/a_1) + 1\}^{1/2} \tag{4.34}$$

Let us use equations (4.25)-(4.34) to describe the process of melt solidification on the assumption that at $x \geqslant -l$ the wave of fluid of thickness s_0 runs onto the solid substrate at a constant velocity v. In this region, we assume the depth of the melt solidification front to be

$$s = s_0 - 2\xi_s (ax/v)^{1/2} \tag{4.35}$$

where the second term in the right side of the equation specifies the thickness of the solidified layer.

The solution is sought in the same manner as that outlined above, with the difference that we apply equation (4.31) to define the parameter ξ_s providing the heat power over the entire region $x \geqslant l$ is zero and the interface changes the direction of its travel:

$$\beta = \xi_s \operatorname{erfc} \xi_s \exp \xi_s^2 \tag{4.36}$$

Since $\lim \beta = 1/\sqrt{\pi}$, then for all the cases where $\beta \geqslant 1$ ($L_m \gamma a \leqslant \theta_m \lambda$), the solidified melt thickness is independent of the shape of the fusion front and is proportional to β:

$$s = s_0 - 2\beta (\pi a x/v)^{1/2} \tag{4.37}$$

Letting $s = 0$, estimate the length of a liquid tail behind the moving heat source:

$$x_m = (v/4a)(s_0/\xi_s)^2 \tag{4.38}$$

Examples of the calculation of fusion zone profiles are shown in Figs. 4.3 and 4.4. The plots for the fusion fronts relate to an actual heat source:

$$X_m' = (\beta/\alpha)^2 - \varkappa_1'$$

Passing to dimension coordinates, we obtain

$$x_n = \varkappa_1' \left[\frac{1}{\pi} \left(\frac{\theta_m \lambda v}{aq}\right)^2 - 1\right] \tag{4.39}$$

where $\varkappa_1' = \varkappa_1/l$.

At low heat source speeds and high power densities q, i.e. when the condition $(\beta/\alpha)^2 < \varkappa_1'$ is met, melting begins ahead of the heat source ($x_m < 0$). This shows up most vividly in materials with a high thermal conductivity. As follows from relation (4.33), with an increase in the melt depth, the amount of heat supplied to the fusion front decreases, so the front propagates at a lower rate. In turn, this causes an overheating of the molten surface layers and

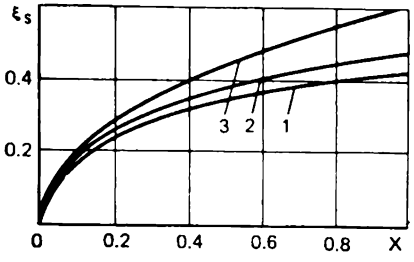

Fig. 4.3. Parameter ξ_s ($\alpha/\beta = 2$) versus X: *1*, $a/a_1 = 2$; *2*, $a/a_1 = 1$; *3*, $a/a_1 = 0$

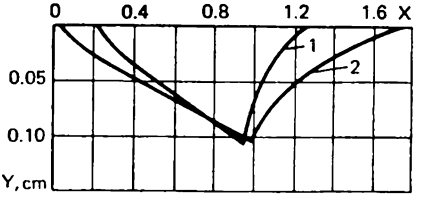

Fig. 4.4. Plots illustrative of the fusion front profiles calculated for silicon: *1*, $v = 5$ cm s^{-1}; *2*, $v = 15$ cm s^{-1}; $l = 0.5$ cm

promotes intensive convective flows in the melt. As obvious from Fig. 4.4, both ξ_s and penetration depth grow with their thermal diffusivity a.

Estimate the intensity of melt motion using the Grashof number

$$\mathrm{Gr} = g\beta_1 \Delta\theta_m l_0^3/\nu^3 \qquad (4.40)$$

where g is the acceleration due to gravity, β_1 the coefficient of volumetric expansion, $\Delta\theta_m$ the temperature difference that can be found from (4.31), l_0 the characteristic length, and ν the kinematic viscosity. The estimates obtained at the typical values of parameters, low values of overheating and comparatively small penetration depths ($\Delta\theta_m \leqslant 50$ K, $l_0 \geqslant 5 \times 10^{-4}$ m) show that $\mathrm{Gr} \gg 1$, i.e. convective mixing of the field is evident.

Under these conditions the temperature in the interaction region approaches the melting point throughout its volume, therewith intensifying the heat transfer to the liquid-solid interface ($a_1 \to \infty$). As a result, the rate of melting rises rapidly and the melt depth tends to the limit at the given heat power density (see Fig. 4.3, curve *3*). In this case, equation (4.33) assumes the form

$$[(\alpha/\beta)(X_n^{1/2} + X_1^{1/2}) - \xi_s/\beta]\,\mathrm{erfc}\,\xi_s \exp \xi_s^2 = 1 \qquad (4.41)$$

From the known dimensions of the molten pool and the speed of the heat source, we can estimate the time it takes the melt to

solidify completely

$$\tau_k = 4a\xi_s^2/s_0 \tag{4.42}$$

and the speed of the phase boundary

$$v_k = (1/4a)\,(s_0/\xi_s)^2 \tag{4.43}$$

So, for each material the melting depth exerts a dominant effect on the speed of travel of the liquid interface and the time of solidification.

4.2. DEFORMATION OF THE MELT SURFACE UNDER REACTIVE PRESSURE

In this section, we shall calculate the deformation of a free melt surface under the reactive vapor pressure in the steady-state conditions of metal melting on the assumption that the heat evolution throughout the volume of the melt can be neglected. In the general case, the problem for calculating the liquid phase deformation under an external local pressure should be solved using the set of Navier-Stokes equations. Because the search for the solution of these equations is an intricate procedure, we first restrict our analysis to the case of the steady process in which v is constant. Denote a deformed surface profile by $Z(r)$. The equation for $Z(r)$ can then be written as

$$Z''/(4+Z'^2)^{3/2} + Z'/[r\,(1+Z'^2)^{1/2}] - Z/a^2 = p\,(r)/\sigma \tag{4.44}$$

where $a^2 = 2\sigma/\gamma g$ is a capillary constant, and $p(r)$ the function describing the external pressure distribution over the melt surface. If the surface deformation is low ($Z' \ll 1$), the equation simplifies to

$$Z'' - Z/a^2 = p\,(r)/\sigma \tag{4.45}$$

where σ is the surface tension coefficient.

Equations (4.44) and (4.45) do not cover the temperature dependence of the coefficients they contain. With this temperature dependence being allowed for, the solution to the equations can only be sought by resorting to numerical methods. Consideration then should be given to the fact that the transition from extremely low to high deformations can occur abruptly in real conditions. This is because the surface tension force grows with fluid deformation, although its growth ceases when the maximum depth of depression becomes equal to the radius of the deformation zone. As the depth of cavity goes on growing, the radius of curvature remains invariable, but the hydrostatic pressure rises.

Let us take a look at analytic solutions to the problem of melt deformation for limiting cases that obey equation (4.44).

Low surface deformation ($Z'^2 \ll 1$). Solve equation (4.44) in the form

$$Z'' + Z'/r - Z/a^2 = p\,(r,\ Z)/\sigma \tag{4.46}$$

If the surface forces causing the melt deformation stem from the reactive pressure due to vapors formed during material evaporation, then in the general case,

$$p\,(r,\ Z) = A\,(r,\ Z)/[T^{1/2}\,(r,\ Z)]\exp[-B/T\,(r,\ Z)] \tag{4.47}$$

where $A\,(r,\ Z)$ is the function accounting for the material properties and surface deformation.

At low values of depression, the effect of variations in the temperature $T\,(r,\ Z)$ with Z at the deformed surface of fluid can be left out of consideration.

Estimate the maximum deformation of the melt surface against the pressure and material parameters. Write the solution of equation (4.46) in the form

$$Z\,(r) = -p/\gamma g + C_1\,[1 + (r/2a)^2 + 1/4\,(r/2a)^4 + \ldots] \tag{4.48}$$

where C_1 is a constant determined from the boundary condition. At $r < 2a$ (for representative metals, a is about 0.5 cm), we may set $1/4\,(r/2a)^4 \ll 1$ and limit ourselves to two terms of the series (4.48). Then,

$$Z\,(r) = -h + [(p/\gamma g) - h]\,(r/2a)^2 \tag{4.49}$$

and the maximum deformation is

$$h = (p/\gamma g)\,\mu^2/(1 + \mu^2) \tag{4.50}$$

where $\mu = \delta/2a$ (δ is the radius of the zone where pressure is different from zero). For the case where $p = 10^2$ Pa, $\gamma = 10^4$ kg/m^3, and $\mu = 0.5$, the numerical estimations give $h = 0.2$ mm.

Consider a specific case of approximation of the function $p\,(r)$. Assume that

$$p = p_0\,(1 - r^2/\delta^2)\exp(-kr^2) \tag{4.51}$$

where p_0 is the maximum pressure, and k the concentration coefficient. In this case, we disregard the dependence of p on Z.

To approximate the pressure by (4.51) we can solve equation (4.46) exactly

$$Z\,(r) = -p_0\exp(-kr^2)/[4\gamma g\,(a\delta k)^2] \tag{4.52}$$

on condition that $r < \delta$ and

$$k = (1/2\delta^2)\,(1 - \sqrt{1 - (\delta/a)^2}) \tag{4.53}$$

From (4.53) we conclude that at $\delta > a$ the steady-state solution does not exist because k becomes a complex quantity. Physically,

this means that at a large radius of the deformation zone the capillary effects prove insignificant. When $\delta = a$, the melt surface depression is $Z = -p_0/\gamma g$.

Large surface deformation, $Z'^2 \gg 1$. In this case, from equation (4.44) we obtain

$$Z = -a^2 [p(r, Z)/\sigma - 1/r] \tag{4.54}$$

Equation (4.54) implicitly defines the shape of the melt surface as a function of r. This equation determines the maximum deformation accurate to a value in the order of $1/Z'^2$ and can be used to estimate the depth of melting. The relation for determining the limiting depth h of the cavity (when $r = \delta$) can be written as

$$a^2 p(h, \delta) + h - a^2/\delta = 0 \tag{4.55}$$

To determine the cavity depth h from equation (4.55), we must explicitly define the function $p(h, \delta)$, i.e. know the mechanism of LR or EB energy scattering as the CEF propagates through the layer of the vaporized material in the cavity. Since $p(h, \delta)$ is a decreasing function relative to h, the solution of equation (4.55) is unique.

Let us have a look at some computer-aided solutions to the problems of melt surface deformation [4]. For Gaussian heat sources, the reactive pressure distribution over the material surface, $p_s(r)$, can, to a certain approximation, be defined by the normal distribution law:

$$p_s = p_0 \exp(-k_g r^2) \tag{4.56}$$

where p_0 is the maximum pressure dependent on the maximum temperature of the molten pool, and k_g the parameter used to account for the degree of decay of the pressure from the center to the periphery of the fusion zone.

The relation between the parameters of the heat source that produces the molten pool on the target surface is rather complex in the general case. To a certain approximation, this relation can be written as

$$k_g = (T^*/A)^n k \tag{4.57}$$

where T^* is the temperature of activation of the vaporization process, A and n are constants, and k is the concentration coefficient.

Equation (4.44) with its right side in the form of (4.56) was numerically solved on a computer. The boundary conditions specified for the problem were

$$Z'(0) = 0, \quad Z(r = l) = 0 \tag{4.58}$$

where l is a certain effective distance from the axis of symmetry, assumed to be equal to $1.5a$.

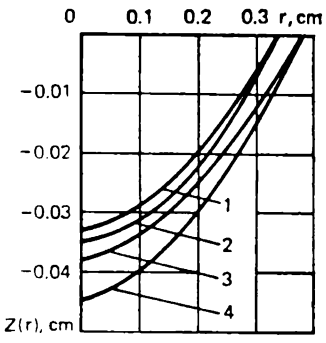

Fig. 4.5. Theoretical curves for hole profiles in liquid phase: $\sigma = 0.5$ N/m; $q = 10^3$ W/cm^2; *1*, $\gamma = 10$ g/cm^3; $k_g = 10$ cm^{-2}; *2*, $\gamma = 10$ g/cm^3, $k_g = 5$ cm^{-2}; *3*, $\gamma = 8$ g/cm^3, $k_g = 10$ cm^{-2}; *4*, $\gamma = 8$ g/cm^3, $k_g = 5$ cm^{-2}

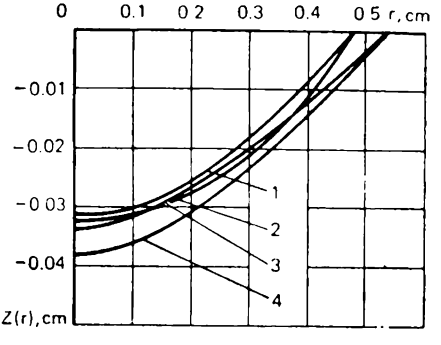

Fig. 4.6. Theoretical curves for hole profiles in liquid phase: $\sigma = 1$ N/m; $q = 10^3$ W/cm^2; *1*, $\gamma = 10$ g/cm^3, $k_g = 10$ cm^{-2}; *2*, $\gamma = 10$ g/cm^2, $k_g = 5$ cm^{-2}; *3*, $\gamma = 8$ g/cm^3, $k_g = 10$ cm^{-2}; *4*, $\gamma = 8$ g/cm^3, $k_g = 5$ cm^{-2}

The second boundary condition in (4.58) is arbitrary to a certain extent since the coordinate of the point of intersection of the function $Z(r)$ with the radius r must be found from an additional condition. The law of conservation of mass obviously represents this condition which involves an approximation of a small compressibility of the liquid and an insignificant loss of the substance during vaporization that gives rise to surface pressure. The profile of a hole near the OZ axis is of particular interest.

The solution to equation (4.44) with boundary conditions (4.58) was sought on a computer by reducing input equation (4.44) to the set of equations

$$Z' = dZ/dr = dy_1/dr = y_2 \tag{4.59}$$

$$Z'' = dZ'/dr = dy_2/dr = (1 + y_2^2) \times [(\sqrt{1 + y_2^2}/\sigma)(p_0 \exp(-k_g r^2) + \gamma g y_1) - y_2/r] \tag{4.60}$$

with boundary conditions

$$y_1 (r = l) = 0, \quad y_2 (r = 0) = 0 \tag{4.61}$$

The set of equations (4.59)-(4.61) was reduced to the Cauchy problem and solved by the trial-and-error method with interpolation. The results presented in our earlier works were used as a first approximation to the boundary condition $y_1 = Z(r)$ at $r = 0$.

Figures 4.5 and 4.6 display the results of hole profile calculations proceeding from a number of parameters specific to CEF metal-

working. The computer-aided solutions based on the parameters typical of the limiting cases are consistent with the results cited in our earlier works.

The curves of Figs. 4.5 and 4.6, which correspond to a weakly developed vaporization at laser power densities q in the range of 10^2-10^3 W/cm^2 and maximum pressures p_0 of 10^2 Pa, illustrate the effect of material density γ on the profile and size of the molten pool. As γ grows, the liquid phase depression decreases. For the case of weakly developed vaporization, Z' is smaller than or equal to 0.2 cm, as follows from calculations, and so $Z'^2 \ll 1$. The calculated results for the given case are close to the estimates presented in our earlier works which dealt with the problem solvable analytically.

V. N. Rodygin calculated the shape of a fusion zone for other relations between the parameters and plotted the profile of the molten pool typical of EB-induced deep-penetration melting. M. I. Tribelskiy [6] more clearly defined the form of function p (r) by working simultaneously the problems of hydrostatics (4.44) and kinetics of evaporation.

Paper [6] examined the process of steady-state heating of a semi-infinite solid by a stationary surface heat source, such as a laser source with the Gaussian distribution of power density q. The solution of the problem rather weakly depends on the kind of distribution of q over the target surface. The basic estimates, accurate to a numerical factor in the order of unity, can be obtained by a dimensional method based on the assumption that there exists a representative value of q (r) which sharply diminishes as r exceeds a certain representative value of $r_0 = k^{-1/2}$.

For simplicity of analysis, we make the following assumptions: vaporization occurs in a vacuum; power density is fairly low, so that the process of heat transfer plays the main part in forming the temperature field; the heat loss by evaporation is negligible; and the radius of curvature of the free melt surface is everywhere much in excess of the characteristic distance within which the reactive pressure changes.

Given the temperature profile T (r, 0) on the target surface, it is possible to evaluate the reactive vapor pressure in a sample. We neglect the reverse flow of atoms returning to the surface as the result of collisions in the gaseous phase, i.e. assume that near the melt surface the distribution of vapor particle velocities within a solid angle 2π ($v_z < 0$) is Maxwellian. In this case, the reactive pressure is

$$p\ (T) = kTn_0\ (T)/2 \tag{4.62}$$

where n_0 (T) is the saturated vapor density at T. Taking into account the deviation of the distribution function from the Maxwell velocity

distribution function leads to the replacement of the factor 1/2 in (4.62) by the factor 0.54 [7], but then the analysis falls beyond the limits of the adopted accuracy.

We can use an Einstein model for a condensed medium to describe the function $n_0(T)$:

$$n_0(T) = (2\pi m\nu_0^2/kT)^{3/2} \times \exp[-(L_v/kT) - 1] \tag{4.63}$$

where m is the atomic mass, L_v the specific heat of vaporization, and ν_0 the Einstein vibrational frequency.

Formula (4.63) adequately defines the process of vaporization if the inequality $kT \ll L_v$ holds, which is the case for the conditions under consideration [6].

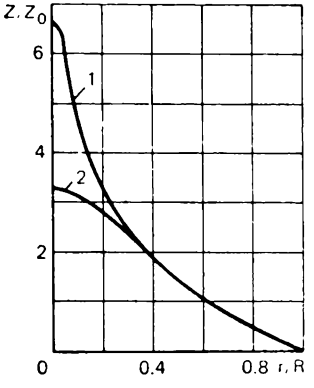

Fig. 4.7. Curves illustrative of the profiles of the free surface of melt at $\beta = R/r_r = 19.6$ (curve *1*) and $\beta = 3.8$ (curve *2*)

The profile of the free surface of melt is deducible from equation (4.45) since according to the conditions of the problem, the surface deformation is small. The pressure here is a function of temperature, $p[T(r)]$, and defined from formulas (4.62) and (4.63). The solution of equation (4.45), which is finite at $r \neq 0$, has the form [6]

$$Z(r) = [K_0(ar)/\sigma] \int_0^r I_0(ar)\, p(r)\, dr + [I_0(ar)/\sigma] \int_r^\infty K_0(ar)\, p(r)\, r\, dr \tag{4.64}$$

where $I_0(x)$ and $K_0(x)$ are the Bessel functions of the imaginary argument.

The characteristic distance over which the reactive pressure of vapors varies is $r_p = r_0 (2kT_s/L_v)^{1/2} < r_0$. Typically, r_0 is equal to about 0.1 cm, whereas $a \approx 1$ cm. In our case, therefore, the function $p[T(r)]$ varies faster than $K_0(ar)$ and $I_0(ar)$. Then, from (4.64) at $ar \ll 1$ we obtain

$$Z(x) = Z_0 [Ei(-x)^2 - 2C - 2\ln(ar_p x/2)] \tag{4.65}$$

where

$$Z_0 = (r_0^2/4\sigma)(\sqrt{kT_s}/L_v)(2\pi m\nu_0^2)^{3/2} \exp[-(L_v/kT_s) - 1]$$

$Ei(-x^2)$ is the exponential integral function; $x = r/r_p$, and $C = 0.577$ is the Euler constant.

At $ar \gg 1$, the function $Z(x)$ exponentially tends to zero. At large distances from the center line of LR, the target temperature drops below T_m and expression (4.64) no longer works.

In Fig. 4.7 are shown the curves of Z/Z_0 against r/R, where R is the radius of the melt boundary $T(R, 0) = T_m$ at various values of the parameter

$$\beta = R/r_p \approx Aq_0r_0L_v/4\sqrt{\pi}\lambda T_m^2 \tag{4.66}$$

It is seen from Fig. 4.7 that even within the confines of perturbation theory, the deformation of the free surface of melt sharply grows near the axis with an increase in the laser power density.

4.3. KEYHOLING

The process of formation of a narrow and deep vapor-gas hole or cavity in the melt by a laser or an electron beam with a power density in excess of the critical value is an interesting physical phenomenon. For practical purposes, the study of this phenomenon is of importance because the knowledge gained enables us to predict certain characteristics and behavior of metal melting: the chemical composition of a weld seam, particularly in welding dissimilar metals, which depends on the intensity of mixing of molten metals; formation of voids in the weldment and uneven penetration depth along the length of the seam; and efficiency of the heating process, which depends on the hole geometry, i.e. cylindrical, tapering, and other profiles of the hole.

Let us examine the process of keyholing based on the experiments carried out on industrial EB setups. That the cavity indeed appears in the melt in the course of the CEF interaction with a material was borne out by direct experiments. In the process of laser welding of aluminum to steel without full penetration through the sheets, the specimen was struck by a pulsating flux of X-ray radiation at a voltage of about 600 kV in order to record the pattern of melting on photographic film. The experiments have confirmed that penetration to a large depth occurs owing to the formation of a hole in the target, which periodically closes as the molten metal flows back into it (Fig. 4.8). The closure of the cavity begins mainly in its upper portion. The rate at which the cavity closes and then opens depends on the time of LR penetration to a specified depth, i.e. on the power density. For corrosion-resistant steel, this repetition rate of cavity sealing is $f = 10$ Hz at $q = 1.7$ to 2.0×10^5 W/cm^2 and for aluminum, it is $f = 7$-12 Hz at $q = 1.7 \times 10^5$ W/cm^2.

The periodic cavity sealing in corrosion-resistant steel heated by a stationary electron beam was also revealed with the aid of

a high-speed framing camera recording at 2 500 frames per second. The parameters of the EB were: $V = 125$ kV, $I = 8\text{-}12$ mA, $q \approx (5\text{-}7) \times 10^6$ W/cm^2, and $t = 23\text{-}45$ s.

A number of researchers modeled the keyholing process and made attempts to describe an actual hole in liquid metal with similarity parameters.

H. Schwarz has established that an air jet issued from a glass nozzle 0.254 mm in diameter and played on the surface of a mercury

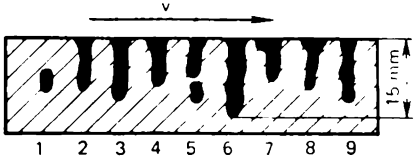

Fig. 4.8. X-ray photorecording of hole profiles in corrosion-resistant steel: $V = 25$ kV; $I = 250$ mA; $v = 2.5$ cm/s; melt depth, 15 mm; $q = 1.5 \times 10^5$ W/cm^2

pool at a pressure close to 4.2 MPa can produce a crater 6.2 mm deep and about 1.6 mm in diameter in the pool. The hydrostatic pressure of the mercury column then reaches 10^3 Pa. Other researchers modeled the process of keyholing in transparent fluids such as water, glycerine, and vaseline oil under the action of a moving air jet forced to oscillate in a sinusoidal manner. It is found that at large linear velocities of the jet played on the fluid surface, the lower portion of the cavity can periodically bend in the direction opposite to that of jet travel. The cavity bends more heavily with an increase in the speed of travel of the jet. There is a critical velocity at which the lower portion of the hole both in transparent fluids and in molten metals begins to vibrate. For aluminum, the critical speed of travel of a keyhole exceeds 1.1 cm/s. The experiments on keyhole modeling suggest that the periodic breakaway of the lower portion of the hole can be responsible for a specific defect of melting, namely, a variation in the weld depth along the length of the bead at large weld rates.

Experimental work was done to disclose the interaction of EB with vacuum-treated oil. The experiments were run on an electron beam setup operated both continuously and pulsed. The characteristic parameters were: $q = 0.6$ to 2.0×10^8 W/cm^2, $V = 50\text{-}100$ kV, $I = 6$ mA, $\tau = 800$ μs, and $f = 20\text{-}250$ Hz. High-speed photography has revealed that a continuous electron beam incident on oil forms a narrow cavity displaying a glow pattern typical of a high-density gas discharge. During the interaction of four successive pulses with a frequency of 250 Hz, the cavity closes in depth at four points. The dwell time t_d for the keyhole is much longer than the

pulse duration τ. At $\tau = 800$ μs, the dwell time t_d is 28 ms, i.e. a factor of a few tens longer than the pulse duration. The time it takes the cavity to close is of the same order as that of the pulse length and reaches units of milliseconds. Ejection of oil from the cavity occurs only during cavity sealing. The keyholing rate that approaches 10^2 m/s at the initial stage sharply drops off with increasing depth, as revealed by high-speed photorecording, and then saturates at about 10 m/s. The rate of ejection of vapors from the cavity reaches about 10^3 m/s and the force acting on the bottom of the cavity produced by the beam with $V = 100$ kV and $d = 100$ μm comes to p^* 0.1 N, which corresponds to the pressure $4p^*/\pi d^2 \approx$ 0.1 MPa.

The authors of work [8] performed similar experiments on the interaction of EB with vacuum-treated oil which was chosen because of its transparence and low vapor pressure at high temperatures. The experiments were made using an electron beam setup at an accelerating voltage of 6-8 kV and beam current of 0.5-5 mA. Higher accelerating voltages caused frequent breakdowns in the electron gun. Oil was left to stand for a few days in a vacuum chamber to degas the oil more completely. The EB-oil interaction zone and the cavity formed were recorded with a high-speed cine camera. The experiments have revealed a number of mechanisms of the electron beam interaction. There are two kinds of cavities, a geometrically stable and a pulsating cavity. For the first kind there correspond lower power densities and smaller aspect ratios (the ratio of depth to diameter). The stable cavity converts to a pulsating one at a certain focusing current which causes the aspect ratio to vary sharply, accompanied by an appreciable variation in the penetration depth. A continuous electron beam of a certain power density initiates bubbles in the oil after a definite time of interaction, which grow fast and float up to the surface where they collapse almost at once and give off splashes or form a spherical cover at the point of entry of the beam. At a longer time of interaction, bubbles can float up one after another. As the electron beam moves over the surface, the most intensive glow occurs at the leading edge and bottom of the hole, which attests to the nonuniformity of physical parameters in the interaction region. The moving electron beam produces a zone similar to that formed in metal welding without through penetration, i.e. the zone whose root of penetration displays a serrate profile. It is possible to obtain a relatively uniform root if the power density of the beam scanned over the surface is such that it ensures a stable shape of the cavity.

The experiments reported in paper [9] were made to investigate the mechanism of interaction of a CW CO_2 laser beam with glycerine. At $q \approx 10^5$ W/cm^2 and a radius of the interaction region of about 0.4 mm, the laser beam, just like the electron beam, was found to produce a cavity in the target.

The results of experiments performed by a number of researchers disclose that the picture of both the formation and behavior of the keyhole in a liquid metal is rather complex. The cavity formed by a stationary electron beam pulsates and periodically closes in its upper portion. The phenomena occurring in the cavity produced by a moving electron beam are still more complex. In the cavity region the molten metal undergoes intensive mixing due to its turbulent motion.

To get a better insight into the processes of formation of cavities in melts, it is necessary to consider a number of problems associated with the hydrodynamic phenomena in the interaction zones.

Critical power density for deep penetration. One of the possible approaches to determining the critical power density of a laser or an electron beam required to provide a deep penetration is to compare the rate of motion shown on the vaporization isotherm with the rate of motion on a certain isotherm of heating at the end of the pulse of duration τ. Equating these rates, we can obtain

$$q_c = A^{-1}\gamma L_v \sqrt{a/\tau} \tag{4.67}$$

where A is the absorptivity of a material, γ the material density, L_v the specific heat of vaporization, and a the thermal diffusivity.

The results calculated by (4.67) correlate with experimental data [10].

M. I. Tribelskiy [6], however, compared the integral heat fluxes removed by heat conduction and expended on the vaporization of matter from the target surface. Let us take a closer look at this approach.

The heat flux extracted by way of heat conduction under steady-state conditions can be found from the relation for the temperature field in a semi-infinite solid:

$$J_T = 2\sqrt{\pi}\,\lambda r_0 T_s = 6\sqrt{\pi}\,n r_0 a \lambda T_s \tag{4.68}$$

where $n = \gamma/m$ is the number of particles in a unit volume of the condensed phase.

The density of the flow of vaporized particles, assuming their distribution to be Maxwellian, is $n_0(T)\sqrt{kT(2\pi m)^{-1}}$, where k is Boltzmann's constant. In this problem both the radius r_r at which the reactive pressure changes and surface temperature T_s are characteristic quantities. So, disregarding the kinetic vapor energy since it is small as against L_v, $kT_s \ll L_v$, the heat flux expended on vaporization can be written as

$$\begin{aligned} J_v &\approx \pi r_r^2 L_v n_0(T_s)\sqrt{kT_s}/\sqrt{2\pi m} \\ &= 4\pi^2 L_v m v_0^3 r_0^2 \exp\left[-(L_v/kT_s) - 1\right] \end{aligned} \tag{4.69}$$

Comparing (4.68) with (4.69) allows us to conclude that $J_v \ll J_T$ at low values of T_s, i.e. at low laser power densities. At large values of T_s, the opposite is true. At $T_s = T_s^*$, both of the heat fluxes are equal, but even an insignificant deviation of T_s from T_s^* results in a large inequality of the fluxes because J_v strongly depends on T_s. It is natural to suggest that when $T = T_s^*$, intensive vaporization sets in a step-like manner at the threshold value of the laser power density. The threshold power density q^* can be found by equating (4.68) and (4.69). The result is a transcendental equation in q^*, the iterative solution of which is given in paper [6]:

$$q^* \approx [2L_v\lambda/(Akr_0\sqrt{\pi})]\,[\ln mv_0^3 r_0/L_v na + \ln\ln mv_0^3 r_0/L_v na + \ldots]^{-1} \tag{4.70}$$

It should be noted that q^* has no relation to the onset of crater formation.

The second representative value of the power density, $\tilde{q}$, can be found proceeding from the condition of triviality of Z_0 against r_r, i.e. smallness of the curvature of the free surface of melt:

$$\tilde{q} = (2L_v\lambda/Akr_0\sqrt{\pi})\,[\ln (m^{3/2}v_0^3 r_0/\sigma L_v^{1/2})]^{-1} \tag{4.71}$$

Comparing (4.70) and (4.71), one can disclose that the regime of deep penetration is realizable if the inequality given below is valid:

$$[\sigma/(n\lambda\sqrt{L_v m})\exp(na\sqrt{L_v m}/\sigma) > mv_0^3 r_0/L_v na \tag{4.72}$$

Otherwise, spherical melting will instantly give way to intensive evaporation with an increase in the power density.

The characteristics of the surface heat source in (4.72) are expressed in terms of r_0. Since the left side of (4.72) heavily depends on the problem parameters, a change in r_0 weakly affects the inequality (4.72). In a physical sense this means that the feasibility of deep penetration largely depends on the properties of the material in question rather than on the characteristics of the heat source.

A finite size of the heat source plays a substantial part in performing the analysis. Therefore, a unidimensional treatment of the phenomenon in the framework of the given statement is in principle impossible. A list of the calculated values of laser power densities q^* and $\tilde{q}$ and experimental values of $\tilde{q}$ [11, 12] for some metals appears in Table 4.2.

The values of A given in the table were estimated indirectly. In experiments conducted on a copper target the maximum spot radius was $r_0 = 0.4$ mm; in all other cases, $r_0 = 0.19$ mm.

TABLE 4.2. **Absorptivity A, Einstein Frequency ν_0, and Threshold Power Densities q^* and $\tilde{q}$ for Some Metals**

Metal	A	$\nu_0 \times 10^{-12}$, s	$q^* \times 10^{-6}$, W cm^{-2} (Theor.)	$\tilde{q} \times 10^{-6}$, W cm^{-2}	
				Theor.	Experiment.
Al	0.3	6.11	1.43	0.95	0.26
W	0.32	11.7	1.31	1.00	0.4
Fe	0.5	9.86	0.16	0.14	0.13
Cd	0.5	2.20	0.19	0.13	0.13
Mo	0.26	7.22	1.72	1.32	0.52
Ni	0.28	10.1	0.57	0.48	0.38
Nb	0.4	12.0	0.72	0.59	0.35
Sn	0.25	2.17	0.54	0.38	0.26
Pb	0.3	1.19	0.17	0.11	0.08
Ti	0.28	13.1	0.11	0.10	0.19
Zn	0.3	3.21	0.29	0.21	0.15
Zr	0.35	8.40	0.19	0.15	0.4
Cu	0.39	5.39	1.04	0.68	1.5

Thus, at $r_0 \approx 0.1$ mm, the typical values of $\tilde{q}$ were in the order of 10^5 W/cm^2 and 10^6 W/cm^2 for fusible and refractory metals respectively.

4.4. THERMOCAPILLARY EFFECTS IN THE LIQUID PHASE

The interaction of laser radiation with metal occurs through the free surface of the molten pool formed on the target. The analysis of vibrations of the free surface of melt is important for laser processing because the surface rippling scatters LR and can affect the heat and mass transfer processes which are essential for the formation of the structure of the surface metal layer after laser interaction.

Crystallization of the molten pool. Let us first consider changes in the rate of freezing of a small volume of melt formed under pulsed laser radiation. To a certain approximation, the problem can be considered unidimensional because the depth of the fusion zone is noticeably smaller than the fusion spot diameter when the laser pulse length τ is about 1 ms. We also assume that by the time the pulse ceases, melt overheating is low and convective flows almost completely equalize the temperature throughout the molten pool. The freezing rate for the melt can then be written as

$$v_m \approx b\,(a/t)^{1/2} \tag{4.73}$$

Here b is the constant which is the root of the equation

$$c(T_m - T_0)/(L_m\sqrt{\pi}) = b\exp(b^2) \tag{4.74}$$

where T_0 is the initial temperature of metal, and t the time after the start of the pulse.

The position of the solidification coordinate is defined by

$$Z(t) = 2b\sqrt{at} \tag{4.75}$$

The estimates determined from formulas (4.73)-(4.75) for iron ($b \approx 0.75$) show that the molten metal freezes for a time in the order of units of milliseconds.

Melt solidification entails a number of concomitant effects resulting in the melt surface deformation and appearance of liquid metal ripples moving from the center to the periphery of the fusion region. The causes of melt surface deformation are the reactive pressure due to evaporation of some fraction of the liquid phase, thermal convective flows in the melt, and other factors.

Dynamic effects initiate a pattern of circular ripple waves on the melt surface, which have no time to decay during fast freezing. The pattern of ripples is usually symmetric about the center of the heat affected zone. The pattern of ripples on the surface of solidified metal arises from the reactive pressure since the effect of rippling shows up more vividly with increasing laser power density.

Let us analyze the process of development of circular waves on the surface of metal. The size of a laser pulse-produced fusion zone and the wavelength of ripples on the surface of solidified metal are commonly small. We should thus consider not gravitational waves but capillary (ripple) waves induced by perturbation factors acting on the central area of the molten pool because the capillary constant

$$a = (2\sigma/\gamma g)^{1/2} \tag{4.76}$$

for the melts of typical metals is certainly much larger than the wavelengths of ripples observed in experiments on the surface of solidified metal ($a \approx 0.5$ cm).

First, consider the vibration of the free surface of melt after the end of the heat source pulse. Assume that the reactive pressure decays as soon as the pulse ends. For an arbitrary amplitude of the capillary wave, the problem is nonlinear in respect of both the equations and boundary conditions. If, besides, crystallization is progressing, both the size of the molten pool and physical parameters undergo changes.

Now suppose the amplitude of the wave is small as against the wavelength, which is in line with experiment. The problem then amounts to finding out the profile of the free surface of melt, $\xi(r, t)$, and melt velocity potential $\Phi(r, z, t)$. The equation for the velocity

potential is written as [13]

$$\Delta\Phi(r, z, t) = 0 \tag{4.77}$$

For oscillations that are purely periodic in time, we try the solution of equation (4.77) in the form

$$\Phi(r, z, t) = \mathrm{Re}\,[\varphi(r, z)\exp(-i\omega_n t)] \tag{4.78}$$

where Re is the real part of $\Phi(r, z, t)$, and $\varphi(r, z)$ the complex function of coordinates that satisfies the Laplace formula

$$\partial^2\varphi/\partial r^2 + r^{-1}\partial\varphi/\partial r + \partial^2\varphi/\partial z^2 = 0 \tag{4.79}$$

Consider a molten pool of depth h which, for a pulse of length τ, can be estimated from (4.74) and (4.75). The boundary conditions for the function $\varphi(r, z)$ have the form [13]:

at the free surface ($z = 0$),

$$\gamma g\,\partial\varphi/\partial z + \gamma\omega_n^2 g - \sigma\partial/\partial z\,(\partial^2\varphi/\partial r^2 + r^{-1}\partial\varphi/\partial r) = 0 \tag{4.80}$$

at the molten pool bottom ($z = h$),

$$\partial\varphi/\partial z = 0 \tag{4.81}$$

The wave amplitude decays at large distances from the center:

$$r \to \infty, \quad \varphi = 0 \tag{4.82}$$

The condition (4.81) is valid only at the initial stage of crystallization. During solidification, the thickness of the molten layer tends to zero in proportion to the square root of time $t^{1/2}$, as follows from formula (4.75). The mechanical momentum on the melt surface decays not instantaneously, but after some time. Since this time is $t_r \approx r_r^2/a$, where r_r is the characteristic radius at which the reactive pressure exerts its action and a is the thermal diffusivity, there is an overestimation of the amplitudes of high-frequency harmonics, the oscillation periods of which are comparable to those of low-frequency components.

The solution of equations (4.77)-(4.81) takes on the form

$$\Phi(r, z, t) = \mathrm{Re}\sum_{n=1}^{\infty} A_n J_0(k_n r)\cosh(h - z)\,k_n \exp(-i\omega_n t) \tag{4.83}$$

where k_n is the wave number related to the wavelength by the expression

$$\lambda_n = 2\pi/k_n \tag{4.84}$$

There is a relation between k_n and ω_n, called the dispersion equation, which is found from (4.80) and written as

$$\omega_n^2 = (gk_n + k_n^2\sigma/\gamma)\tanh(k_n h) \tag{4.85}$$

For the wavelength that is much smaller than the capillary constant and for the molten pool depth that is much greater than the wavelength, equation (4.85) becomes

$$\omega_n^2 = k_n^3 \sigma \gamma^{-1} \tag{4.86}$$

The shape of a capillary wave, $\xi(r, t)$, can be defined if we apply the relation between the deflection of a melt particle from its equilibrium position and the velocity potential:

$$z = 0, \quad \partial \xi / \partial t = \partial \varphi / \partial z \tag{4.87}$$

Then,

$$\xi(r, t) = \sum_{n=1}^{\infty} (k_n A_n / \omega_n) J_0(k_n r) \sinh(k_n h) \sin \omega_n t \tag{4.88}$$

From equation (4.88) we can infer that, in accordance with experimental data, the distance between two neighbor wave crests grows with increasing r, but the wave amplitude decays.

The attenuation factor for capillary waves, which accounts for the dissipation of energy in the wave [13], is given by

$$\gamma_n = 2\omega_n^{4/3} \mu / \gamma^{1/3} \sigma^{2/3} \tag{4.89}$$

where μ is the dynamic viscosity.

Let us calculate the time it takes a perturbation factor to vanish and the time of freezing of a perturbation volume. In the conditions of melt solidification, account should be taken of the fact that the perturbation front $\xi(r, t)$ may take a fixed position during fast crystallization. Compare both the perturbation decay time

$$t_1 \approx \gamma_1^{-1} \tag{4.90}$$

and the time of freezing of a substance volume with a linear dimension of the perturbation quantity in the order of ξ:

$$t_2 \approx \xi(r, t) / v_m(t) \tag{4.91}$$

where $v_m(t)$ is the freezing rate which can be estimated from (4.73).

The condition $t_2 \ll t_1$ corresponds to the onset of the fixed shapes of circular ripples in the course of freezing. The estimates point out that t_1 and t_2 can be of the same order of magnitude for the first harmonic, i.e. the ripples fairly distant from the perturbation center may stop moving and freeze during crystallization. The freezing rate decreases in proportion to $t^{-1/2}$ and thus tends to increase t_2 and decrease t_1 if we allow for the temperature dependence of the melt viscosity [see (4.89)]. Nevertheless, the central area of the solidified melt surface must be free of ripples because the rate of decrease of freezing is faster than the rate of growth of the viscosity, for which

reason $t_1 \ll t_2$ in this area. This statement is in line with experimental results. The melt surface does not respond to spikes if the laser operates in the spiking mode since the time interval between individual spikes is about 10^{-6} s, which is much smaller than the relaxation time for the reactive pressure, $t_r \approx 10^{-4}$ s.

References

1. N. N. Rykalin, A. A. Uglov, and A. N. Kokora. *Laser machining and welding.* Moscow, Mir Publishers, 1978.
2. L. I. Rubinshteyn. *The Stefan problem.* Riga, Zvaygzne, 1967 (in Russian).
3. A. A. Uglov and D. I. Cherednichenko. *Calculation of the fusion front profile in surface melting with a moving heat source.* Fizika i Khimiya Obrabotki Materialov, No. 1, p. 3, 1980.
4. A. A. Uglov, V. V. Ivanov, and V. I. Korenkov. *Calculation of the hole profile in the liquid phase formed by a concentrated heat source.* Fizika i Khimiya Obrabotki Materialov, No. 3, p. 148, 1977.
5. T. R. Anthony and H. E. Cline. *Surface rippling induced by surface-tension gradients during laser surface melting and alloying.* Journal of Applied Physics, 48: No. 9, p. 3895, 1977.
6. M. I. Tribelskiy. *On the surface shape of the liquid phase in laser-induced melting of strongly absorbing mediums.* Kvantovaya Elektronika, 5: No. 4, p. 804, 1978.
7. S. I. Anisimov, Ya. A. Imas, G. S. Romanov et al. *Effect of high-power radiation on metals.* Moscow, Nauka, 1970 (in Russian).
8. V. V. Bashenko, N. N. Detsik, and L. K. Fomin. *On the behavior of the keyhole formed in the liquid by an electron beam.* Fizika i Khimiya Obrabotki Materialov, No. 3, p. 146, 1977.
9. A. V. Antonov, G. I. Kozlov, and V. A. Kuznetsov. *A stationary crater formed in metal by a high-power CW CO_2 laser.* Kvantovaya Elektronika, v. 4, p. 1747, 1977.
10. N. N. Rykalin, I. V. Zuev, and A. A. Uglov. *Fundamentals of electron beam material processing.* Moscow, Mashinostroenie, 1978 (in Russian).
11. M. S. Baranov, B. A. Vershok, and I. N. Geynrikhs. *On determining the melt depth in metal interacting with laser radiation.* Teplofizika Vysokikh Temperatur, 13, No. 3, p. 566, 1975.
12. M. S. Baranov, B. A. Vershok, and I. N. Geynrikhs. *Experimental check on models of keyholing by way of interaction of laser radiation with metal.* Fizika i Khimiya Obrabotki Materialov, No. 5, p. 3, 1976.
13. L. D. Landau and E. M. Lifshits. *Hydrodynamics.* Moscow, Nauka, 1986 (in Russian).

Chapter 5
VAPORIZATION OF MATERIALS

If a concentrated energy flux (CEF) delivers a power per unit area in excess of $q_c^{(3)}$ to a target, the target material begins to disintegrate after a certain dwell time depending on the material properties. The term disintegration used here is conditional since even low power densities can trigger a number of physical processes associated, for example, with diffusion, adsorption, desorption, development of structural imperfections, etc., which lead to irreversible changes in the HAZ.

In the text below, by CEF-induced disintegration will be meant, unless otherwise specified, the formation of holes during vaporization of a fraction of the molten material from the heat affected zone. Disintegration of a material with the formation of craters and through holes in thin plates can also arise in the course of melting and ejection of the liquid material due to the reactive pressure of the vapor jet, followed by solidification of the melt. Thermal stresses induced in brittle materials may cause fractures during and after CEF interaction.

5.1. MODELS OF SURFACE VAPORIZATION

Thermal theory of vaporization. The theory of surface disintegration of metals due to the absorption of LR in the range of power densities from 10^6 to 10^9 W/cm^2 is set forth in a number of works by S. I. Anisimov et al. [1], V. A. Batanov et al. [2], J. F. Ready [3], etc. They analyze the processes on the assumption that the removal of the material from the laser interaction zone occurs through surface vaporization. The authors of work [1] describe the material removal due to vaporization from the surface of the solid phase and the authors of work [2] take into account the fact that the laser energy coupled into the target forms a thin surface layer of melt. The mathematical description of the process is done on the basis of a heat-transfer equation for a condensed medium in the coordinate system involving a moving boundary at which vaporization takes place.

To simplify calculations and single out the basic mechanisms of vaporization, we shall disregard the temporal profile of a laser pulse. Also, in accordance with work [1], our analysis will not take into account a thin liquid layer formed on the surface because the latent heat of melting usually makes a small energy contribution to the enthalpy as compared to the latent heat of vaporization. However, the liquid phase can be an important factor of vaporization on account of the hydrodynamic effects resulting from the motion of the melt due to the reactive pressure of the vapor jet. At low power densities, all the factors conducive to vaporization will depend on the value of the saturated vapor pressure at the melting point. This fact was drawn attention to back in 1970 by Academician A. I. Shalnikov, as mentioned in work [4].

The time to reach the quasistationary condition at a constant rate of vaporization, v_0, when $q \geqslant 10^6$ W/cm^2, is small, and therefore we shall not dwell on this stage of the process. If the inequality

$$r_f \gg (a\tau)^{1/2} \tag{5.1}$$

holds, where τ is the dwell time of the energy flux focused on a spot of radius r_f, the problem on the quasistationary motion of the vaporization boundary in a semi-infinite body simplifies into the unidimensional form

$$\begin{aligned} &\frac{\partial^2 T}{\partial z^2} + \frac{v_0}{a}\frac{\partial T}{\partial z} = 0 \\ &-\lambda \frac{\partial T}{\partial z} = q - v_0 \gamma \Delta w|_{z=0} \\ &T(z, 0) = T(\infty, t) = 0 \end{aligned} \tag{5.2}$$

where Δw is the difference in specific enthalpies between the solid and gas phases:

$$\Delta w = L_v - RT/2 \tag{5.3}$$

Here L_v is the latent heat of vaporization, and R the universal gas constant.

The solution of the system of equations (5.2) in the moving coordinate system has the form

$$T = T^* \exp\left(-\frac{zv_0}{a}\right) \tag{5.4}$$

where T^* is the surface temperature of the condensed phase, which, in the general case, is not equal to the vaporization temperature, but depends on the power density q.

The relation between v_0 and T^* is given as

$$v_0 = \frac{q}{\gamma (L_v + 2.5RT^*)} \tag{5.5}$$

where q is the laser power density absorbed at the target surface.

Expression (5.5) includes two parameters v_0 and T^*, the estimation of which requires an additional equation. The thermal model of material disintegration commonly employs a vaporization rate equation [1]

$$v_0 = c \exp(-L_v/RT^*) \tag{5.6}$$

where c is the velocity approaching the sound velocity in metal and is dependent on the adopted model of the crystal lattice. Thus, for the Debye lattice model,

$$c = \left[\frac{4\pi}{9}(c_l^{-3} + 2c_t^{-3})\right]^{-1/3} \tag{5.7}$$

where c_l and c_t are the velocities of longitudinal and transverse waves respectively.

Solving simultaneously equations (5.5) and (5.6) allows us to express v_0 and T^* in terms of the physical parameters of a material. In the general case, a transcendental equation in v_0 or T^* results, which is solvable by one of the methods. If $L_v \gg RT^*$, we can derive an analytic expression for T^*

$$T^* = (-L_v/R) \ln^{-1}(q/c\gamma L_v) \tag{5.8}$$

and define the steady speed of the vapor front as

$$v_0 = q/\gamma L_v \tag{5.9}$$

Given v_0 and T^*, it is possible to estimate the motion of the vapor front, i.e. vaporization depth,

$$\Delta z = v_0 (t - t_0) \tag{5.10}$$

where t_0 is the time of reaching the quasistationary condition, and t the dwell time. The time t_0 is

$$t_0 = \frac{a}{v_0^2} \frac{9\pi}{4(p+2.5)^2} \tag{5.11}$$

where $p = L_v/RT^*$.

It should be pointed out that surface vaporization problems differ from the ablation problems discussed in Ch. 3 in certain respects, let alone the values of L_v and L_m, although the statements of both types of problems are rather similar. In the ablation problem, the surface temperature is preset and equal to the melting temperature T_m, while in the model of surface vaporization the temperature T^* is not a specified value and is found from the solution of the problem.

Let us note that the model with a constant surface temperature equal to the boiling temperature at normal pressure has been used by J. F. Ready [3] to develop the model of surface vaporization pro-

ceeding from the fact that the surface temperature, as evident from (5.8), is weakly dependent on the power density. Therefore, in the range of power densities from 10^5 to 10^7 W/cm^2 the surface temperature can be taken equal to the vaporization (boiling) temperature T_v. The calculations performed by F. V. Bunkin and A. M. Prokhorov [5] confirm the above supposition. In the general case, however, the supposition of Ready is inaccurate.

The quantitative analysis carried out by S. I. Anisimov et al, leads to the conclusion that there is an optimal condition of vaporization of a given material, at which the volume of the vaporized material and the motion of the vapor front are maximum. The optimal pulse length is

$$t^* = \frac{0.15}{a}\left(\frac{Q}{\gamma L_v}\right)^2 \frac{p^*}{p^*+0.5} \tag{5.12}$$

Here Q is the energy density in J/cm^2, and p^* the parameter defined as the root of the transcendental equation

$$\exp(p) = K\frac{2p+5}{2p+1} \tag{5.13}$$

where $K = 100\, c_0/9\pi a\gamma L_v$.

In optimal operation, the laser power density is

$$q^* = (2.8a/Q)(\gamma L_v)^2 \tag{5.14}$$

The motion of the vapor front under optimal conditions is defined by $\varepsilon\sqrt{at^*}$, where $\varepsilon \sim 1$. So, the optimal vaporization is achieved if the speed of the vapor front during the pulse dwell time is close to the average speed of propagation of the heat wave in the material.

Under the above statement of the problem on the motion of the vapor front into a target, the analysis disregards the temperature dependence on thermal and optical properties of a material, but allows for the reflectivity-temperature dependence. The absorptivity $A(T)$ of metals can be assumed to grow linearly with temperature up to the melting point. The analysis involving the unidimensional statement of the problem shows that optimal vaporization occurs at higher power densities of LR and at shorter pulse lengths.

What places an upper limit on the applicability of the above analysis is the condition of negligible absorption of radiation by the vaporized material, i.e. the absence of shielding of the incident flux by the blowoff material. The analysis of the vaporization process should account for the kinetic effects in a thin vapor layer (the Knudsen layer) near the target surface, for example, the effect of colli-

sions of vapor particles, causing them to propagate back toward the surface.

To clarify the conditions near the vaporization surface, we have to solve a gas-kinetic problem [1].

The speed of the vapor front in a vacuum is given by

$$v_0 = \frac{q}{\gamma (L_v + 2.2kT^*/m)} \tag{5.15}$$

where k is Boltzmann's constant, and m the atomic mass.

With allowance made for the kinetic effects in the Knudsen layer, expression (5.15) becomes different from a similar relation that does not include the solution to the gas-kinetic problem. If the CEF-induced vaporization occurs in a gas medium rather than in a vacuum, the analysis of the process proves rather complex. The analytic relation is then impossible to derive, and the only approach to obtain the quantitative information comes down to solving gas-kinetic problems on a computer [6, 7].

A number of works [8-11] contributed to a further development of the thermal model of the CEF-induced surface vaporization of metals, which analyzed nonstationary vaporization, cratering, and film disintegration along with quasistationary vaporization.

5.2. VOLUMETRIC VAPORIZATION

As is known, the depth and diameter of a crater depends on the purity of a material, its structure, and the amount of both the dissolved gas and free gas contained in pores [12, 13]. Since the physical parameters such as the latent heat of vaporization L_v and material density γ change little at relatively small contents of admixtures and contaminants, it is natural to infer that other processes different from surface vaporization and melting-induced ejection are responsible for notable changes in the parameters of the heat affected zone. Volumetric vaporization can be one of these processes. The mechanism of volumetric vaporization substantially differs from that of surface vaporization. For ideally absorbing mediums that are free of impurities, admixtures, gases, and structural microdefects such as microcracks and pores, the estimates show that in an absorption layer about 10^{-4} cm thick, volumetric vaporization can be an effective tool of material removal in comparison with surface vaporization only at temperatures close to $0.3\omega/k$, where ω is the latent heat of evaporation per atom. The value of ω/k for common materials is equal to tens of thousands of degrees C. Since laser pulses with $q_0 < < 10^9$ W/cm^2 coupled into the target are not able to raise the material to such temperature, the effect of volumetric vaporization is insignificant as against that of surface vaporization. Notice also

that the value $0.3\omega/k$ as a rule exceeds the critical temperature, for which reason the contribution of the volumetric vaporization to the process of material destruction must be appreciable at temperatures below $0.3\omega/k$.

Consider the effect of volumetric vaporization on the destruction of opaque materials such as metals when they absorb the energy of LR with a power density $q_0 > 10^6$ W/cm^2.

A distinct rate of vapor nucleation in fluids free of inclusions and gas bubbles calls for appreciable overheating. In actual conditions, however, various defects can promote the liquid phase boiling, such as blowholes, contraction cavities, pores, impurity clusters, nonmetallic inclusions, and dissolved gases. These and other intrinsic defects act as the ready nuclei of vaporization. The effect of each defect can be different depending on the specific conditions of the laser-material interaction.

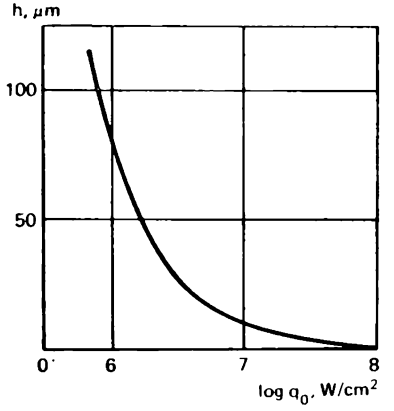

Fig. 5.1. Thickness of molten iron layer versus power density q_0

Look into the conditions at which the liquid phase exists on a target surface that absorbs the energy of LR. The temperature distribution in the course of steady-state vaporization over the bulk of the material absorbing the laser radiation can be defined, as a first approximation, by exponential expression (5.4).

Using expression (5.4), we can calculate the thickness of a molten layer as a function of power density (Fig. 5.1). The thickness of the liquid layer where volumetric vaporization can occur varies with q_0 from hundreds to units of μm, as seen from Fig. 5.1. This thickness is essential for the dynamic process of vaporization in the bulk since it determines an upper limit on the growth of a supercritical bubble.

The critical size of a bubble, r^*, which is in thermodynamic and mechanical equilibrium, can be estimated from the stability conditions

$$p_b(r^*) = p_{ex} + 2\sigma/r^*, \; V_b \leqslant V_c \tag{5.16}$$

$$p_b(r^*) = p_l^* \exp\left(-\frac{2\sigma V_l}{kTr^*}\right) \tag{5.17}$$

where V_b is the bubble volume, V_c the critical volume, p_b the internal bubble pressure, p_{ex} the external pressure, p_l the liquid pressure,

V_l the liquid volume per molecule, and σ the surface tension coefficient.

The minimum critical radius of a bubble for metal melts is $\sim 10^{-2}$ μm, i.e. comparable to the depth of LR absorption in metals. Since the thickness of the molten layer adjacent to the surface vapor front varies from hundreds to units of μm, we determine the upper limit on the sizes of various defects which can serve as centers of vaporization in the bulk of the molten metal. The calculated critical size of a bubble in copper at $q_0 = 10^6$ to 10^7 W/cm^2 ranges from 10^{-5} to 10^{-6} cm. The growth of a bubble in a uniformly heated liquid due to evaporation in the bubble volume is proportional, in a first approximation, to the square root of time t:

$$r(t) = \frac{A2c_p\gamma_l \Delta T (\pi at)^{1/2}}{\pi L_v \gamma_v} \tag{5.18}$$

where A is a constant equal to about 1.7, c_p the specific heat at constant pressure, γ_l the specific volume of liquid, ΔT the temperature difference between T_v and T_m, and γ_v the specific volume of vapor at a given temperature.

As a laser beam interacts with a target surface, a bubble grows in the conditions of increased heat transfer to its envelope with time due to surface vaporization (the bubble moves toward the vapor boundary in the coordinate system related to the vapor front). The calculations reveal that the speed of floating of a bubble to the surface is small; the bubble practically stays at rest in the melt for a few microseconds. Disregarding its floating to the surface, each bubble has a definite lifetime depending on the value of q_0. A plot of the lifetime t_b of a bubble in liquid copper against the flux density appears in Fig. 5.2. The calculated values of the radius of a bubble in molten copper at the end of its lifetime as a function of the laser power density are given in Fig. 5.3.

Under experimental conditions, it is possible to observe the separate removal of liquid droplets due to the mechanisms of volumetric evaporation and melting flushing. The second mechanism causes the droplets to scatter essentially at a certain angle to the surface of the laser interaction zone, whereas the first mechanism is also responsible for droplet scatter normal to the melt surface.

With an increase in the laser power density and decrease in the pulse length, which is the case of the Q-switched operation, the thickness of the molten layer adjacent to the vapor boundary diminishes to a value of the laser pulse penetration depth in the limit, while the melt temperature grows to the critical value or above and the lifetime of bubbles gets shorter. Conversion to these conditions means that the intrinsic centers of vaporization are already less important than the spontaneous centers of the fluctuation origin because the material in the absorption layer can be thought of as a

high-density gas. At a laser power density approaching 10^8 W/cm^2, the lifetime of a bubble reaches $\sim 3 \times 10^{-7}$ s, which is sufficient for it to grow to a size comparable to a fusion region thickness of a few micrometers.

An increased overheating of the molten layer intensifies the growth of bubbles and may cause ejection of the liquid from the interaction zone. One more cause of liquid material blowoff is the pulsation of the reactive power.

Ejection of liquid droplets in the case of normal pulse operation occurs at instants immediately after the power density of the

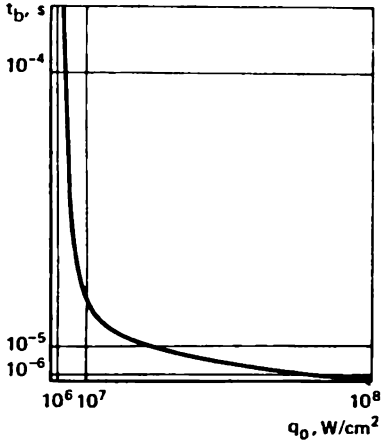

Fig. 5.2. Lifetime t_b of a bubble in copper melt versus power density q_0

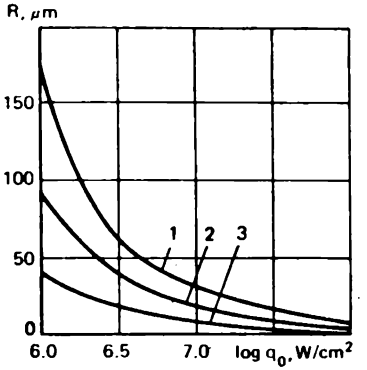

Fig. 5.3. Radius R of a bubble in copper melt as a function of power density at different values of overheating ΔT: *1*, 1 deg C; *2*, 0.5 deg C; *3*, 0.2 deg C

laser pulse sharply drops off. Such a phenomenon was observed experimentally [14]. A steel plate 2 mm thick was struck by an Nd-doped laser pulse with $\sim$ 9 ms duration. The interaction time was varied by a mechanical modulator which was a rotating shutter in the form of a disk with an aperture through which the LR impinged on the target. By changing the rotational speed of the disk and thus the time of onset of the laser pulse interaction it became possible to initiate the injection of liquid in definite periods of pulse interception. This effect developed over certain intervals of time after the start of pulse interaction and did not occur if the laser decoupling took rather a long time. The laser power density was $\sim 10^5$ W/cm^2, and the pulse was almost rectangular in shape [14].

The experiments on the process of initiating the ejection point to the instability of the volume of the removed material after the

interaction of one pulse of the same power density. Thus, the ejection of large droplets occurs once every 4 or 5 pulses under the same conditions of metal treating and then the emission of small droplets follows.

The mass of the removed melt as a function of laser pulse decoupling time t_d for the case of pulse interception with the disk at a frequency of $\sim$ 4 kHz is as follows:

t_d, ms	0.124	0.115	0.107	0.99
$m \times 10^{-3}$, kg	—	0.08	0.2	0.13

The plot of the function m (t_d) has a peak in the frequency range close to 4 kHz. The minimum pulse length after which the material ejection begins from a fusion region 1.25 mm in diameter is approximately 2.5 ms. The maximum time of pulse decoupling that initiates the liquid ejection does not exceed 0.75 ms. A decrease in the decoupling time to $\sim$ 0.03 ms does not discontinue the blowoff process. With an increase in the fusion zone diameter as the result of laser beam defocusing, the time of decoupling conducive to the blowoff grows.

Compare the representative time of change in the temperature at the gas-liquid interface with the time of change in the temperature of the liquid phase at the bottom of the absorption layer. Since heat conduction is the most inertial process to effect temperature changes in the absorption layer $\sim \lambda$ thick and is the only process in this respect for a surface layer of thickness h, the characteristic times of cooling, τ_λ and τ_h, of the absorption layer and melt zone, respectively, can be found from the relations $\tau_\lambda \approx \lambda^2/a$ and $\tau_h \approx h^2/a$. At $q_0 \approx 10^6$ W/cm^2, the melt thickness is $h \approx 0.1$ to 0.01 mm, and therefore the most conservative estimates give $\tau_h \gg \tau_\lambda$. This is because during variations in the laser power density, the internal layers of the melt fall within the overheating region where both the temperature and pressure are relatively stable.

A number of researchers have conducted experiments to get a qualitative understanding of the explosive behavior of the melt flushing mechanism during stable vaporization at laser power densities which raise the target material to critical temperatures. For example, the interaction of CW CO_2 laser beam of a power density of 6×10^3 W/cm^2 with ethanol and acetylene causes an outburst of the liquid, the initiation of which depends on the degree of overheating. It is found that an increase in both the mass removed and the recoil momentum due to explosive evaporation must occur over a narrow range of power densities which raise the surface temperature close to critical values.

A large amount of research work has been done to reveal the effect of gas bubbles and foreign impurities on the development of volumetric vaporization in molten metals. There is a certain criti-

cal value of the laser powder density q_c above which the process of volumetric vaporization prevails over surface vaporization. A useful approach to compare both mechanisms of vaporization is to equate the irradiated area to the total area of all the intrinsic and randomly originated bubbles grown to critical sizes during the time they have dwelt in the melt.

The results of the analysis presented in work [15] disclose the quasistationary temperature distribution for a stable plane wave of vaporization from the free liquid surface with consideration for the energy spent on metal melting, temperature jump in the Knudsen layer, and energy loss due to vapor ejection.

Let us look into the causes of disturbance of the mechanism of surface vaporization. First, volumetric vaporization promotes an additional vapor flow via the bubbles flowing out to the surface. Second, the process of bubbling requires a certain amount of energy, which includes the surface energy, energy of vaporization, and energy expended on dilation. Third, the rising bubbles distort the surface as they produce undulations of the size in the order of the bubble radius. Each of these surface disturbances can be judged by its own criterion deduced for the purpose [15].

The replacement of one mechanism of vaporization by the other can occur with an increase in the power density. The bubbles most heavily distort the surface if the area of these bubbles, $N_b \pi d_b^2 S$, is equal to the area of the plane surface, S, of the melt. Comparing these areas, we get

$$K = \pi d_b^2 N_b = 1 \tag{5.19}$$

where d_b is the average bubble diameter, and N_b the average number of bubbles in a unit volume.

The condition (5.19) means that the area of the surface on which the radiation falls appreciably exceeds the area of the plane surface of the melt. This situation may affect the absorption efficiency. From the condition (5.19) it follows that the distance between neighbor bubbles is equal to about the diameter of each bubble. Therefore, the structure of the absorption layer strongly differs from that typical for surface vaporization. The bubbles rising to the surface can eject the liquid metal lying above and between them in the form of droplets, the radius of which is approximately the same as that of bubbles. With the condition (5.19) satisfied, the mass flow of droplets, $\gamma_0 \mid u_0 \mid N_b d_b^3$, where u_0 is the speed of the fusion front, proves to be of the same order of magnitude as the total mass flow, $\gamma_0 \mid u_0 \mid$, if the collapsed bubble generates a droplet of its size. The ejection of droplets can thus have a strong effect on the mass transfer. Besides, droplets can heavily shield the surface from the incident radiation.

The diameter of a bubble at the instant it touches the surface is

$$d_b = \int_0^{t_b} v(t)\,dt = \int_0^{t_b} \sqrt{(2/3)\,\Delta p\,(t)/\gamma_0}\,dt \tag{5.20}$$

where t_b is the lifetime of a bubble in the liquid until it touches the surface and collapses, and v the rate of growth of the bubble, which is equal to the Rayleigh rate. The growth rate is given as $v = \sqrt{(2/3)\Delta p/\gamma_0}$, for which an approximate estimate is sufficient:

$$d_b \cong v_{\max} t_b = \sqrt{(2/3)\,\Delta p_m/\gamma_0}\,t_b \tag{5.21}$$

where $v_{\max} = \sqrt{(2/3)\,\Delta p_m/\gamma_0}$ is the characteristic rate of growth of bubbles, and $\Delta p_m = p_0\,(T_{\max}) - p$.

The lifetime and the diameter of a bubble before it flows out to the surface are

$$t_b = \delta/(\mid u_0 \mid + v_{\max})$$
$$d_b = \delta v_{\max}/(\mid u_0 \mid + v_{\max}) \tag{5.22}$$

Estimates show [15] that at power densities close to critical values, $v_{\max}$ must be much in excess of $\mid u_0 \mid$ to initiate the changeover of the mechanisms of vaporization.

The mean number of bubbles per unit volume is

$$N_b \cong 10^{-10}/2r_m^{*3} \tag{5.23}$$

where $r_m^* = 2\sigma_m/\Delta p_m$ is the critical radius, and $\sigma_m = \sigma\,(T_m)$.

The function $\sigma\,(T)$, just like $L_v\,(T)$, is well approximated in a linear fashion:

$$\sigma\,(T) = \sigma_0\,(T^* - T)/(T^* - T_0) \tag{5.24}$$

where $T^* - T_0$ is the temperature range, and σ_0 the value of $\sigma\,(T)$ at T_0.

For aluminum the value of σ_0 is equal to 0.737 N/m at the melting point.

The rate of growth of fluctuation-induced bubbles is

$$v_f = n_b \sqrt{\frac{2\sigma}{\pi m}} \exp\left(-\frac{L_v m}{kT}\right) \exp\left(-\frac{4\pi r^{*2}\sigma}{3kT}\right) \tag{5.25}$$

The number of such bubbles grown in a unit volume is given by

$$N_{bf} \cong v_f\,(T_m)\,t_b = v_f(T_m)\,\frac{\delta_T + \delta_q}{\mid u_0 \mid + v_m} \tag{5.26}$$

where δ_T is the heat diffusion depth, and δ_q the radiation penetration (absorption) depth.

The calculations of the critical power density q^* at which sur-

face vaporization gives way to volumetric vaporization with regard to fluctuation and intrinsic bubbles point to the fact that neglect of the growth of intrinsic bubbles at large LR penetration depths may introduce large errors [15].

Figure 5.4 illustrates the relation between q^* and penetration depth δ_q with consideration for the growth of fluctuation bubbles (curve *1*) and intrinsic bubbles (curve *2*). The intersected curves *1* and *2* form a boundary *ABC* between a lower region I and upper region II representative of the prevailing mechanism of surface and volumetric vaporization respectively.

As shown by calculations, fluctuation boiling is the main mechanism of volumetric vaporization in the range $\delta_q < 5.6 \times 10^{-3}$ cm.

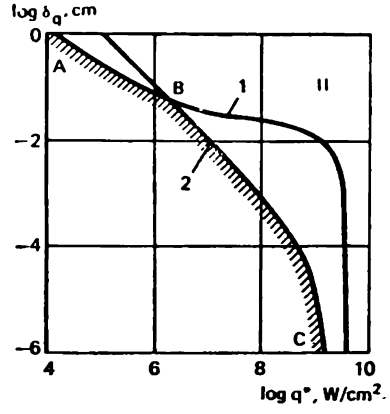

Fig. 5.4. Critical power density q^* at different values of LR penetration depth δ_q

5.3. VAPOR EXPANSION IN VACUUM

As a CEF interacts with the surface of a condensed body placed in a vacuum, the gas formed as the result of vaporization freely expands in empty space. The rate of vacuum vaporization of a substance, whose temperature is substantially lower in magnitude than the binding energy of atoms, depends on the process of forward flow of atoms from the target surface due to thermal motion and the process of backward flow of atoms due to collisions in the gas medium. If the vacuum vaporization proceeds rather slowly, the vapor density near the surface is small and collisions are rare, so the backward flow of atoms to the surface can be disregarded.

In the case of surface vaporization, the velocity distribution of particles within a solid angle 2π is Maxwellian. Temperature T_0 of particles is equal to the surface temperature and particle density n_0 is equal to the saturated vapor density at this temperature [1].

The density dn of a number of vaporized particles whose velocities lie in the interval $\vec{v}, \vec{v}+\vec{dv}$ at the surface ($x=0$) is defined by

$$dn = n_0 \left(\frac{m}{2\pi kT_0}\right)^{3/2} \exp\left(-\frac{mv^2}{2kT_0}\right) \vec{dv}, \quad v_x \geqslant 0 \tag{5.27}$$

where m is the atomic mass of a vaporized particle.

The mass rate of vapor flow, u, directed normal to the target surface is $u = \bar{v}/4$, where $\bar{v} = (8\,kT_0/\pi m)^{1/2}$ is the rms velocity of vapor particles which exhibit the Maxwellian velocity distribution. If the gas has a fairly low density, u determines the rate of flow of the gas from the surface, which is the case when the free path length of particles is $l = 1/n\sigma$, where n is the number of particles per unit volume and σ is the gas kinetic cross section. For the case under analysis, collisions between particles can be left out of consideration. But if the vaporization is intensive, the backward flow must be taken into account.

Motion of the main mass of vapors generated by laser or electron beams is commonly described by gas dynamic equations. In our case, the free path lengths of atoms are smaller than all the specified geometric parameters of the problem of interest and the gas motion occurs in two characteristic regions. In the first region of width l_k that is adjacent to the target surface, the particle collisions culminate in a new gas state defined by an isotropic function of the distribution, which is different from the Maxwellian distribution by temperature $\bar{T}$ and particle density $\bar{n}$. The mass flow rate $\bar{u}$ is also different from $\bar{v}/4$.

In the second region, the gas motion obeys gas dynamic equations. But the gas dynamic approximation is for certain inapplicable to a thin Knudsen layer l_k near the target surface since its thickness is equal to 2 or 3 path lengths of an atom. For gas dynamic equations, the Knudsen layer is the discontinuity surface [1]. To define the boundary conditions for the discontinuity surface, we need to search for the function of atom velocity distribution within the Knudsen layer.

The solution of this problem of vacuum vaporization has been found using the Boltzmann equation [1]. The solutions to kinetic equations are mainly sought with the aid of moment, variational, and Monte Carlo methods [16]. Let us briefly outline these methods.

The moment method [16] consists in multiplying a kinetic equation by the functions which form a complete orthogonal system for the atom distribution function and integrating this equation with respect to all velocities of atoms. Since the orthogonal system is infinite, the infinite system of equations for the distribution function results. The solution is sought after reducing this system to a finite number of equations and imposing a number of constraints on the selected system of functions. The method most commonly relies on five equations identifying the five selected functions with such basic moments for the Boltzmann kinetic equation as the density γ, three components of atom velocity $\vec{v}$, and temperature T [16]. In a number of cases, the method deals with 13 functions which include, apart

from the above moments, the components of pulse power P_{ij} and energy. These types of the method received the name Grad's 5-moment and 13-moment methods. To try the solution of moment equations, recourse most often has to be made to special numerical methods of solving problems on a computer. The moment method involves difficulties in selecting the boundary conditions which are to be met after solving the equations [16].

The variational method applies to problems of seeking for the moments of the distribution function rather than for the function itself, such as the temperature, speed, density, etc., which are first approximated by the functions containing a number of unknown constants.

The Monte Carlo method is in essence used to model numerically a physical process rather than to solve a specific kinetic equation. For example, setting different values of the system distribution function, we find its changes and simulate the motion of a few thousand particles [16].

The main equation of gas kinetics theory is the Boltzmann equation. Its solution presents difficulties because of the complex form of the collision integral in the right side of the equation

$$\frac{\partial f}{\partial t}+\bar{v}\,\frac{\partial f}{\partial r}=I(f) \tag{5.28}$$

where f is the distribution function, and $I(f)$ the collision integral that defines changes in the distribution function due to particle collisions. The form of this integral depends on the mechanism of interaction of gas particles.

One of the approaches to simplify the integral of collisions is to write it in a relaxation form

$$I(f)=\nu\,[f_0(\bar{v})-f(\bar{v})] \tag{5.29}$$

where $\nu=\tau^{-1}$ is the collision frequency assumed to be constant and dependent on the mechanism of interaction of atoms, $f_0(\bar{v})$ the Maxwellian distribution function, and $f(\bar{v})$ the unknown function.

This method suggested by J. Bhatnagar, E.P. Gross, and M. Krook [16] received the name BGK model. This seemingly simple model is in fact fairly complex. It commonly applies to three problems stated to find the distribution function in a half-space with the unknown integral of collisions.

In the analysis of the processes of high-power-laser-induced vaporization of materials in a vacuum, workers [1] used the BGK model in a steady-state unidimensional form and estimated the fraction of vaporized atoms returning to the target surface, which was equal to about 18%.

Given below are the formulas for the calculation of the temperature, speed, and other parameters as functions of q_0 [1]:

$$q_0 = 0.32 \times 10^{-23} A v_0^3 (y_0 + 2.2) e^{-y_0}$$

$$y_0 = \frac{L_v}{kT_0}, \quad A = \frac{m}{1.67 \times 10^{-24}} \tag{5.30}$$

$$j_m = \bar{n}\bar{u} = \frac{q_0}{L_v (1 + 2.2/y_0)} \tag{5.31}$$

$$v_0 = j_m / \bar{n}_0 \tag{5.32}$$

$$\bar{T} = 0.65\, T_0 = 0.65 L_v / k y_0 \tag{5.33}$$

$$\bar{u} = 0.81 \times 10^{12} (L_v / A y_0)^{1/2} \tag{5.34}$$

$$\bar{n} = j_m / \bar{u} \tag{5.35}$$

$$\bar{p} = 0.65\ \bar{n} k T_0 \tag{5.36}$$

Here j_m is the flow of vapor particles to the surface; $\bar{n}$, $\bar{u}$, and $\bar{T}$ are the density, velocity, and temperature of the gas at the surface respectively; and $\bar{n}_0$ is the number of particles in a unit volume of the saturated vapor.

The values of the parameters entering relations (5.30)-(5.36) are given in Table 5.1.

Table 5.1 lists the values of two quantities v_0 and v_0^*, of which

TABLE 5.1. **Parameters of Some Metals**

Metal	A	γ, g/cm³	$n_0 \times 10^{-22}$, cm⁻³	$v_0 \times 10^{-12}$, s⁻¹	$v_0^* \times 10^{-12}$, s⁻¹	L (4.2×10³), J/mol	$L_v \times 10^{-10}$, J/g
Al	27	2.7	6.0	8.11	8.24	74.4	5.16
Bi	209	9.8	2.8	1.66	2.62	47.5	3.29
W	184	19.4	6.3	6.24	6.94	200	13.9
Fe	56	7.9	8.5	8.32	11.9	99.3	6.88
Cu	64	8.9	8.3	6.55	5.39	80.8	5.60
Mo	96	10.2	6.4	7.90	7.74	157.1	10.9
Ni	59	6.6	6.7	7.49	13.7	101	7.0
Sn	119	7.3	3.7	2.29	2.04	72	4.99
Pb	207	11.3	3.3	1.83	1.18	47	3.26
Ag	108	10.5	5.8	4.47	3.99	68.3	4.74
Cr	52	7.2	8.3	8.63	13.4	94.5	6.55
Zn	65	7.1	6.5	4.37	3.3	31	2.15
Mg	24.3	1.74	2.5	—	4.58	34.9	2.42

the value of v_0^* is equal to its experimental value at a saturated vapor pressure of 0.1 MPa proceeding from the condition of a uniform density of the number of saturated vapor particles n_0.

The vapor parameters $\bar{n}$ and $\bar{T}$ in most cases conform to a sharply supersaturated vapor state. This must entail an almost instanta-

neous condensation of the vapor during its expansion just near the surface. But supersaturation cannot markedly change the calculation of hydrodynamic boundary conditions, which neglects the process of condensation near the target surface [1].

The qualitative picture of vapor flow at the target surface is the following. At a distance l_k, equal to 2-3 free path lengths of a particle, the vapor reaches the equilibrium values of the mass flow rate, density, and temperature. As it leaves the Knudsen layer, the vapor is found to be in the supersaturated state and partially condenses at a distance $l \simeq l_k \bar{n}_0/\bar{n}$. The latent heat of vaporization, L_v, evolved as the result of condensation causes the vapor temperature to increase, and the vapor approaches the saturation state. These conditions in the region fairly distant from the surface downstream of the flow are such that the vapor has time to come to equilibrium during gas dynamic expansion.

This approach to the analysis of vapor expansion during vaporization in vacuum is approximate in the general case. The thing is that the hydrodynamic flow of the main mass of vapor sets in only after the transient process, whose analysis calls for the solution of the kinetic problem on vapor motion for the entire stream as well as for the Knudsen layer. Such a solution enables us to follow the transition from the free molecular scattering of vaporized particles to the hydrodynamic flow, determine the character of motion in the region of low densities, and estimate effective boundary conditions on the target surface.

5.4. INTERACTION OF RADIATION WITH BLOWOFF PRODUCTS

The interaction of a concentration energy flux of power density in excess of $q_c^{(3)}$ with the surface of a solid leads to the process of intensive vaporization and motion of vapors which absorb the incident laser radiation or the flow of accelerated particles. Neglect of the interaction of the energy flux with blowoff materials may introduce errors in the calculated values of the parameters of the material disintegration process because the shielding of the target surface by the vaporized particles can appreciably change the spatial and temporal characteristics of the incident flux.

The hydrodynamic problems of vapor particle scattering and absorption of radiation by disintegration products have been dealt with in a number of works, for example, in [1, 5]. Proceeding from these works, let us take a closer look at the problems of vapor heating, vapor motion, and surface shielding by the products of disintegration.

Vapor heating with laser radiation. The vapor jet emitted from the target surface vaporized in a vacuum interacts with the incident

laser beam. Over a certain range of power densities q_0, the vapor does not convert to the state of a strongly absorbing plasma. Under these conditions, the shielding of the incident LR proves insignificant, although the LR raises the vapor to a higher temperature.

Let the target surface be plane. During vaporization, a thin layer, whose thickness is equal to 2-3 free path lengths of atoms, appears near the phase boundary. Although the thickness of this Knudsen layer is $\sim 10^{-2}$ mm, which proves small for most laser experiments, the consideration of the effect of the Knudsen layer is undoubtedly important in the analysis of vaporization processes. The point is that the structure of the gas dynamic flow builds up just in this layer l_k thick. The entire vapor flow consists of two characteristic regions interconnected at the boundary of the Knudsen layer. The collisions between vapor particles in the layer l_k cause a fraction of particles to return to the surface and condense on it since the adhesion coefficient for metals is close to unity.

From the viewpoint of gas dynamics, the boundary between the layer l_k and the gas dynamic flow is the interface of partial discontinuity, beyond which an unsteady wave of the rarefied vapor propagates [17]. On the discontinuity surface itself, the vapor flow velocity is equal to the local sound velocity, i.e. $c_0 = \sqrt{\gamma_v T_0/m}$, where γ_v is the constant of Poisson's adiabat for the vapor, T_0 the vapor temperature related to the surface temperature T_1 by a simple equation $T_0 = \beta T_1$, and m the mass of vapor particles. The vapor flow pressure is $p_0 = \beta_2 p_s(T)$. Here, β_1 and β_2 are smaller than unity and $p_s(T)$ is the saturated vapor pressure at T. The coefficients β_1 and β_2 relating to vacuum evaporation were found from the kinetic equation for the vapor particle distribution function [1]. For the metal vapor, $\beta_1 \cong 0.65$ and $\beta_2 \simeq 0.18$.

If the laser beam diameter is d_f, then the time to reach the gas dynamic parameters must satisfy the condition $t \gg d_f/c_0$. In the layer of thickness $x \ll d_f$, which is adjacent to the target surface, the vapor flow is plane and unidimensional. Beyond this layer, the lateral expansion of the vapor jet begins, and so the density γ_1, pressure p_1, and temperature T_1 of the vapor steadily decrease with increasing coordinate x, whereas the flow velocity $u_1 = u_1(x)$ grows from $(u_1)_{\min} = u_1(0) = c_0$; the vapor flow velocity at all the points in this region is supersonic because $u_1(x) > c_1(x) = \sqrt{\gamma_v T_1(x)/m}$. Even if the lateral expansion of vapors is small, the vapor parameters γ_1, p_1, T_1, and u_1 can change significantly. With an increase in the diameter of the monatomic vapor jet ($\gamma_v = 5/3$) by 30%, the vapor density, temperature, and pressure drop off by factors of 3, 2.1, and 6.2 respectively. The calculated vapor velocity then increases 1.7 times on the assumption that the expansion is adiabatic. Even the pressure that drops to such a fairly low value commonly exceeds the atmospheric. So, the effect of the external pressure p

on the vapor flow in the region $x \sim d$ can be neglected if this pressure is not higher than the atmospheric [17].

Consider the interaction betweem the vapor flow and LR. Designating the total absorption coefficient for the vapor and particle condensation as $\varkappa_\nu = \varkappa_\nu(x, t)$, the laser power density q incident on the metal surface becomes [1]

$$q = q_0 \exp\left[-\int_0^\infty \varkappa_\nu(x, t)\, dx\right] = q_0 \exp\left[-\Lambda(t)\right] \tag{5.37}$$

where q_0 is the laser power density before the interaction with the vapor, and $\Lambda(t)$ the total optical thickness of the absorbing gas.

At vapor temperatures $T \approx T_v$, corresponding to the single ionization of vapor atoms, the dominant LR absorption processes are the process of photoelectric absorption by excited atoms and the process of inverse Bremsstrahlung due to electrons falling in the field of ions and neutral atoms [18]. The laser radiation can also be absorbed and scattered by condensate particles and liquid droplets emitted from the laser interaction region.

The photoelectric absorption and inverse Bremsstrahlung due to ions at $h\nu < I$, where I is the ionization potential, are found from the Kramers-Unzold formula:

$$\varkappa' = \varkappa_{\nu 1} + \varkappa_{\nu 2} = \frac{16\pi^2}{3\sqrt{3}} \frac{e^6 Z^2 kT n_v}{h^4 c \nu^3} \exp\left(-\frac{I - h\nu}{kT}\right) \tag{5.38}$$

where Z is the ion charge, ν the LR frequency, n the density of vapor atoms, c the sound velocity, and h the Planck constant.

The coefficient of inverse Bremsstrahlung due to electrons in the field of neutral atoms at an electronic energy of less than 3 eV is given by [1]

$$\varkappa_{\nu 3} = \frac{46 e^2 \sigma_e \sqrt{\bar{h}}}{(2\pi)^2 c \omega^{3/2} m_e^{3/2}} \left[1 + \frac{3}{2} \frac{kT}{h\omega} + \frac{27}{2} \left(\frac{kT}{h\omega}\right)^{3/2}\right] n_e n_v \tag{5.39}$$

where σ is the cross section of elastic scattering of electrons by atoms, m_e the electron mass, $\omega = 2\pi\nu$, and n_e the electron concentration defined by the Saha formula for equilibrium conditions [18]:

$$n_e^2 = n_v \left(\frac{2\pi m_e kT}{h^2}\right)^{3/2} \exp\left(-\frac{I}{kT}\right) \tag{5.40}$$

In the case of equilibrium ionization,

$$\varkappa_{\nu 3} \approx \frac{46 e^2 \sigma_e}{(2\pi)^{5/4} hc \nu^{3/2}} \left(\frac{kT}{m_e}\right)^{3/4} n_v^{3/2} \exp\left(-\frac{I}{2kT}\right) \tag{5.41}$$

Let us derive the relations for the thickness Λ_g of the gaseous component of disintegration products. Assuming that the ionization is of the equilibrium type and defined by the Saha formula, rep-

resent Λ_g as the sum of two terms corresponding to $\varkappa'$ and $\varkappa_{\nu 3}$ [1]:

$$\Lambda_g = \Lambda_{12} + \Lambda_3, \quad \Lambda_{12} = \int_0^\infty (\varkappa_{\nu 1} + \varkappa_{\nu 2})\, dx$$
$$\Lambda_3 = \int_0^\infty \varkappa_{\nu 3} dx \tag{5.42}$$

The calculations of Λ_{12} and Λ_3 presented in [1] are made for two cases: the gas in the entire region of flow is a saturated vapor, and the gas expands according to Poisson's adiabatic curve.

The numerical estimations present difficulties because regular data on σ_e are absent. In the range of low electronic energies from 1 to 5 eV, σ_e for alkali metals ranges from 1×10^{-14} to 3×10^{-14} cm^2. But it is the photoelectric absorption and inverse Bremsstrahlung that make the main contribution to the absorption process.

The calculated values of $\Lambda_{12}^{(1)}/t$ and $\Lambda_3^{(1)} \times 10^{-14}/\sigma_e\, t$ for some metals as functions of $y_0 = L_1/kT_0$ are given in Fig. 5.5. As a rule, the photoelectric absorption and inverse Bremsstrahlung prevail, i.e. $\Lambda_{12}^{(1)} \ll \Lambda_3^{(1)}$.

The absorption coefficient of metallic vapors at laser power densities of about 10^6 W/cm^2 proves rather small, i.e. the vapor formed during the developed vaporization of metal is so transparent that its heating by the incident radiation is negligible. Here we did not touch the problem of absorption by condensate and liquid droplets ejected from the interaction zone. Yet, the laser beam can heat the "cold" vapor flow transparent to LR if it triggers a stable optical discharge in the vapor. The physical cause of development of this discharge is the following. The vapor fluctuations at a certain distance from the target surface can produce a vapor layer of increased temperature, which begins to absorb LR more intensely. When the speed of the detonation wave, v_d, becomes higher than the speed of the vapor jet, u_1, this layer begins to expand in both directions until it acquires a steady state. The result is the optical discharge initiated in the vapor jet. The steady-state values of the discharge width Δx and discharge temperature T_2 are defined by the expression $Q = Q(T_2, \Delta x)$ [5]:

$$Q = \frac{1 + R\exp(-\Lambda)}{1 - R}(\exp\Lambda - 1)\, q \tag{5.43}$$

where R is the reflectivity, and Λ the optical thickness at which the detonation wave velocity v_d is equal to the velocity $u_1 = u_1(x)$ of the "cold" vapor impinging on the discharge, i.e.,

$$u_1(x) = v_d(Q) \tag{5.44}$$

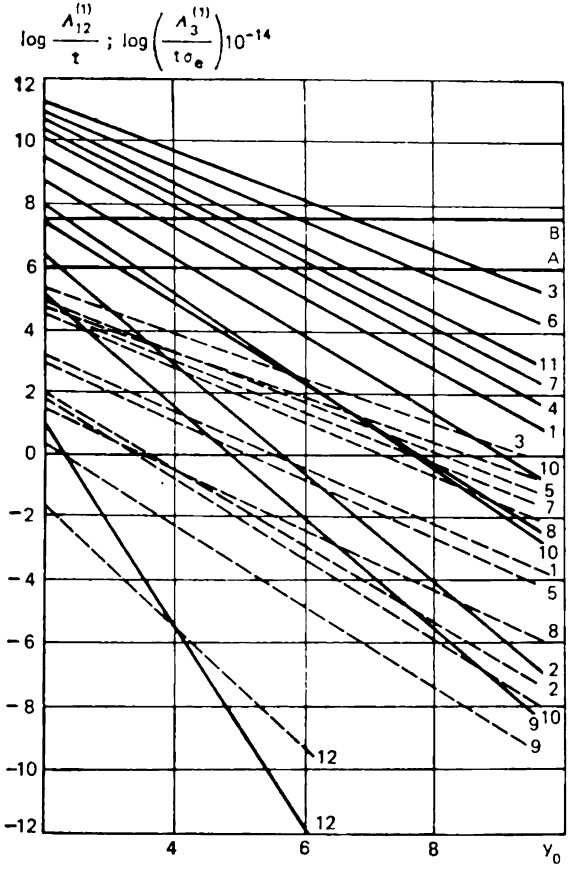

Fig. 5.5. Quantity $\Lambda_{12}^{(1)}/t$ (solid lines) and quantity $\Lambda_3^{(1)} \times 10^{-14}/\sigma_e t$ (dash lines) versus parameter y_0; AB is the region where $\Lambda \approx 1$ for pulses 10^{-6} to 3×10^{-8} s long at the end of interaction. Theoretical curves correspond to metals: *1*, Al; *2*, Bi; *3*, W; *4*, Fe; *5*, Cu; *6*, Mo; *7*, Ni; *8*, Sn; *9*, Pb; *10*, Ag; *11*, Cr; *12*, Zn

while the gas velocity u_2 (Q) beyond the detonation front is equal to the sound velocity $c_2 = \sqrt{\gamma_D T_2/m}$ (the Chapman-Jouguet condition), i.e.,

$$T_2 = (m/\gamma_D)\, u_2^2\, (Q) \tag{5.45}$$

To determine the discharge temperature T_2 and width Δx, it is necessary to define the function u_1 (x). For this, we should solve the gas dynamic problem. If only the temperature T_2 is to be found, the solution need not be sought since T_2 weakly depends on Δx. So, we can set $\Delta x \approx d$. Equation (5.44) then becomes

unnecessary and equation (5.45) can be simplified if $u_2 = \gamma_v \sqrt{2(\gamma_v + 1) Q/(\gamma_v - 1)}$, i.e. if the detonation wave is assumed to be strong.

Proceeding from the Kramers-Unzold relation, the temperature T_2 is found from the equation $\widetilde{\Delta}/T_2 = \ln(\Lambda_0/\Lambda)$, where $\Lambda_0 = \varkappa_0 \Delta x \approx \varkappa_0 d$. The approximate solution of this equation has the form

$$T_2 = \widetilde{\Delta}/\Lambda^*$$

$$\Lambda^* = \ln\left\{\frac{2\gamma_v(\gamma_v-1)}{\gamma_v+1}\,\frac{1+R}{1-R}\,\frac{L_v}{\widetilde{\Delta}}\,\Lambda_0 \ln\left[\frac{2\gamma_v(\gamma_v-1)}{\gamma_v+1} \times \frac{1+R}{1-R}\,\frac{L_v}{\widetilde{\Delta}}\Lambda_0\right]\right\} \tag{5.46}$$

where $\widetilde{\Delta} = \Delta - h\omega$, and Δ is the energy of single ionization of vapor atoms.

The quantity Λ^* is weakly dependent on both the thermal properties of a material and laser power density q, and is close to 10; at $\Lambda_0 = \varkappa_0 d \approx 10^3$-$10^4$, the volume of Λ^* ranges between 9 and 11.

The steady-state vapor temperature T_2 near the target surface ($x \leqslant d$) thus mainly depends on the vapor particle ionization energy Δ and in most cases markedly exceeds the surface temperature T. The heated plume of vapors is separated from the less heated target surface by the "cold" vapor layer moving at a supersonic speed. The optical thickness Λ of the plume is always $\sim \Lambda^{-1}$, i.e. it remains small as against unity, so the target surface shielding is insignificant.

The numerical estimates show that for most metals, excepting refractory metals such as tungsten and molybdenum, the vapor temperature T_2 is 2.5-4.5 times higher than the surface temperature [5].

The steady-state heating of vapors by LR has been treated in a number of works. Work [2], for example, described the vapor heating by the beam from an Nd-doped laser operated at $\lambda = 1.06$ μm. There are the results of spectroscopic measurement of the temperature of vapors struck by pulses of about 1-ms duration at power densities approaching 10^7 W/cm^2.

The optical discharge, also called the laser-induced spark, develops in vapors spontaneously as the result of vapor fluctuations.

The developed vaporization under the conditions of steady-state vapor heating near the target surface ($x < d$) proceeds so long as the power density is not too high and the optical discharge does not originate [19]. When the plasma shields the target surface, vaporization decreases appreciably; with continued irradiation, the beam may trigger a self-sustained process in which a fraction of the laser power will go into maintaining the optical discharge.

The regime of pure vaporization without optical breakdown is realizable only when the laser power density q lies in the range $q_v < q < q_{op}$, where q_{op} is the power density threshold for the onset of optical breakdown in the vapor. At an ambient pressure $p \leqslant 0.1$ MPa, the process of pure vaporization by lasers generating in the visible and near-infrared regions is easy to maintain since q_{op} is much higher than the vaporization threshold q_v. In the far-IR region and also in the CO_2 laser region, the thresholds q_v and q_{op} may lie too close to each other, so that the task of ensuring pure vaporization will be difficult.

Shielding of laser radiation by particles. We shall now consider the effect of shielding of LR by particles of the condensed phase formed during condensation of supercooled vapor [1]. Because of its strong initial supercooling, the vapor begins to condense just near the surface at the instant of the condensation shock. Since supersaturation exceeds the critical value, all the nuclei of the condensed phase prove stable and start growing. The number of nuclei is mainly determined by the degree of vapor ionization. The total number of centers must be approximately equal to the initial number of ions since the vapor supersaturation falls off fast on account of condensation. Besides, the rate of nuclei growth also decreases, which varies with the degree of supersaturation $\theta = (T_s - T)/T_s$ as exp $(-b/\theta^2)$, where b is a constant [18]. To a certain approximation, the total number of condensation centers per atom can be taken constant and equal to the degree of vapor ionization at the instant of the condensation shock, $\alpha_{es} = n_{es}/n_s$, whese n_{es} is the number of electrons in a unit volume near the surface at T_s, and n_s is the number of atoms near the surface.

To calculate the optical thickness Λ_l of the condensed (liquid) phase, we should know the coefficient of attenuation $\overline{K}$ of the laser beam by droplets, which is the sum of absorption coefficient K_{ab} and scattering coefficient K_{sc} [1]:

$$\overline{K} = n_d K = n_d (K_{ab} + K_{sc}) \tag{5.47}$$

where n_d is the concentration of droplets.

For the typical case when the laser emits at a wavelength λ of about 1 μm, the attenuation coefficient can be written as

$$\overline{K} \cong \frac{9\nu\nu_{col}}{\nu_0^2} \frac{n_d V_d}{\lambda}, \quad \nu_0^2 = \frac{Ne^2}{\pi m_e} \tag{5.48}$$

Here ν is the laser frequency, ν_{col} the electron collision frequency, V_d the droplet volume, m_e the electron mass, and N the electron concentration.

The degree of condensation α is defined as the ratio of the number of atoms in the condensed liquid phase, n_l, to the total number n of atoms per unit volume in the two-phase system consisting of the

saturated vapor and condensed phase:

$$\alpha = n_l/(n_l + n_v) = n_l/n \tag{5.49}$$

where $n_l = n\alpha$, and $n_v = (1 - \alpha)\, n$.

It can be shown by the use of relation (5.45) that the quantity $\overline{K}$ is independent of the number of droplets in the flow and only depends on the total amount of the substance in the condensed phase:

$$\overline{K} = \frac{9\nu\nu_{col}}{v_0^2}\,\frac{\alpha n}{\lambda \bar{n}_0} = \delta\alpha n, \quad \delta = \frac{9\nu\nu_{col}}{\lambda \bar{n}_0 v_0^2} \tag{5.50}$$

From the above expressions, we can determine the optical thickness Λ_l [1]:

$$\Lambda_l = \delta n_s u_s t/y_s \tag{5.51}$$

Using the continuity equation $n_s u_s = \bar{n}_0 v_0$, relation (5.51) can be written in the form

$$\Lambda_l \cong \delta \bar{n}_0 v_0 t/y_s \tag{5.52}$$

For clarity, compare Λ_l with Λ^* which is the number of "totally absorbing" layers of metal vaporized by the time t [1]:

$$\Lambda^* = \varkappa_0 v_0 t \tag{5.53}$$

where $\varkappa_0$ is the metal absorption coefficient. Then the ratio

$$\overline{\Lambda} = \Lambda^*/\Lambda_l \tag{5.54}$$

gives the number of metal layers to be vaporized to form a condensate layer near the surface, which reduces the energy of the incident radiation to $1/e$ of its original value:

$$\overline{\Lambda} = \frac{\Lambda^*}{\Lambda_l} = \frac{\varkappa_0 y_s}{\delta \bar{n}_0} = \frac{4\pi}{9}\,\frac{\nu_0^3 y_s}{\nu^2 \nu_{col}} \tag{5.55}$$

where $\varkappa_0 = 4\pi\sigma_0/c\bar{n} \simeq 4\pi\nu_0/c$.

For the typical case of interaction of LR with metal, the value of $\overline{\Lambda}$ is in the order of 10^4 at $\bar{\nu}_0 \approx 2 \times 10^{15}\ s^{-1}$, $\nu \approx 3 \times 10^4\ s^{-1}$, $\sigma_0 \approx 10^{17}\ s^{-1}$, and $y_s \approx 10$.

The calculations presented above for the one-dimensional case are tentative in character since the actual process of vaporization is three-dimensional. Besides, along with condensate droplets, the vapor contains the material ejected as liquid droplets ranging in size from units to tens of micrometers, which can additionally shield the target. The ejected liquid droplets interact with the incident laser radiation and can return to the molten pool.

5.5. EFFECTS OF LASER-INDUCED PLASMA ON THERMAL PROCESSES IN THE INTERACTION REGION

The processes of laser interaction with materials generally involve either (1) heating of a target surface without vaporization or (2) melting with vaporization and plasma formation. To gain an understanding of the physical phenomena in the first type of process, it is sufficient to restrict the analysis to the solution of the heat problem, therewith allowing for the nonlinear changes in the thermal parameters of a target material, phase transitions, reflectivity, and spatial-temporal pattern of the pulse. The range of laser power density q for the process of melting without vaporization does not exceed a threshold value of 10^6 W/cm^2. This region of small power densities has received the most study in the domain of laser technology and is useful for welding and heat treating of materials [21]. In the range of moderate power densities from 10^6 to 10^8 W/cm^2, the second type of process employed, for example, in cutting and hole drilling, becomes dominant. The analysis of this process calls for handling both the heat problem and the problem on target vaporization, plasma wave excitation, and plasma effects during and after laser beam interaction.

The features specific to the second region of interaction in the normal conditions of vaporization are the following.

1. Absorption of laser radiation by the products of erosion, ionization of the vapors of the target material, and surface shielding.
2. Shift of the region of energy release from the target surface to the gaseous phase.
3. Increase in temperature and pressure in the region of laser energy absorption.
4. Strong thermal radiation from opaque plasma.

The main task of investigations in this region is to define the thresholds for ignition of plasma waves depending on the specified conditions of interaction and to study the plasma effects on the irradiation process.

The interaction of laser radiation with metals leads to the absorption of electromagnetic energy in a thin surface area 10^{-5} to 10^{-6} cm thick. The absorbed energy raises the temperature of the surface which begins to melt and vaporize. At this initial stage of interaction, the processes of heating and phase transitions play the main role. The dynamics of surface heating depends both on the laser parameters (wavelength, beam energy density, and temporal and spatial distribution of energy) and on the temperature dependence of the thermal and optical parameters of the metal target, such as the specific heat, thermal diffusivity, phase transition energy, and reflectivity. In the specified conditions of irradiation, there exists a critical power density q_c. This is the threshold above which the metal

begins to vaporize intensely late in the pulse. Where long pulses interact with a target surface, the period of heating includes an initial time t_i after which vaporization begins. Let us note that the definition of the onset of vaporization is rather conditional in view of the fact that diffusive vaporization occurs at any temperature. However, since this type of vaporization proceeds at an extremely slow rate, we may neglect the motion of the vapor front here.

The surface temperature which rises to such a value that the pressure of saturated vapors begins to exceed the pressure of the environment is taken as the point of onset of intensive vaporization into the gaseous medium (under normal conditions, this is the vaporization temperature T_v). The gas dynamic ejection of vapors then begins and the plume of erosion products appears. This is the condition which determines the experimental values of q_c and t_i.

At comparatively low laser power densities the vapors are transparent and the target surface freely absorbs the incident radiation. The vaporization wave propagates into the metal target and the target vaporizes under the conditions at which the vapors do not shield the surface. In such conditions of metal disintegration, the thermal model presented in papers [20, 21] works fairly well. This model involves the solution of a one-dimensional heat-transfer equation with consideration for the moving boundary of vaporization (vapor front). Here, the vapor front velocity is assumed to be exponentially dependent on surface temperature, but the role of the target environment is not taken into account whatever. Other workers, for example, A. A. Golubeva and V. S. Savinich [21], have further developed this model. They investigated the motion of the melting interface in the target and obtained the conditions for the steady-state temperature.

As an example, we shall consider the dynamics of heating and vaporization of an aluminum target, proceeding from the solution of the nonsteady-state heat-transfer equation with regard to the solid and the liquid phase. The equation stated in the form similar to that presented in paper [21] is subject to nonlinear boundary conditions at the moving fronts.

The calculations have been made with consideration for the difference in thermal parameters between the solid and the liquid phase of aluminum [22]. Fig. 5.6 illustrates the calculated results for absorbed power densities q of 10, 1, and 0.1 MW/cm^2. From the time dependence of the target surface temperature (Fig. 5.6*a*) it is evident that the time of onset of vigorous vaporization is $t_i \sim q^{-2}$ (arrows indicate that the surface reaches its vaporization temperature $T_v = 2\,330$°C). After this, the stage of heating continues until the power coupled to the target becomes equal to the power going into the vaporization wave to enable it to move at a constant speed. Now the melt thickness counted off from the vapor-liquid interfa-

ce reaches its steady-state value and the vaporized layer thickness grows at a constant rate (Fig. 5.6*c*).

The steady-state temperature of the target surface increases with the absorbed power density. The overheating with respect to T_v can be rather significant. From Fig. 5.6*b* which illustrates the energy balance as a function of time, it is seen that at the initial stage of absorption, the laser energy goes into heating the target material (thermal energy amounts to 100%). At the instant (marked with a cross in Fig. 5.6*a*) when the melt front starts moving, the energy expended on the melt front motion grows with depth into the specimen.

It is worthy of note that the observed peak of the share of energy that goes into melting the material reaches 22% for all power densities. But this peak of absorbed energy sets in at the instant when the melt thickness is still much below its limiting value specific to the steady-state conditions of interaction. This means that before the fusion front penetrates through the material to a significant depth, the surface starts to vaporize, so that a large amount of laser energy is inefficiently lost through vaporization. A possible way to achieve larger penetration of the fusion front without vaporization is to deliver lower peak powers per unit area and simultaneously stretch the pulse length (see Fig. 5.6*c*). In this case, the steady-state value of the melt thickness sharply increases. It is thus in principle possible to select the optimal conditions of heat treatment of the workpiece to the desired depth.

The above results relate to the time-constant irradiance, with the laser radiation assumed to be totally absorbed at the vapor-liquid interface. But even if account is taken of the abrupt changes in the thermal conductivity, heat capacity during melting, and evolution of the latent heat of melting, the dependence of the surface temperature on q and t strongly deviates from the relation $T \sim q\sqrt{t}$.

Thus, the results calculated at constant values of the thermal coefficients and represented in Fig. 5.6*a* by a dash line for $q = 1$ MW/cm^2 reveal that neglect of the temperature dependence of these coefficients can introduce a few times larger errors in the estimates of the time of onset of vaporization and, hence, of plasma generation.

Most metals subjected to melting display a decrease in the thermal diffusivity that determines the effective depth of heating of a specimen. This leads to an increase in the rate of heating and decrease in the time of onset of vaporization and plasma wave excitation. Apart from the temperature dependence of the thermal parameters of a target material, other factors, too, cause the surface temperature to vary in a different manner rather than as the square root of time, thereby disturbing the process of melting. These are the variation of power density with time and the behavior of the absorptivity and its

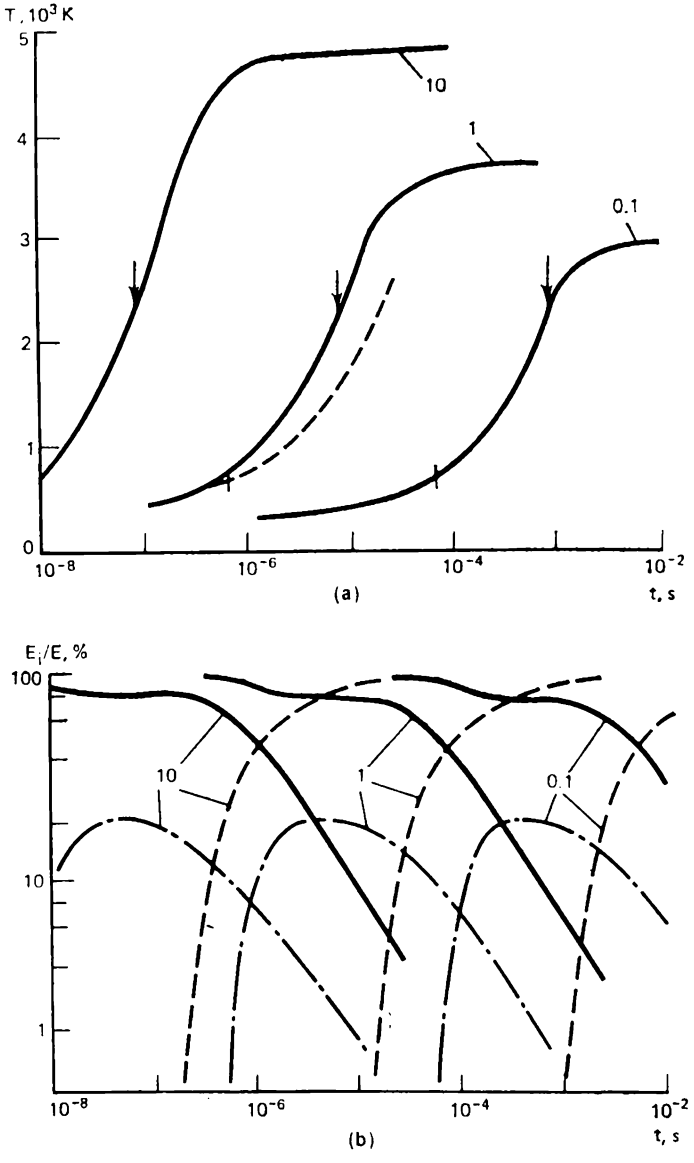

variation with temperature. Therefore, in selecting the optimal conditions for the specific process of metalworking, one must consider most thoroughly the temperature dependence of the thermal and optical parameters of the target material on temperature.

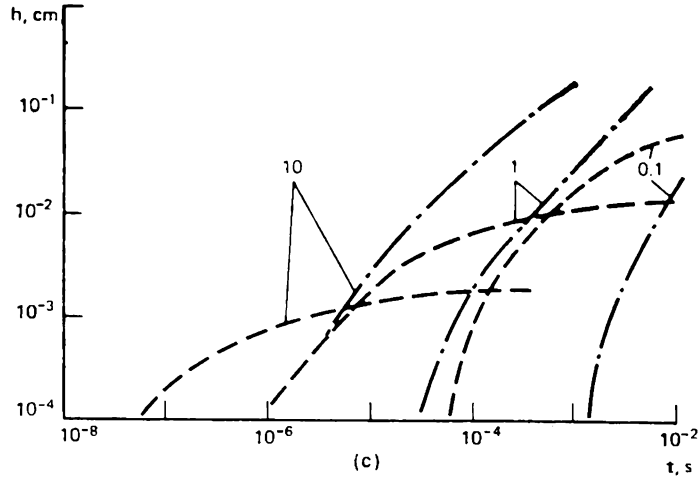

Fig. 5.6. Plots illustrative of the time-dependent parameters of an aluminum target at absorbed laser power densities q = 10, 1.0, and 0.1 MW/cm^2: (*a*) temperature; (*b*) thermal energy (—), energy of melting (— · —), and energy of vaporization (— — —); (*c*) thickness of molten layer (— — —) and vaporized layer (— · —)

But the choice of the optimal conditions of metalworking can be limited to a large degree by the potentialities of laser setups and rather rigid requirements on their parameters. The temporal pattern of a laser pulse depends on the type of laser and the mode of laser operation [23]. For convenience, it will be appropriate if we divide laser pulses into two groups, short pulses of about 1 μs duration, with peak power densities ranging from 10^7 to 10^9 W/cm^2, and long pulses with 10^2-10^3 μs duration and power densities of about 10^6 W/cm^2.

An important parameter from the viewpoint of effective application of lasers in material processing is the reflectivity R of a metal surface. Its value actually determines the amount of absorbed irradiance and, hence, the absorption efficiency of the target surface. The reflectivity generally depends on many factors, including the degree of surface treatment and the presence of oxide films on the target surface. Many metals exhibit a number of common features. For example, the reflectivity of all metals grows with the wavelength in the far IR region. For wavelengths in excess of 5 μm, R for almost all metals exceeds 90% [23]. In the far infrared, the reflectivity is a function of the electrical conductivity of metals; the value of R grows with conductivity. Therefore, the use of lasers emitting at shorter wavelengths, at which the value of $1 - R$ is much higher, looks more promising. However, during the dwell time of the pulse,

the energy coupled into the workpiece heats the surface and its conductivity decreases, with the result that R drops off and promotes a more effective energy absorption. This feature makes CO_2 lasers attractive for use in metalworking.

As regards long pulses which encourage intensive vaporization as they interact with materials, the thermal model alone cannot disclose the entire complex picture of interaction. Along with this model which accounts for the dynamics of heating, temperature distribution in a solid, and motion of phase boundaries, we need to employ an additional model of radiative gas dynamics to describe the process of vapor motion and, in general, the flow set up in the target environment. The boundary conditions required to solve the gas dynamic problem are found from the solution of the gas kinetic problem for the Knudsen layer. The input parameters for the latter problem are the velocities in the gas dynamic region (obtained from the solution of the set of gas dynamic equations) and target surface temperatures determined from the solution of the heat transfer equation. S. I. Anisimov et al. [1] have considered the gas dynamic problem on boundary conditions with vaporization in a vacuum, and C. J. Knight [24] generalized this problem for the case of vaporization with back pressure. The most complete model for the heat transfer problem related to the radiative gas dynamic problem by boundary conditions has been set forth in papers [25-27]. But we should note that there is an alternative model which assumes that vaporization is volumetric and the temperature beyond the quasi-equilibrium vapor zone is equal, at a definite pressure, to the equilibrium temperature at the liquid-vapor interface. However, certain circumstances do not yet allow us to draw an unambiguous conclusion in favor of any of these models. On the one hand, theoretical models embody the uncertainty of the temperature dependence of the target surface reflectivity and the thermal properties of the vapor and condensate. On the other, experimental measurements are liable to errors in the pressure, surface temperature, pulse shape, and irradiance distribution over the focused spot.

As the surface starts to vaporize, the jet of vapors moving from the target expands in the environment. A major share of energy absorbed at the surface is now spent on converting the target material to vapors. At this stage of vaporization, the flow pattern depends on the pressure and composition of the gas surrounding the target, apart from the factors mentioned above. Next a shock wave builds up in the flow, the intensity of which grows with the thrust of vapors spreading away from the surface. For most materials interacting with laser beams of moderate power densities, this flow exhibits high temperatures in the order of a few thousand degrees at pressures approaching a few tens of atmospheres. The rate of expansion of the flow carrying along the blowoff material is a few hundred meters per second.

Under definite conditions, the vapor begins to absorb the incoming laser light, so that its temperature and ionization continue to increase. The thermal radiation of the plume now plays a significant role: it determines both the energy lost in the external medium and the behavior of the absorbed radiation front. The collective effect of the energy transfer by thermal radiation and the gas dynamic energy transfer thus becomes dominant.

It is not only the conditions of heating and vaporization that determine the plasma wave excitation, but also the pattern of the flow being set up and, which is of particular importance, the dependence of the absorptivity on the temperature and density of target material vapors. In Fig. 5.7 are shown the plots of the spectral absorption coefficient A of an aluminum plasma at density $\rho = 10^{-3}$ g/cm^3 and temperatures T equivalent to 0.316 and 1 eV (in the region of first ionization of the aluminum plasma). These data are taken from work [28] which presented the calculated values of the absorption coefficient with consideration for such elementary processes as inverse Bremsstrahlung (absorption by electrons in the field of neutral atoms and ions), photoionization, and bound-bound transitions

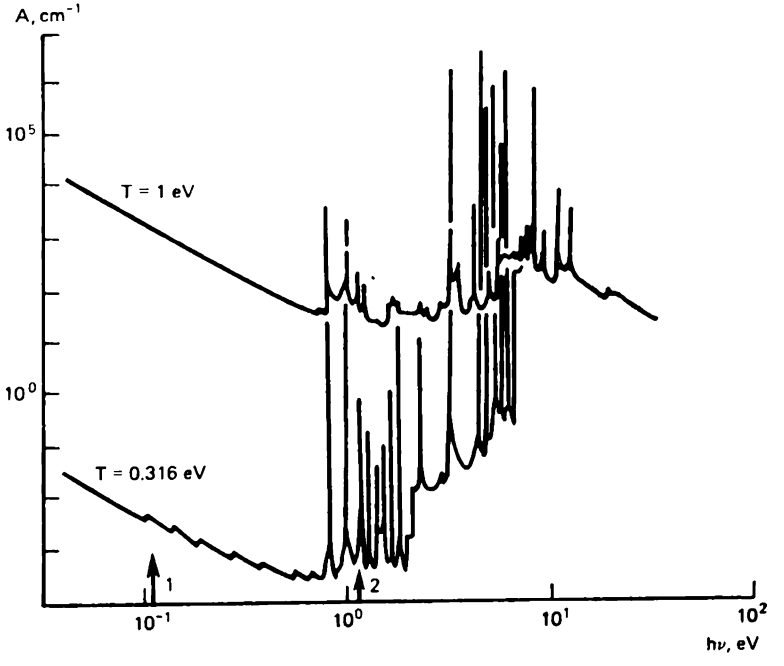

Fig. 5.7. Spectral absorption coefficient of aluminum plasma at a density of 10^{-3} g/cm^3 as a function of quantum energy $h\nu$: (*1*) and (*2*) quantum energy at CO_2 laser frequency and Nd-doped laser frequency respectively

with regard to spectral line spreading. Referring to Fig. 5.7, it follows as an important consequence that the absorption coeffcient in the region of first ionization sharply increases by a few orders of magnitude. The result is a fairly fast shielding of the target surface since the optical thickness of the plume rapidly grows at a relatively slow rate of temperature rise. This leads to a strong reduction in the effective reflectivity which is now dependent on the absorption in the plasma region rather than at the surface.

Surface shielding conducive to laser light absorption persists for a short time as against the characteristic gas-dynamic time. In the literature on the subject this type of absorption has received a widely used name *flash absorption.*

The absorption coefficient grows with lasing wavelength, therefore the power density thresholds for the plasma wave ignition by CO_2 laser pulses are lower than they are in the case of interaction of Nd-doped laser pulses. So, despite a hindered heating of the target by the long-wave radiation at the initial stage of interaction because of a large value of reflectivity, the laser energy absorbed by vapors may activate a plasma early in the pulse.

The temperature of the plume absorbing the laser radiation grows from a few thousand degrees to a few electron volts; the pressure rises to a few hundred atmospheres. Under the prescribed conditions of interaction, the plasma can appear at a definite power density q^* after an interaction time t^*. Let us note that laser pulses excite a plasma wave in the medium with a target at much lower power densities than in the medium without a target; this phenomenon received the name *low-threshold gas breakdown.* The heated vapors begin to absorb laser radiation at appreciably lower temperatures than the environment without a target because the ionization potential for most materials is much smaller than that for gases, though this effect is not yet well known.

The dynamics of the plume after plasma generation by laser pulses greatly depends on the ambient pressure and the kind of atmosphere surrounding the target and also on the spot diameter and temporal structure of the pulse.

At relatively low power densities, $q = 1\text{-}10$ MW/cm^2, and long laser pulses, $t = 10^{-4}\text{-}10^{-3}$ s, when the effect of two-dimensional motion becomes appreciable, the plume assumes the form of a nonadiabatic plasma jet. The factors accounting for the complex physical pattern of development of the laser-supported plume are the following: the two-dimensional motion of the plasma, highly nonadiabatic jet due to laser energy absorption, and nonsteady-state behavior of the jet because of the time dependence of the laser power density. We shall look at some important features of the laser-induced erosion jet using the results reported in work [29]. The authors of this work have studied the character of the interaction process conditioned by

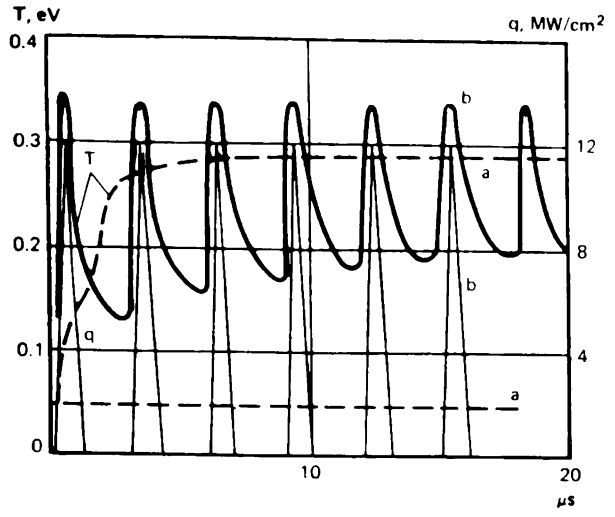

Fig. 5.8. Time dependence of laser energy density ($\lambda = 1.06$ μm) and temperature at the center of focused spot ($D = 1$ mm) on a bismuth target in air; (*a*) continuous laser operation; (*b*) repetitive-spike laser operation

the temporal pattern of the pulse that models the steady-state, quasisteady-state and spiking operation of a laser emitting at 1.06-μm wavelength and delivering in each type of operation an average power density of 2 MW/cm² to a focused spot of 1 mm in diameter on a bismuth target in the air. Fig. 5.8 illustrates the dwell time curves for the power density and temperature at the target surface in the center of the focused spot for continuous operation (dash lines) and spiking operation with a duty cycle of 1/3 (solid lines). The surface struck by a steady-state pulse is found to reach its quasisteady-state temperature after 4 μs; the plume of the blowoff material has the form of an adiabatic jet emitted into the air.

In Fig. 5.9*a* is shown the temperature distribution in a plume along the beam axis at different moments of time. As seen, the normal shock wave (Mach shock) is set up at a distance of about 4 mm from the target surface in a time of about 20 μs. The plume now weakly shields the target surface (the optical thickness is $l \approx 0.1$ mm); the pressure at the vaporizing surface is ~ 45 at.

In the case of spiking operation, each spike produces a plume that effectively shields the target surface ($l \approx 1$ mm), so that vaporization ceases and the target cools down (see Fig. 5.6). The pressure at the surface when it absorbs a maximum of power per unit area reaches a few hundred atmospheres. A highly nonadiabatic behavior of the temperature profile along the z axis is apparent (Fig. 5.9*b*).

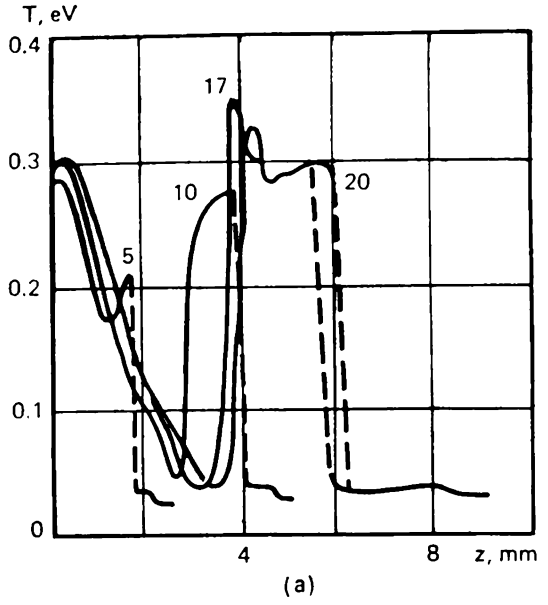

Fig. 5.9. Temperature distribution along the symmetry axis z on exposure of a bismuth target to pulses from an Nd-doped laser operating in CW mode (a) and repetitive-spike mode (b). Digits denote the time of interaction (μs)

It is obvious that the absorbed laser radiation strongly heats the plasma (up to 1 eV). But during the space width the plasmoid formed near the surface has the time to expand, and before the next spike arrives, the plume becomes transparent to the incident radiation.

The normal shock wave where the temperature is at a maximum weakly shields the target since the vapor density in this area is low. It should be pointed out that the spiking mode of irradiation makes itself felt only in the initial section of the jet (as far as the rarefaction region that is in the order of the focused spot diameter), and the shock wave hardly responds to the variation of pressure at the target surface. That this is so is clearly seen from Fig. 5.10 which demonstrates the temperature and density distributions at an instant $t = 30$ μs after the start of the pulse for the cases of the continuous laser interaction (a) and spiking laser interaction (b) with the target.

In these regions of operation, the laser-induced plasma mainly shields the target surface and reduces the efficiency of interaction. The release of the absorbed energy by the plume is insignificant since the optical thickness of the plume is rather small, and the tempera-

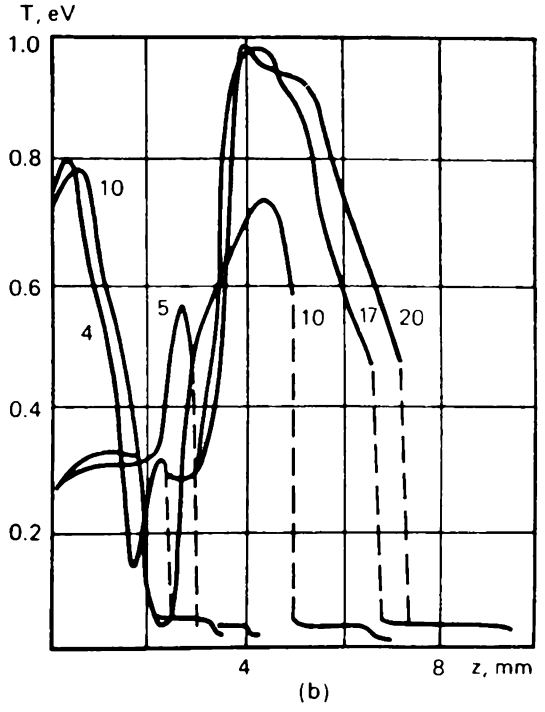

(b)

ture is insufficiently high ($\sim$ 1 eV) for the thermal radiation of the plasma to be comparable in power density to the laser radiation. Besides, during plasma generation, a large amount of laser energy is lost through ionization, therefore the conversion of laser radiation to thermal radiation of the plasma is ineffective.

At high values of laser power density ($q > 100$ MW/cm^2), the plasma effect dominates. Here the plasma appears at the stage of one-dimensional ejection when the surface temperature is still far from reaching its steady-state value predicted by the heat source model. The excited plasma extends above the target surface and the laser-supported absorption (LSA) wave propagates back toward the laser. Of importance for laser material processing is the fact that the laser beam can generate a plasma at the instant when the thickness of the vaporized material is still so small that no damage to the surface is discernible. But since the temperature reaches high values (equivalent to a few eV) and the pressure runs into the kilobars, the plasma region expands fast back toward the laser and also in the radial direction at a speed of several kilometers per second. A number of works analyzed this type of laser interaction, for example [27, 30, 31].

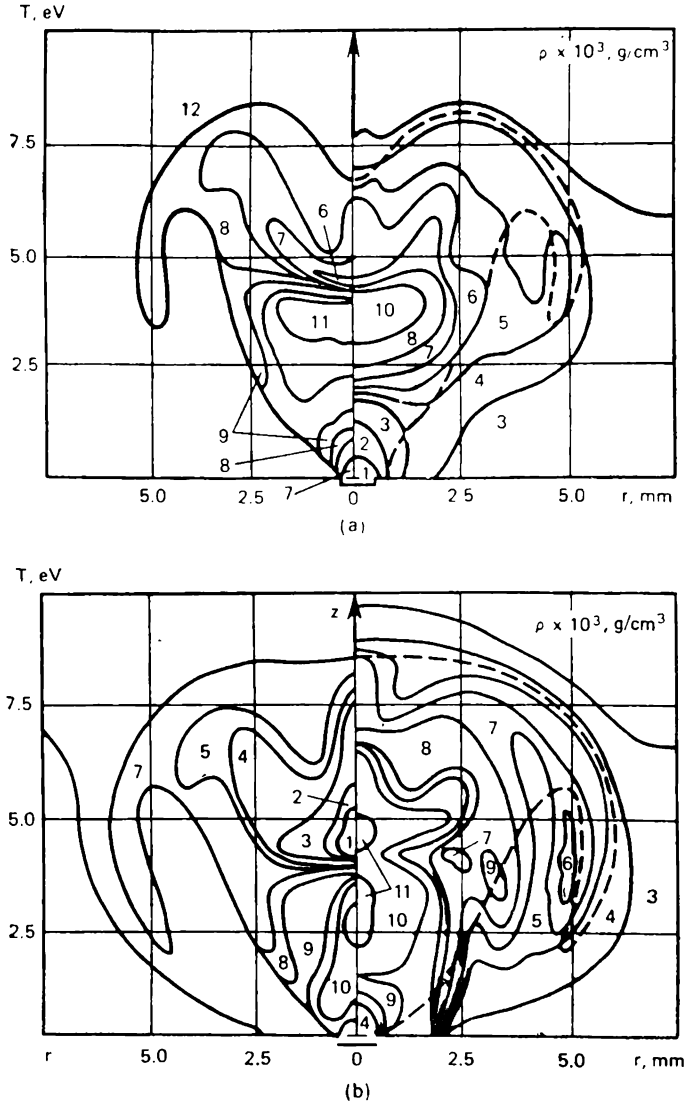

Fig. 5.10. Temperature field and density 30 μs after the start of the pulse from an Nd-doped laser operating in CW mode (*a*) and spike mode (*b*). Temperature T (in eV): 1, 1; 2, 0.8; 3, 0.6; 4, 0.55; 5, 0.5; 6, 04; 7, 0.3; 8, 0.2; 9, 0.15; 10, 0.1; 11, 0.05; 12, 0.025. Density ρ (in 10^{-3} g/cm³): 1, 10; 2, 3; 3, 1.3; 4, 1; 5, 0.8; 6, 0.6; 7, 0.5; 8, 04; 9, 03; 10, 0.2; 11, 01

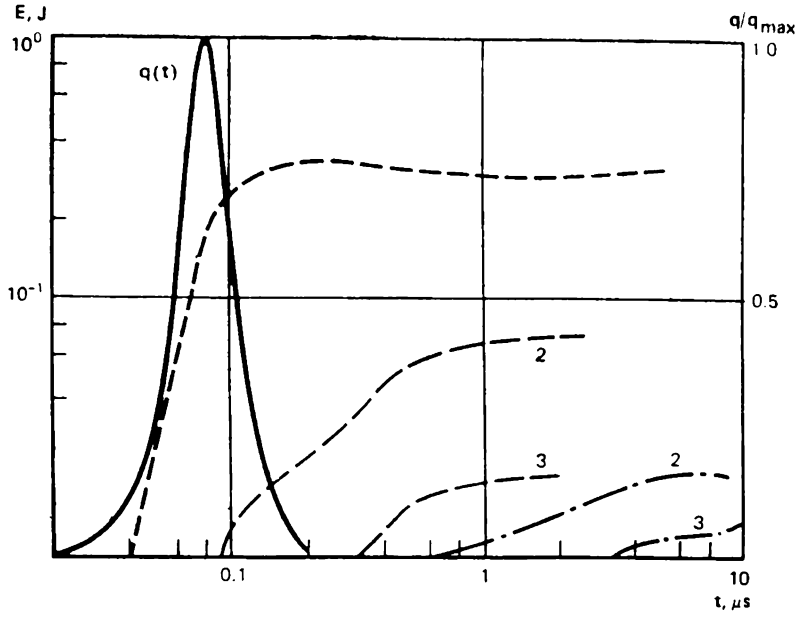

Fig. 5.11. Time dependence of total plasma plume energy E_p (*1*), energy E_a (*2*) re-emitted in air, and energy E_t (*3*) re-emitted on an aluminum target struck by an Nd-doped laser pulse. Dash line and dot-and-dash line represent data obtained with consideration for Planck's mean absorption coefficient and for spectral behavior of the absorption coefficient

Figure 5.11 displays the shape of a laser pulse of 1.06 μm wavelength radiation interacting with an aluminum target in air at power density $q = 600$ MW/cm^2 uniformly distributed over the spot of 0.65 mm radius [31]. The energy plots reveal that the plume emits merely 7% and 5% of its entire energy into the environment and on the target surface respectively. However, the characteristic time is much longer than the pulse dwell time and the interaction zone can markedly exceed the spot of irradiation in size. The dash lines of Fig. 5.11 are the plots of energies emitted into the environment and on the target surface. These energy estimates are obtained from the solution of the heat-transfer equation with allowance made for Planck's mean absorption coefficient. Here, neglect of the spectral dependence of the absorption coefficient appreciably overstates the energy loss by thermal radiation because the capacity of cold air for short wavelength quanta is not given consideration in the context of the "gray body" approximation. Taking into account the spectral response leads to an increase in the de-excitation time since the plume cooling through thermal emission within the region of hot and low-density plasma proceeds at a lower rate.

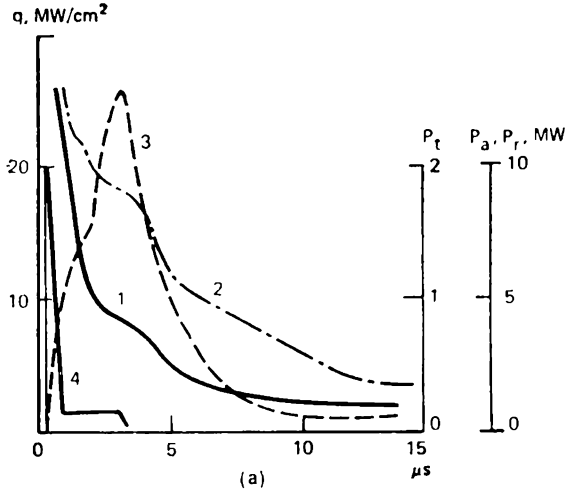

Fig. 5.12. Time dependence of the power of radiation re-emitted by the plasma plume on to a target, P_t (*1*), into air, P_a (*2*), and in radial direction, P_r (*3*), in interaction of a CO_2 TEA laser pulse with an aluminum target

The role of the radiative transfer of energy from the plasma becomes significant at relatively low power densities ($q \approx$ 10 MW/cm²) and large areas of focused spots. Work [27], for example, has considered the case of plasma generation using a CO_2 TEA pulse that delivered a total of 700 J of energy to a 32-cm²

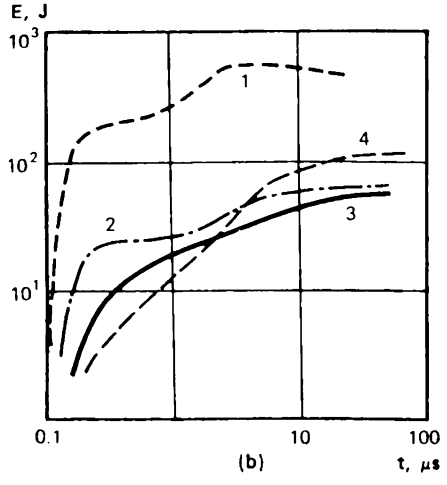

Fig. 5.13. Time dependence of total energy of a plasma plume, E_p (*1*), its kinetic energy E_k (*2*), and energy re-emitted on to a target, E_t (*3*), and into environment, E_a (*4*)

spot on an aluminum plate held in the air [32]. The pulse produces a plasma in ~ 1 μs and then maintains a high temperature in the plasma near the target surface.

The power of plasma radiation re-emitted in the radial direction is fairly small since during the pulse dwell time the plasma moves away from the surface for a short distance of about 7 mm. The radiation loss is mainly brought about by the re-emission of energy from the plasma on the target surface and toward the laser. The total power of radiation from the plasma over the entire spectrum approaches 5 MW during the time of pulse interaction, so that this power per unit area is less than 0.2 MW/cm^2 and is much lower than the laser power density (Fig. 5.12).

Figure 5.13 illustrates how the total energy of the plasma plume, its kinetic energy, and energy re-emitted into the environment and on to the target surface vary with time. The internal energy of the plume is seen to grow markedly after plasma activation. The total energy re-emitted on the surface is of the order of 8%, which is in good agreement with an experimental value of about 6% [32]. The entire energy lost by the plume through radiation amounts to about 15%, and the time of radiative transfer of energy from the plasma to the surface much exceeds the pulse duration.

References

1. S. I. Anisimov, Ya. A. Imas, G. S. Romanov, et al. *Interaction of high-power radiation with metals.* Moscow, Nauka, 1970 (in Russian).
2. V. A. Batanov, F. V. Bunkin, A. M. Prokhorov, et al. *Vaporization of metal targets by high-power optical radiation.* Zhurnal Eksper. i. Teoretich. Fiziki, 63: No. 2, p. 586, 1972.
3. J. F. Ready. *Effects of high power laser radiation.* New. York, Academic Press, 1971.
4. S. I. Anisimov, S. M. Golberg, B. A. Malomed, et al. *Two-dimensional, weakly supercritical structures in laser waves of sublimation.* Dokl. AN SSSR, 262; No. 5, p. 1117, 1982.
5. F. V. Bunkin and A. M. Prokhorov. *Use of a laser as a source of jet thrust.* Uspekhi Fizich. Nauk, 119: No. 3, p. 425, 1976.
6. A. P. Guskov and A. A. Uglov. *Kinetic model of metal surface vaporization in gaseous atmosphere.* Zhurnal Tekhnich. Fiziki, 50: No. 10, p. 2050, 1980.
7. A. A. Uglov and A. P. Guskov. *On metal vaporization in the atmosphere of cover gas.* Fizika i Khimiya Obrabotki Materialov, No. 6, p. 49, 1980.
8. B. Ya. Lyubov. *Theory of crystallization in large volumes.* Moscow, Nauka, 1975 (in Russian).
9. B. Ya. Lyubov and E. N. Sobol. *Quasistationary creation of a hole in a material vaporized by laser radiation.* Zhurnal Tekhnich. Fiziki, 46: No. 7, p. 1517, 1976.
10. B. Ya. Lyubov and E. N. Sobol. *Quantitative analysis of the kinetic mechanism of laser-induced metal film vaporization.* Fizika i Khimiya Obrabotki Materialov, No. 6, p. 8, 1976.
11. B. Ya. Lyubov and E. N. Sobol. *Nonsteady-state vaporization of a semi-infinite solid by high-power radiation flux.* Fizika i Khimiya Obrabotki Materialov, No. 5, p. 3, 1975.

12. A. A. Uglov and V. A. Grebennikov. *Interaction of laser radiation with porous materials.* Kvantovaya Electronika, 8: No. 11, p. 2479, 1981.
13. A. A. Uglov and V. A. Grebennikov. *On interaction of laser radiation with porous materials.* Fizika i Khimiya Obrabotki Materialov, No. 5, p. 144, 1980.
14. A. A. Balatskiy, A. A. Uglov, and T. Ya. Lobacheva. *On liquid flushing from the melt region in metal melting by laser radiation.* Fizika i Khimiya Obrabotki Materialov, No. 5, p. 9, 1976.
15. A. V. Burmistrov. *On the role of bubbling in the interaction of high-power radiation with a material.* Zhurnal Priklad. Mekhaniki i Tekhnich. Fiziki, No. 3, p. 35, 1979.
16. C. Cercignani. *Theory and application of the Boltzmann equation.* Edinburgh and London, Scottish Academic Press, 1975.
17. L. D. Landau and E. M. Lifshits. *Hydrodynamics.* Moscow, Nauka, 1986 (in Russian).
18. Ya. B. Zeldovich and Yu. P. Rayzer. *Physics of shock waves and high-temperature hydrodynamic effects.* Moscow, Nauka, 1966 (in Russian).
19. Yu. P. Rayzer. *Foundations of modern physics of gas discharge processes.* Moscow, Nauka, 1980 (in Russian).
20. B. Ya. Lyubov and E. N. Sobol. *A heat source model for predicting surface vaporization of metals under the effect of concentrated energy fluxes.* Fizika i Khimiya Obrabotki Materialov, No. 1, p. 12, 1979.
21. A. A. Golubeva and V.S. Savinich. *On nonsteady-state vaporization of a plate.* Teplofizika Vysokikh Temperatur, 15: No. 3, p. 674, 1977.
22. I. K. Kikoin (ed.) *Tables of physical quantities.* Reference Book. Moscow, Atomizdat, 1976 (in Russian).
23. J. F. Ready. *Industrial application of lasers.* New York, Academic Press, 1978.
24. C. J. Knight. *Theoretical modelling of rapid surface vaporization with back pressure.* AIAA Journal, 17: No. 5, p. 519, 1979.
25. A. N. Kokora, G. S. Romanov, Yu. A. Stankevich et al. *Laser-induced plasma and its effect on the thermal processes in the laser-metal interaction zone.* Fizika i Khimiya Obrabotki Materialov, No. 1, p. 34, 1986.
26. G. S. Romanov and Yu. A. Stankevich. *Numerical modeling of gas dynamic process in interaction of laser radiation of moderate power density with a metal target in air.* Fizika Goreniya i Vzryva, 17: No. 6, p. 77, 1981.
27. M. A. Elyashevich, G. S. Romanov and Yu. A. Stankevich. *Calculation of the parameters of plasma-erosion jets with consideration for the spectral dependence on the emission characteristics of plumes.* In Proceedings of the 4th All-Union conference on "Dynamics of emitting gas". Moscow State University Publishing House, v. 1, p. 90, 1981.
28. G. S. Romanov, K. L. Stepanov, and M. I. Syrkin. *Optical properties of high-temperature aluminum plasma.* Optika i Spektroskopiya, 53: No. 4, p. 642, 1982.
29. G. S. Romanov and Yu. A. Stankevich. *Some features of formation of a plasma-erosion jet in interaction of a spiking laser with a target.* VINITI, No. 1973, 82nd dispatch, 1982.
30. G. S. Romanov and Yu. A. Stankevich. *Calculation of a recoil momentum arising in interaction of laser radiation with an absorbing target surface in air.* Fizika i Khimiya Obrabotki Materialov, No. 4, p. 16, 1981.
31. A. M. Bonch-Bruevich, V. I. Zinchenko, Ya. A. Imas, et al. *Experimental and theoretical studies on laser-induced plasma during developed absorption.* Zhurnal Teknich. Fiziki, 51: No. 5, p. 919, 1981.
32. R. W. Mitchell, R. W. Conrad, and E. J. Roy. *The role of radiative transfer in pulsed laser plasma target interaction.* JQSRT, 20: No. 3, p. 519, 1978.

Chapter 6

LASER-INDUCED PLASMA EFFECTS AND THERMOCHEMICAL PROCESSES

Material processing with lasers refers to a number of industrial operations associated with heating, melting, and vaporization of workpieces. These operations include heat treatment (surface hardening), annealing, welding, cutting, hole drilling (piercing), etc. A laser can work a material in any atmosphere and thus offers certain advantages over electron beam processing which must be done in a vacuum. Nevertheless, some laser treatment operations need be performed in a vacuum or in a shielding atmosphere of inert gases to minimize the oxidation of reactive metals, for example, in welding, and to raise the threshold for kindling the LSA wave above the interaction region. Jets of cover gases are often used in CO_2 laser metal welding to provide protection against oxidation and to disperse the plasma in the vapor plume that shields the target from the laser beam and inhibits deep penetration.

It is of practical importance to raise the question of how to take advantage of the plasma for its thermochemical and thermal interaction with the target in the most effective way. As regards lasers emitting at both 1.06 and 10.6 μm, the threshold for laser-induced gas breakdown decreases with increasing ambient pressure. Experiments show that the use of a gaseous atmosphere of a controllable composition and pressure near a target surface can change the character of laser-material interaction. This offers the possibility for evolving new processes of material treatment, namely, the processes of laser-plasma treatment since plasma is found to play a substantial role in imparting certain surface properties to a material [1].

A trend today in laser technology is to make the best use of the processes that initiate thermochemical reactions to effect the desired surface treatment in an oxidizing atmosphere or in any suitable gas at laser power densities which do not cause gas breakdown. In the last years this problem has been treated in many works, for example, in [2-4].

6.1. LASER-MATERIAL INTERACTION AT HIGH AMBIENT PRESSURE

A high-power laser beam focused to a spot in a high-pressure gaseous medium is able to trigger an avalanche gas breakdown and a light flash called a *laser spark* in the focal area. This phenomenon, discovered in 1962, has at once become the subject of extensive investigations which disclosed in a fairly short time both the conditions and mechanisms responsible for the origin of optical breakdown.

Optical breakdown in a gas develops at rather high threshold power densities ranging from 10^{10} to 10^{11} W/cm^2, which correspond to an electric field strength of $\sim 10^6$-10^7 V/cm. The breakdown threshold for most gases decreases in the conditions of an increased gas pressure and also on exposure of a gaseous medium to a microwave field or electric field. But even under these conditions the threshold is still high and, besides, it is a function of the laser wavelength.

Placing a solid target in the focal area of the laser beam and increasing the gas pressure cause the breakdown threshold to decrease by a factor of 10 to 100 as compared to that observed in a pure gas without the target. A CO_2 laser beam at $\lambda = 10.6$ μm was found to initiate a low-threshold gas breakdown in the vapors of the target material. A number of papers reported the results of experiments on laser-induced gas breakdown in metal vapors at the atmospheric pressure. For example, an incoming neodymium laser beam with a power density of about 2×10^7 W/cm^2 struck a discharge in air at the lens focus $\sim$ 10 mm distant from the target surface where the power density delivered by the beam approached 2×10^6 W/cm^2. In other experiments, millisecond pulses from a neodymium laser producing average power densities of (1-10) 10^7 W/cm^2 were used to investigate the LR interaction with molybdenum and corrosion-resistant steel in nitrogen at a pressure of (1-120) 10^5 Pa. The targets were held in a high-pressure chamber with two windows; the beam brought into sharp focus by a lens with $f = 150$ mm entered the chamber through one window and a photorecorder operated at a high-speed slow-motion camera traced the processes near the target surface through the other window. Experiments were also made to study the interaction of LR with dielectric plates.

Laser-material interaction at high ambient pressures leads to shielding of the interaction zone and to changes in the character of material disintegration. In the text below, we shall consider the results of experiments on the phenomena occurring above the specimen surface and also the changes caused by the joint action of the laser beam and plasmoid in the physical parameters of the surface layer. We shall also take a look at experiments conducted with nitrogen, argon, and helium since each of them displays its specific features in the target treatment processes.

Development of opaque plasma in nitrogen. Studies on the process of plasmoid generation were undertaken with the aid of high-speed photography. The time span between frames was from 15 to 80 μs depending on the desired detail of study of one process stage or another. The experimental data have revealed that 30-50 μs after the start of the LR interaction a plasma cloud appears above the surface and almost entirely shields the interaction zone from the laser beam. The degree of target shielding conditionally specified in terms of the mass of the material removed strongly depends on pressure changes and, somewhat weaker, on laser power density. The plasma cloud that forms near the target surface moves toward the laser delivering $\sim 10^6$-10^7 W/cm^2 at a speed of 2-5 m/s. Its speed rises to a maximum value of $\sim$ 5 m/s at the end of the pulse and then begins to drop off. The lifetime of the plasmoid before its complete expansion is almost twice as long as the pulse duration ($\sim$ 0.8 ms) for molybdenum and corrosion-resistant steel. For dielectrics, this time is longer, about 4 ms. The cross-sectional dimension of a plasmoid above a metal target changes with time: first, it increases, then diminishes to a certain value, and, later, varies little until vanishes completely. This points to the fact that the pressure in the plasmoid at the end of the pulse differs little from the gas pressure in the chamber.

Laser-material interaction in nitrogen. The target shielding by plasma sharply reduces the ejection of disintegration products whatever the material of the target. A laser beam delivering a power density in the range 10^6-10^7 W/cm^2 to a plate 1-2 mm thick at a nitrogen pressure of 2-3 MPa pierces a through hole and insignificantly melts the material on the surface. In the given range of power densities, an increase in the nitrogen pressure leads to an almost complete shielding of LR. In this case, the target surface only gets "burnt", i.e. covered with a thin layer of combustion products, and generally has no microregions with small droplets of melt. But the size of the zone of laser-material interaction increases several times: at an initial focal spot radius of 0.25 to 0.30 mm, the diameter of the burnt zone reaches a few millimeters. It is natural to attribute this fact to changes in the spatial and temporal characteristics of the heat source acting on the target surface after onset of shielding. As the plasma begins to shield the laser beam, the power density of the heat source on the surface falls off and the effective radius of the HAZ increases markedly as against the focal spot radius r_f. A possible mechanism responsible for this effect is the thermal defocusing of LR as it passes through the plasma region, which thus reduces the heat power density at the surface. On the other hand, since the plasmoid size exceeds the focal spot size during the pulse dwell time, the plasma re-emits the absorbed laser energy on to a larger surface area, thereby augmenting the interaction region. The intensity of

the heat source on the material surface must decay with time according to the relation $\sim$ arccot $(t/t_0)^{1/2}$, where t_0 is the time it takes the material to reach the melting temperature. As the plasma cloud moves further away from the target, the maximum value of q of the surface heat source decreases. In the plasma formed near the target surface, self-sustained oscillations can be set up [5, 6]. Let us consider this phenomenon in more detail.

Researchers of [6] detected the oscillatory state in a laser-induced plasma at high pressures of N_2 and CO_2 by testing the plasma wave in its longitudinal direction. A neodymium laser beam was allowed to travel to a recorder through a hole in a plate near which the beam ignited the plasma plume [7]. Using a probe technique, workers of [5] disclosed an oscillatory character of time-dependent changes in the physical parameters of plasma near a copper target surface both in nitrogen at 1-8 MPa and in carbon dioxide at 0.5-5.5 MPa. The obtained experimental data allow us to conclude that the LR-plasma-target system can pass to an oscillatory state under definite conditions [8].

As reported in [9], for the case of interaction of LR with metals and dielectrics in gases of enhanced pressure, the power density threshold, q, for breakdown initiation and also the pressure p become conditional and are not amenable to a unique assessment because of the presence of the material vapors and cover gas in the focal area. This fact can probably account for why there is a certain intermediate stage of the process between the developed optical breakdown at $q > 3 \times 10^6$ W/cm^2 and ordinary melting or vaporization of the material at $q \ll 3 \times 10^6$ W/cm^2. At $q > 3 \times 10^6$ W/cm^2 and at a definite value of gas pressure p, the material surface rises to its vaporization temperature in time t_v and begins to vaporize, thus heating the cover gas. On the oscilloscope trace of Fig. 6.1*a*, this moment of time, including the time delay of plasma wave propagation from the target to the probe, corresponds to a probe current spike. The optical breakdown does not yet occur because the power density is not great and the degree of ionization is insufficient to trigger the avalanche process. Next the plasma formed partially decouples LR from the target surface, whose temperature drops off, vaporization then slows down and, hence, heating of the cover gas becomes less intensive. The wave with an increased concentration of charge particles thus gives way to the wave of a lower charge particle concentration. This corresponds to a decay of the probe current on the oscilloscope trace of Fig. 6.1*a*. The plasma then expands and becomes transparent to the laser pulse. The vaporization now grows in intensity and the process recurs in an oscillatory manner.

For a copper target, the period of oscillations of the probe current is $T_c = 50\text{-}60$ μs ($f_c = 16\text{-}20$ kHz), which differs somewhat from the period of changes in the optical density of plasma under the

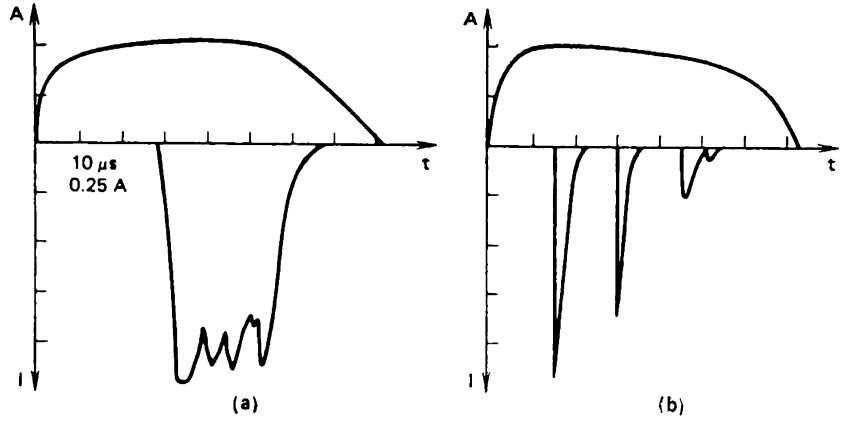

Fig. 6.1. Envelopes of the Nd-doped laser pulse (top) at $\lambda = 1.06$ μm incident on Cu in nitrogen at $p = 6$ MPa and oscilloscope traces of probe current (bottom); (*a*), $q \cong 3 \times 10^6$ W/cm^2; (*b*) $q \cong 1.5 \times 10^6$ W/cm^2

same conditions [6]. From the experimental values of the optical density of plasma, it is found that the free-running plasma frequency is $f_p = 10$ kHz. The values of this frequency calculated by the technique presented in [8] reach 7 kHz, which well agrees with experimental data.

With a decrease in q to 1.5×10^6 W/cm^2, the pattern of probe current fluctuations changes: the oscilloscope trace of Fig. 6.1*b* displays a few current spikes above the zero level. As the power density q drops further below 1.5×10^6 W/cm^2, this pattern of current fluctuations vanishes and only one current spike occurs, which is representative of the vaporized material ejection.

The studies on the parameters of the oscillatory process versus cover gas pressure disclose that in the range of N_2 pressures from 1 to 8 MPa and CO_2 pressures from 0.5 to 5.5 MPa it is the target material that plays a dominant role in initiating and maintaining the oscillatory state. The cover gas mainly affects the velocity of the blowoff material; an increase in the scatter velocity is probably responsible for the decay of the oscillatory state as the pressure of N_2 and CO_2 drops below 1 MPa and 0.5 MPa respectively. The probe current signals then vary in a stochastic manner [5].

There is negative feedback in the LR-target material system, which can be built via the material-vapor plasma, optical-breakdown plasma, or ejection products [10]. Depending on the feedback factor, such a system can pass to an unstable state, i.e. the state of self-sustained oscillations. Oscillatory phenomena can be of substantial importance in shaping the zone of laser-material interaction and can also be harnessed for control of the process.

Consider in brief the changes produced by the joint action of the plasma and LR in the surface layer of material. The distribution of surface microhardness H_μ in the zone of interaction of a laser beam with corrosion-resistant steel is shown in Fig. 6.2. As seen, the microhardness reaches a maximum value on the center line and decreases away from it down to an initial value of 200 MPa at the zone edges. Changes in the surface microhardness can be accounted for

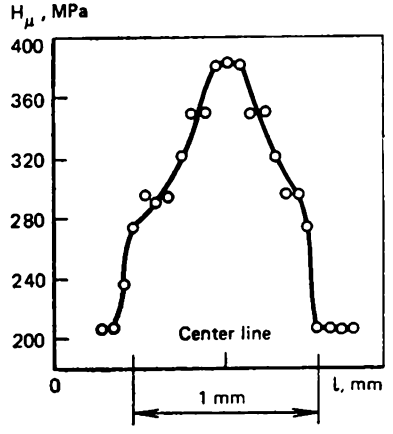

Fig. 6.2. Microhardness as a function of depth in the zone of interaction of an Nd-doped laser with corrosion-resistant steel in nitrogen at p = = 6 MPa after $\tau = 0.8$ ms

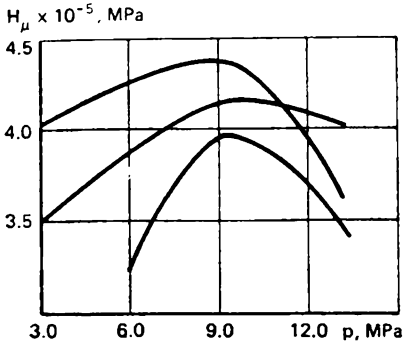

Fig. 6.3. Steel microhardness versus nitrogen pressure

by two causes: (1) structural modification due to high rates of heating and cooling of the surface layers; (2) surface nitriding.

A great deal of experimental work has been done to estimate the surface microhardness of steels treated in nitrogen at increased pressure. The plots of the surface microhardness of steel versus gas pressure in the steady conditions of laser interaction display peaks in the range 7.8.-8.0 MPa (Fig. 6.3).

The results of investigations on the interaction of pulses from a neodymium laser with a revolving corrosion-resistant steel specimen held in nitrogen and other gases were given in paper [11]. The pulse dwell time reached 0.7-1.0 ms, with the power density varying between 10^5 and 10^7 W/cm^2. The linear speed of travel of the specimen was varied from 15 to 40 m/s, which made it possible to determine the onset of plasma excitation accurate to 10-15 μs. It is found that at a nitrogen pressure of $\sim$ 8.0 MPa and power density of around 10^6 W/cm^2, the plasma formed above the surface begins to absorb laser energy not later than 50-200 μs after the start of the la-

ser pulse. With the pressure p and speed v kept constant, changes in q result in changed dimensions and shapes of the fusion regions on the surface. As the power density q decreases, the heat-treated region assumes an elongated form and its length increases until q drops to a certain value (Fig. 6.4). The length of the fusion region comes to 10-12 mm at an N_2 pressure of 2-3 MPa, $v \approx 25$ m/s, and $q \approx 10^6$ W/cm^2. When $p > 3$ MPa, this length decreases with increasing q. When $q > 3 \times 10^6$ W/cm^2, $p < 3.0$ MPa, and $v \approx 20$ m/s, the heat-treated region develops breaks at some points.

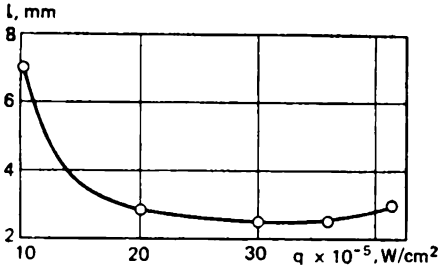

Fig. 6.4. Length l of a fusion region on the surface of a material target moving at $v = 10$ m/s in nitrogen at $p = 3$ MPa as a function of q

The state and structure of the material surface were estimated from changes in the microhardness of regions exposed to LR only, to both LR and plasma, and to plasma only. The measurements show that neither the joint LR-plasma action nor the plasma effect alone essentially contribute to changes in the microhardness if the metal surface is not molten. In the region where LR alone interacts with a specimen, whether moving or stationary, the microhardness grows. As the feed rate of the specimen rises, the microhardness decreases since the dwell time of the laser pulse incident on the given region of the surface gets shorter. The analysis of microhardness in heat-treated regions points out that at the specified values of q, p, and v, the steel microhardness grows mainly due to the plasma effect if the metal in the given region is molten.

Laser-material interaction in argon. Work [12] gives the results of experiments on the interaction of Nd-doped laser pulses at $q = 10^6$-10^7 W/cm^2 with 1-2-mm thick plates of aluminum, molybdenum, and corrosion-resistant steel and also with 2-mm thick graphite plates and thin polished-silicon plates about 10^{-1} mm thick in argon at pressures ranging from 0.1 to 13.0 MPa.

The laser-material interaction here essentially initiates gas breakdown at high pressures and supports a plasma cloud near the surface, the evolution of which determines the character of damage at the spot of incident radiation. These processes are typical of argon in the pressure range above 30 MPa. Experiments confirm that the physical properties of a material have a strong effect on the kinetic characteristics of the plasma cloud, such as the speed of travel, temperature, radiant emittance, and geometric dimensions. The material not only encourages the ignition of plasma near the target sur-

face but also definitely contributes to the development of the plasma plume. Such an effect exerted by the target is most appreciable at the initial stage of pulse interaction when the particles removed begin to form the plume that shields the target. Late in the pulse, this effect on the parameters of the plasma decreases.

A feature common to all the materials tested in the pressure range 0.1-13 MPa is that the target shielding inevitably occurs at a gas pressure of above 3 MPa if the power density exceeds $\sim 10^6$ W/cm^2. With other conditions being equal, an increased argon pressure causes the plasma cloud to increase in average diameter d_p and decrease in length. These changes, at least in the plasma plume diameter, are not monotonic. In particular, in the interaction of LR with metal targets, the plasmoid diameter reaches its maximum value at $p = 1$ MPa. Also, for metal targets, the length l of the plume monotonically grows with decreasing gas pressure. Similar, though less pronounced, regularities of changes in the plasma parameters show up in the interaction of neodymium laser pulses with metal and dielectric targets in nitrogen at increased pressures.

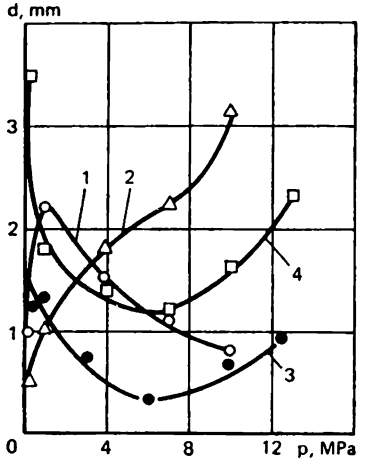

Fig. 6.5. Laser interaction zone diameter d as a function of argon pressure p on the surface of aluminum (*1*), graphite (*2*), molybdenum (*3*), and corrosion-resistant steel (*4*)

The ratio of the length of the plasma cloud to its average diameter can serve as an indirect characteristic of breakdown evolution. If $l \gg d_p$, the gas breakdown does not generally occur, but it does when $l \approx d_p$. This criterion is valid for both metals and dielectrics.

The parameters of the zone of laser-material interaction vary with increasing pressure of cover gases. There is a certain range of argon pressures at which the diameter d of the zone of laser interaction with metals is at a minimum (Fig. 6.5): $p \approx 5$-7 MPa for molybdenum and corrosion-resistant steel (for Al, however, d does not drop to a minimum even at 10 MPa). The diameter of the interaction region on a graphite target is seen to rise steadily with gas pressure. A change in d correlates in a definite way with the average diameter d_p of the plume of incandescent particles, although the relation here is not totally consistent. Specifically, d steadily grows with gas pressure under similar experimental conditions. The interaction zone dia-

meter d characterizes the integral effect due to direct LR, plasma radiation, refracted LR, and plasma proper. From what we have said above, it is clearly seen that the target not only serves as a "seed" for kindling the plasma, but also effectively acts on the process of shielding.

The diameter d commonly decreases with an increase in both the thermal conductivity and melting temperature of a material. In the range of pressures from 1 to 5 MPa, d for aluminum is larger than that for corrosion-resistant steel. In the interaction of LR with graphite and silicon, the plasma cloud stays close to the target surface generally until the end of the interaction time, and since the damage threshold for these materials is low, the interaction zone diameter here is larger than that for metals. Let us point to a common regularity concerning the lifetime of the plasma cloud. This lifetime grows with the argon pressure in the chamber. That this is so is most clearly seen from the results of experiments on the interaction of LR with corrosion-resistant steel.

As follows from the experimental results of interaction of Nd-doped laser pulses with a moving specimen in argon at $p > 8$ MPa and $q > 5 \times 10^6$ W/cm^2 [11], the plasma growth rate v_p in this atmosphere is a few times that in nitrogen and helium. In argon plasma, LR is more liable to refraction and absorption. At $p < 8$ MPa and $q < 5 \times 10^6$ W/cm^2, the process of interaction of LR with a moving specimen in argon stands midway, as regards its characteristic parameters, between similar processes occurring in nitrogen and helium. At argon pressures $p > 4$MPa, LR interacts with a target surface generally in the same way as it does in nitrogen. At argon pressures below 4 MPa, the character of laser interaction is similar to that in helium. The microhardness of the steel surface treated in argon essentially remains equal to the original value. The effect of the pressure of inert gases on the character of changes in steel microhardness was dealt with comprehensively in reference [13].

Laser-material interaction in helium. The results of studies into the interaction of neodymium laser pulses about 1 ms long at q ranging from 10^6 to 10^7 W/cm^2 with molybdenum, corrosion-resistant steel, aluminum, polished silicon plates 0.1 mm thick, fabric-based laminates, and other materials are available in work [14].

As with nitrogen and argon, the properties of a material in helium affect the characteristics of plasma, which, in turn, exerts its influence on the surface properties. The difference is that LR interacting with a material in helium always produces a fusion region on the target surface at any pressures of helium. This means that the plasma cloud forms in the vapors of the removed material.

As is evident from the photographs of a high-speed photorecor-

der, plasma appears near the target surface and exerts its effect on the structure of the interaction region. The size of the plasma plume as a rule diminishes with increasing pressure of helium, while the lifetime of the plume grows, as it does in N and Ar.

Since helium has a high ionization potential, $\varphi = 24.5$ eV, the breakdown in helium at power densities of around 10^6-10^7 W/cm^2 does not occur [14]. The lifetime of plasma generated by LR incident on a fabric-based laminate target in helium is half that of plasma excited in N.

A specimen of polished silicon does not disintegrate in the range of helium pressures from 4 to 8 MPa, as it does not at argon pressures of 3-6 MPa. This means that the mechanism of specimen disintegration under LR is the same in either of the gases and is due to the development of thermal stresses above the strength threshold for the treated material.

In the interaction of a neodymium laser beam with a target moving at 10 to 30 m/s in helium at pressures varying from 0.1 to 9 MPa, the plasma formed has a higher transmissivity than that excited in nitrogen since, as evident from experiments, even at $p =$ 9 MPa the laser beam produces a molten track on the target surface during its entire time of interaction.

Effect of a gaseous medium on laser-induced erosion of refractory metals. Material removal from the laser interaction zone greatly depends on the laser power density, time of interaction, thermal properties of the irradiated metal, the structure and the gas content of the metal.

A growth of the pressure of air surrounding a specimen is found to lead to an increase in the laser-induced erosion of metals. The calculations of mass removal by evaporation from the metal surface in a gaseous medium confirm that the material removal reaches its peak in a definite range of pressures.

An extremal character of specific mass removal $\Delta m/E$, which is the amount of material removed per unit incident energy E, shows up in a wide range of gas pressures from 0.1 to 8 MPa. Fig. 6.6*a* contains the curves of $\Delta m/E$ for hafnium iodide and titanium plotted versus helium pressure [15]. The results presented in [15] reveal that the amount of liquid melt flushed from the cavity on to the specimen surface decreases with increasing helium pressure. A gas pressure stepped up from 0.1 to 1.0 MPa gives rise to a reactive pressure which speeds up the motion of the melt beyond the specimen surface, so that the amount of melt splashed out over the crater edges decreases. Starting at $p \approx 1$ MPa, the gas pressure strongly affects the dynamics of removal of liquid particles: namely, it slows down the motion of particles and even impedes their scattering. An enhanced gas pressure raises the vaporization temperature and thus aids in reducing the specific mass removal $\Delta m/E$. So, the peaks observed

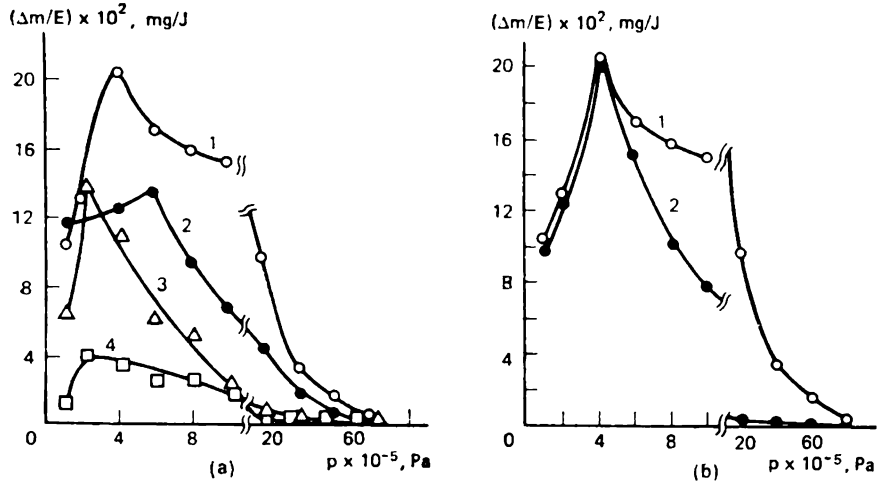

Fig. 6.6. Specific mass removal as a function of pressure of helium (*a*): *1*, E = = 30 J; *2*, E = 21 J; *3*, E = 15 J (for hafnium); *4*, E = 30 J (for titanium); and as a function of pressure of helium and nitrogen for hafnium (*b*): *1*, E = 30 J (helium); *2*, E = 30 J (nitrogen)

on curves of $\Delta m/E$ against p, as shown in Fig. 6.6*b*, arise from the action of two competing processes [15].

A further increase in pressure above 1 MPa sharply reduces the material removal, with the result that the depth melted in the specimen considerably decreases. At $p = 4$ MPa, the cavity depth is merely one third or one fourth that melted at $p = 0.4$ MPa.

The experimental curves of Fig. 6.6*b* illustrate the effect of the plasma optically excited near the target surface on the mass removal from specimens irradiated in nitrogen and helium raised to a wide range of pressures. In the pressure range 0.1-0.4 MPa, the curves of $\Delta m/E$ versus nitrogen and helium pressures are practically coincident in shape. At pressures above 0.4 MPa, the specific mass removal in nitrogen (curve *2*) falls off with increasing pressure much faster than it does in helium (curve *1*) and in essence drops to zero even at $p = 2$ MPa. This is due to the shielding of the target by an opaque plasma formed at high pressures near the surface. The behavior of $\Delta m/E$ as a function of CO_2 pressure in a wide pressure range is similar. Therefore, the plasma only affects the slope of the descending branch of the curves of $\Delta m/E$ against p, but does not determine the extremal behavior of this dependence.

6.2. THE MECHANISMS OF OPTICAL BREAKDOWN IN HIGH-PRESSURE GAS AT THE TARGET SURFACE

The stage of optical breakdown of a gas that determines a further process of interaction of LR with the target surface is of interest to specialists engaged in laser material processing. The phenomenon of laser-excited gas breakdown includes a large number of short-time interdependent and interrelated events which are responsible for the difficulties in studying this phenomenon [16]. Gas breakdown occurs at threshold values of both the power density and gas pressure. Other factors that rather strongly affect the course of gas breakdown are electric and magnetic fields, laser setup parameters, laser frequency and pulse duration, kind of gas, impurity content of the gas, and focal spot radius.

Two mechanisms of optical breakdown are known: the first depends on the phenomenon of multiphoton ionization, and the second on electron avalanche. Either of the two mechanisms dominates depending on the range of LR and its power density: avalanche ionization, at low power densities of ~ 1 GW/cm^2 and high gas pressures $p \geqslant 0.1$ MPa; multiphoton ionization, at ~ 100 GW/cm^2 and $p \ll 0.1$ MPa. There are a number of complex situations in which both mechanisms show up simultaneously or sequentially, one replacing the other.

Locating a specimen in the focal plane of the optical focusing system reduces the threshold values of the power density. A large variety of factors promote a gas breakdown and facilitate its development, for example, target vaporization, thermionic emission [17], and generation of shock waves during intensive vaporization and mechanical destruction of the surface.

The process of optical breakdown in gases always involves a large concentration of chemically active particles and excited atoms, molecules, and ions. Also, most of the collision reactions proceed in the conditions of the strongly unbalanced system, in which case the relation between the parameters of chemical kinetics and the parameters of hydrodynamics and mass transfer are rather complex. The most consistent approach to investigating such a system is to develop fairly comprehensive mathematical models and subsequently solve the problems on a computer.

Considering that the gas breakdown attended by laser-supported plasma generation is a continuous process and that modern computers have definite capabilities, it will be expedient to divide conditionally the process of plasma generation into three stages.

The first stage covers the laser-supported cold-gas breakdown involving elementary reactions. At this stage, the analysis deals with the processes of chemical kinetics and mass transfer. Hydrodynamic processes are still absent since the gas temperature is not yet

high. The second stage is the stage of formation of the plasma cloud that is slightly transparent to LR. Here, account should be taken of the initial gas-dynamic process of plasma excitation. Collision reactions can often be omitted depending on the gas pressure and power density. The third stage, which has been treated by workers of [16], is the stage of the quasistationary distribution of plasma discharges.

Consider the first stage of plasma formation, namely, the molecular nitrogen breakdown near, for example, a molybdenum target surface exposed to LR at $\lambda = 1.06$ μm of $q = 10^7$-10^9 W/cm^2 in the gas pressure range $p = 1$-20 MPa, therewith focusing attention on the digital simulation of the process [18-21].

The basis for the physical model of breakdown is the mechanism of thermal emission of electrons from the molybdenum plate surface, which entails the laser-supported electron-ion avalanche in the dense gas. A high ambient pressure slows down the diffusion of electrons and raises the metal boiling temperature. As a result, the target surface heated to a high temperature does not yet disintegrate, but the space near the surface now contains electrons of a rather high concentration, the value of which is a function of the target emission properties and space charge potential. As they fall into the gaseous medium, thermoelectrons gain energy required to ionize neutral particles owing to the laser energy absorption through inverse Bremsstrahlung in the field of ions and neutrons. The avalanche then develops in conformity with the known concepts.

The first attempts to simulate the process in the framework of this physical model [18, 20] have confirmed that there is in principle a possibility of avalanche buildup at $p = 10$ MPa and a laser power density above 100 MW/cm^2.

An electron avalanche developed in molecular gases is governed by a complex kinetics of collision reactions. The given model considers the processes of chemical kinetics and mass transfer, which proceed in parallel with one another in both atomic and molecular components of the gas. The following processes occur in nitrogen:

(1) electron impact excitation and deexcitation of atoms and molecules,

$$N + e \rightleftarrows N^* + e, \quad N_2 + e \rightleftarrows N_2^* + e$$

(2) vibrational excitation of molecules by electron collisions,

$$N_2 + e \rightleftarrows N_2^* + e$$

(3) thermal dissociation and electron impact dissociation,

$$N_2 + N_2 \rightarrow 2N + N_2, \quad N_2 + e \rightarrow 2N + e$$

(4) reactions of association,

$$N_2 + 2N \rightarrow N_2^* + N_2, \quad N + 2N \rightarrow N_2^* + N$$

(5) ionization of atoms and molecules, causing them to move from ground and excited states, and their three-particle recombination,

$$N_2^+ + e \rightarrow 2N, \quad N_3^+ + e \rightarrow 3N, \quad N_4^+ + e \rightarrow 2N_2$$

In the analysis of mass transfer processes, account has been taken of the diffusion and drift of N_e and N_i^+ particles of the space charge in the electric field and also the thermal conductivity of the electron gas and heavy particles.

The above reactions are defined by the equations of chemical kinetics [19]. The analysis of collision reactions has proved that the reaction rate coefficients are functions of three temperatures: T_e and T_g of electrons and heavy particles, respectively, executing translational motions, and T_v of molecules in the vibrational state. The set of kinetic equations must then be supplemented by three energy balance equations. The inelastic loss of energy by electrons in the molecular component of the gas has been allowed for using an experimental factor δ (ε) which shows how much the total electronic energy loss due to inelastic collisions is larger than the elastic loss. The field of space charge appearing near the target surface is given by the Poisson equation.

Figures 6.7 and 6.8 present the generalized data for the process simulated on a computer in the pressure range 1-20 MPa at $q = 0.9$ GW/cm^2.

Referring to Figs. 6.7 and 6.8, consider the general picture of breakdown development at a nitrogen pressure of 10 MPa. Under optical breakdown one understands a definite state of the substance in its local region where the electron temperature T_e climbs abruptly to cause an avalanche ionization and, hence, an increase in the temperature T_g of heavy particles. This local region is the site of intense LR absorption.

Under normal conditions, nitrogen is transparent to LR with a quantum energy $h\nu = 1.17$ eV and the entire energy flux falls on the target surface which partially reflects it and absorbs the remaining flux $q_a = (1 - R)\, q_0$, where R is the reflectivity. The absorbed energy initiates thermal emission of electrons from the surface. The electrons that undergo elastic collisions with molecules in the LR field gain energy $T_e = 1.1$ eV in time $t \approx 0.2$ ns. The thermal emission gives rise to a space charge near the surface, the potential of which impedes a further emission of electrons, so they have to do more work to be able to escape the target. When the space charge potential u rises to about 3 V in $t = 2$ ns, the emission of electrons from the surface ceases. In the region $x \leqslant 0.4$ μm, the electron density N_e approaches 2×10^{18} cm^{-3} and the surface temperature rises to 0.34 eV. The spatial density distribution N_e can be regarded as a minimum electron density sufficient to initiate gas breakdown. But

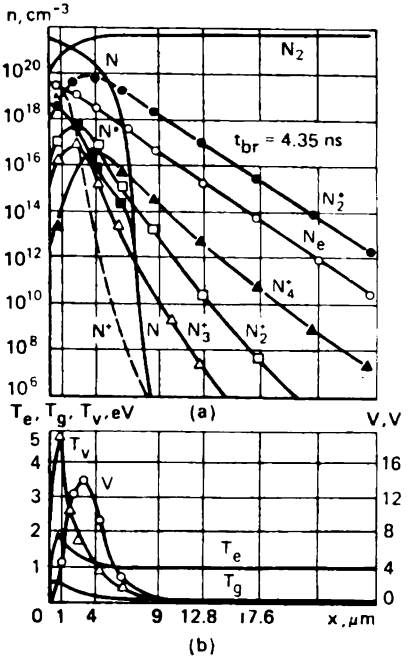

Fig. 6.7. Particle concentration (*a*), temperature and potential (*b*) as functions of distance from the target surface at instant $t_{br} = 4.35$ ns

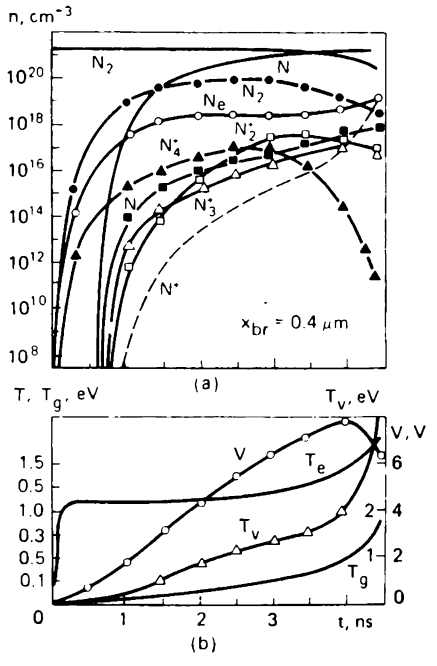

Fig. 6.8. Time dependence of particle concentration (*a*), temperature and potential (*b*) at distance $x_{br} = 0.4$ μm from the target surface

despite a high electron density, the discharge through the gas does not occur over this length of time. All processes in the irradiation zone are governed by collisions in the molecular component of the gas. The ionization of molecules proceeds rather slowly because of an insufficiently high electron energy whose value is limited by inelastic losses since the inelastic loss factor $\delta\ (T_e)$ falls sharply with increasing temperature. The density of atoms is still small due to a low vibrational temperature, $T_v \approx 0.3$ eV (see Fig. 6.8), which determines the degree of thermal dissociation.

The main mechanism of dissociation at $T_v < 0.6$ eV is the dissociation by electron impact. In the molecular nitrogen, electrons quite readily give up energy to sustain the vibrational degrees of freedom. As a result, the energy picked up by electrons in the LR field mainly goes into the vibrational excitation of molecules. Since the inverse process of deexcitation in the nanosecond range does not in essence take place and, besides, the reactions of thermal asso-

ciation

$$N_2+2N \rightarrow N_2^*+N_2, \quad N+2N \rightarrow N_2^*+N$$

still make up for the loss in vibrational energy, the vibrational temperature can be higher than the electron temperature over a certain length of time.

By the time $t \approx 3$ ns, the temperature T_v at a distance $x = 0.4$ μm reaches 3 eV, while $T_e = 1.2$ eV, as seen from Fig. 6.8. In time $t \approx 4$ ns, a vigorous thermal dissociation of the gas climbs to a high value of $\sim 90\%$ (see Figs. 6.7 and 6.8). The collision processes in the atomic component of the gas now dominate. The electron temperature at a level $x = 0.4$ μm above the surface depends on the electron-neutral and electron-ion collisions in the atomic gas. The density of N^+ and N_3^+ ions grows and gives rise to the electron-ion collision frequency ν_{ei}^a, where the superscript a stands for the atomic ion. At the instant the frequency ν_{ei}^a approaches the frequency of collisions of neutral particles with electrons, ν_{en}^a, the temperature T_e begins to rise, with the result that the ionization process grows in intensity and raises still more both ν_{ei}^a and T_e, thus causing onset of an electron avalanche. The increased density of N^+ ions reaches the value of electron density N_e, so that the potential u gets smaller in this region. The electric field becomes self-consistent, and diffusion now exhibits a bipolar pattern.

The stage of breakdown is complete when T_e reaches a maximum at the breakdown point. The temperature $T_{e\,\max}$ is equal to 1.79 eV for $x = 0.4$ μm at an instant of time $t = 4.35$ ns, in which case $N_e \approx N^+ = 3 \times 10^{25}$ m^{-3} and $T_v \approx 4.5$ eV. Late in the pulse, the diffusion causes the breakdown region to shift upward away from the target.

The target surface temperature during the breakdown time reaches 0.45 eV, which is close to the boiling temperature of molybdenum at a gas pressure of 0.1 MPa. This fact allows us to infer that intense vaporization will not occur at 10 MPa.

The calculations of the threshold power density required to initiate the optical discharge show that the threshold q_0 lies between 0.4 and 0.5 GW/cm^2. At lower values of q_0 the mean electron energy does not rise above 0.7 eV, which is insufficient for it to initiate both the step ionization and effective excitation of vibrational states responsible for thermal dissociation. Under these conditions, molybdenum vapors cannot exert a crucial effect on the course of the process. That this is so is borne out by the estimates of the condition at which the electron avalanche builds up by way of ionization that raises atoms from the ground state:

$$\frac{d\varepsilon}{dt} = \frac{4\pi e^2 q_0}{mc\omega^2}\nu_{ef} > \left(\frac{d\varepsilon}{dt}\right)_{i\,\max} = \frac{2m}{M}\nu_{ef} q_0 \qquad (6.1)$$

where $(d\varepsilon/dt)_{l\ max}$ is the maximum rate of energy loss due to elastic collisions, m the electron mass, M the heavy particle mass, and ν_{ef} the effective collision frequency.

From this condition, we determine the laser power density threshold for molybdenum: $q_0 > 6 \times 10^9\ I/\lambda A > 0.4$ GW/cm^2, where $A = 95.95$, $I = 7.1$ eV, and $\lambda = 1.06$ μm.

So, the laser power density responsible for an avalanche either in molybdenum vapors or in nitrogen at 10 MPa is approximately the same in magnitude. However, the process of vaporization begins much later than thermionic emission and cannot precede it; the molybdenum vapors present in a high-pressure atmosphere can only intensify the process of development of an avalanche set off earlier in nitrogen.

Figure 6.9 illustrates the simulated results illustrative of nitrogen breakdown at various pressures. The breakdown region ($x_{br} = 0.25$ μm) shrinks at 20 MPa and the electron temperature T_e rises to a maximum of 2.1 eV, with a breakdown time t_{br} going to 5.6 ns.

As the pressure drops down to 3 MPa, the breakdown point x_{br} moves away from the surface for 4 μm and $T_{e\ max}$ falls to 1.6 eV due to a decreased collision frequency ν_{ei}^a. The breakdown time t_{br} rises to a high value of 6.1 ns.

There is no clearly defined breakdown site when the pressure drops to 1 MPa. The electron temperature $T_{e\ max}$ in the region 12 to 15 μm above the surface is rather high, about 1.4 eV, but it is insufficient to initiate the electron avalanche. Because of heavy diffusion losses, the condition $\nu_{ei}^a > \nu_{en}^a$ is not met. The ion density $\Sigma_i^4 N_i^+$ approaches 7×10^{23} m^{-3}, but the electron density N_e is much higher, about 5×10^{24} m^{-3}. Under these conditions, the surface rises to a fairly high temperature.

Thus, optical breakdown due to thermionic emission in molecular nitrogen can be expected to arise at $p \geqslant 3$ MPa. At lower pressures, for example, at 1 MPa, the breakdown time grows appreciably, so there is a greater possibility of appearance of the vaporized material in the zone of irradiation. Besides, the power density threshold for nitrogen breakdown exceeds 1 GW/cm^2, which is much higher than the threshold for molybdenum vapor breakdown.

Surface target disintegration observed in experiments at $p = 3$-5 MPa does not guard against the possibility of nitrogen breakdown since this process of damage can be governed by the thermal conditions of the target at a later, gas dynamic, stage of plasma generation near the surface.

The results of studies of optical nitrogen breakdown in the absence of a specimen show that the power density threshold q_{br} versus pressure p displays a clear-cut pattern with a minimum at 10.2 MPa.

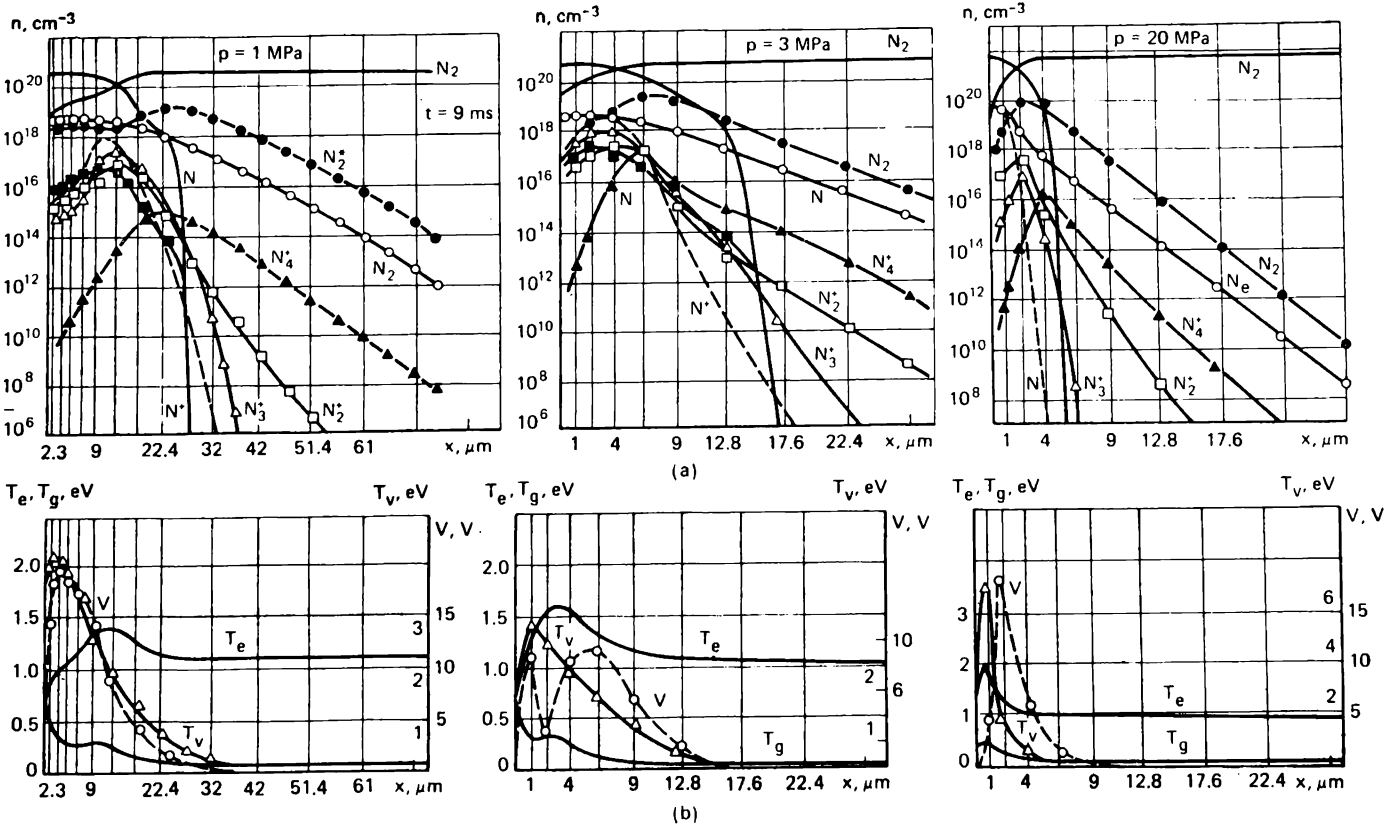

Fig. 6.9. Particle concentration (*a*), temperature and potential (*b*) as functions of distance from the target surface at various pressures

Figure 6.10 contains the plots of t_{br}, x_{br}, and $T_{e\,max}$ versus pressure p at $q_0 = 0.9$ GW/cm^2. The curve of t_{br} (p) qualitatively agrees with the experimental curve of q_c (p) and exhibits the same sharply defined shape with a minimum at 10 MPa. As the pressure falls off, diffusion processes gain in importance, so the electron-neutral collision frequencies ν^a_{en} and ν^a_{ei} start to decrease and the electrons need to travel a much longer diffusion path before they acquire energy in the order of 1 eV and the condition $\nu^a_{ei} \geqslant \nu^a_{en}$ becomes valid. Consequently, the breakdown time gets longer, the distance to the breakdown region increases, and the maximum electron temperature decreases.

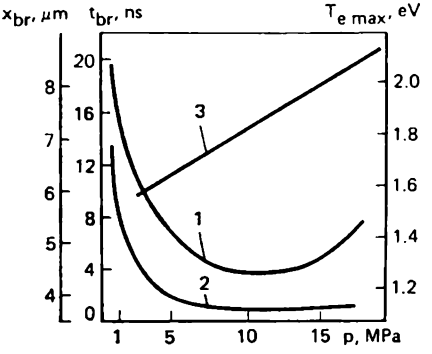

Fig. 6.10. Breakdown time t_{br} (*1*), distance x_{br} from the target surface to breakdown site (*2*), and electron temperature $T_{e\,max}$ (*3*) as functions of p at $q_0 = 0.9$ GW/cm^2

However, if the pressure is too high, above 10 MPa, the time to reach the breakdown grows since at the instant of onset of the avalanche, the conditions for the electrons to gain energy become unfavorable. The inequality $\omega^2 \gg \nu^2_{ef}$ changes to $\omega^2 > \nu^2_{ef}$, where ω is the laser frequency, when the electron-neutral collision frequency ν^a_{en} gets larger than ν^a_{ei}. Besides, the breakdown condition $\nu^a_{ei} > \nu^a_{en}$ ($N^+_{ei} \approx 0.008$ N) is more difficult to fulfil since the process of laser interaction is now unable to ionize a larger number of neutral particles. For this, the time of interaction must be longer, as must be the time required to initiate the breakdown when the electron temperature reaches its maximum value $T_{e\,max}$.

What is remarkable is that $T_{e\,max}$ (p) steadily rises. Hence, at pressures above 10 MPa, the conditions at which electrons gain energy do not vary on the whole. This suggests that the optical breakdown in nitrogen at $p > 10$ MPa can always occur when q_0 corresponds to a minimum of q_c (p) if the laser pulse is indefinitely long.

Consider how various reactions contribute to the process of breakdown. As shown by calculations, it is vibrational excitation, dissociation, and step ionization that are most important for the initiation of nitrogen breakdown. Conversion reactions become of no consequence at $T_g \approx 0.2$ eV. The process of dissociative recombination of molecule ions and clusters plays an essential part in a molecular gas: N^+_2, N^+_3, and N^+_4. Because of their high rates, these reactions limit the breakdown process in a molecular gas (reaction rate coefficients range from 1 to 10^{-2} m^3/s).

The ionization reactions that excite atoms and molecules from the ground state contribute little to the process and can be left out of consideration if the problem stated involves an electron source. The process of associative ionization can be of significance when the gas temperature is high, $T_g \geqslant 1$ eV, while free electrons are few. For the problem with an electron source, the associative ionization may not be taken into account.

Note the main features of laser-induced breakdown in a dense molecular gas:

(a) optical breakdown develops in nitrogen when it totally passes from the moleclular to the atomic state;

(b) characteristic values of breakdown times and laser power density thresholds allow us to interpret an experimentally observed breakdown as a discharge due to a laser spike;

(c) at high pressures, the metal surface serves as an electron source, for which reason the breakdown process is relatively insensitive to the content of impurities;

(d) the processes of heat conduction by way of electrons and heavy particles are essential only at the initial stage during which the temperatures T_g and T_e grow to steady-state values;

(e) space-charge fields are weak to be able to distort the Maxwellian distribution function and thus need not be always given consideration;

(f) an avalanche builds up when the pair collision frequency predominates over the electron-neutral collision frequency, the condition being stable when

$$\Sigma_{i=1}^{4} N_i^+ \approx 0.008 (N + N^* + N_2 + N_2^*)$$

6.3. PLASMA DYNAMICS NEAR A SOLID SURFACE AT HIGH NITROGEN PRESSURE

In Sec. 6.2 we have conditionally divided the process of plasma generation into three stages: gas breakdown, opaque plasma excitation, and quasistationary distribution of plasma discharges. The last stage most easily lends itself to experimental treatment, while the study of the first two stages presents difficulties because of many short-time interrelated processes occurring in the plasma. For the investigation of initial stages, digital computer simulation methods proved effective. They were used to study the stage of laser-induced ignition of molecular nitrogen near a metal surface [19].

Applying the methods of digital simulation and subsequently interpreting the spatial-temporal distributions, the researchers of [22, 23] have obtained the main gas dynamic and thermal characteristics of a plasma cloud in nitrogen at a pressure of 10 MPa on the

assumption that a neodymium laser emitting at $\lambda = 1.06$ μm delivers near-threshold values of power.

The feature peculiar to the process under discussion is that along with the hydrodynamic mechanism of energy transfer, the mechanism of radiative transport is essential. Heat conduction processes are of little consequence. Besides, if the laser pulse is long, about 0.5 μs, and the radius r_f of the focal spot is comparatively large, about 250 μm, the process is also strongly dependent on two-dimensional effects arising from the radial expansion of the laser-induced plasma. It is assumed that the condition of local thermodynamic equilibrium is met in the laser-produced plasma.

The mathematic model of the process comprises a system of two-dimensional axisymmetric equations of radiative gas dynamics in Lagrange variables.

The assumptions made to simulate the breakdown stage are: the preliminarily specified hot region located along the specimen surface is 15 μm thick; its temperature is 1.8 eV; and the laser power density is 5×10^7 W/cm^2.

LR is incident along the z axis. Early in the pulse, intense LR absorption occurs only in the hot region and causes a strong gas dynamic scattering of the material, therewith entailing the excitation of a shock wave in the cold gas.

The spatial-temporal patterns of temperature T, pressure p, and plasma density ρ, which describe the dynamics of plasma generation in the transient period for the case where $p_0 = 10$ MPa are shown in Fig. 6.11. Conditionally, the stage of plasma formation terminates at $t \approx 0.533$ μs, when the gas dynamic velocity becomes lower than the sound velocity.

LR rapidly raises the temperature and pressure in the hot region. By the time $t = 5$ ns, the pressure reaches a maximum of 6×10^2 MPa. Later, despite the temperature growth, the pressure in the hot region falls off because the intense gas dynamic scattering reduces the material density in the damaged region. The shock wave excited in these conditions does not reach a maximum velocity $v \approx 1.3$ km/s by the time $t \approx 10$ ns (Fig. 6.12). The maximum temperature T_{sw} of the gas of the shock wave reaches 0.36 eV, which is insufficient to initiate intense LR absorption. The shock wave is in fact transparent to the laser light, so the conditions are unfavorable for the generation of a laser-supported detonation (LSD) wave that effectively shields the target. Since the shock wave velocity v_{sw} is higher than the velocity of the plasma front, v_{pf}, the shock wave breaks away from the hot region, as is evident from Fig. 6.11. Cold nitrogen ($T \leqslant 1$ eV) is transparent to LR in the visible and near UV, but absorbs well the radiation with energy $h\nu \geqslant 14$ eV. From Fig. 6.11 it is seen that absorption occurs near the hot region about 50 μm from the target. The shock wave decoupled from the energy

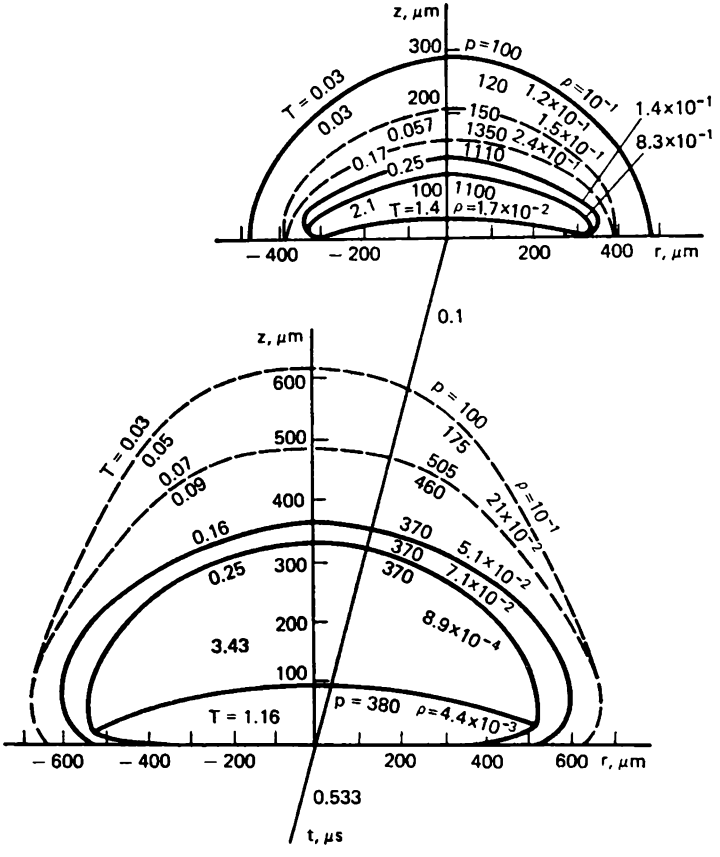

Fig. 6.11. Spatial-temporal profiles of T, p, and ρ in the transient period, showing the regions of shock waves bounded by dash lines

source begins to decay, its speed and temperature fall rapidly, and by the time $t = 0.533$ μs the shock wave dissipates, leaving behind a subsonic perturbation site (see Figs. 6.11 and 6.12).

As revealed by calculations, the flow is initially unidimensional, but after a time of around 0.1 μs the plume extends radially at a rather high speed, and the motion becomes two-dimensional, which is obvious from Fig. 6.11. Since "hot" layers of nitrogen shield LR from the target, near the surface there forms a plasma layer whose temperature is much lower than that of the adjacent upper layer, which assumes the crescent form shown in Fig. 6.11. The joint action of two factors is responsible for the shape of the "hot" region as well as for the shape of the "cold" region adjacent to the surface, na-

mely, the factors of gas dynamic motion and almost complete absorption of LR. The temperature of the region adjacent to the surface gradually falls from 1.8 to 1.1 eV due to LR shielding and gas dynamic scatter of the material. Starting from $t \approx 15$ ns, plasma products become almost totally transparent to LR; it is mainly the flux of laser radiation alone, whose incident power density q_e reaches $10^5 W/cm^2$, that interacts with the target surface.

The maximum temperature of the hot region comes to 3.6 eV and does not climb above this limit because the hot region begins to

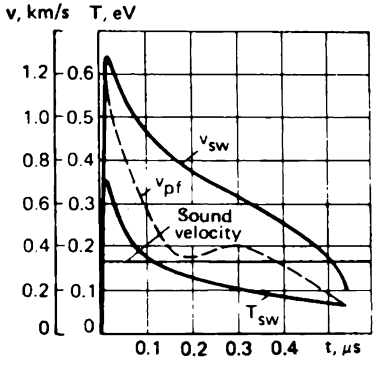

Fig. 6.12. Maximum temperature and speed of a shock wave in gas versus time

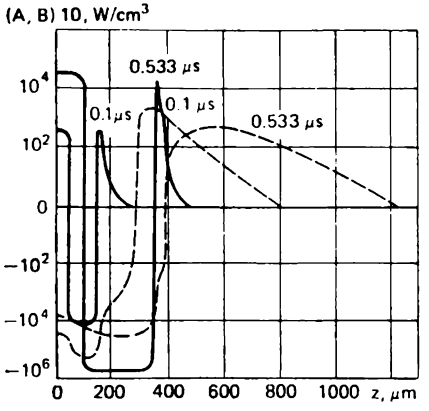

Fig. 6.13. Spatial-temporal distribution of power components in gas due to gas dynamic forces (dashed curves) and radiation transfer (full curves) at $r = 0$

emit radiation much more intensely. So, from the analysis of the shielding effects and the values of radiant fluxes incident on the target, it is possible to explain why the laser beam does not damage the surface at nitrogen pressures above 7 MPa.

The calculated data show that the area of the HAZ is a few times larger than the area of the initial focal spot of incident radiation. These data agree with experimental results. As follows from calculations, the process of propagation of plasma products at the initial stage of interaction is transient in character; it progresses from LSD wave excitation to slow burning. Although the laser-supported detonation process does not come into play, gas dynamic forces contribute markedly to the plasma wave excitation. Fig. 6.13 illustrates the spatial-temporal distribution of the gas power components

$$A = p\left(\frac{1}{r}\frac{\partial}{\partial r}(ru) + \frac{\partial v}{\partial z}\right)$$

due to gas dynamic forces (dashed curves) and due to radiation transfer (full curves):

$$B=\frac{1}{r}\frac{\partial}{\partial r}(rq_r)+\frac{\partial q_z}{\partial z}$$

The amount of energy emitted from the hot region and absorbed by cold nitrogen grows with time, while the amount of energy that goes into heating the gas through gas dynamic compression decreases.

Let us take a closer look at the process of plasma formation near the target surface in nitrogen at 3 MPa. According to the calculations, the temperature of the breakdown region is 1.6 eV and the thickness is ~15 μm.

The results of digital simulation show that initially at $t \leqslant 0.1$ μs, the process of plasma excitation is similar to that obser-

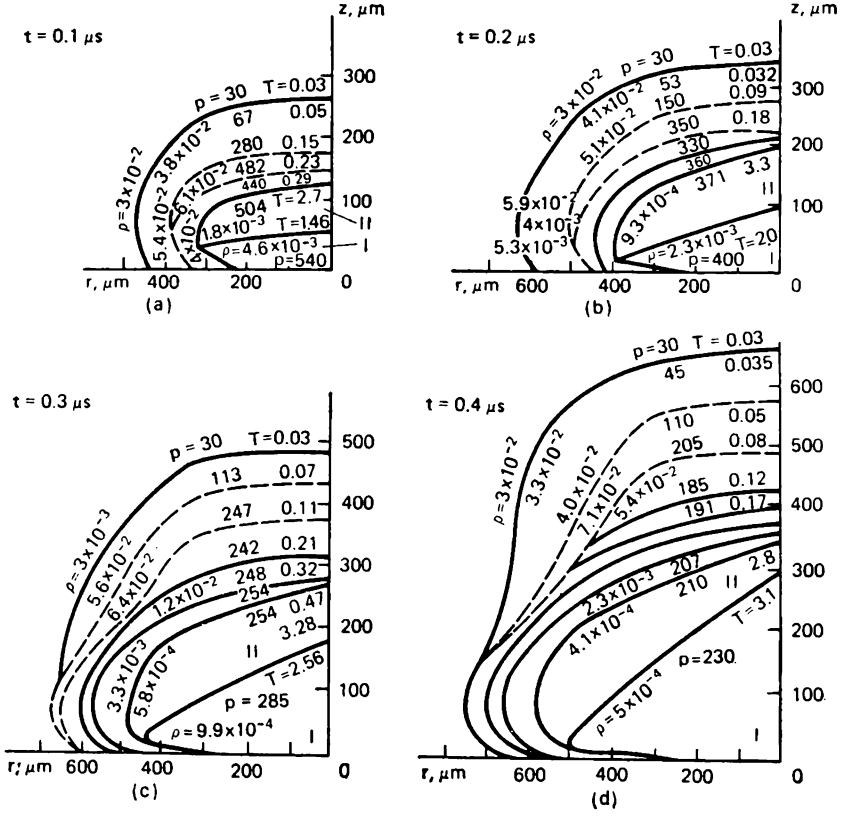

Fig. 6.14. Profiles of temperature, density, and pressure of plasma at instants t = 0.1, 0.2, 0.3, and 0.4 μm

vable at 10 MPa. The incident laser radiation, now being mainly absorbed in the hot zone, leads to an intense dissipation of the hot plume, followed by the generation of a supersonic shock wave in time $t = 10$ ns, which propagates into the cold gas. The velocity v_{sw}^{max} of the shock wave along the z axis at $r = 0$, temperature T_{sw}^{max}, and density ρ_{sw} are 1.9 km/s, 0.36 eV, and 6.1×10^{-2} g/cm^3 respectively.

The profiles of T, p, and ρ of the plasma cloud at $t = 0.1$, 0.2, 0.3, and 0.4 μs, with the shock wave bounded by dash lines, are shown in Fig. 6.14. The hot plume first extends upward along the z axis. As in the case of laser interaction in nitrogen at 10 MPa, here too the thickness Δz of the hot zone becomes much larger than the absorption length l of a laser light quantum because of the expansion of this zone (Fig. 6.14*a*). As a result, a major fraction of LR is absorbed in the upper region of the hot zone (region II), while region I adjacent to the target surface is in fact decoupled from LR and at time $t = 0.1$ μs its temperature T_I is much lower than T_{II}, as seen from Fig. 6.14*a*. At $t = 0.1$ μs, the plume extends radially at appreciable velocities. The effect of gas dynamic expansion of region II at $t = 0.1$ and $t = 0.2$ μs (Fig. 6.14*b*) is quite apparent. From this time on, the processes of plasma formation at 3 and 10 MPa are no longer similar. In view of a lower gas density at 3 MPa, the hot plume in region II dissipates at $t \geqslant 0.1$ μs to such an extent that it becomes transparent to laser radiation. The laser pulse now efficiently couples to region I where the nitrogen density ρ_I is higher than ρ_{II} and, hence, the absorptivity is higher too. The rate of expansion of region I grows fast. The profiles of velocities v (z) at $r = 0$ are shown in Fig. 6.15, where the region of plume dissipation exhibits a second peak; the first peak on the curves corresponds to the speed of the shock wave.

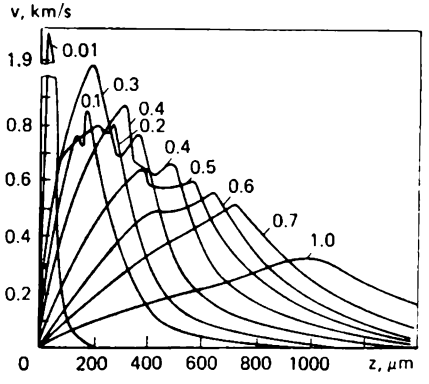

Fig. 6.15. Velocity profiles v (z) at $r = 0$

By the time t of the order of 0.3 μs (Fig. 6.14*c*), the spread velocity v of the hot zone approaches a maximum of 1.1 km/s and exceeds the shock wave velocity v_{sw}, which is around 0.75 km/s. Nevertheless, the second shock under the first does not appear since the plume in region I disperses into region II where the density is low, $\rho_{II} < \rho_I$. But the density of the gas within the confines of the shock

wave grows from 59×10^{-2} g/cm^3 at $t = 0.2$ μs to 71×10^{-2} g/cm^3 at $t \cong 0.4$ μs (Fig. 6.14*d*).

Returning to Fig. 6.14, the temperature T_{II} climbs to a maximum of 3.6 eV at $t = 0.18$ μs and then drops to 2.0 eV at $t \cong 1$ μs as the plume releases the absorbed energy and attenuates the laser beam to a less extent. The temperature T_I first decreases at $t \cong$ $\cong$ 0.1 μs because of the gas dynamic dissipation, but later, as region II gets more transparent and region I absorbs more laser energy, this temperature increases (at $t = 0.2$, 0.3, and 0.4 μs) and reaches

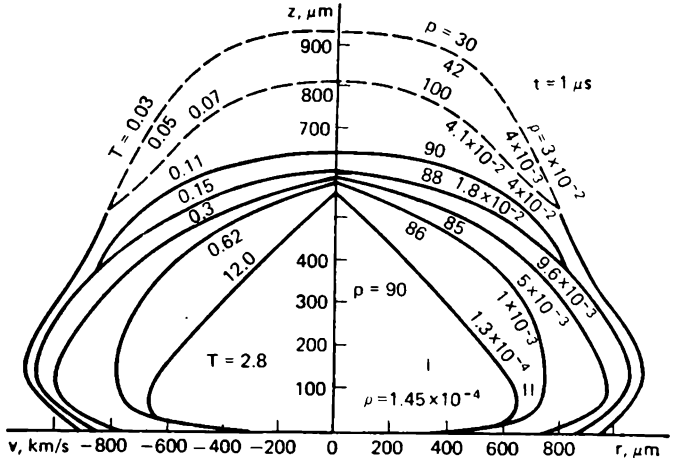

Fig. 6.16. Profiles of temperature, density and pressure of plasma at $t = 1$ μs

a maximum of 3.6 eV at $t = 0.49$ μs. Late in the pulse, as the gas density decreases, the hot zone becomes more transparent, its temperature and pressure fall off, so that the amount of laser energy coupled to the target increases.

Figure 6.16 illustrates the profiles of temperature, density, and pressure of the plasma cloud at $t = 1$ μs.

As in the case of a nitrogen pressure of 10 MPa, at 3 MPa too, the shock wave rapidly decouples from the plasma front. In view of its low temperature, $T_{sw}^{max} = 0.36$ eV at $t = 10$ ns and $T_{sw} \leqslant$ 0.075 eV at $t \geqslant 0.5$ μs, the shock wave is transparent to LR and absorbs the laser energy only at initial moments of time. The shock wave then rapidly decays and dissipates by the time $t \approx 1.0$ μs, leaving behind subsonic perturbations.

The analysis of the contributions which the gas dynamic and the radiative mechanism of energy transfer make into the plasma formation discloses that the first mechanism dominates at the initial stage, $t < 0.2$ μs. At $t \cong 0.1$ μs, the pulse energy proper that goes

into heating the gas is merely one tenth that resulting from the work done by compressive forces. The energy spent on gas dynamic expansion and the plasma-released energy are approximately equal. But even at $t = 0.3$ μs the ratio changes markedly. The ratio of the energies spent on the heating and compression of the gas is 50 : 1, while the radiation loss becomes 4 times the loss due to expansion. At $t > 0.8$ μs, gas dynamic processes are practically immaterial. However, the radiant flux delivered to the target decreases with time because of a temperature decrease in region II, as is apparent from Fig. 6.17. The power density of the laser beam (irradiance) leaving region II is $q_e \cong 10^6$ W/cm², which is almost an order of magnitude higher than that attainable at $p = 10$ MPa.

It is certainly of importance for laser material processing to know the estimates of the laser power density q_e and the total power density $q(t)$ delivered to the target surface. These estimates are given in Fig. 6.17. The laser power density q_e coupled to the target surface amounts to 3×10^6 W/cm² and then drops to 1.6×10^6 W/cm². The radius of the focal area at $t = 1$ μs is $r_f \cong 600$ μm. At $r_f = 250$ μm, the curve of q versus time has two clearly defined minima. The first minimum at $t \cong 0.01$ μs ($q = 6.5 \times 10^6$ W/cm²) is indicative of the intense absorption of LR in region II ($q_p \approx 0.9\ q$). The second minimum at $t = 0.3$ μs ($q = 6 \times 10^6$ W/cm²) results from LR absorption in region I. Later, as the hot zone becomes transparent due to a decrease in ρ_I and ρ_{II} to 1.4×10^{-1} g/m³ and 1.3×10^{-1} g/m³, respectively, the laser power density delivered to the target surface rises to 3.9×10^7 W/cm². So, 1 μs after the start of the laser pulse, the laser power density delivered to the focal spot reaches about 80% and the plasma cloud does not shield the target surface at an initial nitrogen pressure of 3 MPa. This is the main reason of why LR damages the specimen surface at 3-5 MPa.

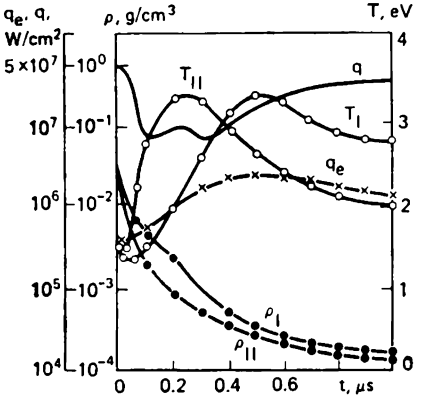

Fig. 6.17. Time dependence of temperatures T_I and T_{II}, plasma densities ρ_I and ρ_{II}, total power density q, and incident irradiance q_e at the target surface

Calculations show that the laser power required to sustain the plasma discharge is practically independent of pressure. The threshold value of power both at 10 and 3 MPa is equal to 92 kW, which corresponds to $q = 4.4 \times 10^7$ W/cm².

6.4. REDUCTION OF METALS AND SYNTHESIS OF INORGANIC MATERIALS

Reduction of metals. The processes of laser-induced reduction of metals, primarily refractory metals, from oxides hold promise in many industrial applications. The reducing mediums that can be used here include gases such as hydrogen and carbon monoxide, liquids such as alcohol, and, sometimes, solids.

What can strongly affect reducing reactions is a thermochemical nonresonant effect, i.e. negative feedback resulting from changes in the oxide surface absorptivity with a growth of the reduced metal layer. A number of works have treated the process of CO_2 laser reduction of metal from an oxide, for example, review [4]. The kinetics of growth of a thin metal layer in hydrogen obeys the equation

$$\frac{dx}{dt} = v \exp(-T_0/T) \tag{6.2}$$

where v is a constant; T_0 the activation temperature of reduction, K; and x, the thickness of the reduced layer.

Equation (6.2) should be supplemented by the equation for the nonsteady-state temperature field in a solid.

The absorptivity of an oxide-metal film system [24] for a small film thickness is given by

$$A(x) = A^* - bx, \quad A^* = \frac{4n}{(1+n)^2}, \quad b = \frac{64\pi}{\lambda A_0^2} \frac{n-1}{(n+1)^3} \tag{6.3}$$

where $A(x)$ is the absorptivity of the layer system, A^* the absorptivity of a pure oxide, λ the laser wavelength, n the refractive index, and A_0 the metal absorptivity ($A_0 \ll 1$).

The dynamics of laser heating of a thin surface layer has been treated in work [4] using a gradient-free approximation and regarding the temperature to be invariable over the thickness.

The thickness of the reduced metal layer varies with time (Fig. 6.18). Starting at a certain moment of time after initiation of the reaction, the thickness changes insignificantly; it is mainly the power rather than the energy of the incident radiation that determines the reaction yield.

Let us consider the experimental data on the reduction of the oxides of refractory metals — tungsten and molybdenum—in hydrogen held at pressures varied over a wide range, from 0.1 to 10.5 MPa. The source of radiation was a neodymium laser emitting pulses of about 1 ms duration with power densities q ranging from 10^4 to 10^7 W/cm^2. The lens with a focal length f of 120 mm focused the laser beam on to the surfaces of specimens under test placed in a high-pressure hydrogen-filled chamber. The specimens were 6-mm diameter pellets prepared by pressing the powders of tungsten trio-

xide WO_3 or molybdenum trioxide and also metal plates oxidized in air for 1 h at 800°C. Interaction zones were studied by metallographic and X-ray diffraction methods. X-ray photographs were taken by standard techniques, with the radiation intensity read out on a scintillation counter.

In Fig. 6.19 are shown the diffraction traces for WO_3 in the initial state and after irradiation in air and hydrogen at a pressure of 10.2 MPa. Irradiation in air and in hydrogen maintained at a low pressure of up to 2.0 MPa does not yield

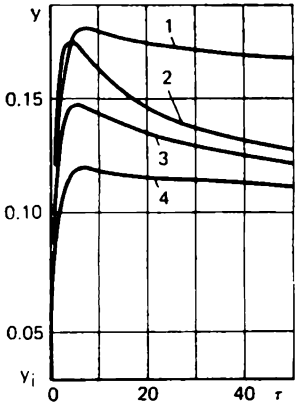

Fig. 6.18. Thickness $y = T_0/T_i$ of a reduced metal layer versus $\tau = (\alpha s/mc)\, t$ for $y_0 = 0.03$ at $\mu = pbmcv/T_0\,(\bar{\alpha}s)^2$: *1*, $\mu = 1$, $y_i = 0.18$; *2*, $\mu = 1$, $y_i = 0.15$; *3*, $\mu = 0.1$, $y_i = 0.18$; *4*, $\mu = 1$, $y_i = 0.12$; T_i, initial temperature; α, heat transfer coefficient; s, target surface area; m, mass; c, specific heat

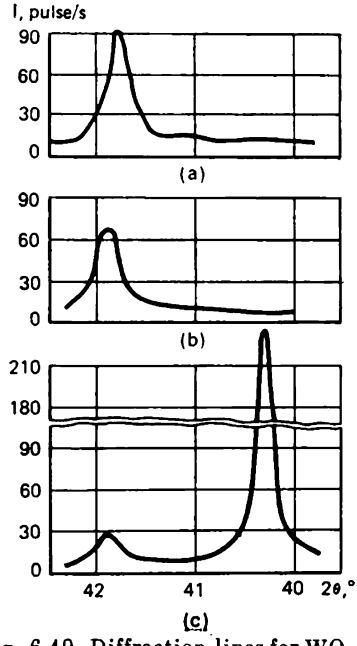

Fig. 6.19. Diffraction lines for WO_3 in the initial state (*a*) and after irradiation in air (*b*) and in hydrogen (*c*) at a pressure of 10.2 MPa

a metal that can be detected radiographically. At higher pressures of hydrogen, the laser beam reduces the trioxide to metal. From the comparison of the intensities of spectral lines of tungsten reduced at various pressures of hydrogen it is obvious that the amount of reduced tungsten grows with pressure in the chamber.

The line strength for WO_3 after irradiation noticeably decreases, and the distribution of intensities between individual lines changes. For example, the (200) line for the standard powder of WO_3 is the strongest, but after irradiation its strength becomes lo-

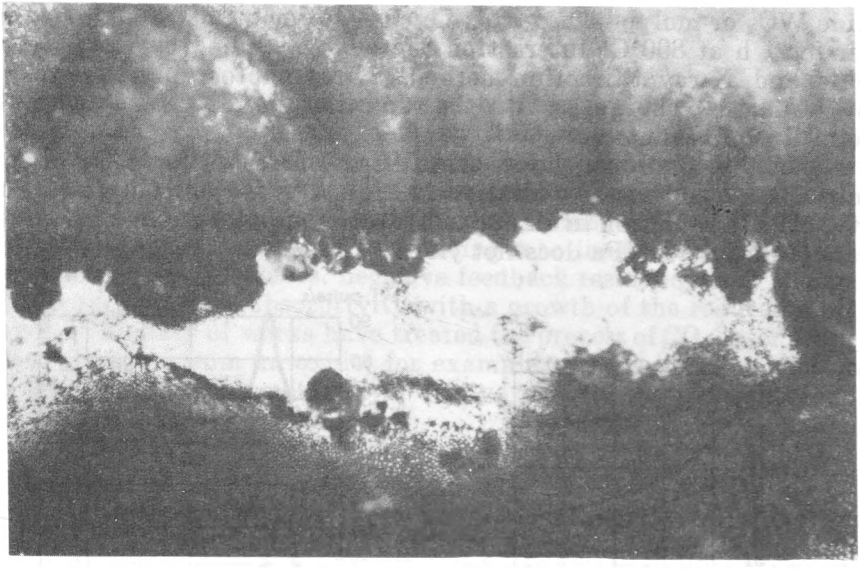

Fig. 6.20. Micrograph of the zone of interaction on the surface of WO_3 struck by a laser pulse at $q = 5 \times 10^6$ W/cm^2 in hydrogen at $p = 10.2$ MPa

wer than that of (001) and (020) lines. The intensity of the (040) line becomes abnormally high and increases 5 times.

In experimental conditions, the irradiation of WO_3 produces the so-called hydrogen-tungsten bronze $H_{0.5}WO_3$ whose structure is given detailed treatment in work [25]. Hydrogen-molybdenum and hydrogen-tungsten bronzes have also been obtained by way of low-temperature reduction of tungsten and molybdenum trioxides in the presence of palladium which promotes an intense penetration of atomic hydrogen into the trioxide lattice.

The data of the X-ray diffraction analysis well agree with the results of metallographic examinations. Fig. 6.20 illustrates a photomicrograph of the WO_3 specimen struck by an Nd-doped laser pulse about 1 ms long with a power density $q = 5 \times 10^6$ W/cm^2 in hydrogen at $p = 10.2$ MPa. The laser interaction zone on the surface of oxides takes the shape of an oval black spot with a bright rim of the solidified metal at the edges. The metal has a large number of pores and cracks separating it from the oxide.

Irradiation in nitrogen at a pressure of less than 5 MPa or at low power densities in the range 10^4-10^5 W/cm^2 gives a surface coat with a blue or violet tint. This is a hydrogen-tungsten or hydrogen-molybdenum bronze of formula H_xMeO_3 detected by the radiographic method, which can be an intermediate product of metal reduction.

Studies reveal that the reduced metal has a preferred orientation of the texture resulting from the directed heat transfer during crystallization of the molten metal. Researchers of [26] have earlier revealed the growth of the texture following the formation of a new compound during the synthesis of titanium nitride on exposure to laser radiation in high-pressure nitrogen. The thickness of the reduced tungsten layer on an oxidized tungsten plate varies from 25 to 100 μm depending on the hydrogen pressure in the chamber; it decreases with increasing pressure since the plasma plume generated at higher pressures shields the target.

From the experimental results we can estimate the mechanism of laser interaction with trioxides of refractory metals. At low hydrogen pressures, laser pulses with power densities of 10^4 to 10^5 W/cm^2 damage the target material. With an increase of the pressure, the plasma formed shields the target and no traces of damage are visible. In these conditions, a fraction of LR and plasma radiation interact with the material and, possibly, protons bombard the surface. This joint action appreciably facilitates the process of chemical transformation in the specimen material and leads to the reduction of the metal from the trioxide. The metal so obtained displays some interesting properties. For example, it exhibits a texture which distinguishes this reduced metal from the metal produced by other methods.

The experimental results of the simultaneous interaction of a laser beam and high-frequency discharge with the surface layers of oxides in a gaseous reducing medium are described in work [27]. It has been found that the rate of the reducing reaction increases 10^4 times and more.

Laser-induced synthesis of nitrides on the surfaces of specimens in high-pressure gases. The interaction of the laser-supported plasma with a metal surface makes it possible to synthesize a number of compounds. Work [26] was the first to present the results of experiments on the plasma-produced synthesis of titanium nitride in high-pressure nitrogen. The experiments were performed on the substrates of as-received titanium. The compound structure was studied by radiographic and X-ray diffraction methods. Let us look at the process of synthesis more closely. As mentioned above, the synthesis requires the plasma which forms at the threshold values of laser power density and nitrogen pressure. According to the results, at a nitrogen pressure of 10 MPa and an average laser power density of 5×10^6 W/cm^2 in a pulse, the microhardness reaches 2.3 to 2.6 $\times$ $\times$ 10^3 MPa and remains invariable ($\sim 2.3 \times 10^3$ MPa) over a wide pressure range. The surface layer of titanium nitride displays the preferred orientation during crystallization. Earlier experiments with some alloys exposed to LR revealed the same phenomenon, but it was not associated with the formation of a new compound. The thick-

ness of the titanium nitride layer on the substrate struck by a laser pulse close to $\sim$ 1 ms in duration ranges from a few units to tens of micrometers depending on the conditions of laser treatment. The layer thickness at its extreme values exhibits a weak dependence on pressure. At $q = 3 \times 10^6$ W/cm^2, a maximum of the layer thickness corresponds to a pressure of 10-10.5 MPa.

Along with titanium, zicronium and niobium are also found to be the most active nitride-forming metals when exposed to a laser beam in nitrogen. These metals treated by a laser beam at a high nitrogen pressure convert to golden-colored nitrides of an enhanced microhardness.

Consider some features specific to the formation of nitrides synthesized during the laser interaction with metals. Experiments [28] established the relation between the processes of self-excited oscillation in the plasma near the surface and the formation of the nitride structure on the metal surface and also revealed how the conditions of irradiation and the methods of nitrogen supply to the test specimens influence the structure and properties of nitrides grown on the surfaces of refractory metal targets.

In the experiments, an Nd-doped laser pulse 1 ms in duration with a power density in the range 10^5-5×10^5 W/cm^2 was focused on the surfaces of specimens from titanium castings. Two arrangements were used to supply nitrogen to the specimen surface. In the first arrangement, nitrogen was brought onto the surface through a nozzle coaxial with the laser beam. The velocity of the gas jet was varied from 1 to 80 m/s. In the second arrangement, provision was made to dispose specimens in a high-pressure chamber where the nitrogen pressure was varied from 0.1 to 8.0 MPa.

The X-ray diffraction analysis revealed that in both cases of nitrogen feed the nitride of the stoichiometric composition was formed on the surfaces of titanium specimens.

The nitrided zone on the specimen irradiated in the chamber with nitrogen held at a pressure close to the atmospheric consists of a thin monolayer of titanium nitride that exhibits a columnar-dendritic structure and a narrow dark strip, probably of an α-phase or a mixture of $\alpha + \varepsilon$ and $\varepsilon +$ TiN phases [28], with the total thickness of both layers varying from 1 to 5 μm. Below this structure there are two layers: a light, softer layer at a depth of $\sim$ 200 μm, which corresponds to the solid solution of nitrogen in α-titanium, and a transition layer with an enhanced microhardness as compared to that of the base metal.

An increase in the gas pressure tends to change the zone structure. The thickness of both the nitride layer and ε-phase layer grows to 15-20 μm, while that of the solid solution of nitrogen in α-Ti gradually decreases, until this layer vanishes completely at a nitrogen pressure of about 4 MPa.

At $p \geqslant 4$ MPa and $q = 3 \times 10^6$ W/cm^2, the microstructure of the treated zone exhibits a few nitride monolayers, one disposed above the other, with an ε-phase strip sandwiched inbetween. This multilayer structure is built up under the effect of the oscillatory process occurring in the plasma near the surface [5, 6]. Self-sustained oscillations in the LR-plasma-surface system can be set up at $p > 1$ MPa [5, 6], but the microstructure analysis of the zone treated at 1-4 MPa has not detected the multilayer structure. This is probably because the amplitude of self-excited oscillations in this range of pressures is still low; the amplitude grows with pressure [6]. So, changes in the physical parameters of the plasma near the surface do not exert a strong effect on the process of synthesis of nitrides on the metal target.

It should be noted that in certain conditions typical of the specimen material and parameters of the process, nitride monolayers show a disturbed pattern of arrangement due to a turbulent motion of the melt in the pool.

The microhardness across the treated zone varies most sharply from the nitride layer to the solid solution layer and from the latter to the base metal. The characteristic values of microhardness of the nitride layer, solid solution layer, and transition layer are: $\sim$ (1-2) 10^4 MPa, (3-9)10^3 MPa, and 2×10^3 MPa respectively. The microhardness within each layer depends on the process parameters: the higher the laser power density and pressure in the chamber, the greater the microhardness. For the solid solution of nitrogen in α-Ti, the microhardness versus pressure and power density displays a clear-cut pattern.

After prolonged etching of specimens (over 10 min) in an aqueous solution of HF (1-2%) and HNO_3 (2-3%), individual portions of the nitride zone have been found to display a different etchability. The most resistant to the attack of the etchant are dendritic pile-ups which form a peculiar skeleton of the nitride zone. This skeleton becomes well discernible after etching the base metal that fills the gaps between dendritic branches. Some areas contain dense dendritic clusters immune from the etchant. The microhardness of these clusters reaches $\sim 2 \times 10^4$ MPa against $\sim 10^4$ MPa for the base metal. The nonequilibrium conditions of crystallization result in the chemical inhomogeneity of the nitride zone. This is particularly the case where the conditions of the process encourage the turbulent motion of the melt in the heat zone.

In the nitrided specimens irradiated in the nitrogen jet issuing at velocities of 1 to 20 m/s, the zone structure is similar to that observable in specimens exposed to LR in the chamber at $p \leqslant 10$ MPa. On changing the laser power density from 10^5 to 5×10^6 W/cm^2 and the jet velocity from 1 to 20 m/s, both the nitride layer and the solid solution of nitrogen in α-Ti first grow in thick-

ness to a certain maximum value, $h_{TiN} \simeq 15$ μm and $h_{\alpha\text{-}Ti} \simeq 200$ μm, and then the thickness diminishes. A further increase in the parameters of the process leads to a turbulent motion of the liquid metal accompanied by the formation of the crater in the interaction zone.

Let us examine the kinetics of the processes in the heat affected zone. With nitrogen forced to the interaction zone through a nozzle and also at nitrogen pressures equal to $p \leqslant 1$ MPa in the chamber, the degree of plume ionization determined experimentally from the values of the charge transferred by the plasma lies between 10^{-2} and 10^{-3}%. In these conditions, the melt is in contact mainly with molecular nitrogen which dissociates on the melt surface and diffuses into the molten pool to form the solid solution of nitrogen in α-Ti and the titanium nitride. As the thickness of the nitride layer goes on growing, the diffusion of nitrogen into the metal slows down with increasing values of the parameters, q, v, and p. A further increase in q, v, and p leads to a decrease in the depth of both the nitride layer and the solid solution layer because the surface begins to vaporize; the plasma then more strongly shields the laser beam, and, besides, a fraction of the melt flushes out of the interaction zone.

While the gas jet adds to the onset of cratering at lower energies, the nitrogen pressure raised above 1.0-1.5 MPa in the chamber augments both the temperature of the plasma and the degree of its ionization to ~ 0.1%. The solubility of nitrogen in the melt then rises, which promotes the growth of the nitride layer at the expense of a decrease in the thickness of the solid solution layer. A rather opaque plasma formed in the process partially or totally shields the target surface from the laser pulse and reduces the penetration depth.

Periodic changes in the physical parameters and, hence, in the chemical activity of the plasma that depends on the oscillatory processes cause the formation fo a multilayer nitride zone on the metal surface. This process of multilayer nitride formation coupled with the development of turbulent motion in the molten pool at high pressures of the cover gas indirectly confirms that self-sustained oscillations exist in the LR-plasma-target surface system.

Lasers emitting at different wavelengths are suitable for nitride synthesis. Work [29] presented the results of titanium nitride synthesis in nitrogen at $p = 0.1$-2.5 MPa using CO_2 pulses 0.5 to 1 μs long with $E = 0.05$-0.5 J. The studies revealed the effect of an external electric field on the process of gas breakdown near the specimen and the intensity of metal nitriding. The efficiency of interaction grows at a rather high field strength, $E/p \geqslant 0.002$ V/cm MPa, that is enough to initiate an arc discharge between electrode and target following the plasma formation. In the interaction zone there

forms a cast structure of columnar crystals of titanium nitride, which is similar to the structure produced on the surface of titanium by the neodymium laser emitting pulses $\sim$ 1 ms in duration with a power density ranging from 10^5 to 10^6 W/cm^2 [26].

Synthesis of carbides. Studies of carbide synthesis on the surfaces of metals in the CO_2 medium were made by workers of [1]. The experiments show that even at pressures of $\sim$ 2 MPa, the diameter of the fused region is a few times the diameter of the focal spot because the plasma in CO_2 contains charged particles of increased density just at the start of the process. The result is a smooth change in the angle of laser light refraction and expansion of the interaction region.

The X-ray diffraction analysis has disclosed the course of carbide synthesis on the surfaces of metals struck by laser pulses [1]. The thickness of a carbide layer reaches 5-10 μm; the microhardness at the center of the focal spot is as high as 2.5 to 2.8 $\times$ 10^4 MPa, but drops to 1.8-1.9 $\times$ 10^4 MPa in the direction toward the spot edges.

The microhardness H_μ of Mo specimens exposed to LR over a wide range of power densities in the CO_2 atmosphere at $p = 3$ MPa comes to 6.0-7.0 $\times$ 10^2 MPa, the initial value of H_μ being in the order of 4.40 $\times$ 10^2 MPa.

As revealed by the X-ray analysis, laser beams falling on tantalum plates placed in a CO_2 medium produce tantalum carbides in the zones of interaction. The microhardness of carbide layers ranges from 1.5 $\times$ 10^4 to 1.7 $\times$ 10^4 MPa.

A laser beam interacting with Ti and Zr specimens changes the structure of the affected zones 2 to 3 mm in diameter and 30-100 μm in thickness. The diameter of the zones on the surfaces of niobium and molybdenum specimens does not exceed 1.5 mm. From the results of metallographic examinations of specimens from Ti and Mo it is evident that the structure of the zones is inhomogeneous in depth. The laser-treated zone consists of a few dendritic layers, each 5 to 15 μm thick, separated by light, poorly etched layers of the same thickness. In titanium specimens, the microhardness of light layers is (1.10-1.40) 10^3 MPa, while that of layers with a dendritic structure is lower, (0.70-0.80) 10^3 MPa.

Synthesis of other materials. In a number of experiments, a CW CO_2 laser was used to obtain silicon carbide, graphite and diamond whiskers from a gaseous phase, diamond films, and homogeneous condensates of diamond in hydrocarbon vapors. Studies were also made of the kinetics of formation of silicon carbide on the surfaces of various materials in the course of decomposition of methyl trichlorosilane. The limiting stage was found to be the stage of decomposition of a methyl radical yielding carbon which then underwent siliconizing. Filamentary crystals of diamond and graphite were grown

from a gaseous phase. Diamond whiskers grew on the surface of a seed crystal. In some cases, their growth discontinued and they assumed a spherical form.

Graphite whiskers were grown on substrates of carbide-forming metals and metals incapable of forming carbides [30]. They appeared on surface defects. The rupture strength of graphite whiskers less than 1 μm in diameter reached 1.5×10^3 MPa.

Diamond films were grown on the laser-heated surfaces of diamond seeds at temperatures of up to 2 000 K, i.e. up to the point of spontaneous graphitization of diamond. These films can form at high temperature only in methane; other hydrocarbons such as ethane, ethylene, and acetylene promote graphitization of the diamond seeds. In experiments on the homogeneous formation of diamond in hydrocarbon vapors, a drop of liquid octane or nonane was allowed to fall and pass through the focus of the CO_2 laser beam. By changing the dropping height, it was possible to vary the time of interaction of the beam with the drop. A homogeneous condensation occurred in hydrocarbon vapors, yielding small particles of the condensated phase of carbon. Electron and X-ray diffraction methods made it possible to detect diamond, graphite, and other substances in the laser-treated zone. Fast quenching of the products of laser synthesis is likely to play the dominant role in this process; the experiments on the solid-solid transition of graphite into diamond confirm this view. Graphite particles were laser-heated to 3 000 K and then cooled in liquid nitrogen. Facte quenching took place in a thin surface layer to yield metastable carbon phases [30].

A CO_2 laser delivering 40 W of power at a focused spot 1 mm in diameter was used to form sufficiently long single crystals of cuprous oxide in an oxidizing atmosphere [31].

The examinations of transverse metallographic specimens reveal that the oxide film forms a plane-parallel layer with a clear-out boundary between Cu, Cu_2O, and CuO. From the X-ray diffraction analysis it is apparent that cuprous oxide Cu_2O grows into a single crystal layer that displays an enhanced resistance to attack by etchants, improved stability to mechanical influences, and adheres more strongly to the substrate than the oxide grown in isothermal conditions. Specimens exhibit sparcely located long crystals of cuprous oxide [31]. These crystals are clearly discernible against the background of the plane-parallel single crystal film.

During 30 min of laser interaction it was possible to obtain crystals up to 1 mm long. A heat source delivering the same amount of average power, with the laser emitting in a wide spectral range, failed to produce long crystals of cuprous oxide.

6.5. LASER-INDUCED THERMOCHEMICAL PROCESSES

A laser beam interacting with materials encourages thermochemical reactions through which it is possible to reduce metals, decompose complex compounds, synthesize materials, oxidize metal surfaces, etc. Detailed treatment of thermochemical phenomena is given in works [2-4].

Oxidation of metals. A laser beam incident on metals in oxygen or air causes the growth of an oxide film on the target surface, which changes the surface absorptivity. As shown by experiments, oxide layers can appear on the target surfaces even when they interact with rather short pulses, $\sim$ 100 ns. Pulses of $\sim$ 1 ms duration promote the growth of oxide films 0.01 to 0.1 μm thick [2], and CW laser beams can encourage oxidation to a depth of tens of micrometers.

The isothermal surface oxidation of metals proceeds in a few stages: surface adsorption of oxygen; binding of the free electrons of the metal or of the oxide with oxygen; diffusion and migration of metal and oxygen ions through vacancies and interstitial sites of the reaction products to phase boundaries; and the chemical reaction proper that yields a new oxide layer [32].

The metal oxidation rate depends on the temperature, oxide thickness, oxygen pressure, and other factors. But, in each specific case, it is the slowest (controlling) step of the process that places the upper limit on the oxidation rate.

The kinetics of the isothermal oxidation of metals can in some cases be described by the equation

$$\frac{dh}{dt} = \frac{B_m}{h^m T^n} \exp\left(-\frac{T_a}{T}\right) \tag{6.4}$$

where h is the oxide thickness, B_m a constant, T_a the temperature of activation at the slowest stage of the reaction, which commonly ranges between 1×10^4 and 5×10^4 K, and m and n the parameters.

Most of the known relations that define the oxidation process can be set up from (6.4). When $m = n = 0$, equation (6.4) describes the linear oxidation, for which the reaction rate is independent of the oxide thickness. When $m = 0$ and $n = -2$, equation (6.4) is linear too, but here it is the thermionic emission from the metal rather than the emission of ions from the metal to the oxide that limits the reaction rate. The case $m = 1$ corresponds to the Mott formula [32] if $n = 1$ and to the Wagner formula if $n = 0$. These formulas conform to the parabolic relations of oxidation controlled by diffusion or ion migration in the oxide. If $m = 2$, a cubic relation for isothermal oxidation follows from (6.4).

The main factor determining the kinetic mechanism of metal oxidation is the heat evolved in the interaction of LR with the metal

target and the metal-oxide system. Temperature exerts a decisive effect on the process of oxidation of thin heat-affected specimens since they cool slower than bulk specimens.

The calculation of temperature for an oxide-metal system exposed to laser radiation is a rather complex problem because the rate of temperature growth depends on the oxide layer thickness at each moment of time. The initial stage of heating of a metal plate oxidizing in air was treated in work [4]. The mathematical statement of the given problem is written as

$$\left.\begin{aligned} &\frac{dh}{dt}=\frac{d}{h}\exp\left(-\frac{T_a}{T}\right), \quad h|_{t=0}=0 \\ &mc\,\frac{dT}{dt}=PA(h)-P_l(t) \\ &T|_{t=0}=T_0, \quad A(h)=A_0+bh^2, \quad P_l=\alpha S(T-T_0) \end{aligned}\right\} \tag{6.5}$$

where h is the thickness of the oxide film on the metal target surface, d and T constants of the parabolic law of oxidation, P incident laser power, $A(h)$ the absorptivity of the metal-oxide system, P_l the heat power lost through convection, A_0 the metal absorptivity, α the heat transfer coefficient, and S the target surface area.

A three-dimensional heat transfer problem on laser heating of a metal with regard to the rate of oxide film growth is more complex. If we neglect the chemical reaction heat, the heat lost from the surface, and the complex structure of the oxide film being grown, the problem of heating of a semi-infinite body by a Gaussian CO_2 laser beam, with allowance made for the oxide film growth, will take the form [33]

$$\frac{1}{a}\frac{\partial T}{\partial t}=\frac{\partial^2 T}{\partial r^2}+\frac{1}{r}\frac{\partial T}{\partial r}+\frac{\partial^2 T}{\partial z^2} \tag{6.6}$$

$$\lambda\frac{\partial T}{\partial z}\Big|_{z=0}=-q_0A(h)\exp(-kr^2), \qquad \frac{dh}{dt}=\frac{d}{h}\exp\left(-\frac{T_a}{T}\right)$$

$$T(r,\ z,\ 0)=T(\infty,\ z,\ t)=T(r,\ \infty,\ t)=T_0, \quad h(t)|_{t=0}=0$$

According to (6.6), the oxide film thickness varies in a parabolic manner that is valid for the growth of "thick" films, $h \geqslant 0.1$ μm. A thin oxide layer grows for a relatively small time, but this stage of growth is of little importance for the problem of metal heating with LR. Since the laser power density is fairly high, in the order of 10^5-10^6 W/cm^2, the surface heat loss may be neglected.

The absorptivity of a two-layer (metal-oxide) system is [4]

$$A(h)=1-(1-A_0)\exp(-2\alpha h)-\frac{2\varkappa}{n}\sin\beta h\exp(-\alpha h) \tag{6.7}$$

where $\alpha=(4\pi/\lambda)\mathrm{Im}\sqrt{\varepsilon}$, $\beta=(4\pi/\lambda)\,\mathrm{Re}\sqrt{\varepsilon}$, $\sqrt{\varepsilon}=n+i\varkappa$, n is the real part, $\varkappa$ the imaginary part, ε the oxide permittivity, λ

the laser wavelength, Im the sign of the imaginary part of the number, and Re the sign of the real part.

At $q_0 \geqslant 10^5$ W/cm^2, the characteristic thickness of an oxide film does not exceed 3 μm. Therefore, an approximate form of the function $A(h)$, as illustrated in Fig. 6.21, can be valid.

For the solution of the problem (6.6), the iterative process is set up so that its zero approximation $T_0(r, z, t)$ can allow for solving equations (6.6) in the absence of the reaction on the target surface.

The oxide film thickness at the hot spot center as a function of dimensionless time at different values of laser power density q_0 is shown in Fig. 6.22. At $t \leqslant t_{st}$, where t_{st} is the time required to reach the steady-state temperature in the absence of the reaction, the oxide film rapidly grows in thickness. The rate of growth heavily increases with the power density since the oxidation reaction then proceeds much more intensely. At $t > t_{st}$, the dependence of the oxide film thickness on time is weaker because the temperature, which is close to zero, reaches its steady-state value and a change in the rate of the reaction becomes smaller.

Figure 6.23 illustrates the curves of the oxide film thickness versus dimensionless distance $k^{1/2} r$ to the hot spot center at different moments of time at point $r = 0$. For comparison, the figure presents the laser power density versus time (curve *3*). At small times of heating, the spatial dependence of the oxide film thickness and, hence, of the absorptivity takes on a sharply defined pattern

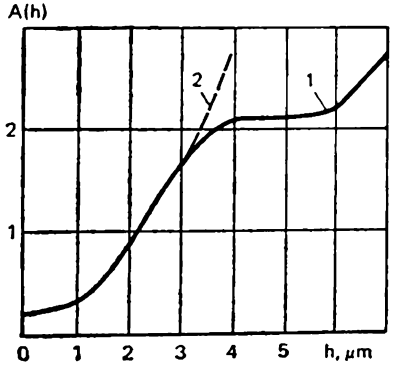

Fig. 6.21. Absorptivity A versus oxide film thickness h: *1*, accurate form of $A(h)$; *2*, approximate form of $A(h)$

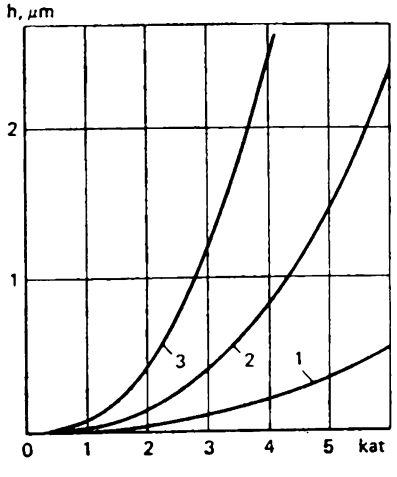

Fig. 6.22. Oxide film thickness versus time in the center of hot spot at different values of q_0: 1, 3×10^5 W/cm^2; *2*, 4×10^5 W/cm^2; *3*, 5×10^5 W/cm^2

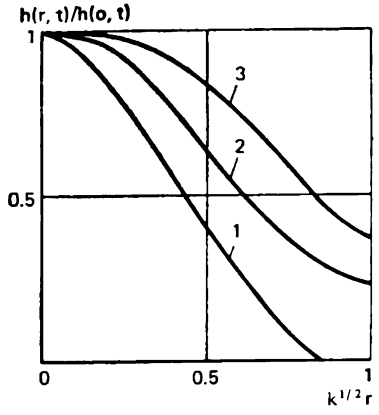

Fig. 6.23. Normalized distribution of oxide film thickness at different moments of time: *1*, $t = 0.6$; *2*, $t = 10$; *3*, specified laser power density

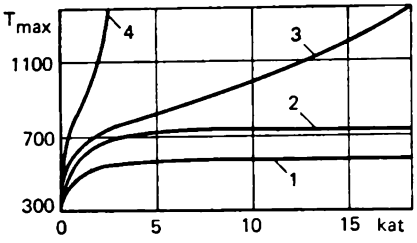

Fig. 6.24. Temperature versus dimensionless time in the center of hot spot at different values of q_0: 1, 2×10^5 W/cm^2; *2*, 3×10^5 W/cm^2; *3*, 4×10^5 W/cm^2; *4*, 5×10^5 W/cm^2; k, concentration coefficient; a, thermal diffusivity

(curve *1*), but then it gets smoother with time due to the effect of heat conduction that "blurs" the distribution of the oxide film in depth. The surface temperature distribution is more complex in character. It becomes sharp or less distinct depending on two competing factors: the peaked distribution of the absorbed laser power due to a nonuniform oxide film thickness and the effect of heat transfer. The oxidation reaction that proceeds on the target surface determines the specific mechanisms of heating depending on the laser power density (Fig. 6.24). At low values of q_0 (for Cu, $q_0 \leqslant 10^5$ W/cm^2 at $\lambda = 10.6$ μm), the absorptivity remains in essence invariable and the nonsteady-state temperature at the center of the focal spot obeys the expression $\operatorname{arctg} 2\sqrt{kat}$ (curve *1*). With an increase in q_0, the temperature rises linearly from the steady-state value that corresponds to the solution of the problem without regard to the chemical reaction on the metal surface (curve *2*). As the density of the radiant flux continues to grow, the temperature begins to rise sharply from a certain moment.

The effect of oxidation on optical properties of metals [2]. The growth of oxide films significantly changes the physical and chemical properties of the surface layers on the metal target, namely, the electrical conductivity, chemical activity, emissivity, hardness, and absorptivity. The mechanisms which are responsible for changes in the absorptivity and are due to the interaction of oxygen with laser-heated metal target surfaces are described in a number of works, for

example, in [2]. These include: (1) direct absorption of radiation in the oxide; (2) coordinate effect of the oxide coat as it absorbs radiation and interference effects in the oxide; (3) temperature-dependent electron-hole absorption in the oxide and changes in the refractive index of the oxide due to charge carrier generation; (4) changes in the plasma frequency and collision frequency of free carriers in the skin layer due to variations of the lattice parameters following the diffusion and dissolution of oxygen [34]; (5) changes in the composition of the skin layer of the alloy and in the optical constants of the layer as the result of oxidation of some elements of the alloy.

The above mechanisms of changes in the absorptivity allow us to qualitatively explain some specific features of laser heating of oxidizing metals: a sharp transition to disintegration, emergence of temperature oscillation, continued heating after the end of laser interaction, etc.

With few exceptions, oxidation entails a decrease in the reflection of light from the metal surface in a wide spectral range. The character of changes in the absorptivity of the oxidized metal depends on the optical thickness of the oxide film, i.e. on the value of $\alpha_1\lambda$. If $\alpha_1\lambda \gg 1$, the absorptivity steadily increases with the oxide growth from an initial value of $A = A_0$ for a nonoxidized surface to a value of A_1 for a bulk oxide layer.

The condition $\alpha_1\lambda \ll 1$ holds more often for oxides, which indicates that they weakly absorb radiation. To these oxides belong Cu_2O, Al_2O_3, and TiO_2, which are impurity semiconductors whose bandgap varies from 1.5 to 3.0 eV. The absorptivity fluctuations due to the interference of LR in the oxide layers are specific to these oxides.

The estimates show that in the interaction of lasers emitting in the visible and in the near infra-red, changes in the absorptivity due to oxidation can occur when the oxide film grows to a thickness of $\sim 10^{-6}$-10^{-5} cm. For the radiation from a CO_2 laser, this thickness is somewhat greater, $\sim 10^{-5}$-10^{-4} cm, i.e. variations in A occur after a longer interaction of radiation [2].

An important factor that determines the behavior of thermochemical processes in metals exposed to LR is the exothermicity of oxidation. In metals with a strong thermal effect of oxidation, the reaction exothermicity can radically alter the character of the treatment desired.

Changes in the absorptivity of titanium, zirconium, hafnium, and other metals laser-heated in air or in oxygen may arise from the diffusion and dissolution of oxygen in the surface layer, since these processes change the plasma frequency and collision frequency of free electrons [2].

A specific mechanism which leads to changes in absorptivity as the result of thermochemical processes in the skin layer is observab-

le in alloys. A predominant oxidation of some elements of the alloy laser-heated in air changes the percentage of these elements entering the skin layer [34].

The actual process of laser-induced oxidation and its effect on the optical properties of metals is by far more complex than the models used to calculate the laser-induced effects. It is found that the composition of oxide films formed on titanium and steel targets during pulsed laser heating varies in depth and exhibits poorly defined boundaries between the oxides of different valences and also between the oxides and metals [26].

The above described theoretical concepts of the formation of plane oxide layers are certainly conditional since the plane front of oxidation is unstable to perturbations in a wide range of spatial frequencies. The deviation of the actual oxide surface from the plane one and of the oxide structure from the homogeneous one was the subject of study in [2].

References

1. N. N. Rykalin and A. A. Uglov. *Laser-and-plasma treatment of metals at high gas pressures.* Kvantovaya Elektronika, v. 8, p. 1193, 1981.
2. A. M. Bonch-Bruevich and M. N. Libenson. *Nonresonant laser chemistry involved in the processes of interaction of strong radiation with materials.* Izv. AN SSSR. Physical Series, **46**: No. 6, p. 1104, 1982.
3. F. V. Bunkin, N. A. Kirichenko, and B. S. Lukyanchuk. *Laser thermochemistry.* Izv. AN SSSR. Physical Series, **46**: No. 6, p. 1150, 1982.
4. F. V. Bunkin, N. A. Kirichenko, and B. S. Lukyanchuk. *Thermochemical effect of laser radiation.* Uspekhi Fizich. Nauk, 138: No. 9, p. 45, 1982.
5. N. N. Rykalin, A. A. Uglov, and M. B. Ignatyev. *Oscillatory character of changes in the parameters of the laser-produced plasma near the target surface in high-pressure gases.* Dokl. AN SSSR, 256: No. 5, p. 1117, 1982.
6. A. A. Uglov and M. B. Ignatyev. *Self-sustained oscillations in the interaction of the laser beam with a solid target surface in high-pressure gases.* Pisma v ZhTF, 8: No. 8, p. 481, 1982.
7. N. N. Rykalin, A. A. Uglov, and A. L. Galiev. *Radiation absorption by a plasma formed near a solid target surface at high pressures of gases.* Fizika Plazmy, 2: No. 2, p. 332, 1978.
8. N. N. Rykalin, V. I. Skobelkin, I. V. Zuev et al. *A model representing self-sustained oscillations in the continuous interaction of a concentrated energy flux with a substance.* Dokl. AN SSSR, 257: No. 7, p. 99, 1981.
9. A. A. Uglov and A. L. Galiev. *On the development of a laser-supported plasma near a solid target in high-pressure gases.* Kvantovaya Elektronika, 7: 2, p. 244, 1980.
10. S. I. Valyanskiy, B. M. Zhiryakov, N. I. Lipatov, et al. *Behavior of the reactive pressure in the interaction of strong optical radiation with metals*: in Proceedings of the 4th All-Union conference on the nonresonant interaction of optical radiation with materials. Leningrad, Nauka, p. 106, 1978 (in Russian).
11. A. A. Uglov and A. L. Galiev. *Interaction of a laser beam with a moving target in high-pressure gases.* Fizika i Khimiya Obrabotki Materialov, No. 3, p. 23, 1978.

12. N. N. Rykalin, A. A. Uglov, and M. M. Nizametdinov. *On laser-material interactions in a wide range of argon pressures.* Kvantovaya Elektronika No. 4, p. 18, 1978.
13. A. A. Uglov, A. G. Gnedovets, and A. L. Galiev. *Changes in the microhardness of steel under laser radiation in inert gases.* Fizika i Khimiya Obrabotki Materialov, No. 4, p. 18, 1978.
14. N. N. Rykalin, A. A. Uglov, and M. M. Nizametdinov. *On pulsed laser-material interactions in a wide range of helium pressures.* Fizika i Khimiya Obrabotki Materialov, No. 1, p. 24, 1978.
15. A. A. Uglov and M. B. Ignatyev. *Effect of a gaseous atmosphere on laser-induced erosion of refractory metals.* Fizika i Khimiya Obrabotki Materialov, No. 1, p. 137, 1984.
16. Yu. P. Rayzer. *Fundamentals of modern physics of gas-discharge processes.* Moscow, Nauka, 1980 (in Russian).
17. C. T. Walters, R. N. Barnes, and R. E. Baverly. *Initiation of laser-supported detonation (LSD) waves.* J. Appl. Phys., 49: No. 5, p. 2938, 1978.
18. V. I. Mazhukin, A. A. Uglov, and B. N. Chetverushkin. *Modeling of laser-induced molecular gas breakdown near a metal surface.* Dokl. AN SSSR, 246: No. 6, p. 1338, 1979.
19. V. I. Mazhukin, A. A. Uglov, and B. N. Chetverushkin. *Optically induced molecular gas breakdown in a wide range of pressures near a solid target.* Kvantovaya Elektronika, 9: No. 5, p. 906, 1982.
20. V. I. Mazhukin, A. A. Uglov, and B. N. Chetverushkin. *Numerical analysis of laser spark initiation in a dense gas near a metal surface.* Fizika i Khimiya Obrabotki Materialov, No. 6, p. 73, 1979.
21. V. I. Mazhukin, A. A. Uglov, and B. N. Chetverushkin. *Numerical analysis of the problem on laser-induced dense gas breakdown.* Zhurnal Vychisl. Matem, i Matemat. Fiziki, 20: No. 2, p. 451, 1980.
22. V. I. Mazhukin, A. A. Uglov, and B. N. Chetverushkin. *On laser-induced low-pressure plasma in high-pressure nitrogen.* Dokl. AN SSSR, 257: No. 3, p. 584, 1981.
23. V. I. Mazhukin, A. A. Uglov, and B. N. Chetverushkin. *A numerical analysis of the dynamics of laser-induced plasma near a solid surface at a high ambient pressure.* Dokl. AN SSSR, 256: 5, p. 1100, 1981.
24. L. D. Landau and E. M. Lifshits. *Electrodynamics of continua.* Moscow, Nauka, 1982, in Russian.
25. S. S. Gorelik, L. N. Rastorguev, and Yu. A. Skakov. *Radiographic and optoelectronic analysis.* Moscow, Metallurgiya, 1970 (in Russian).
26. A. L. Galiev, L. L. Krapivin, Mirkin L. I., et al. *Laser-supported synthesis of titanium nitride in high-pressure nitrogen.* Dokl. AN SSSR, 251: No. 2, p. 336, 1980.
27. P. A. Skiba and A. G. Nepokoychitskiy. *On phase transformations of oxide systems under the joint effect of laser radiation and HF discharge*: in Proceedings of the 5th All-Union conference on nonresonant interaction of optical radiation with materials. Leningrad, Nauka, p. 315, 1981 (in Russian).
28. N. N. Rykalin, A. A. Uglov, V. A. Grebennikov, et al. *On formation of nitrides in laser interaction with metals.* Dokl. AN SSSR, 272: No. 3, p. 930, 1983.
29. A. G. Gnedovets, V. A. Grebennikov, V. I. Konov, et al. *CO_2 laser synthesis of titanium nitride at high nitrogen pressures*: in Proceedings of the 5th All-Union conference on nonresonant interaction of optical radiation with materials. Leningrad, Nauka, p. 361, 1981 (in Russian).
30. D. V. Fedoseev and I. G. Varshavskaya. *Use of laser heating for synthesis of refractory materials*: in Proceedings of the 5th All-Union conference on nonresonant interaction of optical radiation with materials. Leningrad, Nauka, p. 285, 1981 (in Russian).
31. D. T. Alimov, F. V. Bunkin, E. Yu. Egorov, et al. *Laser-induced growth of "giant" single crystals*: in Proceedings of the 5th All-Union conference on non-

resonant interaction of optical radiation with materials. Leningrad, Nauka, p. 292, 1981 (in Russian).
32. P. Barret. *Cinetique heterogene.* Cauthier-Villars, Paris, 1973.
33. A. A. Uglov, I. Yu. Smurov, and A. A. Volkov. *Calculation of laser heating of metals in an oxidizing atmosphere*: in Proceedings of the All-Union conference on application of lasers in machine building. Moscow, Nauka, p. 100, 1982 (in Russian).
34. A. G. Akimov, A. M. Bonch-Bruevich, A. P. Gagarin, et al. *Effect of the elementary composition on the optical properties of alloys during pulsed laser heating.* Pisma v ZhTF, 6: No. 10, p. 1017, 1980.

Part 2
LASER MATERIAL PROCESSING

Chapter 7
HEAT TREATMENT

Heat treatment, or surface hardening, is one of the recent successful applications of lasers to industrial material processing, which opens up new possibilities for improving service characteristics of metal parts and tools.

There are several potential advantages to laser heat treatment.

1. Selective hardening of workpieces to a required depth and width at the sites of excessive wear without affecting the desirable properties of the substrate metal; the attainable hardness is 15 to 20% higher than that achieved by conventional methods.

2. Surface hardening of difficult-to-reach cavities and areas since there is a possibility of directing the beam to any point by means of focusing optics.

3. Formation of hardened bands of any desired pattern on the target surface rather than of the layer hardened over the entire surface, which is prone to cracking, deformation, and spallation.

4. The ability to impart the surface the desirable mechanical and chemical properties through laser alloying, hard coating, and skin melting (cladding, or hardfacing).

5. The ability to obtain fine roughness of hardened surfaces, if required.

6. Negligible distortion of parts owing to localized heat treatment, which generally allows dispensing with post-hardening machining.

7. Lack of tool contact along with the ability to scan the beam over the part, which affords ease of automation of the process for hardening complex shapes.

The methods of laser heat treatment are advantageous for use in the following cases: the surfaces are complex in shape, the distortion of which must be brought to a minimum; the heat input to the treatment zone by conventional methods involves difficulties; and the zone is small in size in comparison with the part.

The main factors that determine wide application of laser heat treatment in various branches of industry are as follows.

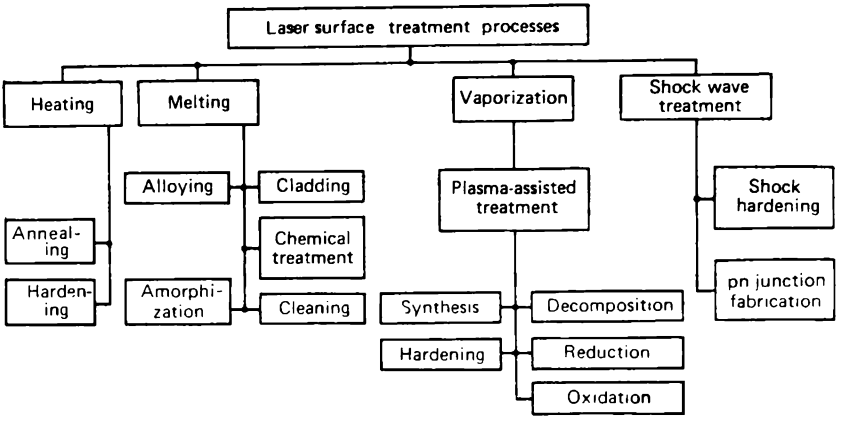

Fig. 7.1. Classification of the methods of laser surface treatment of materials

1. Standard high-capacity laser equipment, both pulsed and CW, is available.

2. Laser hardening is a comparatively simple process as against laser hole piercing, welding, and cutting, so it is easy to select the optimal conditions of treatment.

3. There is a wide range of parts requiring local hardening.

4. The process is highly efficient.

In some cases, the shape and size of parts do not allow the use of common methods of surface hardening since they induce high stresses in surface layers, which cause cold and hot cracking and distortion of parts. That is why the strength of such parts made, for example, from as-cast structural steels is generally low.

It is often desirable that the machinery parts should have a maximum strength at the surface to enable them to stand up to impact loads and to resist abrasive wear, while retaining the original toughness in the bulk where the hardness decreases in depth from a maximum to a minimum value. Lasers applied in material processing provide the desired properties of the surfaces of parts.

The classification of the methods of laser surface treatment is shown in Fig. 7.1. These methods fall into several groups according to the dominant process involved in laser interaction: heating, melting, vaporization, and treatment under laser-induced shock affects (shock hardening).

Laser heating determines such processes as material annealing and surface hardening through solid phase transformations. The latter process involving a very rapid heating and subsequent cooling of metals and alloys is most popular. Surface hardening with melting (liquid phase quenching) also belongs to this group of the methods of

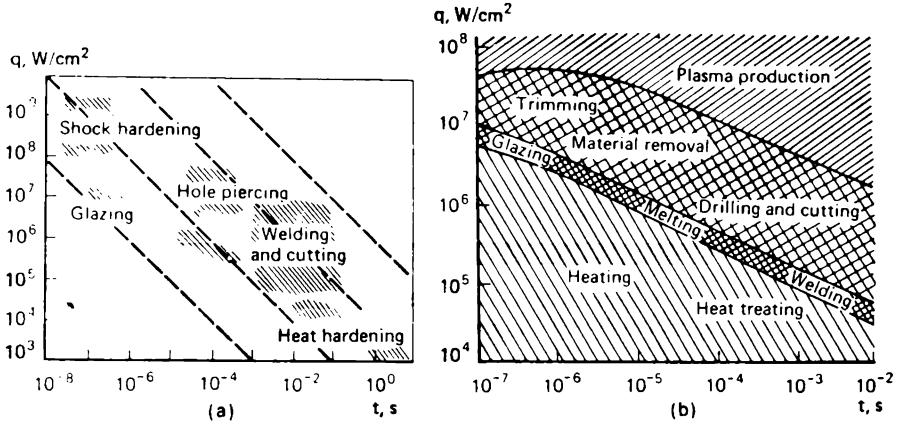

Fig. 7.2. Regions of laser power density and pulse duration suitable for various surface treatment processes (*a*) and diagrams of the processes (*b*) [1, 2]

treatment. Melting can provide surface alloying, amorphization, cladding, and cleaning of metal and alloy grains. Laser shock hardening is the process of surface treatment by giant pulses of very high peak power densities.

Figure 7.2 identifies the regions of laser power density suitable for various material-processing applications and diagrams of corresponding processes [1, 2]. Laser hardening based on phase transformations in surface layers (transformation hardening) covers the region of low power densities from 10^3 to 10^4 W/cm² with times of laser interaction ranging from 10^{-2}, to 1 s, whereas shock hardening covers the region of maximum power densities from 10^8 to 10^{10} W/cm², with the time of laser-solid surface interaction held at a minimum, $\sim 10^{-6}$-10^{-8} s [1, 3].

7.1. PHYSICAL PRINCIPLES OF MATERIAL HARDENING

In many industrial applications of lasers, material processing relies on the heating effect due to absorption of high-power beams incident on opaque mediums. The process of laser-material interaction is fairly well studied and can be adequately described in a wide range of power densities up to 10^9 W/cm² in terms of the heat model, by which we can conditionally divide the process of laser interaction with opaque mediums into a few characteristic stages [4]:

(a) absorption of the laser beam and conversion of its energy to thermal lattice vibrations;

(b) heating without material damage;

(c) onset of vaporization in the interaction region and scatter of disintegration products;

(d) cooling (quenching) after the laser interaction ceases.

Along with these stages, diffusion and chemical processes take place and phase transformations occur, which have a considerable effect on the character of laser-material interactions.

The amount of absorbed energy depends on the optical and thermal properties of materials, especially on the properties of metals; it decreases with increasing wavelength. For example, at room temperature polished aluminum and polished copper reflect 97% and 99%, respectively, of incident radiation at the 10.6 μm wavelength, as seen from Table 7.1.

TABLE 7.1. **Reflectivity of Metals at Various Laser Wavelengths**

Wavelength, μm	Au	Cu	Mo	Ag	Al	Cr	Fe	Ni
0.4880	0.415	0.437	0.445	0.952	0.85	—	—	0.597
0.6943	0.930	0.831	0.498	0.961	0.82	0.555	0.575	0.676
1.06	0.981	0.901	0.582	0.964	0.733	0.570	0.650	0.741
10.6	0.975	0.984	0.945	0.989	0.970	0.930	—	0.941

The reflectivity of most metals in the optical range of wavelengths reaches 70-95%, and the absorption coefficient is also rather high, $\sim 10^5$-10^6 cm^{-1}.

The heating stage is the main stage for a number of industrial processes such as surface hardening and welding, which do not involve material removal.

The analysis of this stage in other processes, for example, laser drilling, which call for material removal, permits determining the disintegration conditions such as the temperature boundary and also the corresponding laser power density.

The process of material heating begins after conversion of the laser energy to heat. The absorbed energy heats up "cold" layers by various mechanisms of heat conduction, of which the mechanism of electronic heat conduction in the temperature interval from hundreds to tens of thousands of degrees is the main one for metals.

For laser material processing, heat treatment including, it is of much importance to consider integral characteristics of the heating stage, such as the temperature distribution in the interaction zone, rates of heating and cooling, heat penetration depth, and others, which can be defined from the solutions of heat transfer problems.

Figure 7.3 illustrates the theoretical curves of temperatures in the laser-steel interaction region without substantial surface disintegration as a function of time (*a*) at fixed values of depth Z and as a function of z (*b*) at certain values of t. The temperature increases

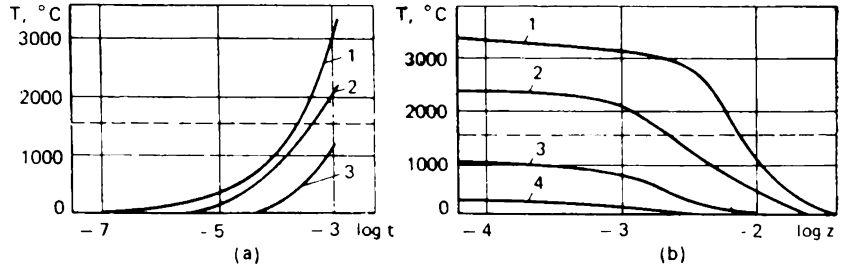

Fig. 7.3. Theoretical curves of temperature of 45 steel specimens as a function of time at fixed values of Z (*a*): *1*, 10^{-4} cm; *2*, 10^{-3} cm; *3*, 10^{-2} cm; and as a function of Z at different values of t (*b*): *1*, 1 ms; *2*, 0.5 ms; *3*, 0.1 ms; *4*, 0.01 ms

with time, the time lengths under consideration being not in excess of the pulse length. First it reaches the melting point T_m at a depth of $\sim 2 \times 10^{-3}$ cm in 5×10^{-4} s after the start of the laser pulse, then it reaches T_m at $\sim 10^{-2}$ cm in 1 ms, etc.

The analysis of the stage of heating of metals and alloys with appreciable surface damage up to temperatures at which phase transformations in the solid state occur is important for heat treatment. Let us introduce the parameter $b = T_h/T_s$, where T_h is the temperature of heating to enable steel hardening and T_s is the surface temperature. We can now determine the depth of heat distribution for any specified isotherm, for example, to estimate the thickness (depth) of the hardened layer, Z_h, on the center line of the focal spot:

$$\text{ierfc}\left(\frac{Z_h}{2\sqrt{a\tau}}\right) = \frac{b}{\sqrt{\pi}} \tag{7.1}$$

where ierfc stands for the integral of the complementary error function, and τ is the pulse duration.

The metal surface in the center of the hot spot ($r = 0$, $Z = 0$) has the highest temperature at the end of the laser pulse:

$$T_s = T(0, \tau) = \frac{2q_s\sqrt{a\tau}}{\sqrt{\pi}\lambda} \tag{7.2}$$

The rate of heating without appreciable metal surface damage can generally be written as

$$\frac{\partial T}{\partial t} = \frac{q_s\sqrt{a}}{\lambda\sqrt{\tau}}\frac{1}{\sqrt{\pi}}\exp(-Z^2/4a\tau) \tag{7.3}$$

For example, given $q_s = 10^5$ W/cm^2, $\tau = 1$ ms, $a = 0.1$ cm^2/s, and $\lambda = 0.335$ W/cm °C, the heating rate $\partial T/\partial t$ for grade 45 steel is 1.7×10^6 °C/s and 1.6×10^6 °C/s at the depth $Z = 10^{-3}$ cm and at $Z = 0$ respectively. As the heat penetration depth grows, with the

laser pulse duration being the same, the heating rate decreases (Fig. 7.4*a*); for example, $\partial T/\partial t$ is 3.38×10^3 °C/s at $Z = 5 \times 10^{-2}$ cm, but $\partial T/\partial t \cong 0$ when $Z = 10^{-1}$ cm.

The distribution of the temperature gradient across the heated layer is

$$\frac{\partial T}{\partial Z} = -\frac{q_s}{\lambda} \operatorname{erfc} \frac{Z}{2\sqrt{a\tau}} \tag{7.4}$$

For the above parameters of the laser pulse, the gradient distribution $\partial T/\partial Z$ at the surface of 45 steel ($Z = 0$) is -4.8×10^5 deg/cm; at $Z = 5 \times 10^{-3}$ cm, it is equal to -2.7×10^5 deg/cm. It should be noted that the same temperature gradient covers a wider range of Z at higher values of time t (that does not exceed the pulse duration) than at lower values (Fig. 7.4*b*). For example, at $t = 1$ ms, $\partial T/\partial Z$ remains equal to 2.5×10^5 deg/cm up to $Z = 5 \times 10^{-3}$ cm; but at $t = 10^{-5}$ s, the same value of $\partial T/\partial Z$ is found to be only at $Z = 5 \times 10^{-4}$ cm.

Expression (7.1) for estimating the depth of laser surface hardening does not allow for the fact that after the end of the pulse the heating still continues and the hardening depth increases owing to the heat conduction into the bulk material. The region below the surface initially heats up and then cools down, and only the surface ($Z = 0$) cools at once after the pulse ceases.

For a one-dimensional problem ($d_0 \gg \sqrt{a\tau}$), the temperature at any point on the Z axis as a function of time t after decoupling of

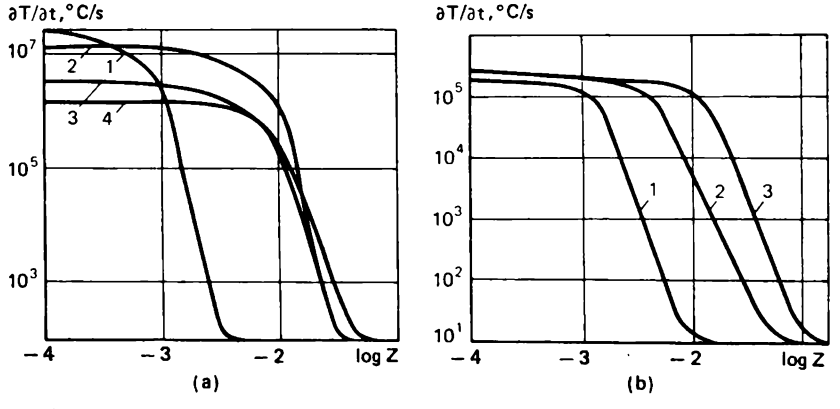

Fig. 7.4. Theoretical curves (*a*) of heating rate as a function of depth Z after t of 1 μs (*1*), 10 μs (*2*), 0.1 μs (*3*), and 1 ms (*4*) and theoretical curves (*b*) of temperature gradient as a function of depth after t of 10 μs (*1*), 0.1 ms (*2*), and 1 ms (*3*) for laser-treated steel specimens

the pulse of duration $\tau \ll t$ can be given by the expression

$$T(Z, t) = \frac{2q_s\sqrt{a}}{\lambda} \times \left\{\sqrt{t}\ \text{ierfc}\left(\frac{Z}{\sqrt{4at}}\right) - \sqrt{t-\tau}\ \text{ierfc}\left(\frac{Z}{\sqrt{4a(t-\tau)}}\right)\right\} \quad (7.5)$$

or by the expression

$$T(Z, t) = T(0, \tau)\frac{\sqrt{\pi}}{\sqrt{\tau}} \times \left\{\sqrt{t}\ \text{ierfc}\left(\frac{Z}{2\sqrt{a\tau}}\right) - \sqrt{t-\tau}\ \text{ierfc}\left(\frac{Z}{2\sqrt{a(t-\tau)}}\right)\right\} \quad (7.6)$$

As follows from expression (7.6), the temperature $T_1 < T_s = T(0, \tau)$ of an arbitrary isotherm shifts into the bulk material after the pulse decoupling, reaches the highest depth Z_{max}

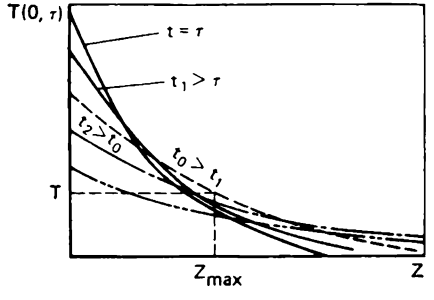

Fig. 7.5. Isotherms for the zone of laser interaction with 45 steel, plotted for different periods of time after the end of laser pulse

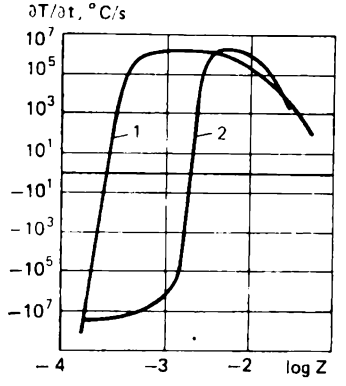

Fig. 7.6. Cooling rate versus depth for 45 steel specimens 0.1 μs (*1*) and 1 μs (*2*) after the end of laser pulse

at time t_0, then moves to the surface and vanishes, i.e. the depth is Z_{max} at $t = t_0$ $(t_1 < t_0 < t_2)$ $Z(T_1)$, as illustrated in Fig. 7.5. So, after the pulse ends, the heat still penetrates into the bulk material and the depth of metal hardening thus increases.

Figure 7.6 illustrates the plots of the cooling rate versus depth Z for the zone of laser-steel interaction without appreciable surface damage at different values of time $\Delta t = t - \tau$ after the pulse ends. Thus, the cooling rate is $\partial T/\partial t = -1.31 \times 10^8$ °C/s at the depth $Z = 10^{-4}$ cm after 10^{-7} s from the moment the pulse ended. It is of practical interest to estimate the heat penetration depth Z_{max} as a function of time t at a specified value of T_1 of the isotherm. For exam-

ple, at $T_1 = T_h$, the value of Z_{max} is the hardening depth of 45 steel. Assuming $T(Z, t)$ to be equal to T_h, expression (7.5) takes the form

$$T_h = \frac{2q_s\sqrt{a}}{\lambda}\left\{\sqrt{t}\ \text{ierfc}\left(\frac{Z_h(t)}{\sqrt{4at}}\right) - \sqrt{t-\tau}\ \text{ierfc}\left(\frac{Z_h(t)}{4a(t-\tau)}\right)\right\} \quad (7.7)$$

In Fig. 7.7 is shown the curve of $Z_{max}/\sqrt{a\tau}$ as a function of $b = T_1/T_s$, where T_1 is the temperature of an arbitrary isotherm, and T_s is the surface temperature at the end of the pulse.

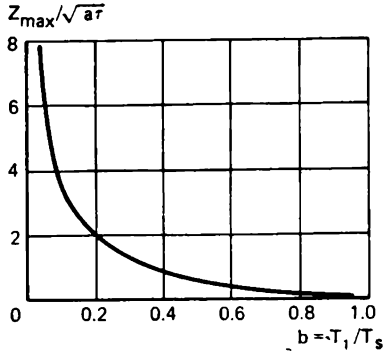

Fig. 7.7. Plot of $Z_{max}/\sqrt{a\tau}$ versus b

When $b < 0.3$, the above relation is written as

$$Z_{max}/\sqrt{a\tau} = 1/\sqrt{2lb}$$

or as

$$Z' = 0.429/b \quad (7.8)$$

where $Z' = Z_{max}/\sqrt{a\tau}$.

To check for the correct calculation of any isotherm representative of the distribution of the constant temperature T_h to a depth Z_h during and after interaction of a free-running pulse, we consider the results of experiments on laser surface hardening of 45 steel [5]. It is possible to determine rather accurately the boundary of the hardened layer from the metallographic analysis or from the difference in microhardness between the zones with the hardened and original structures.

The characteristic temperatures for the specimens from 45 steel were the following: vaporization (boiling) temperature $T_v = 3\,100$°C, melting temperature $T_m = 1\,500$°C, and hardening temperature $T_h = 850$°C. The energy of a ruby laser pulse with 4-ms duration was 7.5 J. The pulse whose power density q_{s0} was 1.1×10^5 W/cm^2 did not cause appreciable damage to the specimen surface ($R = 0.46$). The hardened depth on the center line of the focal spot was 300 μm. The values of Z_h calculated from (7.1) and (7.8) with and without regard to the cooling effect were 250 and 280 μm respectively. The calculated results thus agree well with the experimental values.

For the case where $b > 0.3$, the following approximation may apply:

$$Z' = 3.8 \exp(-3.3b), \quad 0.3 < b < 0.75$$
$$Z' = 1.24(1 - b), \quad 0.75 \leqslant b \leqslant 1 \quad (7.9)$$

The above methods for estimating any isotherm can be used to calculate the parameters of laser surface hardening and other types of heat treating.

As with pulse heat treatment, in continuous laser treatment of metals, we need to know how the hardening depth varies with the scan speed of the CW beam, beam diameter, and power.

An approach that provides insight into the variation of Z with the above parameters is to use a uniform irradiance model. This model allows for the solution of the temperature distribution in a solid heated by a plane surface heat source of constant power for a certain time t which is assumed to be equal to the time it takes the laser beam to cross a surface spot as it travels along the target surface, $t = 2r/v$, where r is the effective radial size of the laser beam and v is the beam scan rate [6]. The temperature distribution for points lying at a distance of less than $\sqrt{at}$ from the surface assumes the form

$$T(Z, t) = \frac{\eta P}{\pi a c r^2 \rho} (\sqrt{4at/\pi} - Z) \tag{7.10}$$

where η is the absorption coefficient for the target surface, P the laser power, c the specific heat, and Z the heat penetration depth.

In industrial applications of lasers, it is important to define the critical values of the laser power density at which melting begins. Using expression (7.2) for estimating the surface temperature at the hot spot center, we can estimate the parameters of a laser pulse, such as the power density and the dwell time corresponding to the onset of material melting.

Assume that the surface reaches the phase transformation temperature T_0 required for hardening at the end of travel of the light beam over the surface point of interest, the hardening depth as a function of the effective radial size of the laser beam, its scan rate, and power density is written as

$$Z = \sqrt{8ar/\pi v} - \pi a c r^2 \rho T_0 / \eta P \tag{7.11}$$

The experiments conducted on steel specimens exposed to a laser power of $\sim$ 1 kW to check the above expression for accuracy showed a satisfactory agreement of the calculated values of Z with experimental results.

In work [7] the analysis was made of the surface heating of a semi-infinite body by an infinite surface source of constant power density $q = AP_0/\pi r^2$ during time $t = 2r/v$ on condition that $r \gg (at)^{1/2}$, where A is the absorption coefficient for the target material, and P_0 is the laser power. From this analysis, an expression was found for estimating a number of parameters of surface hardening with a CW CO_2 laser.

The calculations were performed on the assumption that the hardening depth reaches Z_{max} when the surface rises to its melting temperature T_m. For this, the power density of the heat source must be equal to

$$q_m = T_m\lambda\,(\pi/4at) \tag{7.12}$$

The required time of hardening is

$$t_h = \frac{\pi Z_h^2}{4a}\,\frac{T_m}{T_m - T_h} \tag{7.13}$$

and the required hardening rate is

$$v_h = \frac{8a\,(T_m - T_h)^{3/2}}{\pi T_m^2 Z_h^{3/2}} \tag{7.14}$$

The hardening depth can be found from the expression

$$Z_h = (4at/\pi)^{1/2}\,(T_m - T_h)/T_m \tag{7.15}$$

The experimental findings of the hardening depth in steel and iron specimens are in good agreement with the predictions, and the deviation in the range of small hardening rates does not exceed 15 % [8].

7.2. CHANGES IN THE STRUCTURES AND PROPERTIES OF MATERIALS IN THE ZONES OF PULSED LASER INTERACTION

A laser beam rapidly heats the target surface at a rate unattainable in other techniques of material processing and so markedly changes the properties of the material in the interaction zone. These factors along with the specified parameters of treatment, determine the effectiveness of laser technology in surface hardening of a number of metals and alloys.

Based on the results obtained by a number of researchers [4, 5, 9], we shall briefly consider the representative examples of changes in the structures and properties of iron and iron-carbon alloys with a carbon content of 0.02 to 3-4%. These materials are chosen for studies because their properties in various initial states are fairly well known and many researchers have used them to investigate the phase transformations during rapid heating with hf currents (induction heating), electric arc, powder gases, etc. Besides, the alloys under consideration are the basic structural materials widely employed in machine building.

We shall also briefly describe the structural changes in other materials—nonferrous metals and alloys.

Interaction of a normal pulse (free-running) laser with iron and iron-carbon alloys. The pulsed laser-heat-treated region in the specimens of armco-iron, steels, gray iron, and white iron consists of two layers exhibiting a clearly defined phase boundary between

the first upper layer recrystallized from the liquid state and the second layer.

In most materials, excepting low-alloyed steels, the first layer has a columnar-dendritic structure. A high crystallization rate causes a preferential growth of the main dendritic branches directed normal to the phase boundary.

Electron microscope investigations relying on a 5 000 × magnification and above also confirm that the structure of columnar crystals in the first layer is dendritic. The microscopic segregation is considerable due to a high crystallization rate. The columnar crystals in cross-section have the appearance of equiaxial grains which consist of separate blocks definitely oriented within each grain and exhibiting fine dendritic branches.

The microhardness H_μ of the first layer in armco-iron reaches a high value of 2 800-3 200 MPa as against an initial value of 1 000 MPa. This high increase in microhardness is likely to be attributable to hardening that gives rise to low-carbon martensite and also to precipitation hardening and plastic deformation caused by thermal stresses.

As shown by metallographic and radiographic examinations, the structure of the first layer in 45 steel corresponds to fine-needled martensite having a certain amount of retained austenite. The microhardness of this layer is $H_\mu = 8\ 200\text{-}8\ 300$ MPa.

The structure of the first layer in carbon steel grade U8 consists of fine-needled martensite and an appreciable amount of retained austenite ($\sim 70\ \%$). Nevertheless, H_μ of this layer ranges from 8 800 to 9 200 MPa, which is due to the specific features of laser treatment, namely, precipitation hardening and high rates of heating and quenching.

In low-alloyed steels, the first layer does not exhibit a distinct dendritic structure and consists of relatively equiaxial grains. It has a martensite-austenitic structure with large martensite needles in the absence of carbides which have dissolved completely since the layer temperature was much in excess of the critical value, Ac_m.

In gray iron, the first layer mainly consists of individual drop-shaped formations, in which liquid metal has crystallized in ledeburite; the eutectic clusters are grown in the direction of heat removal. The layer is almost completely free of graphite precipitates. A considerable porosity of the structure probably results from the evolution of gases adsorbed on graphite inclusions during the primary crystallization of iron. The spheroidal, smooth internal surface of pores attests to the origin of the porous structure due to gas evolution. The microhardness of the first layer is 9 500 MPa. This is indicative of the dissolution of graphite in liquid metal and the subsequent chilling and quenching due to a rapid transfer of heat into the bulk material.

By controlling the chemical composition of gray iron and conditions of its treatment, it is possible to obtain a chilled layer of a comparatively uniform thickness and high wear resistance. However, the microhardness of the first layer decreases in depth evidently because of an incomplete dissolution of graphite inclusions.

The structure of the first layer in white hypoeutectic iron exhibits a columnar dendritic crystallization of the original austenite, which spreads from the melt boundary. High residual stresses that arise in this layer can often cause cracking. The structure of this layer has a lower carbon content than the first heat-treated region in gray iron and is typical of strongly supercooled hypoeutectic white iron. The first layer has a highly refined structure in comparison both with its original structure and with the structure of ledeburite in the second layer (in the heat affected zone). The diameter of austenitic columns in cementite is less than 0.5 μm; in the original structure it reaches 2 μm.

The absence of large precipitates of the original austenite is evidence that the crystallization process is rather nonuniform. The microhardness of the first layer at its surface is H_μ=9 000-9 700 MPa. The microhardness of deeper regions of the first layer is different and dependent on the original structure. The microhardness in the order of 9 000-9 250 MPa is specific to the original pearlite regions. In the original ledeburite regions, H_μ is 7 500 MPa, which increases to 12 000 MPa after treatment. Such a large difference suggests that carbon does not diffuse between the grains since the metal solidifies very rapidly without mixing.

The structures of the second layers in the above mentioned alloys are different because of the differences in carbon contents, alloying elements present, original structures, and temperature gradients across the layers.

In armco-iron, the second layer features a fine-grained structure with a grain diameter of 3-20 μm; in the original structure, it is equal to 80-100 μm. The grain refinement arises from the phase recrystallization $\alpha \rightleftarrows \gamma$ and plastic deformation due to thermal stresses and subsequent recrystallization. The electron microscope investigations show that the structure of the second layer in the zone of contact with the first layer is similar to lamellar pearlite with an interlamellar distance of $\sim$ 1 μm. Since armco-iron is deficient in carbon to form pearlite of an equilibrium structure, the obtained structure should be considered pseudopearlitic, grown during fast cooling of superheated austenite with a reduced carbon content. The microhardness diminishes with increasing depth from 2 800 to 1 000 MPa.

The structure of the second layer in 20 steel exhibits a two-phase zone attributed to a rather wide temperature interval in

which α- and γ-phases remain in equilibrium. In this two-phase zone, the α-phase consists of both low-carbon martensite that is closer to the melt region and ferrite that is away from this region.

In 45 steel specimens, the sites of prior pearlite grains have the structure that repeats the periodicity of carbon distribution in accordance with the position of cementite lamellas in original pearlite. The specimens retain the ferrite network at grain boundaries because the time during which the steel temperature is equal to or in excess of T_h is not enough for austenite to go through diffusion annealing and for ferrite to undergo sufficient carburizing. The microhardness of pearlite grains is 8 200-8 500 MPa and that of ferrite grains is 3 200-3 500 MPa (the original value is 1 000 MPa). Such an increase in H_μ of ferrite results from its precipitation hardening during phase recrystallization $\alpha \rightleftarrows \gamma$ and ferrite grain deformation due to volumetric changes in neighbor grains following their martensite transformation. It is also possible that a certain amount of carbon has diffused from prior pearlite grains into ferrite grains and added to the hardness.

The inhomogeneity of the second layer in U8 carbon steel is due to a large gradient of temperatures which vary from the melting point to the critical point Ac_1 across a layer from tens to hundreds of micrometers wide.

Since laser radiation heats the alloy at a rate of $\sim 10^5$-10^6 °C/s, complete austenizing shifts into the region of rather high temperatures, thus extending over a wider temperature interval. The diffusion process that equalizes the carbon concentration in the bulk of the alloy may not terminate even in the region of temperatures which are much in excess of Ac_3. This results in inhomogeneous austenite and, hence, in inhomogeneous martensite after hardening.

In U8 steel, a deeper region of the second layer that is adjacent to the original structure undergoes complete transformation. However, because of a high heating rate and a low dwell time at temperatures upward of Ac_m, diffusion annealing of austenite does not occur, and the structure exhibits pseudopearlite, or banded martensite. The banded structure in the region of prior lamellar pearlite is probably due to the microscopic inhomogeneity of the formed austenite of manganese and silicon, which determine the distribution of carbon.

In specimens with granular pearlite, the complete dissolution of cementite does not occur. In specimens with the original structure of both lamellar and granular pearlite, the second layer in the region adjacent to the first layer does not contain carbides. After prolonged etching of the second layer, fine-needled martensite is visible against the background of retained austenite.

The structure of the second layer in low-alloyed steels is also inhomogeneous. The upper section adjacent to the first layer consists

of minute regions of austenite with H_μ = 3 500-4 500 MPa and also has regions of the martensite-austenite structure whose microhardness reaches 6 600-7 500 MPa. Since the temperature in the upper section of the second layer was in excess of the critical value Ac_m, carbides dissolved completely, thus causing an increase in the chromium content and, hence, in the amount of retained austenite. The lower section of the second layer at the boundary of the original structure is fine-needled martensite with retained austenite and carbides uniformly distributed over the entire section, for which reason the microhardness is high, 8 700-9 500 MPa.

Investigations were also made of the effects of the free-running laser pulse interaction with preliminarily hardened steel specimens. The structure of the first layer in 45 steel is found to be similar to the above described structure of 45 steel. The first layer in U8 steel features a high degree of dispersion. At the boundary of the HAZ, the second layer as a rule has a tempering region with a lowered microhardness as against the original value.

In gray iron, the pearlite structure of the second layer has transformed into fine-needled martensite on heating above the critical point and fast quenching. As revealed by electron microscope examinations, the region adjacent to the substrate metal has residues of cementite and ferrite lamellas, which is indicative of a short-time holding of the metal in the austenite state and of the absence of uniform distribution of carbon in austenite and, consequently, in martensite.

The second layer in the melt zone near graphite precipitates displays wedge-shaped protrusions extending into the zone for 10-20 μm.

The HAZ structure of white iron consists of ledeburite sites and original austenite grains of a modified structure.

At the boundary of the solidified melt there is a layer 10-20 μm thick with a large-needled martensite structure that passes into fine-grained martensite with distance away from the melt front. At still larger distances, the layer exhibits the inclusions of sorbite and contains fine carbides up to 0.5 μm in size, which have had no time to dissolve. The second layer inherently retains the needles of secondary cementite.

The metallographic and electron microscope studies of cementite in ledeburite formed in heat affected zones showed that cementite was brought to melting without decomposition (graphitization) after dissolution of a certain amount of austenite in it. During solidification the retained austenite precipitated in the form of fine dendrites.

In the HAZ there are two varieties of cementite precipitates.

The first variety of cementite has fine dissiminations of austenite (martensite), the dispersity of which is one or two orders of

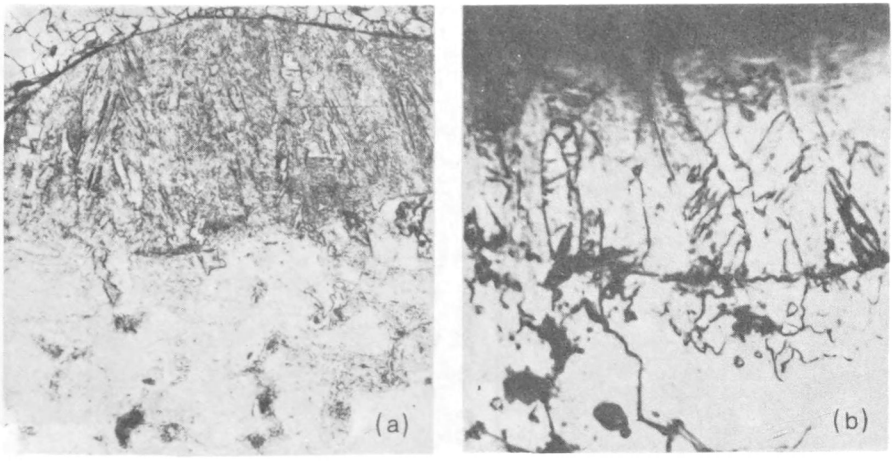

Fig. 7.8. Results from heat treating of armco-iron with a pulsed laser: (*a*) longitudinal section (70×); (*b*) grain structure (450×); (*c*) hardness as a function of depth

magnitude higher than that of austenitic dendrites in the melt zone. The microhardness of such a two-phase structure component is as high as 12 700-14 840 MPa.

The second variety of cementite has no signs of "decomposition", but its microhardness is somewhat higher than that of original cementite away from the zone of laser interaction and reaches 9 600-12 700 MPa, while H_μ of original cementite is 8 900-9 600 MPa. The anomaly of this cementite lies in a high etchability of its microsections in alcoholic solutions of nitric acid and other etchants which do not attack common cementite. It is evident from electron microscope examinations that this anomalous cementite contains austenite along (001) lattice planes, namely, austenite and martensite precipitated after cooling to room temperature. This new structure component received the name "baikovit" [5].

It should also be noted that the melt front is not even: the front line delays near large grains of primary austenite whose melting temperature is higher than that of ledeburite. In the region of secondary cementite needles embedded in the grains of austenite (pearlite), the penetration (melting) depth is greater. A feature common to all investigated iron-carbon alloys is that they have the regions of

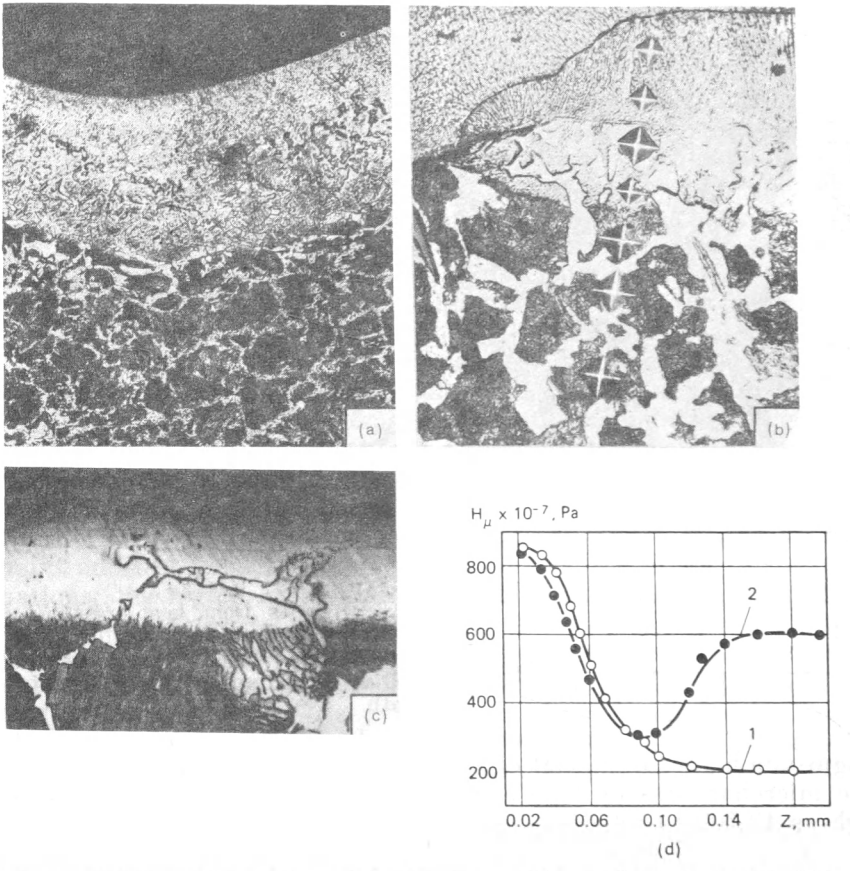

Fig. 7.9. Micrographs of 45 steel heat-treated with a pulsed laser: (*a*), 340× (*b*), 600×; (*c*), 450×; (*d*), hardness versus depth for unhardened (*1*) and hardened (*2*) specimens

hardening with and without surface melting (regions of melt quenching and transformation hardening respectively).

In Figs. 7.8-7.13 are shown the micrographs of the zones of iron-carbon alloys heat-treated with a normal pulse laser and also the graphs of microhardness distributions in the interaction zones. The radiographic analysis of iron-carbon alloys reveal that changes in the substructure after laser heat treatment are largely similar to changes produced after hardening and plastic deformation. The interaction of pulses from a normal pulse laser with iron-base alloys causes an appreciable decrease in the size of blocks and increase in the density of defects and lattice distortions in the HAZ. For example, in 45 steel specimens, the block sizes in the metal splattered

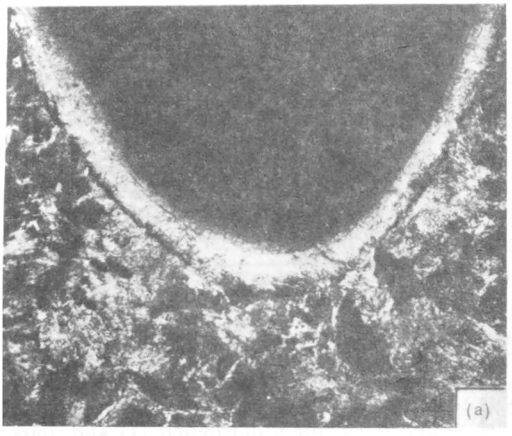

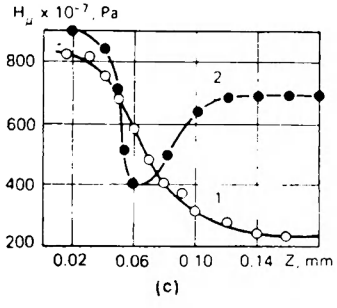

Fig. 7.10. Micrographs of U8 steel specimens heat-treated with a pulsed laser: (*a*), changed structure of original lamellar pearlite (200×); (*b*), changed structure of globular pearlite (600×); (*c*), hardness versus depth for unhardened (*1*) and hardened (*2*) specimens

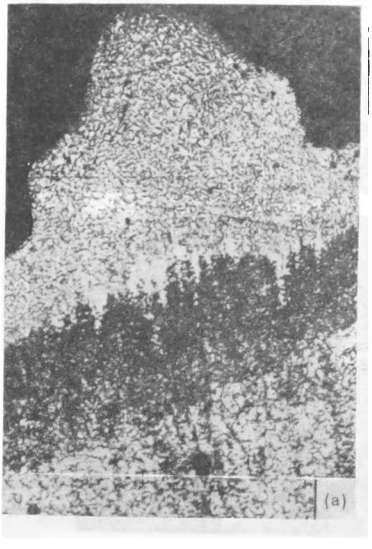

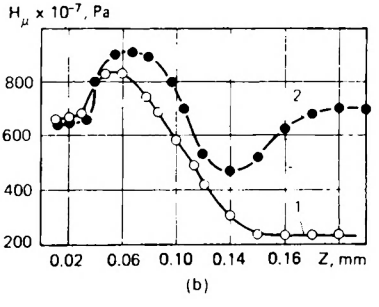

Fig. 7.11. Structure (*a*) of low-alloyed steel treated with a pulsed laser (340×) and hardness versus depth (*b*) for unhardened (*1*) and hardened (*2*) specimens

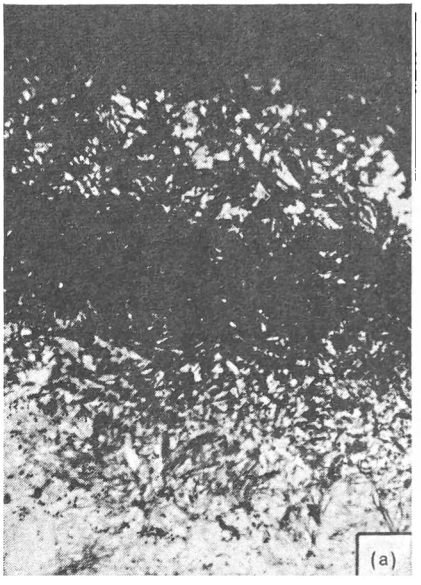

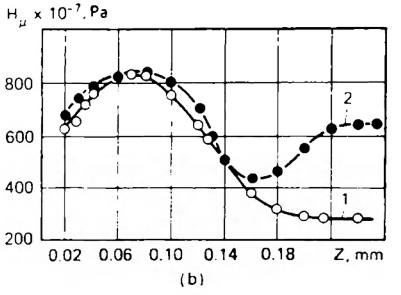

Fig. 7.12. Structure (*a*) of low-alloyed steel grade 15 treated with a pulsed laser (340×) and hardness versus depth (*b*) for unhardened (*1*) and hardened (*2*) specimens

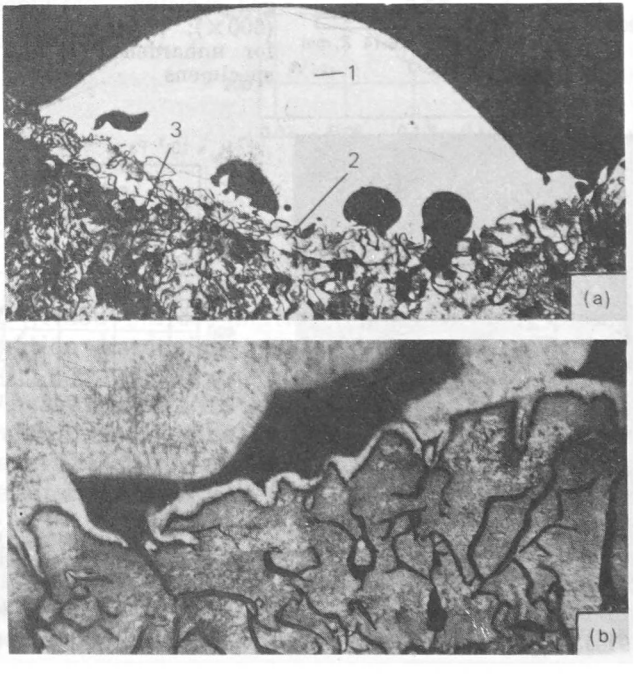

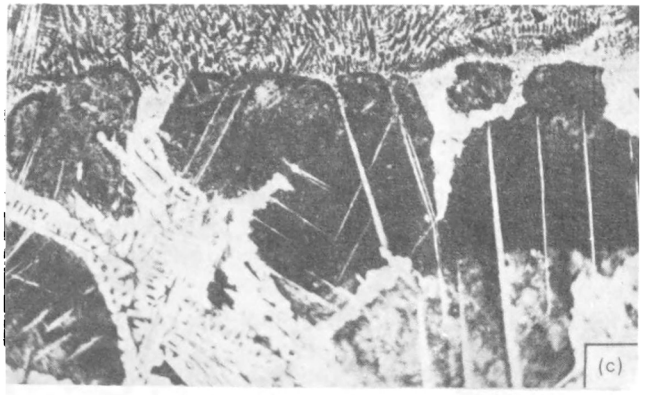

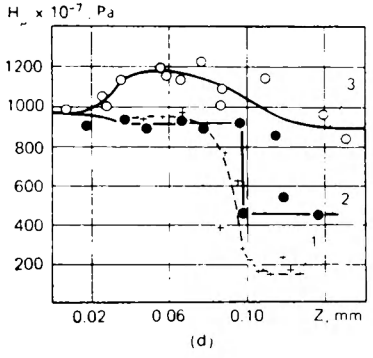

Fig. 7.13. Structure of pulsed-laser-treated iron: (*a*), general view of gray iron specimen (125×); *1*, region of melted and rapidly solidified iron; *2*, HAZ; *3*, original structure of HAZ (600×); (*b*), gray iron HAZ structure (600×); (*c*) white iron structure at boundary between melt zone and HAZ (450×); (*d*) hardness versus depth curves for gray iron (*1*), pearlite sites in white iron (*2*), and ledeburite sites in white iron (*3*)

around the melt zone edges and also those in the metal recrystallized in the first layer are 0.33×10^{-5} and 0.57×10^{-5} cm respectively as against 3.0×10^{-5} cm in the original structure. Lattice distortions $\Delta a/a$ in the solidified melt increase 26% over the initial value.

The defect density in the two areas of the solidified melt reaches 30×10^{10} and 9×10^{10} cm^{-2}, respectively, against an initial value of 0.3×10^{10} cm^{-2}.

Transmission electron microscope examinations of 0.1-mm thick foil of carbonyl iron subjected to double vacuum refining ($\sim$0.02% C) showed that the laser treatment of foil specimens considerably increased the dislocation density over the original value (Fig. 7.14). For example, with a power density of about 8×10^4 W/cm^2 delivered to the foil the pulse causes liquid metal flushing and melting through the entire target. The foil specimens then exhibit a cellular dislocation structure similar to that observed in strongly deformed metals. The density of individual dislocations along the boundaries of cells amounts to $\sim 10^{11}$-10^{12} cm^{-2}, which is approxi-

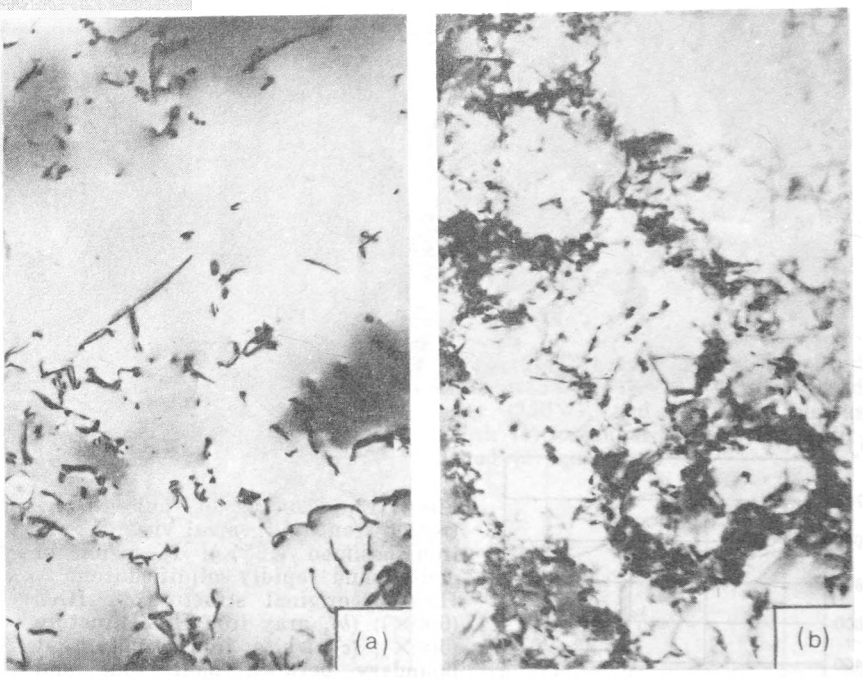

Fig. 7.14. Dislocation distribution in preliminarily annealed foil of carbonyl iron: (*a*), before pulsed laser interaction (3 400×); (*b*) after interaction with a laser pulse at $q = 8 \times 10^4$ W/cm^2 (31 000×)

mately three orders of magnitude higher than the initial value. A few factors are responsible for such an increase in dislocations. Of these, mention should be made of high heating and cooling rates and enhanced temperature gradients in the interaction region, which, apart from causing the $\alpha \rightleftarrows \gamma$ recrystallization, bring about thermal stresses due to the difference in the specific volumes and linear expansion coefficients between the coexistent phases. These stresses relax on account of the growth, motion, and interaction of dislocations.

So, alloy hardening with a pulsed laser results from the cumulative effect of the increased number of defects appearing in a thin crystalline structure during laser radiation and subsequently in the course of both the fixation of nonequilibrium structures due to rapid heating and the martensite transformation.

Of much interest is the study of the causes of abnormally high values of hardness, up to 15 000 MPa, obtained in tool steels after double hardening—first, ordinary hardening and then laser hardening. Calculations disclose that the high-rate laser heating of untem-

pered martensite or tempered martensite formed after low-temperature tempering causes a reverse martensite transformation, martensite → austenite. For example, in laser hardening of the edges of blanking dies preliminarily hardened by a conventional method [10], three martensite transformations occur—two direct and one reverse. As a result of a sharp increase in the density of dislocations and other lattice defects, the metal acquires an abnormally high hardness and enhanced wear resistance despite a large amount of retained austenite [5].

7.3. CW LASER-IRON ALLOY INTERACTION

Consider the most typical structural changes in iron-base alloys treated with a CW CO_2 laser which delivered 700-1 000 W of power to both stationary targets during the time of interaction of up to 5 s and to moving targets traveled at a speed of 1 m/min and above.

A laser beam interacting with a stationary armco-iron specimen ensures the refinement of ferrite grains from an original size of 50-60 μm down to a size of 10-15 μm in a layer up to 0.55 mm thick, the refinement being most intensive at a depth of 0.35-0.55 mm. Large grains are found near crater edges. The grain refinement results from the processes of austenizing during heating and the subsequent decomposition of austenite during cooling. The different rates of nucleation and growth of ferrite grains involved in these processes are probably attributable to the different sizes of austenite grains formed in close vicinity to the liquid phase and away from it [5].

The microhardness H_μ of armco-iron is about 4 000 MPa. The melt front is not clear-cut. The layer formed at the site of the earlier molten metal is rather porous due to a deficient amount of deoxidizing agents.

In steels with an adequate amount of deoxidizers (Mn and Si), treated for rather a long time with a CO_2 laser beam at power densities $q \geqslant q_c$ sufficient to initiate melting, the solidified layer is less porous, but the upper slag layer is still present.

In all iron alloys treated for a long time, the interaction region enhibits a slag layer in its upper portion and, sometimes, also beyond the porous region. The slag layer largely consists of the oxides of iron and other products of thermochemical interaction of the continuous beam with the alloys in air and in gases dissolved in the metals.

In low-carbon steel with 0.2-0.3% C, the treated zone exhibits a coarse-grain Widmannstätten structure whose microhardness is little different from the original value.

A prolonged interaction of the continuous laser at $\lambda = 10.6$ μm with normalized specimens of 45 steel, whose original structure consists of pearlite grains with ferrite interlayers, produces, apart

from the slag layer, the layer of molten and porous metal up to 75 μm thick. This layer and the portions adjacent to it are appreciably decarburized. At a distance of 100 μm from the crater, the steel structure contains martensite, the amount of which increases with distance away from the crater. At a depth of 300-400 μm, the steel has a completely hardened layer disposed above an incompletely hardened layer.

In preliminarily hardened specimens of 45 steel subjected to laser treatment, a layer $\sim$ 400 μm thick has formed, which consists of an upper decarburized zone and a lower laser-hardened zone where martensite needles are finer than they are in the substrate metal. Below the hardened zone, there lies a tempering zone $\sim$400 μm thick with products of martensite decomposition.

The structural changes in specimens from normalized and preliminarily hardened U8 carbon steel are in the main analogous to those in 45 steel specimens. The only difference is that in the pretreated carbon steel, the hardened layer adjacent to the solidified melt contains grains with markedly corroded boundaries. The loss of strength is evident in decarburized zones. In carbon steel, for example, the hardness of these zones is about half that of the original value.

In low-alloyed steel specimens the structural changes are similar to those in carbon steel specimens, the difference being that the hardened zone, just like the original hardened substrate metal, contains globular carbides. The columnar structure of the earlier molten layer is quite discernible.

In specimens of high-speed steel, whose original structure consists of globular pearlite with a hardness of 300 MPa and carbides, the first zone has a dendritic structure with H_μ = 7 650-9 250 MPa [9]. This is the zone of melt quenching with a martensite-austenite structure. The next zones in succession are the troostite-martensite zone with H_μ = 5500 MPa, troostite-sorbite zone with H_μ = 3 200-4 700 MPa, and the zone of original metal.

The CW CO_2 laser beam interacting for a long time with pearlite gray iron targets causes the melt zone $\sim$ 110 μm deep to chill completely. The zone is free of graphite precipitates, little porous, rather hard, and wear resistant [5]. Below this zone is the hardened layer $\sim$ 275 μm thick, which retains graphite inclusions. It is important to note that if the iron contains coarse graphite inclusions, the solidified layer, too, partially retains coarse graphite.

As regards white eutectic iron, the structure here changes to a large depth of $\sim$ 900 μm. It is worthy of note that heat treatment considerably refines pearlite grains from an original size of 30-40 μm to a size of 4 μm. The HAZ spreads to a depth of about 500 μm from the modified layer. At the sites of the earlier coarse conglomerate within the HAZ, cementite melts completely, while

the austenite interlayer does so only partially, and fine ledeburite appears between the residues of austenite after solidification.

The microhardness of iron-base alloys in the melt zone and HAZ up to 0.6-0.8 mm deep reaches 11 000 MPa and over after quenching.

We shall now consider the results of treatment of iron-base alloys with a CO_2 laser beam delivering up to 1 kW of power to moving targets. The speed of specimens, or the scan rate of the laser beam, was varied from 0.4 to 0.6 m/min. The power densities delivered to the targets ranged from 5×10^3 to 2×10^5 W/cm^2. The heat-treated zones were found to consist of clearly defined layers differing in the level of phase transformation.

The experiments show that in the first layer, the heating temperature exceeds the upper critical values Ac_3 and Ac_m for hypoeutectoid and hypereutectoid steels, respectively, and is often above the melting point. The layer has a martensitic structure.

The second layer corresponds to heating in the temperature range between the critical points, which results in incomplete hardening. In hypoeutectoid steels, this layer has a reduced hardness in comparison with the first layer because it retains ferrite grains. In hypereutectoid steels, the hardness of the second layer is higher than that of the first owing to highly dispersed cementite which gives an added strength to the steel [11, 12]. The microhardness of heat-treated steels as a function of depth is shown in Fig. 7.15. The hardness of the laser-treated zones in grade 20 steel specimens traveling at a speed of $v = 0.6$-1.8 m/min amounts to 7 500 MPa, which is impossible to attain in the process of ordinary hardening. The hardened depth is equal to 500 μm. The HAZ in carbon steel

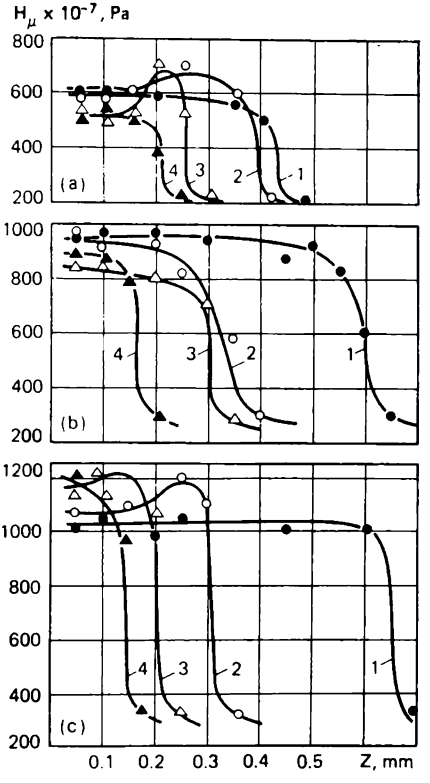

Fig. 7.15. Microhardness versus depth for specimens treated with a CW CO_2 laser at different feed rates: (*a*), 20 steel; (*b*), 45 steel; (*c*), U12 steel; *1*, 0.6 m/min; *2*, 1.8 m/min; *3*, 3.0 m/min; *4*, 4.2 m/min

specimens displays an inhomogeneous structure, which is evident from the reduced etchability of portions located at the sites of the network of secondary cementite. This is because the diffusion process for the equalization of the carbon concentration in the conditions of short-time laser heating at all the speeds of specimens has no time to reach completion and the above mentioned portions contain an increased amount of austenite.

The analysis of the hardness distribution curves for U12 steel specimens shows that when the speed of travel (treating rate) of the specimen is a minimum (0.6 m/min), the hardness of the first layer is close to that of the second, whereas at higher treating rates the hardness of the second layer becomes much greater. In the first case, the longer dwell time of the laser beam results in a more uniform distribution of carbon in austenite. The hardness of martensite at a carbon content of up to 0.6% is linearly dependent on carbon and is practically independent of it at a higher content, which is in accord with the experimental findings presented in [5, 11, 13].

Below are given the results of experiments on specimens of 35 steel with the original ferrite-pearlite structure (0.37% C, 0.25% Si, 0.7% Mn, 0.06% Cr, 0.025% S, and 0.02% P) at treating rates (speeds of travel of specimens) ranging from 0.6 to 2.6 m/min. The CO_2 laser beam melts the surface at treating rates of up to 2.4 m/min; at v of $\sim$ 2.6 m/min and over the surface melting does not occur [14].

At treating rates of 0.6-1.8 m/min, the laser-treated zone consists of four layers which appreciably differ from one another in microstructure and hardness. The first layer formed from the melt at $v \leqslant 1.8$ m/min is noted for a reduced etchability and high hardness, $H_\mu = 8\,000$ MPa, which is four times the hardness of the original steel and 1 500 MPa higher than that of the same steel after ordinary hardening. The microstructure of this layer consists of martensite with a certain amount of retained austenite; the degree of dispersion of martensite is 1.5-2 times the dispersity obtained after ordinary hardening. Despite the metal fusion at the surface, dendrites in the first layer are not present. A reduced etchability of the white layer results from high stresses and the absence of decoration of the boundaries of the first and the second order because the impurity atoms and lattice defects do not have enough time for the redistribution.

A few factors are responsible for a high hardness of the first layer [4, 5]: (1) an appreciable degree of supersaturation of the α-solid solution by the impurity interstitial atoms due to high quench rates; (2) increased density of structural defects both new and earlier ones partially inherited from the original structure; (3) fine-grain structure of martensite.

In the second layer, the microstructure is martensite whose needles are 2 to 4 times larger in size than those in the first layer.

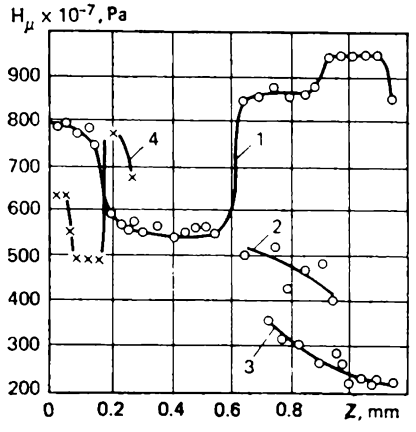

Fig. 7.16. Hardness versus depth for 35-steel specimens treated with a CW CO_2 laser at different scan rates: *1* (martensite), *2* (troostite), *3* (ferrite), 10 mm/s; *4* (martensite), 40 mm/s

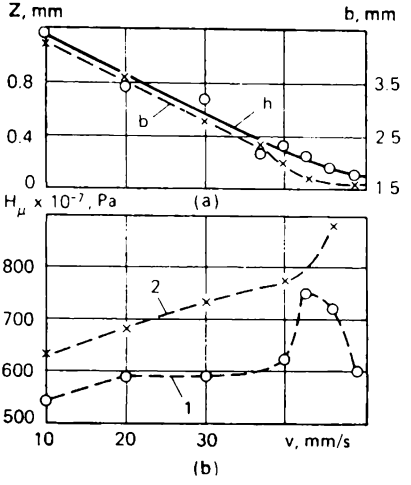

Fig. 7.17. Depth, width (*a*), and hardness (*b*) of laser-treated zone as functions of laser scan rate: *1*, first (surface) layer; *2*, fourth layer

The structure of this layer has the hardness and dispersity comparable to those of the steel structure after conventional hardening.The third layer is the zone of incomplete hardening with a structure consisting of martensite, troostite, and ferrite. The fourth layer is also the zone of incomplete hardening, but differs from the third layer in that it is completely free of troostite, has a ferrite network and exhibits a higher hardness.

An example of the hardness of the CO_2 laser-treated steel region as a function of depth at different scan speeds (sweep rates) of the laser beam is shown in Fig. 7.16.

Figure 7.17 illustrates the effect of the sweep rate on the hardened depth h, hardened width b, and hardness in the two layers of the heat-treated region, in the first and the fourth layer mentioned above.

The differences in the structure and hardness between the layers in the 35 steel zone treated with a continuous CO_2 laser are due to different conditions of heating and cooling of the layers.

In analogy to the investigations on the dislocation structure of carbonyl iron by electron microscope methods [5], studies were made of the structure of commercial purity aluminum [12, 15] treated with a high-power CW CO_2 laser (the aluminum base includes 0.25% Si, 0.4% Fe, 0.05% Cu, 0.05% Mn, 0.05% Mg, 0.05% Zn, and 0.03% Ti). It is found that the heat-treated region consists of three types of microstructure with the corresponding values of

hardness. The main and the largest portion of the zone located beyond the visible track produced by laser radiation on the target surface has a high average hardness 395 MPa and even 445 MPa at some sites. A narrow portion between the main portion and the visible track has a low hardness, lower than the original value; $H_\mu =$ $= 308$ MPa, while at some sites, the value is as small as 282 MPa. The third portion within the boundaries of the track exhibits an intermediate value of hardness 341 MPa which varies at some sites from 365 to 325 MPa.

Electron microscope studies have revealed that the portion of the highest hardness contains fine dislocation loops of an appreciable density, which attests to the intense processes of a structure deformation similar to the deformation in metals treated by a powerful electron beam or subjected to ion bombardment and shock hardening.

Approximately the same increase in the density of dislocations was noted in aluminum specimens after treating welds with giant pulses of a 25-ns duration and peak power density of 1 to 2×10^9 W/cm^2 [12].

The second portion is free of dislocations, although the dislocation network is apparent near the crystal.

The third portion displays some dislocation loops which afford a slight increase in the microhardness as against that of the second portion, but its value is lower than that of the first portion.

The distribution of the dislocation loops and, hence, of the hardness depends on the motion of a shock wave in the material, which arises after the rapid heating of the target with a laser pulse. The laser-supported absorption (LSA) wave drives the shock front into the material, thereby producing work hardening.

The results of treatment of irons of various grades with a a CW CO_2 laser in a wide range of feed rates for specimens were presented in a number of works [5, 9, 16-20].

For example, specimens from gray irons of different compositions and microstructures were treated on a CW CO_2 laser setup with an output power of up to 700 W. The laser power density at a target was 5×10^4-5×10^5 W/cm^2 and the speed of specimens ranged from 5 to 0.1 m/min. Let us consider the experimental results.

In heat treating at a feed rate of 5 m/min, the laser beam has no time to melt the iron target. The transformation hardening occurs at a small depth only through the conversion of the gray iron matrix to martensite and troostite without any changes in the surface roughness of the specimen. But the temperature interval of heating in this type of hardening is narrow because austenization of pearlite terminates only at $\sim 1\,000$ °C [19], while at $\sim 1\,150$ °C, iron begins to melt. It is thus apparent that in this region of laser interaction, the range of the parameters of treatment is rather narrow. Besides, the stability of laser parameters must be fairly high.

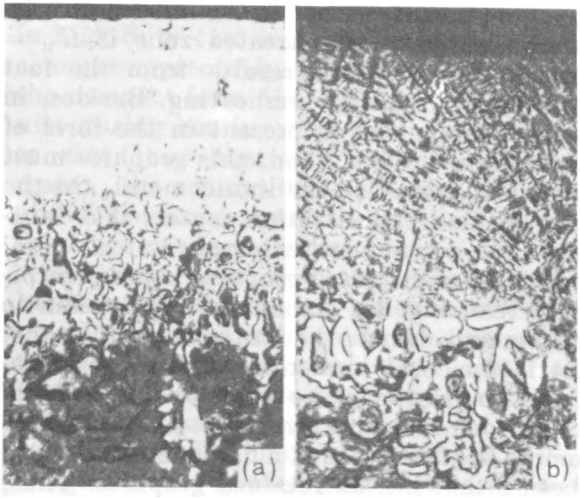

Fig. 7.18. Surface structure of white iron in regions uniformly melted with a CW CO_2 laser: (*a*), 150×, (*b*), 250×

Fig. 7.19. Structure across the hardened bands in a gray iron specimen treated with a 300-W CW CO_2 laser at a speed of specimen travel of 1.0 m/min (250×)

Appreciable advantages of laser hardening of irons show up where the heat treatment involves some surface melting and surface layer chilling at a high rate.

The microstructure of a surface layer after uniform surface fusion is shown in Fig. 7.18. The solidified layer of melt is practically immune to attack by the alcohol solution of nitric acid, which is a common feature after laser hardening because of a poor etchability of cementite and martensite. Multiple etching by nitric and picric acids with subsequent polishing makes it possible to reveal the structure of this layer. Low-temperature tempering can be used to render martensite more susceptible to etching.

A fact peculiar to the CW beam treatment is that dendrites in the molten zone grow at an angle to the target surface, which can be accounted for by an additional temperature gradient appearing in the direction of travel of specimens.

The zone lying directly under the molten layer is a partially fused layer containing the primary dendrites of hypoeutectic iron and the residues of graphite lamellas. In the completely chilled zone, the microhardness is H_μ = 10 700-12 110 MPa and in the partially chilled zone, H_μ = 4 290-10 700 MPa.

In the case of shallow melting of the iron surface (Fig. 7.19), dendrites can grow in the chilled zone in the direction from the

untreated substrate material to the surface, not in the reverse direction. In this case, the microhardness of the treated zone is H_μ = 6 320-7 050 MPa. A lower hardness here results from the fact that the melt pool does not undergo strong overheating. Besides, in the treated gray iron the graphite phase is present in the form of fine flakes (graphite eutectic). On the one hand, this graphite must rapidly dissolve in the melt and carburize the liquid metal. On the other hand, a large number of the graphitization centers that saturate the melt do not dissolve at a low overheating of the melt pool. Even at a high quench rate, a rather dispersed graphite phase precipitates in the melt, thereby reducing the amount of the ledeburite component in the chilled zone and, hence, the hardness of this zone.

Of practical interest is the local hardening of iron bearings, sleeves, and joints subjected to friction. The pearlite structure of the matrix of anti-friction irons and fine graphite flakes readily dissoluble in the melt promote the formation of a hardened layer with a completely chilled structure that has no retained graphite. Thus, the metallographic analysis of a guide bush of iron (3.32% C, 2.33% Si, 0.71% Mn, 0.18% P, 0.11% S, and 0.05% Sb) has shown that there is a clear boundary between the chilled layer and the substrate metal with the unchanged graphite structure. At the points of intersection of this boundary by a graphite flake the melt region penetrates deeper into the bulk as a consequence of contact melting. Inlets of the solidified melt are found in the bulk material near the fusion front at the sites of inclusions of the phosphide eutectic, which have a low melting temperature, down to 950°C.

It should be pointed out that coarse graphite flakes as a rule have no time to dissolve completely in the melt and remain there in the form of individual lobes in the zone whose height often reaches half the height of the entire fusion layer. In the remaining portion of this layer there are sometimes the traces of dissolved graphite flakes which leave sulfides, oxides, and other nonmetallic inclusions in this portion. Let us also note that fine lobes peeled off the flake surface are well visible around the yet incompletely dissolved flakes of graphite.

Graphite lamellas in the fusion zone are the sources of bubbles blown off these lamellas at the faces surrounded by the liquid metal. The bubbles so formed are filled completely or partially with the melt.

The blowhole porosity of the hardened region can often be a substantial drawback of surface hardening of iron workpieces. One way to eliminate this defect is to preliminarily degas workpieces in a vacuum or to heat them in a dry atmosphere at a temperature of up to 210-300°C, which is sufficient to remove a large fraction of hydrogen from the graphite phase. In going from gray irons with lamellar graphite to irons with compact forms of the graphite phase,

namely, flaky graphite in malleable cast iron and globular graphite in high-duty cast iron, the workability of alloys by the laser beam changes appreciably. The thing is that the inclusions of graphite of the compact form dissolve slowly in the molten metal (and in austenite during heating). The liquid solution is then carburized at a lower rate than that of the metal with lamellar graphite. For this reason, the zones with the hardened structure are rather suggestive of the hardened zones in high-carbon steels. They mainly exhibit the austenite-martensite structure and have a much lower amount of cementite in ledeburite than the hardened zones in gray iron. The hardness of the treated zones is lower accordingly.

As in the case of gray irons, in malleable and high-duty irons treated by a laser beam, the fusion front penetrates deeper into the bulk metal at the sites of graphite inclusions. But in irons with compact forms of graphite inclusions, around the globules of graphite or around the inclusions of temper carbon there are liquid metal fringes formed as the result of contact melting [9, 20].

The metallographic analysis of malleable ferrite cast iron [20] has revealed that in surface treating with melting, the hardened zone consists of four layers: (1) the surface layer of ledeburite; (2) sublayer of austenitic dendrites (austenite-martensite dendrites at room temperature) with ledeburite inbetween; (3) interlayers largely of the austenite structure with a small number of martensitic needles; (4) troostite-sorbite layer with $H_{\mu} = 4\,160$-$2\,850$ MPa.

Austenite-martensite-ledeburite portions occur not only on the iron surface but also inside the troostite-sorbite layer around the partially dissolved inclusions of graphite (temper carbon). A shallow fusion penetration in malleable ferritic iron (and local fusion at the sites of graphite inclusions) even at low feed rates ($v \approx 0.1$ m/min) is attributable to a long time of irradiation required for carburizing of the metal matrix.

Laser treating of ferrite gray irons causes a partial dissolution of graphite, with the result that a weakly etched region forms around the graphite. Earlier, work [9] pointed to the probability that ferrite could melt in the regions of contact with graphite.

It is important to note that the hardness of ferrite after CW laser surface treating increases to 2 200-3 200 MPa [9, 20, 21], probably because a large number of defects and distortions appear in a thin surface layer.

Paper [21] presented the results of investigations into the microstructure of laser-heat-treated specimens of malleable ferritic iron after tempering for 1 hour at temperatures of up to 600°C at an interval of 100 deg C. With an increase in the tempering temperature, austenite dissociates into a ferrite-graphite mixture and carbon diffuses to graphite. Tempering at 500°C leads to the complete dissociation of austenite and to a certain coarsening of the ferrite grains

of the matrix. The structure tempered at 600°C is similar to the original structure. In irons treated by a pulsed solid-state laser, austenite dissociates and carbon diffuses to graphite at lower temperatures.

Thus, an increased tempering temperature reduces the matrix ferrite hardness, which becomes equal to the original value after tempering at 600°C. The investigations suggest that laser surface hardening is advisable for malleable iron parts designed for operation at up to 300°C.

In papers [3, 22, 23] were given the results of studies into the thermal stability of specimens from pearlitic, troostite-sorbite Cr-Ni-Mo high-duty, and malleable ferritic irons treated by a CW CO_2 laser at a power from 1 to 5 kW with and without surface melting.

The specimens were tempered at 200, 400, 600, and 700°C. According to the results of the X-ray diffraction analysis and nuclear gamma-resonance spectroscopy, an increase in the tempering temperature up to 600°C reduces the amount of retained austenite from 30-60% to $\sim$ 8%, depending on the iron grade. At a temperature of up to 400°C, austenite dissociates into a ferrite-carbide mixture and the hardness of the structure slightly increases, but then sharply drops off as the temperature rises to 700°C, which is attributable to the coagulation of cementite in ledeburite and its graphitization. The troostite-sorbite iron is most stable to tempering.

The corrosion resistance of pearlitic irons increases ten times after laser treatment due to the absence of graphite inclusions.

Let us note that the wear resistance of irons, depending on their grades and conditions of laser treatment, increases from 2 to 5 times after hardening with a continuous laser [16, 17] and up to 5 times after pulsed laser hardening.

7.4. SURFACE ALLOYING

Laser alloying is the method of metal surface modification to improve corrosion resistance, high-temperature strength, red hardness, and other properties of metals and alloys. The method involves spreading of a powder containing alloying elements over the surface portion to be hardened and melting the powder and a thin surface layer with a laser beam to produce a true alloy layer on the surface after solidification.

In comparison with the conventional methods of nitriding, carburizing, hardfacing, etc., metal surface modification by laser alloying at high rates of melting and recrystallization offers a number of added advantages:

(a) reduced alloy material consumption;

(b) minimum volume of work involved in subsequent machining of laser-treated critical precision parts;

(c) no need for postprocessing of minor parts;
(d) fairly good control of melt depth;
(e) reduced requirements on the surface geometry due to the presence of electric and magnetic fields;
(f) high-speed processing and high quality;
(g) good reproducibility of the parameters of the hardened layer;
(h) saving of labor.

In the text below, we shall consider the main results of investigations into the process of laser alloying and examine some particular features of the process.

A number of works reported studies on various grades of irons and steels alloyed with C, Cr, Ni, W, and a single-carbide alloy applied in powder form on the target surface in a thin layer up to 0.1 mm thick, which was melted and alloyed into the surface by pulsed laser delivering up to 20 J of energy in a pulse of 1 to 3 ms duration. The same materials were also heat-treated with a laser. Metallographic examinations and also chemical, spectral, and X-ray analyses disclosed that the chemical composition and structure of heat-treated and alloyed zones differed from those of base metal zones. According to the quantitative spectral analysis for carbon, the content of carbon in the microvolume of graphite-alloyed armco-iron increases more than 10 times, 0.6% against 0.04% for the base metal; in the surface layer of armco-iron treated with the single-carbide alloy, the carbon content grows to 0.2% and the spectrum displays the spectral lines of tungsten and cobalt.

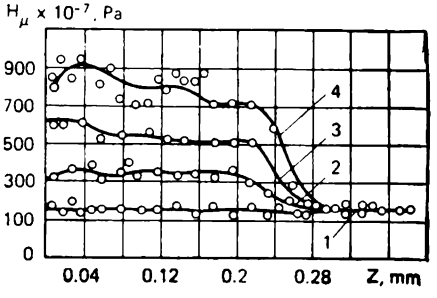

Fig. 7.20. Microhardness versus depth for steel specimens after laser treatment: *1*, original hardness; *2*, hardness of laser-heat-treated steel; *3*, hardness in layer mixed with graphite; *4*, hardness in layer mixed with single-carbide solid solution

As seen from Fig. 7.20, the hardness of the same steel in the laser-alloyed layer is much higher than that in the laser-heat-treated layer.

Works [9, 24] contain the results of experimental studies on pulsed and continuous laser alloying of a wide range of iron grades, including compound-alloyed high-speed steels, with C, Cr, Ni, W, WC, Co, etc., applied in powder form on the target surfaces to the appropriate thickness as dry powders or as powders mixed with water or liquid glass. After the passage of the laser beam, the alloying elements, the solubility of which was found to be higher than that attainable in conventional processes, resolidified in the mixture of

the base metal melt to form iron-carbon, iron-tungsten, and other solid solutions. The thin alloy layer so produced on the surface differed from the substrate in chemical and phase composition, microstructure, hardness, and heat stability.

So, this process can form alloy layers of the specified properties on the surfaces of high-carbon metal parts and thus increase the heat stability of the parts to 300-400°C. However, the experiments have revealed that the alloying elements added to the composition of high-speed steels do not improve their cutting properties. It is advisable to produce alloy layers of the desired properties on the surfaces of parts and tools made of cheap metals.

Diffusive saturation of iron with carbon and tungsten during the interaction of pulses from a neodymium-glass laser was described in [9]. The Nd-glass laser delivered up to 35 J of energy in a pulse of $\sim 10^{-3}$ s duration. The iron surfaces were coated with different compounds in powder form that contained carbon and also graphite. The pulses caused the compound to melt, following which the melt on the surface resolidified to form a white, etch-resistant layer, the size and shape of which depended on the conditions of treatment. The laser alloyed zone had 1.5 times the hardness of the original structure of α-iron. This fact pointed to the presence of the supersaturated solid solution. As revealed by the X-ray diffraction analysis, the molybdenum concentration in α-iron varied from 28 to 36%. Such an enhanced concentration resulted from the convective mixing of liquid metals and intense diffusion of alloying elements into the liquid metal.

Work [12] presented the results of alloying of iron and steel with pure elements such as nickel, molybdenum, titanium, tantalum, uranium, chromium, and vanadium. It was found that all alloying elements, excepting nickel, added to the hardness of the zone irradiated with 4-ms pulses delivering up to 9 J of energy. The steel target exhibited three clearly defined regions: the first region 300-400 μm deep, which was the solid solution of the alloying element mixed with base metal and was the largest in volume; the region of hardening; and the region of tempering. The choice of alloying elements has a significant effect on the characteristics of the treated surface layer; molybdenum and titanium afford a higher increase in hardness than niobium does. A nonuniform distribution of a large amount of the alloying element may give rise to local stresses in the heat-treated regions, attended by the formation of cracks and cavities.

The process of surface saturation of metals and alloys with alloying elements can be controlled in a wide range by changing the parameters of laser heat treatment [10]. The content of an alloying element and the depth of the zone of alloying is governed by the pulse duration, pulse energy E, and the number n and shape of the pulses delivered to the interaction zone [12].

The curves illustrative of the hardness of a vanadium-alloyed layer on the surface of armco-iron coated with graphite as a function of laser energy qualitatively agree with the hardness curves for the laser-heat-treated iron with a 3% carbon content. The analysis for low-temperature tempering (160-170°C) of iron coated with graphite shows that the laser treatment produces an iron-carbon solid solution layer on the target surface. The hardness of the surface layer is as high as 14 000 MPa and the hardness of the heat-treated layer below the first layer reaches 10 000 MPa.

Laser heat treatment can also afford the saturation of refractory materials with carbon. For example, irradiation of a graphite-coated tungsten surface yields an alloy layer with a changed structure and a small amount of tungsten carbide. The hardness of the layer amounts to 7 000-8 000 MPa [9].

After irradiation of iron coated with tungsten or a mixture of iron and tungsten in powder form, the specimen exhibits an iron-tungsten solid solution layer with a greater lattice constant; the solid solution contains an increased amount of tungsten, 15-18% against 13% attainable in the ordinary process of heat treatment at a temperature of up to 1 530°C. This solid solution can form only after transformation from the liquid phase in sharply nonequilibrium conditions. Also, a high quench rate in the order of $\sim 10^{6}$°C/s adds to the solution of tungsten in alfa-iron.

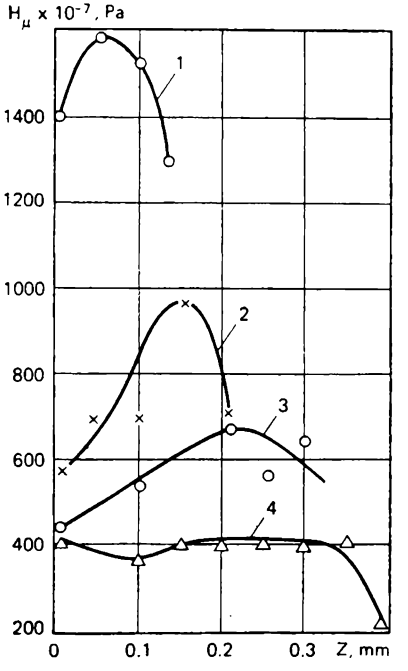

Fig. 7.21. Microhardness across the surface layer of armco-iron alloyed with molybdenum: *1*, one 8-J pulse; *2*, three 3.5-J pulses; *3*, three 5-J pulses; *4*, three 6-J pulses

In studies [12, 25], mild steel coated with molybdenum was irradiated with pulses from an Nd-doped laser. The surface of mild steel was coated with molybdenum foil produced by electron-beam melting. The number of 9-J pulses, each 4 ms long, incident on different target portions was varied from 1 to 15. The depth of penetration of Mo into the base metal reached 450-500 μm owing to the convective mass transfer. The microhardness across the alloy layer as a function of depth is shown in Fig. 7.21.

There are a few methods of applying an alloying element on the surface to be hardened: foil rolling; electrolytic deposition, shock wave deposition; plasma spraying, spraying of powders with binders and powder-solvent slurries, and other methods [12]. All these methods suffer from a disadvantage of an appreciable thermal resistance between the alloying element and base metal. A promising method is one that combines electric spark alloying with subsequent laser melting. This method ensures good thermal contact between the deposited layer and base metal owing to the formation of an inhomogeneous transition layer between the interacting metals [12].

The method for electric spark deposition of alloying elements prior to laser melting can be used to form fairly thick multilayer coats without impairing heat conduction between the alloying metals and base metal.

Work [12] described the results of experimental studies on laser treatment of steels and titanium alloys preliminarily coated with alloying materials such as T15K6 alloy, VK8 alloy, tungsten carbide, nichrome, aluminum, silver, titanium, and tungsten on an industrial setup of electric spark deposition. The thickness of alloy layers produced by a pulsed laser delivering power densities of about 10^5 W/cm^2 to substrates ranged from 30 to 50 μm. In this process of surface alloying, the quality of the alloy layer depends on the conditions of electric spark deposition, parameters of the laser beam, conditions of melting and solidification, and other factors. The use of fusible metals or compounds as alloying materials decreases the effectiveness of laser alloying. For example, in the process of laser treatment of calorized specimens of 45 steel, the laser beam has vaporized an appreciable amount of electric-spark-deposited aluminum and only an insignificant fraction of this metal penetrated into the melt [12].

The analysis of the concentration of alloying elements was made [12] after CO_2 laser treatment of aluminum and corrosion-resistant steel samples coated with a mixture of a nonmetallic powder, zinc, and copper. Aluminum specimens contained zinc only in the upper portion of the solidified melt region, and the copper content of steel was higher in the lower portion of the alloy layer than it was in the upper portion. The difference in the degree of convective mixing of the melt was due to the different values of thermal diffusivity for aluminum and corrosion-resistant steel.

In reference [12] were also given the results of the X-ray microanalysis of a laser-heat-treated titanium alloy preliminarily coated with nichrome deposited on the target surface by the electric spark method. An appreciable fraction of nichrome was found to alloy into the surface layer to a depth in excess of the thickness of the nichrome coat.

One analysis [26] afforded the data on the phase composition of the layer formed on the surface of tool steel and the distribution of chromium and tin in the zones irradiated with a CO_2 laser beam. The solid solution of chromium in ferrite was present in the entire layer covered with the film of chromium oxide. The surface layer of the steel sample preliminarily coated with tin contained intermetallic phases in the form of fine precipitates of tin in iron.

A technique for calculating the maximum concentration of an alloying constituent in the surface layer was put forward in [12]. The process of surface alloying was assumed to proceed most effectively in the liquid phase due to its uniform mixing. If we take the profile of the pulsed laser-melted region to be a paraboloid of revolution with a generating line corresponding to the isotherm of melting, the expression for an alloying element content k_2 can be written as

$$k_2 = k_1 V_2/(V_1 + V_2) \tag{7.16}$$

where k_1 is the content of the element in the layer deposited on the target surface, V_1 the volume of this layer, and V_2 the volume of molten metal.

It is also possible to produce laser surface alloying in a gaseous medium in contact with the surface to be hardened. Gas nitriding of annealed steel in NH_3 at a pressure of 0.1-0.4 MPa on the Kvant-10 laser setup was described in [26].

Since the laser setup could deliver power densities in the range from 0.1×10^5 to 1.0×10^5 W/cm^2, alloying was done with and without surface melting, using care to exclude optical breakdown in the gas.

Treatment without surface melting resulted in an inhomogeneous austenitic structure with martensite formed in the upper portion of the alloy layer due to a supercritical quench rate. In the process of alloying with surface melting, the treated zone contained martensite with an appreciable amount of nitrogen. The hardness of the recrystallized molten layer reached 4 000 MPa; in the transition region, the hardness was 150-200 MPa, and at a depth of 100-120 μm it was equal to the original value. A simultaneous increase in both the number of pulses incident on the same spot and the pressure of the NH_3 gas significantly increased the steel hardness, while a separate increase in either the number of pulses or the gas pressure produced a modest effect.

In [27], chromium and titanium were alloyed into the surface layers of armco-iron and steels in the conditions of high-rate laser heating. Carbon steels used in the experiments had the original structure of sorbite with a Rockwell C hardness of 28-30.

The slurries used as a saturation medium consisted of the powders of chromium and titanium mixed with a coal-tar varnish;

Al_2O_3 served as an energy-releasing agent and one of the salts of halogen hydracid, NH_4Cl, as a catalyst of the process.

The composition of the slurry utilized for alloying of armco-iron with chromium and titanium comprised a 55% mixture of powders of 30% Cr_2O_3 and 70% TiO_2, 35% carburizer, and 10% NH_4Cl. The slurry for alloying of carbon steels comprised a 70% mixture of 30% Cr_2O_3 and 70% TiO_2 powders, 25% Al_2O_3, and 5% NH_4Cl. The choice of slurries was made from the practical considerations of chemical heat treatment.

The specimens coated with a slurry layer 0.2-0.3 mm thick were treated on a laser unit permitting up to 4 J/mm^2 of energy density in a beam.

The results of studies confirm that the laser-treated zone has a sharply defined profile, the properties of which are different from those of the parent metal; U8A steel mixed with Cr and Ti and also armco-iron with C, Cr, and Ti are found to have the highest (statistical average) microhardness, in the order of 10 130-10 790 MPa.

The hardness of 45 steel after alloying is lower, 920 to 960 MPa, because the steel is deficient in carbon (0.45%) that takes part in the formation of superhard structures. Since chromium retards the diffusion of carbon into the bulk, the depth of the laser alloyed zone is smaller than that attainable in laser surface hardening. The depth alloyed in armco-iron is minimum; the reason is that the iron lacks an agent to promote a greater growth of the layer in depth, such as pearlite in carbon steels. The metallographic analysis reveals the difference in the boundaries between base metals and laser alloyed regions: armco-iron exhibits a distinct boundary; Cr-Ti steels feature a fairly smooth transition from the base metal to the alloy layer, which attests that the hardened layer well adheres to the base and is less susceptible to peeling and cracking. The alloy layers in all specimens are similar in morphology which displays an acicular structure typical of diffusionless transformation.

Concurrent with the diffusion in the liquid phase, which is conducive to the saturation of the surface layer with alloying elements, the diffusion in the solid phase also occurs.

A number of works [12, 26, US Pat. No. 212900 and No. 4015100, Japanese Pat. No. 54112710 and No. 55117584] contain specific recommendations for implementing the processes of surface hardening and alloying. For example, it is suggested to harden the surface of nitrided steel with a laser beam which partially decomposes nitrides and leads to the formation of a hardened layer of martensite and nitrides. The diffusion layer formed under the surface layer displays a higher hardenability and greater quench hardness, with the result that the total hardened layer increases in thickness.

In one method intended for increasing the corrosion resistance of heat-resistant nickel alloys, it is suggested to place an Al sheet

on the surface of Ni alloy, cover the Al sheet with an Ni sheet, and then sweep a CO_2 laser beam over the Ni sheet to melt it through. Since the melting point of Al is much lower than that of Ni, aluminum melts to form a liquid alloy layer which fuses into the Ni layer. A feature of the method is that the liquid metal does not splash over. The liquid aluminum fairly well spreads over the surface of the heat-resistant alloy, thereby improving the alloy corrosion resistance and resistance to scaling.

Alloying is made by means of a pulsed laser, with the power density at the hot spot and pulse duration selected so that the base metal can heat to a minimum, while the rate of crystallization (quench rate) can be the highest.

Recommendations for laser alloying and examples of treatment of particular workpieces are given in work [28] and US Patent No. 4015100; the latter work suggests the method of alloying with a CO_2 laser coupling 1 to 20 kW of power to a spot 0.59 to 1.80 mm in diameter. The laser can also produce a rectangular beam or a beam of any other shape and size in cross section.

The scan speed of the laser beam ranges from 12.7 to 1 270 cm/min, and the time of metal melting at a given spot does not exceed 0.1-1.5 s. The time of metal recrystallization is approximately the same. High temperature gradients, shock wave effects, and other factors contribute to good mixing of the alloying agent and substrate metal. Preheating of a workpiece allows the beam to be swept over at a higher rate.

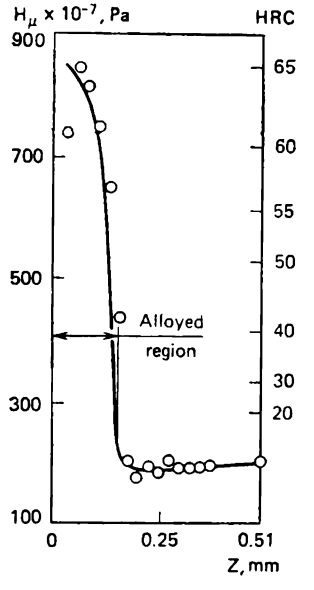

Fig. 7.22. Microhardness versus depth for the alloy layer produced by a laser on the surface of low-carbon steel

The melt depth can be varied from 0.05 to 5 mm, with the degree of alloying adjusted from 0.1 : 1.0 to 0.81 : 1.0.

The composition of the alloying paste sprayed onto target surface to thickness $\sim$ 4.5 mm is: 6 g of graphite, 3 g of chromium, 3 g of manganese, each in powder form, and 40 ml of binder. An underlayer of manganese phosphates and alumina increases the absorptivity of target at the laser wavelength 10.6 μm. The microhardness versus depth for the alloy layer on the surface of low-carbon steel laser-alloyed with C, Cr, and Mn is shown in Fig. 7.22.

As an example of laser alloying, US Pat. No. 4015100 describes the process of hardening the working surfaces of ICE valves. The beam was swept across the valve surface at a rate of 508 cm/min, with the valve held stationary to exclude the deformation of liquid metal due to centrifugal forces. The coat consisted of 20% Cr and 80% W in powder form. The output of the setup with the laser delivering 3 to 19 kW of power to the target surface was 2 400 pieces per hour.

7.5. CLADDING

Laser cladding, or laser hardfacing, is the process of melting of an appropriate metal or alloy placed on a metallic surface, which then spreads over the surface and quickly solidifies to give the surface layer with specified properties. In distinction from laser alloying, laser cladding involves a minimum fusion of the base metal, which must be only enough to produce a metallurgical bond between the alloy material and the substrate. A large amount of the base metal fused into the alloy material may impair the properties of the cladding.

The materials used in this work are commonly high-melting-temperature alloys applied to the surfaces of low-melting-temperature metals and alloys.

The typical cladding materials called upon to increase the surface hardness, therewith reducing the wear rate and imparting the surface the corrosion-resistant properties, are Co, Ni, and iron-base alloys [26]. Cladding is a fairly well studied and proven technique. Experimental results of cladding can be found, for example, in work [29] which described the process of melting of the alloy material and its fusion to the base metal of gear wheels, shafts, cams, inside surfaces of cylinders, piston ring channels, valve seats, etc. Flame plating was used to coat the target surfaces with self-fluxing high-chromium Ni-Co alloys which were then melted with a laser beam. Rather high contents of boron, silicon, and tungsten carbide of these alloys lowered the melting point of the alloys and promoted the process of self-fluxing.

The method of plasma spraying is also suitable for applying alloy materials [US Pat. Re 29815]. A moving or stationary laser beam then fuses such a coat to the base, thus producing a bond of the homogeneous chemical composition and microstructure with the specified wear-resistant and corrosion-resistant properties [29].

Optimal experimental conditions for laser cladding were suggested in works [26, 29], which also described cladding materials, operating practices, and specific features of the process. Let us consider some examples of coatings.

Co-base alloy coating. The details of the process of cladding of parts with Co-base alloys to make the parts wear- and corrosion-

resistant were given in [26]. An increase in the wear resistance of these alloys was due to a hard intermetallic phase in the form of dendrites present in the solid solution of the eutectic base. This phase of the hexagonal close-packed structure had a composition intermediate of those of CoMoSi and Co_3Mo_2Si. The corrosion resistance resulted from an adequate distribution of chromium, about 33% in the intermetallic phase and about 67% in the solid solution. To inhibit carbide formation, the carbon content was not allowed to exceed 0.08%. The volume of the intermetallic phase reached 50%. The alloy of this composition was fused to the surface of steel with 2.25% Cr and 1% Mo. The scanning beam melted the alloy material applied in powder form and produced a coating 7 to 6 mm thick and 10 mm wide in a single pass. The dilution of the cladding by the base metal was below a 5% fraction of total mass.

Stellite (Co-base alloy) coating. In experiments, 3-mm diameter stellite rods placed on a steel substrate were successively melted by a 3-kW scanning beam to produce the cladding on the base metal fused to a negligible depth. The rate of deposition was $\sim$ 1 kg/h. The alloy layer contained up to 51% Co, 31% Cr, and 13% W, and had a rather uniform microstructure in depth. The amount of the substrate metal dissolved in the layer was not in excess of 5%. The cladding hardness amounted to 730 MPa.

In the process of cladding, the temperature conditions were adequately chosen to dissolve the coarse carbides of the stellite. The alloy was melted with a laser beam at $\sim$ 1 335°C and then overheated to 1 649°C, following which the melt was allowed to cool at a quench rate of 650 deg C/s down to 1 335°C and then at a rate of 40 deg C/s down to room temperature.

The cladding process in a carburizing medium enables the melting point of the substrate surface to be raised to 1 426°C.

Silicon coating. The coating in silicon with a melting temperature of 1 430°C was formed on an aluminum alloy substrate melted over the temperature range 508-649°C. The aluminum alloy contained 17% silicon. The layer beam melted the silicon powder ground to a particle size of 44 μm and also a thin layer of the substrate surface. The microstructure so produced had silicon particles implanted in the Al-Si eutectic base, the volume of which reached 53-73%, corresponding to a 53-69% silicon content by mass. Silicon particles with an original hardness of $\sim$ 9 800 MPa raised the coat hardness to 4 000 MPa. The hardness of the aluminum alloy was an average of 1 250 MPa.

Coating composed of a dense base with tungsten carbide. The material used for cladding was the mixture of an iron powder ground to a size of $\sim$ 44 μm and tungsten carbide with a particle size of 0.5 mm. The mixture without a binder was sprayed onto the surface of low-carbon steel and melted with a laser beam. The temperature

conditions selected for the purpose were such that the beam did not melt tungsten carbide particles, which decomposed little as they submerged into the fine iron powder. After laser treatment, an average hardness of tungsten carbide particles was 11 000 MPa and that of the iron base was 8 700 MPa. The metallographic analysis revealed the regions of interaction of carbide with iron on tungsten carbide particles.

Alumina coating. In laser cladding of an aluminum alloy with alumina, whose melting temperature was 2 063°C, the hardness of the coat produced was as high as 20 000-23 500 MPa.

7.6. SHOCK WAVE EFFECTS

A Q-switched laser can produce single giant pulses with a duration of $\sim$ (20-70) $\times$ 10^{-9} s. The peak power density of the pulse in the focus of the optical system can be very high, in the range of 10^9-10^{12} W/cm^2 and even above with a duration of the pulse front of $\sim$ 10^{-9}-10^{-8} s. The interaction of such a laser with metals appreciably differs from that of a normal pulse laser. A short giant pulse incident on the target can effect local hardening of steels, work (strain) hardening under the action of the wave front driven into the material by an LSA wave, surface etching by gas and ion jets issuing from the zone of interaction, etc. [4].

A number of works, for example, [4, 5, 9], treated the subject of the shock wave action on the structure and properties of materials and also discussed some other aspects, for example, wave-induced structural defects, thermal and ionic etching, and point defects in annealed copper plates 0.1 mm thick struck by giant pulses with 80-ns duration and a peak power of 5-6 MW. Crystal defects arise from high quench rates, of the order of 10^8 deg C/s, increased temperature gradients (10^5 deg C/cm), appreciable pressures during metal vaporization (1 000 MPa), and ion bombardment. An increased number of point defects in the heat-treated zone raise the metal hardness.

Work [9] contains the results of studies on the plastic deformation of low-carbon steel with the original structure of ferrite (H_μ = 1 700 MPa) and pearlite (H_μ = 2 000 MPa) in the interaction of a 10-ns duration pulse.

In the zone of interaction, 35-J, 10-ns giant pulse forms a 0.9 mm dia. crater 0.5 mm deep. A thin surface layer of the solidified melt 10 to 20 μm thick has a fine-acicular martensite structure with a hardness of 7 600 MPa; below this layer is a heat affected zone $\sim$ 20 μm thick with transformed grains of pearlite, the hardness of which reaches 6 500 MPa. Next in succession is the zone of "mechanical" influence 700-750 μm deep, in which the ferrite grains contain twins.

Based on experimental findings, a qualitative model of giant pulse interaction has been put forward, at the root of which is the formation of a powerful shock wave whose pressure is so high that the wave near the target surface causes thermal melting, vaporization, and material blowoff. At a certain distance from the crater, the intensity of the shock wave is still sufficient to induce plastic deformation, which is apparent from the twinning of ferrite grains.

Works [9, 12] have pointed out to an essentially mechanical character of interaction of a single giant pulse, the dwell time of which is too short to produce the HAZ of a large size. An example of shock hardening of an aluminum alloy by the impact of Nd-glass laser pulses causing the formation of a tangled dislocation substructure was given in work [12].

Experiments were made to trace the onset of twinning and to analyze the effect of a giant pulse on an iron alloy with 3% Si [5]; the pulse gave rise to a shock wave whose pressure reached 5 600 MPa. It was found that the slip effect was partially responsible for material deformation.

As noted in [12], laser shock hardening of various aluminum alloys causes a temporal increase in the fatigue of the metals due to residual compressive stresses. The estimates of pressure pulses arising in the zones of giant pulse interactions are available in a number of works. For example, works [5, 12] presented the results of measurement of the shock wave pressure on the target struck by a CO_2 laser pulse with a minimum duration of $\sim$ 100 ns. The estimates were taken using a technique which relied on the measurement of motion of a target whose back surface served as a mirror of the Michelson interferometer.

The maximum pressure produced by a laser pulse with $q = 2 \times 10^8$ W/cm^2 was equal to $p = 10^4$ MPa. The experimental and theoretical relations between the shock wave pressure and the environmental pressure p_e, laser power density q, and laser beam diameter d where found to take the form [5, 12]: $p = p_e{}^{0.51} q^{0.89} d^{-1.95}$; $p_{th} = p_e{}^{0.48} q^{0.7} d^{-1.67}$.

As mentioned above, the shock wave resulting from the rapid surface vaporization exerts pressure on the target. The intensity of this mechanical influence depends on the laser power density delivered to the interaction region and on the thermal and optical parameters of the material. Let us consider an example of shock hardening with an Nd-glass laser which generated single giant pulses 25-30 ns long with energies of up to 500 J. The lens with a focal length of 100 cm focused the beam to a spot 3 mm in diameter. The pulse delivered a power density in the range 5.23×10^2-1.58×10^9 W/cm^2 to iron specimens 0.3 cm in thickness and under, with and without coatings from quartz glass, lead foil, and glass-lead composites.

The results of experiments show that the deformation of plates without coatings is insignificant and does not occur at a depth in excess of 50 μm away from the surface even at a maximum power density q. A decrease in q leads to a lower degree of deformation. The quartz coating, too, reduces the deformation effect, which can be accounted for by the shielding effect of the plasma cloud above the coating. In the interaction of the giant pulse with the lead coating, the recoil momentum (impulse transmitted to the target) increases because the sublimation energy of lead is much lower than that for iron.

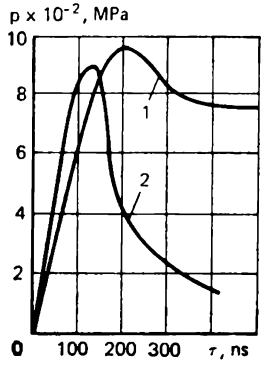

Fig. 7.23. Shapes of the pressure wave at pulse durations of 200 ns (curve *1*) and 30 ns (curve *2*)

Decreasing the thickness of plates increases the material hardness. The length of the laser pulse has an appreciable effect on the formation of the shock wave. Figure 7.23 illustrates the shape of the pressure wave on the back surface of the target irradiated with a comparatively long pulse 200 ns in duration (curve *1*) and a rather short, 30-ns pulse (curve *2*). At a long pulse, the pressure decays slower due to a more uniform distribution of stresses in the target.

Studies on the deformation of materials raveal that very short giant pulses produce a shear deformation effect. The data on the measurement of impulses transferred to the target are available in many earlier works. As follows from the comparative investigations, a 0.3-J, 50-ns pulse from a ruby giant pulse laser transfers to a copper target placed in a vacuum ($\sim 4 \times 10^{-3}$ Pa) a momentum of 0.18×10^5 N s as it causes the gas dynamic motion of the blowoff material. The momentum due to the sunlight pressure for the case of total reflection reaches merely 2×10^{-9} N s. It is found experimentally that an average speed of the blowoff material in the interaction of a giant pulse delivering power densities in the 10^{10}-10^{11} W/cm^2 range is equal to (0.4 to 3.0) $\times 10^6$ cm/s. The impact of a giant pulse mainly causes the ejection of disintegration products as liquid droplets. The character of target damage largely depends on the intensity of the shock wave produced, which propagates into the material and leads to an additional melting and vaporization of the material, accompanied by the formation of a crater (Fig. 7.24).

Works [4, 5, 9] presented the results of experimental studies of the thermal and mechanical effects produced by a giant pulse on

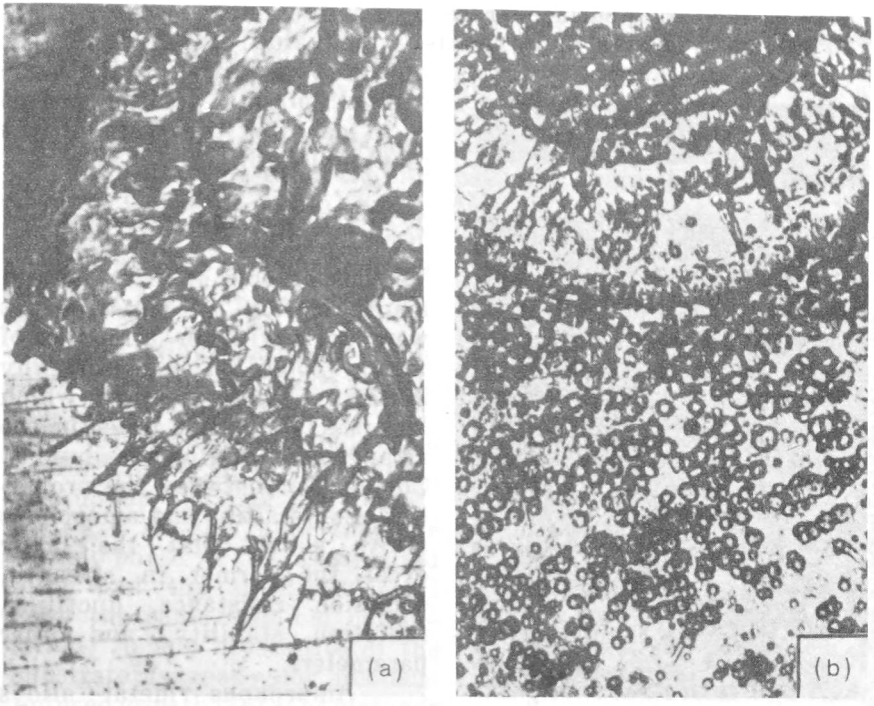

Fig. 7.24. General view of the regions on corrosion-resistant steel specimens (70×) irradiated by a Q-switched laser in air (*a*) and in vacuum (*b*)

iron-carbon alloys (carbonyl iron foil subjected to double-stage vacuum refining and foil of corrosion-resistant steels).

A ruby laser giant pulse 8×10^{-8} s long that delivered 0.4 J of energy to the surface of corrosion-resistant steel failed to increase the hardness of the surface layer in the crater.

In the interaction of an Nd-doped laser pulse of $\sim 10^{-7}$ s duration, plasma-induced heat effects played a significant role. The rates of heating and cooling after the formation of the plasma plume reached 10^7-10^8 deg C/s, and the maximum hardened depth in corrosion-resistant steel did not exceed 10 μm at an average power density of 10^{11} W/cm^2; the microhardness of the solidified melt was 7 500 MPa (Fig. 7.25).

The models suggested in [4, 5] afford a satisfactory agreement between the calculated and experimental values of the hardened depth in the zone of giant pulse interaction. During a very short interaction time, neither electrons nor the radiant flux can ensure a noticeable heat transfer deep into the solid phase. The effect of hardening to a depth of 10 μm can be produced only if the heat power

density on the target surface struck by a 100-ns pulse reaches $\sim 5 \times \times 10^6$ W/cm^2. This is approximately the value of the power per unit area re-emitted by the laser-excited plasma to the surface ~ 10 ns after the start of the giant pulse [5].

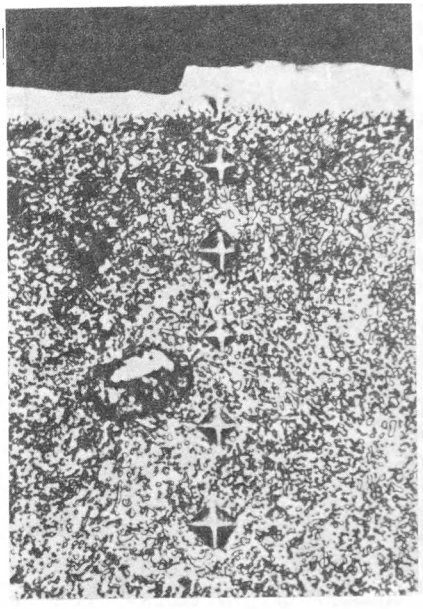

Fig. 7.25. Section through the hardened zone produced on the surface of corrosion-resistant steel by a giant pulse laser in vacuum (600×)

7.7. AMORPHIZATION

Various aspects of laser-induced amorphization of metal alloys were dealt with in a number of works [30-36]. The reason why interest is taken in alloys which lack the long-range order in the arrangement of atoms is obvious. Comparison between the properties of crystalline and amorphous alloys shows that the latter excel the former in strength, corrosion resistance, ductility, radiation stability, and other parameters.

Amorphous metal alloys are metastable systems [35]. That is why the melt must be cooled at high rates, $\sim 10^6$ deg C/s and above, to ensure highly nonequilibrium conditions required for the amorphization of alloys. There are several conventional methods for the superfast cooling of melts: flattening of liquid droplets by moving disks, ejection of the melt onto a heat-conducting substrates, liquid metal quenching in the jet of a liquid or gas, etc. The laser method affords fast quenching of the irradiated regions at a rate of 10^7 deg C/s and over on condition that heat removal from the melt is sufficiently efficacious. It should be noted that the laser-melted alloy zone has improved thermal contact between the liquid phase and the solid substrate, whereas the melt produced and cooled by the conventional methods contains a thin layer of adsorbed impurities and gases. The rates of heating and cooling can be adjusted by changing the parameters of laser treatment.

It is difficult to convert pure metal elements to the amorphous state by melt quenching [35]. For convenience, it is suggested to divide all binary alloys, in which X-ray methods trace amorphous phases, into the following categories proceeding from the character

of the interatomic bond, atomic structure of the elements, and types of constitution diagram:

(1) alloys of Group I elements (Ag, Au) and Group VIII elements (Pd, Pt, Rh, Fe, Ni, Co) with 20% of metals, semimetals (metalloids) and nonmetals such as Si, Ge, Sb, P, and C;

(2) alloys based on the compositions of rare-earth elements (La, Ce, Pr, Nd, Y, Gd, Sm) and metals of ordinary valence (Ag, Au, Cu, Al, Ga, In, Sn);

(3) alloys of transition metals (Ti, Zr, Nb, Ta) with Cu, Fe, Co and Ni;

(4) alloys based on tellurium Te with additions of Ag, Ga, Cu, In, and Tl;

(5) binary compounds such as Pb-Sb, Pb-Si, Pb-Ag, Pb-Au, Tl-Au, Sn-Cu, and Au-Su.

Let us also note that the liquid phase of a laser-melted alloy and the substrate metal have the same chemical composition, so any crystallite of the substrate is ready for nucleus-induced growth [28]. The methods of preparing specimens for laser beam refining have been put forward in US Pat. No. 4122240, which describes laser heat treatment of massive specimens of alloys liable to amorphization or thick substrates coated with these alloys.

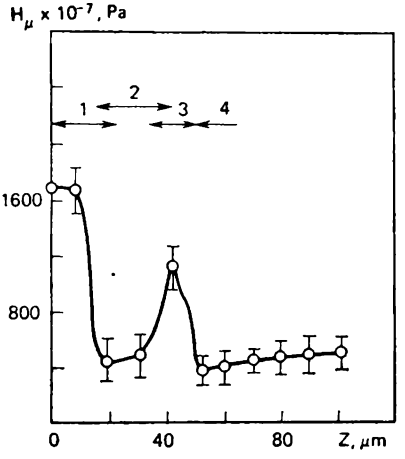

Fig. 7.26. Microhardness versus depth for laser treatment of tool steel coated with $Fe_{80}B_{20}$ alloy: *1*, amorphous zone; *2*, dendritic zone; *3*, hardened zone; *4*, original structure

Readily amorphizing coatings were deposited on the surfaces of massive specimens prepared from tool steel of the ledeburite class (2.1% C and 12% Cr) and from single crystal niobium. Various methods of coating were tried out: electroplating, plasma spraying, flame plating, and dusting [28]. The surface of tool steel was given a $Fe_{80}B_{20}$ alloy coat 40 μm thick which was remelted by a 3-kW CO_2 laser beam focused to a spot 3 mm in diameter. The beam also melted a substrate layer 20 μm thick. The linear velocity of the scanned beam relative to the specimen was 20 cm/s.

Electron microscope and diffractometer microexaminations have revealed an amorphous layer on the specimen surface; still deeper into the specimen, there lie the dendritic zone, HAZ (for steel), and base metal in succession. The hardness versus depth plot for the tested specimens is shown in Fig. 7.26. The microhardness is as high as 17 000 MPa. It is important to note that the curve displays

a secondary increase in microhardness for the HAZ (hardened zone).

Heat stability tests indicate that annealing for 15 min at 960°C decomposes the amorphous layer and forms the polycrystalline structure with a grain size of 0.5-1.0 μm. Bend and compression tests show that the adhesion of amorphous layers to substrates is fairly strong.

Pd-Cu-Si alloy specimens arranged on a revolving table were irradiated with a CO_2 laser beam at $q = 10^4$-10^7 W/cm^2 in a cover gas medium. The linear rate of melting was 76.2 cm/s, which ensured an amorphization coverage rate of $\sim$ 300 cm^2/min at a quench rate of $\sim 10^4$-10^{10} deg C/s.

The analysis of the laser-treated steel specimens have revealed the complete dissolution of carbides and the absence of cracks in the amorphous layer. This layer also had a higher corrosion resistance than the substrate metal.

A 0.15-μm thick amorphous layer was formed on the surface of a pure aluminum specimen (99.9999% Al) after irradiation in air with a 15 ns ruby laser pulse at a pulse fluence of 3.5 J/cm^2 and subsequent solidification at a quench rate of 10^{10} deg C/s [28]. The amorphous phase was detected with the methods of transmission electron microscopy and microdiffraction. The laser treatment in air probably facilitated the pure metal amorphization owing to the presence of amorphizing elements. The amorphous layer also contained adsorbed nitrogen N_2 and oxygen O_2. The electron diffraction analysis detected the hexagonal nitride AlN with a grain size of $\sim$ 0.01 μm.

In other experiments [28], the equiatomic mixture of fine Cu and Zr powders deposited on a thick copper plate was struck by a laser pulse delivering power density in the range from 5.6×10^4 to 6.2×10^4 W/cm^2. The X-ray diffraction analysis revealed the amorphized portion of the surface layer up to 50 μm thick, the hardness of which was 7 900 MPa.

The results of studies of the Ni-Nb and Cu-Zr systems point to the possibility of obtaining partially amorphized metal alloys from the irradiated mixture of requisite crystalline powders. Work [28] have also reported the growth of amorphous layers on the surfaces of $Ni_{60}Nb_{40}$ cast alloy specimens.

The first amorphous alloy based on a ferrous metal was produced from a ternary phosphide eutectic of the Fe-C-P system quickly quenched from the liquid state [37]. Later, researchers [36] obtained the amorphous metal in the Fe-C alloy without phosphorus. Irons high in carbon and silicon and also fairly rich in phosphorus must be capable of conversion to the amorphous state on fast cooling.

The study presented in paper [36] has examined the structural transformation in iron specimens irradiated with an Nd-doped normal-pulse laser which provided about 100 J of energy in a 1.8-ms

pulse. The beam was so focused as to form a shallow crater on the surface of the melted iron.

The chilled zone on the surface of iron showed evidence of the transformation expected. Iron contained 3.20% C, 2.67 Si, 0.64 Mn, 0.014 S, and 0.060 P. At an appreciable distance from the fusion boundary, the surface layer was found to have a rather coarse crystalline structure with large martensitic needles in the base of retained austenite. This was the result of averaging of the carbon content of the melt and even melt decarburization in the superheated surface layer. The quench rate in the order of $\sim 10^5$-10^6 deg C/s for such a melt with about 3% C was insufficient to produce the amorphous metal [36].

The solidified melt zone nearest the fusion boundary contained an aggregate of sites both stable and unstable to attack by the etching agent nital. The insoluble sites were the sites formerly occupied by cementite in ledeburite and the soluble sites were the former sites of pearlite (austenite in high-temperature conditions). Decarburized cementite dissociated into two crystalline phases: stoichiometric cementite and austenite with its interlayers disposed along (001) planes of the original Fe_3C crystal. Such a finely dispersed mixture of the phases received the name "baykovit". It is readily etched with nital. So, this allows us to presume that the insoluble sites are the sites of an amorphous metal, i.e. a metallic glass which has not had time to solidify at a high quench rate of $\sim 10^5$-10^6 deg C/s because the dissolved carbon content of this metal is higher (around 6%) than that of alloys sited in reference [36].

The X-ray diffraction analysis of these small regions of the supposed amorphous phase is still difficult to carry out. Therefore other methods were used to identify this phase. Electron microscopy showed no evidence of the crystalline structure even with a 24 000× magnification. The microhardness H_{20} of insoluble and soluble regions was 12 000 MPa and 8 000-10 000 MPa respectively.

Tempering at 200°C did not lead to substantial changes in the structure and hardness of the structural components of the metal, but tempering for 2 h at 400°C rendered the metal slightly prone to etching and increased its hardness by an average of 500 MPa. If the regions of the fused and solidified cementite had a fine-crystalline structure, the hardness of the regions would increase on tempering. Crystallization of the amorphous phase containing less than 6.67% C must yield a fine two-phase structure of the type of baykovit with enhanced hardness. In the experiments described above, this apparently was the case.

Electron microscope examinations of a variety of baykovit (let us call it baykovit II) have provided evidence that the modification observed in earlier experiments conducted with laser-irradiated white iron samples was indeed baykovit II.

A thick specimen of cementite was shot by laser pulses to obtain an amorphous phase (6.67% C) undiluted with iron. But the quench rate of the metal after laser pulse heating of the surface layer proved insufficient because of a low thermal conductivity of cementite. This led to a strong superheating and, hence, to decarburizing of the melt which solidified into a classical mixture of crystals of primary cementite with ledeburite interlayers.

Definite scope exists for laser processing of alloys which are not subject to amorphization at quench rates of $\sim 10^5$ deg C/s [28]. Superfast crystallization of melts favors the growth of superfine-grain structures or structures with finely dispersed phases and thus affords the formation of surface layers with improved service properties [28]. For example, this approach was used to obtain a refined uniform structure with a hardness of 14 000 MPa on the surface of a homogeneous nickel alloy containing 15% Ni, 15% Co, 5% Cr, and 2.75% Mo and B. In other experiments, it became possible to achieve the refinement of a carbide eutectic with an increased volume fraction of the carbide phase (from 13.8 to 50%) and the refinement of primary carbides in tool steel. In a certain way, this is the process of laser glazing. Let us point out that the notion of laser glazing has a broad meaning: the process involves surface melting to produce the layers with enhanced dispersivity of crystalline phases as well as the layers with amorphized phases [28].

7.8. ON SOME FEATURES OF LASER HEAT TREATMENT

Three kinds of laser surface heat treatment, namely, heat hardening of layers 0.05 to 1.0 mm thick, cladding, and alloying, require power densities in the range of 10^4 to 10^5 W/cm^2 with a total energy per unit area (fluence) delivered to the target of $\sim 10^4$ J/cm^2.

Amorphization proceeds at a power density of 10^6-10^7 W/cm^2 with energies coupled to a unit area ranging from 1 to 10^2 J/cm^2. In shock hardening, a short pulse of $\sim 10^{-7}$ s duration must deliver a peak power density of $\sim 10^9$ W/cm^2 at a pulse fluence of 10^2 J/cm^2.

Certain requirements need be met to implement the processes of laser heat treatment [3]: (a) cover the surfaces to be treated with laser-light-absorbing coatings; (b) employ high-power lasers and adequate beam-scanning systems in certain processes called upon to work large surface areas; (c) ensure a high level of automation of the entire process with due regard for variations in the surface properties of materials. In this connection, a large amount of theoretical and experiment work has yet to be done to study the aspects of material adhesion in laser cladding and the ways of increasing the wear and corrosion resistance of surface layers.

Laser surface treatment is the main domain of industrial laser application, which, unlike laser welding and cutting, competes successfully with the established surface treatment techniques.

Laser surface treatment accounts for up to 70% of the entire volume of work done with lasers. It is expected that this technique will soon reach production status in automotive, road-building, agricultural machinery, mining, and steel industries for treatment of various critical parts; hardening of tools, dies, rolls of mills and bloomers; alloying of cutting edges of farm implements, road-building machines, and head-roaders. For this, it is necessary to develop industrial lasers with powers in the 2-5 kW range and put them in production. High-power lasers are more preferable, for example, in hardening of the rolls of machinery employed in ferrous metallurgy. Gas dynamic lasers may prove effective for the solution of this problem.

It is advisable to harden tools with 2-kW lasers [3]. Examples of the successive use of pulsed lasers for tool hardening are given in [10, 38, 39]. Workpieces of motor-car engines and power drives can be hardened with lasers delivering 5-10 kW of powers [3].

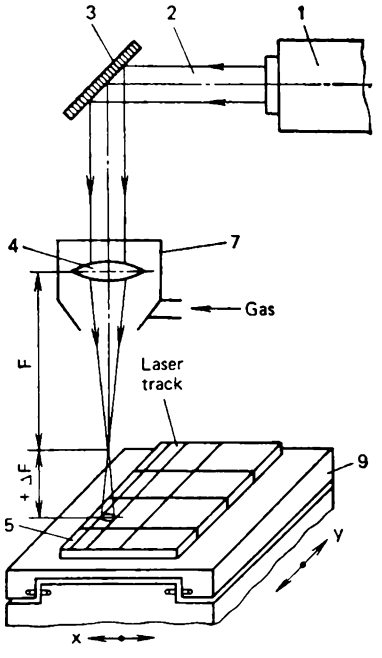

Fig. 7.27. Schematic diagram of laser surface heat treatment: *1*, pulsed or continuous laser; *2*, laser beam; *3*, mirror; *4*, lens; *5*, target; *9*, worktable; *7*, cap with gas jet nozzle

Figure 7.27 presents the schematic diagram of a laser unit for surface treatment of materials. The beam *2* from a laser source *1* falls on a turning mirror *3* which reflects it at a right angle on to an optical system *4* focusing the beam to a desired spot on the surface of a target *5* placed on a worktable *9* that moves in the *X-Y* coordinate system at a definite speed. The optical system is as a rule an objective used at a pulsed laser wavelength of up to 1.06 μm and, for example, a KCl or ZnSe lens at a CW laser wavelength of about 10.6 μm. The cover gas such as argon or nitrogen at a pressure of $(0.5\text{-}1.0) \times 10^5$ Pa is brought into the cup 7, from which the gas jet issues through the nozzle coaxial with the beam and falls on the

target. The size of the light spot (laser impingement point) can be adjusted in a wide range by shifting the focal plane of the focusing lens with respect to the target surface, i.e. defocusing the beam by ΔF as shown in Fig. 7.27. Defocusing the beam with the aim to bring the spot to the requisite size varies the power density delivered to the spot over a definite range. For example, the Kvant-16 laser setup can adjust the light spot from 2 to 4 mm in diameter depending on the amount of pulse energy and the task specified.

In most cases, except for stable laser operation [4], lasers do not provide for a uniform distribution of energy across the beam and, hence, over the spot. For this reason, it is good practice to treat workpieces at a maximum pump energy of the lasant and to stop down the lens, thereby cutting off the outer edges of the beam and minimizing the size of the tempering zone.

As mentioned above, a defocused beam is generally used to treat the surfaces of parts. The energy in the beam and the amount of defocusing are so adjusted that the power density at the hot spot should not cause damage to the specimen due to melting and vaporization of the material on the target surface. The profile of the hardened zone irradiated by one laser pulse resembles an upset bell-shaped (Gaussian) curve with strongly elongated edge sections. Therefore, in an effort to produce broader hardened bands of a more even case depth, recourse is made to partial overlapping of single-pass hardened spots. The spot overlap ratio K defined as the ratio of the difference between the spot diameter D and treatment step S (spot center-to-center pitch) to the diameter D, $K = (D - S)/D$, ensures an approximately even depth of hardening in two overlapping passes if the value of K approaches 0.5 (Fig. 7.28). In the laser treatment of comparatively large areas, individual heat-treat tracks overlap to form adjacent bands irradiated three or four times by the outer edges of successively scanned beams (Fig. 7.28*c*). These narrow bands with a decreased hardness due to the anneal effect of the multiple passes separate the tracks of high hardness, $H_\mu = 10\,000$ MPa and above. Since the power density at the outer edges of the beam is lower than that at the center, the temperature at the edges of the hot spot is lower too. So, during the overlapping, the earlier hardened peripheral regions of the spots undergo tempering, which decreases their hardness. Nevertheless, the hardness of these regions is somewhat higher, by 2 000 MPa or more, than that of the regions surrounding the laser-treated spots on the surfaces of preliminary hardened specimens.

Experiments performed on steel specimens irradiated in air have revealed a considerable oxidation of the treated surface and the formation of a softened region up to 20 μm thick in the surface layer. For example, in chromium steel the hardness of the zone is $\sim$ 11 000 MPa, while that of the softened region is 9 000-9 200 MPa.

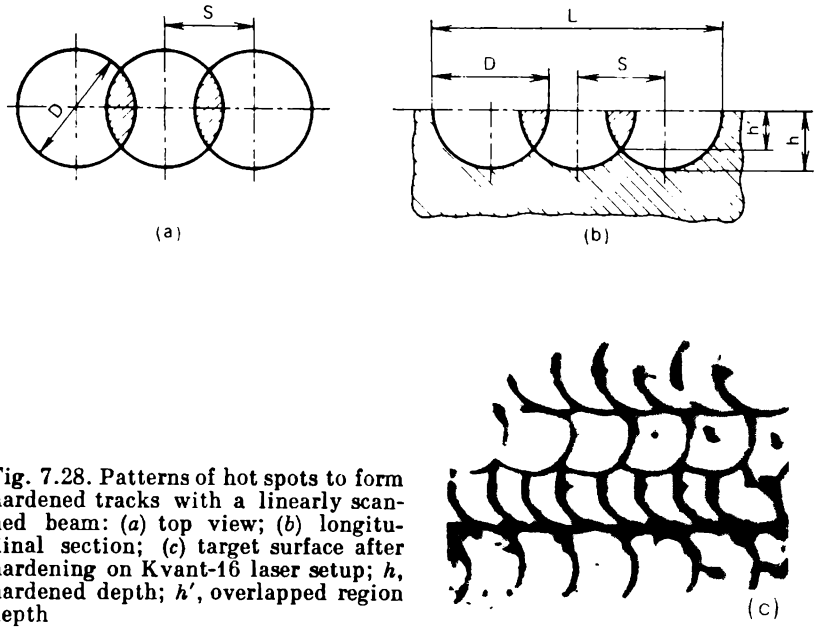

Fig. 7.28. Patterns of hot spots to form hardened tracks with a linearly scanned beam: (*a*) top view; (*b*) longitudinal section; (*c*) target surface after hardening on Kvant-16 laser setup; h, hardened depth; h', overlapped region depth

The surfaces of specimens treated in the atmosphere of argon and nitrogen to prevent oxidation have shown no traces of the softened layer.

For steels hardened both in air and in cover gases such as argon and nitrogen, the microhardness and hardness penetration grow with power density q at the hot spot up to the critical power density q_c, at which the material begins to melt and the surface profile changes at the hot spot. The heat treatment in cover gases calls for a much higher power density q_c than when treating the same materials in air. For example, q_c for the surface hardening of chromium steel specimens in nitrogen and in air approaches $3.2 \times \times 10^4$ W/cm^2 and 2.5×10^4 W/cm^2, respectively. The second pulse impinging on the specimen in nitrogen or argon does not cause any changes in q_c, but does in air, in which case q_c drops down to $\sim 2.1 \times \times 10^4$ W/cm^2, and then remains stable since the oxide layer has had time to form even at the end of the second pulse. In the presence of the oxide layer which begins to build up during the first pulse, the absorptivity of specimens increases appreciably.

The studies of changes of the microscopic surface irregularities from the original values show that over the power density range up to q_c, only structural transformations contribute to these changes,

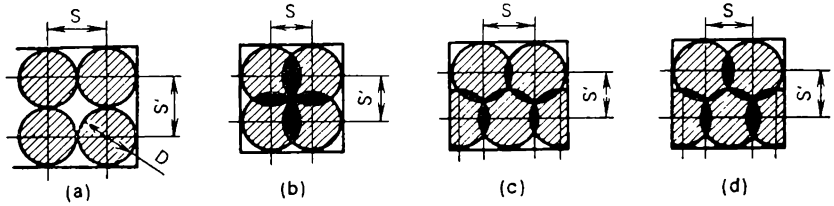

Fig. 7.29. Patterns of hot spots to form a hardened band on the target surface irradiated with a pulsed beam focused by a spherical lens

and then, at q above q_c, both the degree of melting and the character of surface damage become the dominant factors.

Let us also note that the hardness penetration for steels treated in argon or nitrogen is smaller than that attainable in air by about 15-20 μm; the hardened depth does not exceed 0.2 mm and typically ranges from 0.08 to 0.135 mm. The hardness of test specimens heat-treated both in air and in protective mediums does not rise above the 10 000-11 000 MPa range.

The results of wear tests on laser-irradiated steel specimens attest to the benefits of laser heat treatment. For example, the intensity of wear (mg/cm² m) of laser-heat-treated carbon steel specimens, both previously untreated and treated, is as follows:

Untreated specimens	120
Heat-treated specimens (*HRC* 54-56)	26
Untreated specimens after laser hardening	40
Heat-treated specimens after laser hardening	15

A CW CO_2 laser beam can yield hardened tracks of a larger penetration depth. For example, a 600-W CO_2 laser beam scanned at a rate of 1.0 m/min over the surface of chromium steel with an original hardness H_μ of 2 500-2 900 MPa produced a hardened band up to 0.35 mm thick, the hardness of which was 8 000 MPa. An increase of the laser irradiance at the hot spot more than 3 mm wide to $\sim 10^4$ W/cm², with allowance made for the steel reflectivity equal to 95% at 10.6 μm, made it possible to raise H_μ of a carbon steel sample from 3 000-4 000 MPa to 12 000 MPa in the hardened zone up to 0.4 mm thick at a sweep rate of 2.7 m/min.

In the process of pulsed laser heat treatment, the hardened region is the total area of individual overlapped spots, therefore the throughput of a surface hardening process depends on the sizes of single spots, overlap ratio K, pulse repetition rate, and other parameters.

Figure 7.29 illustrates the rows of hardened spots produced on the target by a laser pulse focused with a spherical lens. As seen, a track along the X or Y coordinate consists of overlapped laser-

hardened spots, one shifted from the other in the direction of beam travel for a certain distance, a treatment step S being equal here to the center-to-center spacing.

The linear speed of surface hardening (linear treating rate) is

$$v = L/t = KfD \tag{7.17}$$

where L is the track length, K the overlap ratio, f the pulse repetition rate, and D the spot diameter.

With an increase in the step S of linear traverse, the speed v grows, but then the untreated area gets larger. For the profile of hardness penetration to be reasonably smooth, K must commonly be equal to 0.2-0.5. To ensure an optimal coverage of the area to be worked, considering that the depth of hardening should be as even as possible, one must select an adequate relation between the step S in the X direction and the step S' in the Y direction [12].

To estimate the most effective way of realizing the spot patterns of Fig. 7.29, it will be expedient to use two coefficients: the coverage factor $K_c = F'/F$, which relates the irradiated area F' (less the overlapped area) to the area F that is subject to coverage; and the pulse utilization factor $K_u = 4F'/n\pi D^2$, which relates the actual area to be irradiated by n pulses to the theoretical area.

The pattern of Fig. 7.29*a*, where there are no overlapped spots, provides a small coverage factor, $K_c = 0.8$, and a rather high utilization factor K_u, thereby, affording a substantial treating rate.

In the pattern of Fig. 7.29*b*, the center-to-center spacing for the spots along the X and Y tracks are the same, $S = S' = 0.7D$. The coverage here is at a maximum ($K_c = 0.96$), but K_u is low and equal to 0.46. The overlapped areas are rather large, so much of the laser pulse energy is wasted. This drawback is overcome to a large extent in the patterns of Fig. 7.29*c* and *d* where the spacing in the X direction between the centers of the intermediate spots in the adjacent tracks is taken equal to $S/2$. The optimal step of traverse for these patterns is $S = S' = 0.8D$. The overlapped sections are not equal in area, but the difference is insignificant and has a little effect on the degree of coverage, so that $K_c = 0.94$ at $K_u = 0.72$.

The coverage rate P, defined as the irradiated area per unit time, takes the form

$$P = \pi D^2 K_u f/4 \tag{7.18}$$

where D is the laser-irradiated spot diameter, and f the pulse repetition rate.

Figure 7.30 illustrates the hot spot patterns of laser surface hardening using a cylindrical lens which focuses the beam to a rectangular spot with rounded sides, each shaped as a semicircle whose radius is equal to approximately half the width of the rectangle, $R = b/2$, or $D = b$. Each laser track consists of rectangular zones,

one shifted from the other by the step S in the X direction and S' in the Y direction. Introducing the parameter $k = S/l$, where l is the length of the heat treated zone, the step of linear traverse in the X direction becomes

$$S = l - b\,(1 - k) \tag{7.19}$$

The pattern of Fig. 7.30*a* does not have overlapped areas and ensures the highest treating rate at a sacrifice in the untreated regions. When $k = 1$, the step in the X direction is

$$S = (l - b) + bk = l \tag{7.20}$$

and the step in the Y direction is

$$S' = bk' = b$$

where $k' = S'/b$.

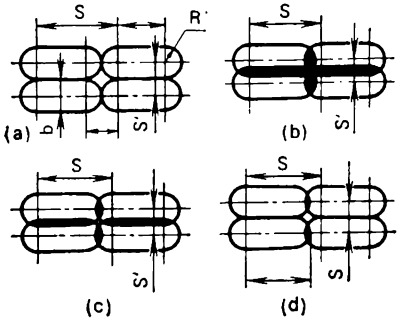

Fig. 7.30. Patterns of rectangular hot spots illustrative of the ways of surface hardening with a pulsed beam using a cylindrical lens

In this case, the coverage rate (disregarding the untreated regions) is equal to

$$P = (lb - 0.21b^2)f \tag{7.21}$$

The approximate estimates of the step of linear traverse and the coverage rate for the patterns of Fig. 7.30*b-d* are given in work [12].

In most cases, the laser heat treatment involves the motion of the laser beam and workpiece with respect to each other; this motion can be continuous or discrete (during the pulse spacings for the pulsed laser treatment). The rate of continuous motion must be lower than the rate of the process of surface treatment such as hardening, melting, etc. If the travel rate of a target is comparable to, or larger than, the rate of a treatment process, for example, the rate of a hardening process, then even the interaction of a pulsed laser becomes similar to that of a continuous laser. Let us point out that the depth to which the material changes its properties depends on the thermal constants of the material, laser beam parameters, and the dwell time, i.e. the time of interaction of the beam with the material of a certain volume, $\tau \approx 2r/v$, where r is the focal spot radius, and v the speed with which the spot traverses a distance equal to the spot diameter. To produce a hardened track on the surface of a cylindrical part with a CW laser, it is possible to keep the laser beam stationary, while the part reciprocates and revolves simultaneously, or to reciprocate the beam, while the part revolves.

Figure 7.31 illustrates the patterns of hardened tracks produced by focused beams and the corresponding spatial intensity pro-

files of the beams. Figure 7.31*a* is an illustration of the multimode laser beam with the Gaussian irradiance distribution at the focused spot. In Fig. 7.31*b* and *c* are shown the examples of the defocused beam incident on the surface. Here, the beam has a more uniform spatial profile, so it can produce the hardened track of a rather even depth. Figure 7.31*d* is an example of the defocused beam caused to oscillate in a direction transverse to the direction of traverse of the target, in which case the hardened track is wide and the area covered is large.

Two methods are commonly suitable for the surface heat treatment with a high-power CW CO_2 laser. In the first method, a defocused beam linearly scans a stationary target; in the second, a focused beam of a sufficient power is forced to dither in the plane normal to the direction of target motion.

The choice of either of the methods depends on the specified properties to be imparted to parts destined for heat treatment. Let us consider in brief these methods.

A defocused laser beam incident on the surface can offer a reasonable compromise on the depth of hardening and scan rate, therewith ensuring the required hardness. Figure 7.32*a* displays the cross section of the hardened zone after irradiation of the target with a scanning beam similar to a Gaussian beam noted for a highly peaked irradiance distribution. The greatest depth of hardening is in the central porti-

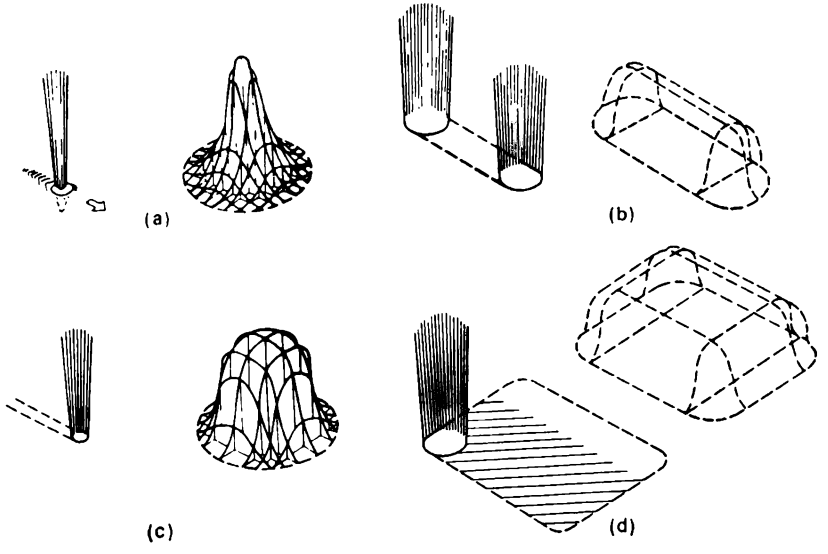

Fig. 7.31. Spatial intensity profiles of multimode laser beams suitably defocused to produce desired hardened tracks

on of the zone since the Gaussian beam delivers the highest power density at the center of the hot spot. The hardened zone is as a rule surrounded by a heat affected zone (HAZ). For example, a 1 500-W laser beam scanned over the surface produces a 2.032-mm wide hardened zone 0.254 mm in depth with a HAZ 0.051 to 0.076 mm thick on both sides of the track. To increase the width of the hardened track, the beam can be scanned repeatedly to cover the required width in several overlapping passes (Fig. 7.32*b*). However, the hardened track so produced has an uneven depth, and the overlapped regions of heat affected zones may transform into softened bands under the effect of annealing. Transverse high-frequency oscillation of the laser beam can provide a more even depth. An example of the hardened zone produced by this technique is shown in Fig. 7.32*c*. As seen, the hardness penetration is uniform over the track width and the HAZ is narrow. Although this technique adds more complexity to the heat treatment system, the advantages it offers can be worth the expenses involved. As mentioned above, the beam is set into vibration in a direction normal to the direction of traverse (Fig. 7.33*a*). The plot of temperature against time (Fig. 7.33*b*) represents the heating-and-cooling cycle, the curve being superposed on the conventional time-temperature-transformation (TTT) curve. The power density in the order of 1.55×10^4 W/cm^2 is high enough to rapidly bring the surface to the required temperature. The oscillation frequency and the linear transport speed are so chosen that the temperature of the given surface region can vary in the temperature range between the melting temperature T_m and transition temperature T_{tr} until the requisite volume of metal below the surface reaches T_{tr}. At this temperature, the hot spot absorbs the heat required to transform austenite into bainite or martensite. For the depth of hardening to be even, the beam must oscillate at such

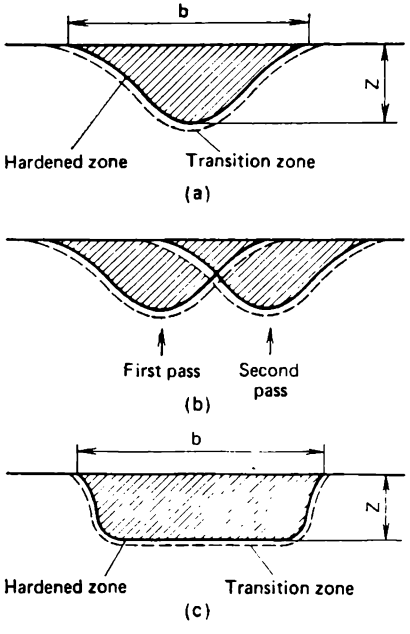

Fig. 7.32. Cross sections of hardened zones produced on the surface of metal by a defocused CW CO_2 laser beam in a single pass (*a*), in two overlapping passes (*b*), and in one pass at a definite frequency of transverse oscillation of the beam (*c*)

a frequency as to transform the oscillating pattern into a constant heat flow under the effect of thermal conduction. By properly shielding the edges of the beam, it is possible to obtain a nearly rectangular cross section of the heat-treated track with a narrow HAZ, as illustrated in Fig. 7.32*c*. If the oscillation frequency is too low for the given power density, the surface temperature may grow to the melting point, thus inducing strains in the part. If the power density is insufficient for the given oscillation frequency, the material will not reach the transition temperature and the process of

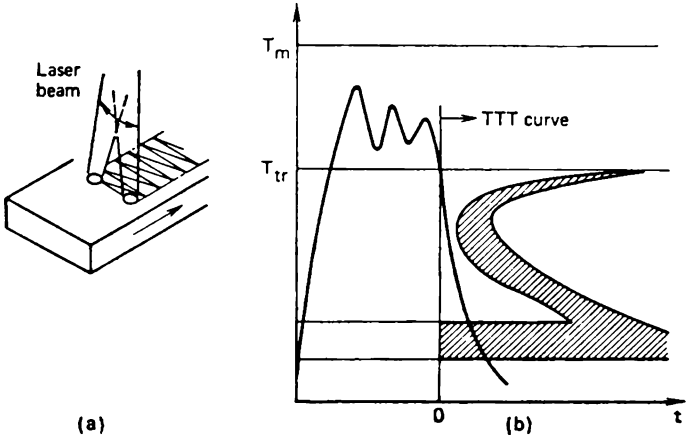

Fig. 7.33. Principle of heat treatment with an oscillating laser beam

hardening will not take place. Should we allow the beam to oscillate or to stay at the same spot over too long a period of time in order to increase, for example, the penetration depth, the entire part can be brought to a temperature at which the effective self-cooling cannot occur. In this case, the cooling curve intersects the "lobe" of the TTT curve and points to the transformation of austenite into pearlite rather than into martensite. This approach is suitable for local annealing of the surfaces of hardened parts to make the local regions more responsive to cutting and also to increase their fatigue resistance.

The diagram shown in Fig. 7.34 rather clearly represents the process of changes in the structure of an iron-carbon alloy (steel). The alloy held in the austenitic state at a high temperature must cool at a supercritical quench rate, so that the entire austenite can be brought to the initial martensitic transformation temperature to cause the formation of the martensitic structure.

Curves *1* and *2* superposed on the isothermal transformation diagram are the theoretical plots of time-dependent temperatures

on the surface of a 10-mm thick sample and at a depth of 0.5 mm respectively. The regions of other structures lie on the right of the curves. Hardening lasts ~ 1 s at an absorbed power density of $\sim 3 \times 10^3$ W/cm^2. The hardened zone mainly consists of martensite.

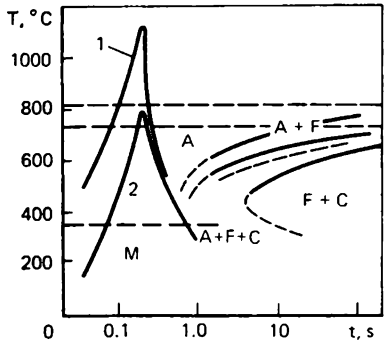

Fig. 7.34. Diagram of isothermal transformations in carbon steel due to an absorbed laser power density of 3×10^3 W/cm^2 for an interaction time of 0.2 s: *1*, curve of temperature changes on the surface of a 10-mm thick sample 2; *2*, curve of temperature changes at a depth of 0.5 mm; A, austenite; F, ferrite; C, cementite; M, martensite

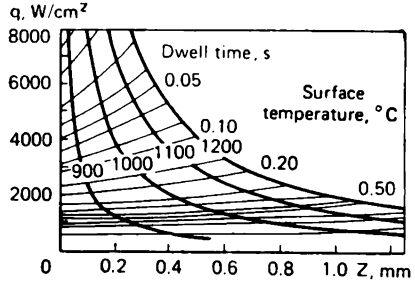

Fig. 7.35. Characteristics of laser hardening

In general, as is clear from Fig. 7.34, the degree of hardening at various cooling rates, i.e. at various rates of changes of metal temperature with time, can qualitatively be estimated by comparing the cooling curves with the continuous cooling transformation diagrams representative of the decomposition of supercooled austenite.

Laser surface hardening lends itself to continuous control. The curves of laser power density as a function of case depth for hardening of iron with 3.5% C ($T_m \approx 1\,200$°C) at different values of dwell time are shown in Fig. 7.35 [1]. With an increase in q, the penetration depth decreases because of a higher rate of heating.

Figure 7.36 illustrates the coverage rate for heat treatment of gray iron with a 1.5 kW CO_2 laser beam as a function of the case depth and the frequency of transverse oscillation of the beam. The estimates have been made by measuring the width of the hardened track at a definite depth of hardening.

The width of the hardened track on the surface depends on the method of heat treatment used and can be much larger than that at a certain depth. As mentioned earlier, a broader area can be covered in a few passes of the beam, with each preceding track partially overlapped by the successive track to provide a more even case depth.

In most cases, continuous laser hardening is done by a stationary beam, with the part traversed according to the specified pro-

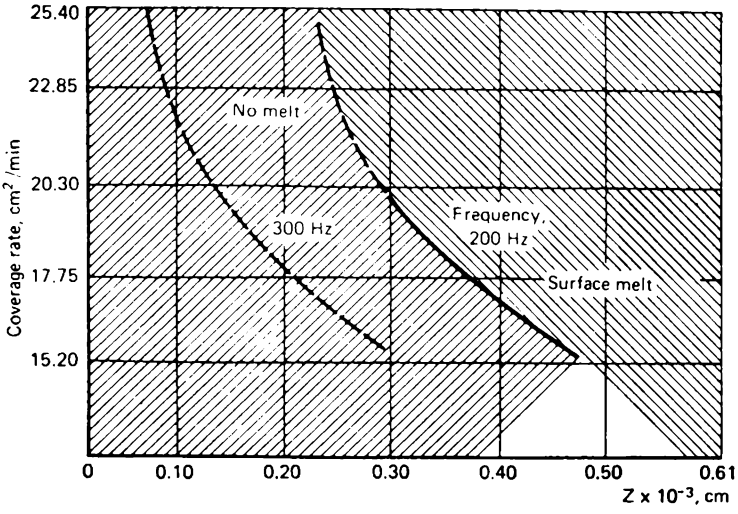

Fig. 7.36. Coverage rate for heat treatment of gray iron with a 1.5 kW CO_2 laser beam as a function of laser hardness penetration. The laser mode structure is a combination of TEM_{00} and TEM_{01}

gram to obtain the desired pattern of hardened tracks. The beam can also be scanned over the target surface if it is necessary to cover appreciable areas. In the latter case, the coverage rate depends on the scan rate, spot size, and contouring desired.

In common use are contact, projection, and optical contouring methods for producing beam images or spots on target surfaces [25, 40].

In the *contact method*, the substrate is brought into direct contact with a stencil screen or mask. The *projection method* uses an off-contact mask with windows to define the desired pattern imaged on the substrate surface. In the *contouring method*, a stationary (or moving) focused beam successively illuminates a moving (or stationary) target, thus tracing the desired path.

The contact method produces an optical image as the beam strikes the mask with windows which define the pattern to be transferred to the target surface in contact with the mask. The disadvantages inherent in this method are the following: fast wear of the mask, possible damage to the substrate when forced too strongly to the mask, lighting at the sites of poor contact, diffraction-induced distortions of the track at these sites, and waste of energy in the areas of the mask without windows.

The mask material must be more stable to radiation than the target material.

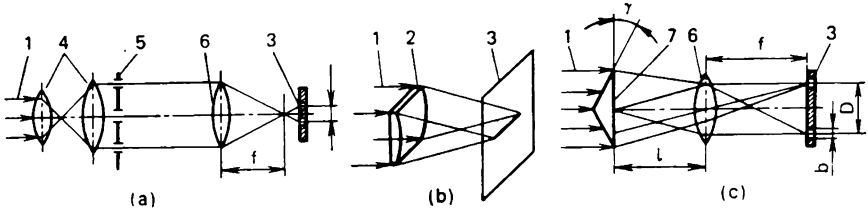

Fig. 7.37. Laser optical systems for shaping beam images on target surface: (*a*) telescope and projection lens; (*b*) cylindrical lens; (*c*) axicon and focusing lens

The projection method has certain advantages over the contact method: the mask does not contact the substrate, so it is not subject to mechanical wear; the substrate surface can be accurately aligned with the image plane to eliminate the diffraction losses. But, as with the contact method, here too the beam wastes much of its energy on the mask surface. In both cases, the optical system must fulfil the rigid requirements for the uniform illumination of the entire mask surface [25].

The schematic diagram illustrative of the projection method [25] is shown in Fig. 7.37*a*. The two-lens telescope *4* expands the laser beam *1* to the size of mask *5* with a requisite contour pattern and the projection lens *6* produces a reduced image of the pattern on the surface of the workpiece *3*. Since the beam emerging from the telescope has a low divergence, which results in a small loss of beam energy, it is possible to place the mask at a large distance from the telescope. An important parameter of the projection system is a linear magnification M, which is the ratio of the size of the image on the target to the size of the pattern on the mask. For the case under consideration, this ratio is smaller than unity. It is easy to obtain the values of M in the order of 1/10 and 1/20. A collecting lens can ensure still lower values of M, $\leqslant 1/100$.

In the contouring method, contour imaging appreciably depends on the parameters of the mechanical system guiding the target or the beam relative to each other [12, 25, 41]. The factors of much importance are the temporal stability of the laser output and the correct choice of the range of target speeds to avoid the image shape distortions and ensure the laser energy input required to achieve the prescribed results of heat treatment.

A cylindrical lens and an axicon, such as illustrated in Fig. 7.37*b* and *c*, can be used to form a rectangular and an annular image of the beam, respectively, in which case the part must be stationary with respect to the beam. The easiest way to implement the beam imaging here is to use a pulsed laser beam.

As seen from Fig. 7.37*b*, the lens *2* focuses the beam *1* on the

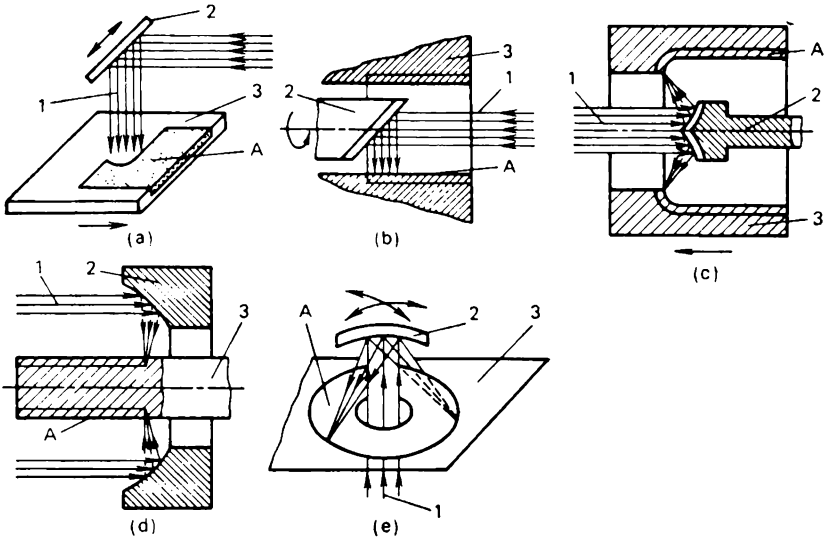

Fig. 7.38. Laser beam guiding systems: (*a*) and (*b*) moving and rotating slanted mirrors to scan the beam over flat and inner surfaces respectively; (*c*) and (*d*) hyperbolic mirrors to scan the beam over inner and outer surfaces respectively; (*e*) vibration deflector to scan the beam over flat surfaces

target *3* to a spot of a rectangular form, the spot size being determined by the lens parameters. This type of optical system is particularly effective for hardening the long edges of cutting tools and parts subject to wear.

An example of the optical system consisting of an axicon *7* and focusing lens *6* to form a ring-shaped image of the beam appears in Fig. 7.37*c*. The diameter D of the ring depends only on the angle γ at the vertex of the cone and on the distance l between the lenses; the width b of the circular band depends on the focal length f of the lens *6*.

A relative motion of the beam with respect to the target can appreciably change the shape of the laser-heat-treated zone. As mentioned above, a suitable mechanism can reciprocate or revolve the part being struck by a stationary beam, or a revolving prism or mirror can guide the beam to enable it to scan the surface of a stationary part.

The systems of Fig. 7.37 can be used to work parts with pulsed and continuous beams.

Figure 7.38*a*, gives an example of hardening the flat surfaces of parts. The optical system with a moving mirror *2* provides the stripwise scanning of the beam *1* by guiding it along one coordinate

axis, while the target *3* periodically moves along the other coordinate axis.

The inner surfaces of the bodies of revolution can be hardened by means of a scanning system demonstrated in Fig. 7.38*b*. An inclined mirror *2* placed inside a cylindrical part *3* both revolves and moves along the cylinder axis, thereby scanning the beam over the entire inner surface *A* of the part. In Fig. 7.38*c* and *d* are shown examples of hardening the inner and outer surfaces *A* of parts *3* moving along the axis of the beam *1* focused into a ring-shaped image on the target surface by means of a hyperbolic mirror *2*. Figure 7.38*d* is an example of the laser beam guiding system using a vibration deflector to scan the beam across flat surfaces.

Deflectors, or scanners, are effective beam guiding devices, which fall into three basic categories: mechanical, electrooptic, and acoustooptic deflectors [41]. Consider some features of mechanical deflectors.

A typical mechanical deflector is a device similar to a galvanometer in design or a device including a mirror or a prism with a piezoelectric driving element or any other type of drive.

The advantages of a mechanical deflector are the following: a large angle of beam deflection; low loss of radiant energy; low power demand; possibility of using a variety of scanning elements.

This type of deflector relies on rotating or vibrating mirrors or prisms and belongs to the inertial class of devices. Low-inertial devices include electrooptic, magnetooptic, and acoustooptic deflectors. The former devices cannot compete with the latter in the resolution, accuracy, scan linearity, and scan speed.

A mirror deflector provides a higher resolution than a prism deflector. Its scanning frequency depends on the rotational speed of the mirror and the number of segments it contains. In a rotating segmented mirror, each segment independently forms, for example, a rectangular image of the laser light that strikes it.

A vibration deflector that uses a galvanometer moving coil carrying a reflecting mirror suspended in a constant magnetic field is free of a number of imperfections inherent in other mechanical scanning systems. A current passed through the coil causes the coil with the mirror to turn through a certain angle, and the mirror thus reflects the light beam at an angle which is twice the angle of rotation. A vibration deflector must be complete with a sufficiently large mirror immune from deformation and ensure a high vibration frequency and appreciable angle of coil rotation. The resonance frequency of this deflector depends on the size and mass of the mirror, rigidity of coil suspension strings, and other factors. The deflector can operate in a wide frequency range up to the resonance frequency, in a narrow range at the resonance frequency, and in the range of frequencies above the resonance value. In the first case, the angle of

rotation of the galvanometer coil is essentially proportional to the amount of current applied to the coil; in the second, the dependence is nonlinear; and in the third, the ballistic effect that comes into play causes the angle of rotation to decrease with increasing frequency at the same current amplitude.

7.9. MASS TRANSFER PROCESSES

The alloying element content of alloys appreciably changes in the zones of interaction of normal-pulse laser beams [4, 5]. As follows from experimental findings, even a short-time interaction of high-energy laser beams with iron alloys gives rise to mass transfer processes, which redistribute the alloying elements and thus significantly change the physical and mechanical properties in the heat-treated zone.

The microscopic layer-by-layer analysis is the most proven method for studying the redistribution of elements in the zones of laser-material interaction. The electron probe X-ray analysis gives a less accurate picture of the distribution of elements.

The spectrum analysis of laser-irradiated samples of steels and armco-iron reveals that the distribution of carbon in depth for all the samples is generally identical (Figs. 7.39-7.41). The curves show the characteristic peaks of carbon content at a depth of 0.20-0.35 mm from the bottom of the cavity surface. At a depth of 0.6-1.2 mm from the surface of the target the carbon content is equal to the initial value. As seen from Fig. 7.40, the curve of chromium distribution in chromium-molybdenum steel is almost similar in shape to that of carbon distribution and the depths of changes in both Cr and C con-

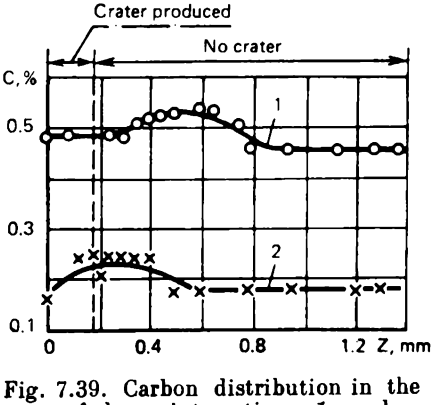

Fig. 7.39. Carbon distribution in the zone of laser interaction: *1*, carbon structural steel with 0.45% C; *2*, carbon steel with 0.3% C

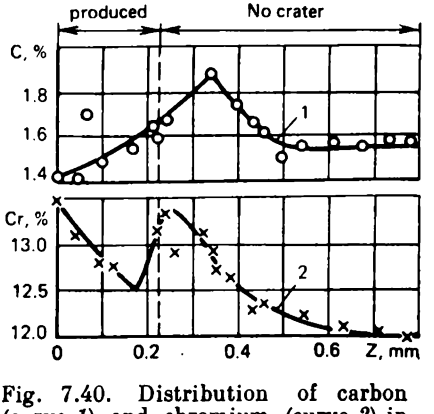

Fig. 7.40. Distribution of carbon (curve *1*) and chromium (curve *2*) in the zone of laser interaction with chromium-molybdenum steel

tents are approximately the same, ~0.5 mm. Since the diffusion factor of carbon in steel is 5-6 orders of magnitude greater than that for chromium, the fact mentioned above does not speak in favor of mass transfer by the diffusion process [4].

The spectrum analysis carried out with the aid of a point source of rectified current on corrosion-resistant steel irradiated with the focused beams from ruby and neodyminum lasers [5] has revealed a considerable redistribution of Mn, Ni, Cr, and C in the irradiated zones. In the layer adjacent to the crater, the carbon content does not differ from the original value, but the contents of other elements are higher or lower than the average content for the given sample. In the layer more distant from the crater, the contents of the above elements become greater. But the contents of Cr and Si in the laser-irradiated zones remain invariable.

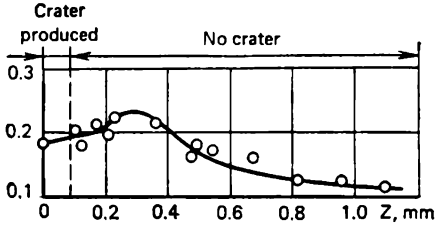

Fig. 7.41. Carbon distribution versus depth of the zone of laser interaction with armco-iron

In analogy with the above method, studies have been made on the distribution of alloying elements in high-temperature alloys and irons [5]. It is found that the content of such elements as Mn, Ni, Ti, Nb, Mg, and Si changes after laser irradiation.

Investigations reveal that the structure of a metal or alloy irradiated with a laser beam may affect the excitation of the optical spectrum of some elements dissolved in the metal, thereby producing a false picture of the redistribution of elements. But this effect does not appear in the case of spark excitation even after hardening which strongly distorts the structure.

Check experiments on chromium-manganese steel samples irradiated with a normal pulse laser have been undertaken [4, 5] to verify the redistribution of carbon in heat-treated regions (Fig. 7.42). In the experiments, each sample was struck by a laser beam to form two craters up to 3 mm in diameter and down to 5 mm deep. The target then was cut into two samples with one crater in each. One of the samples was annealed for 2 hours at 650°C to check the carbon content. The carbon distribution profile obtained from the microscopic analysis of the unannealed sample is shown in Fig. 7.42*a*. As is apparent from the figure, the carbon content significantly decreases at the edges of the crater and slightly increases 100-120 mm away from the edges. The diffusion factor of carbon in ferrite at an annealing temperature of 650°C reaches 3.6×10^{-7} cm²/s, so the effective diffusion length must be ~1 mm in 2 hours. This explains why the

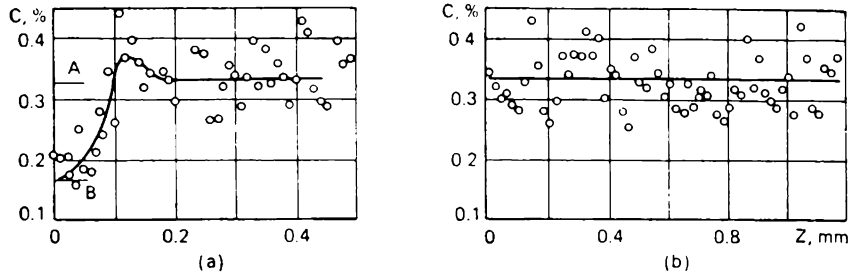

Fig. 7.42. Carbon distribution in the bottom region of the crater formed on a chromium-manganese steel sample (zero on the X axis corresponds to the crater bottom); (a) unannealed sample; A, original carbon content; B, carbon content after melt solidification; (b) sample annealed for 2 h at 650°C

microscopic analysis has failed to trace any changes in the carbon content of the annealed sample (Fig. 7.42b).

The detailed analysis of the redistribution of alloying elements in the zones of laser-alloy interaction is difficult to perform for a number of reasons. The mathematical definition of the distribution process involves the most substantial difficulties because the problem stated includes the system of nonlinear differential equations with nonlinear boundary conditions for describing the element distribution and temperature field. The nonlinearity of these equations stems from a sharp variation of the diffusion coefficients of materials with temperature.

The effects of the processes of thermal diffusion and diffusion associated with pressure and plastic deformation on the element redistribution in pulsed laser-irradiated alloys have been treated in work [4]. The calculations reveal that, whatever the conditions of diffusion, even if account is taken of plastic deformation, theory does not agree at all with experiment. The redistribution of elements in the zones of laser-alloy interaction is governed by mass transfer processes of the nondiffusive nature. A laser beam incident on the target surface melts the material to form a thin liquid layer at the liquid-solid interface; the higher the power density, the thinner the liquid layer. The calculated results of liquid layer thickness h against power density q are shown in Fig. 7.43. For steel, the melt thickness

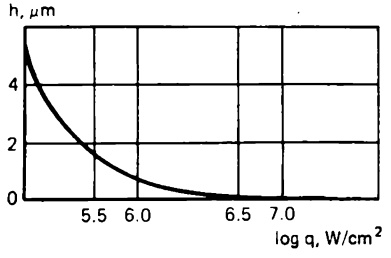

Fig. 7.43. Thickness of the molten layer of metal versus power density in the region of laser interaction with iron and steel

is about half that for iron due to the difference in thermal constants.

The melt layer on the target surface can be enriched with or depleted of the alloying elements in view of the difference between the vapor pressures of the alloying elements and base metal. The bonding energy for alloying elements is lower than that for the base metal per alloy atom. Therefore, when the fusion front propagates into the sample, there is a possibility of vaporization of atoms from the surface and also a fraction of atoms moving from a layer of a definite thickness h'. This thickness is close to the light absorption thickness for metals, in which the effective values of temperature and pressure are rather high, with the result that the diffusion coefficients increase significantly.

One more possible cause of an increase in the mobility of alloying elements is the volumetric vaporization in the liquid layer [4], which tends to increase the fraction of the element vaporized into bubbles forming in the melt zone. The rate of this process is a function of the radiant intensity, element concentration, amount of gases dissolved in the material, and other factors. The layer thickness h' is smaller than the melt thickness. If the above concepts are valid and the binding energy for the elements is lower than that for the base metal, the thin layer adjacent to the crater must have an increased or a decreased content of alloying elements depending on their vapor pressure. Last, let us point to one more possibility of changes in the concentration of elements in the layer adjacent to the crater. The liquid-solid interface moves into the target and takes off from the solid phase the elements the solubility of which in the liquid phase is higher than that in the solid phase. This allows us to introduce the notion of an nonequilibrium distribution coefficient k_n which, proceeding from the equilibrium distribution coefficient, can be written as

$$k_n = C_s/C_l \tag{7.22}$$

where C_s and C_l are the concentration of alloying elements in the solid and the liquid phase respectively.

The rate of propagation of the fusion front depends on the liquid metal temperature, the time of contact between the liquid and the solid phase, physical nature of element atoms, and element content. Most of the elements dissolve faster in the liquid phase than they do in the solid phase, for which reason a layer with a decreased content of elements builds up in front of the liquid phase boundary. The liquid-solid interface stops moving after the end of the pulse, and the melt begins to crystallize. At this instant, vaporization from the surface is of no significance. In the course of crystallization, a fraction of atoms return to the zone adjacent to the crater edges. This must equalize to a certain extent the number of element atoms in the region near the crater, although the complete equali-

zation may not occur since the temperature in the work area does not appreciably exceed the melting temperature.

These qualitative considerations lead us to the conclusion that the initial distribution of elements in the region adjacent to the crater must be different from the final distribution. The effective depth at which changes in the element content are considerable must not exceed the thermal diffusion depth, $\sqrt{at}$, where t is the total time of heating and cooling, and a is the thermal diffusivity. At t of about 10^{-2} s and $a = 0.1$ cm^2/s, the effective depth is equal to about 0.6 mm, which is in agreement with experiment. The diffusion depth heavily depends on the temperature in the crater area since the diffusion coefficient in most cases is

$$D = D_0 \exp(-E/kT) \tag{7.23}$$

where D_0 is the limiting value of D, and E the activation energy.

So, the process of redistribution of alloying elements in the laser treated zone can be broken down into several stages.

The first stage is a transient stage leading to a quasistationary distribution of temperature in the crater area. At $q \geqslant 10^6$ W/cm^2, this stage is short and does not result in a perceptible redistribution of elements. The next stage is the stage of quasistationary target damage, at which the temperature field in the zone of interaction can be thought of as reaching a steady state. At this stage, the alloying elements diffuse into or from the liquid layer.

The last stage involves the crystallization of the melt after the end of the pulse. A fraction of the elements return from the liquid to the solid phase and also move to the edges of the zone by the action of a mechanism similar to that of zone cleaning. Since this stage is very short, diffusion of the elements from the solid phase can be disregarded.

The diffusion problem so outlined does not cover all the possible mechanisms of mass transfer. Consideration of all the effects would certainly afford a better agreement between theory and experiment. An example of the mechanism of mass transfer is a strong penetration of CO_2 or N_2 into the zone irradiated with a laser.

7.10. LASER SURFACE HARDENING IN NITROGEN

Laser surface hardening is the process of heat treatment of metal parts to provide a hard surface, for example, in areas of dry friction, thus significantly decreasing the wear rate. It is common practice to use air for economic reasons in the process of heat treatment of weakly oxidizable materials. Where there is a need to do away with oxidation completely, the process must be run in a vacuum or in the environment of inert or active gases. An active gas penetrates

into the laser-heat-treated zone and reacts with the melt to form a compound, the properties of which differ from those of a similar compound obtainable by conventional techniques [42, 43].

The use of cover gases makes it possible to create new processes of laser heat treatment. A great body of information is available on the gas-assisted laser treatment of materials at high pressures of gases in excess of 5×10^5 Pa [44] and at pressures slightly above the atmospheric, below 0.5×10^5 Pa [45].

Work [45] has presented the results of experiments on the surface hardening of titanium and steel samples with a laser beam assisted by a jet of nitrogen. A Kvant-16 laser setup used in experiments was able to produce 2-ms duration pulses with a power density of 10^5-10^6 W/cm^2. Nitrided samples were put to metallographic and X-ray diffraction analyses. The X-ray analysis based on the photoionization effect was performed on a setup equipped with a scintillation-counter spectrometer. Titanium samples were prepared from the powder of electrodeposited titanium. The porosity of samples was 13%. The samples prepared from various grades of steel were pretreated to raise their microhardness H_μ to (690-780) $\times 10^7$ Pa. Let us consider the results of experiments.

A laser beam delivering a power density over 10^5 W/cm^2 to the surface of a titanium sample produces a pale-yellow spot with a high degree of porosity. Increasing both the laser energy and the gas jet velocities to values corresponding to intense vaporization and melt flushing causes the color to change to a golden yellow and the porosity to decrease down to a value at which a practically nonporous cast structure builds up after solidification. A further increase in the above parameters leads to the formation of a crater or cavity, the walls and the bottom of which have a light gray color indicative of the unoxidized metal. In this case, nitrogen acts as a cover gas.

The X-ray analysis of the surfaces of laser-treated zones has detected titanium nitride of the stoichiometric composition. From the examination of X-ray photographs it follows that the lattice constant a depends on nitriding conditions. It is thus possible to obtain the nitride layer of a definite composition by properly selecting the nitrogen jet velocity.

The thickness of the titanium nitride layer is small, as evident from the X-ray patterns which display the lines of pure titanium along with the lines of titanium nitride. Metallographic examinations of the microsections of nitrided zones reveal that each zone consists of three layers sharply differing from one another. The upper layer composed of columnar crystals extending in the direction of maximum heat transfer is the solidified melt of titanium nitride. The intermediate layer is a narrow band of the ε-phase. The lower layer formed on the base metal is a weakly etched solid solution of nitrogen in titanium. In the text below, we shall deal with the

total thickness of the cast titanium nitride and the solid solution of nitrogen in α-Ti.

The microhardness H_μ heavily depends on the conditions of treatment. Increasing the laser energy E in the range 2-10 J causes an increase in the depth of nitriding. At a greater depth, H_μ begins to vary faster with growing energy, which is attributable to a lower intensity of the diffusion processes as nitrogen penetrates deeper into the material. As seen from H_μ-E curves, H_μ tends to saturation at E = 8-10 J since the nitride layer becomes thick enough to exclude contact between the liquid metal and nitrogen.

Let us look at the results of nitriding with a pulsed laser delivering two repetitive pulses to the same spot. The repeated shots increase the depth and microhardness of the nitrided zone by 30-35% and 20-25% respectively. Also, the treated zone exhibits a lower porosity and improved quality of the surface.

As follows from the studies of pulsed laser nitriding of high-speed steel, the nitrided zone consists of two layers which differ in microhardness. Steels nitrided at T = 813 K for 38 h display a similar character of changes in H_μ due to the specific feature of nitrogen dissolution in metals [46].

The nitrides of such metals as titanium, zirconium, and hafnium have a high wear resistance. It is therefore desirable to obtain the nitride layers of these metals on the surfaces of parts subject to wear due to dry friction. In one experiment [45], a special arrangement was used to deliver steel workpieces to the zone of plasma produced by a laser beam near a titanium substrate in nitrogen at a pressure of $\sim 4 \times 10^6$ Pa. Provision was made to locate the parts at a distance of (2-3) $\times 10^3$ m from the substrate surface. The layer of titanium nitride obtained on the surfaces of steel parts consisted of large grains 5×10^{-6}-5×10^{-5} m in size. According to the metallographic analysis, the nitrided layer was 0.04×10^{-3} m thick and had a microhardness of 9.8×10^9 Pa.

Consider the results of experiments [47] on the structure and corrosion resistance of a zirconium alloy containing 1% niobium by mass. This alloy has been given the most study as regards its structure, hardness, strength, creep, and corrosion resistance in water both before and after laser irradiation. In experiments conducted in the atmosphere of nitrogen and argon, 10 × 10 × 1.5-mm alloy samples were shot with beam pulses from a laser operated both in the free running and in the Q-switched regime. The laser power density was varied by a factor of 10^4 so as to harden the target surface with and without melting.

Niobium, just like the high-temperature modification of β-zirconium, has a body centered cubic lattice, and the atomic radius of Ni is close to that of β-Zr. Alloying Zr with Ni at high temperatures yields a continuous series of solid solutions; alloying

at low temperatures results in the constitution diagram of the monotectic type. The maximum solubility of Ni in the low-temperature modification of α-Zr at a monotectic temperature of 590-610°C reaches 0.7-1.0% by mass. The structure of the binary alloy of Zr with 1% Ni at room temperature consists of the solid solution of α-Ni in Zr and the solid solution of β-Zr in 85% Ni.

The laser-irradiated zone consists of two regions: the inner region of the solidified melt, the size of which corresponds to the diameter of the laser light spot, and the outer region of the aggregate of microscopic craters.

The inner regions of the zones irradiated in nitrogen differs from those produced in argon. In the alloy sample irradiated in nitrogen, the recrystallized melt is surrounded by the ring of nitrides which are the products of the reaction of ejected liquid particles with nitrogen. The central region of the solidified melt produced in argon is surrounded by microcraters without any traces of burning. The size and density of these microcraters decrease with distance away from the center of the spot.

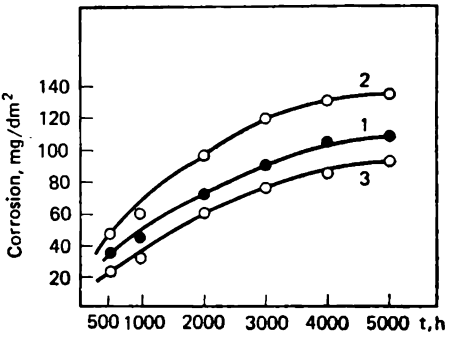

Fig. 7.44. Kinetic curves of corrosion of zirconium alloy with 1 wt. % niobium in water at 350°C: *1*, alloy nonirradiated; *2*, alloy irradiated with laser pulses in nitrogen; *3*, alloy irradiated with a CW laser beam in argon

The microhardness of laser-treated zones has increased three times after melt quenching. In samples subjected to hardening without melting, H_μ in the region near the surface decreases by 20% and then remains the same with distance along the depth. This is the region of tempering of a reduced hardness as against the original value.

The effect of laser radiation on corrosion resistance of alloys. The process of corrosion of zirconium alloys is rather complex because the kinetics of oxidation depends on many factors, among which we can single out the following: (a) the chemical composition of the alloy as regards the contents of its impurities and alloying elements; (b) structural state that is dependent on the process of production of samples at all the stages of the process; (c) sample surface quality; and (d) composition and properties of the heat-transfer agent, namely, the water purity, contents of hydrogen and oxygen, and hydrogen ion (pH) value.

Figure 7.44 displays the kinetic curves of corrosion of alloy samples in water at 350°C. It is seen that the curves of corrosion

rates for samples both nonirradiated and irradiated with a laser beam are similar. Laser radiation does not change the character of corrosion specific to zirconium and its alloys.

7.11. LASER-ASSISTED MACHINING

One of the methods of increasing the machinability of metals is to preheat the workpiece by a suitable source of energy. Resistance heating and plasma heating are the most widely used techniques of heat pretreatment, which effectively reduce the tool force required for cutting and increase cutting speeds [48]. In the process of resistance heating, the heat source raises the temperature of the material

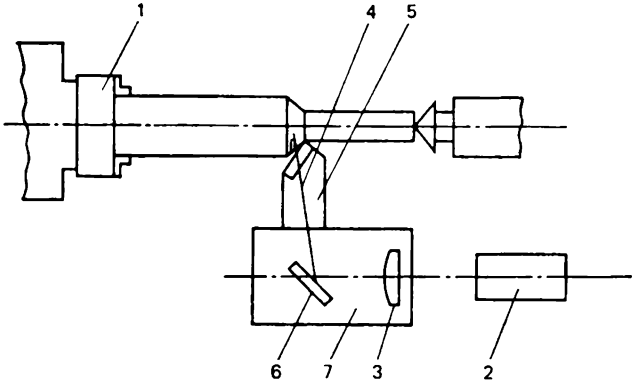

Fig. 7.45. Schematic diagram of a LAM setup: *1*, lathe; *2*, laser; *3*, lens; *4*, beam; *5*, cutting tool; *6*, mirror; *7*, carriage

ahead of the cutting tool and does not essentially affect the surface adjacent to the transient surface. The plasma heat source can heat up the layer being cut throughout its thickness before the tool arrives at the area of chip formation, but suffers from a disadvantage that it cannot afford a sufficient local heating, which may lead to thermal deformation of the workpiece and to changes in the structure of the work surface.

A substantial advantage of laser heating is the ability to couple a large amount of laser energy to a small volume of the target. Other advantages that make laser-assisted machining (LAM) a promising technique include: (a) ease of adjusting the energy-related and spatial parameters of LR, (b) ability to deliver laser energy to difficult-to-reach areas, and (c) high stability of the process.

Work [49] has described a LAM setup, the schematic diagram of which appears in Fig. 7.45. Cutting (turning) of samples was done on a 250-W bench-type universal lathe using the 10.6-μm

output of a 1-kW CO_2 laser to preheat the samples. The system of metal mirrors with a 0.210-m focal length lens from KCl was used to deliver and focus the laser beam to the workpiece.

The beam guiding mirrors (not shown) directed the beam parallel to the axis of rotation of the workpiece. The focusing system located on the carriage consisted of a lens and a turning mirror. The entire arrangement ensured a fixed location of the focal spot on the surface of the workpiece. By adjusting the turning angle of the mirror, it was possible to select a desired position and size of the focal spot so as to heat the work surface ahead of the cutting edge in the cut area. The center of the focal spot was at a distance of about 250 μm from the cutting edge.

The aim of experiments [49] was to study the conditions of LAM and compare the results with those obtained by the conventional technique. The comparison involved the following parameters: (1) tool life at a specified cutting speed; (2) components of cutting force; and (3) quality of the machined surface.

The workpieces were 22×10^{-3}-m diameter samples of a Mo alloy with 3% Nb. The cutting tools had carbide tips. The cutting edge was made to the USSR state standard 18878: tool clearance $\alpha = 8°$; tool rake $\gamma = 10°$; tool cutting edge angle $\varphi = 45°$; cutting edge radius $r = 0.5 \times 10^{-3}$ m. The cutting conditions were the following: cutting speed $v = 60$ m/min; feed per revolution $s = 0.05 \times 10^{-3}$ m/rev; depth of cut $t = (0.15\text{-}0.20) \times 10^{-3}$ m; and focal spot diameter $d = 0.5 \times 10^{-3}$ m.

Tool wear tests under these cutting conditions were made for both types of lathe work: "cold" turning and turning with preheating by a laser which delivered 0.5 and 1.0 kW of power to the workpiece.

The height of the wear land of the flank up to $h = 0.5 \times 10^{-3}$ m was taken as the limit value of tool wear. In excess of this value, the tool began to wear very fast and soon broke off.

The wear rate of the tool was slower at a higher power of the beam, and at 1 kW the intense wear commenced in 8 min, i.e. the service life of the tool was four times the life attainable in "cold" turning (Fig. 7.46).

Laser preheating enabled the tool to wear evenly, and the sintered-carbide tip showed no evidence of chipping. In tests performed on workpieces of corrosion-resistant steel, the character of tool wear was similar. Since the work surface was irregular, the tool cut the material intermittently, but the tip did not chip out and its wear approached the limit value in 10 min. In the case of "cold" turning of such a workpiece, the tool nose began to break off as it touched the work surface.

What distinguishes LAM from conventional machining is an appreciable reduction in tool chatter owing to a reduced tool force required for cutting. The measurements of power P_m taken off the

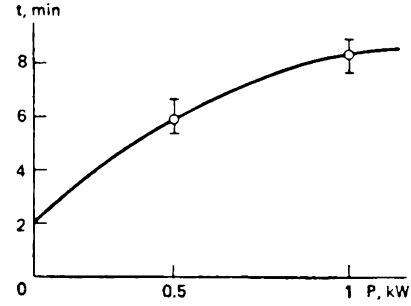

Fig. 7.46. Wear rate of a carbide-tipped tool in turning Mo alloy with 3% Nb as a function of laser power

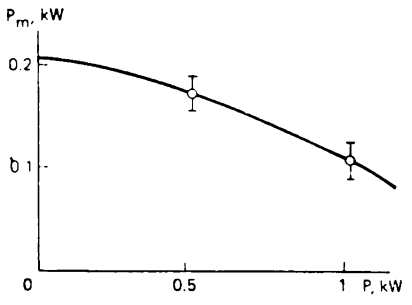

Fig. 7.47. The effective power P_m taken off the main drive motor of the lathe versus laser power P

main drive motor in both types of operation revealed that laser preheating considerably reduced the power demand. With an increase of the laser power up to 1 kW, the effective power P_m expended in cutting the molybdenum alloy with 3% Nb was reduced by 30-40% as against that required for conventional machining (Fig. 7.47).

The studies of the effect of laser preheating on the quality of the machined surface were conducted by comparing the surface roughness of parts machined with and without laser preheating. Contour records were taken from a modular profilograph-profilometer.

The analysis of the obtained results shows (Fig. 7.48) that LAM aids in reducing the surface roughness. It is found that 1-kW laser assisted turning can decrease the surface roughness (ten-point height of irregularities) from $R_z = 30$ typical of "cold" turning to $R_z = 15$ and thus upgrades the surface finish by two classes. Besides, the time during which the turning tool provides a constant value of R_z increases (Fig. 7.49). As apparent from the curves of Fig. 7.49,

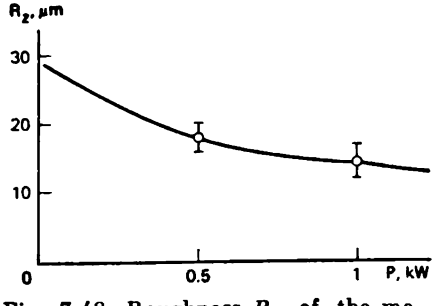

Fig. 7.48. Roughness R_z of the machined surface as a function of laser power

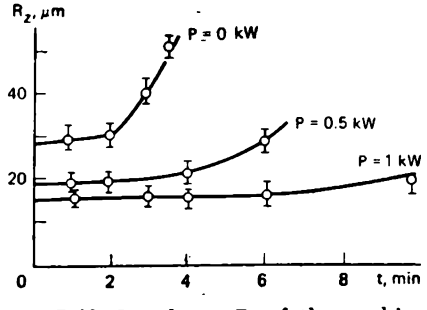

Fig. 7.49. Roughness R_z of the machined surface as a function of the time of turning at various laser powers: *1*, $P = 0$; *2*, $P = 0.5$ kW; *3*, $P = 1.0$ kW

"cold" turning ensures a constant value of $R_z = 30$ for 2 min; with LAM, the initial value of $R_z = 15$ remains stable for as much as 8 min. After these periods of time, the surface roughness increases, and does so more sharply in the case of "cold" turning. Tool wear is likely to be the cause of this increase in roughness because the above periods coincide with the times after which the tool wears to a limit value of $h = 0.5 \times 10^{-3}$ m.

The machined surface also shows changes in structure due to work hardening. It is known that dynamic loading (turning) considerably increases the microhardness of the machined surface against the original value [50].

Checks for changes in microhardness due to turning with and without laser preheating were undertaken on polished sections of tubes from the alloy of Mo with 3% Nb. The transverse specimens were 22×10^{-3} m in external diameter and 10×10^{-3} m in internal diameter. The microhardness was measured both at the surface and below the surface in order to determine the depth and degree of work hardening. The latter quantity was estimated as the ratio of the difference between hardness H_1 of the work-hardened layer and original hardness H_0 to H_0, $H_1 - H_0/H_0$.

The original value of microhardness was $H_0 = 244 \pm 9$ kg/mm^2. "Cold" turning raised the surface microhardness to $H_1 = 317 \pm 15$ kg/mm^2, which dropped to H_0 at a depth of 50 μm. The use of 0.5 kW laser preheating caused H_1 to grow to 264 ± 14 kg/mm^2. The original value of microhardness was found to be at a depth of ~ 25 μm.

7.12. EXAMPLES OF LASER HEAT TREATING

Surface hardening of iron bases of flats for carding machines. The bases of revolving flats were heat treated with laser pulses to form a thin hardened layer on the surface at a minimum size of the HAZ. This treatment made it possible to meet the operating requirements placed on the wearing faces of strips, whose limit of wear was 300 μm.

The test specimens were gray iron castings used for the flats. Industrial laser setups employed for heat treatment of base surfaces provided 100 J, 20 J, and up to 30 J of energy in a pulse with a duration varied from 1 to 6 ms. The laser power density delivered to the target surface could be adjusted from 10^4 to 10^5 W/cm^2 by varying the degree of beam focusing. The beam spots successively focused at the surface slightly overlapped one another.

The optimal power density for melt quenching of the surfaces of strips reached 8×10^4 W/cm^2, which was enough to provide a hardness penetration down to 300 μm at a minimum depth of the molten layer. Surface tension forces caused a thin layer of melt to shrink at some spots, thus forming beads up to 30 μm high with

a smooth profile. The surface layer exhibited ledeburite sites imparting the surface antiscuffing and wear-resistant properties. The optimal power density for solid-state transformation hardening was 2×10^4 W/cm^2.

The Vickers hardness (VH) of the surfaces of unhardened iron specimens was 262. The values of VH in the laser hardened zones ranged from 666 to 677.

The service tests revealed that the laser hardening afforded about a six-fold increase in the wear resistance of base strips of flats (Fig. 7.50).

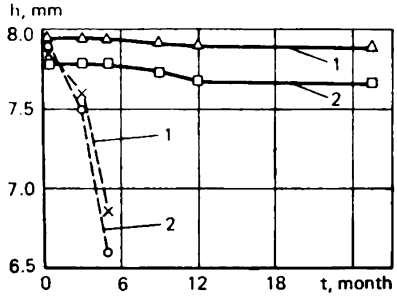

Fig. 7.50. Wear rate of iron base strips of flats: with unhardened strip (dashed line); hardened strip (solid line); *1*, left strip; *2*, right strip

In Fig. 7.51 is shown the general view of an industrial laser work station for hardening the wearing faces of the bases of flats for carding machines. It comprises a commercial laser setup of the Kvant-16 type and an arrangement for clamping the base and moving it in the work area according to the specified program. This arrangement consists of a right table mounted directly on the laser setup, a left table supported on a special post, and a control cabinet for a hydraulic system with a pump unit and an automatic control system for clamping and moving the workpiece.

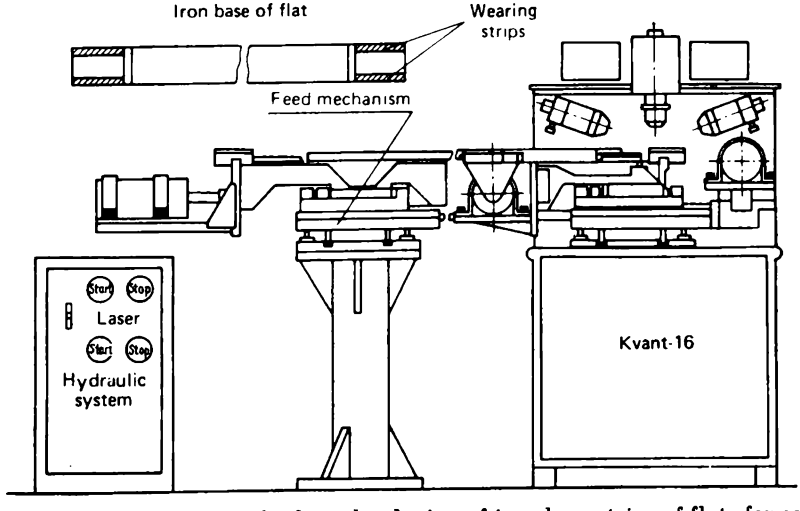

Fig. 7.51. Work station for laser hardening of iron base strips of flats for carding machines

Structure and properties of blanking dies after laser hardening of cutting edges [10]. Let us consider an example of pulsed laser surface hardening of tool steels subjected to pre-laser heat treatment by conventional methods.

Tests were run on blanking dies from good-quality carbon tool steel grade U8, subjected to quench hardening in oil at 790°C and low tempering at 150°C (Fig. 7.52). The die lips were hardened at the work station using a Kvant-16 laser setup which could provide up to

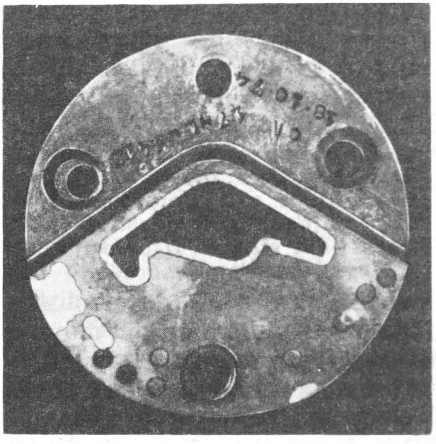

Fig. 7.52. External view of the blanking die after laser surface hardening of cutting edges

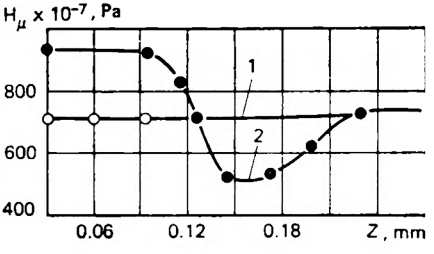

Fig. 7.53. Microhardness of the die surface layers versus hardened depth

30 J of energy in a pulse with 6 ms duration at a pulse repetition rate of 0.1 Hz. The diameter of the defocused beam spot at the die surface was 4 mm and the overlap ratio for irradiated spots was 0.5.

As found from microexaminations, the structure of the hardened layer consists of a large amount of residual austenite and fine-acicular martensite. The microhardness of the laser hardened surface of the die is higher than that obtained after conventional hardening although the surface layer contains an increased amount of residual austenite as revealed by the X-ray analysis (Fig. 7.53). An increase in the microhardness of the laser-hardened surface layer of U8 steel is attributable to the following factors.

1. Martensite formed at high cooling rates of about 10^6 deg C/s has an increased hardness, as is known from experience of induction hardening of steel.

2. Austenite resulting from high-rate heating of martensite (at about 10^6 deg C/s) has a high hardness since its structure is oversaturated with crystal lattice defects. High rates of heating may cause

reversible diffusionless martensite transformation so that austenite inherits the defect structure of martensite since in the process of rapid heating the effects of disorder and regrowth practically have no time to come into play.

3. Martensite accumulates lattice defects in the course of two direct martensite transformations and one reversed transformation.

Despite the severe conditions of hardening without tempering of hardened zones, the hardened layer is free of such defects as quenching cracks and microcracks. This can be accounted for by the presence of the temper regions of two types that have appeared after laser treatment.

1. The tempered sublayer with H_μ of 5 000 MPa that separates the hardened surface layer from the primarily hardened matrix.

2. The arched tempered regions on the hardened surface of the die, which result from the overlapping of irradiated spots. The volume of these regions does not exceed 5% of the total laser-hardened volume of metal, so they little affect the wear resistance of the die on the whole. They virtually play the role of relaxation zones for quenching stresses and thus serve as peculiar thermal joints.

Service life tests of laser-after-heat treated dies used for blanking swivel-window drop channels of front car body doors were conducted at a Moscow automobile plant. The channels were made from scale-resistant steel. The material of dies was a carbon tool steel hardened and tempered to a hardness of Rockwell C 58. The Kvant-16 laser unit hardened the dies (punches) by two variants: at the end faces and at the lateral faces. Laser hardening raised H_μ of die steel from an initial value of 6 300 MPa to 13 500 MPa.

The thruput of commercial dies over the period of uptime to regrinding was 4 500-5 000 pieces per die. After laser hardening, the thruput capacity of the dies hardened at end faces and those hardened at lateral faces increased to 10 000 and 14 000 pieces respectively.

One more example of wear life tests of dies designed for punching, upsetting, and trimming tool steel parts has been given in paper [39]. The dies were pretreated to raise their hardness to Rockwell C 52-56. The roughness R_a of dies (arithmetic mean deviation of the profile) was 0.63-1.25 μm.

Laser hardening was done in argon using the Kvant-16 laser setup which sequentially scanned the laser beam over the target surface to form heat-treat tracks at a spot overlap ratio of 0.5. The energy in a 6 ms pulse was 22-26 J and the irradiated spot was 3.0-3.2 mm in diameter. The wear life of laser-hardened dies increased 1.6-3 times. Table 7.2 lists the results of tests for the thruput capacity of laser-hardened and heat-treated dies over the period of lifetime to regrinding.

TABLE 7.2. **Thruput of Dies after Laser Hardening and after Conventional Hardening**

Die part	Die material	Material of piece worked	Thruput of die, number of pieces worked	
			laser hardened	heat treated
Bed die to pierce 1.8 mm holes	Kh12	65 steel	6 000	2 000
Punch to form 1.2 × 15 mm notches	Kh12	12Kh18N9T	3 000	1 500
Gasket for die to pierce 1.8 mm holes	Kh 12	65 steel	6 000	3 500
Punch to pierce 1.8 mm holes	KhVG	65 steel	10 000	3 200
Bed die to form a dimple in umbrella tie-rod	KhVG	65 steel	8 000	4 000
Bed die to form 2 × 10 mm notches	Kh12	12Kh18N9T	3 000	1 500
Bed die to cut out clamps	Kh12M	65 steel	20 000	10 000
Bed die to form a spherical portion of umbrella tie-rod head	Kh12	65 steel	10 000	3 000
Blade to cut 3-mm die wire	U10	A12 steel	60 000	20 000
Bed die to trim 3-mm dia screws	U10	20 steel	50 000	30 000
Bed die to head 3-mm dia rivets	Kh12M	St 3 steel	50 000	20 000
Bed die to head 4-mm dia rivets	Kh12M	St 3 steel	60 000	22 000
Punch to cut out clamps	Kh12	40 steel	20 000	10 000
Finishing punch to head 3-mm dia screws	U10	A12 steel	40 000	20 000
Blade to cut off 3-mm dia rivets	U8	St 3 steel	50 000	30 000
Finishing punch to head 10-mm dia screws	U10	20 steel	50 000	15 000
Punch to form a dimple in umbrella tie-rod	KhVG	65 steel	8 000	4 000

Notes: 1. The Latin letter-symbols G, Kh, M, N, T, and V denoting Mn, Cr, Mo, Ni, Ti, and W, respectively, in ferrous metal grades are the transliteration of respective Russian letters. For example, 12Kh18N9T is the transliterated designation of a scale-resistant steel which contains 0.12% C, 18% Cr, 9% Ni, and 0.5-0.8% Ti.

2. The symbol St denotes various grades of carbon steel. Designations 20 steel, 40 stecl, and 65 steel identify good-quality carbon structural steel grades containing 0.20, 0.40, and 0.65% C respectively.
3. The letter A in A12 denotes a free cutting steel with 0.12% C.
4. The letter U, for example, in U10, denotes a good-quality carbon tool steel with 1% C. The letter A attached to U10 (U10A) denotes a high-quality carbon tool steel.
5. The letter A in nonferrous metal grades stands for Al. For example, BrA7 is aluminum bronze containing 7% Al and 93% Cu.

References

1. C. M. Banas and R. Webb. *Macromaterials processing.* Proc. of the IEEE, vol. 70, No. 6, p. 556, 1982.
2. J. F. Ready. *Material processing.* An overview. Proc. of the IEEE, vol. 70, No. 6, p. 533, 1982.
3. G. A. Abilsiitov and V. S. Golubev. *Basic problems of laser technology and industrial lasers.* Troitsk, NITS-TL AN SSSR, 1981 (in Russian).

4. N. N. Rykalin, A. A. Uglov, and A. N. Kokora. *Laser machining and welding.* Moscow, Mir Publishers, 1978.
5. M. A. Krishtal, A. A. Zhukov, and A. N. Kokora. *The structure and properties of laser treated alloys.* Moscow, Metallurgiya, 1973 (in Russian).
6. V. V. Korneev, F. K. Kosyrev, S. F. Moryashchev, et al. *On some aspects of laser heat treatment.* Fizika i Khimiya Obrabotki Materialov, No. 3, p. 3, 1980.
7. V. M. Andriyakhin, V. S. Mayorov, and V. P. Yakunin. *Calculation of CW laser surface hardening of iron-carbon alloys.* Poverkhnost, No. 6, p. 140, 1983.
8. V. M. Andriyakhin, V. S. Mayorov, N. T. Chekanova, et al. *Experimental check on the calculation of CW CO_2 laser hardening of iron-carbon alloys.* Poverkhnost, No. 9, p. 145, 1983.
9. L. I. Mirkin. *Physical principles of laser treatment of materials.* Moscow, Publishing House of Moscow State University, 1975 (in Russian).
10. A. A. Zhukov, A. N. Kokora, A. N. Zarya, et al. *On the structure and properties of heat-treated blanking dies after laser surface hardening.* Fizika i Khimiya Obrabotki Materialov, No. 1, p. 141, 1977.
11. L. F. Golovko, V. S. Kovalenko, and V. S. Chernenko. *On iron-carbon alloy hardening with a high-power CW CO_2 laser.* Elektronnaya Obrabotka Materialov, No. 6, p. 26, 1980.
12. V. S. Kovalenko, L. F. Golovko, G. V. Merkulov, et al. *Laser hardening of parts.* Kiev., Tekhnika, 1981 (in Russian).
13. I. I. Novikov. *The theory of heat treatment of metals.* Moscow, Metallurgiya, 1978 (in Russian).
14. V. V. Goryushin and A. V. Martyakova. *Effects of laser irradiation on the structure and properties of 35 steel.* Metalloved. i Termich. Obrabotka Metallov, No. 1, p. 53, 1978.
15. V. S. Kovalenko, K. Enami, E. Arata, et al. *On the mechanism of material hardening with a CW laser.* Elektronnaya Obrabotka Materialov, No. 1, p. 35, 1980.
16. V. M. Andriyakhin, Ya. G. Kletskin, A. G. Osmantsev, et al. *Gray iron hardening with a CO_2 laser.* Avtomobil. Promyshlennost, No. 6, p. 25, 1980.
17. V. M. Andriyakhin, V. K. Sedunov, V. N. Belov, et al. *Changes in the structure and properties of laser-hardened ICE cylinder liners.* Metalloved. i Termich. Obrabotka Metallov, No. 9, p. 10, 1980.
18. A. N. Kokora. *Laser heat treatment and prospects of its application at engineering plants of food industry.* Moscow, TSNIITEIlegpishchemash, 1977 (in Russian).
19. A. N. Kokora, A. A. Zhukov, and L. Z. Epshteyn. *CW laser surface hardening of gray iron parts.* Fizika i Khimiya Obrabotki Materialov, No. 3, p. 28, 1977.
20. A. N. Kokora, A. A. Zhukov, and L. Z. Epshteyn. *CW laser surface hardening of irons with compact graphite inclusions.* Fizika i Khimiya Obrabotki Materialov, No. 4, p. 23, 1977.
21. V. E. Arkhipov, A. N. Grechin, and M. L. Khina. *Laser treatment of ferritic cast iron.* Metalloved. i Termich. Obrabotka Metallov, No. 4, p. 16, 1980.
22. V. M. Andriyakhin, S. V. Zemskiy, V. I. Gorodetskiy, et. al. *Effects of laser radiation on carbon redistribution in irons.* Tekhnologiya Avtomobilestr., No. 5, p. 30, 1980.
23. V. M. Andriyakhin, N. V. Edneral, N. T. Chekanova, et al. *Structural and phase changes in laser-treated surface layers of gray irons.* Izv. Vuzov. Ferrous Metallurgy Series, No. 9, p. 12, 1981.
24. E. F. Semiletova. *Laser hardening and alloying of tool materials*: in Problems of developing and introducing high-performance cutting tools with a reduced content of tungsten. Tbilisi, GPI, 1978 (in Russian).
25. V. S. Kovalenko. *Pulsed laser treatment of materials.* Kiev, Visshcha Shkola, No. 2, p. 43, 1977 (in Russian).

26. S. S. Khayurov. *Heat and diffusion-heat treatment of metals and alloys with ion and laser beams*: in Achievements of science and engineering. Physical metallurgy and heat treatment. Moscow, VINITI, v. 14, 1980 (in Russian).
27. V. A. Burakov and S. S. Fedosienko. *Metallographic examinations of carbon steels laser-cladded with Cr and Ti*: in Advanced foundry practice in agricultural machinery industry. Rostov-on-Don, Institute of Agricultural Machinery Industry, 1980 (in Russian).
28. V. S. Kraposhin. *Laser metal surface treatment.* Poverkhnost, No. 3, p. 1, 1982.
29. E. A. Arzamastseva, B. F. Mulchenko, V. M. Zinchenko, et al. *Laser applications in industry.* Tekhnologiya Avtomobilestr., No. 5, p. 16, 1980.
30. A. A. Zhukov, R. L. Snezhnoy, and A. N. Kokora. *Formation of an amorphous phase in iron.* Metalloved. i. Termich. Obrabotka Metallov, No. 12, p. 41, 1980.
31. V. M. Kyashkin, G. S. Zhdanov, and L. I. Mirkin. *Laser induced amorphization of alloys.* DAN SSSR, 249: No. 3, p. 1118, 1979.
32. V. M. Kyashkin and L. I. Mirkin. *Amorphous metals formed under laser radiation*: in Proceedings of the 9th All-Union conference on strength and plasticity of metals and alloys. Kuybyshev. Politechnical Institute, 1979 (in Russian).
33. V. M. Kyashkin, L. I. Mirkin, and N. S. Saburova. *Laser-induced formation of amorphous metals*: in Applications of lasers in science and engineering. Leningrad, LDNTP, 1981 (in Russian).
34. L. I. Mirkin and V. M. Kyashkin. *Laser-amorphized alloys and their properties*: in Structure of amorphous alloys. Moscow, MISiS, 1980 (in Russian).
35. I. S. Miroshnichenko. *Liquid phase quench.* Moscow, Metallurgiya, 1982 (in Russian).
36. I. S. Miroshnichenko and V. F. Bashev. *Amorphous phases formed in Fe-B and Fe-C alloys at rapid melt quenching.* Izv. AN SSSR, Metals Series, No. 3, p. 206, 1977.
37. B. M. Grinberg, A. A. Zhukov, A. D. Sherman, et al. *Effect of the rate of cooling on the phase composition of ternary eutectic in the Fe-C-P system.* Fizika i Khimiya Obrabotki Materialov, No. 3, p. 114, 1976.
38. V. S. Velikikh, V. P. Goncharenko, and V. S. Kartavtsev. *Laser hardening of tool steels.* Tekhnologiya i Organizats. Proizvodstva, No. 11, p. 45, 1976.
39. A. N. Kokora, V. B. Zulaev, and E. N. Koryalev. *Laser surface hardening of equipment parts and tools*: in Electrophysical and electrochemical methods of material processing. Moscow, MDNTP, 1978 (in Russian).
40. F. F. Vodovatov, A. A. Chelny, V. P. Veyko, et al. *Industrial lasers.* Moscow, Energiya, 1975 (in Russian).
41. K. I. Krylov, V. T. Prokopenko, and A. S. Mitrofanov. *Laser applications in machine building and instrument making.* Leningrad, Mashinostroenie, 1978 (in Russian).
42. N. N. Rykalin and A. A. Uglov. *Processes of laser-plasma-induced compound synthesis and refractory metal reduction.* Fizika i Khimiya Obrabotki Materialov, no. 4, p. 3, 1985.
43. N. N. Rykalin and A. A. Uglov. *CEF-material interaction*: in CEF interaction with materials. Moscow, Nauka, 1985 (in Russian).
44. N. N. Rykalin and A. A. Uglov. *Laser-plasma treatment of metal at high gas pressures.* Kvantovaya Elektronika, 8: No. 6, p. 1193, 1981.
45. A. A. Uglov, V. A. Grebennikov, V. G. Panaetov, et al. *Nitrogen-jet-assisted laser hardening of metals.* Fizika i Khimiya Obrabotki Materialov, No. 2, p. 3, 1984.
46. Yu. M. Lakhtin and Ya. D. Kogan. *Steel nitriding.* Moscow, Mashinostroenie, 1976 (in Russian).

47. I. A. Tregubov, L. N. Evseeva, S. B. Maslenkov, et al. *Effect of laser radiation on the structure and corrosion resistance of zirconium alloys.* Fizika i Khimiya Obrabotki Materialov, No. 2, p. 30, 1984.
48. A. N. Reznikov. *Thermal physics of the processes of machining.* Moscow, Mashinostroenie, 1981 (in Russian).
49. B. S. Gavryushenko, L. V. Okorokov, N. N. Rykalin, et al. *Laser-assisted metal cutting.* Fizika i Khimiya Obrabotki Materialov, No. 2, p. 4, 1985.
50. A. N. Strozhkov, Sh. L. Tesler, S. P. Shabashov, et al. *Cutting of preheated low-machinability materials.* Moscow, Mashinostroenie, 1977 (in Russian).

Chapter 8
LASER WELDING

There are two basic types of laser welding, CW (continuous) and pulse (spot). Seam welding is done by CW laser beams or overlapping pulses. Pulse or spot welding (microwelding) is done using pulsed lasers or CW lasers with shutters. Deep penetration welding became possible with the advent of multikilowatt continuous lasers. The main advantages of laser welding are [1, 2]:

(1) heat input to the welding spot by the focused laser beam of high power density;
(2) low heat release in weldments;
(3) small heat-affected zone (HAZ);
(4) low deformation of weldments;
(5) the keyholing effect that enables deep penetration welding;
(6) high weld rates;
(7) possibility of welding dissimilar metals difficult to weld by other techniques;
(8) an easily automated process.

The above advantages depend on the parameters of the laser beam that creates a heat source in the target, the character of interaction of the beam with materials, and on other factors. Let us look at the results of the analysis of thermal processes during welding, which can be used to make simple engineering calculations and estimates.

8.1. THERMAL PROCESSES

High-power laser radiation incident on metals gives rise to the following processes [2, 3]:

(1) electron and ion emission due to heating effects;
(2) melting, vaporization, and ejection of the droplets of melt from the interaction region;
(3) thermal radiation and X-radiation of up to 2 keV;
(4) ultrasonic vibrations in metal due to the periodicity of heating and thermal expansion in the interaction of pulses whose substructure consists of spikes.

In the range of moderate power densities, $q \leqslant 5 \times 10^5$ W/cm², the laser energy coupled to the target mainly heats the surface and brings about thermionic emission and the photoelectric effect. An increase in q to a certain critical value causes the surface to vaporize, and a still higher increase above this threshold leads to an appreciable overheating of the material and its recoil against the surface, so that the shock produced disintegrates the surface layer [3, 4].

Part of the energy of incident radiation is reflected from the target surface. For example, at a laser pulse fluence of 5 kJ/cm², such materials as copper, aluminum, and iron reflect 83, 66, and 40%, respectively, of the energy of the incident pulse, thus heavily decreasing the efficiency of laser metalworking. The curves of changes in

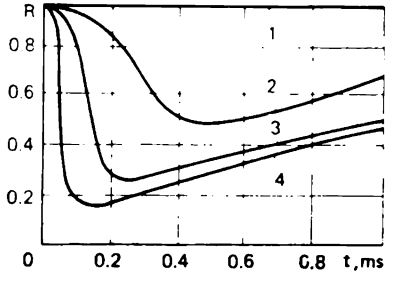

Fig. 8.1. Reflectivity R of silver at laser pulse fluence of 2.0, 2.6, 4.2, and 7.3 kJ/cm² (curves *1*, *2*, *3*, and *4* respectively)

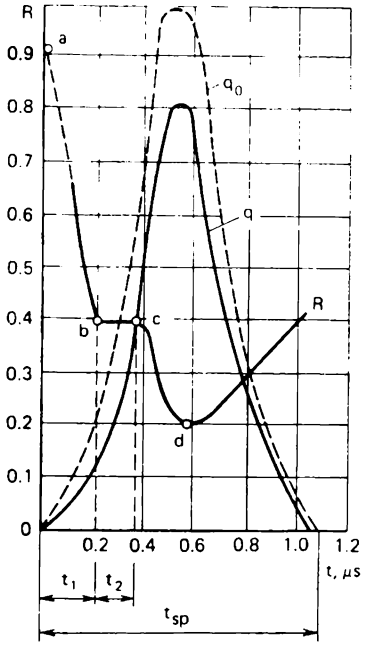

Fig. 8.2. Reflectivity R of silver during one spike at $Q = 7.5$ kJ/cm² and $q = \times 10^7$ W/cm²

the reflectivity R of silver during the pulse dwell time at different values of pulse fluence Q are shown in Fig. 8.1. The reflectivity R drops to a minimum in the range of maximum values of Q and then begins to increase as the result of a gradual decrease in the temperature of the target surface (2, 4). When Q exceeds a certain critical value, the reflectivity changes most heavily. With an increase in the temperature of the material at the point of interaction up to the melting temperature T_m and above, R drops markedly.

When an individual spike of the laser pulse strikes the silver target, R decreases with increasing power density q (points *b* and *c*) and drops to a minimum (point *d*) approximately at a maximum

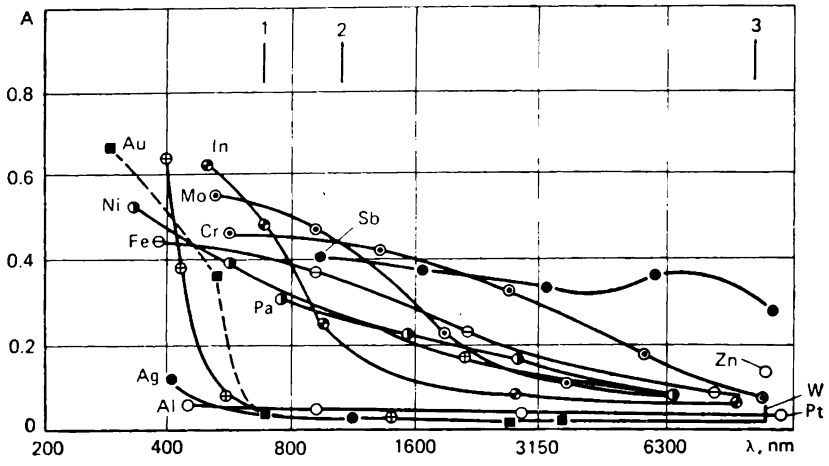

Fig. 8.3. Absorptivity A of metals versus laser wavelength: *1*, 0.694 μm, ruby laser; *2*, 1.06 μm, Nd-YAG laser; *3*, 10.6 μm, CO_2 laser

value of q (Fig. 8.2). The bend on the curve of R corresponds to metal melting. Late in the spike, R grows as q decreases.

In the region of power densities $q \leqslant 10^6$ W/cm^2, the value of R greatly depends on the laser wavelength, type of target material, surface finish, presence of oxide films, etc.

TABLE 8.1. **Reflectivity of Metals of Various Laser Wavelengths**

Metal	Wavelength λ, μm		
	0.7	1.06	10.6
Al	0.87	0.93	0.97
Cr	0.56	0.58	0.93
Cu	0.82	0.91	0.98
Ni	0.68	0.75	0.95
Ag	0.95	0.97	0.99
Steel	0.58	0.63	0.93-0.95
Zr	—	—	0.917
Ti	—	—	0.906

Consideration of the reflectivity of metals is of importance since it allows us to calculate the weld efficiency which is defined as the ratio of the absorbed power used to melt the material to the total power input. The power absorbed per unit area of the target surface with consideration for R is

$$q(r) = (1 - R)\, q_0(r) = Aq_0(r) \qquad (8.1)$$

where q_0 is the total power density, and A the absorptivity.

The values of R for some metals at different values of the laser wavelength are listed in Table 8.1 [3, 5]. Figure 8.3 illustrates how A for some metals varies with λ.

The reflectivity R of Al and Fe as a function of the target surface temperature is shown in Fig. 8.4. Preheating can markedly increase the laser power input [2].

The weld efficiency can be increased by depositing a thin absorptive layer of, say, Fe_2O_3 on the surfaces of parts to be joined. The keyholing process greatly increases the weld efficiency since the hole walls effectively absorb the laser energy throughout the depth of the hole [2].

Work [2] contains the results of experimental studies on the character of changes of A for some materials as a function of the speed of welding with a YAG laser operating at 1.06 μm and CO_2 laser at 10.6 μm. The experimental results obtained by the colorimetric technique are given in Fig. 8.5*a*.

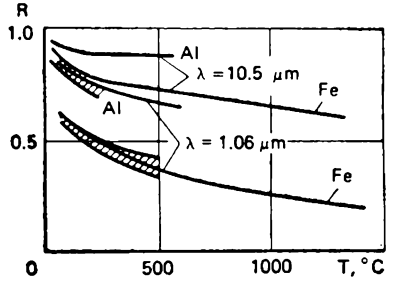

Fig. 8.4. Reflectivity versus temperature for Al and Fe (hatched regions, experiment; full lines, theory)

The researchers [2] explain an increase in A with weld speed in the laser keyholing process as being due to changes in the shape of the keyhole. Otherwise, an increase in weld speed and a corresponding decrease in hole depth, providing the hole absorbs laser radiation through its multiple reflection from the hole walls, would cause the absorptivity to decrease. The shapes of conventionally drilled holes affect the values of R and thus confirm that R depends on the profile irregularities, i.e. on the shape of the keyhole (Fig. 8.5*b*).

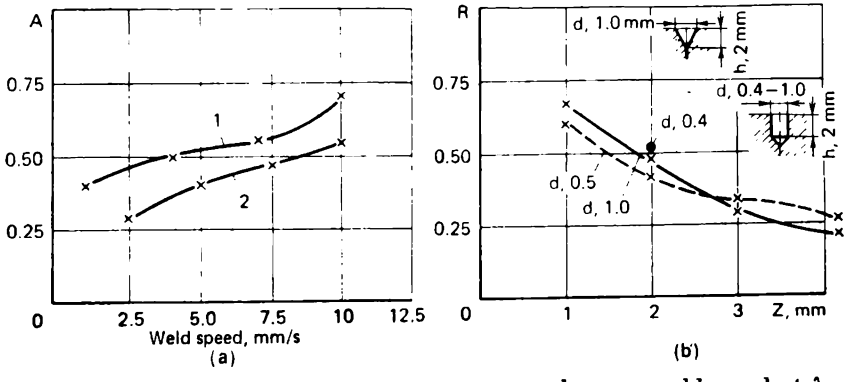

Fig. 8.5. Absorptivity (*a*) of corrosion-resistant steel versus weld speed at $\lambda =$ $= 1.06$ μm and $P_0 = 500$ W (curve *1*) and at $\lambda = 10.6$ μm and $P_0 = 2$ kW (curve *2*); reflectivity (*b*) of same steel versus shape and depth of holes preliminarily drilled in steel specimens

In the general case, the heat flux density at the target surface is a complex function of the coordinates and time; the heat source can be thought of as the surface source if the laser power density is insufficient to effect the keyholing process, i.e. if the penetration depth is small as against the radius r_f of the focused spot (hot spot). The relation for the absorbed power density can be given as a product of two functions dependent on the spatial coordinates and time respectively [3].

Pulsed laser heating can be treated as a one-dimensional problem if the hot spot radius satisfies the condition $r_f \gg \sqrt{a\tau_p}$, where a is the thermal diffusivity and τ_p is the pulse duration. The problem disregards the temperature dependence of optical and thermal constants. The surface being heated can in most cases be considered adiabatic.

For pulsed laser welding, the laser power density must exceed a critical value $q_c^{(1)}$ at which the surface reaches its melting point T_m in a time equal to τ_p, but must not be in excess of $q_c^{(2)}$ at which the surface begins to vaporize intensely, i.e. $q_c^{(1)} \leqslant q \leqslant q_c^{(2)}$.

If q exceeds $q_c^{(2)}$, the rate of vaporization increases still more and becomes comparable to the heating rate at $q_c^{(3)} = L_v \rho \sqrt{a\tau_p}$, where L_v is the latent heat of vaporization and ρ the material density. The expressions for the heating rate v_h and cooling rate v_c take the form [3]

$$v_h = (q_0/\lambda)\sqrt{q/\pi t} \quad \text{at} \quad t = \tau_p \tag{8.2}$$

$$v_{cl} = (q_0/\sqrt{\pi\lambda c\rho})\,(1/\sqrt{t} - 1/\sqrt{t-\tau_p}) \tag{8.3}$$

where c is the specific heat.

The plots of v_h and v_{cl} for a semi-infinite body heated by a Gaussian source are shown in Fig. 3.23. As seen from the graphs, the rates of heating and cooling are high.

The analysis of three-dimensional heat transfer problems allows us to consider the thermal processes in pulse welding at a pulse duration of about 10^{-3} s and a hot spot radius of about 10^{-2} cm. Since $r_f \approx \approx \sqrt{a\tau_p}$, the pulse is considered constant in time, with the power density being distributed in Gaussian fashion over the spot on the surface [3].

The calculations of temperature fields and energy-related characteristics for laser welding of plates can be made by using the models of a semi-infinite body, a single-layer plate with various boundary conditions, and a two-layer plate with ideal and nonideal contact between the layers. The boundary conditions allow for the geometry of welded pieces, physical properties of materials, and energy-related characteristics such as the temporal pattern of the pulse and reflectivity.

The quality of contact between the pieces to be welded, the pulse length, and other factors affecting laser weldability have been treated in work [3]. Calculations and experiments show that the quality of contact is of much importance. The surface of poor contact between the pieces to be welded can act as an adiabatic boundary responsible for melt overheating and blowoff, which sharply reduces the strength of the weld joint and impairs its operating characteristics. The spikes of a laser pulse are conducive to vapor pressure pulsations and melt ejection [6]. In any case, the use of nonspiked pulses with a smoother envelope greatly reduces the probability of material blowoff.

Proceeding from the analysis of problems on laser material heating, workers [3] have formulated the main requirements for the laser pulse duration, pulse energy, and power density which ensure the optimal conditions of welding.

For the calculations of thermal processes involved in continuous laser welding, use can be made, in the framework of heat transfer theory, of a continuous moving surface heat source with the Gaussian distribution of the power density over the hot spot [3]. In this case, the expression for temperature at the surface of a semiinfinite body takes the form

$$T(x,\ y,\ z,\ \tau) = \frac{2P_0 \exp(-vx/a)}{c\rho(4\pi a)^{3/2}} \int_0^{\tau} \frac{dt'}{\sqrt{t'(t_0+t')}} \times \exp\left[-\frac{Z^2}{4at'} - \frac{r^2}{4a(t_0+t')} - \frac{v^2(t_0+t')}{4a}\right] \quad (8.4)$$

where P_0 is the power entering the surface, v the speed of travel, a the thermal diffusivity, c the specific heat; ρ the material density; $t_0 = 1/4\ ak$, k the concentration coefficient, t' the integration variable, z the position of a point on the target, and $r = \sqrt{x^2 + y^2}$.

The calculated data for the estimation of the thermal processes and conditions of laser seam welding for sealing the crystal vibrators of electronic watches are given in work [2]. Flange welds in copper and kovar with a total thickness of plates of 0.5 mm were made using a Kvant-12 setup delivering 2.5 J of energy in a pulse of 2.5×10^{-3} s duration at a pulse repetition rate of 10 Hz.

To estimate limiting temperatures at which it is permissible to heat the workpieces to be welded, the researchers used the expression for T_{max} at a point of a massive sample in the course of heat propagation from a powerful quick-acting source:

$$T_{max}(r_0) = \frac{1}{e} \frac{q}{vc\rho(\pi/2) r_0^2} \quad (8.5)$$

where v is the speed of travel, and r_0 the distance from the source.

The suggested technique gave good agreement between the experimental and calculated results for the temperature and penetration depth.

The plots of penetration depth h versus subcritical laser power P at different speeds of travel of the heat source are shown in Fig. 8.6.

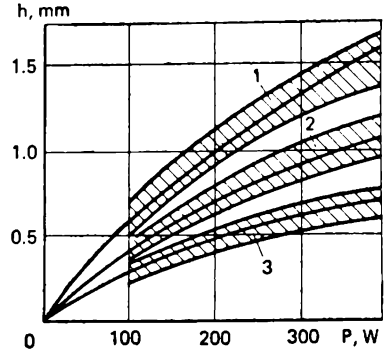

Fig. 8.6. Weld penetration h versus laser power P for welding corrosion-resistant steel at subcritical power densities and at rates of 1.0, 3.0, and 10.0 mm/s (curves *1*, *2*, and *3* respectively)

As the power density reaches a critical value of $q_c^{(2)}$, the surface begins to vaporize and the surface source can convert to a cylindrical source. Figure 8.7 illustrates the curves of $q_c^{(2)}$ and critical laser power P_c as functions of the radius r_f of the focused beam spot on the surface of corrosion-resistant steel samples.

To derive the expressions for calculating the parameters of interest at $q \geqslant q_c^{(2)}$, workers [2] used the model of a linear heat source and heat transfer in the course of keyholing.

At multikilowatt laser levels, keyholing is the predominant process which affords a fairly deep penetration of the laser energy into the workpiece. To carry out heat-transfer calculations, it is advisable to employ the model of a linear heat source moving at a constant speed, therewith disregarding the mechanism of keyholing [3].

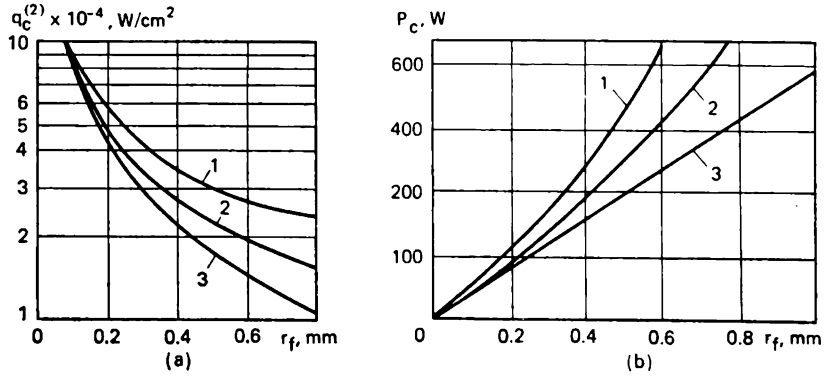

Fig. 8.7. Critical power density $q_c^{(2)}$ (*a*) and critical power P_c (*b*) versus focal spot radius r_f at weld rates of 30, 10, and 0 mm/s (curves *1*, *2*, *3* respectively)

Keyholing depends on the parameters of a laser beam at the given thermal constants of the material being welded. It begins at 100 to 500 W for a YAG laser and at 1.5 to 5.0 kW for a CO_2 laser [2].

Work [2] contains formulas for temperature distribution in a semi-infinite body, which can be used to determine the weld shape and find the relation for hole wall coordinates. Besides, it shows how the shape of the fusion zone varies with the angle of beam convergence and the location of the focal point relative to the surface of the workpiece. The penetration depth h as a function of laser power P in excess of P_c is illustrated in Fig. 8.8.

In investigating the process of molten pool formation to study the kinetics of metal melting and keyholing, the targets were struck

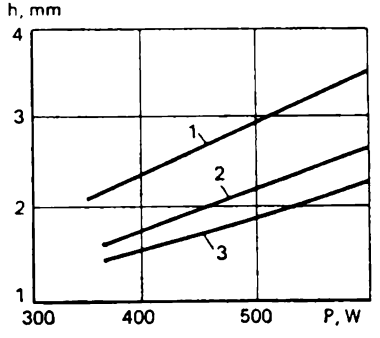

Fig. 8.8. Penetration depth h versus supercritical power P at weld rates of 1.0, 3.0, and 5.0 mm/s (curves *1*, *2* and *3* respectively)

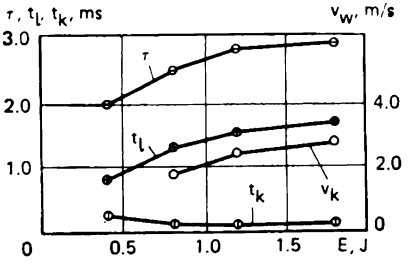

Fig. 8.9. Time t_k to form a keyhole, keyhole lifetime t_l, and keyholing rate v_k versus pulse energy E at pulse length τ

with ruby laser pulses containing up to 1.2 J and delivering $2.5 \times \times 10^5$ W/cm^2 to the surface [2]. It is found that the laser beam drills a through hole in the sample at a rate of 2-3 m/s; the volume of melt increases with the time of interaction. Figure 8.9 displays the curves of the time t_k required to form a keyhole in the sample, the keyhole lifetime t_l, and keyholing rate v_k versus the energy of a pulse of duration τ.

The analysis of the process of pulse welding with an Nd-YAG laser providing up to 20 J of energy in an 8 ms pulse has revealed that the length of time to melting to a depth of 0.5 mm is 7 ms for titanium and steel, 3 ms for aluminum, and 1 ms for silver. The melting temperature remains stable during 25, 12.5, 6, and 2 ms for Ti, steel, Al and Ag respectively.

Work [3] presents data on the penetration depth (melt depth) for pulse welding as a function of maximum laser power density. power density distribution over the spot, and pulse length. For

rather thick metal pieces welded at a temperature below the boiling point, the isothermal of melting has an approximately spherical shape (the aspect ratio is 2). Experiments [7] confirm this calculation result for some values of the power density.

In the experiment described in [3], a laser setup delivering up to 20 J of energy in a 1.45 ms pulse was used to determine how the penetration depth varies with the average laser power density q_0 (incident irradiance) at the spot on the metal surface and with the location of the focus relative to the surface. The relation between the absorbed power density q (absorbed irradiance) and q_0 is $q = q_0 A$, where A is the absorptivity.

The melt depth h at low values of the laser power density slowly increases as q_0 rises to a certain critical value, q_{01} (curves *1* and *2*

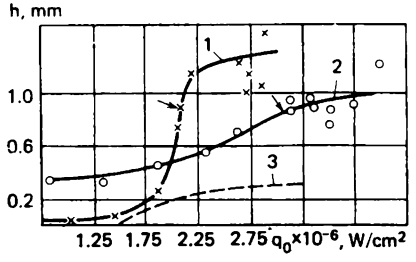

Fig. 8.10. Penetration depth versus average laser power density for welding copper (*1*, *3*) and nickel (*2*): curves *1* and *2*, experimental; curve *3*, theoretical

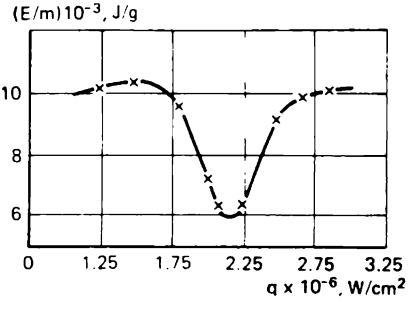

Fig. 8.11. Specific energy versus laser power density for melting copper

in Fig. 8.10). A further increase in q_0 above q_{01} causes a faster increase in h (in proportion to q_0) until the laser power density q_0 reaches another critical level q_{02} (shown by arrows in Fig. 8.10), following which the vapor pressure pushes the melt away to the sides of the fusion zone, forming a cavity whose depth increases at a slower rate with a further increase in q_0. The threshold values of q_0 at which intense vaporization begins are equal to 3.0×10^6, 1.75×10^6, and 2.1×10^6 W/cm² for Ni, Al, and Cu respectively. In the initial region of the plot, the theoretical curve *3* coincides with the experimental curve in shape. In the range of q_0 in excess of 2×10^6 W/cm² (for copper), the rate of growth of h with q_0 is much faster than is found from the heat transfer theory (curve *3*) since the mechanism of deep penetration involves the motion of the liquid metal in the fusion zone.

The character of input of laser energy E per unit mass m of molten copper is shown in Fig. 8.11. As apparent from the graph,

the specific energy E/m is at a minimum in the definite range of absorbed laser power density q. Notice that the effect of deep penetration shows up most strongly just in this range of q. This supports the statement that deep penetration welding is energetically the most advantageous welding technique. Deeper penetration in copper samples is due to the following [3]. A high irradiance of the beam falling on a small region causes the metal to vaporize very rapidly. The recoil force produced by the partially enclosed vapor pushes the molten metal from the hottest region, thus forming a hole. Keyholing proceeds so long as the recoil force due to the vapor jet is greater than the sum of the surface tension force and gravitational force, which tend to impede the melt flow to the hole walls. The beam penetrates through the vapor hole and heats the hole walls more strongly than it is done by convective heat transfer. At some instant the tension force and gravitational force become higher than the vapor recoil force, so the liquid metal flows back into the hole and this determines the depth of penetration. A low metal loss involved with this technique of welding is evidence that keyholing results from the above described effect. Penetration increases when the focal point of the beam is located slightly below the surface.

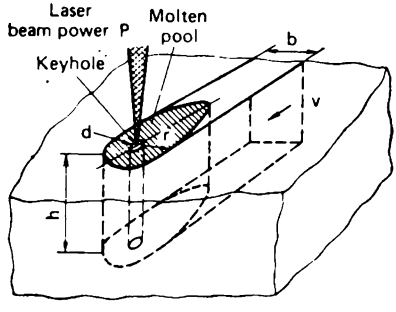

Fig. 8.12. Laser keyholing: d, spot diameter; h, penetration depth; v, speed of travel; b, melted zone width

The penetration depth markedly grows at higher power levels [8]. This is because the beam delivers energy to the surface so rapidly that it drills a hole into the material and thus penetrates more deeply into the sample as it deposits energy at the hole bottom. Thermal conduction does not any longer limit the heat penetration depth. The keyholing process here is the same as that described above, but affords deeper penetration. If the beam or sample is moved, the molten metal flows in behind the hole translated through the material, thereby effecting the weld bead. The analysis of deep penetration welding with continuous YAG lasers is given in [8], and with CO_2 lasers in [9].

The schematic diagram of the progress of deep penetration welding is shown in Fig. 8.12 [9]. As the laser power density at the hot spot reaches 10^6 W/cm^2, a small region of material begins to vaporize since the beam delivers energy so rapidly that the mechanisms of thermal conduction, convection, and radiation have no time to remove it. The metal vapor pressure does not allow the hole

vaporized to close under the action of hydrostatic forces of the liquid metal. At a definite speed of traverse of the laser beam, the hole translated through the material acquires the dynamic stability.

The metal melts ahead of the hole and solidifies behind it after the beam has passed. As noted above, the hole allows the beam to penetrate into the part, thus enabling a more effective absorption of energy. The penetration depth comes to saturation when the vapor pressure in the hole becomes insufficient to counteract the hydrostatic and hydrodynamic forces, so the melt fills the hole, forming a narrow weld bead with a large depth-to-width ratio (aspect ratio). As distinct from the hemispheric shape of the fusion zone formed in welding by conventional techniques [9], the fusion zone formed in laser keyholing has a more sharply defined shape since the beam creates a nonsteady-state cylindrical heat source in the target [10].

Laser keyholing makes it possible to weld metals at high speeds with a minimum of heat input to the region adjacent to the fusion zone, which results in a very little distortion and improved quality of the weld. The fusion penetration is as a rule inversely proportional to the weld speed at a given laser power input. Correspondingly, the fusion penetration is proportional to the power at a constant weld speed [9].

The expressions presented, for example, in work [3], relate such quantities as the weld rate, material thickness, and laser power. With a decrease in the weld rate at a constant laser power, the size of the molten pool around the keyhole increases in proportion to the energy per unit seam length. The penetration depth then sharply decreases and fusion zone becomes hemispheric, which corresponds to the conditions of thermal conduction melting [3]. The maximum penetration varies approximately as $P^{0.7}$, where P is the laser power [9].

It is not only the heat input, but also the angle of beam convergence, α, and the focal spot size that are of importance in shaping the weld. Work [11] contains the results of experiments for weld efficiency using two double-mirror Cassegrain reflectors. The angle α was 10 and 45° and the diameter of the spot at the focus of both reflectors was not greater than 0.3 mm.

Deep penetration welds with penetration of 6 to 8 mm were made at a weld speed of 60-70 m/h, laser power of 6-8 kW, and $\alpha = 45°$. An increase in power input added little to penetration but increased the weld width, largely in the middle and in lower portions of the cross section of the weld.

In the experiments performed with the beam whose angle of convergence was 10°, the weld penetration proved much in excess of 8 mm and reached up to 24 mm. The weld penetration as a function of laser power P at different values of α is shown in Fig. 8.13.

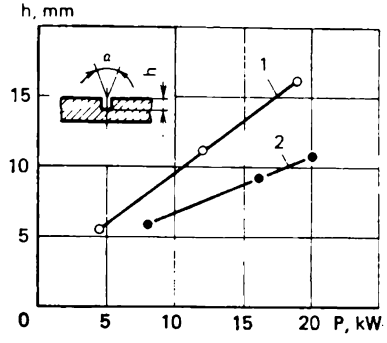

Fig. 8.13. Weld penetration h as a function of laser power P: *1*, $\alpha = 10°$ and $v_w = 86$ m/h; *2*, $\alpha = 45°$ and $v_w = 36$ m/h

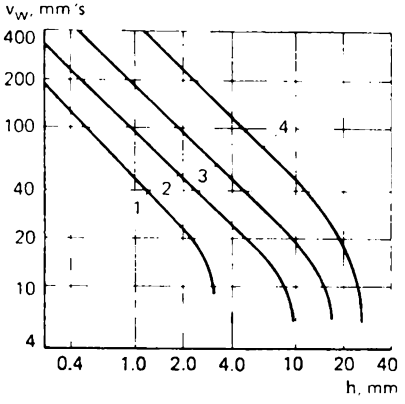

Fig. 8.14. Characteristics of laser welding: *1*, 1.5 kW; *2*, 5 kW; *3*, 10 kW; *4*, 25 kW

As is evident from the plots, the penetration depth h is smaller at a large angle of convergence. This is because the beam focused at a point slightly below the surface irradiates too large a spot and so delivers a decreased power per unit area. The requisite condition for obtaining weld depths in excess of 10-12 mm in the welding of carbon steel at a rate of 80 m/h is to reduce the angle of beam convergence.

Work [9] presented the results of deep penetration welding of steel plates up to 50 mm thick. The estimates point to a high weld efficiency, which, to a certain extent, makes up for a commonly low efficiency of the laser proper. The weld efficiency is the ratio of the power needed to melt the volume of metal in the fusion zone to the power delivered to the metal by the laser beam. The melting efficiency which determines the efficient use of the laser power to produce a weld joint is

$$\eta_m = (mcT'_m)/P \tag{8.6}$$

where m is the mass of melted metal, c the specific heat, T'_m the normalized melting temperature corrected for the latent heat of fusion, and P the laser power.

The total efficiency of the welding process is

$$\eta = \eta_T \eta_m \tag{8.7}$$

where η_T is the thermal efficiency.

Direct calorimetric measurements of the absorbed irradiance indicate that the absorption of the beam during the process of deep penetration welding is greater than 90%. Figure 8.14 illustrates the

plots of weld speed v_w as a function of controllable penetration depth h, which determine the efficiency for the use of the incident laser power in melting of a number of pure metals. The melting efficiencies in excess of 70% are attainable in practice for materials with lower thermal diffusivity. This means that over 70% of the absorbed energy goes into melting the material and the losses due to heat removal from the fusion zone do not exceed 30%.

The results show that the amount of laser energy required to produce a weld is generally about one tenth the energy expended per weld in the conventional process of fusion welding. This suggests that the total energy per unit weld length, including the energy lost in converting electric to optical energy is comparable to that required in arc-welding processes [9]. These factors along with the ability of lasers to produce weld joints of improved characteristics at high rates explain why the laser has become an important tool in many welding applications.

8.2. LASER WELDING TECHNOLOGY

In general, it is necessary to take the following steps to develop the desired laser welding process and to optimize its parameters [2]:

(1) select the proper type of laser;

(2) design the weld joint of the adequate configuration;

(3) estimate the optimal pattern of the beam and beam parameters depending on the materials of joint elements, their thickness, and limitations on heating temperature;

(4) design the equipment so as to make the most of laser welding practice.

Before deciding on a laser welding process or any other process of metalworking, a thorough technical and economic analysis of laser use must be performed proceeding from the point that laser processing justifies the cost and effort where conventional techniques are difficult or impossible to realize.

The choice of the type of laser depends on the total laser power required, power loss due to reflection from the surfaces of pieces to be welded, weld efficiency, and other factors [2]. Comparison between the weld efficiencies attainable with the use of YAG lasers and CO_2 lasers shows that pieces more than 5 mm thick should be welded with CO_2 lasers since they afford a higher weld efficiency, have a longer service life, and can produce welds with penetration of 20 mm and more. YAG lasers are more suitable for welding thin pieces because the power loss due to reflection from the pieces is very low and, besides, the laser setup incorporating a solid-state laser is small in overall dimensions. For example, a 200-W YAG laser can weld aluminum and copper foil up to 30 μm thick at a

rate of 1 m/s, while the beam from a 200-W CO_2 laser scanned at 0.1 m/s does not melt the surface at all [2].

Both continuous laser welding and pulsed (spot) laser welding find practical applications. Pulse welding can be used to make spot welds and butt seam welds by overlapping pulses. The advances in laser engineering have led to the development of high-power YAG lasers and repetitively pulsed CO_2 lasers yielding appreciable average powers at a high pulse repetition rate. These lasers can seam-weld pieces up to 2 mm thick.

Continuous laser seam welding is practically done only with CO_2 lasers.

Pulse welding. Since seam welding with early lasers was impractical because of the slow speed along the seam, the efforts were primarily made to develop pulse welding.

The pulse welding technique has become a versatile tool used to perform a variety of jobs [2, 3]:

(1) spot-weld and seam-weld electronic device parts from refractory metals and alloys;

(2) butt-seam-weld thin wall elements which must comply with stringent requirements for residual stresses and weld face quality;

(3) weld dissimilar metals and alloys;

(4) spot-weld elements of integrated circuits and precision instruments;

(5) weld part sections that are otherwise difficult to access, readily deformable pieces, strongly heat-liberating parts, and parts which call for small heat-affected zones and thorough cleanliness in manufacture.

To implement the process of spot welding, it is first necessary to select the proper type of laser and pulse parameters, determine the position of the focal point relative to the target surface, and duly prepare the joint faces for welding. Besides, depending on the task to be dealt with, it may be desirable to meet one of the following requirements:

(1) limit the HAZ size if the job to be done is to weld metal foil to semiconductors or to produce welds near heat-sensitive elements;

(2) limit material blowoff from the interaction region to obtain the weld joint of high strength;

(3) limit the temperature gradient;

(4) minimize the time of contact between the solid and the liquid phase to exclude the formation of intermetallic bands and brittle layers after HAZ solidification;

(5) increase the weld penetration without material ejection so as not to reduce the weld strength;

(6) apply cover gases or weld in vacuum to protect the parts against oxidation.

It is certainly impossible to meet all or most of these requirements simultaneously. Considering that the material in question is a solid with definite thermal constants, the solution to the problem stated can be sought by defining the optimal pulse length, power density required, and power density distribution in space. This problem can be regarded as a specific case of the problem on control of the system with distributed parameters [3], but the general solution is difficult to obtain since not all the requirements are compatible. For example, an increase in the power density may favor a greater penetration but at the sacrifice of the increased volume of blowoff material.

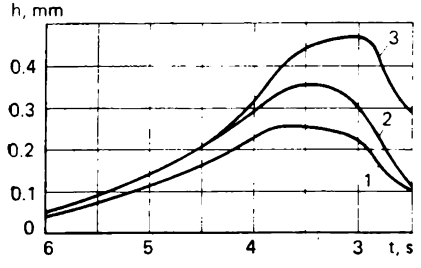

Fig. 8.15. Maximum penetration depth versus pulse duration at $E = 15$ J: *1*, tungsten, *2*, copper; *3*, aluminum; the scale of t is logarithmic

The analysis of the laser heating problem leads to the following main requirements to be imposed on the laser pulse parameters.

Pulse duration. For each material and for each thickness of the workpiece to be welded there is an optimal range of pulse lengths, within which a weld joint can be made without excessive ejection of the melt from the fusion zone. This pulse length range varies with the type of material. With an increase in the pulse energy, the optimal range of pulses shifts toward larger values of τ_p. A definite pulse length, at a given constant pulse energy, can yield a spot weld with a maximum penetration depth (Fig. 8.15). The peak of the curve is obvious since a short pulse with energy E has little time to melt the material, while a long pulse with the same energy E delivers a low power density to the surface. A similar tradeoff between these parameters exists in the conditions of "pure" evaporation. If we limit the irradiance to avoid material blowoff, it will be impractical to raise τ_p above $\tau_3 = 10\, r_f^2/a$ [3].

Pulse energy. This parameter has a strong effect on the welding process since it determines the total amount of heat absorbed in the fusion zone and entails changes in the pulse length, pulse structure, and beam divergence. Filters or aperture stops are commonly used to adjust the pulse energy.

The choice of the laser power density can be made by way of computations if the absorption coefficient of a material at a given laser wavelength is known and also the angle of beam incidence and the state of the target surface are allowed for. The desired parameters of the laser setup that has to adjust E and τ_p over definite ranges should be chosen after estimating $q_c^{(1)}$ on the basis of the known

values of the thermal and optical constants of the material of interest and the focal spot radius. The value of τ_p enables us to compare it with one of the characteristic times involved in the choice of the procedure of calculation of thermal processes. It is then possible to determine the optimal pulse length and specify the pulse energy required for welding. Pulse parameters are defined more exactly from experimental findings.

A rough estimate of the penetration depth along the z axis of a semi-infinite solid at the instant t_v when the surface rises to the vaporization temperature T_v can be made using the equation

$$h = 3.54/T_m \tag{8.8}$$

A more accurate value of h can be found by solving the transcendental equation

$$hT_m = 3.54 \text{ erfc } (h/2\sqrt{at_v}) \tag{8.9}$$

Consider how the weld penetration into a material varies with the pulse duration τ_p. Use the model for a semi-infinite solid with a surface Gaussian heat source. The temperature along the z axis can be estimated using the formula

$$T(0,\ Z,\ \tau) = \frac{P_0}{4\pi\lambda\sqrt{\pi a}} \int_0^{\tau} \frac{\exp(-z^2/4at')\,dt'}{\sqrt{t'}\,(\tau_0 + t')} \tag{8.10}$$

where P_0 is the effective constant power, a the thermal diffusivity, τ the pulse length, $\tau_0 = t_0 = (4ak)^{-1}$, and t' the integration variable.

Equation (8.10) can be used to perform calculations by setting T on the left side of the equation equal to T_m and then evaluating the integral of various values of h and τ_p. The calculated results for copper, aluminum, tungsten, and corrosion-resistant steel at a concentration coefficient k of 0.74×10^6 cm^{-2}, focal spot radius r_f of 25 μm, and different values of laser energy E are shown in Figs. 8.16 and 8.17. As the pulse energy grows, the upper limit of the pulse length that does not yield the melt spot shifts into the region of longer pulses. A shorter pulse with a higher power effects deeper penetration but vaporizes a large volume of material. This explains why it is necessary to bound the pulse length range both below and above at a constant pulse energy. This optimal range for copper, aluminum, and corrosion-resistant steel lies within $10^{-4} < \tau_p < 5 \times 10^{-4}$ s, $5 \times 10^{-4} < \tau_p < 2 \times 10^{-3}$ s, and $5 \times 10^{-3} < \tau_p < 8 \times 10^{-3}$ s respectively.

Metal blowoff is commonly assigned to two causes: the reactive vapor pressure resulting from the nonuniform power distribution over the hot spot and the combined effect of admixtures and

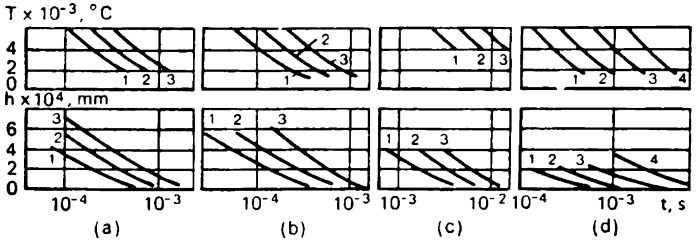

Fig. 8.16. Temperature at the center of the hot spot and penetration depth as a function of pulse length: (*a*), copper, *1*, 10^{-2} J, *2*, 2×10^{-2} J, *3*, 3×10^{-2} J, (*b*), aluminum, *1*, 2.5×10^{-3} J, *2*, 5×10^{-3} J, *3*, 10^{-2} J; (*c*), tungsten, *1*, $5 \times \times 10^{-2}$ J, *2*, 10^{-1} J, *3*, 0.3 J; (*d*), corrosion-resistant steel, *1*, 10^{-3} J, *2*, $2 \times \times 10^{-3}$ J, *3*, 4×10^{-3} J, *4*, 10^{-2} J

dissolved gases in the molten pool. The melt flushing process can be controlled by both reducing the laser power and selecting the requisite conditions of beam focusing [3].

Figure 8.18 illustrates examples of the laser weld joints of metal sheets, wires, wires to massive parts, and case walls butt welded to form leak-tight cases [2, 3, 6]. For good quality welds to be made, it is essential that the fixturing should ensure the specified fit-up tolerances for weld joints since excessive misalignments and gaps between the parts to be joined have an adverse effect on the absorption of laser energy. The vertical misalignment and the gap between the parts to be butt welded should be no larger than 0.25 and 0.15 of the part thickness, respectively. The gap between the sheets to be lap welded should not exceed 0.25 of the sheet thickness [2]. Adherence to these restrictions will lead to a higher weld efficiency and good reproducibility and quality of welds.

A number of suggestions have been put forward to improve the quality of laser welds. For example, in Pat. No. 51-32870 (Japan), a proposal has been advanced for butt welding of parts with a laser

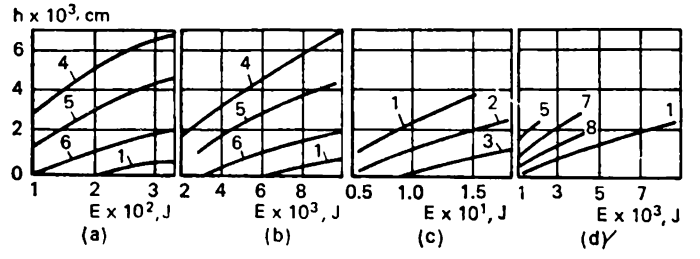

Fig. 8.17. Penetration depth versus pulse energy for welding copper (*a*), aluminum (*b*), tungsten (*c*), and corrosion-resistant steel (*d*) at pulse lengths of 10^{-3} s (*1*), 2×10^{-3} s (*2*), 4×10^{-3} s (*3*), 10^{-4} s (*4*), 2×10^{-4} s (*5*), 5×10^{-4} s (*6*), 4×10^{-4} s (*7*), and 6.5×10^{-4} s (*8*)

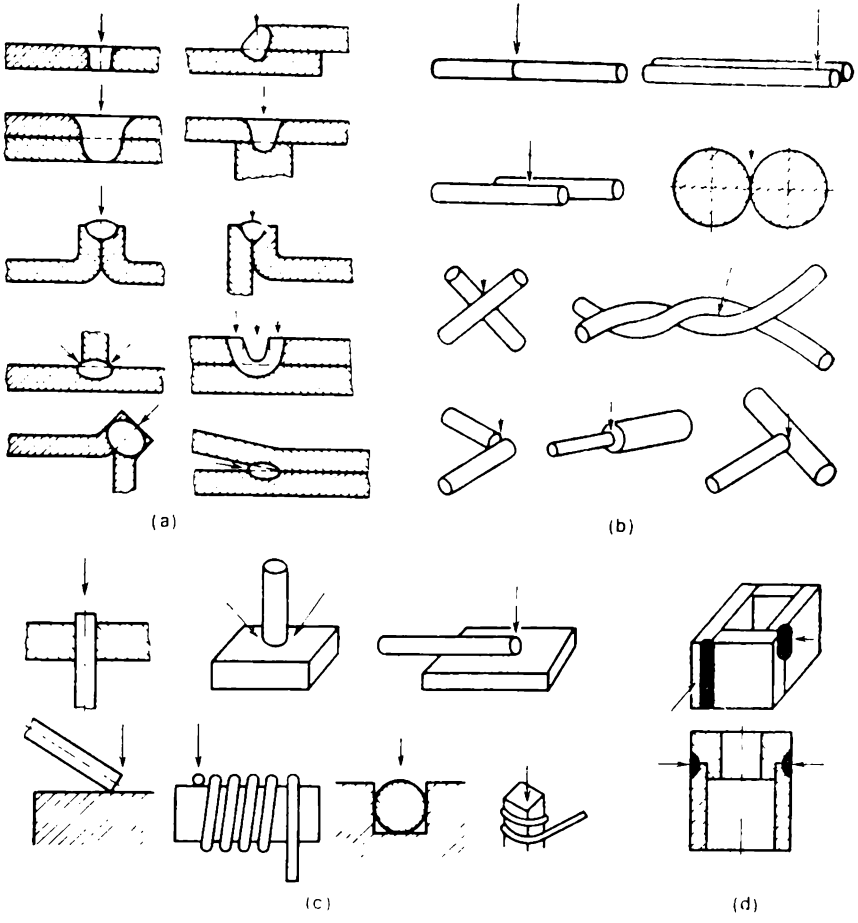

Fig. 8.18. Types of weld joints between sheets (*a*), wires (*b*), wires and massive pieces (*c*), and walls to form air-tight cases (*d*)

beam whose focal point is forced to shift during the pulse dwell time by the focusing lens as it reciprocates along the beam axis. Welding is begun with a defocused beam which melts the butt edges to a small depth. The focusing system is then moved downward to shift the focus to a position in which the beam effects a maximum penetration. At the final stage, the focal point is brought back to its original position.

The suggested method reduces the probability of melt flushing, improves the weld appearance, and increases the joint strength.

In one more variant of the welding technique described in the above patent, an oscillating beam was used to ensure a more even power density distribution over the hot spot and better control of the depth of penetration. To achieve the effect, one of the cavity mirrors is brought into a vibratory motion in step with the emission from the pump lamp. Transverse oscillations of the beam can be set up by periodically shifting the focusing unit of the laser head [2].

In Japanese Pat. No. 50-108737, a method of welding with two successive pulses has been described to afford better conditions of

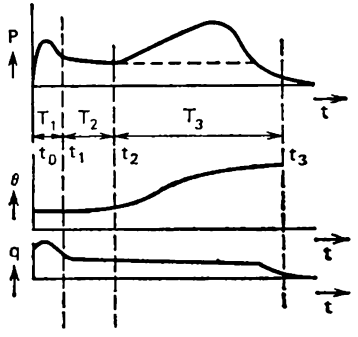

Fig. 8.19. Laser power P, angle of beam divergence θ, and power density q of two pulses shot in succession

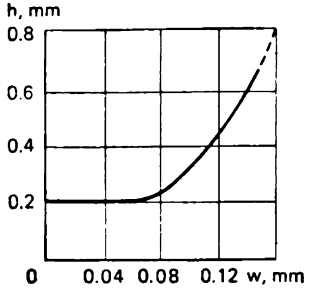

Fig. 8.20. Penetration depth h versus air gap w between two plates

shaping the weld. The effect is illustrated in Fig. 8.19. The first pulse with a lower energy and smaller divergence than the second is focused to a spot of a smaller size but with a higher power density to effect intense absorption of the irradiance at the start of the laser-material interaction. The second pulse with a higher energy and greater divergence is focused to a larger spot to provide for the desired penetration. Laser beams from a pulsed CO_2 laser and a CW CO_2 laser can be used for welding in the above described manner.

An increase in the gap between the pieces to be lap welded decreases the fusion area and, hence, reduces the joint strength. The effect of the air gap and fusion area on the strength of spot-welded lap joints has been treated in [2].

The plot of the weld penetration h versus the air gap w between the plates 0.2-0.6 mm thick from corrosion-resistant steel and titanium is shown in Fig. 8.20 [12]. At a gap of up to 0.07 mm, the penetration depth does not change since the melt fluidity is insufficient for the liquid metal to penetrate more deeply into the narrow gap. Increasing the gap from 0.08 to 0.12 mm results in an almost linear increase in penetration since the melt flows more freely into the gap as the beam penetrates into it and additionally heats up

the side surfaces. An increase in the gap size up to 0.15 mm leads to a further increase in the melt depth due to cratering, as revealed by the metallographic analysis. At a 0.2-mm wide gap, the beam does not produce a good quality weld since the melt has no time to fill the gap before its solidification. In welding the parts used in instrument making, the thickness of which reaches 50-80 mm, a gap of about 0.10-0.12 mm is advisable.

Coatings on the parts to be welded are regarded as separate plates of definite thermal conductivity. Practice shows that even a large difference in thermal conductivity between the parts and coatings does not change the total penetration since the coating thickness is small.

Welding of plates, wires including, which have intermediate layers of adhesives, vanishes, and enamels, in the conditions of higher laser energies suitable for welding pure materials involves a partial evaporation of the material and cratering. A reduction of laser energy by 30-40% ensures a good weld since the insulation cannot vaporize completely and therefore decreases the total thermal conductivity of the fusion zone. This reduces the size of the fusion zone and raises the temperature of the surface layer to the boiling point of the base metal.

Pulse welding of the parts and elements of electric low-power machines should be done with a convergent beam. Investigations reveal that the molten pool produced by a divergent beam tends to assume a convex shape under the action of surface tension forces and internal pressures, which push the melt into the region where the incident irradiance is higher, thereby intensifying the vaporization process. In contrast, the metal melted by a convergent beam tends to flow into the region of a lower power density, which results in a more uniform heating and better quality of the weld. A convergent beam also ensures better conditions of heating of the parts located at an angle to the incident radiation.

In welding parts to wires, it is good practice to reduce the thickness b of the flanges of necks relative to the wire diameter d (Fig. 8.21). In this case, a greater amount of heat removed along the wire length will be offset by the heat transferred from the flanges into the plate.

The laser energy coupled to the weld zone should not be too high, but only enough to bring the material to melting without intense vaporization. As shown by experiments, a reduction of energy at which intense vaporization occurs by 30-45% ensures the required balance. The thermal conditions balanced out over the entire cross section of the plate provide a good weld despite the fact that the two wire ends in the slot begin to melt earlier than the flanges.

The effect of the geometry of joints on laser weld quality. In the experiments described in work [13], steel and alloy instrument components with edges 0.3 to 1.0 mm thick were laser welded and

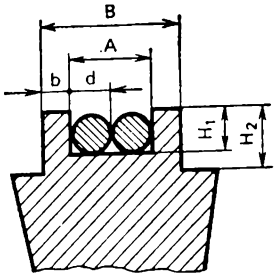

Fig. 8.21. Detail of the joint to be made by welding armature winding ends to the commutator of a low-power motor

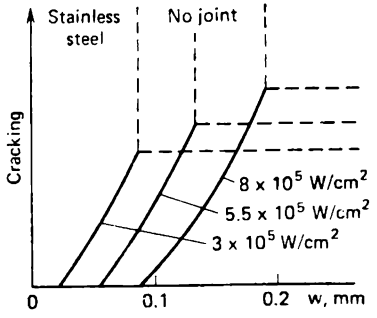

Fig. 8.22. Tendency of weld metal to develop cracks depending on the size of root gap between parts

checks were made to determine the quality of welds depending on the types of joint, edge preparation, and gap sizes. The laser setups used for the purpose provided 2 ms and 4 ms pulses containing 3 to 15 J of energy. The focused spot on the target surface was 0.2 to 1.0 mm^2 in area.

As mentioned above, the gaps between the parts to be laser welded must be held to a minimum to avoid hot cracking in weld joints. In experiments [13], pulses of the same energy and duration produced a number of spot welds on 10 $\times$ 100-mm^2 samples positioned with a gap that was varied from 0.01 to 1.0 mm in welding operations. At a definite gap w, the spot welds developed cracks extending in the radial direction from the spot center. Beyond this gap limit, the spot welds exhibited a network of cracks. At a still greater value of the gap size, the pulse failed to produce a spot weld, although it melted the edges of workpieces. A longer pulse delivering a higher power density to the target was able to shift the onset of hot cracking toward the range of larger gaps, as seen from Fig. 8.22. However, although a longer pulse promotes the formation of a better weld, an increase in the laser power density leads to a more intense ejection of the melt and, hence, to cracking. It was found that scale-resistant and nickel steels were less prone to hot cracking.

Grooves, chamfers, and curved faces impair the welds since they are conducive to hot cracking.

The choice of the type of joint depends on the construction of the unit to be welded. In laser welding, however, a small volume of the molten pool largely determines the choice. Butt welding can be done in the most favorable conditions of metal melting and recrystallization. It is certainly not always possible to butt weld the bodies. The use of other types of joint raises the problem of pro-

ducing quality welds, while ensuring the proper accuracy of unit assemblies.

Experiments [13] revealed that hot cracks sometimes appeared in longitudinal and circular fillet joints. To clarify the causes, overlapping pulse welding of the simulators of various parts was done under different conditions. The direction of the beam coincided with the bisectrix of the angle between the parts to be joined. The laser setup delivered 2 to 8 J of energy in a 4 ms pulse to seam weld the simulators at a speed of 5 to 15 cm/min.

The second pass failed to eliminate the cracks since the laser energy lower than or equal to the energy coupled initially could not

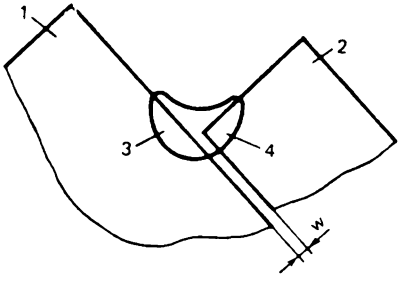

Fig. 8.23. Corner joint preparation: *1*, *2*, pieces to be welded; *3*, *4*, areas to be melted; *w*, root gap

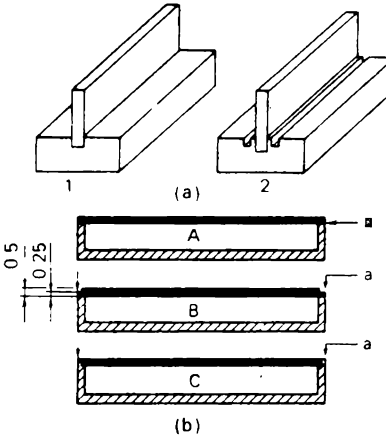

Fig. 8.24. Joint designs (*a*) without butt edges (*1*) and with butt edges (*2*) and laser weld joints in device casings (*b*)

effect the penetration to the single-pass weld root which contained cracks. An increase in energy led to melt ejection and to an imperfect seam.

The corner joint is most unfavorable for laser welding. The profile of the joint is such that the beam impinging directly at the point of joint causes a sharply nonuniform heating of the spot. The fusion areas in parts *1* and *2* are different (Fig. 8.23). Since in actual conditions the gap *w* is unavoidable, the area *3* is generally two or three times as large as the area *4*. Consequently, each part contributes a different fraction of the metal to the formation of the molten pool.

In producing circular welds or longitudinal double-sided welds with or without fixation of joint edges in slots, as illustrated in

Fig. 8.24*a* on the left, either radial or transverse stresses appear, which cause throat cracks along the weld seam.

To ensure uniform heating, melting, and recrystallization of the weld zone, a suggestion was put forward to groove one of the parts to be joined so as to raise edges on one or two sides, as shown in Fig. 8.24*a* on the right. This type of joint calls for a 10 to 15% decrease in the pulse energy because of the limited propagation of heat only into the flanges formed by grooving. In this case, the laser beam in fact produces a butt-welded joint as it melts the raised edges. The joint in section has the shape of a transition region from one part to the other, which decreases the concentration of stresses in the weld.

The suggested method made it possible to produce longitudinal corner welds practically without cracks and to reduce cracks in circular and double-sided welds by 20%. In the latter case, the stresses arising from the contraction of the metal in the radial and transverse directions and increasing the assembly rigidity were responsible for cracking.

Grooving, such as illustrated in Fig. 8.24*a* on the right, ensures good conditions of heating, molten pool formation, and metal crystallization. The volume of the weld pool formed after flange melting is enough to fill the gap up to 0.2 mm wide at a thickness of each part of 0.5 mm.

This type of groove welding with lasers can be used to advantage for sealing the cases of instruments and packages of integrated circuits.

Package sealing with electron-beam and argon-arc welding results in a large percentage of rejects due to cracking of the glass insulators of leads located near the seam under the action of heat and contraction of the metal.

Overlapping pulse welding does away with the problem of cracking without resorting to complex equipment, which simplifies the welding process. Besides, hermetic weld joints, as shown in Fig. 8.24*a*, make the welded assembly repairable.

A laser welder [13] used for hermetic sealing of cases provided 4 ms pulses with 2 to 6 J of energy at a pulse repetition rate of 5 to 15 Hz. Air-tight welds were made by overlapping spots at a spot overlap ratio of 60%. The metallographic analysis showed that the welds produced with a very narrow HAZ had no cracks, pores, and voids.

So, the gap between the parts to be laser welded and edge preparation such as employed in conventional welding techniques promote hot cracking at the weld spot. Square edges formed by grooving enable the laser beam to produce a quality corner weld. This overlapping pulse welding technique used to seal IC packages improves the reliability of the welded assemblies.

The technique of sealing flat kovar cases with a 1-kW continuous laser operated in a pulse mode was described in [2]. The case walls were 1.02 mm thick and the cap was 0.51 mm thick (Fig. 8.24*b*).

The simplest variant *A* of Fig. 8.24*b* does not prevent the melt splashes from falling on IC elements. The variant *B* with a 0.25-mm thick step on the cap requires a less amount of heat. The variant *C* with a centering flange cut out on the case wall is an optimal choice but is more costly to produce. Welding is done by preliminarily tacking the cap at several points.

Welds were made in argon and other gases to protect the bead against oxidation with 230 W of laser power in a 0.5 ms pulse at a speed of 65 cm/min and a pulse spacing of 1.2 ms.

Laser welding of similar and dissimilar metals. The strength of laser welds depends on the geometry of the molten pool, structural changes in the cast nugget, and the properties of the melt of dissimilar metals. The alloy in the molten pool of dissimilar metals can form by way of diffusion and mixing of the metals [6].

The diffusion process depends on the melt temperature, melt lifetime, mutual solubility of metals, as well as the kinds of metals. The mechanical mixing of the liquid metal in the fusion zone can occur as the result of nonuniform heating and the metal-vapor back pressure against the melt surface.

If the lifetime of the melt is long, a homogeneous solid solution generally forms in the weld zone. In pulse welding, the melt produced in a very short time rapidly cools and solidifies. Under these conditions, the weld zone of dissimilar metals commonly consists of large portions of component metals with smeared boundaries between the portions [6]. This structure attests to the mixing of metals, and the smeared boundaries are likely to be the evidence of mutual diffusion of dissimilar metals.

Table 8.2 lists the results of tests for the strength of butt-welded joints of similar and dissimilar metals and alloys [3].

The welds of similar metals have a rather high strength and appreciable ductility and mainly display a columnar crystal structure.

Laser welding of dissimilar, mutually insoluble metals, for example, copper to tungsten, molybdenum, and tantalum gives a poorly shaped seam; an interface that serves as a bond between the welded metals is apparent. The weld joint ruptures under mechanical load.

In welding the metals that display an unlimited solubility in the solid state, such as copper to nickel, tantalum to titanium, the seam welded is chemically inhomogeneous, and its microhardness is nonuniform over the cross section, but, on the average, is higher than that of base metals.

As for the welds produced between the metals exhibiting a limited solubility in the solid state, for example, between nickel

TABLE 8.2. **Strength of Butt Welds of Similar and Dissimilar Metals**

Metal	σ, MPa	VT-7	T4	MRN	N4	M1	Bronze	N1	12Kh18N9T	St08kp	VT1	A1
Al	5	100%, M, B	100%, 110°, B	100%, 180°, B	100%, 110°, B	40%, 80°, S, b	60%, 30°, S, b	100%, M, B	—	—	100%, M, B	100%, M, B
VT1	50	80%, 30°, T, b	65%, 90°, S, b	45%, 5°, S, b	100%, M, B	50°, 110°, S, b	55%, 110°, S, b	—	—	—	100%, M, B	
St08kp	33	90%, 170°, S, b	—	50%, 90°, S, b	—	30%, 180°, S, b	75%, 270°, T, d	65%, 45°, S, b	100%, M, B	100%, M, B		

Bronze	50	90%, 180°, T, b	75%, 160°, S, b	100%, 270°, T, d	100%, 150°, T, d	80%, M, S, d	100%, M, B					
M1	25	57%, 90°, S, d	35%, 60°, S, d	35%, 180°, S, d	100%, 180°, S, d	95%, M, S, d						
N4	27	—	100%, M, B	—	100%, M, T							
MRN	73	75%, 0°, S, b										
T4	48	—	60%, M, T, d									
VT-7	45											

Notes: 1. In the designations of grades, the transliterated Russian letters denote the following elements: V, tungsten; T, titanium; kp, rimming steel; Kh, chromium; N, nickel; M, copper in nonferrous metal grades, as M1; M, molybdenum in ferrous metal grades,as MRN, where RN stands for refining.

2. Percentages indicate the ratio of the ultimate strength σ of a weld metal to that of a stronger metal. Degrees stand for the angle of bending of welded specimens at 0.7 mm radius of punch curvature.

3. The letters following percentages and degrees identify the following: M, multiple bending; S, weld seam; T, transition zone (HAZ); B, base metal; b, brittle failure; d, ductile failure.

and niobium, corrosion-resistant steel and molybdenum, and copper and titanium, the chemical analysis shows that the weld seam has regions with various contents of the welded elements, which include intermediate phases and eutectic layers. At the junctions between the parent metal and the weld zone, alternate interlayers of the eutectic and intermediate phases are often present, which reduce the weld joint strength.

Examples of pulse welding applications. *Welding of armature winding ends to the commutator of a low-power motor* [6, 14]. Joints between the winding ends and commutator bars are commonly made by various soldering techniques using, for example, tin-lead solders. The soldering process that includes such preliminary operations as mechanical or chemical wire stripping does not lend itself to automation.

From the analysis of the capabilities of such welding techniques as resistance, ultrasonic, argon-arc, electron-beam, and laser welding, it has been found that a laser is the best choice for welding copper wires 0.08 to 0.3 mm in diameter to the copper segments of commutators.

Since the laser beam acts as a surface heat source, it is necessary to arrange the conductors at the same level on the outer surface of the commutator. For this, the commutator bar illustrated in Fig. 8.25 has a neck with a slot where the coil ends are laid in one row [6]. The neck dimensions are: $A \cong 2d$; $b = 0.8d \geqslant 0.15$ mm; $H_1 = (1.2 \text{ to } 1.5)\, d$; $H_2 \geqslant H_1 + 0.2$ mm; $B = A + 2b$, where d is the wire diameter and b the flange thickness.

The slots are cut with a block of three mills separated by washers. The width of the block is chosen such that the slots milled allow space for the desired number of conductors. The use of the block of cutters speeds up the job and makes the sizes of slots and flanges identical.

The coil ends placed in slots are pressed out with adjustable-jaw pliers to secure them in position and provide good thermal contact with neck walls. This operation makes the assembly ready for automatic welding.

Figure 8.25*a* illustrates a commutator built up of segments *1* separated by mica punchings *2*. In Fig. 8.25*b* is shown the schematic diagram of an automatic laser welding machine comprising a laser, a mechanism to rotate the armature, and a system for automatic location of the site of joint to be welded. This system affords the stability of the process and enables the laser beam to fall accurate to 0.1 mm relative to the center of the site of joint and produce good welds on the revolving armature.

The system for automatic location of the joint site operates on the principle of the difference between the reflectivities of the segment *1* and mica punching *2*. Referring to Fig. 8.25*b*, let us briefly

describe the operating principle of the system. The light source *10* shapes a rectangular light spot 0.21 × 1.0 mm in size on the commutator bar neck. Since the light is incident at an angle to the commutator, the reflected light beam falls on a photosensor *7*. With the armature revolving, the light spot passes from the insulation

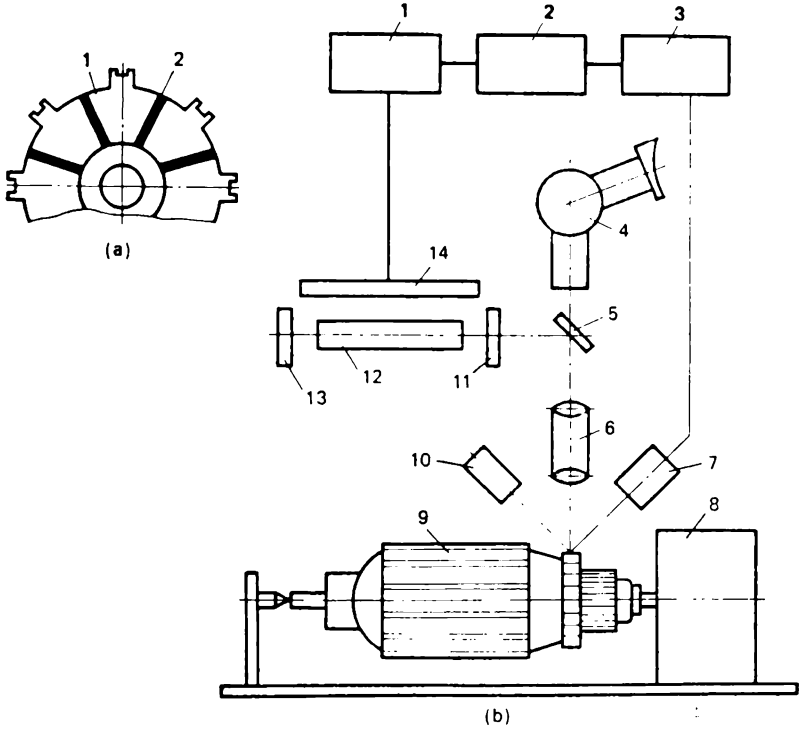

Fig. 8.25. Commutator: (*a*) shows copper segments *1* insulated with mica punchings (*2*) and schematic arrangement (*b*) of a laser setup for welding armature winding ends to the commutator: *1*, power unit; *2*, control unit; *3*, trigger pulse-shaping unit; *4*, lens for visual control; *5*, turning mirror; *6*, focusing column; *7*, photosensor; *8*, armature rotating mechanism; *9*, armature; *10*, light source; *11*, 50% reflectiong mirror; *12*, laser rod; *13*, 100% mirror; *14*, pump flashtube

to the segment, and a more intense light beam reflected from the segment causes the photocurrent in the sensor *7* to increase. As the photocurrent flowing to a trigger pulse-shaping unit *3* reaches a specified value, the unit *3* sends a trigger pulse to a thyristor which turns on and switches the laser welder. The system is set up so that at the instant when the trigger pulse enables the control unit *1*, the focusing column *6* faces the center of the bar neck. The focused

laser beam strikes at the center exactly at this instant irrespective of the commutator pitch and the rotational speed of the armature. The system does not need changeover for the tasks involving the operations on the armatures of the same type. After completing the last weld, the system is cut off automatically.

In the system described above, the laser emits approximately rectangular pulses 2 or 3 ms in duration which contain 1 to 10 J of energy coupled to a spot 0.6 to 0.9 mm in diameter, depending on the wire diameter and the number of wires in the slot.

The described welding systems produces good weld joints without the need to strip wires of insulation, but calls for about a 10% increase in pulse energy as against the energy required to weld bared conductors. Wire stripping enables a 10 to 15% increase in the weld strength. However, this operation adds very little to the weld strength with a decrease in the wire diameter.

Welding of clockwork parts. In experiments [6], a quasi-continuous laser emitted 8 J pulses 0.5 to 0.8 ms in duration to weld a 1.0×0.2-mm steel filament of a spiral hair spring to a 2.5-mm diameter block 1 mm thick. The beam delivered a power density of about 4×10^5 W/cm^2 to a spot 0.15 to 0.2 mm in size to effect a weld penetration of 0.5 mm.

Since the HAZ was very narrow, the weld showed no evidence of cracking or other defects impairing the mechanical properties of the hair spring.

Prior to testing the balance-wheel in service conditions, the metallographic analysis of the weld pool was made and checking conducted for the weld joint strength. Selection checks for the spring rupture strength on 100 pieces from the batch of 1 000 pieces revealed that a force needed to break away the spring from the block ranged from 3 to 12 N. From the metallographic analysis it was found that the weld nugget was quite sound, and without pores and cracks. Laser welding in air imparted temper colors to the metal surface, but the welds produced in a nitrogen or an argon atmosphere showed no temper colors. After welding of the balance units, there was no need to straighten the coils of the spiral spring in its plane; in the conventional process, this operation must be done on all the balance assemblies. Functional tests on watches with laser-welded hair springs were run at the reliability laboratory of the 2nd Moscow watch-making plant. An average daily isochronous error was 25 s as against 60 s observed in watches with hair springs fastened in the conventional manner.

8.3. CONTINUOUS LASER CUTTING

Multikilowatt continuous lasers are promising tools for use in material removal applications, namely, hole piercing and material shaping or cutting to separate the pieces, or to perform scribing,

fracturing, marking, and trimming operations. Cutting operations mostly involve CO_2 and Nd-YAG lasers. CO_2 lasers possess the highest practical promise because they produce high values of continuous power at efficiencies ranging from 15 to 20% and emit radiation at 10.6 μm that is absorbable by many materials, both organic and inorganic: metals, glass, quartz, plastics, ceramics, paper, wood, and cloth.

Cutting can be done in three ways, namely, by moving the laser with respect to the material to be cut, moving the material below the stationary focused spot, and moving the beam of the stationary laser by a series of lenses and mirrors. The second and the third method are most practical.

Direct cutting by vaporization involves the total removal of the material along the line of the kerf. Scribing is the process of cutting a continuous groove into the surface or drilling closely spaced small holes with the subsequent splitting of the material along the scribed line. A variant of scribing used for brittle materials is thermally induced fracturing, i.e. shaping without vaporization. The moving heat source produces stresses in the material, which cause small cracks. The material can then snap easily along the path of travel of the heat source.

Laser cutting is generally a gas-assisted process. In cutting readily inflammable materials, the jet of an inert gas such as nitrogen delivered to the point of incidence of the laser beam assists in increasing the cutting rate by blowing the molten material out of the hole. In cutting metal materials, a reactive gas such as oxygen both blows away the molten material and contributes to the material removal owing to the energy of an exothermal chemical reaction between the metal and oxygen.

The amount of energy required to cut materials with a CW laser greatly depends on the optical and thermal properties of the target. Polished metals strongly reflect radiation emitted at 10.6 μm, but as the laser heats the material to its ignition point in the atmosphere of the oxygen-assist gas, the absorption of the beam greatly increases.

The principle of gas jet assisted laser cutting is shown in Fig. 8.26. The laser beam is focused by a suitable optical system onto the workpiece. The jet of oxygen is brought onto the workpiece through a nozzle which is coaxial with the laser beam. As mentioned above, oxygen serves a dual purpose: it blows away the molten material through the kerf or out from under the nozzle and oxidizes the surface, thus increasing the material absorptivity and, hence, the cutting rate. The laser beam is a high-intensity heat source, therefore it is able to produce cuts with a narrow kerf width and a small HAZ and can cut at higher rates than any other conventional heat source. The kerf width is equal to or smaller than the focal spot diameter and the HAZ is 0.05 to 0.2 mm thick.

In the oxygen-assist cutting process, the cutting rate grows with the laser power, but it certainly depends on the optical and thermal constants of a material and sheet thickness. Plots of the cutting speed as a function of laser power P, oxygen flow rate, and material thickness h appear in Fig. 8.27. At power levels of 300 to 500 W, the cutting rate of steel and titanium reaches a few meters per second, but this power is still insufficient to cut strongly heat-conducting materials such as copper and aluminum. A laser with a power of up to 20 kW can rapidly cut copper and aluminum even without the oxygen assist [3].

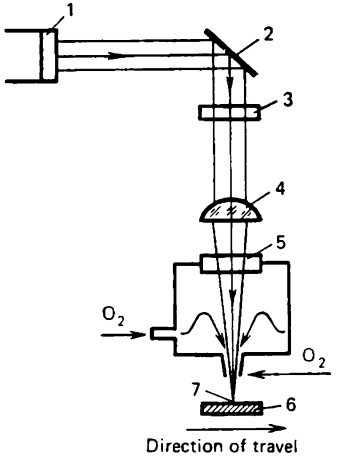

Fig. 8.26. Laser cutting with an assist-gas jet coaxial with the laser beam: *1*, laser; *2*, mirror; *3*, shutter; *4*, lens; *5*, window; *6*, workpiece; *7*, focal point at surface

The cutting rates for some materials of various thicknesses cut at different values of laser power are listed in Table 8.3.

In the case of incombustible materials, the gas jet mainly serves to blow away the products of vaporization and liquid droplets from the kerf and to remove heat from the cut edges. This cooling effect is of much importance in cutting dielectric materials since it

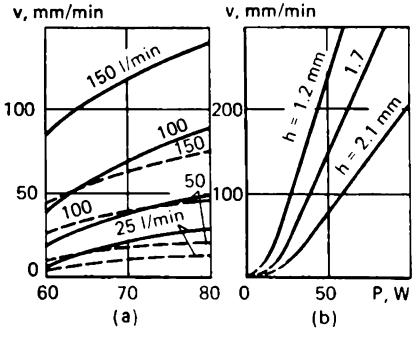

Fig. 8.27. Cutting rate v as a function of laser power P: (*a*) for 1-mm thick low-carbon and corrosion-resistant steels (full and dashed curves respectively) at different oxygen flow rates; (*b*) for quartz glass 1.2, 1.7, and 2.1 mm thick

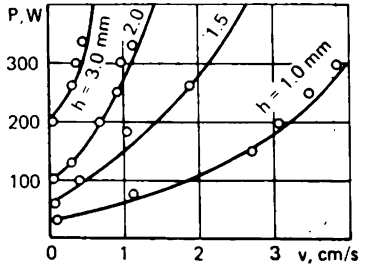

Fig. 8.28. Laser power P versus cutting rate threshold v for scale-resistant steel 3.0, 2.0, 1.5, and 1.0 mm thick

TABLE 8.3. Gas-Assist Laser Cutting of Materials

Material	Laser power, W				
	100	200	250	850	1 000 (no assist gas)
Low-carbon steel	1.0/1.6	4.75/0.635	0.5/0.635	2.2/1.8	6.3/2.3 (15)
Corrosion-resistant steel	1.0/0.94	0.46/0.635 0.15/0.762	0.5/2.6	9.0/0.36	4.7/1.27 (20)
Titanium		0.51/0.203[a]	0.6/0.2[a]	0.5/3.24	
Niobium		0.13/0.127[a]			
Tantalum		0.13/0.127[a]			
Zirconium		0.25/0.914[a]			
Plastic-coated steel		0.89/0.635			
Carborundum		1.57/0.762			
Wood		17.5/0.203	18-50/0.1-0.2	5.0/4.5[n]	
Asbestos cement		6.35/0.025	6.3/0.025[a]		
Glass		0.381/0.101 1.57/0.381 0.20/0.101	4.0/0.1[a]		9.5/1.52 (20)
Nylon		0.76/6.10			
Plexiglass					25.4/1.52 (8)
Aluminum					12.7/2.3 (15)
Quartz	1.2/0.5				
Rubber	2.0/1.9				
Ceramics				6.5/0.6[n]	

Notes: 1. The numbers in the numerator and denominator denote the material thickness (mm) and cutting rate (m/min), respectively; the numbers in brackets denote laser power in kW.
2. The superscripts *a* and *n* stand for air and neutral gas (argon), respectively. The numbers without superscripts are the data on cutting with oxygen assist.

does not allow the edges to melt and scorch. The gas jet also protects the focusing optics against damage due to spatter or smoke.

CW laser cutting with a jet of inert gas blown around the cut is especially applicable to brittle and flammable materials such as ceramics, glass, plastics, paper, and wood. These materials strongly absorb radiation at 10.6 μm.

In one experiment, metals and dielectric materials were cut with a multimode CO_2 laser in the 500 W range. A 150-mm focal length lens focused the beam to a spot of ~0.5 mm in diameter. The conical nozzle for the beam and the gas jet had an exit diameter of 1.5 mm. The gas pressure in the cup was 0.3 MPa and the gas flow rate was ~0.5 l/s.

The cutting rate for metals with the assist oxygen markedly depended on gas pressures at low pressure levels, but weakly depended on pressures in the range above 0.25 MPa. The quality of cuts was better at higher gas flow rates and at shorter distances from the nozzle exit to the target. Figure 8.28 illustrates the plots of laser powers against maximum cutting rates for corrosion-resistant steel of various thicknesses [3]. The laser power and sheet thickness have a considerable effect on the upper limit of cutting rates.

The data on the parameters of CO_2 laser cutting of dielectric materials are available in [3]. Laser cutting of nonmetallic materials offers a number of advantages over conventional techniques: a high cutting rate and improved edge quality, ease of process automation, low distortion of samples, lack of tool wear, and clean surfaces of parts due to a reduced spatter of the molten material around the cut. The kerf is always clean, straight-sided, and has smooth edges; the thickness of the scorched layer is less than 0.1 mm. The edges of cuts made in organic materials show traces of slight charring. It is interesting to note that the width of the kerfs produced in relatively thick materials is narrower at the bottom than one would expect considering the beam divergence with distance away from the lens. This is due to the beam self-trapping (self-guiding) effect which appears as a result of the multiple reflections from the kerf sides.

Plastics, wood, ceramics, glass, and other materials up to 50 mm thick can be cut with a laser. The kerf width does not generally exceed 1 mm, although the beam diameter at a distance of 20 mm from the lens focus can reach about 7 mm. The reason is that the laser beam focused onto the sample surface partially vaporizes the sides of the narrow slit, thus forming a shielding layer of gases which absorb radiation and protect the kerf walls from further damage. The assist gas issuing from the nozzle mixes up with the vaporized material, and a very hot gas jet so produced cuts through the sheet material.

Laser cutting is a promising technique for textile industry. Laser cloth cutters are now available, which can cut cloths in a single ply or in multiple plys of a total thickness of 20-30 mm. The properly adjusted cutting process yields clean, unscorched cut edges. In multiple-ply cutting of such materials as capron and glass cloth, the plys are wetted or separated by tissue paper interlayers to prevent the ply cut edges from sticking together.

Scribing. Direct gas-assisted cutting of such brittle materials as ceramics, silicon, and glass often yields poor cuts because of a low thermal conductivity and large modulus of elasticity of these materials. A large power input along the line of cut overheats the cut edges and causes uncontrolled fracturing due to high thermal stresses. To minimize the total power input, it is common practice to use a laser operating in a pulsed mode. The laser delivers a high power density at a moderate power in a pulse to the substrate surface and drills a series of closely spaced holes. The substrate can then be easily split along the scribed line.

Some theoretical aspects. The simplest dynamic model for laser cutting is a heat source of constant power P that moves at a constant velocity v along the surface of an infinite plate of thickness h. For the steady-state conditions in the moving system of coordinates, the power of the heat source is equal to the absorbed laser power P_a in the case of cutting without the gas assist. If laser cutting is done with an assist gas, which initiates a chemical reaction after the surface reaches the temperature T_0 indicative of the effective material removal, an additional heat source of power $P_1 = Qm$ appears, where Q is the energy per unit mass, J/g, released as the result of chemical reactions and phase transitions; $m = b\gamma\, hv$ the material removal rate, g/s; $b = 2y_0$ the kerf width equal to the width of the isotherm for T_0; and ρ the material density.

Considering that the gas jet removes a certain amount of power, P_2, the expression for the total power of an equivalent heat source can be written as

$$P = P_a + P_1 - P_2 \tag{8.11}$$

For a nonuniform heat source, the power distribution over the spot and into the depth of the material is a complex function of coordinates. To simplify the problem, we can use a point source model, i.e. combine the heat source due to the chemical reactions with the laser heat source and assume that the kerf width is equal to the width of the material band heated to $T \geqslant T_0$. Besides, we assume that the thermal constants are independent of temperature and the kinetics of chemical reactions does not limit the cutting speed. The solution to the problem on heating a sheet of thickness h in the steady-state conditions will then take the

form [3]

$$T(r, x) = \frac{P}{2\pi\lambda h} \exp\left(-\frac{vx}{2a}\right) K_0\left(\frac{vr}{2a}\right) \tag{8.12}$$

where $r = \sqrt{x^2 + y^2}$ is the radius vector, λ the thermal conductivity, $K_0(u)$ the modified Bessel function of the second kind of order zero, and $u = vr/2a$ the dimensionless parameter proportional to the heat source speed.

Introduce the dimensionless variables $\varepsilon = vx/2a$, $\eta = vy/2a$, and the dimensionless parameter of total power W, absorbed laser power W_a, and power W_1 due to chemical reactions:

$$\begin{aligned} W &= P/2\pi\lambda h T_0 \\ W_a &= (P_a - P_2)/2\pi\lambda h T_0 \\ W_1 &= (2/\pi)\psi\eta \end{aligned} \tag{8.13}$$

where $\psi = Q/cT_0$ is the dimensionless thermochemical parameter which does not depend on the cutting conditions and accounts for the properties of the material and assist gas. From expression (8.12) for the isotherm of $T(r, x) = T_0$ we can obtain

$$W_a = \exp(\varepsilon) K_0^{-1}(u) - (2/\pi)\psi\eta \tag{8.14}$$

To determine the kerf width, we need to define a maximum width of the isotherm at T_0 from the condition $\partial T/\partial x\,|_{r=r_0} = 0$. Performing the requisite computations yields a system of equations:

$$\begin{aligned} W_a &= K_0^{-1}(u_0) \exp\left[-u_0 \frac{K_0(u_0)}{K_1(u_0)}\right] - \frac{2}{\pi}\psi\eta \\ \eta &= \pm u_0 \sqrt{1 - \left[\frac{K_0(u_0)}{K_1(u_0)}\right]^2} \end{aligned} \tag{8.15}$$

where $K_1(u_0)$ is the modified Bessel function of the second kind of order one.

From equations (8.15) we can calculate the values of W_a as a function of $u = vr_f/2a$, which is a dimensionless parameter proportional to the speed. The plots of W_a as a function of U are shown in Fig. 8.29 [3]. At large values of the argument, expanding $K_0(u_0)$ and $K_1(u_0)$ into a series gives

$$W_a = (2/\pi)\eta(1.9 - \psi) + 0.3 \tag{8.16}$$

From (8.16) it follows that $\partial W_a/\partial\eta$ is above zero when $\psi < 1.9$, i.e. W_a grows with η and points to steady conditions of cutting. When $\psi > 1.9$, $\partial W_a/\partial\eta$ is below zero and the conditions become unsteady. The value of W_a can be negative, in which case the actual cutting occurs by the reaction of the material with oxygen.

Let us estimate the region where the above model is applicable. It does not work at slow cutting speeds since the heat transfer from

the plate cannot be disregarded. At large values of the cutting speed, the model is inaccurate because the kerf width b can be smaller than the actual diameter of the focused beam spot. The heat source speeds for which the model is valid lie within $\sqrt{aB} < v < 2a/r_f$, where B is the coefficient of heat loss in 1/s. For metals this range is $0.1 < v < 1$ cm/s.

The quasistationary temperature at the center of a Gaussian heat source is

$$T(0, 0) = P/(4\pi\lambda h) \times \times [-E_i(-U^2/4)] \quad (8.17)$$

where E_i is the exponential integral function. In analogy with equations (8.13), we can write $W_1 = (2/\pi)\,\varphi U$, where $\varphi = (y_0/r_f)\,\psi$. Here, the parameter φ depends on the kerf width. Considering the contribution the chemical reactions make to the total power, expression (8.17) can be rewritten in the form

$$W_a = \frac{2}{-E_i(-U^2/4)} - \frac{2}{\pi}\varphi U \quad (8.18)$$

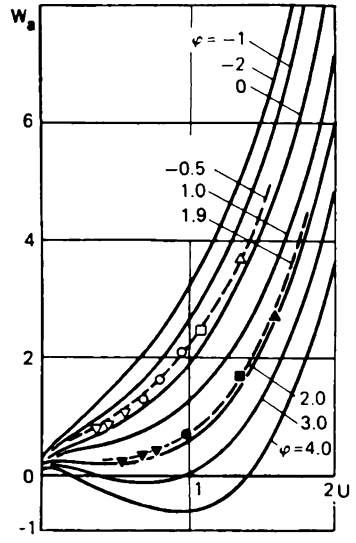

Fig. 8.29. Dimensionless power W_a versus dimensionless speed U calculated for a Gaussian heat source used in laser cutting. Light and dark symbols represent experimental results for scale-resistant steel and St3 steel, respectively, cut in thicknesses 0.5 mm (△, ▲), 1.0 mm (light and dark squares), 1.5 mm (light and dark circles), and 3.0 mm (▽, ▼)

As seen from Fig. 8.29, the regions of steady and unsteady conditions exist at $\varphi < 1.9$ and at $\varphi > 1.9$ respectively. In the range of low values of U, the results calculated for a point source and a Gaussian source coincide. As U exceeds 0.8, the results become different. From Fig. 8.29 it follows that even at $\varphi > 1.9$ in the range of high values of U, the unsteady conditions convert to steady ones. For example, the steady operation is apparent at $U > 1.4$ when $\varphi = 4$.

At a large speed v of travel of the Gaussian source, the temperature field tends to a simple shape in the limit [3]. This source, which rapidly moves along the surface of a plate of thickness h, can be thought of as a continuous source of power P_a distributed in a Gaussian fashion on the surface transverse to the direction of motion and uniformly into the depth of the plate. The heat thus flows only in the direction normal to the direction of motion of

this source. In this case, the temperature is only a function of η and can be defined by the relation [3]

$$T(y) = P_a/vh\sqrt{4\pi c\rho t_0}\exp(-y^2/4at_0) \tag{8.19}$$

where c is the specific heat, ρ the material density, $t_0 = 1/4\ ak$, a the thermal diffusivity, and k the concentration coefficient. A minimum absorbed laser power P_{min} required to reach the temperature T_0 for material removal is found from (8.19) at $y = 0$:

$$P_{min} = T_0 vhc\rho\sqrt{\pi/\lambda k} \tag{8.20}$$

where λ is the thermal conductivity.

As is obvious from (8.20), P_{min} increases with T_0 and v.

The energy input required to cut a material is a function of the specific energy Q_0 of cutting, which is the characteristic of a material and is independent of the conditions of cutting. The results of tests on defining the values of Q_0 for a number of materials cut in a wide range of speeds and powers are available in pertinent literature. Table 8.4 lists the values of the specific energy Q_0 for some materials.

TABLE 8.4. **Specific Energy for Cutting Some Materials**

Material	Q_0, kJ/g	Material	Q_0, kJ/g
Cloth-base laminate	50	Pine	0.9
Glass-cloth-base laminate	47	Oak	5.4
Lining plastic	2.0	Plywood	5.4
Board	0.8	Rigid PVC	1.8
Plexiglass	2.0	Oil-gasoline-resistant rubber	2.5
Asbestos cement	28	Gas-tight rubber	2.1
Asbestos	20	Opaque glass ceramic	25
Ceramics	30	Window glass	31
Composites	80	Quartz glass	45

Since the specific energy is $Q_0 = cT_0$, we can define the range of $\psi = Q/cT_0$ for most of the dielectric materials cut with the air assist, which lies within $-1 \geqslant \psi \geqslant -2$. The low values of ψ allow us to conclude that it is the air jet rather than the vaporization mechanism that mainly contributes to the removal rate by blowing fine fractions and droplets out of the kerf. But this is not the case for materials based on phenol-formaldehyde resins, such as cloth-base laminates, glass-cloth-base laminates, and composite materials. Assuming that the temperature T_0 at which these materials begin to disintegrate is about 1 000°C, the values of ψ are found to lie in

the interval $-5 > \psi > -10$. When irradiated with a laser beam, these materials transform into a sintered viscous mass which is not blown away by the gas jet, and so more energy must be coupled to cut them by vaporization.

CO_2 laser cutting of nonmetals. As noted above, most cutting operations involve continuous CO_2 lasers whose efficiency reaches 15-20%. Many nonmetallic materials have high absorption at 10.6 μm. These include leather, wood, linen, cotton cloth, leather substitutes, rayon, synthetic-base fibers, etc. In the text above, we have mentioned the advantages of laser cutting.

The experimental data on gas-assist cutting of footwear materials and fancy leather using an automatic computer-controlled laser cutter have been given in work [15]. The multimode CO_2 laser could emit 500 W and above. The optical cutter contained KCl lenses which focused the laser beam with a divergence of about 2×10^{-3} rad to a spot 0.5 to 0.8 mm in diameter.

The effect of gas pressure on cutting conditions. Let us consider an example of cutting artificial leather (imitation-leather cloth) 1.5 mm thick and leather-like rubber 4.5 mm thick [15].

The aim of the experiments was to determine the effect of pressure p of assist gases on the depth h of cut, kerf width b, and quality of the cut-edge surfaces. The CO_2 laser delivered 350 W of power to the target. The optical system with a focal length F of 240 mm focused the beam at the surface. The cutting rates v of artificial leather and leather-like rubber were 16.8 and 1.5 m/min respectively. With an increase of air pressure from 0.1 to 0.4 MPa and above, the depth of cut continued to grow until the ply was cut through; at pressures of 0.1, 0.2, and 0.3 MPa, the depth of blind cuts was 1.0, 1.2, and 1.4 mm respectively. The kerf width measured at a level of one-fourth the thickness of the ply below the surface increased with pressure from 0.19 to 0.52 mm.

Cutting with the nitrogen-assist gas led to an increase in the kerf width from 0.28 mm at 0.1 MPa to 0.52 mm at 0.5 MPa. The materials were cut through at 0.2 MPa and over. The different values of the depth of cut achieved in the nitrogen and the air atmosphere can be accounted for by the different conditions of beam shielding from the target surface.

In air-assist cutting of leather-like rubber, the depth of cut increased from 2.35 to 2.80 mm with an increase of air pressure from 0.1 to 0.5 MPa.

In Fig. 8.30 are shown the cross sections of kerfs produced in 2-mm thick texon (a variety of board) with a 350-W CO_2 laser at an air pressure ranging from 0 to 0.4 MPa and at cutting rates of 4, 5, and 8 m/min. Table 8.5 lists the dimensions of kerfs illustrated in Fig. 8.30, namely, the depth of cut, h, and the kerf width b at the top and bottom of the blind and through cuts. It is found that

TABLE 8.5. **Dimensions of Cuts Made in 2-mm Thick Texon with a 350-W Laser Beam Focused at the Surface ($F = 280$ mm)**

Air, p, MPa	b, mm		h, mm	b, mm		h, mm	b, mm		h, mm
	at top	at bottom		at top	at bottom		at top	at bottom	
	$v = 8$ m/min			$v = 5$ m/min			$v = 4$ m/min		
0	0.42	Blind	0.85	0.48	Blind	1.76	0.54	0.24	2.0
0.1	0.48	cuts	0.97	0.54	cuts	1.82	0.60	0.30	2.0
0.2	0.48		0.97	0.54		1.94	0.67	0.36	2.0
0.4	0.50		1.10	0.54	0.09	2.0	0.79	0.48	2.0

the kerf width at the surface and the bottom of the ply increases with air pressure at slower speeds of cutting. For example, at $v = 8$ m/min, the entrance width b increases from 0.42 to 0.50 mm as the pressure rises from 0 to 0.4 MPa, while at $v = 4$ m/min, this width grows from 0.54 mm at zero pressure to 0.79 mm at 0.4 MPa. The HAZ along the line of cut is very narrow and cut edges are rather smooth.

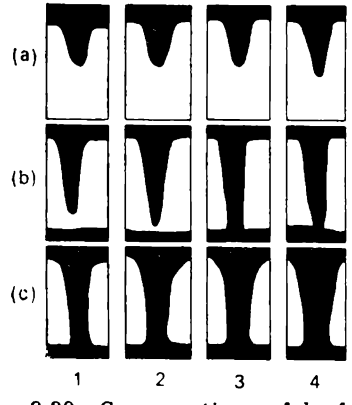

Fig. 8.30. Cross sections of kerfs in 2-mm texon cut with a laser beam in air at a rate of 8, 5, and 4 m/min (*a*, *b*, and *c* respectively) at an air pressure of 0, 0.1, 0.2, and 0.4 MPa (*1*, *2*, *3*, and *4* respectively)

The effect of beam focusing on the parameters of cut. The lens focal length F and the location of the focal point, ΔF, relative to the target surface have an appreciable effect on the profile of the cuts produced. In experiments [15], the lens focused the 500-W laser beam both above the surface of leather-like rubber from 0 up to 6 mm and below the surface from 0 down to 10 mm (Fig. 8.31). The rate of gas-assist cutting at an air pressure of 0.2 MPa was 10 m/min.

As is apparent from Fig.8.31, changing the distance ΔF from the beam focus to the surface changes the profiles of cuts in leather-like rubber. The beam focused by a 280-mm focal length lens above the surface gives a kerf width of 1.17 mm as against 0.82 mm when focused below the surface at the same value of ΔF. Shifting the focal point more deeply into the material down to 10 mm increases

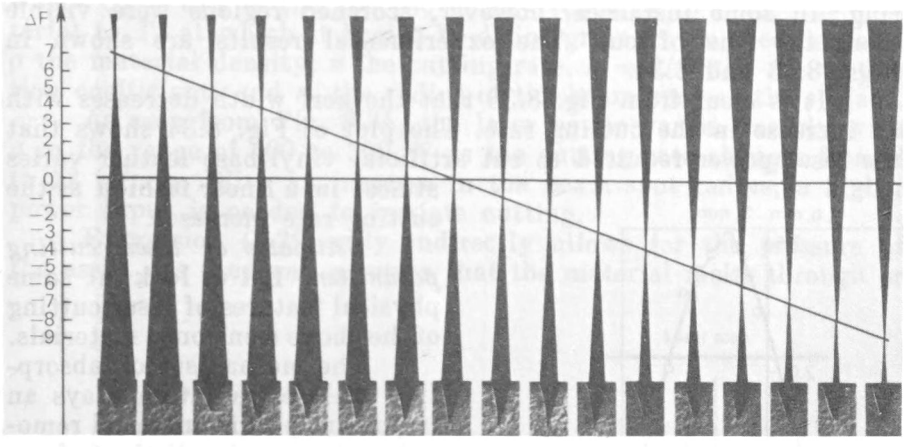

Fig. 8.31. Kerf profiles in leather-like rubber as a function of focal position for cutting at $v = 10$ m/min with 500 W

the kerf width to 1.10 mm. The focal point shifted 3 mm below the surface is an optimal choice, which yields the narrowest and deepest kerf, down to 2.48 mm deep. With an increase in ΔF in excess of 0.3 mm above and below the surface, the focal spot increases in size and so the kerf width becomes larger, while the depth of cut becomes smaller; it decreases to 1.03 mm and 1.45 mm when the focus is 6 mm above the surface and 10 mm below the surface respectively. Figure 8.32 shows how the kerf width b, depth of cut, h, and cross-sectional area S of the kerf vary with the position of the focal point above and below the surface.

The effect of laser power on the kerf width and cutting rate [15]. Ten materials for footwear and heberdashery were cut with a 500-W laser at an air pressure of 0.2 MPa. A 240-mm focal length lens focused the beam to a spot of up to 0.8 mm in diameter at a maximum laser power. The focal point was one-half the thickness of the ply below the surface.

The laser cut through most of the materials, excepting kersey, asbestos, and artificial fancy leather, at cutting velocities of up to 24 m/min. The kerf width was generally less than 0.8 mm in all the material with the exception of asbestos cloth, where it reached 1.25 mm, despite the fact that the light spot was 0.8 mm in diameter. This was probably because the effective diameter of the focused spot, where the power density exceeded the threshold value required for material disintegration, was less than the total diameter of the light spot. The cut edges were clean, smooth, and slightly fire-polished. The HAZ size ranged between 0.05 and 0.1 mm owing to a low thermal diffusivity of the materials and high rates of cut-

ting. In some instances, however, scorched regions were visible along the line of cut. The experimental results are shown in Figs. 8.33 and 8.34.

It is clear from Fig. 8.33 that the kerf width decreases with an increase in the cutting rate. The plot of Fig. 8.34 shows that the laser power required to cut artificial vinyl-base leather varies almost in a linear fashion as the cutting rate increases.

Estimates of laser cutting parameters. Let us look at some physical features of laser cutting of the above mentioned materials.

The mechanism of absorption of laser radiation plays an important part in material removal processes. As distinct from

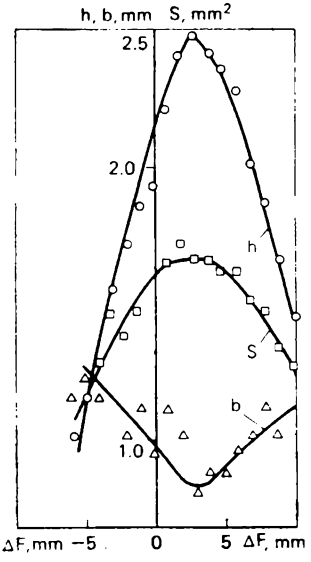

Fig. 8.32. Width b, depth h, and cross-sectional area S of cuts in leather-like rubber versus the position of the foeal point below and above the surface

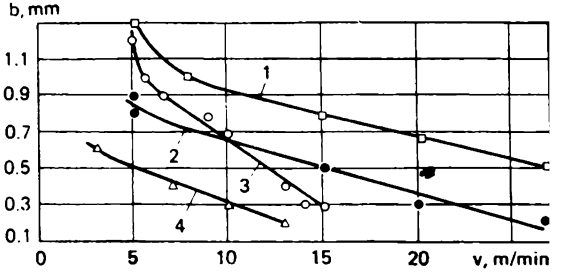

Fig. 8.33. Kerf width versus cutting rate for imitation-leather cloth (*1*), gloving leather (*2*), solid film (*3*), and kersey (*4*) cut with air assist ($p = 2 \times 10^5$ Pa) at 500 W using 240-mm focal length

metals, dielectric materials display a three-dimensional character of laser energy absorption, the penetration depth being determined by the physical properties of the material in question. After a certain time of interaction, the laser energy coupled to the material produces a heat source which begins to destroy the interaction region as its temperature reaches a certain threshold value, T_0. The products of disintegration are blown out of the kerf by the gas jet and drawn off. Let us make some estimates using the same models as those applied to metal removal processes. A minimum power required to disintegrate a material of thickness h can be defined as

$$P_{\min} = Q_0 h \rho v \sqrt{\pi/k} = Q_0 h \rho v r_f \sqrt{\pi} \qquad (8.21)$$

where $Q_0 = cT_0$ is the specific energy required to bring the material to T_0 at which it begins to disintegrate, c the specific heat, ρ the material density, v the cutting rate, $k = 1/r_f^2$ the concentration coefficient, and r_f the radius of the beam spot at the surface.

As seen from Fig. 8.34, the laser power varies linearly with v in the range of 100 to 500 W as the cutting rate changes from 3 to 12 m/min. With an increase in the beam spot radius, a higher power input is needed to initiate cutting.

Expression (8.21) only indirectly allows for the pressure of the assist gas used and assumes that the material melts through or

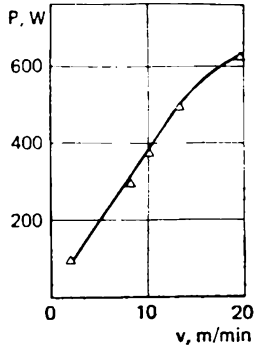

Fig. 8.34. Laser power versus cutting rate for artificial vinyl-base leather

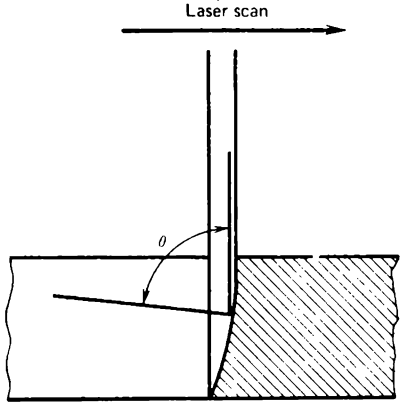

Fig. 8.35. Schematic of metal cutting with a laser beam at angle θ between the normal to the generating line of the surface of cut and the beam axis

disintegrates as it is brought to T_0. However, it is of importance to account for the differences in the properties of materials since they are responsible for the differences in the character of interaction of the beam with vapors and in the degree of ionization of the plume above the surface. The calculations of P_{min} by expression (8.21) involve difficulty for most materials discussed here since the data on their thermal properties are not yet available. Qualitative estimates can be made for a rigid PVC (polyvinyl chloride) plastic, for which the specific energy is known, $Q_0 = 1.8$ kJ/g [15]. Substituting the experimental values into (8.21), namely, $h = 1.5$ mm, $\rho = 1.5$ g/cm^3, and $v = 25$ cm/s, we find that P is equal to about 1.7 kW as against 0.5 kW observed in experiments. The difference is likely to result from the overstated values of Q_0 used in calculations.

The HAZ width can be found from a simple expression for the temperature due to a continuous Gaussian heat source [3]:

$$T(y) = \frac{P}{vh\sqrt{4\pi c\rho t_0}} \exp\left(\frac{-y^2}{4at_0}\right) \tag{8.22}$$

Here, $T(y)$ is the temperature distribution in the direction normal to the line of cut, $t_0 = 1/4\ ak$, and a the thermal diffusivity.

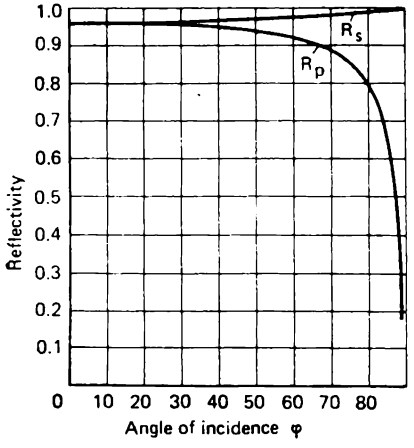

Fig. 8.36. Reflectivity of iron as a function of the angle of beam incidence to the sheet surface

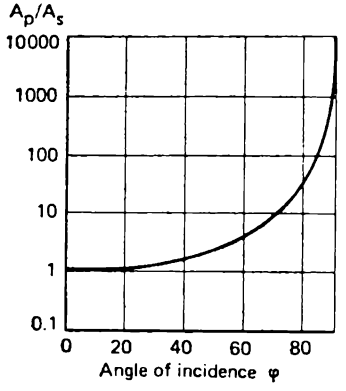

Fig. 8.37. A_p/A_s versus angle of incidence

If we assume that the HAZ width y_0 is the distance over which the temperature is only a certain fraction of T_0, then from (8.22) we can derive the expression

$$y_0 = 2\sqrt{at_0 \ln A/T(y_0)} \tag{8.23}$$

where

$$A = \frac{P}{vh\sqrt{4\pi c\rho\lambda t_0}}$$

Since $at_0 = r_f^2/4$, the HAZ width is

$$y_0 = r_f \ln^{1/2} A/T(y_0) \tag{8.24}$$

This means that y_0 increases with the beam spot radius r_f and weakly varies with P.

The values of y_0 calculated by (8.24) for the typical values of the parameters of the materials under study qualitatively agree with experimental findings. A more accurate agreement is difficult to achieve since the data on the thermal properties of the materials used in experiments are not available.

The effect of laser polarization on cutting conditions. Laser polarization is one more factor that determines the cutting rates and the quality of cuts made with CO_2 lasers in different materials [16, 17]. The laser beam scanned along the target surface produces a cut whose normal to the surface forms an angle θ with the axis of the incident beam (Fig. 8.35). The reflectivity of a surface irradiated with a plane-polarized beam depends on the optical properties of the material, angle of incidence φ of the beam, and angle ψ between the plane of polarization and the plane of incidence. An example

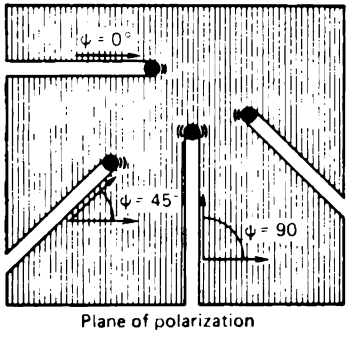

Fig. 8.38. Sites of intense absorption of laser energy at different angles

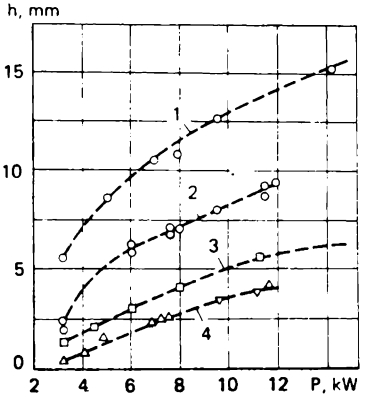

Fig. 8.39. Weld penetration h as a function of laser power P at weld rates of 12.7, 42.3, 84.6, and 12.7 mm/s (curves *1*, *2*, *3*, and *4* respectively)

of the angular dependence of the reflectivities R_p and R_s of iron for the polarization directions p and s, with the 10.6-μm radiation incident on Fe at room temperature, is shown in Fig. 8.36; p and s are polarization vectors lying in the plane and normal to the plane of beam incidence respectively.

An average angle of incidence of the beam focused to a spot of diameter d_f on the surface of a material of thickness h is $\varphi \approx \text{arctg}\,(h/d_f)$. For example, at $h = 0.7$ mm and $d_f = 0.15$ mm, the angle of incidence is approximately equal to 80°. Knowing the absorptivities A_p and A_s for p and s polarization, we then find that the ratio A_p/A_s at $\varphi = 80°$ is equal to about 20, as illustrated in Fig. 8.37 [17]. This means that if the plane of cutting is coincident with (parallel to) the plane of beam polarization, the absorbed laser power is 20 times that when these planes are normal to each other.

Since the reflectivity of metals heavily changes with temperature, the ratio A_p/A_s decreases with increasing temperature. Oxy-

gen-assist cutting decreases the parameters of cuts produced by the laser beam polarized in two directions.

Figure 8.38 illustrates the sites of the most intense absorption of laser radiation in cutting low-carbon steel sheet at different angles ψ between the plane of polarization and the plane of cutting. If these planes are coincident ($\psi = 0$), the site of the highest absorption, which is shown by two curved line segments, is ahead of the kerf. In this case, the absorbed energy ensures a maximum cutting rate at a minimum kerf width. If these planes are normal to each other ($\psi = 90°$), the kerf sides absorb most of the energy. At other angles, absorption is asymmetrical, which leads to a wider and distorted kerf.

Investigations reveal that gas-assist cutting of sheet metals under optimal conditions should be done with a plane-polarized beam so that the laser cutter can automatically rotate the plane of polarization ahead of the focusing system depending on the direction of cut. However, since there are no arrangements for polarization of a laser beam of high power density, it is expedient to use polarization-free lasers.

8.4. SEAM WELDING WITH MULTIKILOWATT CW LASERS

Continuous laser welding owes its origin to the development of CW CO_2 lasers with powers in excess of 1 kW. By its capability, laser welding competes with electron beam welding and offers some advantages, for example, allows welding in the atmosphere and does not initiate X-radiation dangerous to health.

Higher power outputs enable lasers to weld at higher rates and at a larger aspect ratio h/d, i.e. the ratio of penetration depth h to diameter d. Figure 8.39 shows penetration depth h as a function of laser power P for high-strength steel at different weld speeds v_w. At multikilowatt levels, the maximum weld penetration can be defined as

$$h_{max} \approx nP^{0.7} \tag{8.25}$$

where n is a proportionality factor [2], and P the laser power.

An example of producing single-pass welds in high-strength steels 38 mm thick with 90 kW of laser power at 2.54 m/min was given in [2]. The weld penetration h versus weld speed v_w at different laser power levels is shown in Fig. 8.40 [2]. For plates 0.1 to 0.3 cm thick, 2 kW of laser power is sufficient to weld at a rather high rate. Thinner plates can be welded at a laser power level up to around 1 kW.

The data on welding of various materials with CW CO_2 lasers emitting 0.25 and 15 kW of power are listed in Tables 8.6 and 8.7.

TABLE 8.6. Welding with a 250-W CO_2 Laser in Argon Supplied at 0.42 m^3/h Using a 63.5-mm Focal Length Lens [2]

Material	Thickness, h, mm	Weld speed v_w, cm/s	Weld width w, mm
	Butt joint		
Stainless steel	0.13	3.8	0.46
	0.25	1.5	0.71
	0.42	0.47	0.76
	0.13	2.1	0.51
	0.25	0.4	1.02
Inconel	0.10	6.3	0.25
	0.25	1.7	0.46
Monel	0.25	0.63	0.63
Titanium	0.13	6.0	0.38
	0.25	2.1	0.56
	Lap joint		
Stainless steel	0.41	7.5	0.63 [1]
	0.76	1.27	0.76 [1]
	0.25	0.33	0.76
	Corner lap joint		
Inconel	0.10	6.8	
	0.25	1.48	
	0.42	1.05	
Monel	0.25	1.05	
	0.51	1.15	

[1] Incomplete penetration.

Let us consider experimental data on the weld penetration achieved in corrosion-resistant (stainless) steel with 20-kW laser beams from electric-discharge and gas-dynamic CO_2 lasers. A 20-kW gas-dynamic laser provided a 19-mm penetration depth in a steel plate with an aspect ratio of 6 : 1 at a weld rate of 2.1 cm/s. The penetration decreased to 12.7 mm at a speed of 4.2 cm/s.

An 8-kW electric-discharge laser was able to melt a 9.5-mm thick steel plate almost to its entire thickness at a rate of 1.27 cm/s. The laser produced a complete-penetration weld in a 6.35-mm thick plate at a rate of 1.7 cm/s. This laser also butt welded two 0.95-cm

TABLE 8.7 Welding with Multikilowatt Lasers

Material	Thickness, mm	Power, kW	Weld speed, cm/s
Steel:			
low-carbon	3.0	15	17
	9.5	14	3.18
corrosion-resistant	3.2	14	16.95
	17.8	17	1.06
high-strength	12.7	15	1.27
Superalloy:			
inconel	5.0	14	4.23
	14.5	15	2.33
aluminum	6.3	10.2	5.9
	11.9	14.5	2.12
titanium	3.2	10	10.7
	9.5	15	5.7

thick plates positioned with a gap of 500 μm and produced a butt joint with an almost full penetration.

The results of these experiments appear in Fig. 8.41. The solid line represents the experimental data on electron beam welding. When the normalized laser power $P_0/T_m h\lambda$ is greater than 100, thermal conduction is of little significance, so the weld rate scales linearly with laser power. At lower powers, the weld rate tends to decrease as the square of power. Figure 8.42 displays the data on the weld penetration h as a function of laser power P required to achieve a 30% efficiency of welding of corrosion-resistant steel, low-carbon steel, aluminum, and copper. As noted earlier, the weld efficiency is the ratio of the power used to melt a material to the total power input with allowance made for the heat lost by thermal conduction.

In experiments conducted with a 20-kW laser welder, the weld efficiency reached approximately 45%. At a lower power level of 8 kW, the efficiency was about 28%. With a decrease in laser power to 3.8 kW, the efficiency dropped to 22%. The power required to achieve 1-cm penetration, as seen from the graphs of Fig. 8.42, is 4, 14, 16, and 60 kW for corrosion-resistant steel, low-carbon steel, aluminum, and copper respectively. The efficiency depends on the product of the weld speed by the weld zone width and is independent of the zone width.

Deep penetration welding with lower laser powers is also possible, but at a sacrifice in weld efficiency.

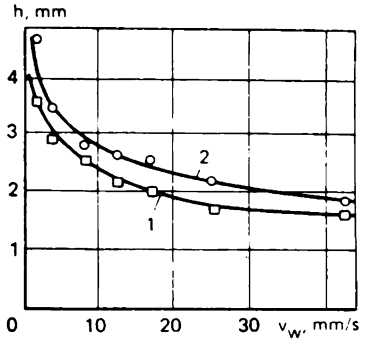

Fig. 8.40. Weld penetration versus weld rate v_w at 1.2 kW (curve *1*) and 1.5 kW (curve *2*)

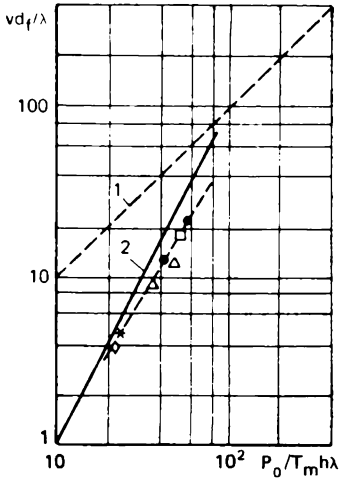

Fig. 8.41. Normalized weld speed as a function of normalized power: curve *1*, laser welding, with heat transfer disregarded; curve *2*, E-beam welding; 8 kW (triangle); 20 kW (dark circle); 3.8 kW (star); 10 kW (square); 4 kW (lowermost light symbol)

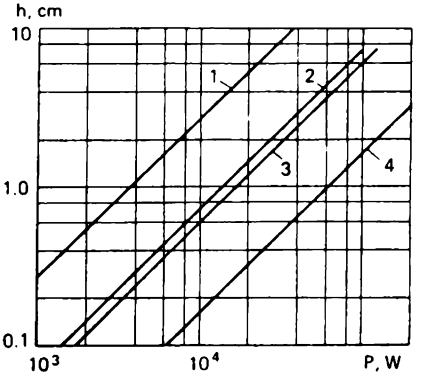

Fig. 8.42. Penetration depth versus laser power for corrosion-resistant steel (*1*), low-carbon steel (*2*), aluminum (*3*), and copper (*4*)

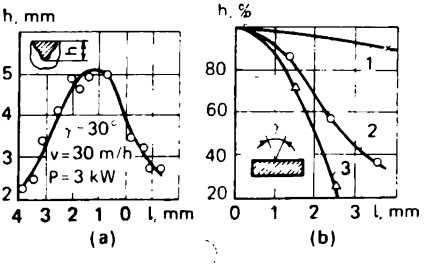

Fig. 8.43. Penetration depth h versus focal position (*a*) and relative penetration h (%) versus focal position (*b*) at an angle of beam convergence of 10° (curve *1*), 30° (curve *2*), and 50° (curve *3*)

The effect of keyholing for continuous seam welding occurs at power inputs equal to or slightly in excess of 1.5 kW. In experiments [2], a 1.5-kW laser was used to weld 2-mm thick plates of nickel steel. The weld bead had a regular width of 0.5 mm with an expanded upper portion in cross section. Full penetration welds with a depth-to-width ratio of 8.0 : 1.6 were made in 5-mm titanium alloy when the weld rate at a power of 3 kW was reduced from 380 to 100 cm/min. In welding 6.3-mm corrosion-resistant steel with a 3.5-kW laser at a rate of 127 cm/min, the aspect ratio of the welds was, on the average, equal to 7 and reached a maximum of 12.

The penetration depth h and the depth-to-width ratio are dependent not only on the focal spot size and weld speed v_w, but also on the position of the focal point relative to the parts to be welded and the angle of convergence γ of the laser beam.

Figure 8.43 summarizes the results of studies [2] on the penetration depth h as a function of the distance l of the focal point below the surface at various values of the angle of beam convergence γ. In Fig. 8.43, h in percent is the ratio of the penetration depth h to an optimal value of h.

Work [11] contains experimental data on the weld penetration and aspect ratio as a function of CO_2 laser power at angles of beam convergence of 10 and 45° achieved by using two-mirror Cassegrain reflectors of different parameters. In the authors' opinion, a decrease in the angle of convergence is a critical requirement for producing deep penetration welds more than 10-12 mm deep in carbon steel at weld rates of up to 80 m/h.

In experiments [11], weld beads in the plates of corrosion-resistant steel were made in an atmosphere of argon supplied through the nozzle and directed at the weld location both normal to the target surface (coaxial with the beam) and parallel to the surface.

It is found that the first method of application of the cover gas produces the deepest penetration. With the second method used, the brightness at the weld spot is higher but the weld seam is much narrower and more uniform in properties. In welding without a cover gas, the vaporized material forms a stationary plume of ionized metal vapors above the surface. The plume effectively shields the target surface from the beam and reduces the penetration depth.

This effect appears when the laser power exceeds a threshold value of 8 kW. The gas jet carries away the vapor, thus preventing the formation of the ionized cloud. It is also possible to apply gases which suppress cloud ionization in the region of beam interaction. To provide cover for the underhead in full penetration welding, an inert gas can be blown on the back side of the weld.

In Fig. 8.44 is shown an arrangement intended to protect the bead against oxidation, suppress plasma ignition, and prevent damage to focusing optics due to metal spatter and vapors. This is a

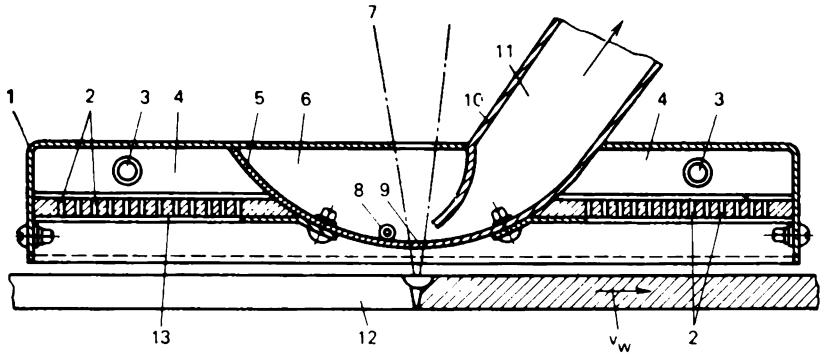

Fig. 8.44. Arrangement for supplying cover and plasma-suppressing gases to the weld zone: *1*, casing; *2*, openings in longitudinal partition; *3*, cover gas inlet; *4*, upper section; *5*, cross baffle; *6*, plasma-suppressing gas chamber; *7*, laser beam; *8*, jet tube; *9*, opening for laser beam; *10*, gas outlet sleeve; *11*, outlet; *12*, weld; *13*, partition with openings

rectangular cup with a horizontal partition *13* which divides the cup into an upper section *4* and a lower open section facing the target surface. A segmental partition *5* with a hole to allow the beam *7* to impinge on the target and cover *1* form a closed space into which a plasma-suppressing gas (helium) is fed through a jet tube *8* and drawn off through an outlet sleeve *10* that provides a slit channel *11*. The cover gas flows into the upper section *4* through inlet tubes *3* and forces its way through holes *2* into the lower section to cover the weld location. The holes *2* equalize the pressure of the gas flow, thereby excluding the mechanical action of the flow on the molten pool.

To improve the process of seam welding, the authors of Pat. No. 51-35758 (Japan) have proposed a method of keeping the required shape of the molten pool under the action of a gas flow. By the method described in Pat. No. 52-119446 (Japan), the gas jet directed at the melt prevents the molten pool deformation or melt outflow under gravity. For example, to produce horizontal welds (Fig. 8.45*a*), it is advisable to play the jet from the bottom upward at a definite angle to the weld plane. For circular welds to be made (Fig. 8.45*b*), the jet must strike the target at a definite angle in a direction opposite to the sense of rotation of the piece.

The composition and pressure of gas mediums have an appreciable effect on the conditions of beam-metal interaction [2]. These aspects have been treated in Chapter 6. As described in the text, helium most strongly opposes the onset of plasma generation; plasma breakdown occurs in the range of power densities from 10^6 to 10^7 W/cm^2. The vapor plasma builds up after the material begins

to vaporize. As compared to other inert gases, helium offers the least opposition to laser radiation and provides good protection against oxidation.

The results of experiments on welding with a 15-kW CO_2 laser in different gaseous mediums reveal that helium allows deeper penetration than air, and small additions of hydrogen of about 1% made to helium promote still greater penetration. The plot of the relative penetration depth n, expressed as the ratio of the weld penetration h with He to the weld penetration h with air, versus the helium flow rate is shown in Fig. 8.46.

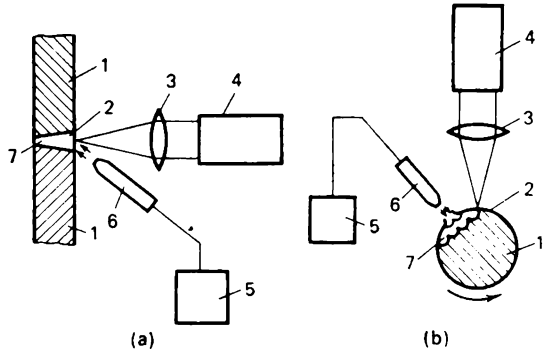

Fig. 8.45. Schematic arrangements of laser work stations using a gas jet to control the formation of horizontal welds (*a*) and circular welds (*b*): *1*, pieces welded; *2*, weld zone; *3*, focusing lens; *4*, laser; *5*, gas cylinder; *6*, jet nozzle; *7*, molten pool

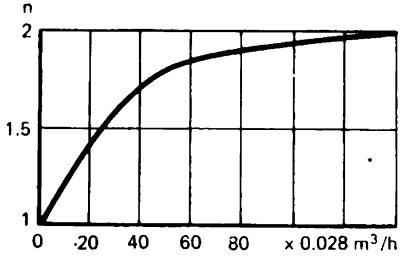

Fig. 8.46. Weld penetration $n = h_1/h_2$ as a function of helium flow rate; h_1 and h_2 are the weld depths achieved with He and air respectively

Unlike He, Ar considerably decreases the laser penetration and its additions to He reduce the penetration depth in proportion to its content of the gas mixture. A mixture of He with a small amount of Ar is found to provide a good protection against oxidation of metals welded at high rates [2]. Other gaseous mediums suggested in [2] for use in welding steel parts are a mixture of helium and oxygen or a mixture of helium and an electronegative gas such as CCl_2F_2 or SF_6 with 10% CO_2.

The weld efficiency can be raised markedly by increasing the absorptivity of the surfaces of the metals to be joined. To achieve

the aim, Japaness Pat. No. 49-23749 suggests a method of coating the surfaces to be joined with a metal powder which strongly absorbs laser radiation and makes up for the weld metal lost by vaporization. The increased absorption allows the welds to be made at a lower laser power.

To overcome the difficulty in welding metals such as copper, silver, and gold which have high reflectivity in the visible and the IR region, a proposal has been made to apply coats of nickel to copper surfaces and coats of palladium to gold and silver surfaces by the method of cladding under high pressure with or without heating (US Pat. No. 570104). The cladding must have a thickness of $\geqslant$0.0127 mm and must vaporize insignificantly. In this case, too, a lower-power laser is needed to produce welds.

The proper choice of the weld rate is important for quality welding. There is an upper limit to the weld rate above which the melt begins to crystallize before it spreads over the edges well enough to provide the required fusion. Too high weld rates result in shrinkage porosity and other defects. The highest weld rate for 0.127-mm thick corrosion-resistant steel welded at 1.5 kW of CW laser power is near 5.0 m/min. The lower limit lies at a value below which the thermal conduction causes the molten pool to spread outside more rapidly than into the bulk, with the result that the weld width and the HAZ size increase considerably. The weld metal zone also exhibits excessively large grains.

For quality weld joints to be made, it is necessary to meet the following conditions: (1) fit up the pieces to be welded with a minimum gap in order to avoid weld recession; (2) thoroughly clean the surfaces of contaminants; (3) employ the proper type of fixturing for the pieces to be held tightly together; (4) ensure the stability of laser beam parameters and preferably rely on single-mode operation; (5) use lasers operating at $\geqslant$2 kW; (6) focus the beam so that the power density at the focus should be in the range of 1.55×10^5 to 1.55×10^7 W/cm^2 to ensure deep penetration welding; (7) protect the weld zone with a cover gas flow that has a preferentially tangential component of the velocity so as to carry away the vapor plume formed above the molten weld pool; (8) ensure an optimal speed of travel of the workpiece or the beam; (9) remove heat from the weld root in order to promote oriented crystallization from the bottom upward, thus excluding shrinkage cavities in the center of the weld; (10) use focusing systems with a sufficient depth of focus to enable straight-sided welds to be made in cross section.

If these conditions are met, the welding process can yield welds with a high depth-to-width ratio, which are free of recessions, nonmetallic inclusions, and gas cavities. Nonmetallic inclusions have higher absorptivity than base metals, so they rapidly vaporize from the weld zone.

Since the laser is able to deliver very high power per unit area to localized regions, the energy input per unit length of the weld seam is fairly low and comparable to that required in electron beam welding. A low amount of heat input results in a very little distortion of the weld zone and a small heat-affected zone (HAZ) because of rapid cooling. The laser beam produces a rather narrow and deep weld similar to an E-beam weld. Laser welds are made without welding electrodes which present a contamination problem. Since the impurities such as sulfur, oxygen, and nitrogen contained in the melt zone absorb CO_2 laser radiation more strongly than the metal and vaporize more readily, the weld exhibits better mechanical properties.

Work [2] contains the results of tests for the impurity content of the weld metal and the impact strength of welded specimens of high-strength alloyed steel used for pipe production. The plates 6.4 mm thick were welded with a 5-kW laser at a rate of 0.85, 1.27, 1.48, and 1.90 cm/s. Argon and the mixture of Ar and He were used to protect the back and the face side of the weld respectively. The total flow rates of gases on both sides were 472 and 157 cm^3/s. Table 8.8 presents the results of the chemical analysis of the weld metal and Table 8.9 shows the results of Charpy impact tests.

TABLE 8.8 **Impurity Contents of the Base Metal (High-Strength Steel) and Weld Metal [2]**

Element	Base metal, %	Weld metal at v_w =0.85 cm/s, %	Base metal, %	Weld metal at v_w =1.27 cm/s, %
C	0.127	0.120	0.122	0.117
N	0.0125	0.013	0.0130	0.0115
O	0.044	0.0021	0.0078	0.0051
S	0.0069	0.0074	0.0073	0.0070
H	0.001	0.001	0.001	0.001

TABLE 8.9 **Notch Impact Strength a_n of Laser Welded Specimens**

P, kW	v_w, cm/s	Temperature, °C	a_n, J/cm²	
			Weld metal	Base metal
5	1.9	−1.1	52.9	35.8
5	1.9	+23.9	52.9	36.6
5	1.48	+23.9	38.4	32.5
5	0.85	+23.9	36.6	33.9

A considerable increase in the impact strength a_n of the metal of welds produced at a rate of 1.9 cm/s over that of the base metal was due to a decreased number of nonmetallic inclusions and their spherical shape, as revealed by the metallographic analysis. The oxygen content dropped by 35-52% evidently on account of the oxidation of manganese silicates which added to the impact strength.

The temperature of transition to brittle failure of single-pass and double-pass weld beads was 9 and 51°C respectively.

Laser welds in titanium alloys also displayed good mechanical properties primarily because they had a structure with finer grains as compared to those attainable, for example, in plasma-arc welding, and did not contain pores in excess of 0.15 mm. In static tests on the welded specimens, the base metal was the first to fail. The fatigue tests showed that the ultimate strength of the weld metal corresponded to that of the base metal and reached 550 MPa. The joints stood up to 10^7 stress cycles.

As noted earlier, the laser can weld various materials, for example, high-temperature alloys based on nickel and iron, which are difficult to weld by other techniques.

Work [18] presented the results of comparison studies of laser welding, electron beam welding, and argon-arc welding to estimate the potential of each technique through such weld parameters as the static and the impact strength of the weld joint, weld metal, parent metal, and HAZ. Welds were made in pearlitic steels, medium-carbon steels, and titanium α-alloys.

Laser welding provided full penetration weld joints and butt joints between the plates positioned with a narrow gap. The weld metal compared favorably with the base metal in strength and excelled the latter in impact strength.

If we disregard the process of keyholing, the distribution of heat required to produce a seam weld can be treated in the framework of the theory of moving heat sources. In particular, the simplest model for describing the deep penetration in thick materials can be taken to be the model of a linear heat source moving at a constant velocity throughout the bulk of the solid.

Such a model was used in works [3, 19] with consideration for the temperature dependence of thermal constants. These works described the solution to the quasistationary heat transfer equation in the moving coordinate system to obtain physical insight, for example, into the dependence of the weld speed on laser power in deep penetration welding. Introducing the normalized power per unit depth, $X = P_0/hS$, and normalized speed $Y = vb/a$, the authors of work [3] derived the expression $Y \cong 0.483\ X$. Here, P_0 is the total laser power, h the penetration depth, S the spot area, b the molten pool width, and a the thermal diffusivity.

7.26

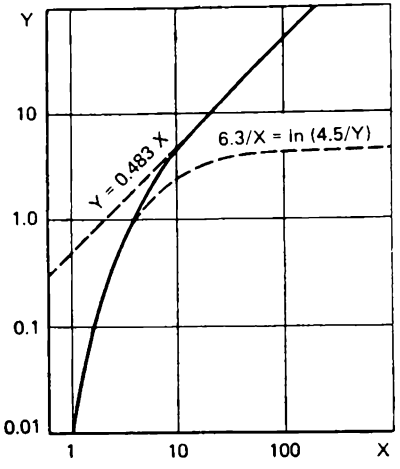

Fig. 8.47. Normalized weld speed Y versus normalized power X for deep penetration welding

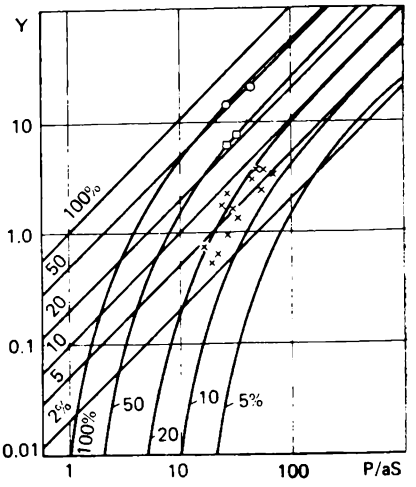

Fig. 8.48. Comparison between theoretical and experimental values for deep penetration welding at 20 kW (light circles), 8 kW (light squares), and 250 W (crosses)

The plot of Y against X is shown in Fig. 8.47. The factor equal to 0.483 represents the weld efficiency, which is the ratio of the energy needed just to melt the metal to the total energy delivered by the laser beam. At low speeds of travel of the laser beam

$$Y \cong \exp(\ln 8 - \mathrm{Eu} - 2\pi/X) \tag{8.26}$$

where Eu = 0.577 is Eulier's constant.

To achieve the specified values of weld penetration and weld speed at lower powers, we need to narrow the melt zone width or to decrease the focused spot area. The full line of Fig. 8.47 represents an intermediate range of speeds.

Figure 8.48 compares the predicted values (straight lines) of Y with experimental values for deep penetration welding by a CO_2 laser at 8 and 20 kW and also at 250 W (for welding thin plates of various materials). The weld efficiency grows with the laser power delivered to the target despite a high reflectivity of metals. As mentioned earlier, in the process of deep penetration, or keyholing, the keyhole produced serves as a trap for the beam and effectively absorbs nearly all the power of the trapped beam [20]. Table 8.10 summarizes data on welding with high-power lasers.

Consider the theoretical data on the temperature fields in materials heated with a CO_2 laser and compare them with experimental

TABLE 8.10 **Deep-Penetration Laser Welding**

Metal	P_0, kw	h, mm	b, mm	v, mm/s	$P_0/h\times10^{-3}$, kW/m	$P_0/hS=X$	$vb/a=Y$
Carbon steel	0.125	0.125	0.45	38.0	2.0	56	3.5
	0.25	0.250	0.70	14.8	1.0	28	1.1
	0.25	0.417	0.75	4.7	0.6	17	0.72
	0.25	0.125	0.50	21.1	2.0	56	1.2
	0.25	0.203	0.50	12.7	1.23	34	1.3
	0.25	0.250	1.0	4.2	1.0	28	0.86
	8	8.9	2.3	12.5	1.0	28	5.9
	8	6.4	2.1	16.7	1.25	35	7.2
	20	20.2	3.3	21.2	0.9	27	14.3
	20	12.7	2.3	42.4	1.57	44	19.9
Inconel	0.25	0.10	0.25	63.5	2.5	74	3.2
	0.25	0.25	0.45	16.9	1.0	29	1.52
Nickel	0.25	0.125	0.45	14.8	2.0	20.6	0.53
Ni-Cu alloy	0.25	0.25	0.62	6.4	1.0	21.3	0.57
Titanium	0.25	0.125	0.37	59.0	2.0	50	3.0
	0.25	0.25	0.55	21.1	1.0	25	1.61

results. In experiments, the CO_2 laser operated from a 60-Hz pumping source and delivered a beam oscillating at 120 Hz (Fig. 8.49). The energy distribution over the beam diameter can be approximated by the Gaussian distribution curve 0.5 mm wide at a $1/e$ level (37%) of the maximum energy.

The profile of the molten pool in a 0.3-mm thick corrosion-resistant steel plate coated with a Fe_2S_3 film agrees well with the calculated results for the Gaussian heat source (Fig. 8.50). The curves of h/r against h are shown in Fig. 8.51, where h is the penetration depth and r is the half-width of the molten pool. The calculated values are valid for point, circular, and Gaussian sources on the assumption that the power of each source is constant. The experimental and theoretical data correlate well for the Gaussian source. For the circular source, the agreement is good at low values of h, but insufficient at high values. As for the point source, the results are poorly consistent.

The data on the penetration depth as a function of the velocity v of the heat source in a corrosion-resistant steel plate coated with a Fe_2S_3 film to increase absorptivity are given in Fig. 8.52. The ex-

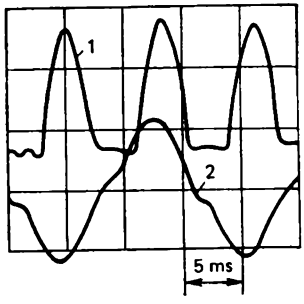

Fig. 8.49. CO_2 laser power (curve *1*) and pump power (curve *2*) as a function of time

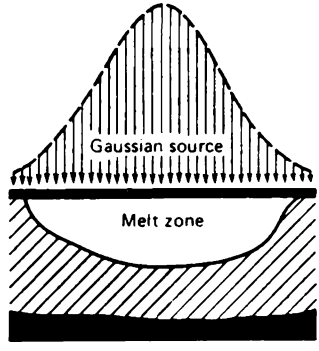

Fig. 8.50. Typical profile of the CO_2 laser melted zone on a 0.3-mm thick corrosion-resistant steel plate coated with Fe_2S_3

perimental and theoretical data are in good agreement at low speeds. At higher speeds, the experimental values of the penetration depth become greater than the predicted values.

Figure 8.53 illustrates an example of the dimensionless temperature distribution (curve *1*) calculated along the weld axis on the back side of a 0.3-mm thick aluminum plate heated with a source whose output power varies at a frequency of 120 Hz (curve 1′). For comparison, Fig. 8.53 shows the temperature curve *2* resulting from a heat source of constant power (curve *2′*).

Regarding the quasistationary heat transfer problem, the dimensionless temperature at the center of the heat source produced

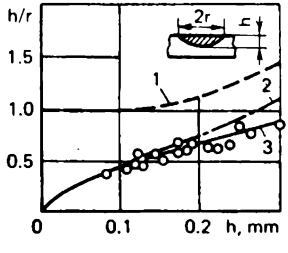

Fig. 8.51. Ratio h/r as a function of h for a point source (*1*), circular source (*2*), and Gaussian source (*3*)

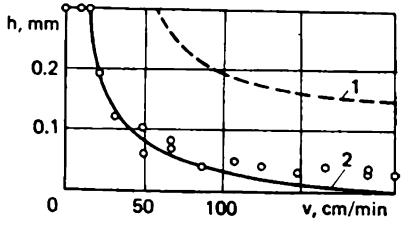

Fig. 8.52. Weld penetration in corrosion-resistant steel as a function of speed of a point heat source (curve *1*) and Gaussian heat source (curve *2*)

by a CO_2 laser beam focused on the surface is given by

$$\theta(0,\ 0,\ \infty) = AP/2\sqrt{\Pi}\,\lambda r_f \tag{8.27}$$

where A is the absorptivity, and λ the thermal conductivity.

A minimum power required to melt the surface of a semi-infinite solid is then defined as

$$P_{\min} = 2\sqrt{\Pi}\,\lambda r_f T_m / A \tag{8.28}$$

The absorptivity of a polished metal at the melting temperature is

$$A = 4\sqrt{\Pi\omega\varepsilon_0 R/\lambda} \tag{8.29}$$

where ω is the light frequency, ε_0 the electric constant, and R the dc resistance at T_m.

Hence, a minimum CO_2 laser power needed to raise the surface to its melting point is

$$P_{\min} = 7.9 \times 10^{-4}\,(\lambda T_m/\sqrt{R}) \tag{8.30}$$

The estimates of $P_{\min}$ for a number of metals show that the following values are enough to melt even the polished surfaces of metals: 200 W, titanium and corrosion-resistant steel; 300 to 400 W, iron and zirconium; and 9 to 10 kW, copper and silver.

Figure 8.54 displays the plots of the effective power P required to melt through 3-mm thick polished plates of aluminum (curve *1*) and corrosion-resistant steel (curve *2*) in the quasistationary heat transfer conditions as a function of the scan speed (weld rate). In the range of linear transport speeds below 150 cm/min, the power input to melt through the corrosion-resistant steel plate is lower

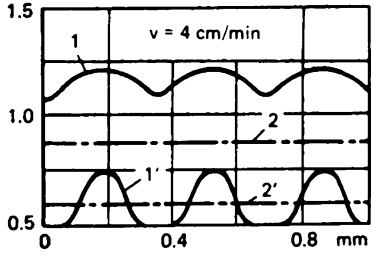

Fig. 8.53. Plots *1* and *2* of temperature distribution on the back side of 0.3-mm thick aluminum plate heated with sources of pulsating and constant powers represented by *1'* and

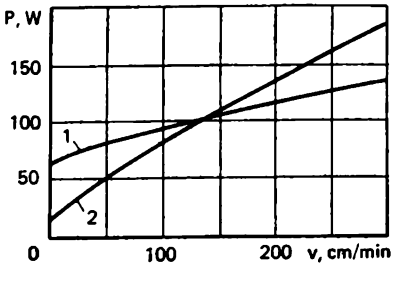

Fig. 8.54. Power required to melt through 0.3-mm thick polished plates of aluminum (curve *1*) and corrosion-resistant steel (curve *2*) as a function of scan speed v

than that for the Al plate, but at scan speeds above 150 cm/min, the reverse is true since v is proportional to a^{-1}, where a is the thermal diffusivity.

8.5. WELDING AT LOW ENVIRONMENTAL PRESSURES

Reports on experimental laser and electron beam welding in mediums of decreased pressures date back to 1976. It is found that the weld penetration h increases with decreasing pressure p in a definite pressure range. The articles of Brown, Banas, Arata, and

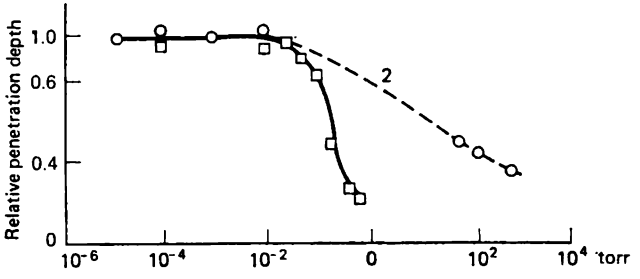

Fig. 8.55. Relative penetration depth versus gas pressure for welding with laser beam at 3.4 kW (curve *1*) and electron beam at 0.9 kW (curve *2*)

other researchers in book [21] describe the experiments on laser and electron beam welding in a medium rarefied to 10^{-6} torr. Let us consider these experiments.

Figure 8.55 shows the plot of the relative penetration depth (ratio of h to h_{max}) in a steel plate irradiated with a laser beam (L-beam) and electron beam (E-beam) as a function of the environmental pressure. It is seen that in the range of 10^{-6} to 10^{-2} torr the penetration depths achieved with the L-beam at 3.6 kW and E-beam at 0.9 kW are essentially the same.

At pressures above 10^{-2} torr the penetration depth decreases in welding both with the L-beam and with the E-beam, but it drops faster in the case of laser welding. For the E-beam, an increase in the medium density leads to a decreased electron path length due to electron scattering by gas molecules. The losses of laser energy result from the generation of plasma during vaporization. According to experiments, deep penetration in metals becomes stable at weld rates of less than 5 mm/s.

For example, at a weld rate of 0.2 mm/s, a laser power of 3.4 kW is enough to melt through a 1.9-cm corrosion-resistant steel plate in a rarefied atmosphere, the penetration depth being twice that achieved at the atmospheric pressure. A 5-kW CO_2 laser is able to melt through a steel plate 4.1 cm thick at a rate of 0.34 mm/s,

which provides three times the penetration depth attainable at the atmospheric pressure. At a laser power of 7 kW and a weld rate of 2.1 mm/s, the weld penetration in steel reaches 3.5 cm.

Researchers [21] explain the increase in penetration depth due to a reduced effect of plasma on the penetration of radiation into the keyhole. Although the pressure threshold above which the weld penetration h begins to decrease is generally the same, $p_{th} \sim 10^{-2}$ torr, both for the L-beam and the E-beam, the mechanisms responsible for a decrease in h are different.

The qualitative concepts accounting for the same pressure threshold value are the following [21]. Deep penetration welding is the keyholing process in which the L-beam or E-beam forms a hole, or cavity, into which the beam deposits more energy which ensures deeper penetration. In turn, the parameters of the keyhole depend on the intensity of vaporization of the material in question. The vaporization (boiling) temperature of a material is a function of external pressure; it decreases with decreasing gas pressure. The pressure of vapors of iron, chromium, and nickel, which are the main components of corrosion-resistant steel, reaches or even exceeds 10^{-2} torr at T_m. This means that at an environmental pressure of $\sim 10^{-2}$ torr the vaporization temperature T_v for the above metals is close to T_m. Consequently, during melting the liquid phase is not blown off completely under the effect of explosive vaporization owing to a transient nature of the process and high rate of energy transfer.

The process of keyholing at the atmospheric pressure calls for steel heating to about 3 150 K. If the pressure is reduced to $\sim 10^{-2}$ torr, T_v drops to 1 800 K. This facilitates the process of keyholing and requires a much lower laser or E-beam power to be coupled to the target to sustain the process. A minimum temperature at which the process occurs is the melting temperature T_m of metal. Since it varies weakly with a decrease in the external pressure, the penetration depth grows insignificantly at pressures below 10^{-2} torr. Keyholing is more stable at lower pressures.

References

1. G. A. Abilsiitov and V. S. Golubev. *Basic problems of laser technology and industrial lasers.* Troitsk, NITsTL AN SSSR, 1981 (in Russian).
2. V. P. Sinev. *Laser welding*: in Advance in science and engineering. Welding series, vol. 11. Moscow, VINITI, 1979 (in Russian).
3. N. N. Rykalin, A. A. Uglov, and A. N. Kokora. *Laser machining and welding.* Moscow, Mir Publishers, 1978.
4. S. I. Anisimov, Ya. A. Imas, G. S. Romanov, et al. *Interaction of high-power radiation with metals.* Moscow, Nauka, 1970 (in Russian).
5. F. F. Vododovatov, A. A. Chelny, V. P. Veyko, et al. Ed. by M. F. Stelmakh. *Industrial lasers.* Moscow, Energiya, 1975 (in Russian).

6. A. N. Kokora, E. A. Korneev, A. K. Fannibo, et al. *Laser welding and prospects of its application at engineering plants of food industry.* Moscow, TsNIITEI legpishchemash, 1978 (in Russian).
7. V. P. Veyko, A. N. Kokora, and M. N. Libenson. *On experimental check of temperature distribution in the zone of laser-metal interaction.* DAN SSSR, 179: No. 1, p. 68, 1967.
8. J. F. Ready. *Material processing.* An overview. Proc. of the IEEE, vol. 70, No. 6, 533, 1982.
9. C. M. Banas and R. Webb. *Macromaterials processing.* Proc. of the IEEE, vol. 70. No. 6, p. 556, 1982.
10. D. T. Swift-Hook and A. E. Gick. *Penetration welding with lasers.* Weld. J., vol. 5, p. 402, 1973.
11. A. M. Belenkiy, G. M. Zuev, F. K. Kosyrev, et al. *Deep penetration welding.* Svarochnoe Proizvodstvo, No. 11, p. 23, 1977.
12. C. M. Banas and R. A. Hella. *High power laser welding.* Opt. Eng., vol. 17, p. 210, 1978.
13. A. A. Uglov, E. N. Vlasov, V. G. Panaetov, et al. *On laser welding and machining instrument parts*: in Laser technology in instrument making and precision machinery industry. 3rd Series, Moscow, Mashinostroenie, 1980 (in Russian).
14. F. A. Sromin. *Application of laser welding in assembly of electric machines.* Leningrad, LDNTP, 1978 (in Russian).
15. A. A. Uglov, A. N. Kokora, and N. V. Berlin. *CO_2 laser cutting of nonmetals.* Kvantovaya Elektronika, 5: No. 7, p. 1553, 1978.
16. F. O. Olsen. *Cutting with polarized laser beam.* DVS Berichte 63. Strahltechnik, p. 197, 1980.
17. E. O. Olsen. *Studies of sheet metal cutting with plane-polarized CO_2 laser.* Optoelektron. Tech. Vort. 5 Zut. Kongr.: Laser 81, München, 1981. Berlin, 1982, p. 227, 1982.
18. A. G. Grigoryants, Yu. L. Ivanov, and A. N. Grezev. *Mechanical properties of laser welded joints*: in Weldment strength and quality control. Proceedings of MVTU, No. 337. Moscow, MVTU, 1980 (in Russian).
19. D. T. Swift-Hook and A. E. Gick. *Penetration welding with laser.* Marchwood Eng. Lab. R/M/N. 637, p. 1, 1972.
20. Y. Arata, I. Migamoto, and M. Kubota. *Some fundamental properties of high power CW laser beam as a heat source.* II W Document, 14/4/69, p. 1, 1969.
21. D. Belforte (ed.). *The industrial laser.* Annual handbook: in Levitt Pennwellbooks, Laser focus, Tulusa, Oklahoma, USA, 1986.

Chapter 9
LASER DRILLING

9.1. LASER-INDUCED MATERIAL REMOVAL

An approximate range of laser power densities required for material removal, in particular, for laser hole piercing, or drilling for short, lies between 10^6 and 10^9 W/cm^2. In Chapter 3 we have defined critical levels $q_c^{(1)}$ and $q_c^{(2)}$ at which materials begin to melt and vaporize respectively.

At a laser power density in excess of $q_c^{(2)}$, a material undergoes intense vaporization accompanied by flushing of the liquid phase and particulate emission, the latter process being associated with thermal stresses which cause material splitting.

In the range of power densities of 10^6 to 10^9 W/cm^2, ejection of particles mostly begins just at the start of the laser pulse, as seen from Fig. 9.1*a*, where the frame of high-speed photography illustrates a jet-like vapor flow suggestive of the spiking pattern of the laser pulse. In this process, the surface temperature at the atmospheric pressure is commonly higher than the vaporization (boiling) temperature T_v and depends on the power density.

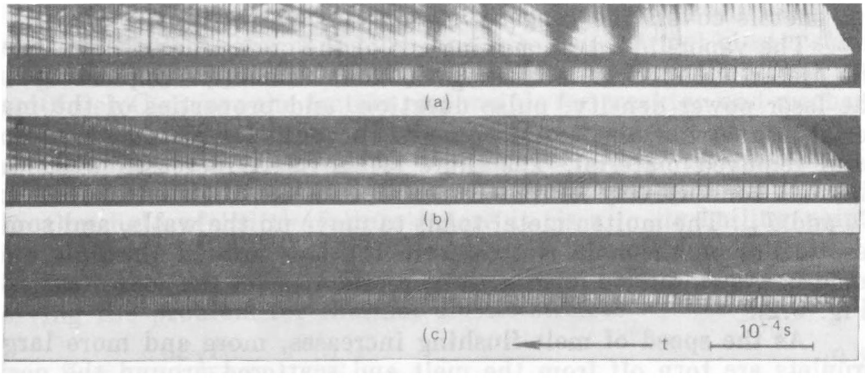

Fig. 9.1. High-speed photorecording illustrative of material removal from a steel surface drilled with 10^{-3}-s duration pulses focused by a 50 mm focal length lens using a 10-mm dia. diaphragm: (*a*) 42 J; (*b*) 9 J; (*c*) 0.5 J

At a power density of up to 10^8 W/cm^2, the blowoff material moves away from the metal surface into the surrounding atmosphere in the form of a jet normal to the surface.

The jet of the vaporized material expands and accelerates in the rarefaction region. Under certain conditions, the metal vapors cool down and condense into droplets up to 10^{-4} cm in size.

The resultant speed of the vapor front v_0 depends on the difference between the vaporization rate v_v and condensation rate v_c due to the flow of particles moving toward the target surface. This flow arises from the collision of the vapor atoms with one another and with the atoms of the environment. The speed of the vapor front is equal to about $0.8\ v_v$.

When the material evaporates in a vacuum the vapors freely expand and the flow of particles to the surface is insignificant. In this case, there is no distinct boundary between the stage of heating and the stage of material removal by vaporization.

A fraction of incident laser radiation does not reach the surface, but is absorbed and scattered by the blowoff material. The vapor of the plume absorbs laser energy most strongly. This is a weakly ionized plasma whose temperature and density determine its transparency to the laser beam. The absorbed energy heats up the plume and increases its brightness; there is a certain relation between the degree of plasma brightness and spike duration. The investigation described in a number of works point out that the laser-induced metal vapor plasma begins to decouple the beam from the surface most intensely at incident laser power densities of $q_{max} \geqslant 10^8$-10^9 W/cm^2. These threshold values determine the upper limit on the range of power densities practicable for laser drilling. The lower limit is set at power densities which are still sufficient to begin to pierce the material. This threshold for opaque materials and metals covers the range of q_{min} from 10^5 to 10^6 W/cm^2.

The vapor-liquid jet moving out of the crater melts and erodes the crater walls, thus increasing the hole diameter. Depending on the laser power density, pulse duration, and properties of the material in question, the liquid phase can account for 30 to 80% of the total removed material. The share of the melt increases with the thermal conductivity of the material and the difference between T_v and T_m. The molten metal tends to move up the walls, and some resolidifies on the hole rim to form the lips around the hole and some is blown out to form a thin, recast rim on the metal surface (Fig. 9.2).

As the speed of melt flushing increases, more and more large droplets are torn off from the melt and scattered around the periphery of the plume. A large number of small droplets ejected from the crater bottom are blown out into the central portion of the plume. The laser beam vaporizes some particles before they fall on

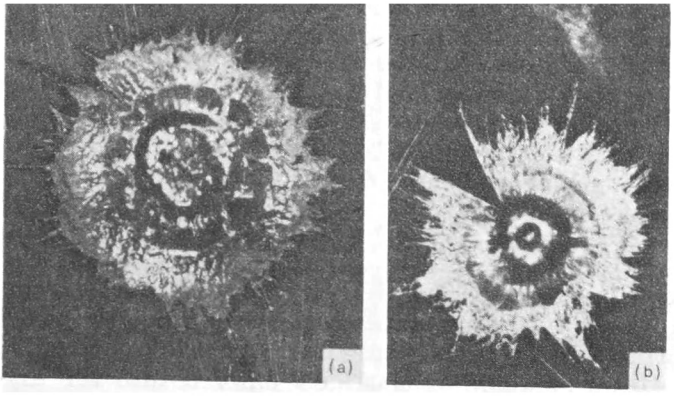

Fig. 9.2. Resolidified metal on the rims of laser-drilled holes (4×) in Cr-W-Mn steel (*a*) and 45 steel (*b*)

the surface. Individual particles 10^{-3} to 10^{-2} cm in size that move at (2 to 5) × 10^2 cm/s can change direction and return to the crater during the action of a few spikes (see Fig. 9.1*a*).

On the surface of the rim of the recast material, one can see concentric bands differing in temper color due to different rates of melt cooling (see Fig. 9.2).

The target surface beyond the rim of the recast material is covered with a layer of oxides, i.e. the products of the reaction of the metal with air. This layer does not appear if hole drilling in iron-carbon alloys is done in vacuum. The bottom and walls of the crater are covered with fine recast droplets $\sim 10^{-5}$-10^{-4} cm in size, which are the products of condensation of the metal vapor.

The recoil momentum produced by the blowoff material and transferred to the crater bottom and also the thermal elastic stresses caused by appreciable temperature gradients ranging from 10^5 to 10^6 deg C/cm are the factors responsible for cracking and mechanical damage to materials (Fig. 9.3). The criterion of transition from damage by vaporization to damage due to thermal elastic stresses is taken to be a condition at which the material reaches the threshold of brittle failure before it rises to its boiling point. The estimate of the threshold for brittle failure of a material in the region of the hole during melting of its walls can be made by solving the problem for thermal elastic stresses

$$\sigma_e = \frac{\beta E_Y T'}{3(1-2E_P)} \frac{r^2(t)}{\rho^2} \tag{9.1}$$

where β is the temperature coefficient of volumetric expansion, E_Y Young's modulus, T' the temperature variation in the region

of the fusion front, t the hole radius, E_P Poisson's ratio, and ρ the material density.

Expression (9.1) suggests that the size of the heated layer is much lower than the hole diameter and the temperature inside the hole is constant. The tangential stress σ_e elongates the material, and if σ_e is larger than the rupture stress σ_r, the material develops a radial crack whose length can be defined as

$$l = \sqrt{\frac{\beta E_Y T'}{3(1-2E_P)\sigma_r} r(t)} \qquad (9.2)$$

Expressions (9.1) and (9.2) apply only to thin plates, for which l is much larger than the plate thickness. However, even in this case the estimates are accurate to within one order of magnitude because the static modulus of elasticity entered into the expressions leads to large errors in the analysis of pulse interaction effects.

Substituting the tabulated values of quantities entering into (9.1) and (9.2), it can be found that l in steel and ferrite runs into the hundreds of micrometers. These values check well with experimental data. For example, the crack length in ferrite is equal to about 400 μm at a hole radius r of 50 μm considering that

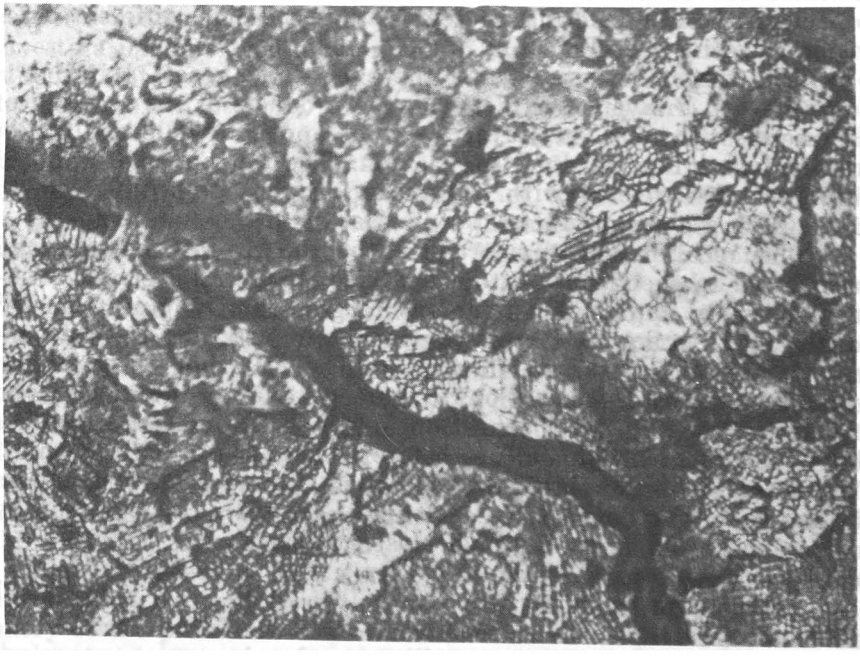

Fig. 9.3. Cracks on the crater surface of a steel specimen (600×)

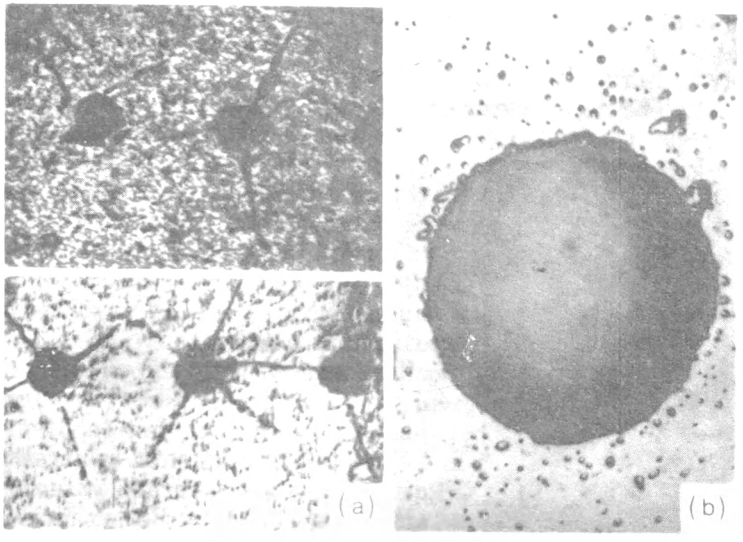

Fig. 9.4. Holes 100 μm in diameter drilled in ferrite with a 1.5-ms pulse (*a*) and 0.1-ms pulse (*b*). As seen, longer pulses lead to cracking

$\beta = 2.3 \times 10^{-5}$ K^{-1}, $\sigma_P \approx 0.1$, $E_Y = 2 \times 10^4$ MPa, and $\sigma_r = 5 \times 10$ MPa. Figure 9.4 illustrates 100-μm diameter holes drilled in ferrites by pulses of different lengths [1]. Longer pulses such as those used to pierce holes of Fig. 9.4*a* tend to increase the zone of thermal stresses which cause cracking. The recoil momentum can additionally damage the crater bottom since it develops a pressure of 10 to 100 MPa at a laser power density of 10^7 to 10^8 W/cm^2. The estimates obtained at the requisite values of vaporization rates point out that the resultant cleavage stresses can be beyond the damage threshold for materials. As follows from experiments, this is indeed the case. In Fig. 9.5 is shown the exit of the hole pierced through a scale-resistant steel plate. The broken underlip and lack of roundness due to recoil forces are apparent.

In single-shot or multiple-shot drilling, the position of the focal point is of importance for control of the hole shape. By adjusting the focal point between shots, it is possible to form, for example, a conical or a cylindrical hole.

The longitudinal sections of holes drilled in various steels exhibit white fringes around the hole sides, which form a poorly etched layer resulting from phase and structure transformations. Its width grows from the bottom upward to 10^{-3}-10^{-2} cm and depends on the thermal properties of the material and the shape and parameters of the pulse.

The temperature across this white layer changes from T_m or from the temperature of the superheated liquid metal to a value that is lower than the hardening temperature for the original structure of the base metal. The temperature gradient at the end of the pulse then reaches 10^5-10^6 °C/cm. This ensures fast heating and cooling, thus leading to phase and structural transformations in the zone of laser interaction.

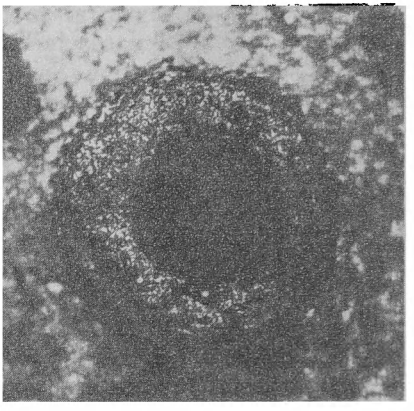

Fig. 9.5. Bottom view of the hole pierced through a steel plate (600×)

The effect of a quasi-continuous (spikeless) laser beam differs from the above described effect produced by the pulse from a spiking laser. The instantaneous power contained in a spikeless pulse does not generally differ from the average value at any instant of time. For example, a 50 J spikeless pulse about 10^{-3} s long delivers a maximum of 5×10^6 W/cm^2 to a focused spot about 10^{-2} cm^2 in area, while the spiking pulse of the same total energy delivers 5×10^8 W/cm^2 to the same area when irradiated by a spike 5×10^{-7} s long [2]. This difference in power density by two orders of magnitude has a strong effect on the character of material removal. Experiments confirm that the products of disintegration of most metals do not contain the liquid phase at laser power densities of up to 5×10^6 W/cm^2, but vaporization begins even at lower values of q and rapidly grows in intensity with an increase in power density.

9.2. MELT FLUSHING MECHANISM

Experimental studies and metallographic examinations of the zones of laser-metal interaction reveal that a large fraction of the melt is left in the crater at the end of the pulse, which recrystallizes at the bottom and on the walls of the cavity. The reason is that the beam delivers a lower power density to the crater bottom with an increase in the hole depth because of its defocusing and shielding by the vapor plume. Besides, since the laser pulse shape is not rectangular, the laser power decreases by the end of the pulse. This decreases the vaporization rate and vapor pressure in the crater, so that the flushing process discontinues and the melt clogs the hole, which is the case in hole piercing with pulses of ~1 ms duration and over.

The photographs of a high-speed framing camera, illustrative of the process of laser hole piercing through thin metal plates, are shown in Fig. 9.6. The melt clogs the hole either at the end of the pulse when the energy coupled to the spot drops off or soon after the end of the pulse. Figure 9.7 illustrates the process of hole plugging by the melt [1].

The power density below $q_{\min}$ only causes the surface to melt to a small depth and the melt flow has a little effect on the process of hole formation (Fig. 9.7*a*). At q above $q_{\min}$, the metal begins to vaporize at the center of the focused spot, and the excess vapor pressure bends down the melt surface such as depicted in Fig. 9.7*b*. As q continues to grow, the hole increases in depth and diameter because the processes of vaporization and flushing become more intense. But the liquid flow is still laminar and its speed is slow. The melt carried along by the vapor jet does not sputter away in droplets but flows over on the hole rim and forms at its edges a lip held in place by surface tension forces (Fig. 9.7*c*). As the pulse ends, the liquid metal on the cavity walls and on the lip side sloping toward the hole flows down and fills the cavity, thus forming the zone of recast metal after its recrystallization. At a still higher value of q, the flushing process becomes partially turbulent, and some liquid droplets break away from the melt flowing along the walls toward the exit aperture of the crater (Fig. 9.7*d*). In this case, the melt fills the cavity only partially, thus forming voids which can also appear when the melt seals the cavity and recrystallizes even before the pulse decays. When the power density reaches such a value that the melt flow becomes totally turbulent, more droplets are blown off, being carried away with the plume and scattered around the crater edges. Nevertheless, the volume of melt is still sufficient to plug the crater near its lip, especially if the laser pulse used is near to 1 ms in duration and its trailing edge is fairly long (Fig. 9.7*e*). Only a power density in the order of 5×10^7 W/cm^2 can provide

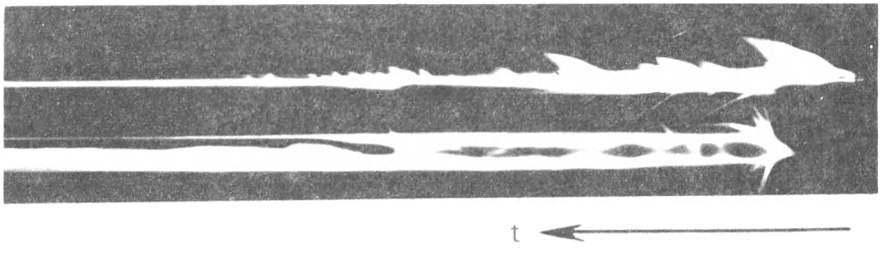

Fig. 9.6. High-speed photorecording of the processes of hole drilling with 1.06-μm laser radiation incident on a 50-μm thick tungsten plate at a focused spot 250 μm in diameter

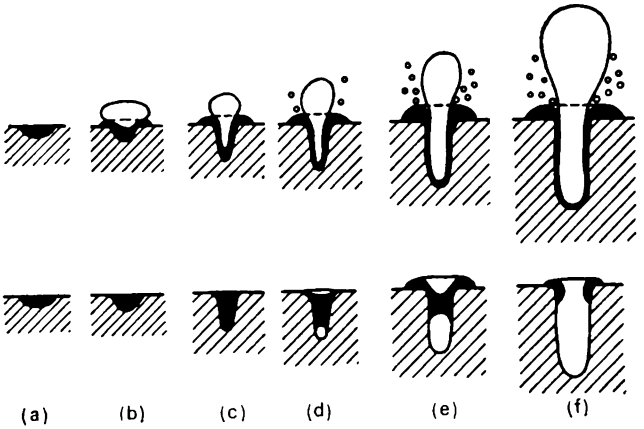

Fig. 9.7. Profiles of holes produced during and after interaction of pulses of various power (shown at top and bottom respectively)

open cavities (Fig. 9.7*f*). But even at this level of q, the melt redistribution after the end of the pulse can strongly distort the initial profile of the hole.

In Fig. 9.8 are shown photographs obtained with a high-speed photorecorder by the transmission microscope method, which demonstrate the process of hole piercing in metal plates about 0.3 mm thick. After approximately 10^{-5} s, the spikeless laser beam focused to a spot of a radius of 180 to 200 μm pierces a hole whose diameter d_1 at the end of the crater reaches $\sim 10^{-3}$ cm and is smaller than the diameter d_2 at the entrance to the cavity, $d_1 < d_2$. So, early in the pulse, the cavity produced tapers downward.

After a few tens of microseconds, the pulse produces a narrow cavity 10 to 20 μm in diameter, with its walls surrounded by the melt layer 10 to 20 μm thick. This melt begins to move in the cavity space under the action of the pressure gradient. If the hole is blind, the back pressure forces the melt at the crater bottom and on the walls to flow out and splatter around the edges of the crater.

The melt can close the cavity. If the energy coupled to the zone of interaction is enough to open the cavity, the pressure in the blind hole rapidly drops, tending to the environmental pressure. This changes the conditions of the melt flow along the cavity walls. After some time, the melt flows down and plugs the cavity if its diameter is not too large. The melt at the crater bottom absorbs the laser energy which increases the temperature and back pressure, so that the cavity becomes open again.

The process of cavity sealing and opening is not purely periodic since the thermal effects are inertial in character. Each cycle leads to an increase in the crater diameter subsequent upon an increased

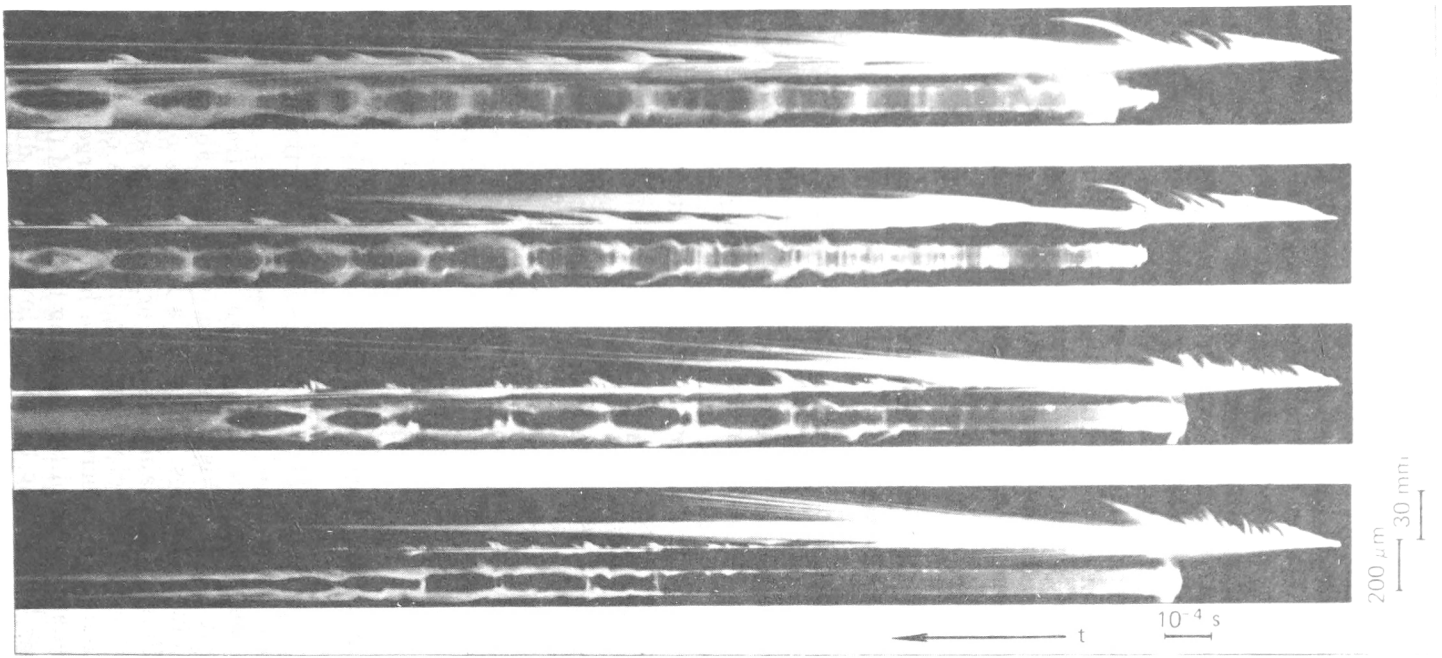

Fig. 9.8. High-speed photorecording of the processes of hole drilling in 0.3-mm thick metal plates

ejection of the fraction of material removed in liquid form. So, at a certain diameter d_1, the melt is no longer able to clog the cavity and the cavity diameter gradually increases until the power density of the heat source delivering heat to the cavity sides drops below the threshold for melting.

The qualitative analysis of liquid metal motion in the cavity allows us to assert that laser drilling should be done at $\geqslant 10^7$ W/cm^2 to improve the quality of holes. At excessively high values of q, however, the evaporating material can strongly shield the target surface at a definite moment of pulse interaction, so the melt will inevitably flow down and clog the cavity. Therefore, it is important that the optimal values of the pulse duration and pulse energy should be chosen to pierce holes of the desired shape and diameter in the most effective way [2].

9.3. EFFECT OF THE PULSE LENGTH AND ENERGY ON HOLE PARAMETERS

Under the specified conditions of beam focusing, the final dimensions of holes largely depend on the energy contained in the pulse and on the pulse length. Many industrial laser systems drill holes with pulses of a definite, invariable duration. In this case, the proper choice of the value of pulse energy is essential for precision laser hole drilling. The variation of the hole depth h and diameter d with laser pulse energy E is one of the main factors which deserves particular consideration.

Account must be taken of the fact that h and d vary with E not in a unique fashion, but depend on the method of pulse energy control. There are three methods for control of pulse energy: (1) adjustment of pump flashtube energy, which is the most popular approach; (2) control by means of light filters; and (3) aperture diameter adjustment. The experimental plots of d and h in steel as a function of pulse energy E adjusted by the above methods are shown in Figs. 9.9 and 9.10. The focal length F of the lens used to focus the beam on the target surface is equal to 60 mm.

It is seen from Fig. 9.9 that the same amount of pulse energy adjusted by the three methods produces holes of different diameters. The hole diameter is smaller in the case of pulse energy control by pumping and beam aperturing than when control is made with the aid of light filters. This difference is considerable especially in the range of lower energies. Thus, at a few joules of energy in the pulse, the difference in diameters is 2 or 2.5 times as large.

A decrease in the hole diameter in the case of the apertured beam is attributed to a decrease in the beam divergence. As for the case of pulse energy control by changing the level of flashtube pumping, a decrease here is due to both a lower beam divergence and a

shorter pulse. Referring to Fig. 9.10, as one would expect, the curve *2* for the case of pump energy control lies above the curve *1* involving the energy adjustment by filters.

Beam aperturing at a constant level of pumping of the lasant leads to the following: the hole diameter varies with the aperture

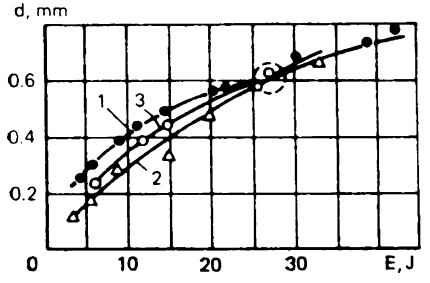

Fig. 9.9. Hole diameter d versus pulse energy adjusted by a light filter at pump voltage $V_p = 4.2$ kV and aperture stop diameter $D = 7$ mm (curve *1*), pump flashtube at $D = 7$ mm (curve *2*), and aperture stop at $V_p = 4.2$ kV (curve *3*)

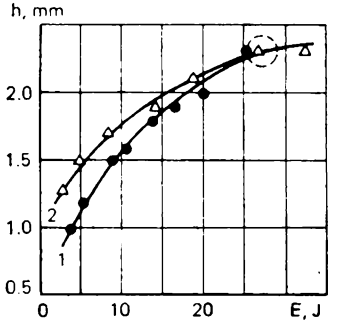

Fig. 9.10. Hole depth h versus pulse energy adjusted by a light filter at $V_p = 4.2$ kV and $D = 7$ mm (curve *1*) and by a pump flashtube at $D = 7$ mm

diameter, but the hole depth changes insignificantly even in the wide range of changes in the diameter of the stop. The dimensions of holes drilled at various diameters of the aperture stop are listed in Table 9.1.

The hole depth remains almost constant whatever the beam aperture because the aperture stop does not change the spatial profile of the beam, i.e. irradiance distribution over the beam cross section, but only changes the divergence angle and the diameter of the beam. Since the rate of hole piercing is a function of the laser power density (irradiance), the hole depth cannot vary appreciably with the beam aperture. At some, relatively small, diameters of the aperture stop, the hole depth increases by 10-12% because the stop cuts out the outer edges of the beam of a lower power density. This decreases the fraction of the material removed in liquid form and provides a saving in the energy required to remove the melt from the hole. The depth and diameter of the hole drilled are a function of the product of the laser power by the pulse length, i.e. the total energy contained in the pulse, $P\tau = E$. Consequently, the final dimensions of the hole are independent of P and τ if E remains constant [2].

Experiments show that the hole dimensions strongly depend on the pulse duration at a constant value of pulse energy. In one ex-

periment, the laser pulse length was varied with the aid of a revolving disk. The beam leaving a 10-mm diameter stop was focused by a 35 mm focal length lens on to the target surface of 45 steel. The level of laser pumping was held constant to have the output parameters of laser radiation invariable. The proper choice of filters made it possible to maintain the energy in each pulse constant.

TABLE 9.1 Hole Dimensions at Various Diameters of the Aperture Stop and at Constant Pump Voltage $V_p = 4.2$kV

Aperture,	Pulse energy, J	h (mm)	d (mm)	h/d
12	42.2	2.2	0.80	2.3
10	38.9	2.3	0.75	3.1
8	30.2	2.2	0.70	3.1
6	21.4	2.3	0.60	3.8
5	14.7	2.5	0.45	5.6
4	11.4	2.5	0.40	6.3
3	6.0	2.1	0.25	8.4

TABLE 9.2 **Depth h and Diameter d of Holes Versus Pulse Length**

E, J	τ, ms	q	h (mm)	d (mm)	h/d
5.4	0.25	2.2×10^8	1.2	0.42	2.9
5.1	0.35	1.5×10^8	1.3	0.39	3.3
5.9	0.55	1.1×10^8	1.5	0.38	3.9
5.7	0.75	7.6×10^7	1.6	0.36	4.4
5.4	0.85	6.3×10^7	1.8	0.30	6.0
5.0	1.15	4.4×10^7	1.6	0.26	6.1

A longitudinal section of the specimen illustrative of the holes drilled by laser pulses of various lengths appears in Fig. 9.11. The values of depths h and diameters d of holes produced by laser pulses, with energy E held constant accurate to 5-10%, are given in Table 9.2.

Increasing the pulse length from 0.25 to 0.85 ms increases the hole depth 1.5 times and decreases the hole diameter by 30%. Variations of the hole depth and diameter with the pulse length at the same pulse energy can be put down to two factors.

First, the irradiance drops in the radial direction from the beam center where q is maximum. Light filters cause a decrease in q. Since the filter transmissivity decreases away from the center, in evidence is an increase in the size of the region at the outer edges of the beam, where the irradiance falls below the threshold at which the material begins to melt and vaporize.

Second, the effect of attenuation of the beam by the material removed from the hole becomes weaker at a lower power density and a longer pulse. The reason is that the fraction of the melt left on the hole walls increases since the vapor pressure is not sufficient to eject the melt which thus adds little to the shielding effect. Indeed, the cross sections of holes in specimens show that short pulses delivering relatively large powers produce holes with smooth sides.

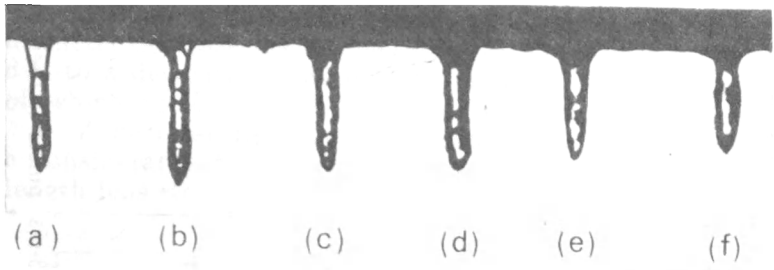

Fig. 9.11. Holes produced in steel by constant-energy pulses 1.15, 0.85, 0.75, 0.55, 0.35, and 0.25 ms long (*a*, *b*, *c*, *d*, *e*, and *f* respectively, 10×)

As the pulse increases in duration, the sides become rougher due to the solidified melt. In the limiting case, when the pulse length is relatively large and the irradiance is low, the melting process dominates, so that the melt seals the cavity and the hole depth decreases (see Fig. 9.11).

Too long a trailing edge of the pulse heavily contributes to the formation of the layer of the recast metal on the hole walls. The tail of the pulse from the laser used in the experiments described above was 350 to 400 μs long and accounted for almost one-third of the entire pulse length. Such a trailing edge promotes the melting process, with the result that a large fraction of the melt is left on the walls of the hole. The experiments conducted with pulses in which the tail about 300 μs long has been cut off show that this approach improves the profile of the hole, whose walls are practically free of the recast metal, although the hole depth varies insignificantly, in the range of 15%.

The profile of the hole and its dimensions considerably depend on the position of the focal point relative to the target surface. Let us consider the results of experiments on hole piercing in steel plates with a laser beam focused by lenses whose focal lengths are $F_1 = 39$ mm; $F_2 = 60$ mm, and $F_3 = 91$ mm. Figure 9.12 illustrates the paths of the beam with its focal point successively shifted above and below the target surface for a distance F. It is seen that the profiles of holes change with changes in the focal position. The energy in the pulse remains constant and reaches ~35 J. The beam aperture is 8 mm.

The diameter of the entrance of the hole drilled with the beam focused above the surface is a few times larger than the diameter of the light spot on the surface. When the focal point lies at the surface, the hole diameter is 4.8, 3.5, and 2.6 times the diameter of the focused spot for lenses with focal lengths of 38, 60, and 91 mm respectively. This is because the beam focusing to a smaller focal area results in a large power density delivered to the target surface.

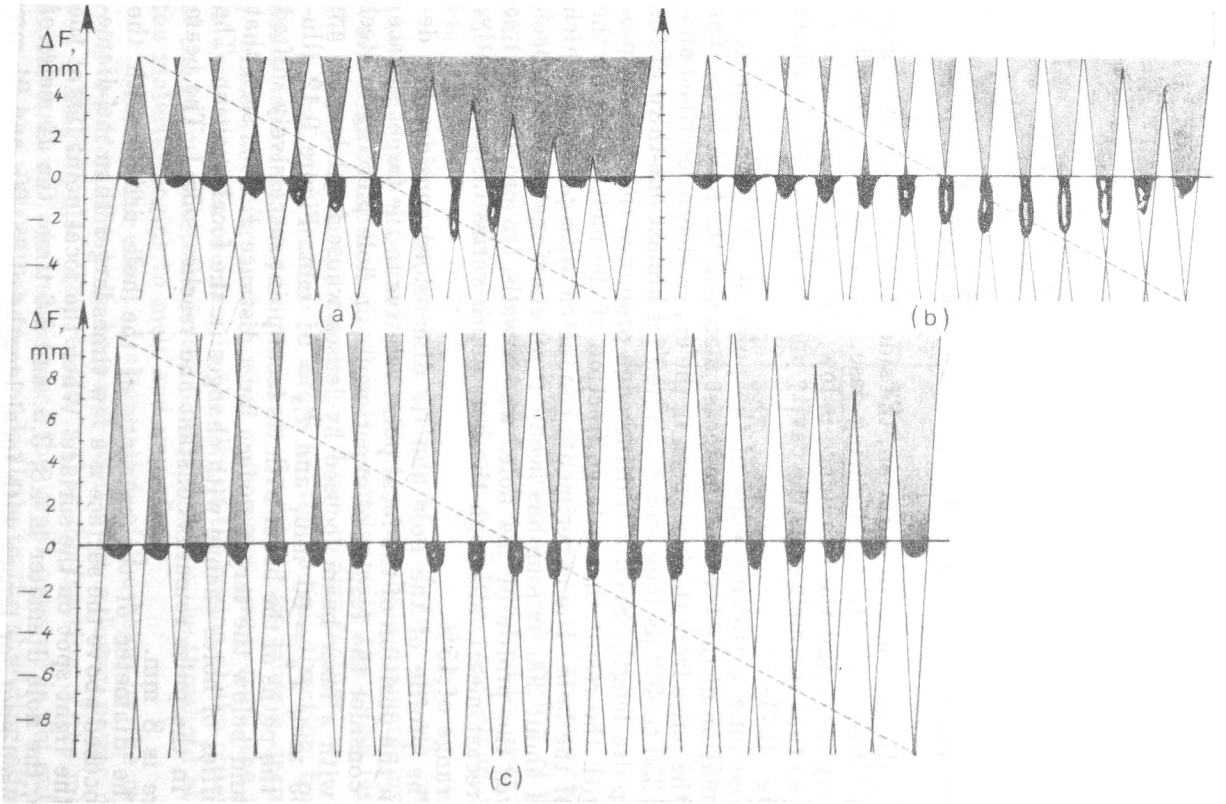

Fig. 9.12. Hole profiles as a function of focal position for drilling holes in steel with 35-J, 1.3-ms pulses focused by lenses with a focal length of 39 mm (*a*), 60 mm (*b*), and 91 mm (*c*)

The ratio of the hole entrance diameter to the focused spot diameter decreases as the focal length of the lens increases. This is due to a decrease in the power density at the focal point, the size of which increases with the focal length.

A decrease in the entrance diameters of holes for the case of a considerable defocusing of the beam focused by a 39 mm focal length lens stems from the fact that the melt seals the hole entrance

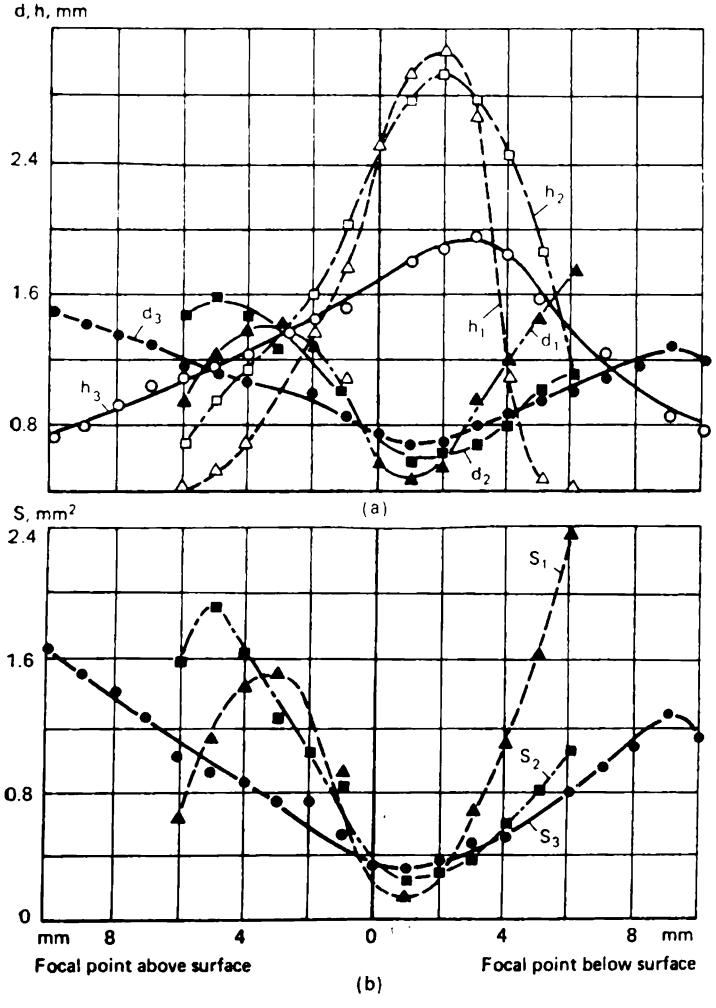

Fig. 9.13. Diameter d (*a*) and entrance area S (*b*) of holes drilled in steel by 35-J, 1.3-ms pulses as a function of focal position for lenses with $F_1 = 39$ mm, $F_2 = 60$ mm, and $F_3 = 91$ mm

because of a low power density. As the location of the focal point gradually changes relative to the surface, the beam produces holes of different shapes: parabolic shapes and conical shapes in the case of a large beam defocusing, cylindrical shapes when the lens focus is above the surface; and bulb-like shapes when the beam is focused slightly below the surface. The results of measurements of holes in the longitudinal sections of specimens have been used to construct the plots of the hole entrance diameter d, hole depth h, and hole entrance area A against the values of distance ΔF of the focal point from the target surface (Fig. 9.13).

As seen from Fig. 9.13*a*, the focal positions corresponding to the largest depths and smallest diameters are different. The beam focused slightly below the target surface for a distance equal to about two-thirds of the depth pierced produces the deepest hole in the order of 1.5 to 2.0 mm depending on the focal lengths of lenses. The use of shorter focal length lenses enables the beam to pierce deeper holes but of a smaller diameter.

9.4. SURFACE FINISH OF HOLES DRILLED BY NORMAL PULSES

Let us consider the results of measurements of the profile irregularities on the walls of five holes pierced in steel plates by 1, 2, 3, 4, and 6 pulses respectively (Fig. 9.14). Each pulse delivered 40 J of energy and lasted about 1.3 ms.

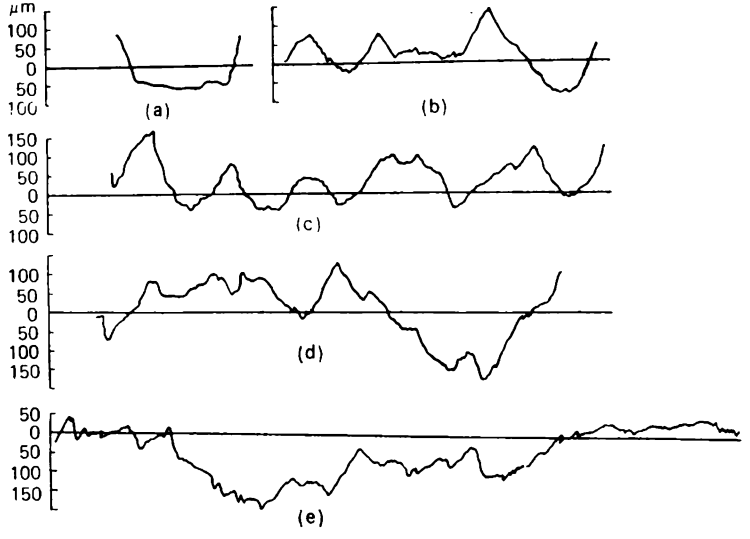

Fig. 9.14. Contour records for holes drilled in steel by one (*a*), two (*b*), three (*c*), four (*d*), and six (*e*) pulses with 40 J energy and 1.3 ms duration

The specimens were cut in the plane parallel to the hole axis at a distance of ~0.1 mm from the diametral line. Next the sections were ground with an abrasive disk to remove burrs and to obtain the cross sections cut exactly in the axial plane of the holes. The tracing head of a profilograph of K.L. Ammon had a diamond needle to trace profiles. The scale factor of a contour record was 0.20 μm and the horizontal magnification was 30 ×. The degree of roughness of hole walls was assessed by comparing the contour records with those taken from the surfaces of roughness comparison specimens.

The contour records show that longer pulses of high energy yield rough walls with protrusions and depressions measuring from 100 to 250 μm. An increase in the number of shots improves the surface finish insignificantly.

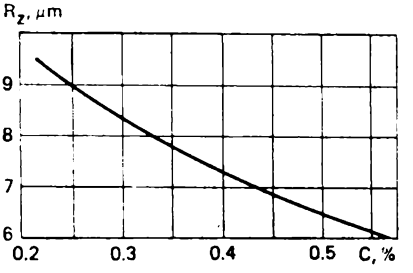

Fig. 9.15. Roughness R_z of laser-drilled holes in carbon steels versus steel carbon content

Hole piercing by a series of shorter pulses of lower energy, which reduce the fraction of the liquid phase in the blowoff material to a minimum, can eliminate these defects. The technique of multiple shot drilling involves the requirement that each pulse delivered to the same spot should provide an aspect ratio of $h/d \simeq 1$.

The roughness R_a (arithmetic mean deviation of the profile) of some regions of hole walls ranges from 0.63 to 0.08 μm. These values of R_a allow us to conclude that the laser beam can find practical applications, at least for piercing initial holes in various parts, for example, in dies. These holes can then be brought to size and smoothed in final finishing operations. The properties of materials affect the hole quality [3]. For example, the height of irregularities, R_z, on the walls of holes drilled in carbon steels containing 0.2 to 0.6% C decreases with increasing carbon content (Fig. 9.15). The thing is that the melt becomes less viscous with an increase in the carbon content, so it is blown off more readily from the cavity.

9.5. FACTORS AFFECTING THE HOLE QUALITY

The reproducibility and quality of laser-drilled holes largely depend on the amount of the liquid metal in the material being removed from the crater and its distribution on the walls and at the bottom of the crater both at the end of the pulse and soon after the pulse ceases. The fraction of the liquid phase can reach 30 to 80%. The longer the pulse, the larger the fraction of the melt in the

hole, which involves difficulties in control of the process of drilling and leads to a large scatter in the parameters of holes. Too long a pulse, longer than 1 ms, causes an appreciable growth of the zone of possible changes in the structure and properties of the material. A long pulse striking a brittle material increases the zone of thermal stresses which can produce cracks (see Fig. 9.4). A shorter pulse greatly decreases the probability of cracking. For example, the pulse length at which no cracks appear near the hole in ferrite does not exceed 100 μs.

The temporal profile of the laser beam and the shape of the pulse envelope have an appreciable effect on the quality of holes. The optical systems of laser setups contribute little to the distortion of the cross section of the hole if they properly position and aperture the beam focused on the target surface [1]. However, errors in aligning the laser beam and the optical system may cause both distortions of the laser power density distribution in the focused spot and the offset of the center line of the hole from the normal to the target surface.

Of much importance is the radiation pattern from a laser and, hence, the spatial profile that characterizes the cross section of the laser beam. A factor that heavily affects the hole profile is the random irradiance distribution over the beam cross section, which is specific to normal relaxation pulses. Asymmetry of the angular divergence results in a distorted shape of the focused spot even if the beam is apertured.

An asymmetric radiation pattern can arise from inhomogeneities of the laser rod and optical pump field and from an inaccurate adjustment of the cavity elements and the cavity itself with respect to the optical system.

A symmetric radiation pattern with the power density attenuating from the center to the edges of the beam, which is typical of many normal-pulse lasers, does not distort the hole profile, but often results in rough sides and large taper of the hole.

Other factors which determine the accuracy of laser drilling are the caustic (envelope curve) of the beam from the optical system, location of the target surface relative to the caustic, and changes in the irradiance distribution with an increase in the hole depth.

In general, the reproducibility of hole dimensions is a function of such laser parameters as the pulse energy, pulse duration, angle of divergence, and the spatial and temporal profile of the beam.

Hole piercing is done with pulsed lasers which can ensure a rather high throughput. The investigations conducted with ruby and Nd-glass lasers show that the laser parameters change significantly during the transient process until the lasant reaches the steady-state heat conditions. Heating impairs the emitting characteristics of the

active medium and causes thermal deformations of the resonator due to a nonuniform temperature distribution over the cross section of the rod.

The duration of the transient, which does not commonly exceed a few tens of seconds, depends on the mass of the lasant and its thermal properties and also on the efficiency of the cooling system. By the end of the transient, the energy in the pulse can be 10-15 times the energy in the first pulse, the pulse length can increase 5 or 6 times, and the beam divergence 2 or 3 times. These changes in the beam parameters must entail changes in the dimensions of holes during the transient.

The output parameters of a laser operating in the steady-state conditions depend on the pump energy and efficiency of the cooling system that ensure the steady temperature of the laser rod and resonator. The laser can pierce holes more or less identical in shape and size only in the steady conditions of operations. In the case of single-pulse drilling, the spread in hole sizes primarily stems from the spread in the laser pulse parameters. A measure of the spread in any parameter is the mean relative deviation $\gamma_x = dx/x$, which is proportional to the standard (rms) deviation $\sigma = 1.25 \mid dx \mid$ for the normal distribution of the spread in x [1]. The quantity γ_x is convenient for use and can readily be found from experimental results. It also offers a means for estimating the particular effects of various factors on the reproducibility of hole dimensions.

TABLE 9.3 **Relative Deviations of Nd-Glass Laser Energy and Hole Diameters**

Material	Thickness, mm	γ_E, %	γ_d, %
Ferrite	0.5-0.6	2.0	6.6
		5.0	11.5
Aluminum foil	0.1	1.5	3.4
		6.5	7.5
Cr film on glass ceramic	0.1	2.0	1.7
		5.0	2.0

In the steady-state operation of a pulsed laser, the energy in a pulse changes most heavily. Its relative deviation γ_E is larger than the pulse length deviation γ_p and beam divergence deviation γ_b. For example, the values of these deviations for a Nd-glass laser pulse delivering 2-3 J of energy are: $\gamma_E = 5\%$, $\gamma_p = 0.5\%$, and $\gamma_b = 1.0\%$. An increase in γ_E leads to an increase in the deviation γ_d of the diameters of through holes; the thicker the plate, the larger the value of γ_d, as seen from Table 9.3.

The output characteristics of a repetitively pulsed laser operating in the steady thermal conditions become more stable the higher the ratio of laser energy to the value of the lasing-action threshold. When this ratio rises from 1.1 to 3.5, the relative deviation of energy from a Nd-glass laser drops from 18 to 2% and only depends on the

variations of both the pump energy and the thermal conditions of the laser rod.

The kind of cooling fluid, its flow rate and temperature, and also the pump pulse repetition rate more weakly affect the stability of Nd-glass laser parameters. The opposite is true for a ruby laser: the generation threshold for a ruby rod noticeably increases with temperature, so the excess over the threshold decreases.

Cavity mirrors, pump reflectors, and optical elements age with time, and lasants change their properties under UV radiation of flashtubes. They determine the service life of a laser and stability of its parameters such as the pulse energy, pulse duration, and beam divergence, which, in turn, affect the diameter and depth of holes and their reproducibility.

Statistical computer-aided processing of the data on a large number of holes pierced in ferrite plates by pulses of the recorded parameters has shown that the mean deviations of both hole diameters and radiation parameters of the laser operating in steady conditions follow the normal distribution law.

A part must be properly held in position and moved with respect to the laser beam so that the normal to the target surface should be coincident with the optical axis of the focusing system. Otherwise, when piercing a series of holes in the part, each focused spot would gradually change in diameter and would lead to corresponding changes in hole shapes. Proper positioning of parts can remedy the situation.

Inhomogeneous properties and structures of materials can also affect the reproducibility of the results. This is particularly the case where the diameters of holes drilled are commensurable with the sizes of inhomogeneous sites or if the number of these sites is large.

9.6. MULTIPLE SHOT DRILLING

The technique of multiple shot drilling (MSD), or percussion, involves the superposition of a series of pulses over the same focal spot to remove percussively the material by vaporization, thereby producing a deeper hole. The final depth of the hole depends on the total energy delivered by the repeated pulses. The hole diameter is a function of the average parameters of each pulse, focused spot diameter, and shape of the caustic.

The thickness of each layer removed with one shot can be rather small. Therefore, as compared to single-pulse drilling, the multiple-shot process of percussion of holes $\sim$1 mm deep and over produces a less amount of melt, which affects to a less degree the hole shapes after its resolidification. So, thin layers successively vaporized by a series of pulses result in smoother hole walls.

A distinguishing feature of laser-induced percussion is the possibility of hole piercing with short pulses, whose space width (pulse spacing) is much larger than the time it takes the material to cool. This feature combined with a high pulse fluence affords a sharp reduction of the melt in the blowoff material.

The use of short pulses makes it possible to drill brittle materials without cracking owing to a more uniform distribution of residual stresses throughout the depth and to a higher dynamic strength with a shorter duration of the thermal shock. As the crater depth increases, the irradiance at the crater bottom changes because of an increased beam defocusing. The part must then be shifted with respect to the focal point to compensate for the thickness of the layer vaporized by each pulse. If the requirements placed on the accuracy of holes are not too rigid, the focal plane can be made coincident with the moving vapor front to avoid the irregularities in the hole shape. More accurate holes of round or other shapes can be drilled by aligning the plane of the image of the aperture stop with the vapor front, seeing to it that the irradiance distribution over the beam cross section is uniform.

One more feature of MSD is that this technique is less vulnerable to the deviations in the laser beam parameters. For example, assuming the deviations to be the same, the use of n pulses of total energy E instead of one pulse of the same energy reduces the rms deviation of hole dimensions by a factor of $\sqrt{n}$.

The MSD technique can be applied to achieve two different aims: to pierce the deepest possible holes without meeting too strict accuracy requirements and to produce precision holes. The processes here only differ in the optimal conditions selected for the purpose. In the first case, the aspect ratio h/d attained with each shot is greater than unity; in the second, the ratio is $h/d < 1$.

Precision holes can be made by ensuring a cylindrical shape of the beam. This effectively reduces the amount of radiation that is directly incident on hole walls and conducive to material melting.

Deep hole drilling. In experiments, a series of 40-J, 1.3-ms pulses were shot at the same spot on the target surface. The focal length F of the lens was 50 mm and the diameter of the aperture stop placed across the beam was 10 mm. The hole depth gradually increased with the number of shots but the diameter changed little after each pulse. A photograph of cross sections of holes, each produced by a different number of pulses, appears in Fig. 9.16. The plot of the depth of a hole as a function of the number n of pulses is shown in Fig. 9.17. Work [2] contains the theoretically predicted values of the final dimensions of holes.

Experiments confirm that it is the parameters of each individual pulse rather than the number of pulses that determine the hole diameter. Starting at a definite depth, a greater fraction of the

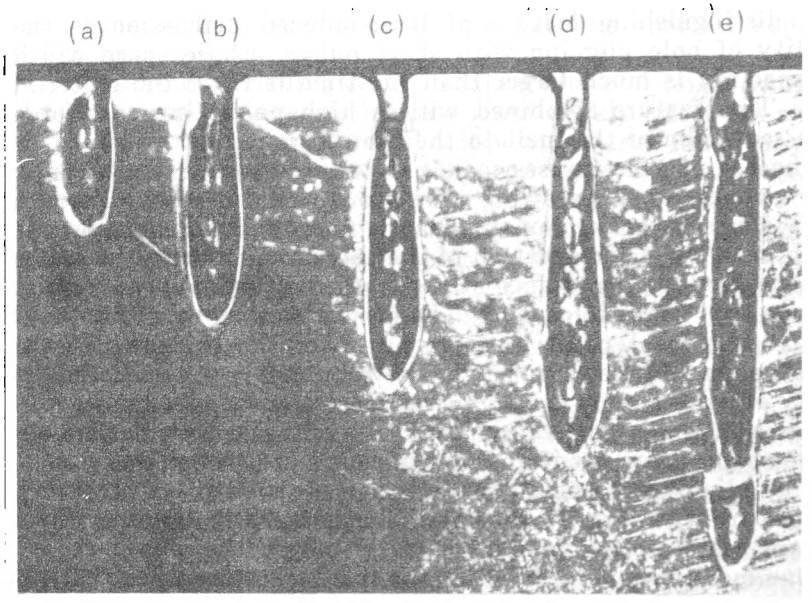

Fig. 9.16. Cross sections of holes (7×) produced in steel by one (*a*), two (*b*), three (*c*), four (*d*), and six (*e*) pulses of 40 J energy and 1.3 ms duration

beam will fall on the hole walls because of the beam defocusing with distance away from the lens focus. It is likely that some rays reflected from the walls will impinge on the crater bottom and contribute to an increase in the hole depth. This contribution must then be taken account of in estimating the limiting depth pierced by a series of pulses. To check whether or not the reflection from the walls adds to the hole piercing, a few pulses were shot to form such a hole that the rays at the outer edges of the beam could fall on the hole sides. The hole was then struck by one more pulse passed through an aperture stop placed behind the lens. The stop diameter was

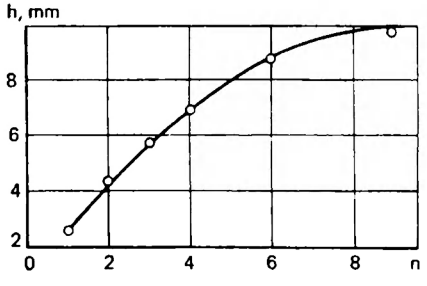

Fig. 9.17. Depth of hole drilled in steel as a function of the number of 40-J, 1.3-ms pulses

TABLE 9.4. **Limiting Dimensions of Holes Produced by a Series of Pulses**

E, J	*d*, mm	*h*, mm	*h*/*d*	*n*
0.1	0.15	0.5	3.3	4
1.0	0.33	1.5	4.5	6
10.0	0.73	5.0	6.9	9

such as to cut off the outer rays of the beam. A similar check was made but without the diaphragm.

Table 9.4 lists the limiting values of d and h of holes produced in carbon steel by a series of 100-μs pulses of various energy E at $\tan \varphi = 0.2$, which is a factor accounting for the shape of the caustic behind the focal plane of the optical system. For the case under consideration, the latent heat of vaporization of steel is 5×10^4 J/cm^3 and pulse fluence is about 300 J/cm^2.

Comparison between the dimensions of holes produced with and without the aperture stop shows that the hole depth is always larger in the second case. The contribution made by the radiation reflected from hole walls to an increase in the hole depth ranges from 2 to 6 % depending on the values of the hole depths pierced.

Experiments confirm that the depth of holes produced by a series of short pulses can be a few times that pierced by a single pulse. The proper choice of radiation parameters and conditions of beam focusing can increase the depth tenfold depending on the material drilled.

The percussion process cannot effect a purely vaporization drilling for the mere reason that the temperature distribution into the material is continuous and the vapor front produces a thin molten layer of thickness $h' = a/v \ln T_0/T_{max}$, where $v = 2r_f/\tau$ is the mean rate of material vaporization. Assuming that this layer is partially blown away under the excess vapor pressure, the residue being uniformly distributed over the hole sides at the end of the pulse, it is possible to estimate the relative deviation of the hole diameter, γ_d, depending on the number n of pulses. A series of 9 or 10 pulses increase the hole depth fourfold. The hole depth reaches ~90 % of the peak value after 6 or 7 pulses ~1.3 ms in duration, with the beam focused by a 50 mm focal length lens.

As noted earlier, the hole depth can be increased by shifting the focal point inside the sample between the shots for a definite distance. This approach enables holes to be made with aspect ratios exceeding 25.

Precision hole drilling. The process calls for a minimum degree of melting on the walls and at the bottom of the cavity. For this, two conditions must be met, which determine the region of optimal regimes:

$$\tau \leqslant r_f^2/a, \quad h(\tau) \leqslant 2r_f$$

The first condition ensures a low heat loss by conduction through the hole walls, thereby minimizing the amount of the melt formed in and around the hole. The second condition places a limit on other factors that encourage melting and ensures a specified hole diameter deviation

$$\gamma_d = 0.1 \ln T_0/T_m$$

For the case under consideration, γ_0 is equal to 8%, which corresponds to the second class of accuracy at a hole diameter of 50 μm.

The above conditions are not universal and are mainly applicable to metals. For nonmetals, whose thermal conductivity is low, the limit on the pulse duration can be set up from other considerations. In drilling brittle materials, for example, too long pulses can induce thermal stresses and, hence, cracking. For such materials, pulses should be kept short to maximize vaporization.

Let us briefly consider the process of hole piercing with repeated pulses of various lengths. Comparison between the sizes of holes produced by a single long pulse and by a series of short pulses at the same energy expended in drilling one hole allows us to conclude that the final dimensions of a hole and its shape depend on the amount of energy lost in the course of both the beam absorption by blowoff material and the heat transfer through hole walls.

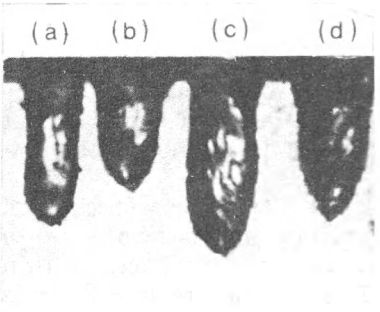

Fig. 9.18. Cross sections of holes produced by five 3.8-J, 0.15-ms pulses and one 19-J, 0.65-ms pulse (*a* and *b* respectively) and by five 6.8-J, 0.25-ms pulses and one 34-J, 1.2-ms pulse (*c* and *d* respectively). The total energy and length of five pulses are the same as those of a single pulse

Indeed, a series of short pulses with a space width sufficient for the removal of the vapor and liquid phases produce a deeper hole than a single pulse whose energy and duration is equal to the total energy and duration of all the short pulses.

For the cases illustrated in Fig. 9.18, the energy loss which increases with the pulse length causes a decrease in the final depth of the hole by 30%. In evidence is an increased taper at the entrance to the hole, which points to a considerable melting of the walls. From the comparison of the cross sections of holes produced by pulses of various lengths, it becomes apparent that shorter pulses appreciably minimize the fraction of the liquid phase solidified on the hole walls.

Of practical interest is the method of splitting a long pulse into a series of short pulses with a revolving disk, for example. In experiments, a long pulse has been split into 10 and more pulses with a different duty cycle and duration of up to ~50 μs. Here, laser-beam modulation with a revolving disk offers the possibility of shaping rapid pulses with a repetition rate of ~10 kHz.

Examples of MSD applications. The MSD technique expands the area of application of lasers and makes it possible to pierce holes

with an aspect ratio of up to 50. The correct choice of working conditions allows dispensing with final finishing operations.

Work [2] gives examples of hole piercing with Q-switched ruby lasers, repetitively pulsed lasers, and lasers equipped with special projection systems for the production of holes 4 to 100 μm in diameter with an aspect ratio of 20 to 50 in alumina, silicon, germanium, zinc, molybdenum, ruby, and ceramics. The holes are well reproducible, have a small taper at the entrance and rather smooth sides.

Multiple shot drilling has reached commercial status in a number of applications. Let us cite several examples: current technology can produce 50-μm diameter holes with a 50-μm hole spacing in ferrite plates for computer memories; 50-μm diameter holes in 0.6-mm thick ceramic-glass boards for the interconnection of leads to printed circuitry; holes in ceramic spacers for coaxial precision cables; and 5 to 80-μm diameter holes in refractory materials up to 0.2 mm thick for use as apertures in electron beam and ion beam setups.

Table 9.5. Typical Dimensions of Holes Produced in Materials by Repeated Pulses

Material	Hole parameter				Pulse parameter			
	d, μm	h, mm	h/d	δ_d, μm	E, J	$\tau\times10^4$, s	q_0, W/cm²	n
High-alumina ceramics	200	3.2	16	—	1.4	5	4×10^6	40
	200	1.0	5	+30	1.6	10	5×10^6	1
Ferrite	200	1.0	5	±4	0.3	1	1.2×10^7	7
	50	1.0	20	—	0.05	0.9	6×10^7	10
	100	0.7	7	±15	1.5	10	2×10^7	1
	100	0.5	5	±5	0.2	0.9	6×10^7	9
Stainless steel	50	1.2	24	—	0.2	0.9	1.2×10^6	12
	50	0.1	2	±2	0.2	0.8	1.5×10^8	1 to 5
Ruby	10	0.4	40	—	0.1	Q-switched	—	—
Brass	30	0.1	3.5	±1.5	0.05	1.0	4×10^7	1 to 3
Glass ceramic	50	0.6	12	—	0.3	1.0	5×10^7	3 to 5

Table 9.5 lists the values of d, h, h/d, and hole diameter tolerance δ_d for holes drilled in some materials by n pulses with different values of average pulse energy E.

9.7. USE OF A CONICAL LENS TO PRODUCE LARGE DIAMETER HOLES

Drilling of holes larger than 1 mm in diameter with the use of a simple lens or a system of simple lenses to shape the beam calls for a large energy in the pulse, which is attainable mainly at laboratory setups.

There is known a method for producing holes of the desired size and configuration, by which the piece is moved so that the focal point traces out the contour of the hole in plan. However, the need to move the part entails complications in the laser setup design and makes automation of the process difficult. The edges of the hole drilled have irregularities no less than the focused spot radius in size. The irregularities can be reduced by overlapping the spots at a large overlap ratio or by decreasing the spot size. Either of the approaches decreases the hole drilling rate and gives holes of poor quality. To drill holes of large diameters, researchers [4] found it advantageous to shape the laser beam to a configuration conformable to that of the hole to be drilled and then guide the beam onto the target surface.

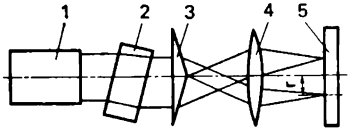

Fig. 9.19. Diagram of an optical system with a conical lens for laser hole drilling

Figure 9.19 illustrates the principle of the optical system using a conical lens to implement the suggested method. The system includes a laser *1*, plane-parallel plate *2*, conical lens *3*, zoom (varifocal) lens *4*, and fixture (not shown) for a part *5*, which can move along the axis of the optical system.

The conical lens *3* and zoom lens *4* focus the beam to a specified contour pattern on the target surface. The size of the contour pattern depends on the conical surface of the lens *3*. The radius r from the optical axis to the contour line is given by

$$r = F\,[\arcsin(n\cos\alpha) + \alpha - \pi/2]$$

where α is the angle between the generator of the cone of the lens *3* and the optical axis in the plane normal to this axis, F the focal length of the zoom lens, and n the refractive index for the conical lens material.

If the value of α is close to $\pi/2$, the above formula reduces to a simpler form

$$r = F\,(\pi/2 - \alpha)\,(n - 1)$$

The size of the contour pattern can be varied in a rather wide range by adjusting the focal length of the zoom lens. This adjustment makes the optical system ready for drilling single-type configuration holes of different sizes. Tilting the plane-parallel plate *2* at different angles to the optical axis and rotating it around this axis yield a smooth power distribution over the contour pattern, which can be of advantage where the material drilled has a different thickness or hardness.

To produce fairly deep cylindrical holes, account should be taken of the following facts. The deviation of the hole profile from the cylindrical shape is stronger the greater the angle of beam convergence behind the cylindrical lens. From the analysis of the geometry of ray paths it follows that the deviation from roundness is smaller the shallower is the hole and the larger is the focal length of the spherical lens.

For the holes to be more accurate in size, the thickness of cut, $h' = \beta F$, must be as small as possible (β is the actual beam divergence). In evidence are two opposing requirements: (1) the focal

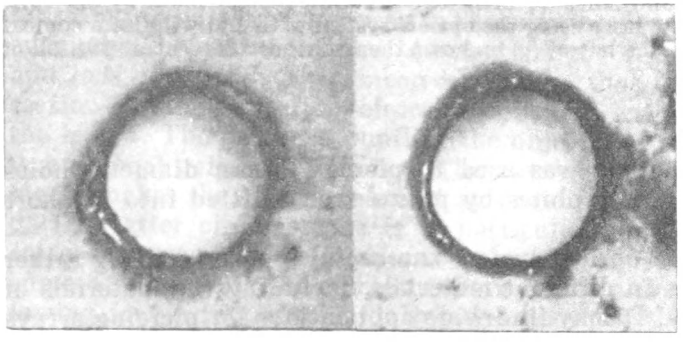

Fig. 9.20. Holes produced in a stainless steel plate by single 50-J, 1.3-ms pulses focused by the optical system of Fig. 9.19

length F must be as large as possible to avoid the lack of roundness; and (2) F must be as small as possible to reduce the width of the contour line to a minimum.

Nevertheless, given the specified values of the hole diameter d, depth h, and deviation from roundness, a lens of the shortest focal length should be chosen to ensure the required precision and to raise the hole-drilling rate.

Figure 9.20 illustrates 3.0-mm diameter holes produced in a 0.3-mm thick stainless steel plate by single pulses from a Nd-glass laser focused by a conical lens. An example of a 2.5-mm diameter hole drilled in a 0.3-mm thick stainless steel plate by six split pulses from a Nd-glass laser focused by a conical lens appears in Fig. 9.21*a* on the right; on the left is shown the nonirradiated central portion of the contoured spot. The Nd-glass laser produced 16 J of energy in a pulse of 1.0 ms duration. Each normal relaxation pulse was split into ten 40-μm duration pulses. The same experiment but without the use of a conical lens was performed to drill holes in the same plate (Fig. 9.21*b*). As seen, the hole diameter is about one-third the diameter of the hole of Fig. 9.21*a*.

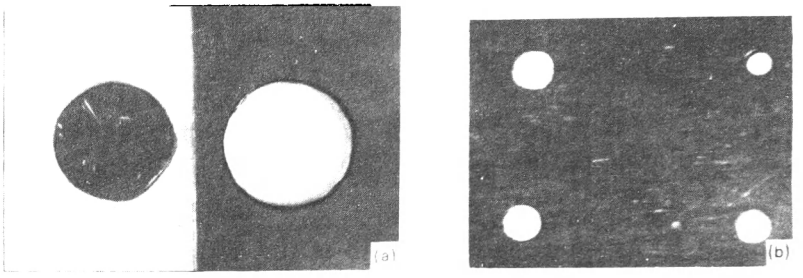

Fig. 9.21. Hole (*a*) and holes (*b*) drilled in a stainless steel plate by six split pulses from a Nd-glass laser using the optical system with and without a conical lens respectively. On the left of (*a*) is shown the nonirradiated central portion of the contoured spot

A similar method was used to pierce 2.5-mm diameter holes in 1.2-mm thick ferrite plates by pulses each splitted into 15 short pulses (Fig. 9.22).

The described optical system is a useful tool for drilling rather reproducible holes in different materials, including the materials of low machinability. It may find wide applications for piercing arrays of orifices larger than 1 mm in diameter in the production, for example, of filters, grids, and sieves of various purposes.

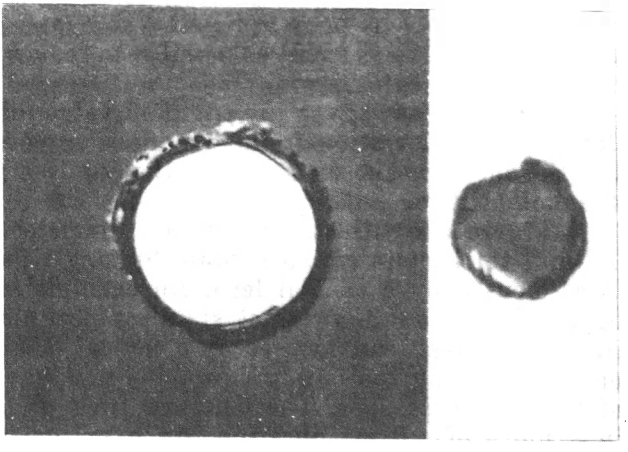

Fig. 9.22. Hole produced in ferrite by 15 split pulses from a Nd-glass laser using the optical system with a conical lens. The spot on the right is the nonirradiated central portion

9.8. WAYS OF IMPROVING THE REPRODUCIBILITY OF HOLES

There are a number of methods in which highly reproducible fine holes ~1 mm in diameter can be made with a focused laser beam.

Consider a way of improving the accuracy and quality of fine drilling with the aid of an axicon commonly applicable for producing large diameter holes [4, 5, 6]. The choice of location of the axicon depends on the type of optical system used.

The layout of the optical system under consideration is shown in Fig. 9.23. The system includes a laser rod *2* placed into a cavity formed by plane mirrors *1* and *3*, axicon *4*, lenses *5* and *6* to form a telescope, tilting cold-light mirror *7*, and lens column *8* to focus the beam onto the target surface *9*. The viewing system consists of an eyepiece *12* with crosshairs, turning mirror *11*, viewing lens *10*, and lens column *8*. The axicon is sited so that the minimum cross section of the beam after refraction coincides with the front focus of the lens *5*. The entrance pupil of the objective *8* coincides with the second focal point of the lens *6*. This mutual arrangement of the elements makes the system compact at a minimum aperture of the lens *6*. The latter circumstance is of particular importance since a decreased aperture of the focusing lens causes the focused beam to assume a more elongated shape in the zone of interaction, thereby allowing for an increase in the relative depth of the hole.

This optical system was used in experimental studies. The energy in a 1-ms duration pulse was varied from 3 to 5 J by adjusting the pump energy. The divergence of the beam emitted from the cavity was ~40′. The experiments were performed using two lenses

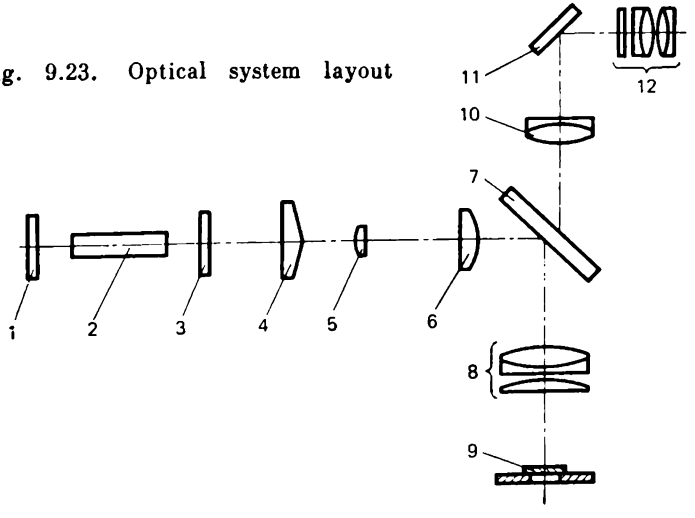

Fig. 9.23. Optical system layout

with $F_1 = 50$ mm and $F_2 = 100$ mm and two telescopes with a magnification of 4 and 1.5 power respectively. The refraction angle of the axicon was 0.04 rad.

The system equipped with a 50 mm focal length lens and a four-power telescope focused the beam to a circular spot $\sim$0.5 mm in diameter.

Hole drilling was done in plates of scale-resistant steel, tantalum, and molybdenum 0.3 to 0.55 mm thick. An array of 50 holes 0.5 mm in diameter were made in each plate. Similar patterns of holes were drilled using the optical system of Fig. 9.23 but without the axicon *4*. In the second variant of the process performed with two combinations of focusing lenses and telescopes, the hole diameter varied from 0.07 to 0.4 mm depending on the focal length of the lens and magnification of the telescope used. The laser setup could not produce large diameter holes probably because the energy delivered to the zone of interaction was low; the energy loss in the optical system was 40-60%.

In both variants of hole drilling, i.e. with and without the axicon, 4 to 8 pulses were shot to pierce one hole. In some series of pulses, each pulse was split into several portions.

The comparison between the results of hole piercing with and without the axicon by the beam having the same spatial and temporal profiles has revealed the advantages of the first variant of the process. Principally, it yielded better shapes of holes and decreased the spread in hole diameters to ± 2 or 3% as against ± 6 to 10% in

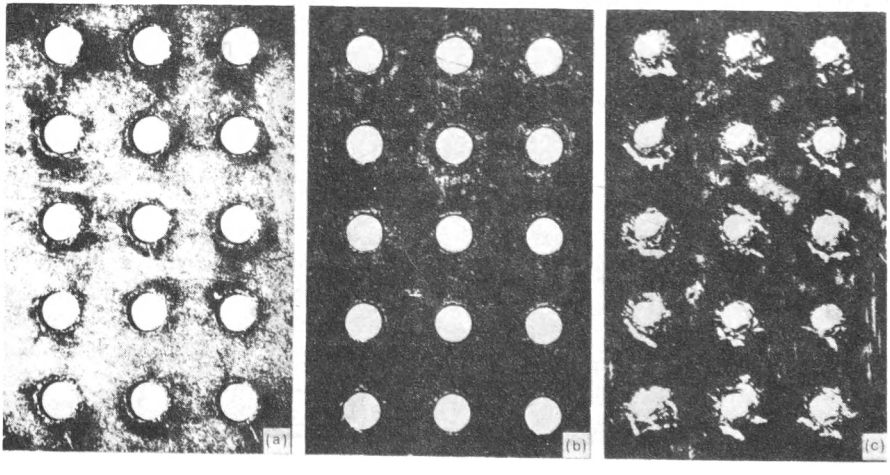

Fig. 9.24. Photographs of fine holes drilled in steel (*a*) and molybdenum (*b*) with the use of an axicon and in molybdenum (*c*) without the use of an axicon in the optical system

steel and ±8 to 12% in Mo typical for the second variant. Also, the lip formed around the hole was thinner and the taper at the entrance to the hole was smaller.

In the first variant, a lower energy in the pulse was needed to drill through holes and the amount of blowoff material going into the plume was lower. The latter fact indicates that the optical system requires simpler means of protection of the focusing lens against spatters and can operate with a short-focus lens if necessary.

Figure 9.24 displays photographs of holes pierced in steel (a) and molybdenum (6) and (c) by split pulses using the optical system with an axicon *(a)* and (6) and without an axicon (c). Pulse splitting led to a slight decrease in the spread of hole diameters to ±1.5-2% for the first variant of the process and to ±5-8% in steel and ±7-10% in Mo for the second variant. The quality of holes also improved especially in the first variant of hole drilling.

9.9. AN EXAMPLE OF HOLE DRILLING WITH SPLIT PULSES

There are a number of methods for producing pulses of higher power and shorter duration, which can effectively drill deeper holes. Let us consider in brief the results of hole drilling with a laser using a mechanical modulator (beam splitter) [61.

The modulator was an opaque disk driven into rotary motion by an electric motor. The disk provided with 7-mm orifices at a pitch of 14 mm around its periphery was set up in a spherical-mirror resonator which housed a 7 X 130-mmNd-glass rod without any additional optical elements. The disk could rotate at speeds in the range of 12 000-16 000 rpm.

In this range of rotational speeds and over a time period equal to a flashtube pulse length of 1.5 ms, the laser emitted ten 40-ps duration pulses, each delivering a peak power which was much in excess of that of the normal pulse. With the disk rotated, the energy stored in the cavity could be emitted in a pulse ot high power at the instant when the pumping intensity at the end

Fig. 9.25. Cross section of holes produced in a 5 mm thick steel plate by split pulses (on the left) and normal pulses (on the right)

of the pump pulse dropped below the normal (free-running) threshold intensity. The energy in the normal pulse emitted at the instant when the center of one of the disk orifices was brought into coincidence with the rod axis reached 10 J. The total energy of ten split pulses was 7 J.

Obviously, beam splitting involves a certain sacrifice in the energy of the pulse, but shortened pulses can effect deeper drilling. Cross sections of a through hole and a blind hole produced by split pulses and normal pulses, respectively, during the same number of flashtube shots appear in Fig. 9.25.

Split pulses drilled a hole to a depth twice the depth pierced by normal pulses despite the fact that the values of energy coupled to the target from the two types of pulses during one shot from the flashtube were 2.8 and 4.0 J respectively; the optical system accounted for 60% of the energy lost.

References

1. M. N. Libenson, G. P. Suslov, A. N. Kokora, et al. *Methods of improving the reproducibility of laser-drilled holes.* Leningrad, LDNTP, 1973 (in Russian).
2. N. N. Rykalin, A. A. Uglov, and A. N. Kokora. *Laser machining and welding.* Moscow, Mir Publishers, 1978.
3. V. S. Kovalenko. *Material processing with pulsed lasers.* Kiev., Vishcha Shkola, 1977 (in Russian)
4. A. N. Kokora, E. A. Korneev, B. M. Manzon, et al. *Use of a conical lens in drilling large-diameter holes with a laser beam.* Fizika i Khimiya Obrabotki Materialov, No. 4, p. 145, 1979.
5. V. P. Vyzhelevskiy, A. N. Kokora, M. V. Orekhov, et al. *On improving the reproducibility of laser-drilled fine holes.* Fizika i Khimiya Obrabotki Materialov, No. 1, p. 148, 1980.
6. A. A. Uglov, M. V. Orekhov, and A. N. Kokora. *Ways of increasing the laser drilling efficiency.* Fizika i Khimiya Obrabotki Materialov, No. 4, p. 135, 1976.

Part 3

ELECTRON BEAM MATERIAL PROCESSING

Chapter 10

ELECTRON BEAM-SOLID INTERACTIONS

10.1. MECHANISMS OF HOLE FORMATION

Material processing with an electron beam (EB or E-beam for short) involves various thermal processes which will be dealt with later in the text. The main effects associated with thermal processes are the following [1]:

(1) phase transformation in solids, during steel hardening, for example;

(2) melting in welding, polishing, alloying, cladding, and marking of metals and nonmetals;

(3) vaporization in drilling, cutting, marking, engraving, scribing, fracturing, trimming of metals and nonmetals;

(4) sublimation which is vaporization from the solid to the vapor state.

Machinability of a material is largely a function of its thermal properties and EB power density delivered to the target. To avoid excessive melting, for example, in hole piercing, it is common practice to work materials with pulses so as to achieve a maximum efficiency under resonant conditions of heating. Material processing can be done with single pulses or repeated pulses and with a continuous beam scanned at a high speed.

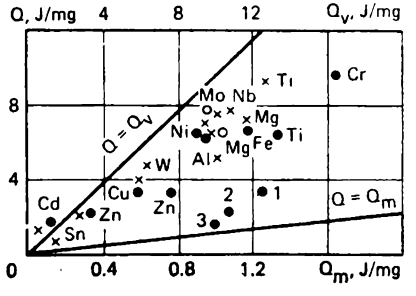

Fig. 10.1. Specific energies Q, Q_m, and Q_v for metal removal, melting, and vaporization respectively

Melt flushing and vaporization. The experimental measurements of the specific energy Q per unit mass m of the material damaged under the action of energy E coupled to the target, $Q = E/m$, reveal that Q for almost all metals is larger than the specific energy of melting, Q_m, and lower than the specific energy of vaporization, Q_v (Fig. 10.1) [2].

The blowoff material contains a considerable fraction of the liquid phase. The amount of absorbed energy that is enough to init-

iate material removal in drilling, cutting, and deep penetration welding, for example, of steels is only 10 to 20% greater than that required for melting. Such a little difference in the energy balance of the processes of evaporation and fusion greatly simplifies heat transfer computations.

The causes of early material vaporization with liquid spatter can be accounted for by the growth of heterogeneous vapor centers and overheating. In the first case, the factors that facilitate boiling are the following: the gas dissolved in metal, which forms bubbles whose volume can be tens and hundreds of times the melt volume; nonideal contact between phases; and local temperature fluctuations due to a nonuniform temporal profile of the beam. The latter factor is responsible for the generation of compression and rarefaction waves in the region of interaction, which act in the same way as ultrasonic vibrations.

Boiling due to overheating is more difficult to explain because the physical processes here are complex. One of the factors responsible for overheating is attributable to the action of the vapor back pressure in the melt region: since relaxation in the melt volume after the pulse dwell time lasts 10^{-8}-10^{-9} s and thus occurs at the speed of propagation of stress waves, or the speed of sound, the melt undergoes practically instantaneous overheating, which is equivalent to a rapid excessive heat release in a local volume.

According to another opinion, overheating results from the fact that the region of interaction has two layers for which the time periods of temperature changes after the end of the pulse are different. In the energy-absorbing layer of thickness h', the relaxation time is $t' = h'/a$; in the melt layer of thickness h that is adjacent to the above layer, the relaxation time is $t = h^2/a$, which is greater than t'. If during variations in the heating rate, the liquid layer undergoes overheating, the melt begins to vaporize because the time t is simultaneously the time of relaxation of the back (recoil) pressure.

One more factor that can cause boiling and melt flushing is the following. Since the vapor plume periodically shields the beam from the target, the vapor back pressure changes accordingly, thereby inducing mechanical vibrations in the melt, which encourage the growth of equilibrium bubbles of the dissolved gas [3].

The volume of dissolved gas contained in 100 g of metal commonly reaches 20 cm^3. For example, the initial volume of hydrogen in aluminum at T_m is equal to 0.69 cm^3 per 100 g or 1.86×10^{-2} cm^3 per cm^3 of metal. In the course of metal melting, the dissolved gas tends to form bubbles which are held in the equilibrium state.

The gas bubbles appearing in the melt do not yet point to the possibility of onset of volumetric vaporization (boiling). However, the variations in the back pressure due to the periodic beam

shielding must give rise to compression waves in the melt and, hence, to the growth of boiling sites [3]. The generation of compression waves is equivalent in a certain way to the generation of ultrasonic vibrations in a liquid. The sound wave shakes, as it were, the site of nucleation of the bubble and causes the bubble to overcome the potential barrier from the subcritical to the critical point of boiling.

In this case, an asymmetric character of bubble deformation can be the main factor accounting for the bubble growth.

The compression wave deforms the bubble (Fig. 10.2). It is safe to assume that this wave is plane since the beam radius is much larger than the radius of an equilibrium bubble.

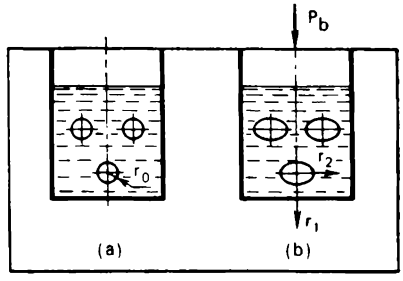

Fig. 10.2. Gas bubbles at equilibrium in molten metal not subjected (*a*) and subjected (*b*) to pressure of the wave

In the equilibrium state, the bubble pressure is $p_b = 2\sigma/r_0$, where σ is the surface tension and r_0 the equilibrium bubble radius. With allowance made for the compression wave pressure p_c, the equilibrium condition for a deformed bubble when $r_1 < r_0 < r_2$ will assume the form

$$p_b = \sigma/r_1 + \sigma/r_2 + p_c \qquad (10.1)$$

where r_1 and r_2 are the main radii of curvature of an oblate bubble.

As the compression wave decays, the bubble region with r_1 can expand to a radius r_0, with the bubble still held in equilibrium. In the region where $r_2 > r_1$, the conditions are such that $\sigma/r_2 < p_c$, so the bubble inevitably tends to expand.

As shown by experiments, $p_c = nkT$ reaches 60 N/cm^2, where n is the concentration of atoms per unit volume. For aluminum, r_1 and r_2 are equal to about 0.4 r_0 and 1.3 r_0, respectively, when $\sigma = 9 \times 10^{-3}$ N/cm and $r_0 = 10^{-4}$ cm. The vaporization (boiling) condition $r_2 > r_0$ for aluminum is set up at $p_c \geqslant 20$ N/cm^2, which is the case for welding and other processes in the range of laser power densities of $q = 10^5$ to 10^6 W/cm^2. This is the threshold above which a material begins to vaporize.

So, periodic changes in the back pressure give impetus to the expansion of the bubbles of the gas dissolved in the liquid metal and lead to volumetric evaporation.

In piercing holes through aluminum, one pulse delivered to the target is able to remove a metal layer 200 μm thick, which corresponds to a volume of $V_1 = 7 \times 10^{-4}$ cm^3.

Since 100 g of aluminum contain 0.69 cm^3 of hydrogen, the volume V_2 of the gas in the aluminum melt is 1.2×10^{-5} cm^3. Considering that the gas volume must reach the volume of the melt to be able to remove the melt completely, the gas must increase in volume by $V_1/V_2 = 60$ times.

If we assume that the radius of an original gas bubble is about 1×10^{-4} cm, each bubble must expand so that its radius r is close to 4×10^{-4} cm. When vaporization involves bubbling at $q = 10^5$ to 10^6 W/cm^2, the rate of travel of the phase boundary for aluminum is $v = 3$ to 30 cm/s. Consequently, the time it takes a bubble to expand until the moment of ejection is $t = r/v = 10^{-4}$ to 10^{-5} s.

The calculated values refer to one recoil momentum (recoil impulse). If we consider that each E-beam pulse induces several pressure pulses during its dwell time t, the probability of splatter increases.

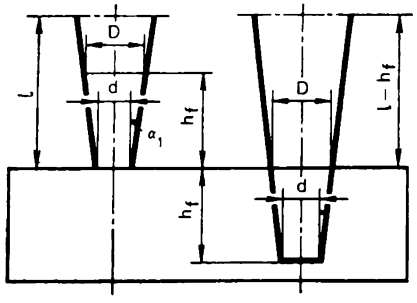

Fig. 10.3. Position of the focal point below the surface without changing the angle of beam convergence α_1

Optimal location of the EB focus below the target surface. As is known from experiments, other conditions being the same, an electron beam focused at a point slightly below the target surface can melt or vaporize the material to a greater depth.

An electron beam focused below the surface can increase the depth of the hole pierced through the material by 30%. The relation between the position of the focal point and EB parameters can be found from simple geometric considerations. If the focus is at the target surface, the beam that penetrates more deeply into the hole diverges more strongly, its power density q at the cavity bottom drops off and the process of hole piercing slows down. Experiments show that the beam focused below the surface provides a deeper penetration at the same rate of welding or hole piercing.

Let us estimate how the location of the focal point relates to the beam parameters. When the focus of the beam with an angle of convergence, α_1, lies at a distance h_f below the surface, as illustrated in Fig. 10.3, the relation between the diameter D of the beam on the surface and the beam diameter d in the focal plane takes the form

$$(D - d)/2 = h_f \tan \alpha_1 \qquad (10.2)$$

Since $D > d$, the power density at the surface, q_s, is lower than the power density q in the focal plane. The condition of deep penetration for the given distance h_f of the focus below the surface is

$q_s \geqslant q_c$, where q_c is a lower critical power density. Assuming that $D = 2\sqrt{P/\pi q_c}$ and $d = 2\sqrt{P/\pi q}$, where P is the beam power, the relation between the maximum distance h_f and EB parameters is given by

$$h_f \leqslant r \cot \alpha_1 (\sqrt{q/q_c} - 1) \tag{10.3}$$

where r is the EB radius in the focal plane.

As is apparent from (10.3), it is always necessary to change the focus of a convergent beam for a distance h_f which must be greater at a lower value of α_1. For a cylindrical beam, h_f is zero because $q = q_c$.

The predicted values of h_f for an industrial EB setup ELU-9B used for welding corrosion-resistant steel at $V = 60$ kV, $I = 60$ mA, $P = 3.6 \times 10^3$ W, $q = 2.7 \times 10^5$ W/cm^2, and $q_c = 2.7 \times 10^4$ W/cm^2 are the following: $h_f = 3.9$ cm at $\alpha_1 = 2^0$; $h_f = 2.8$ cm at $\alpha_1 = 3^\circ$; and $h_f = 1.5$ cm at $\alpha_1 = 5^0$. The results are consistent with experimental data.

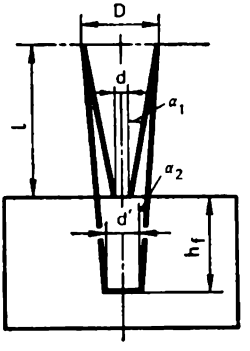

Fig. 10.4. Position of the focal point to depth h by changing α_1 with l held constant

In the case under study, shifting the focus below the surface does not entail changes in the angle of convergence α_1. In the practice of EB-induced material removal and EB welding (EBW), a focusing coil is used to adjust the position of the focal point along the depth and thus to distribute energy more uniformly in the zone of interaction and avoid variations in the penetration depth. In this method employed to achieve deeper penetration (Fig. 10.4), the focus of the beam with an angle of convergence α_1 penetrates into the material to a depth h_f owing to changes in α_1; at a depth h_f, the angle of convergence becomes equal to α_2.

The expression relating the beam diameter d at the focus, diameter D of the beam along the axis of the focus coil, and distance l from the center of the focus coil to the target surface can be written as

$$(D - d)/2 = l \tan \alpha_1 \tag{10.4}$$

The relation among D, h_f, and d', which is the maximum possible beam diameter due to beam defocusing, is

$$(D - d')/2 = (l + h_f) \tan \alpha_2 \tag{10.5}$$

The value of d' is related to q_c in the same way as $D = 2\sqrt{P/\pi q_c}$.

Proceeding from expressions (10.4) and (10.5), we can obtain

$$h_f \leqslant l\left(\frac{\tan\alpha_1}{\tan\alpha_2} - 1\right) + \frac{r}{\tan\alpha_2}\left(\sqrt{q/q_c} - 1\right) \qquad (10.6)$$

When $\tan\alpha_1 = \tan\alpha_2$, in which case there is no changes in the angle of convergence and the beam is incident on the surface, expression (10.6) converts to (10.3).

Given $l = 10$ cm, $r = 0.05$ cm, and $q/q_c = 4$, let us change the mean value of $\alpha_1 = 10°$ by $\pm 2°$. When $\alpha_2 = 8°$, the focal spot depth is $h_f = 2.46$ cm and when $\alpha_2 = 12°$, we have $h_f = -1.66$ cm. The term in the right side of (10.6), which represents relation (10.3) leads to asymmetry of h_f.

Formulas (10.3) and (10.6) do not allow for the EB attenuation due to the blowoff material and, therefore, have limited areas of application.

The choice of conditions of hole piercing and cutting (grooving). An electron beam pierces a hole in a free-running manner. It periodically vaporizes a layer of thickness h. In the intervals between vaporization cycles, a fraction of the EB energy left in the cavity, the density of which is by a factor of 10 or 100 lower than the initial density, melts the cavity walls. Consequently, the process of continuous interaction of the EB with the material is similar to the interaction of a pulse of duration τ and pulse spacing t_s; in the interval t_s between pulses the heat source only melts the material. Converting from a continuous beam to pulses with duration τ and pulse spacing t_s enables us to drill a hole rather than melt the material to a certain depth.

It is the amount of the liquid phase formed during beam interaction that determines the type of process, melting or hole piercing.

In the general case, the amount of the melt produced depends on the duty cycle, $G = \tau/(\tau + t_s)$. For the continuous beam process, in which $t_s = 0$, the duty cycle is $G = 1$. For the process of treatment with pulses, $G < 1$. The duty cycle can be defined as

$$G = [1 + qd^2/(\rho' v_v d_h^2 L_v)]^{-1} \qquad (10.7)$$

where d is the beam diameter, ρ' the critical material density, v_v the speed of vapor particles, d_h the hole diameter, and L_v the latent heat of vaporization.

The pulse duration and pulse spacing can be chosen proceeding from the conditions

$$\tau \leqslant \rho h L_v/q \qquad (10.8)$$

$$t_s \geqslant \rho h d^2/\rho' v_v d_h^2 \qquad (10.9)$$

where h is the hole depth.

The pulse repetition rate with regard to the critical power density q_c is

$$f = 1/(\tau + t_s) \geqslant a/d^2 \tag{10.10}$$

where a is the thermal diffusivity.

The duty cycle for the process of drilling is

$$G \geqslant \rho h L_v a/qd^2 \tag{10.11}$$

Figure 10.5 illustrates how the amount of the melt in the zone of interaction varies with G. Experimental data confirm that the optimal values of G for the processes of EB-induced material removal lie in the range

$$\rho h L_v a/qd^2 < G < 0.1 \tag{10.12}$$

For the case of EBW in pulsed conditions, the limits to G are $0.3 < G < 0.9$.

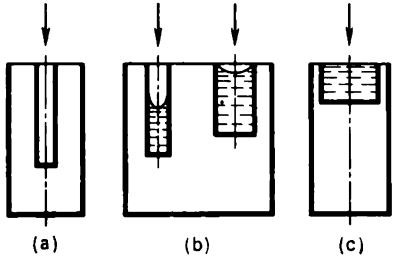

Fig. 10.5. Fraction of melt in the zone of EB-material interaction at $G \ll 0.1$ (*a*), $G > 0.1$ (*b*), and $G = 1$ (*c*)

The relation between EB parameters and the depth of cut, h, and kerf width b can be found from the expression for the cutting rate v, or the speed of travel of the beam:

$$v = \frac{d(1-K)}{(\tau + t_s)} = \frac{d(1-K)}{\rho h \left[\frac{L_v}{q} + \frac{hd^2\alpha}{v_v b^2 \ln (q/q_c)}\right]} \tag{10.13}$$

where d is the beam diameter, K the pulse overlap ratio, L_v the latent heat of vaporization, and α the angle of beam convergence.

The above expressions can be used for selecting the conditions of E-beam microprocessing and machining with the aid of commercial setups.

The optimal pulse duration should be chosen with consideration for the periodic EB scattering by the blowoff material in the case of pulsed microprocessing.

EB drilling has reached commercial status in a number of applications. For example, an industrial EB system operating at $V = 65$ kV, $I = 1.5$ mA (mean value), $\tau = 1$ ms, $t_s = 9$ ms, and $f = 100$ Hz can drill through holes in superalloy plates up to 10.5 mm thick. At $V = 70$ kV, $I = 0.5$ mA, $\tau = 1$ ms, $t_s = 9$ ms, and $f = 100$ Hz, the system pierces 6.5-mm deep holes 200 to 300 μm in diameter on the back side of the plate. The rate of drilling reaches 10 mm³/min at a specific energy of 0.05 J/mm³.

During a dwell time of 0.5 s, the beam drills holes 8 to 10 μm in diameter through 0.8- to 1.6-mm thick superalloy plates at $V = 60$ kV, $I = 0.1$ mA, $f = 1\,000$ Hz, and $\tau = 0.1$ ms. With an increase in the dwell time up to 1 s, the hole diameter reaches 12-15 μm.

The blowoff material propagating upward from the target scatters and defocuses the beam, thus reducing the rate of drilling (Fig. 10.6). To achieve an optimal length of the pulse, the beam must be cut off (chopped) at the instant when the process of material removal becomes rather ineffective (Fig. 10.6*b*, curve *3*). The amount of material removed with short pulses is small, and the process discontinues when the rate of travel of the heat source becomes too large (Fig. 10.6*c*).

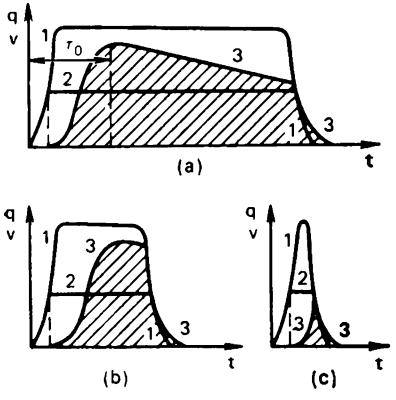

Fig. 10.6. Power density q and rate v of material removal versus time of interaction of a long pulse (*a*), optimal pulse of length τ_0 (*b*), and short pulse (*c*): curves *1*, initial values of q; curves *2*, lower threshold values of q; curves *3*, rates of material removal

Figure 10.7 displays the plots of the rate of drilling, v, of holes in stainless steel (curve *1*) and the specific energy Q coupled to the target (curve *2*) as a function of the pulse length without regard to the pulse spacing at $V = 75$ kV, $I = 2$ mA, and $f = 100$ Hz.

Figure 10.8 shows how the diameter at the end of a through hole drilled for 0.5 s in stainless steel at $V = 75$ kV, $I = 0.2$ mA, and $f = 100$ Hz varies with the pulse duration.

It is found that the total mass m of the material removed from the target surface of such metals as tungsten, molybdenum, zirconium, niobium, copper, and steel struck by a single pulse is a function of the pulse energy E, pulse duration τ, and thermal properties of the metals in question. The amount of material removal is $m = BE^n$, where B and n are factors accounting for the properties of the material. The effects of other parameters such as the beam current, accelerating voltage, and pulse duration under optimal conditions of focusing are more complex. For example, the mass removal from a stainless steel surface at $V = 100$ kV, $q = 10^7$ W/cm^2, and $\tau = 4$ to 25 μs is defined by

$$\log m = 1.2\, I^{0.2} \log \tau - 7.22 \qquad (10.14)$$

Under these conditions, an increase in pulse energy from 10^{-4} to 10^{-1} J leads to a thousandfold increase of the mass removal.

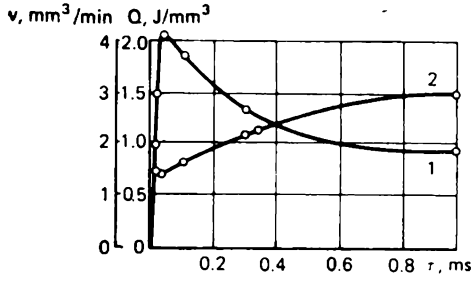

Fig. 10.7. Rate of material removal (curve *1*) and specific energy input (curve *2*) versus pulse length disregarding pulse spacing

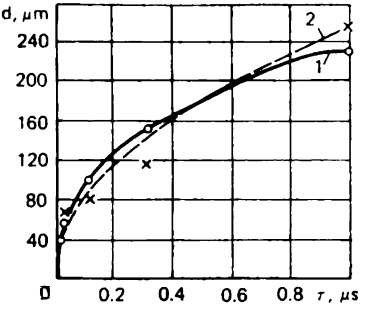

Fig. 10.8. Hole diameter as a function of pulse length: *1*, low-frequency supply source; *2*, high-frequency supply source

The material is blown off in a recurrent manner in the form of outburst of vapor atoms, ions, and liquid droplets. The repetition rate of blasts depends on the energy in a pulse and reaches tenths of megahertz.

The rate v of material removal grows as the exponential function of the beam current and can reach an extremum depending on the pulse duration.

For stainless steel, the rate is

$$v = B_1\tau^n \exp(-c_1\tau) \qquad (10.15)$$

where B_1 and c_1 are factors allowing for the parameters of the process.

If a pulse with its length reduced from 45 to 4.5 μs delivers 5×10^{-3} J of energy, the rate v increases by a factor of 2.8; 10.1×10^{-3} J of energy in the same pulse provides a 6.3-fold increase in the rate.

The diameter d_h and depth h of a hole increase linearly with E, but vary in an exponential manner with the pulse duration τ and beam current I:

$$d_h = B_E E + a, \quad h = C_E E + b_E, \quad d_h = B_I I^n$$
$$h = (aI^2 + bI + cI)^{-1}, \quad d_h = B_\tau \tau^m, \quad h = c_\tau \tau^N$$

where B, C, a, b, and c with corresponding subscripts are factors and n, m, and N are exponents, which account for material properties and the type of machining.

The angle of convergence and the location of the focal point relative to the target surface determine the dimensions and shape of a hole. A single pulse can pierce a hole of the maximum depth and smallest diameter when the beam focus is 0.1-0.3 mm below the surface.

The efficiency of material removal, m/E, i.e. the amount of material removed per unit incident energy, shows an extreme character. It reaches a maximum when the pulse length is shorter than is necessary for an optimal rate of material removal. The efficiency of utilization of the incident energy for material removal varies as an exponential function of the beam current:

$$m/E = \tau (B_e\tau^2 + c_e\tau + n_e)^{-1} \tag{10.16}$$

where B_e, c_e, and n_e are factors.

In drilling massive parts of any materials to a large depth, the current per unit area of the solid angle must be maximum and the beam focus must be at a certain point below the surface. Where thin plates are involved, the beam must have a maximum angle of convergence and its focus must be above the target surface.

The manner in which the dimensions of fine blind holes vary with EB characteristics can be defined using empirical formulas:

$$d_h = a_d I^{x_d}, \quad h = a_h I^{x_h}, \quad d_h = m\tau^n$$
$$h = a_V V^{x_V}, \quad h = c_\tau \tau^N \tag{10.17}$$

where a_d, a_h, m, a_V, and c_τ are factors used to account for the thermal properties of materials, and x_d, x_h, x_V, n, and N are exponents specific to the material worked and the conditions of material processing.

The depth of a fine hole is

$$h = a + b \log n \tag{10.18}$$

where a and b are factors characteristic of the conditions of metalworking, and n is the number of pulses. The graphs of Fig. 10.9 confirm the validity of expression (10.18).

As is apparent from relations (10.17), assuming the single pulse duration and focal position to be optimal, the hole dimensions heavily depend on I, V, and the number n of pulses. Investigations into the effect of each factor in a traditional way take much time, and therefore the requisite relations are found using the method of the full factorial experiment.

The mathematical model taken as the reference assumes the form

$$h = BV^c I^p n^q \tag{10.19}$$

where c, p, and q are exponents, and B is the factor accounting for the thermal properties of the material and the conditions of machining.

The statistical processing of the data yields the expression

$$h = 4.4 \times 10^{-13} V^{6.02} I^{1.2} n^{0.6} \tag{10.20}$$

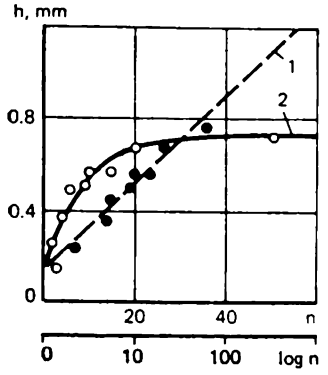

Fig. 10.9. Depth of hole drilled in steel at $V = 130$ kV, $I = 6$ mA, $f = 500$ Hz, and $\tau = 10$ μs as a function of the number of pulses: *1*, linear scale; *2*, logarithmic scale

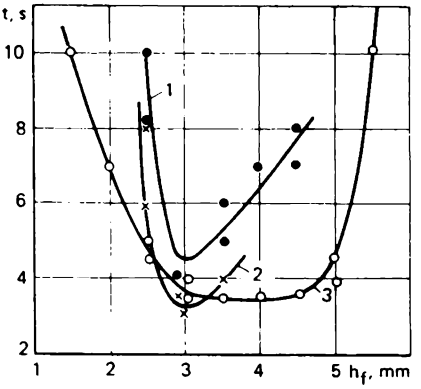

Fig. 10.10. Time t of hole piercing in Ti (curve *1*), stainless steel (curve *2*), and Al-Mg alloy (curve *3*) at $V = 100$ kV, $I = 35.5$ mA, $f = 50$ Hz, and $\tau = 100$ μs as a function of the depth h_f of the focal point below the target surface [3]

The process of pulsed EB drilling in optimal conditions with consideration for EB scattering by the blowoff material is notable for the lowest fraction of the material removed in the liquid state.

In some cases, for example, in the process of cutting or piercing semiconductor materials, the melt flushes the region of interaction and makes the edges of cut rough because the surface tension of the melt is lower than that of the solid phase.

To get an insight into the process of a flow of a laminar melt layer on to the solid surface, recourse can be had to a model which allows for the fact that a fraction of the molten layer adjacent to the solid crystallizes during the flushing process.

10.2. EXAMPLES OF EB MATERIAL PROCESSING

Drilling in metals. To get an understanding of how the beam power, position of the focal point, pulse length, and pulse repetition rate determine the parameters of the drilling process, let us consider examples of practical EB drilling in scale-resistant steel, titanium, and aluminum-magnesium alloy [4]. The parameters of the beam used for hole piercing are: $V \leqslant 100$ kV, $I \leqslant 100$ mA, beam diameter $d \geqslant 20$ μm, pulse repetition rate $f = 2$ to 3 000 Hz, and pulse length $\tau = 30$ to 10 000 μs.

The rate of drilling appreciably depends on the location of the focal point relative to the target surface. At $V = 100$ kV,

$I = 35.5$ mA, $f = 50$ Hz, $\tau = 100$ μs (for Ti and steel), and $\tau = 70$ μs (for Al-Mg alloy), the beam drills at the highest rate when the focal point is approximately one-half the thickness of the plate below the surface (Fig. 10.10).

Changes in the pulse length at a constant repetition rate affect the speed of drilling. When $V = 100$ kV, $I = 50$ mA, $f = 100$ Hz, and $\tau = 10$ to 500 μs, the beam does not practically pierce the material (Fig. 10.11). With an increase of the pulse length from 50 to 100 μs, the rate of the process increases 6 or 7 fold. The optimal length of a pulse is 100 μs and the time required to pierce a 6-mm thick plate is 2 or 3 s.

At $V = 100$ kV, $I = 50$ mA, $\tau = 100$ μs, $f = 25$ to 500 Hz, and $h_f = 3$ mm, the rate of drilling is the highest in the range of f from 100 to 150 Hz (Fig. 10.12). With a decrease in f, the rate diminishes by 50-75%.

The efficiency of process is the highest and the quality of holes is better at the following values of the beam parameters: $V = 100$ kV, $I = 50$ mA, $f = 100$ Hz, $\tau = 100$ μs, and $h_f = 3$ mm.

EB-silicon interaction. A schematic arrangement for melting localized regions on a silicon sample with an electron beam appears in Fig. 10.13.

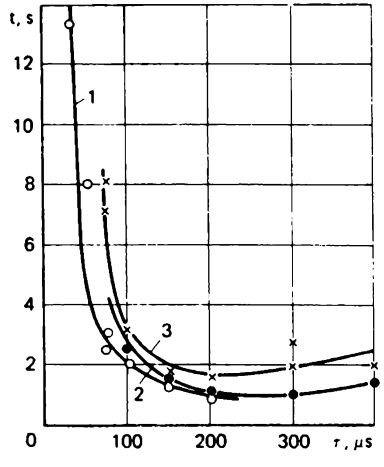

Fig. 10.11. Time t of hole piercing in 6 mm thick plates of Ti (curve *1*, $I = 50$ mA), Al-Mg alloy (curve *2*, $I = 35$ mA), and stainless steel (curve *3*, $I = 50$ mA) at $V = 100$ kV and $f = 100$ Hz as a function of the pulse length [4]

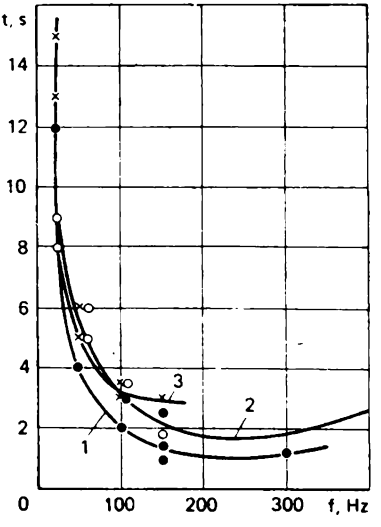

Fig. 10.12. Time t of hole piercing in 6 mm thick plates of Ti (curve *1*, $\tau = 100$ μs), Al-Mg alloy (curve *2*, $\tau = 70$ μs), and stainless steel (curve *3*, $\tau = 100$ μs) at $V = 100$ kV and $I = 50$ mA as a function of the pulse repetition rate [4]

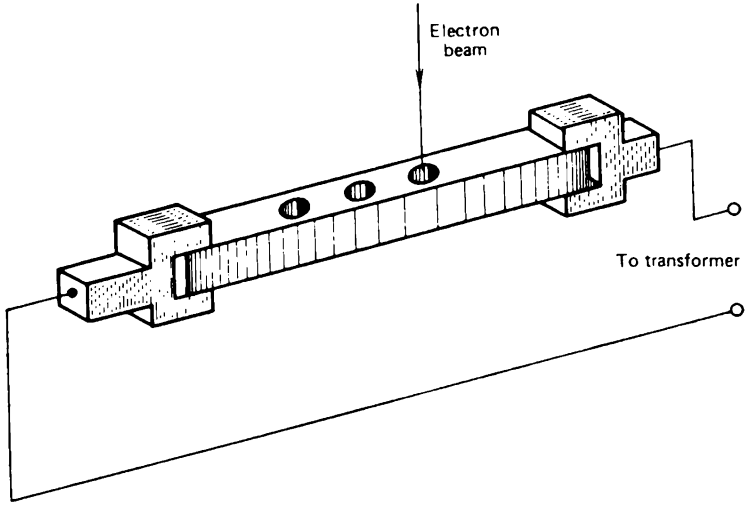

Fig. 10.13. Schematic arrangement for EB-induced melting of a silicon sample

The sample is housed in a chamber and its ends are inserted into holders with electrodes connecting the plate to a transformer via leads in bushings passed through the chamber walls. As the chamber is pumped to a specified vacuum, the plate is slowly heated to 300-400°C with a defocused electron beam and then the transformer is switched into the circuit to allow the current to heat the sample to 700°C. A chromel-alumel thermocouple built into one of the holders enables the operator to control the process of preheating. The plate is allowed to stay at 700°C, held accurate to ~30 deg C for 0.5 to 1.0 min and then is struck by the EB to melt a local region on its surface. The aim of preheating to 700°C is to prevent the sample from cracking during intense heating and cooling. The area of contact of the sample ends with the holders must be as small as possible in order to reduce the temperature gradient along the plate. With the same aim in view, the three spots to be melted must lie in the middle portion of the plate.

The process is run at the specified values of the accelerating voltage, beam current, time of interaction, and distance from the center of the focusing system to the target surface.

In Fig. 10.14 is shown the top view of the EB-irradiated spot on the surface of a silicon substrate and the region partially surrounding the spot. In the surface region directly adjacent to the melt boundary, there is a high density of slip bands (dislocations), which decreases with distance away from the melt boundary. The rows of dislocations intersect at an angle of 60°. Near the melt boundary

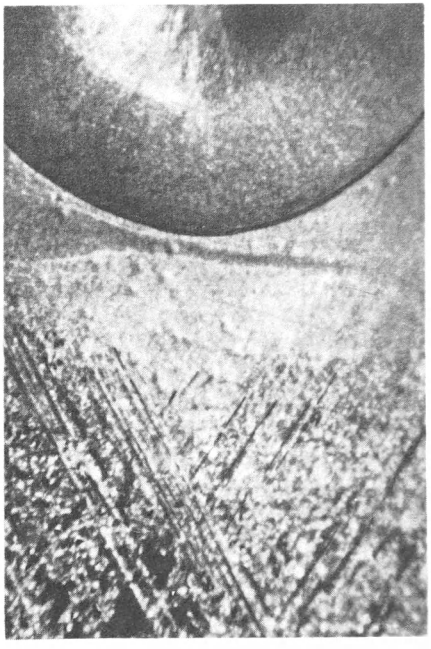

Fig. 10.14. Top view of the melt zone (20×) on the surface of silicon struck by a 30-ms pulse at $V = 20$ kV, $I = 80$ mA, and lens-to-part distance $l = 60$ mm

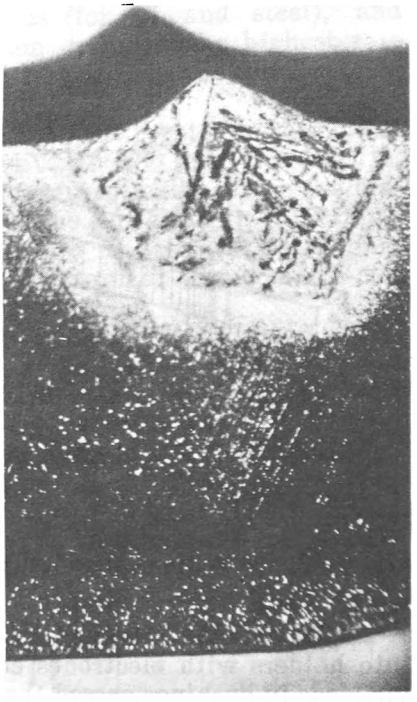

Fig. 10.15. Cross section of the melt zone in n-type [111] silicon crystal bombarded by a 50 ms pulse at $V = 24$ kV, $I = 150$ mA, and $l = 60$ mm (25×)

and at a certain distance from the boundary, etch pits are visible on the dense background of slip bands. These etch pits are larger in size than the original dislocations.

Figure 10.15 demonstrates a cross section of the fusion zone in the [111] plane of a silicon specimen heated by an electron beam. The trapezoidal shape of the melt region and rows of new slip bands intersecting at 60° are clearly seen. The fusion zone is part of a triangle formed by slip bands. At the lower edge of the specimen under the triangle, one can observe a pileup of etch pits (dislocations) separated from the triangle by the dislocation-free region.

The most clearly defined fusion zone of the keyhole shape is evident in p-type silicon specimens in the [100] plane. For example, during the time of interaction of 2 ms, the beam provides a fusion region in the [100] plane of p-type silicon with an aspect ratio h/b (melt depth-to-width ratio) of about 5; in the [100] and [111] planes of

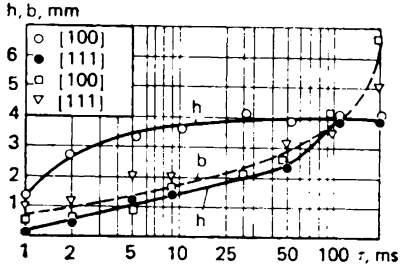

Fig. 10.16. Depth h and width b of the melt zone in p-type silicon as a function of the time of EB interaction at $V = 20$ kV, $I = 40$ mA, and $l = 45$ mm

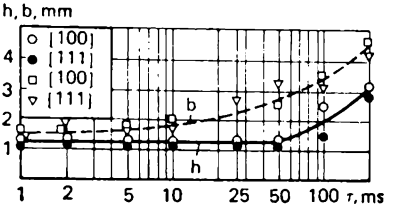

Fig. 10.17. Depth h and width b of the melt zone in n-type silicon as a function of the time of EB interaction at $V = 20$ kV, $I = 40$ mA, and $l = 45$ mm

n-type silicon and in the [111] plane of p-type silicon, the aspect ratio ranges between 1 and 2.

The shape of a fusion zone changes with an increase of the dwell time, as seen from the graphs of Figs. 10.16 and 10.17.

It is evident from Fig. 10.17 that the melt depth in both planes of n-type silicon practically remains the same as the dwell time increases from 1 to 25 ms. Above this time threshold, the melt depth grows sharply, as does the melt spot width in both slip planes. As seen from Fig. 10.17, anisotropy of silicon does not affect the depth of melting. The difference in the values between melt depths in planes [111] and [100] lies within the limits of the experimental error.

From Fig. 10.16 it is obvious that anisotropy for n-type silicon plays a substantial part. The difference in the values of h in the [100] and [111] planes reaches 200 to 300%. The melt depth sharply increases with the dwell time in the [100] plane and reaches the plate thickness (4 mm) in about 10 ms. In the [111] plane, h increases slowly and reaches 4 mm in about 100 ms. The width of the melt region grows at the same rate in both planes. It increases most heavily when the time of interaction ranges from 50 to 100 ms.

All the melt regions in both slip planes of n-type and p-type silicon plates display a zone of high dislocation density, the shape of which is similar to the shape of the melt region (Fig. 10.18). In some specimens, for example, in n-type [111] silicon irradiated for 25 ms, there are sites of high dislocation density under the melt region. Of much practical interest is the profile of the melt region in silicon containing twins. Figure 10.19 shows the cross section of the melt region in a p-type [100] silicon substrate irradiated for 5 ms. The profile of the melt region intersected by twin boundaries sharply deviates from the EB axis. The fusion column schematically represented in Fig. 10.19*b* in the center of the zone of interaction noticeably changes its direction as it intersects the twin boundary.

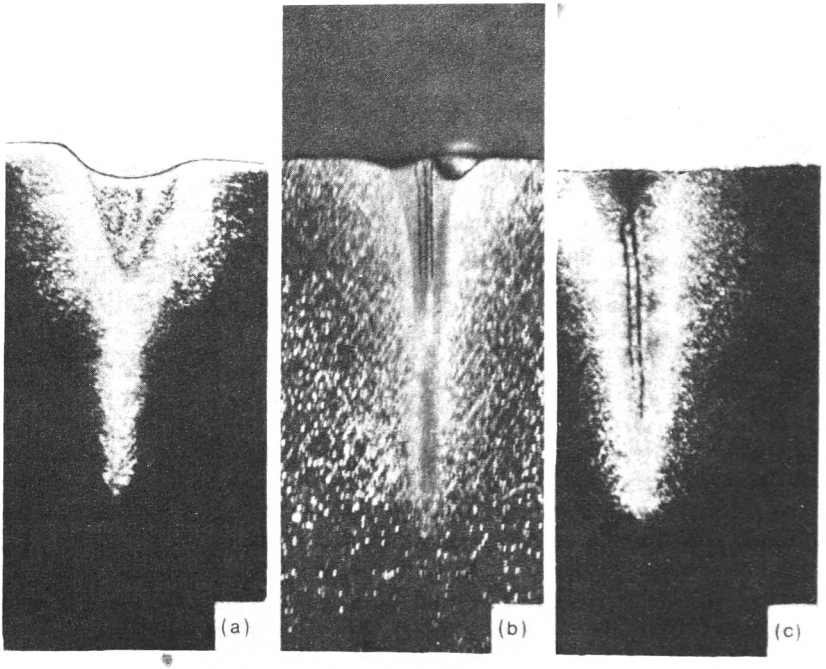

Fig. 10.18. Cross sections of the melt zones in *p*-type [100] silicon crystal struck by a 1 ms pulse (*a*), 2 ms pulse (*b*), and 5 ms pulse (*c*) at $V = 20$ kV, $I = 40$ mA, and $l = 45$ mm (20×)

The angles of deflection of the melt zone axis at the entry to and exit from the twin area are equal to 11 and 18° respectively.

Drilling in brittle materials. EB processing of brittle materials such as glass, ceramics, ruby, and diamond has specific features because of a peculiar character of material disintegration in the zone of EB interaction [5].

At a voltage of 20 to 40 keV, the beam produces a crater, or cavity, in a glass sample, the radius of which is greater than the beam diameter. The crater exhibits traces of the solidified melt in the center and also spallings and fine cracks at the outer edges. With an increase in the power density, the area of spallings becomes larger and cracks grow in size.

A crater produced in a ceramic plate by a single pulse has a diameter which is approximately equal to the beam diameter. Other conditions being the same, the diameter of the crater formed in the ceramic plate is much smaller than that of the crater produced in the glass plate.

The bottom of the crater in a ruby plate is covered with a thin layer of the material of a different structure, which poorly

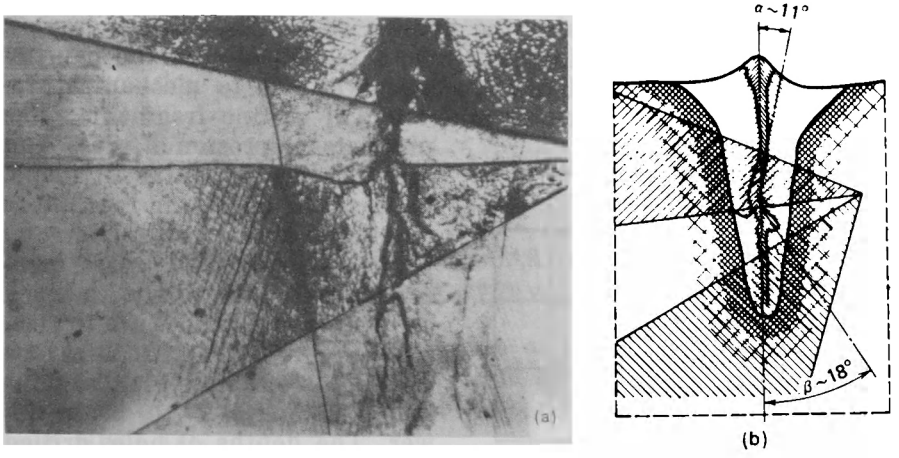

Fig. 10.19. General view (*a*) and schematic representation (*b*) of the cross section on the melt zone in Si with twins (200×)

adheres to the base material and readily peels off. The zone of contact of the layer with the base exhibits many fine cracks, which grows in size with the beam power. A very high power density of the beam causes breakage of ruby plates.

A crater drilled in a diamond plate is always covered at the bottom with a layer of graphite 2 to 10 μm thick. At $V = 80$ to 100 kV and $q = 3 \times 10^7$ W/cm², fine cracks appear in the crater center, while the thickness of graphitized layer decreases. When the

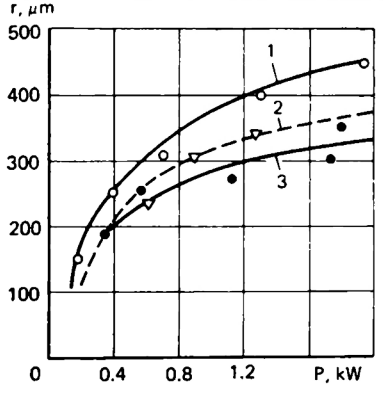

Fig. 10.20. Radius r of a hole vaporized in glass as a function of electron beam power [5]: *1*, 32 kV; *2*, 24.1 kV; *3* 23.4 kV

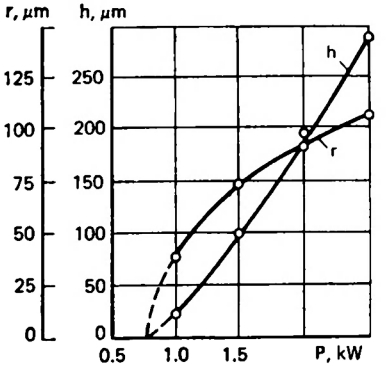

Fig. 10.21. Radius r and depth h of a hole vaporized in diamond versus pulse power [5]

power density rises up to 5×10^7 W/cm^2, the dimensions of the craters and cracks and also the number of cracks become greater.

The traces of spallings and cracks in and around the cavities attest that the beam-induced heating gives rise to mechanical factors responsible for cracking and removal of fine fragments. The products of erosion of glass and ceramics are irregular in shape, have sharp edges and reach tens of micrometers in size. Diamond particles display an almost regular shape of crystals with black coats and are up to 3 μm in size.

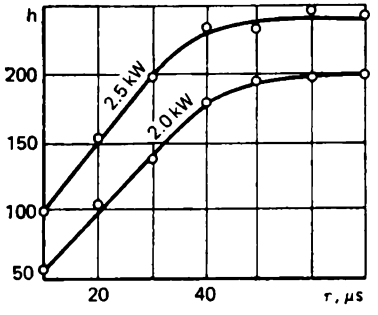

Fig. 10.22. Depth h of a hole vaporized in diamond as a function of the pulse length

Figure 10.20 illustrates how the radius of a hole pierced through glass varies with beam power. The depths of holes drilled in glass do not exceed 10-15 μm at $V = 20$ to 30 kV. It is seen from Fig. 10.21 that in diamond the radius r varies with P in the same manner as in glass. The critical values of q at which glass and diamond begin to vaporize are equal to 0.8×10^6 and 1.2×10^7 W/om^2 respectively.

The relations between the depth of a cavity produced in diamond and the pulse length at two values of EB power are shown in Fig. 10.22. It is worthy of note that the hole depth increases with the pulse length up to 50-60 μs. Above this threshold, the blowoff material begins to shield the EB from the surface and the efficiency of drilling decreases. The deepest holes in diamond are made when the beam is focused at a point 0.7 mm below the surface. Material removal is discontinuous when the focal point is shifted to a depth that is 2 or 3 times the optimal depth.

References

1. D. K. Biegelsen, G. A. Rozgonyi and C. V. Shank (eds.). *Energy beam-solid interactions and transient thermal processes.* Vol. 35, MRS, Pennsylvania, 1984.
2. V. M. Kirillov and A. I. Ulyakov. *Fractions of the material removed as liquid and gas in the interaction of a laser with metals.* Fizika i Khimiya Obrabotki Materialov, No. 1, p. 8, 1971.
3. N. N. Rykalin, I. V. Zuev, and A. A. Uglov. *Fundamentals of electron beam material processing.* Moscow, Mashinostroenie, 1978 (in Russian).
4. I. P. Voronkov, A. N. Kabanov, and V. K. Titov. *Processing of metals with a pulsed electron beam of up to 10 kW power.* Proceedings of MIEM, Series 35, Electron-Beam Technology, Moscow, 1974 (in Russian).
5. D. A. Noskov and N. G. Pankovets. *Some mechanisms involved in pulsed EB-induced erosion of brittle materials.* Fizika i Khimiya Obrabotki Materialov, No. 4, p. 128, 1975.

Chapter 11
ELECTRON BEAM WELDING

11.1. EFFECT OF THE GUN-TO-PART DISTANCE ON THE FUSION ZONE GEOMETRY

As mentioned in Ch. 10, the location of the focal point below the target surface can increase the depth of a hole. The same is true for deep-penetration electron beam welding (EBW) relying on the keyholing effect [1].

To determine how the focal position affects the geometry of the weld fusion zone, workers [2] conducted experiments with a variable working distance l between the exit section of the electron gun and target surface.

Although the spatial position of the focal point when welding along the slanting plane remains invariable (I_f is constant), the degree of beam focusing, dI_f, changes since the current I_0 of point focusing required to ensure a maximum penetration depth takes on a new value with each new value of the gun-to-part distance l. The relation between the current for point focusing, I_0, and distance l for the optical system is linear in shape (Fig. 11.1).

By the degree of beam focusing, dI_f, is meant an algebraic difference between the focusing current I_f adjusted for certain working conditions and minimum control current I_0, $dI_f = \pm (I_f - I_0)$. The zero reference point is taken to be the point at which $I_f = 88$ mA.

If welding is carried out at other values of I_f, the curve of dI_f is shifted up or down for equal distances in accord with the increase or decrease of I_f. But the inflection point at $l = 90$ mm, which is indicative of the specific features of the electron gun of interest, will remain on the same vertical.

The nomograph of Fig. 11.1 is in essence the focusing characteristic of an electron gun of the specified type, which enables the engineer to quickly solve the problem on estimating the degree of EB focusing in two stages. First, he determines the control values of I_f and I_0 for the given distance l and the selected value of dI_f. Second, when welding with a variable value of l, he estimates dI_f and I_0 for each value of l proceeding from the preassigned value of I_f.

To obtain quantitative estimates of how the position of the focal point above or below the target surface affects the geometry of

fusion zones of seam welds produced with continuously varying values of $l = 90 \pm 50$ mm at a constant value of $I_f = 88$ mA, use is made of the alignment chart of Fig. 11.1 to define the values of l at which dI_f takes on successive values of +4, 0, —4, and —8 mA. The distances l are equal to 132, 90, 70, and 48 mm respectively. After welding, the weld joints are ground at an angle of 19° 30′ to the normal to obtain microsections.

The weld fusion profiles, preliminarily enlarged eightfold, are superposed on the respective profiles of weld zones obtained at a

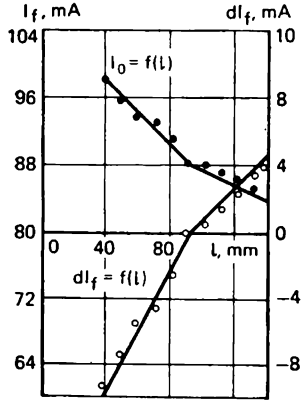

Fig. 11.1. Nomograph relating the degree of focusing, dI_f, and focusing currents I_f and I_0 to the electron gun distance l

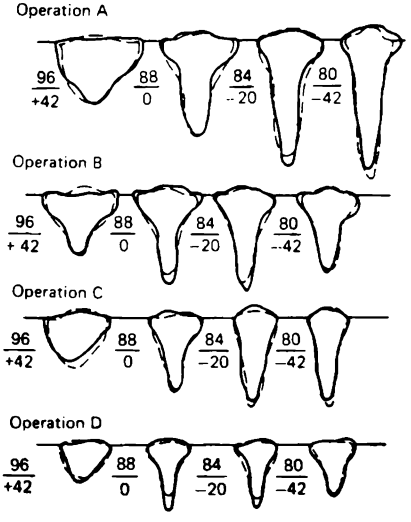

Fig. 11.2. Cross sections of fusion zones produced at various currents I_f and at constant distance l (solid lines) and various distances l (dash lines)

constant value of l to compare their configurations and areas. The noncoincident portions are measured with a planimeter to determine the difference in area. The results of comparison between the areas of fusion zones produced in welding conditions of four types A, B, C, and D are shown in Fig. 11.2. It is seen that the profiles of zones obtained at a constant value of l and at various values of l (solid and dash lines respectively) register well. In Fig. 11.2, the numerator denotes the focusing current for a solid profile and the denominator denotes the distance (mm) of the focal point above the target surface (plus sign) and below the surface (minus sign).

The relative difference in percent between the areas of dash profiles and those of solid profiles for the four values of dI_f reaches about 12% (Table 11.1). The highest deviation occurs at low values

TABLE 11.1. **Percentage Deviation of the Areas of Two Registered Fusion Zone Profiles**

Operation type	V, kV	I, mA	v, cm/s	P, W	Q, J/cm	Percentage deviation, dI_f, mA, at l=constant			
						+8	0	−4	−8
A	60	60	0.55	3600	6540	−5.8	+3.6	+7.7	−2.7
B	60	40	0.55	2400	4360	+3.0	−2.4	−5.0	−2.4
C	60	60	1.10	3600	3275	+10.5	−8.2	−2.3	−7.3
D	60	40	1.10	2400	2180	+12.0	−10.1	−1.0	−12.0

Note: The plus and minus signs point to an increase and decrease of cross section, respectively, at dI_f=constant.

of energy input: three cases in operation *D* and one case in operation *C*. The cause is the instability of the accelerating voltage and current.

Figure 11.3 displays the cross sections of welds produced at l of 70, 90, 110, and 130 mm, respectively, at the same value of energy

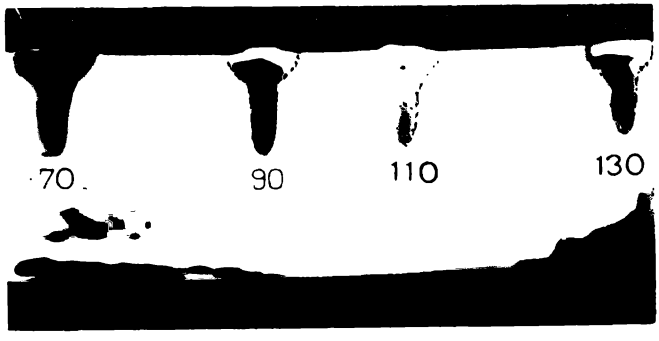

Fig. 11.3. Four cross sections of fusion zones produced in stainless steel at gun distances of 70, 90, 110, and 130 mm and at constant value of dI_f

input and the same value of $dI_f = 0$, i.e. $I_f = I_0 = 92$, 88, 86, and 84 mA respectively ($V = 60$ kV, $I = 60$ mA, and $v = 0.55$ cm/s). The profiles are rather identical, which is apparent from the dimensions of the four welds (Table 11.2). A large width of the weld produced at $l = 130$ mm is due to the edge effect since this weld is made near the plate edge.

So, with the degree of beam focusing dI_f held constant, the welds are fairly reproducible in cross section whatever the distance l. This is of much practical importance because the shape of the

TABLE 11.2. **Dimensions of Welds of Fig. 11.3**

Weld parameter	Gun-to-part distance l, mm			
	70	90	110	130
Depth h, mm	8.65	8.30	8.10	8.10
Width b, mm	6.40	6.80	6.60	7.00
Reinforcement, mm	0.79	0.72	0.67	0.33
Aspect ratio, h/b	1.35	1.22	1.23	1.16
Cross section, mm^2	25.7	27.0	24.7	26.5
Mean area deviation, %	−1.1	+3.8	−5.0	+1.9

fusion zone can be kept constant at various values of the distance l specified in the certificate of the electron gun for the given electron-optical system.

Experiments confirm that the location of the EB focus above or below the target surface is equivalent to a certain decrease or increase in the EB power density. The maximum experimental value of the depth h_f of the focal point below the surface well agrees with the predicted value determined by the formula

$$h_f \leqslant r \cot \alpha \, [(q/q_c) - 1] \tag{11.1}$$

For the operation of type A, in which $V = 60$ kV, $I = 60$ mA, $q = 2.7 \times 10^5$ W/cm^2, and $q_c = 2.7 \times 10^4$ W/cm^2, the predicted value of h_f is equal to 39 mm at an angle of convergence $\alpha = 2°$, which is close to an experimental value, $h_f = 42$ mm.

11.2. RELATION BETWEEN EB AND WELD PARAMETERS

According to the normal distribution law, the volume bounded by the fusion zone surface is

$$V = (\pi/k)\, h \tag{11.2}$$

where k is the concentration coefficient for the power density distribution, and h the maximum penetration (melt) depth.

From (11.2) it follows that the volume melted per second is

$$vA_m = IV\eta_e\eta_T/[\rho\,(cT_m + L_m)] \tag{11.3}$$

where v is the weld speed, A_m the melt area, η_e the effective (net) efficiency, η_T the thermal (weld) efficiency, ρ the mass density, c the specific heat, and L_m the latent heat of melting (fusion).

Dividing both sides of (11.2) by the time t required to obtain the melt of volume V yields

$$V/t = \pi h/kt$$

Since $V/t = vA_m$, equation (11.2) can be written in the form

$$\pi h/kt = IV\eta_e\eta_T/[\rho\ (cT_m + L_m)] \tag{11.4}$$

Denoting $Q = IV\eta_e/v$, $t \approx d/v$, and $k = 4/b^2$ gives

$$\eta_T Qd = [\pi b^2/4)\ h\rho\ (cT_m + L_m)] \tag{11.5}$$

where d is the beam diameter and b the weld width at a level of $1/e$ as shown in Fig. 11.4.

Equation (11.5) relates the energy input Q, with consideration for power density at the given d, to the depth h and width b of a weld.

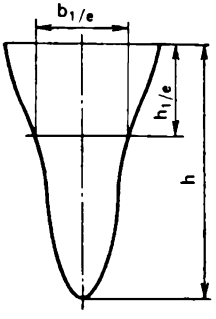

Fig. 11.4. Typical dimensions of the fusion zone

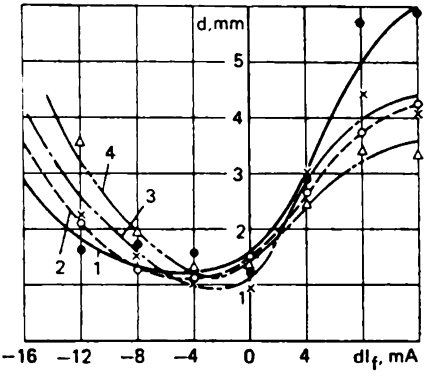

Fig. 11.5. Beam diameter d as a function of dI_f for four conditions of welding, A, B, C and D (curves *1*, *2*, *3*, and *4* respectively)

The thermal (weld) efficiency η_T specifies with fraction of energy required to heat and melt a metal of volume $\pi b^2 h/4$.

The experimental values of A_m, b, h, and η_T and also the values of beam diameter d calculated by (11.5) are given in Table 11.3. Figure 11.5 illustrates how d varies with dI_f for four types of welding operations.

The experimental value of η_T is found from the formula

$$\eta_T = \rho v A_m C_m / P \tag{11.6}$$

where C_m is the volume specific heat and $P = \eta_e IV$ the beam power.

As follows from Table 11.3, the average value of η_T varies from 0.382 (operation A) to 0.514 (operation C). For all the types of operation the mean of η_T is equal to 0.452, which is very close to the maximum theoretical value of the weld efficiency, $\eta_T = 0.484$, for a linear source moving along an infinite plate. The experimental values of the EB power density q for operations of types A, B, C,

TABLE 11.3. **Experimental Values of Fusion Zone Dimensions**

I_f, mA	Operation	A_m, cm²	h, mm	b, mm	η_T	d, mm
76	*A*	0.35	11.2	2.8	0.423	1.8
	B	0.24	7.8	3.1	0.436	2.4
	C	0.21	7.0	3.1	0.510	2.9
	D	0.12	4.4	3.8	0.436	4.0
80	*A*	0.29	14.0	2.3	0.350	1.5
	B	0.22	7.8	2.3	0.400	1.4
	C	0.22	9.2	2.4	0.535	2.2
	D	0.14	5.7	2.7	0.510	3.0
84	*A*	0.34	11.0	2.7	0.413	1.7
	B	0.22	8.0	2.2	0.400	1.2
	C	0.20	9.3	1.8	0.486	1.3
	D	0.13	5.8	2.1	0.474	1.6
88	*A*	0.31	9.5	2.5	0.376	1.3
	B	0.24	7.6	2.6	0.436	1.6
	C	0.23	7.2	2.1	0.560	1.4
	D	0.14	5.8	2.3	0.510	2.0
92	*A*	0.30	7.5	4.1	0.364	2.7
	B	0.25	6.9	3.8	0.464	3.1
	C	0.21	5.9	4.0	0.510	4.0
	D	0.14	4.9	3.2	0.510	3.0
96	*A*	0.32	5.5	6.7	0.388	5.2
	B	0.24	5.0	5.1	0.436	4.1
	C	0.20	4.0	5.8	0.486	5.7
	D	0.14	3.5	4.5	0.510	5.0
100	*A*	0.30	4.5	7.5	0.364	5.3
	B	0.23	5.5	5.1	0.417	4.4
	C	0.21	3.3	6.2	0.510	5.3
	D	0.12	2.4	4.9	0.436	4.0

and D are 2.7×10^5, 2.1×10^5, 2.7×10^5, and 1.2×10^5 W/cm^2 respectively.

Equation (11.5) describes the heat energy balance for the process of EB welding of metals accurate to 10%, disregarding vaporization and overheating of some fraction of the liquid phase. The energy coupled to the target to enable deep penetration due to the keyholing effect does not commonly exceed 10%.

An accurate quantitative description of the process calls for consideration of both melting and vaporization. For this, we need to use the system of two equations

$$Q = (1/4)\,\pi d\rho h L_v \times [1 + q/\rho' v_v L_v)] \qquad (11.7)$$

$$\eta Q d = (\pi b^2/4)\, h\rho \times (cT_m + L_m)$$

where ρ' is the critical mass density, v_v the speed of vapor particles, and L_v the latent heat of vaporization.

TABLE 11.4. Experimental and Predicted Values of Fusion Zone Dimensions

Experiment			Theory
d, mm	b, mm	h, mm	h, mm
0.10	0.40	8.5	8.1
0.15	0.50	8.2	7.8
0.20	0.60	8.0	7.3
0.30	0.75	7.1	7.0
0.37	0.90	6.1	5.9
0.43	1.00	5.0	5.6

However, a 10% accuracy proves sufficient for the practical cases of the estimates of the EB diameter made from the dimensions of the fusion region or of the estimates of the metal melt volume from the known diameter of the EB. This is obvious from Table 11.4 which lists experimental data for welding stainless steel at $V = 130$ kV, $I = 13$ mA, and $v = 1$ cm/s. The calculation of the weld penetration h is made at $\eta_T = 0.484$ and at the known thermal constants of the steel. The discrepancy between the predicted and experimental values of h lies within 10%.

11.3. CALCULATION OF THE WELD DEPTH AND WIDTH

Equation (11.5) relates EB parameters to the weld penetration h and weld width b, which must be defined independent of each other. Expression (11.7) can be used to estimate the penetration depth h. It is easy to determine the weld width b using the model for a semi-infinite solid heated by a moving Gaussian source [2].

Weld penetration can be treated proceeding from the relationship among the following dimensionless quantities: (1) Peclet number $\mathrm{Pe} = vy_m/a$; (2) criterion vr_0/a which defines the degree of concentration of the source heat flux; and (3) criterion $\varepsilon = Pv/a^2C_m$. Here, v is the speed of travel of the source, y_m the half-width of the fusion

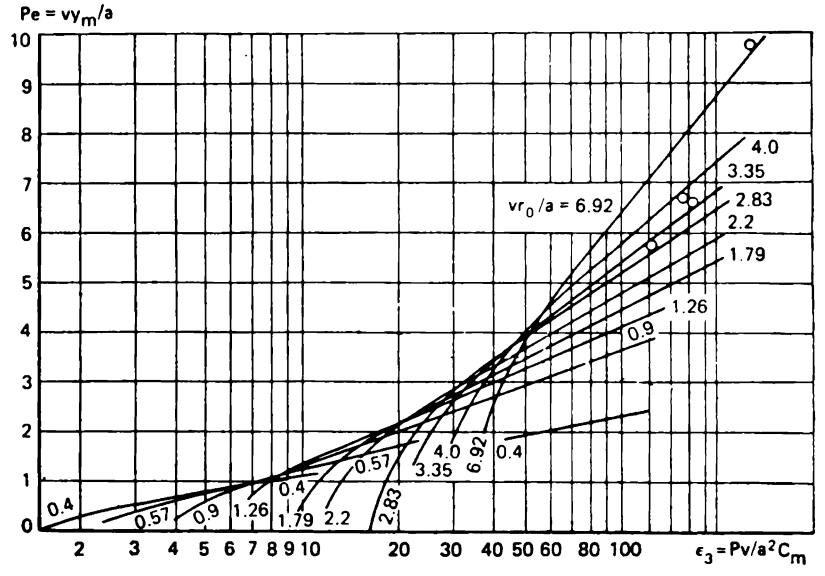

Fig. 11.6. Nomograph relating dimensionless quantities Pe, vr_0/a, and ε

zone, a the thermal diffusivity, $C_m = c\rho T_m$ is the specific heat per unit volume at the melting point.

Since the criterion ε goes beyond the limits of the chart relating Pe, vr_0/a, and ε for EBW in the conditions of types A, B, C, and D under consideration, N. N. Rykalin and coauthors have extrapolated the requisite curves and plotted an additional curve for $vr_0/a = 6.92$ (Fig. 11.6).

Comparison between the experimental and theoretical values of the weld width b, illustrated in Table 11.5, shows that the values are well consistent for all the four types of EBW process.

In Fig. 11.7 are shown the plots of the dimensionless weld width $b_{1/e}/b$ versus the degree of focusing dI_f.

To calculate the fusion area A_m corresponding to the depth h and width b in a given cross section, we need to estimate the weld filling factor $\mu = A_m/hb$. The analysis of 60 welds has revealed that the weld filling factor μ ranges between 0.50 and 0.95. For deep penetration welds in which the aspect ratio is $h/b \geqslant 1$, the factor μ is 0.5-0.7. For welds produced by a softly focused beam, in which case $h/b < 1$, this factor ranges from 0.7 to 0.9. The values of μ advisable for use in computations are given in Table 11.6.

The calculation of the weld depth with a sufficient accuracy for practical applications can be made with the aid of the expres-

TABLE 11.5. **Predicted Values of EBW Parameters Involving a Moving Gaussian Heat Source**

Operation type	$\varepsilon=\frac{Pv}{a^2C_m}$	vr_0/a	$h=\left(\frac{v/a}{vr_0/a}\right)^2$	Pe	Weld width, mm	
					$b=\frac{2\text{Pe}}{v/a}$	b (exper.)
A	99	4.0	9.8	5.8	9.2	—
		3.35	14.0	5.3	8.5	7.9
		2.83	19.5	5.1	8.2	7.8
		2.2	32.3	4.8	7.7	7.6
		1.79	48.8	4.4	7.0	7.3
		1.26	100.0	4.0	6.4	6.0
		0.9	193.0	3.5	5.6	4.7
		0.4	975.0	2.3	3.7	—
B	66	4.0	9.8	4.6	7.3	—
		3.35	14.0	4.4	7.0	—
		2.83	19.5	4.2	6.8	7.0
		2.2	32.3	4.0	6.4	6.5
		1.79	48.8	3.75	6.0	6.3
		1.26	98.2	3.5	5.6	5.5
C	198	6.92	13.0	8.7	6.9	—
		4.0	39.1	7.25	5.8	5.5
		3.35	55.7	6.75	5.4	4.7
		2.83	78.2	6.4	5.1	4.3
		2.2	129.0	5.8	4.6	4.2
		1.79	195.0	5.4	5.3	4.1
D	135	6.92	13.0	7.4	5.9	—
		4.00	39.1	6.3	5.0	5.5
		3.35	55.7	5.9	4.7	4.9
		2.83	78.2	5.7	4.6	4.5
		2.2	129.0	5.2	4.2	4.3

TABLE 11.6. **Variations of the Weld Factor μ with Aspect Ratio h/b**

$h/b \geqslant 1$		$h/b < 1$	
μ_{min}-μ_{max}	μ_{av}	μ_{min}-μ_{max}	μ_{av}
0.51-0.69	0.59	0.76-0.83	0.80
0.53-0.58	0.56	0.69-0.80	0.75
0.58-0.72	0.64	0.91-0.95	0.93
0.55-0.61	0.58	0.75-0.81	0.78
0.49-0.64	0.54	0.76-0.81	0.79
0.48-0.64	0.56	0.59-0.70	0.66
0.50-0.70	0.60	0.64-0.88	0.79
0.50-0.72	0.62	0.71-0.95	0.83

TABLE 11.7. **Experimental Parameters of Welding in Stainless Steel**

I_f, mA	P, kW	h, cm	P/v, kJ/cm	d, cm	P/h kW/cm	P/hv, kJ/cm^2	η_T	b, mm	b, mm (theor.)
76	3.6	1.1	6.5	0.18	3.2	5.8	0.42	2.8	2.4
	2.4	0.8	4.4	0.24	3.0	5.6	0.43	3.1	2.8
	3.6	0.7	3.3	0.29	5.1	4.7	0.51	3.1	3.0
	2.4	0.4	2.2	0.40	5.5	5.0	0.44	3.8	3.4
80	3.6	1.4	6.5	0.15	2.6	4.7	0.35	2.3	1.8
	2.4	0.8	4.4	0.14	3.0	5.5	0.40	2.3	2.0
	3.6	0.9	3.3	0.22	3.9	3.5	0.53	2.4	2.3
	2.4	0.6	2.2	0.30	4.2	3.8	0.51	2.7	2.8
84	3.6	1.1	6.5	0.17	3.3	6.0	0.41	2.7	2.4
	2.4	0.8	4.4	0.12	3.0	5.5	0.40	2.2	1.9
	3.6	0.9	3.3	0.13	3.9	3.5	0.48	1.8	1.7
	2.4	0.6	2.2	0.16	4.1	3.8	0.47	2.1	1.9
88	3.6	1.0	6.5	0.13	3.8	6.9	0.37	2.5	2.0
	2.4	0.8	4.4	0.16	3.2	5.7	0.44	2.6	2.3
	3.6	0.7	3.3	0.14	5.0	4.6	0.56	2.1	2.1
	2.4	0.6	2.2	0.20	4.1	3.7	0.51	2.3	2.2
92	3.6	0.8	6.5	0.27	4.8	8.7	0.36	4.1	3.3
	2.4	0.7	4.4	0.31	3.5	6.3	0.46	3.8	3.4
	3.6	0.6	3.3	0.40	5.1	5.5	0.51	4.0	3.8
	2.4	0.5	2.2	0.30	4.9	4.4	0.51	3.2	3.0
96	3.6	0.6	6.5	0.52	6.5	11.9	0.39	6.7	5.6
	2.4	0.5	4.4	0.41	4.8	8.7	0.43	5.1	4.5
	3.6	0.4	3.3	0.57	9.0	8.2	0.48	5.8	5.4
	2.4	0.3	2.2	0.5	6.8	6.2	0.51	4.5	4.5
100	3.6	0.5	6.5	0.53	28.8	14.5	0.36	7.5	6.0
	2.4	0.5	4.4	0.44	4.4	7.9	0.42	5.1	4.3
	3.6	0.3	3.3	0.53	10.9	9.9	0.51	6.2	5.9
	2.4	0.2	2.2	0.40	10	9.1	0.43	4.9	4.5

sion

$$h = \eta_e \eta_T Qd/[(\pi/4)\, b^2 \rho\, (cT_m + L_m)] \qquad (11.8)$$

where b is the weld width which can be found from the chart of Fig. 11.6.

The choice of the EBW conditions for steels can be clarified by considering the data on the character of changes in the weld efficiency η_T with the beam power P, penetration depth h, and weld speed v.

Figure 11.8 illustrates the relation between η_T and P/h for various conditions of beam focusing. The experimental data related to Fig. 11.8 are given in Tables 11.7 through 11.9. From Fig. 11.8 it is seen that the η_T versus P/h relation can be approximated by a curve with a maximum corresponding to $\eta_T = 0.4$-0.5, which is close to the maximum theoretical value for a linear source in a plate, $\eta_T = (2/\pi e)^{1/2} = 0.484$ and $P/h = 4$ to 5 kW/cm.

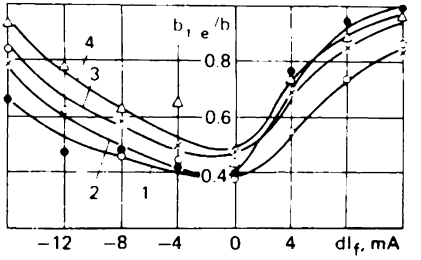

Fig. 11.7. Dimensionless weld width $b_{1/e}/b$ as a function of dI_f for welding operations A, B, C, and D (curves *1*, *2*, *3*, and *4* respectively)

It is of interest to note the fact that the relation of Fig. 11.8 applies for a wide range of penetration depths, namely, from 3 to 160 mm.

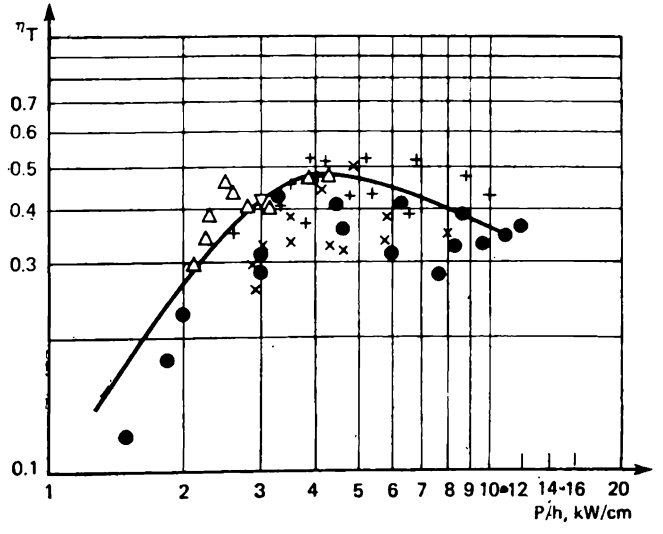

Fig. 11.8. Thermal efficiency η_T of EBW as a function of P/h for various steels

TABLE 11.8. **Experimental EBW Parameters**

Metal	P, kW	h, cm	v, cm/s	P/h, kW/cm	P/hv, kJ/cm²	d, cm	η_T	b, mm	b, mm (theor.)
Cr steel	1.5	1.0	0.4	1.5	3.6	0.05	0.12	0.6	0.52
	7.5	4.0	0.4	1.9	4.5	0.05	0.1	1.1	0.7
	1.5	0.75	1.0	2.0	1.9	0.05	0.23	0.6	0.5
	7.5	2.5	1.0	3.0	2.9	0.05	0.29	1.1	0.7
	15.0	3.7	2.1	3.0	1.4	0.1	0.31	1.2	0.9
	1.5	0.5	3.1	3.3	1.0	0.05	0.43	0.6	0.5
	7.5	1.6	1.0	4.0	3.8	0.05	0.23	1.1	0.8
	15.0	2.6	4.1	4.5	1.1	0.1	0.41	1.2	0.8
	22.5	2.9	2.1	4.7	2.2	0.1	0.36	1.4	1.0
	1.5	0.5	2.1	6.0	2.9	0.03	0.31	0.6	0.6
	7.5	1.2	3.1	6.3	2.0	0.1	0.41	1.1	1.0
	15.0	1.8	2.1	7.8	3.8	0.1	0.28	1.2	1.2
	22.5	2.3	3.1	8.3	2.7	0.1	0.33	1.4	1.0
	1.5	0.3	4.1	8.8	2.1	0.03	0.39	0.6	0.6
	7.5	0.8	3.1	9.8	3.1	0.1	0.33	1.1	1.1
	15.0	1.4	4.1	10.7	2.6	0.1	0.35	1.2	1.0
	22.5	1.9	4.1	11.8	2.8	0.1	0.37	1.4	1.2
Austenitic stainless steel	5.2	1.2	2.1	4.3	2.0	0.1	0.33	0.9	0.9
	5.2	1.1	2.7	4.6	1.7	0.1	0.32	0.8	0.8
	5.2	0.92	3.4	5.7	1.7	0.1	0.34	0.8	0.9
	5.2	0.88	4.0	5.9	1.5	0.1	0.39	0.8	0.8

In Fig. 11.9 is shown the plot of η_T versus tabulated values of P and h, but with consideration for the weld rate v: $\eta_T = f(P/hv)$. As is apparent from the curve, the maximum of η_T lies within the range of $P/hv = 4$ to 5 kJ/cm², i.e. corresponds to $P/h = 4$ to 5 kW/cm,

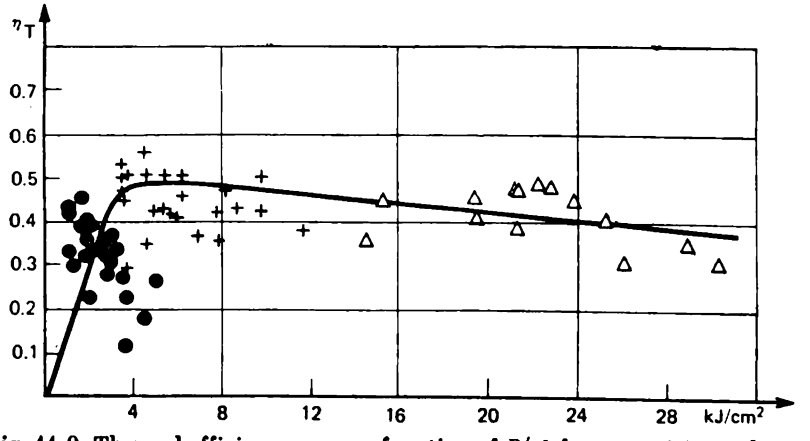

Fig. 11.9. Thermal efficiency η_T as a function of P/vh for austenitic steels (points and crosses) and pearlitic steels (triangles)

TABLE 11.9. Experimental EBW Parameters

Metal	P, kW	v, cm/s	h, cm	P/h, kW/cm	P/hv, kJ/cm²	η_T	b, mm	b, mm (theor.), at d=1cm
Boiler steel 22K	25.9	0.17	10.0	2.6	15.2	0.44	9	9
	28.9	0.09	10.0	2.9	32.0	0.30	12.5	11.1
	36.2	0.16	11.5	3.1	19.7	0.41	10.5	10.2
Boiler steel 16 GNMA	27.6	0.13	10.8	2.5	19.7	0.46	12	11.0
	45.0	0.18	11.2	4.0	22.3	0.49	14	12.0
	30.1	0.11	11.5	2.6	23.8	0.45	14	12.0
	45.0	0.18	11.8	3.8	21.2	0.47	13	11.3
Turbine steel	25.3	0.11	9.0	2.8	25.3	0.4	13	11.4
Stainless steel	21.9	0.11	9.4	2.3	21.2	0.4	11	10.5
Scale-resistant steel	49	0.19	11.5	4.3	22.6	0.48	14	11.9
	47	0.20	11.5	4.1	20.5	0.59	16	12.5
	37	0.08	16	2.3	28.8	0.34	13	11.2
Pearlitic steel	30	0.08	14	2.1	26.3	0.30	10	10.1

which is typical of a rather high weld rate, 1 cm/s. With an increase inthe weld penetration h and, hence, a decrease in the weld speed to $v = 0.1$ to 0.2 cm/s (the right branch of the curve) the energy coupled to the metal sharply increases to 20-30 kJ/cm², but η_T still remains high.

Let us consider the factors responsible for a sharp decrease in the weld rate and a corresponding increase in the energy absorbed per unit area in the case of deep penetration welding.

Welding with a high concentrated energy flux proceeds in a free-running manner as the electron beam penetrates into the part throughout its thickness and continues to move relative to the part. Obviously, the electron beam with a specified power density q must have a definite time to be able to vaporize a cavity, or hole, in the sample to a depth h.

The speed with which the beam forms the cavity, i.e. the speed of the vapor front, is

$$v_v = q/C_v$$

where $C_v = \rho (cT_v + L_v)$ is the heat content per unit volume of the metal vaporized, J/cm^3; ρ the mass density of evaporating metal, g/cm^3; c the specific heat, or heat capacity, J/g K; T_v the vaporization temperature, K; and L_v the latent heat of vaporization, J/g.

The time it takes to form a cavity of depth h is

$$t_c = h/v_v = hC_v/q$$

In order that the beam should not move away from the cavity to be produced during the time t_c, it is necessary to observe the condition

$$d/v \geqslant t_c,\ d/v \geqslant hC_v/q$$

or

$$v \leqslant \frac{4}{\pi} \frac{P}{dhC_v} \tag{11.9}$$

where v is the weld speed, cm/s; P the beam power, W; d the cavity diameter taken equal to the beam diameter, cm; and h the weld penetration, or weld depth, cm.

Given that $P = 60$ kW, $d = 0.5$ cm, $h = 10$ cm, $q = 3 \times \times 10^5$ W/cm^2, $\rho = 7.9$ g/cm^3, $c = 0.45$ J/g K, $T_v = 3\,273$ K, $L_v = 6\,070$ J/g, and $G_v = 58\,600$ J/cm^3, the weld speed for steel according to the above condition is $v \leqslant 0.25$ cm/s. For welding to be performed at a maximum value of η_T, P/h must be equal to 4-5 kW/cm, as follows from Fig. 11.8. For the weld speed specified above, we have $P/hv = (4 \text{ to } 5)/0.25 = 16$ to 20 kJ/cm^2, which is in agreement with the graph of Fig. 11.9.

The above analysis shows that we can judge of the value of q from the maximum weld rate which provides the desired weld depth h.

The result of Fig. 11.8, according to which the maximum efficiency η_T of the EBW process corresponds to the absorbed heat power in the order of $P/h = 4$ to 5 kW/cm, is likely to be accounted for in the following way.

Obviously, the beam ensures a maximum value of η_T when it sustains metal vaporization so as to form a stable cavity translated through the material to a given depth and with a specified linear speed. The condition to be met here is

$$P/h \geqslant C_v a$$

where a is the thermal diffusivity, cm^2/s.

For the case of steel welding, we have $C_v a = 5.86 \times 10^4 \times \times (4 \text{ to } 6) \times 10^{-2} = 2.4$ to 3.6 kW/cm, and so the above condition is valid.

Expression (11.5) can be used to define the weld width

$$b_{1/e} = \left(\frac{4}{\pi} \frac{\eta_e \eta_T P d}{vhC_m} \right)^{1/2} \tag{11.10}$$

As for through penetration, account should be taken of a fraction of power P_l (up to 40%) lost by the beam as it passes through the cavity on the back side of the plate. The loss factor is given by

$$F_l = \frac{\eta_e P - P_l}{\eta_e P}$$

Measuring the current of the beam of the given voltage V at the exit from the cavity and considering that the energy of electrons leaving the cavity does not change, we can estimate F_l.

For the case of through penetration, expression (11.10) takes on the form

$$b_{1/e} = \left(\frac{F_l \eta_e \eta_T P d}{v h C_m} \right)^{1/2} \tag{11.11}$$

We can now select the conditions for steel welding: (1) set $h = 10$ cm and $d = 0.5$ cm; (2) take the weld power to be $P = 40$ kW in accordance with Fig. 11.9 and with regard to η_e and F_l; (3) select the weld speed v from condition (11.9); (4) correct the value of η_T using the curve of Fig. 11.8; and (5) calculate the desired weld width b from (11.10) and (11.11).

For the case under consideration we have: $h = 10$ cm; $P = 40$ kW at $\eta_e = 1$ and $F = 1$; $v = 0.17$ cm/s; $P/hv = 23.5$ kJ/cm^2; $\eta_T = 0.45$; $C_m = 9\,800$ J/cm^3; $b = 0.83$ cm; and aspect ratio $h/b = 12$.

Work [1] has considered the extreme behavior of η_T as a function of welding parameters. It is found that the η_T versus ε relation for a Gaussian source has a maximum at $n_m = 0.1$ and $\varepsilon = 300$, $n_m = 0.2$ and $\varepsilon = 80$, $n_m = 0.3$ and $\varepsilon = 30$, and $n_m = 0.4$ and $\varepsilon = 15$. Here, $\varepsilon = 8\sqrt{\pi p / n_m}$; $n_m = T_m / T_c$; $T_c = \eta_e P / 2\lambda \sqrt{4\pi a t_0}$; $p = v^2 t_0 / 4a$; λ is the thermal conductivity, W/cm K; a the thermal diffusivity, cm^2/s; t_0 the heating time constant; and v the weld speed, cm/s.

The extremum does not appear when $n_m = 0$ for a point source on the surface of a semi-infinite solid. Researchers [1] explain the appearance of extreme points due to the fact that at high weld rates the weld width may become smaller than the Gaussian source diameter. This situation is theoretically impossible for a point source. If we compare the results presented in [1] with experimental findings, we can see that they correlate well probably because the aspect ratio h/b is very large since the weld width b is rather narrow. In the cases of welding of massive pieces, the beam diameter is known to be in the order of the weld width or sometimes even smaller than b.

11.4. EFFECT OF BEAM VOLTAGE ON THE PENETRATION DEPTH

As shown by experiments, other conditions being equal, the weld penetration increases with accelerating voltage (Fig. 11.10). This is due to a reduced electron scattering by vapor atoms. For example, at $V = 20$ kV, the absorption coefficient is $\alpha = 2.4 \times 10^6/V^2 = 6 \times 10^3$ cm^2/g, while at 100 kV it decreases to 2.4×10^2 cm^2/g, i.e. by a factor of more than 10. An increased voltage thus leads to a higher kinetic energy of electrons and increases the free path of electrons in metal vapors.

The effect of V on h has been given detailed treatment in work [3], which contains the results of experiments on welding of stainless steel with an electron beam to a weld depth of about 80 mm at $P = 10$ kW, $q \approx 5 \times 10^5$ W/cm^2, $V = 30$ to 100 kV, weld speed $v = 0.3$ to 2.2 cm/s, and a pressure in the chamber of $5 \times 10^{-3} = 1 \times 10^{-2}$ Pa. Figure 11.11 illustrates the experimental plots of the penetration depth h against the weld rate v_w and accelerating voltage V. The experiments confirm that the vapor pressure is

$$p(z) = \frac{\gamma(T)}{r_c} \frac{1}{r_c/h + 3(1 - z/h)} \qquad (11.12)$$

where $\gamma(T)$ is the surface tension of the melt as a function of temperature, r_c the cavity radius at a depth h/e, and h the maximum cavity depth equal to the weld penetration.

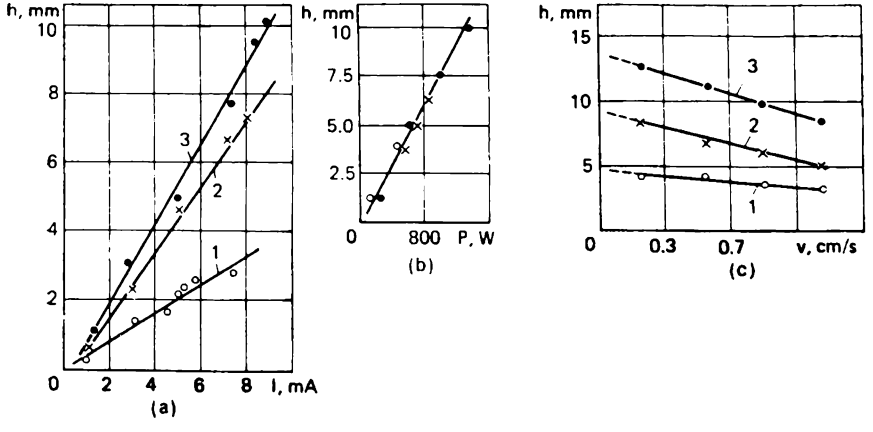

Fig. 11.10. Penetration depth as a function of beam current (*a*), power (*b*) and weld speed (*c*); (*a*) stainless steel at $v = 1.2$ cm/s, $V = 100$ kV (curve *1*) $V = 130$ kV (curve *2*), and $V = 150$ kV (curve *3*); (*b*) stainless steel at $v = 1.2$ cm/s and $V = 100$ to 150 kV; (*c*) low-carbon steel at $V = 100$ kV and $I = 7$ mA (curve *1*), $V = 125$ kV and $I = 10$ mA (curve *2*), and $V = 150$ kV and $I = 13$ mA (curve *3*)

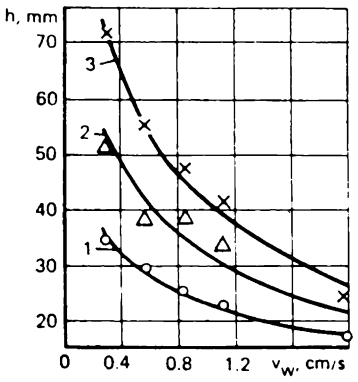

Fig. 11.11. Penetration depth as a function of weld speed and accelerating voltage V at constant power of 10 kW and power density of about 5×10^5 W/cm^2 ($r_e = 0.25$ mm): *1*, 30 kV; *2*, 63 kV; *3*, 100 kV [3]

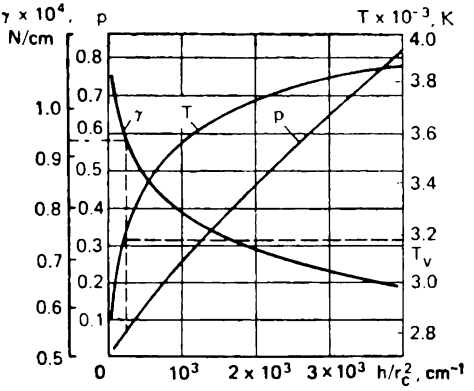

Fig. 11.12. Maximum values of T (K) and vapor pressure p (MPa) and minmum values of surface tension γ/(N/cm) along the cavity axis versus parameter h/r_c^2 defining cavity dimensions [3]

The surface tension $\gamma\,(T)$ linearly decreases with increasing temperature and drops to zero at a critical temperature $T_c = 1.7\,T_v$, where T_v is the vaporization temperature at the atmospheric pressure (for iron, $T_c \approx 5\,670$ K):

$$\gamma\,(T) = \gamma_0\,(T_c - T)/(T_c - T_0) \tag{11.13}$$

where γ_0 is the surface tension at T_0. For iron, $T_0 = 2\,090$ K and $\gamma_0 = 1.5 \times 10^{-2}$ N/cm.

The saturated vapor pressure is

$$\log p = B - A/T \tag{11.14}$$

where A and B are constants characteristic of the type of material.

If h and r_c are known, equations (11.12)-(11.14) solved simultaneously yield the maximum values of p, γ, and T along the cavity axis. The curves of these values plotted versus h/r_c^2 are shown in Fig. 11.12. It is seen that the vapor pressure along the cavity axis can reach 10^5-10^6 Pa.

The Gaussian function can be applied for defining the current distribution over the path length z in the metal vapor traversed by the electron beam with an effective radius

$$r_e(z) = r_e(0) \exp\left[(\sigma/2) \int_0^z n(z)\,dz\right] \tag{11.15}$$

where r_e (0) is the initial EB radius, σ the total effective electron-by-atom scattering cross section, and n (z) the atom concentration.

With allowance made for elastic and inelastic collisions, the scattering cross section assumes the form

$$\sigma = (47.8/V)\, Z^{1/3} \left\{ Z - 1 - \frac{4 \ln 0.0678 V_i}{Z^{1/3} V^{1/2}} \right\} 10^{-16} \qquad (11.16)$$

where V is the accelerating voltage, V; Z the atomic number; and V_i the ionization potential of iron. For iron, $Z = 26$, $V_i = 7.9$ V and

$$\sigma = (142/V)\,[25 - 4 \ln (0.181/V^{1/2})]\, 10^{-16}$$

Considering equation (11.12) and expressing the atom concentration in terms of pressure, the expression for r_e after the EB travels a path of length z in metal vapors takes the form

$$r_e(h) = r_e(0) \exp\left(\frac{\sigma \gamma h}{6 k T_{\max} r_c} \ln \frac{12h}{r_c} \right) \qquad (11.17)$$

where k is the Boltzmann constant and $T_{\max}$ the maximum temperature.

The temperature $T_{\max}$, which is independent of the speed of a heat source, is defined as the temperature in the center of a circular source on the surface of a semi-infinite solid [2]:

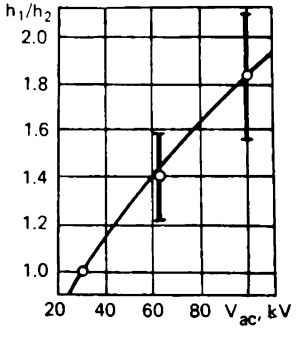

Fig. 11.13. Penetration depth h_1/h_2 as a function of V_{ac} at constant P and q [3]

$$T_{\max} = \eta_e P / [\pi \lambda r_e (h)] \qquad (11.18)$$

where $P = IV$ is the beam power and λ the thermal conductivity.

The thermal efficiency for stainless steel is $\eta_T = 0.38$ at $P = 10$ kW, $v = 0.28$ cm/s, and $V = 63$ kV. The volume of metal melted per second is

$$V = vhr_b = 0.38 \eta_e P / \rho c T_m \qquad (11.19)$$

where r_b is the half-width of the weld pool.

Expressions (11.12), (11.14), and (11.17)-(11.19) form the system of equations for determining six unknown quantities: r_e (h) at $z = h$, $p_{\max}$, $T_{\max}$, $\gamma_{\max}$, h, and r_c on condition that the shape of the cavity obeys the Gaussian function.

Solving (11.17) and (11.18) and in view of (11.19), we obtain the result after some simplification, which well agrees with experiment:

$$h_1/h_2 \approx \sqrt{V_1/V_2} \qquad (11.20)$$

A graphical representation of (11.20) appears in Fig. 11.13. The depth at $V = 30$ kV is taken as the initial value.

Comparison between the experimental and theoretical values obtained from the above expressions shows that the weld penetration h for stainless steel reaches 5.2 cm at $P = 10$ kW, $V = 63$ kV, $v = 0.28$ cm/s, and $r_e(0) = 0.25$ mm (see Fig. 11.11).

The predicted values are the following: $\sigma = 1.2 \times 10^{-17}$ cm^2, $r_c = 0.075$ cm, $b = 0.6$ cm, $h/r_c^2 = 1 \times 10^3$ cm^{-1}, $T_{max} = 3\,560$ K, $\gamma_{max} = 7.9 \times 10^{-3}$ N/cm, $p_{max} = 3.3 \times 10^5$ Pa, and $h = 5$ cm. The weld width b agrees well with the experimental value. The same is true for h, the experimental value of each is 5.2 cm.

11.5. POSITIONS OF WELDING

The pressure due to free fall acceleration of the metal melt strongly affects the process of weld seam formation and may contribute to defects especially when welding is done in massive parts 20 to 200 mm thick. For this reason, measures are taken to harness the force of gravity as a factor beneficial for shaping the weld. Work [4] has analyzed the methods of EB welding of massive parts and suggested an optimal angle of incidence of the beam.

There are three basic EBW methods differentiated by the weld positions: (1) horizontal welding, in which the direction of gravity force is coincident with the EB direction (Fig. 11.14*a*); (2) vertical welding along the vertical wall, with the force of gravity acting at right angles to the beam axis (Fig. 11.14*b*); and (3) horizontal welding along the vertical wall, with the force of gravity directed normal to the beam (Fig. 11.14*c*).

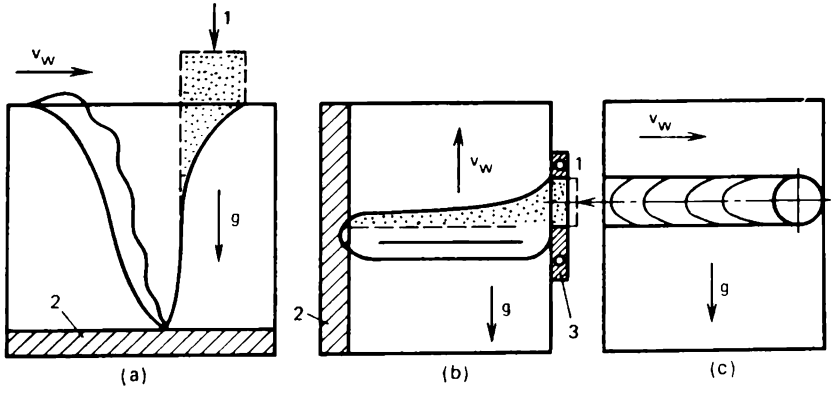

Fig. 11.14. Schemes illustrating EBW methods: *1*, EB; *2*, support; *3*, water-cooled slide block; v_w, weld speed; *g*, force of gravity

To eliminate defects in welds produced by these methods, provision is made to achieve the following: (*a*) prevent the melt from flowing out of the pool; (*b*) ensure favorable temperature pattern at all points of the pool; and (*c*) guard the pool against local and overall hydrodynamic perturbations.

The method illustrated in Fig. 11.14*a* satisfies well the first two conditions, but poorly satisfies the third condition. The scheme of Fig. 11.14*b* meets the first and the third condition. The scheme of Fig. 11.14*c* does not meet the first condition.

To satisfy all the three conditions, a suggestion is made to tilt the weld seam plane with reference to the horizontal through a certain angle α at which the pool pressure in the weld root does not exceed 4 500 Pa.

Since the static pressure of the melt column of height h, tilted to the horizon at an angle α is $p = \rho gh \sin \alpha$, then we have $\alpha \leqslant \leqslant 450/\rho h$ at a maximum pressure of 4 500 Pa. Here, ρ is the metal density, g the force of gravity, and h the weld penetration.

High-quality welds in steels are made at $V = 80$ kV, $I = 0.7$ A, $\alpha = 24°$, and $v = 0.15$ and 0.25 cm/s.

The effectiveness of welding with a tilted beam is treated in work [5].

References

1. T. M. Berezovskiy. *The thermal efficiency of metal welding with a surface weld arc.* Avtomatich. Svarka, No. 10, p. 18, 1979.
2. N. N. Rykalin, A. A. Uglov, and I. V. Zuev. *Electron beam processing of materials.* Moscow, Mashinostroenie, 1978 (in Russian).
3. K. S. Akopyants, Yu. V. Zubchenko, V. E. Lokshin, et al. *Effect of accelerating voltage on EBW parameters.* Avtomatich. Svarka, No. 11, p. 11, 1972.
4. G. I. Leskov and L. N. Zhivaga. *EB welding of thick steel pieces in various weld positions.* Avtomatich. Svarka, No. 10, p. 1, 1980.
5. V. V. Bashenko, V. A. Lopota, E. A. Mitkevich, et al. *Welding with a tilted electron beam.* Svarochnoe Proizvodstvo, No. 7, p. 19, 1981.

Chapter 12
THERMAL PROCESSES

12.1. EB-PLASMA INTERACTION

Experiments confirm that the beam whose power density q ranges from 10^7 to 10^8 W/cm^2 generates a thermally non-equilibrium plasma in the zone of interaction. In the process of deep penetration, for example, due to the keyholing effect, the plasma produced in the cavity enables electrons to penetrate more deeply into the solid since the plasma electrons lose an insignificant amount of energy. To gain a better understanding of the mechanism of EB-solid interaction, it is of interest to clarify the possible ways in which slow secondary and thermionic electrons interact with the primary electron beam in the work areas on the target surface [1].

A minimum number of slow electrons, in terms of the order of magnitude, required to shield (scatter) the beam is $n_1 \approx S/S'$, where S is the beam cross-section area and S' the cross-section area where electron scattering occurs.

Primary electrons travel at a speed v_1 across a layer of thickness h' (depth of electron penetration) and give rise to secondary electrons of number sI, where s is the secondary emission ratio and I the beam current expressed in terms of the number of electrons per unit time. Secondary electrons leave the layer of thickness h' at the speed v_2 during the time t_2. Since $t_2 = h'/v_2$ is much greater than $t_1 = h'/v_1$, the number of secondary electrons left in the layer is $t_2 n_2 = sIt_2\,(t_2/t_1)$.

The condition of primary-by-secondary electron scattering can then be written as $sIt_2\,(t_2/t_1) \geqslant S/S'$. From this expression we obtain the critical value of current at which the beam begins to interact with slow electrons at an appreciable rate:

$$I > \pi d^2 v_2^2 / 4S' v_1 s h' \qquad (12.1)$$

where d is the beam diameter.

For the case of EB-dielectric interaction, at $s = 10$, $h' = 10$ μm, $V = 25$ kV, $d = 0.5$ mm, and $E = 10$ eV, we have $v_1 \approx 1 \times \times 10^{10}$ cm/s, $v_2 = 1.8 \times 10^8$ cm/s, $S' \approx \lambda^2 = 1.6 \times 10^{-15}$ cm (where λ is the wavelength of a slow electron), and $I \geqslant 63.5$ A which corresponds to a power density $q \geqslant 8 \times 10^7$ W/cm^2.

For the typical case of formation of a cavity in metal of depth $h = 1$ cm and cross-sectional area of 1×10^{-2} cm^2 at an ionization coefficient η of 1.0 and at the above values of other quantities, the current is $I \geqslant 3$ A or $q \geqslant 7.5 \times 10^6$ W/cm^2. If we allow for the fact that the vapor layer of thickness h has a particle concentration of $n \leqslant 10^{18}$ cm^{-3}, then $I \geqslant 3 \times 10^4$ A or $q \geqslant 7.5 \times 10^{10}$ W/cm^2 for the vapor layer reduced to an equivalent solid layer that is approximately 1×10^{-4} cm thick.

So, the interaction with secondary electrons in the range of power densities of 10^5 to 10^6 W/cm^2 typical of welding and heat treatment is insignificant, but makes itself felt when q becomes higher than 10^8 W/cm^2.

From expression (12.1) we can estimate the critical EB parameters at which the beam begins to interact strongly with the vapor or plasma. When $V = 25$ kV, $S' = 1 \times 10^{-18}$ cm^2, $v_1 = 1 \times \times 10^{10}$ cm/s, $d = 0.5$ mm, and $\eta = 1$, the current is $I \geqslant 5 \times 10^{-2}$ A or $q \geqslant 5 \times 10^5$ W/cm^2, which is indeed the fact in the conditions of material processing with an electron beam and its interaction with the vapor. If the degree of gas ionization is $\eta = 0.1$ and 0.01, then the respective values are $I > > 5 \times 10^{-1}$ A or $q \geqslant 6 \times \times 10^6$ W/cm^2 and $I \geqslant 5$ A or $q > 6 \times 10^7$ W/cm^2, in which case the interaction with the neutral vapor is appreciable and begins at relatively low values of q, i.e. when $q > 1 \times 10^5$ W/cm^2.

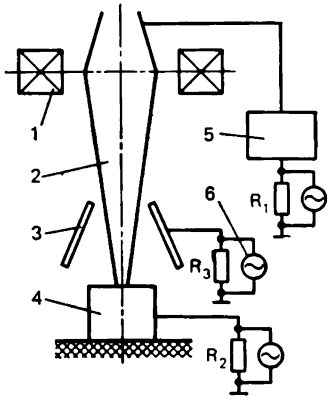

Fig. 12.1. Schematic diagram of system for studying the kinetics of cavity formation: *1*, focusing system; *2*, electron beam; *3*, collector; *4*, target; *5*, supply source; *6*, oscilloscope

12.2. KINETICS OF CAVITY FORMATION

Figure 12.1 demonstrates schematically an arrangement for experimental studies of the kinetics of cavity formation at $V = 20$ kV and $I = 5$ to 250 mA in the interaction of a single pulse of 50 ms to 5 s in duration. A metal sample 30 mm in diameter and 30 mm in height is set up on the insulator in a chamber and connected to ground via a resistor R_2. On inserting a resistor R_1 into a beam source circuit, an oscilloscope *6* begins to record both the current I_t through the target and beam current I_b of the source. The oscilloscope screen displays the traces, the photographs of which are taken to analyze the process. The oscilloscope can also record traces on tracing paper. This arrangement made it possible to analyze I_t at

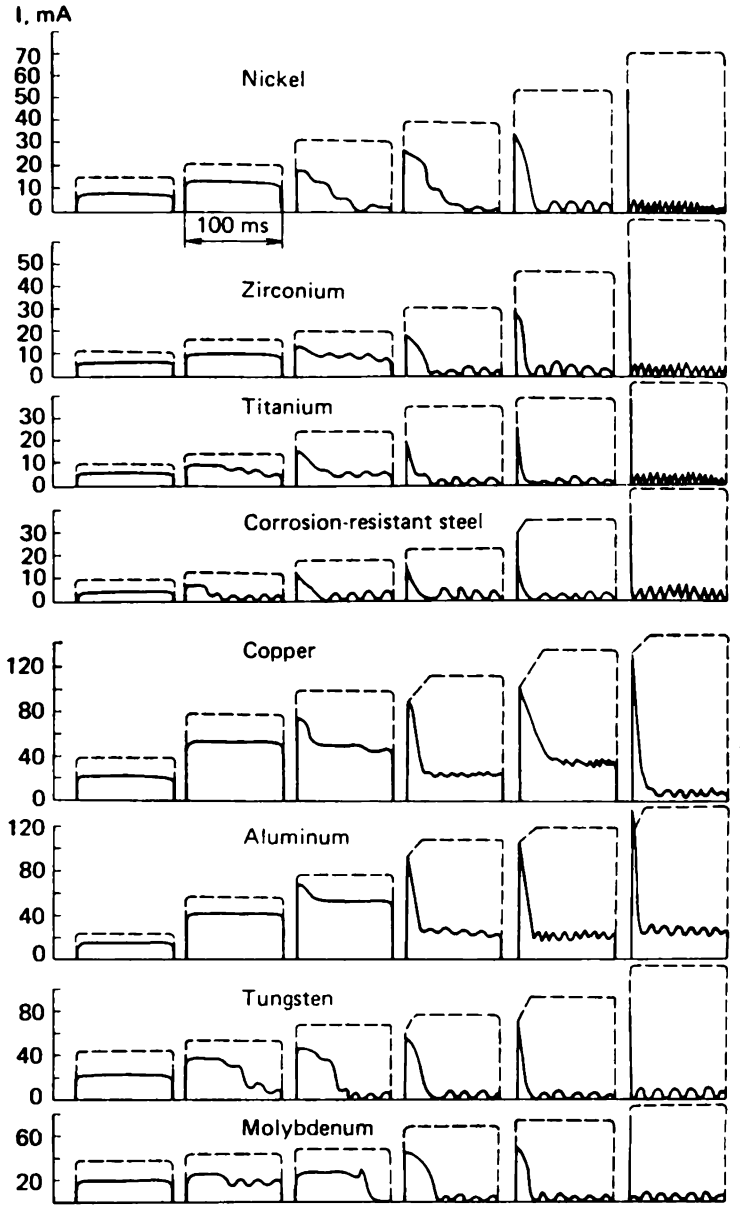

Fig. 12.2. Changes in the shape of a 100-ms current pulse taken from the supply source (dash lines) and passed through the targets (solid lines) with an increase in the beam current

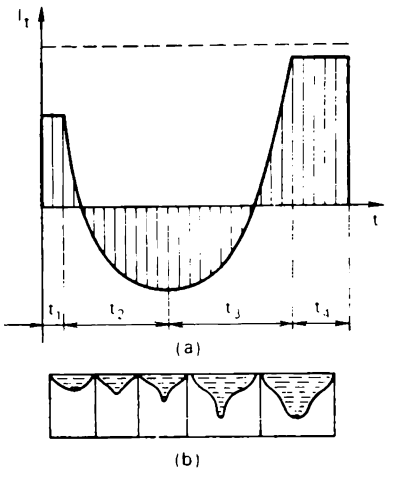

Fig. 12.3. Typical oscilloscope trace (*a*) of current passing through a stainless steel target struck by the beam for $t = 1$ s and melt zones (*b*) corresponding to pulse lengths of t_1, t_2, t_3, and t_4

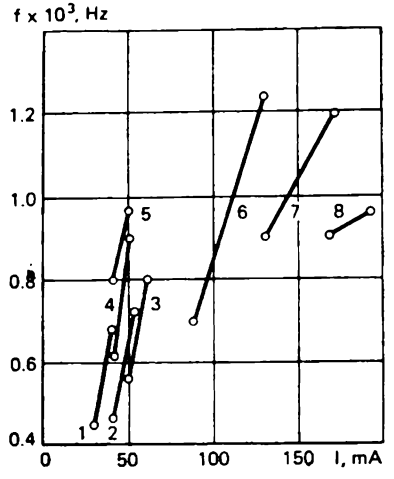

Fig. 12.4. Oscillation frequency of current through targets in the period t_3 of the trace of Fig. 12.3 as a function of the beam current: *1*, Ti; *2*, stainless steel; *3*, Ni; *4*, Zr; *5*, Al; *6*, Mo; *7*, Cu; *8*, W

I_b = 5 to 250 mA and V = 20 kV for W, Mo, Ti, Zr, Ni, Cu, Al, and stainless steel.

Figure 12.2 displays the oscilloscope traces of 100 ms current pulses passing in the source (dash lines) and through the targets of metals under investigation (solid lines) with an increase in the beam current over the range indicated in the figure. At the initial stage, an increase in I_b does not principally cause any change in the pulse shape apart from a slow rise of the ratio I_t/I_b. But when I_b reaches a definite critical value which depends on the thermal properties of metals, the pulse of current through the target begins to display a somewhat deformed shape. During a certain time t_1 the target carries a constant current, but then the current through the target becomes pulsating over the remaining time of the pulse length, $t - t_1$. The time t_1 decreases with increasing I_b, while the ripple frequency of I_b increases during $t - t_1$.

In Fig. 12.3 is shown the curve of changes in I_t through the target during the time $t = 1$ s of interaction of the beam. The current I_t does not vary during the time t_1, then drops down in an increasingly oscillating manner. After some time, I_t starts to grow and reaches an approximately constant value equal to 80-95% of I_b. High-frequency pulsations now give way to low-frequency pulsations.

The analysis of the curve of Fig. 12.3 discloses that the current through the target changes in four stages, each lasting a definite time: (1) constant current, for t_1; (2) pulsating current with increasing frequency f and decreasing amplitude, for t_2; (3) pulsating current which grows in frequency and mean amplitude, for t_3; (4) pulsating low-frequency current with a constant mean amplitude, for t_4.

It is found that the pulsating character of current through the target results from of a few types of oscillation. Referring to Fig. 12.3, in the time period t_2 the current oscillates at a frequency of 50 Hz and displays oscillations of 300 Hz superimposed on the main oscillations. During the time t_3, the character of oscillations becomes more complex since these two types of oscillation experience an added effect of oscillations of up to 10^3 Hz superimposed on them (Fig. 12.4). At the end of time t_3, these oscillations decay, excepting low-frequency oscillations in the range of 6 to 50 Hz.

An independent recording of I_t and a simultaneous recording of changes of the pressure in the weld pool region with an ionization gage give identical results of changes in the oscillation frequency. To a maximum of I_t there periodically corresponds a minimum of the pressure in the region of interaction.

From the shapes of melt pools produced in stainless steel during t_1, $t_1 + t_2$, $t_1 + t_2 + t_3$, and t, as illustrated in Fig. 12.3, we can picture the kinetics of deep penetration, or keyholing. During the time t_1 the beam heats the sample and a fraction of heat is removed from the zone of interaction by thermal conduction. For most metals, excepting Mo and W, the irradiated spot begins to melt at the end of t_1. Emission from the molten pool during this time is mainly brought about by secondary and back-scattered electrons. The share of secondary emission diminishes with an increase in the pulse current, i.e. with an increase in the rate of heating.

Over the period t_2, intense thermionic emission from the pool is evident. The thermionic current flows in the opposite direction to that of primary electron current. Therefore, the current I_t is an algebraic sum of currents, $I_t = I_b - I_e$, where I_e is the current of emission from the sample of both back-scattered secondary electrons and thermionic electrons.

As mentioned above, by the end of time t_1 the metal is generally found to be in the molten state. Over the period t_2, the temperature of the melt increases and the thermionic current grows accordingly. The oscillation frequency of current at t_2 is 50 Hz with a superimposed frequency equal to 300 Hz, the latter resulting from the instability of accelerating voltage. The voltage stabilization accurate to 1-2% removes the harmonic with a frequency of 300 Hz. The harmonic with a frequency of 50 Hz probably appears as a result of pulsations in other supply sources.

At the start of the period t_3, the metal begins to vaporize intensely. The material is blown off the pool because of the periodic vaporization of layers, each having a thickness of the same order of magnitude as the electron free path. The face of the molten pool lowers down at a certain rate, thereby resulting in a cavity or hole, whose walls absorb the secondary emission electrons. Starting from this moment, the current through the target increases. By the end of time t_3 the depth of the cavity reaches such a value that the cavity walls practically absorb the entire secondary electrons. The current through the target approaches the value of the primary electron current. The period t_3 is thus the net period of cavity formation. During the time t_4 the cavity does not increase in depth. The pulsations of the current at 6 to 50 Hz, which are characteristic of this period, result from the periodic clogging of the cavity in its upper portion.

A number of experiments have confirmed the concept of the intermittent process of cavity formation due to the periodic scattering of the electron beam. It is assumed that the process of continuous interaction of the beam with a material, for example, during one second, is analogous in some way to pulse interaction: the pulse duration is equal to the time of evaporation of the elementary layer whose thickness is of the same order of magnitude as the electron path length at the cavity bottom and the pulse spacing t_s is equal to the time of scattering of the EB which only forms the liquid phase, but does not increase the cavity depth. If we convert from the continuous to the pulsed process using pulses of duration t_p and pulse spacing t_s, then the beam must pierce a hole of depth $h_0 \geqslant h$ over the period t rather than melt the material to a depth h. In this case, the beam is "switched on" to vaporize a layer and then is "switched off" to avoid excessive melting due to the EB scattering by the blow-off material. Because of the high-frequency pulsations of the current through the target during the time t_3, it has been possible to pierce 2-mm diameter holes 15 to 60 mm deep in stainless steel and aluminum parts under the following conditions: $t_p = 1 \times 10^{-3}$ s, $f = 100$ Hz, $V = 20$ kV, $I = 150$ mA, and $q \approx 10^5$ W/cm^2 (Fig. 12.5). Holes up to 5 mm deep have also been drilled in other metals and alloys, including molybdenum.

So, both calculations and experiments support the conclusion that the process of deep penetration occurs in a pulsating manner. In the interaction of a softly focused beam that does not lead to keyholing, pulsations depend on the equipment used and the stability of the rated values of power supply sources. The ripple frequency of the current here is 50 Hz, with a frequency of 300 Hz being superimposed on this frequency. In the case of strong focusing that results in keyholing, the ripple frequency is a function of the power density and reaches 0.5 to 1.2×10^3 Hz. High-frequency

pulsations of the current are due to the periodic scattering (shielding) of the EB as it penetrates more deeply into the material. The cavity which receives energy in a pulsating manner has its upper portion periodically clogged at a frequency of 6 to 50 Hz. A knowledge of the effects described above opens up possibilities for control of the process of EB-solid interaction.

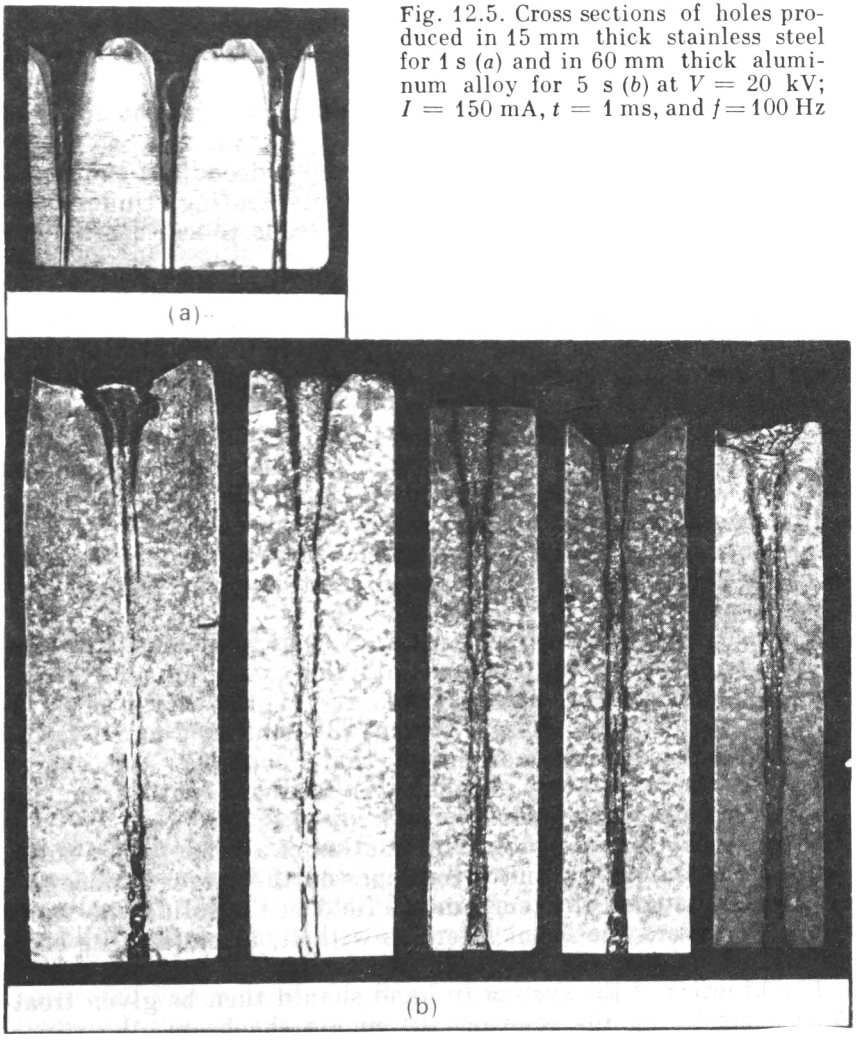

Fig. 12.5. Cross sections of holes produced in 15 mm thick stainless steel for 1 s (*a*) and in 60 mm thick aluminum alloy for 5 s (*b*) at $V = 20$ kV; $I = 150$ mA, $t = 1$ ms, and $f = 100$ Hz

12.3. FREE OSCILLATION

Experimental studies into the interaction of an electron beam (EB) of $q = 10^5$ to 10^7 W/cm^2 with metals reveal the following.

1. With the flow of energy held constant in time, certain physical parameters specific to the beam-solid system, such as the vaporization rate, beam power density, and electron emission rate, undergo variations.

2. There is a critical value of beam energy above which oscillations are set up. This value varies with the type of target material and the beam parameters.

This behavior of the beam-solid system is inherent in free-oscillation systems [2].

The vapor moving from the metal target decouples the beam from the surface and affects the process of its heating. Under definite conditions, the shielding of the target leads to self-excited oscillations [3-6].

When a time-constant flow of energy heats up a solid, the pattern of changes in the surface temperature considerably differs from the conventional pattern: the temperature does not tend to a constant value, but varies in a self-sustained manner. This is also the case for the vapor density. The mechanism of self-excited oscillations stems from the shielding of the beam by the vapor and from the relaxation processes involved in the gas dynamics of the vapor. The critical values of the energy and the amplitude and frequency of oscillations depend on the parameters of the energy flow, thermal constants of the material in question, gas-dynamic characteristics of the vapor, and the pattern of interaction of the beam energy with the vapor.

Work [2] defines the free-oscillation system as one that converts the energy of a steady source into the energy of oscillation. The requisite elements of such a system are: (1) the oscillatory system proper; (2) constant-energy source; (3) "shutter", namely, the beam-by-vapor scattering mechanism that "controls" the energy delivered to the oscillatory system; (4) feedback path from the oscillatory system to the shutter.

Let us consider the model of interaction of a beam with a solid. The beam from an energy source impinges on the target surface and heats it, thus changing the temperature field in the solid. The vapor traveling up toward the beam interacts with it, attenuates its energy, and thus reduces the intensity of heating.

The kinetics of the system in hand should then be given treatment by considering the relationship among the beam, the vapor, and the material, i.e. its temperature field.

The free-oscillation system schematically illustrated in Fig. 12.6 includes all the elements mentioned above: the EB source;

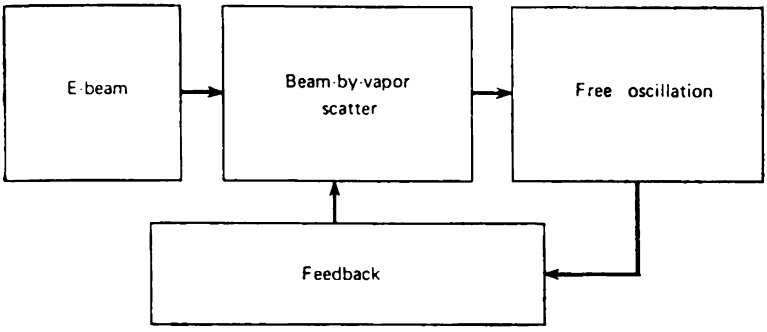

Fig. 12.6. Schematic representation of oscillatory system

the shutter, i.e. the mechanism of beam scattering by the vapor plume; the oscillatory system, i.e. the mechanism involving the relaxation processes in the kinetics of the vapor density and dissipative processes of heat removal from the zone of interaction; and the feedback path which relates the vaporization rate to the surface temperature.

A simple mathematical model of the free-oscillation system comprises an independent set of two common first-order differential equations [7].

Let us write the equations describing the kinetics of the process represented in Fig. 12.7 in the form

$$dT/dt = -(a/l_e^2)\,(T - T_0) + Q \exp(-\alpha_1 \rho b) \tag{12.2}$$

$$d\rho/dt = (v/b)\,\{n(t) - n[T(t - \tau(b))]\} - (\eta/\rho b^2) \times \times [\rho - n(T)] \tag{12.3}$$

$$T(0) = T_0, \quad \rho(0) = \rho_0$$

$$n(T) = (A_n/T) \exp(-B_n/T) \tag{12.4}$$

$$\tau(b) = b/v - \rho b^2/\eta$$

Here T is the target temperature; α_1 the absorption factor; t the time of interaction; a the thermal diffusivity of the target material; l_e the effective heat propagation length (the target thickness); $Q = q/l_e c\rho'$ the effective rate of heating; q the beam power density; c the specific heat; ρ' the material density; ρ the vapor density; $b \approx (1$ to $10)\,r$, where r is the beam radius; $v(T)$ the vapor speed; $n(T)$ the saturated vapor density; η the vapor viscosity; A_n and B_n the phenomenological constants determined from the relations of the saturated vapor pressure to the temperature T.

When the beam delivers a power density of 10^5 to 10^7 W/cm^2 to the target, the temperature at the irradiated spot reaches about

(2 to 5) $\times 10^3$ K. In this temperature range the saturated vapor density is such that the free path of an atom becomes smaller than the size of the vapor plume. Consequently, when considering the gas dynamics of the vapor, we need to allow for the interaction of atoms with one another.

The gas jet moving up from the irradiated spot forms a vapor plume above the target surface. The free jet is known to become turbulent at a low Reynolds number. Besides, the density of the gas jet varies in a pulsating manner.

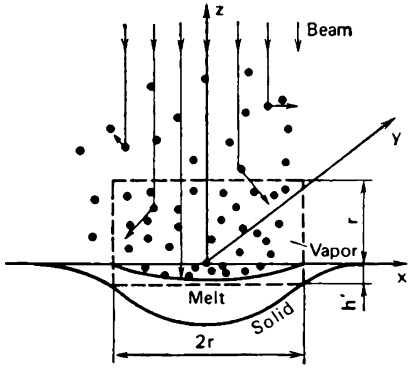

Fig. 12.7. Model illustrative of EB-solid interaction: r, EB radius; h, electron penetration depth; x, y, z, coordinates

Since the energy delivered to the target depends on the vapor plume density which, in turn, depends on the beam spot temperature, large-scale pulsations (in the order of the plume size) of both the vapor density and the temperature in the beam spot lead to the buildup of self-sustained oscillations under certain conditions.

The vapor flow traveling from the irradiated spot conditionally consists of two components: one sustains the plume itself and the other traverses the plume. So, the first convective term in expression (12.3) corresponds to the appearance of pulsations at τ and the second diffusion term represents the pulsation decay.

Let T_e and $\rho_e = n\,(T_e)$ be the steady-state solutions of equations (12.2) and (12.3).

Introduce the following designations:

$$u = (1 - T_0/T_e)\,(B_n/T_e - 1)\,a/l_e^2$$

$$U = \alpha_1 \rho_e b u, \quad W = \eta_e/\rho_e b^2, \quad f_0^2 = p\,(U + u)$$

$$\rho' = \nu_e \rho_e b/\eta_e, \quad \varepsilon = [(\rho' - 1)\,U - u - W]$$

Self-excited oscillations are set up at $\varepsilon > 0$. In this case we have

$$\rho\,(t) = \rho_e + (u/U)\,\rho_e A_e \cos f_e t + (f_0/U)\,\rho_e A_e \sin f_e t$$

$$n\,[T\,(t)] = \rho_e + \rho_e A_e \cos f_e t$$

The ripple amplitude of temperature is

$$A_e = 2\sqrt{\frac{\varepsilon}{W\,(2u/U + 3u^2/U^2 + 3f_0^2/U^2)}}$$

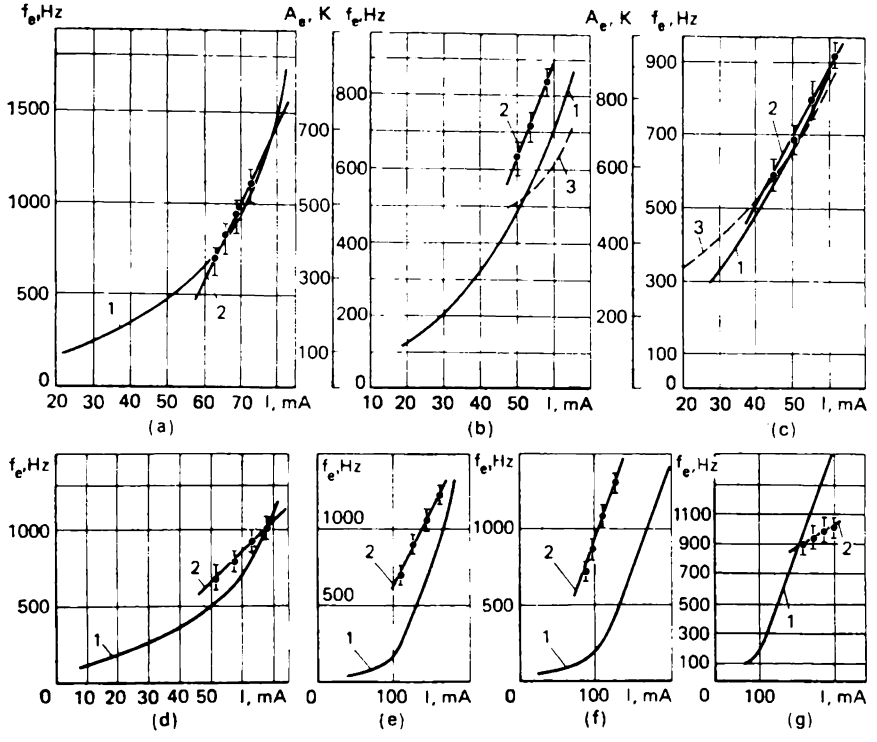

Fig. 12.8. Comparison between the predicted values of frequency (*1*) and amplitude (*3*) of free oscillations and the experimental values of frequency (*2*) in the interaction of EB with materials at $V = 20$ kV and $\tau = 100$ ms: (*a*) Zr, $T_e = 4830$ K; (*b*) Ti, 3640 K; (*c*) Ni, 3240 K; (*d*) Al, 2800 K; (*e*) Cu, 2920 K; (*f*) Mo, 5020 K; (*g*) W, 5900 K

The free-running (oscillation) frequency is

$$f_e = f_0 + f_0 (U\dot{W}/f_0^2) \left[\frac{3}{8} (u^2/U^2) (1 + u/U) + \frac{1}{8} (f_0^2/U^2) (1 + 3f_0/U) A_e^2 \right]$$

The values of the free-running frequency calculated by the above formulas well agree with the experimental data. The free frequency is $f_e = 10^2$ to 10^4 Hz and the ripple amplitude of temperature is $A_e = (1 \text{ to } 5) \times 10^2$ K. A more detailed analysis of A_e and f_e has revealed that these quantities depend on the beam power, i.e. on T_e (Fig. 12.8). The vapor flow, electron emission, and irradiance from the zone of interaction depend on the target surface temperature, and so they vary with the beam spot temperature. The experi-

mentally observed flash evaporation corresponds to the oscillatory state because the latter entails a sharp increase in the amplitude of vibration of the vapor plume.

Since the temperature field in a target determines the thermal processes in the interaction zone, the described mechanism of continuous free oscillations enables workers engaged in scientific and applied researches to treat the physics of these processes from a qualitatively new point of view. In particular, we have ground to conclude that there are resonant conditions of heating of solids.

The use of resonant conditions offers considerable scope for further improvements of the methods of EB material processing.

References

1. N. N. Rykalin, I. V. Zuev, and A. A. Uglov. *Fundamentals of electron beam processing of materials.* Moscow, Mashinostroenie, 1978 (in Russian).
2. P. S. Landa. *Self-excited oscillation in systems with a finite number of the degrees of freedom.* Moscow, Nauka, 1980 (in Russian).
3. N. N. Rykalin, A. A. Uglov, I. V. Zuev, et al. *Oscillatory processes in CEF-metal interactions.* Zhurnal Eksperiment. i Teoretich. Fiziki, 85: No 6 (12), p. 1953, 1983.
4. I. V. Zuev, S. V. Selishchev, and V. I. Skobelkin. *Self-excited oscillation in CEF-solid interactions.* DAN SSSR, 225: No. 6, p. 1372, 1980.
5. I. V. Zuev, S. V. Selishchev, and V. I. Skobelkin. *Self-excited oscillation in CEF-solid interactions.* Fizika i Khimiya Obrabotki Materialov, No. 6, p. 3, 1980.
6. N. N. Rykalin, V. I. Skobelkin, I. V. Zuev, et al. *A model of self-excited oscillation in CEF-solid interactions.* DAN SSSR, 257: 1, p. 99, 1981.
7. A. N. Tikhonov and A. A. Samarskiy. *Equations of mathematical physics.* Moscow, Nauka, 1977 (in Russian).

Chapter 13

ELECTRON BEAM APPLICATIONS IN MICROELECTRONICS

13.1. VACUUM FILM DEPOSITION

In experiments [1], aluminum, nickel, and titanium samples were shot with EB pulses at a duty cycle of $G < 0.1$ to produce deep holes from which the vaporized material was allowed to condense on glass plates and form films at a rate of 1-3 μm/s. In contrast to laser-induced, pulsed plasma, and flash evaporation methods, this method produced films, the surfaces of which were free of droplets and splashes.

Since in this method the rate of condensate deposition is two or three orders of magnitude higher than that obtainable in conventional methods of thermal evaporation in vacuum, the basic aspects of evaporation with EB pulses deserve attention. Let us also note that EB welders produced in lots can be adapted to implement the process of high-rate film deposition.

Film deposition by thermal vacuum evaporation is one of the widely used techniques [2]. However, it suffers from several disadvantages: a limited rate of deposition; necessity of maintaining a vacuum to 10^{-3}-10^{-5} Pa to reduce the effect of residual gases; and difficulties involved in evaporation of multicomponent materials. This led to the development of principally different methods: ion plasma spraying, cathode sputtering [3], EB deposition of films from chemical compounds [4], etc.

The above shortcomings of thermal evaporation stem from steady-state heating. Some approaches, such as "multiple-source" heating and "explosive" (flash) evaporation, bring certain advantages, but they do not dispense with steady-state evaporation.

Pulsed methods of film deposition relying on a pulsed plasma, laser beam, electron beam, and flash evaporation of wire or foil [5, 6] considerably increase the rate of evaporation. High rates of film deposition lead to specific features of the process of condensation.

Efficiency of continuous and pulsed methods of film deposition. As mentioned above, the main advantage of pulsed deposition of films is a very high rate of film growth, from 1 to 10 μm/s. Also,

this approach permits retaining the stoichiometric composition of the vaporized material.

In paper [7], comparison is made between the two types of method proceeding from the estimates of the vapor particle density n and particle energy E in the vapor stream. The comparison diagram is shown in Fig. 13.1.

The energy E is laid off along the x axis. The point of reference of E is taken to be the origin of coordinates, at which $E = L_v$,

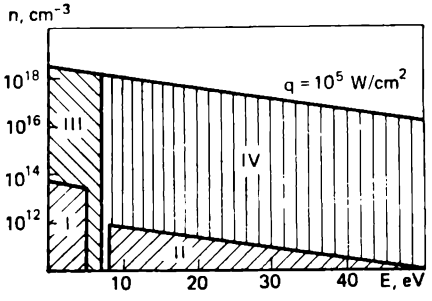

Fig. 13.1. Diagram illustrative of the capacities of various film deposition techniques [7]: I, continuous evaporation; II, cathode sputtering; III, pulsed EB and laser-induced evaporation; IV, pulsed evaporation using plasma accelerators

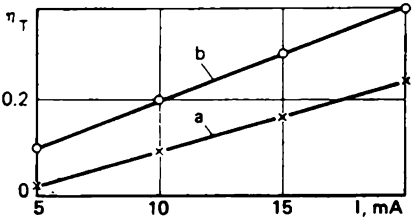

Fig. 13.2. Thermal efficiency η_T of penetration depth for stainless steel as a function of EB current at $V = 20$ kV: (*a*) continuous operation; (*b*) pulsed operation at $G = 0.37$, $t = 0.025$ s, and $f = 15$ Hz

where L_v is the latent heat of vaporization per iron atom, equal to about 4 eV. The point of reference on the y axis corresponds to the particle concentration of air rarefied to 10^{-4} Pa; this is a vacuum maintained in an evaporator, at which films are commonly grown.

The upper bound on E and n lies at $q = 10^5$ W/cm², which is the maximum absorbed power density maintained during condensation and is indicative of the onset of vaporization.

The continuous methods of evaporation, namely, thermal (vacuum), and EB and laser-induced evaporation, occupy narrow region *I*, which covers a few tenths of an electron volt along the x axis and extends along the y axis up to the concentration n which corresponds to the rate of deposition of $\sim 10^{-9}$ m/s. Second region *II* is that of cathode sputtering, which covers a long range along the x axis, but insignificantly rises up along the y axis and affords a deposition rate of merely up to 0.3×10^{-9} m/s.

Regions *I* and *II* in essence embrace all conventional techniques of film deposition. Electric flash evaporation, for example, falls within region *III*, and the region of condensation of ion beams is practically coincident with the x axis or lies below the x axis on the diagram drawn to the scale selected here.

Region *III* of pulsed electron beam and laser-induced evaporation shifts away from region *I* along the x axis for merely 2 or 3 eV, but extends along the y axis to the highest value of n. These methods ensure a deposition rate of up to 10^{-4}-10^{-2} m/s. Region *IV* is the region of pulsed plasma evaporation realizable with the aid of plasma accelerators.

As a whole, pulsed evaporation, including plasma spraying, features higher values of n and E than continuous evaporation and can provide deposition rates of up to 10^{-4}-10^{-1} m/s. Also, the first type of method has a higher thermal efficiency η_T. As shown by experiments with stainless steel, other conditions being the same, the value of η_T for pulsed evaporation is about twice as high (Fig. 13.2).

A high rate of heating at $G \leqslant 0.1$ sharply reduces the amount of the liquid phase, which is in essence completely blown off the hole and sprayed. The specific energy required to evaporate, for example, aluminum, is only one-sixth of or lower than that expended in continuous evaporation ($G = 1$).

The choice of the conditions of pulsed EB evaporation [1] is similar to the choice of drilling conditions since this process is identical to hole piercing by vaporization [8].

Industrial pulsed EB evaporators. The process of pulsed EB evaporation calls for the requisite equipment ensuring stable operation for a long time at frequencies of up to 1 kHz and source powers in the range of 1 to 3 kW. Industrial setups are now commercially available, which can operate at $V = 25$ to 30 kV, $P = 3$-5 kW, $q = 10^5$ to 10^6 W/cm^2, a pulse length of 1 to 50 ms, and a pulse repetition rate of 1 to 200 Hz.

EB setups are complete with deflecting systems which, in combination with EB scanning and modulation devices, can vaporize one or a few targets simultaneously, thereby depositing the films of any desired composition from any materials. One pulse can spatter a fraction of the material of 10^{-6} to 10^{-5} g.

13.2. INTEGRATED CIRCUIT PACKAGING

Wire bonding. Thermocompression bonding and ultrasonic bonding are the conventional methods of connecting the lead-out pins of an integrated circuit (IC) to 1-μm thick contact pads of copper, gold, nickel, and aluminum using for the purpose a copper, gold, nickel, or aluminum wire with a 30-to-100-μm diameter globule (ball) formed at its end to produce a bond by pressing it against the pad or pin. Electron beam welding (EBW), or bonding, gives more reliable and reproducible bonds.

To estimate visually the quality of bonds between wires and bonding pads, it is useful to judge them by an aspect ratio $K = h/d$,

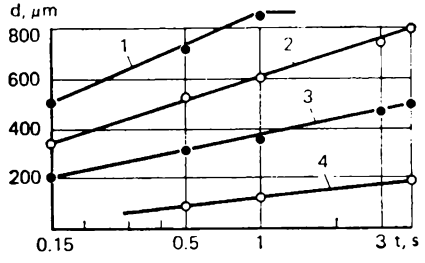

Fig. 13.3. Contact diameter as a function of the time of bonding at $V =$ = 35 kV and various values of EB current I: 1, 200 μA; 2, 150 μA; 3, 100 μA; 4, 50 μA

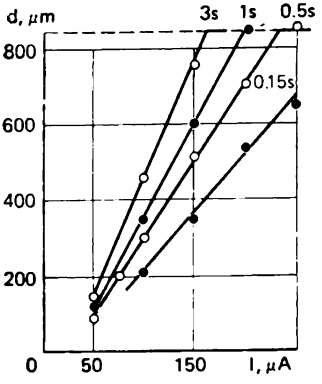

Fig. 13.4. Contact diameter versus EB current at $V = 35$ kV and various times of bonding

where h is the height of the bond, i.e. the height of the solidified ball, and d the base diameter of this ball.

Figures 13.3-13.6 show how the EBW parameters such as the accelerating voltage V, beam current I, and welding (bonding) time t influence the geometry of a bond.

The optimal value of K is chosen proceeding from the studies of the external appearance, microstructure, and electrical and physical characteristics of bonds.

The bond strength is higher than the wire strength at $K < 1$, but lower at $K > 1$. In the latter case, if the bonded metal adheres

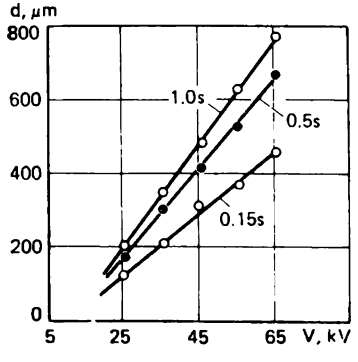

Fig. 13.5. Contact diameter versus accelerating voltage at $I = 100$ μA and various times of bonding

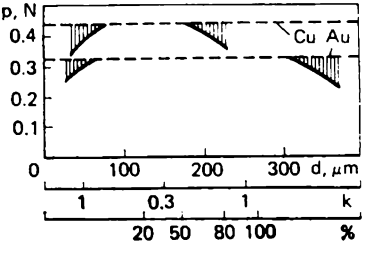

Fig. 13.6. Strength of the bond as a function of contact area and aspect ratio

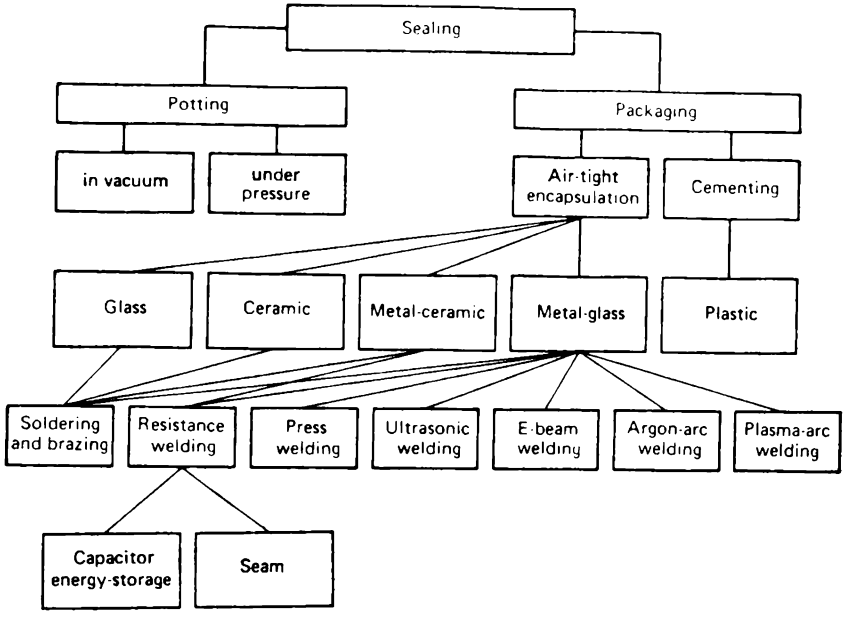

Fig. 13.7. Methods of molding of uncased chips and sealing of packages to protect ICs against environmental influences

well to the substrate, the wire can tear out a piece of the substrate material in the break test.

EBW provides a 100% reproducibility of the aspect ratio. In wire bonding required to ensure continuity between the IC elements and package, the aspect ratio is the figure of merit for the EB-produced bond.

Package sealing. There are a number of sealing techniques for protecting ICs against the environment (Fig. 13.7). Potting is the simplest method of encapsulation of uncased ICs. A popular method is to seal ICs in plastic packages. To render ICs more reliable in operation, the mounted chips are sealed in metal, glass, and ceramic packages. In wide use are metal-glass packages sealed by fusion welding (EB and plasma-arc welding) and by resistance welding of the seam, butt, and spot types.

In sealing packages by fusion and resistance welding, one must first tackle three basic tasks: select the source power that affords the desired penetration depth for package edges; make sure that the temperature of heating during welding operations does not impair IC characteristics; and minimize the evolution of gas from the electroplating parts, which can result in a porous (nonhermetic) weld.

As seen from Fig. 13.7, the techniques of packaging of hybrid or other integrated circuits are diverse, each designed to meet the environmental, mechanical, power, and heat-dissipation requirements.

A package must be mechanically strong and airtight or even vacuum-tight in the conditions of prolonged storage at temperature variations from 208 to 423 K, must afford protection at a 98% humidity and 313 K, and must remain operative after long exposure to a temperature of 423 K.

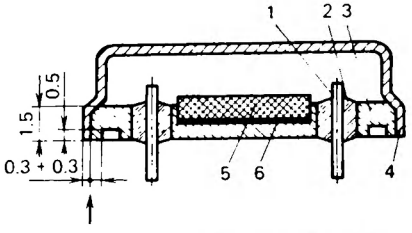

Fig. 13.8. IC package: *1*, lead-out wire; *2*, glass insulator; *3*, header; *4*, cap; *5*, chip; *6*, solder

Packages mostly come in circular or rectangular configurations. The basic components of a package are shown in Fig. 13.8. Chip *5* is mounted on a metal or ceramic header *3* with an appropriate interconnection pattern and electrically connected to lead-out wires or pins *1* arranged around the perimeter of the header. Figure 13.9 illustrates typical encapsulations for integrated circuits.

Dielectric materials and metals used for IC packages and envelopes must be so chosen that their coefficients of thermal expansion should be identical (Fig. 13.10).

Calculation of temperatures of a package during its sealing. Consider some theoretical aspects concerned with the sealing of a

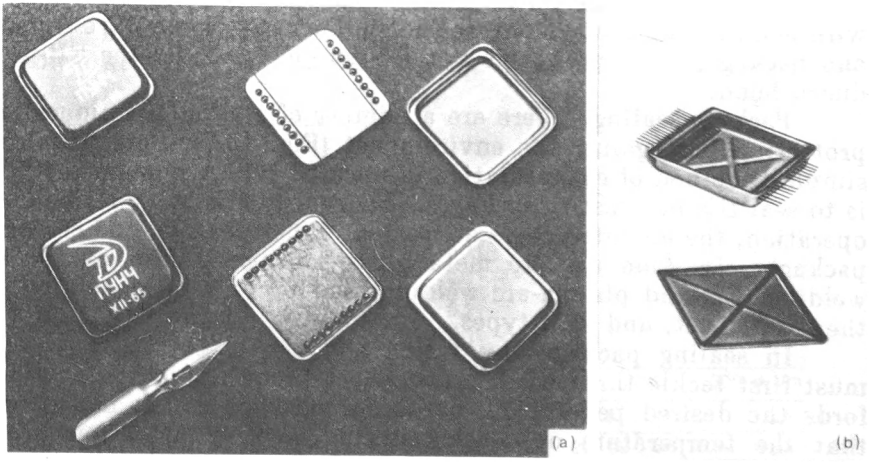

Fig. 13.9. Components of IC metal-glass packages: (*a*) dual in-line packages; (*b*) flat pack showing lead-out frame with cap removed

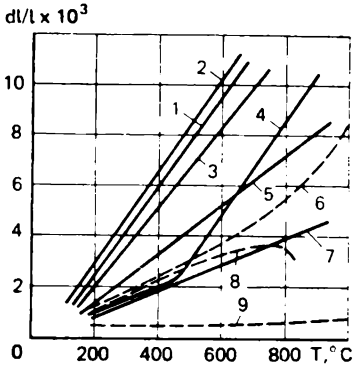

Fig. 13.10. Elongation dl/l versus temperature: *1*, copper; *2*, nickel; *3*, stainless steel; *4*, precision alloy; *5*, titanium; *6*, high-alumina ceramics; *7*, molybdenum; *8*, aluminosilicate glass; *9*, quartz

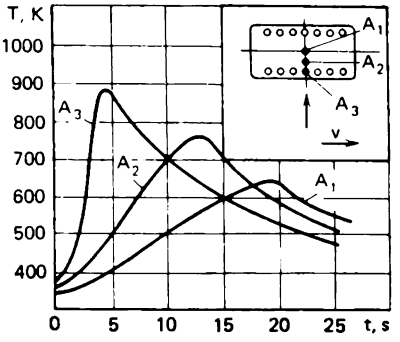

Fig. 13.11. Thermal cycles at various points on the package header during its sealing by fusion welding

rectangular package. The problem reduces to estimating the heat propagation in a finite plate heated by a linear source. The limited size of the plate, with welding being done along the edge of the plate, is offset by doubling the source power.

In sealing a kovar package, let us assume the following values: $P = 200$ W; $\eta_e = 0.7$; $h = 1$ mm; $v_w = 1$ cm/s; $c = 0.5$ kJ/kg K; $\rho = 8.35 \times 10^3$ kg/m^3; $\lambda = 20$ W/m K; $a = 4.6 \times 10^{-6}$ m^2/s; $\gamma = 38$ W/cm^2 K; and $B = 2\gamma/c\rho h = 1.85 \times 10^{-2}$ s^{-1}. Here, h is the weld penetration, v_w the weld rate, c the specific heat, ρ the mass density, λ the thermal conductivity, a the thermal diffusivity, γ heat transfer factor; and B temperature loss factor.

Use the equation of heat transfer from a fast-moving linear source on the plate:

$$T(y_0, t) = [P/(v_w h \sqrt{4\pi\lambda c\rho t})] \exp[-y^2/(4at) - Bt] \qquad (13.1)$$

At point $y = 0.1$ cm after time $t = 1$ s, the temperature is $T = 820$ K. At point $y = 1$ cm, which lies approximately in the middle of the header, the temperature is 135 K after 9 s. The maximum temperature is

$$T_{max} = [0.484P/(v_w c\rho h^2 y)](1 - By^2/2a) \qquad (13.2)$$

where $0.484 = \sqrt{2/\pi e}$. At point $y = 1$ cm, we have $T_{max} = 135$ K.

With the cap placed on the header and all the four sides welded, the temperature in the middle of the package with consideration for room temperature is $T = 4 \times 135 + 300 = 840$ K (Figs. 13.11 and 13.12).

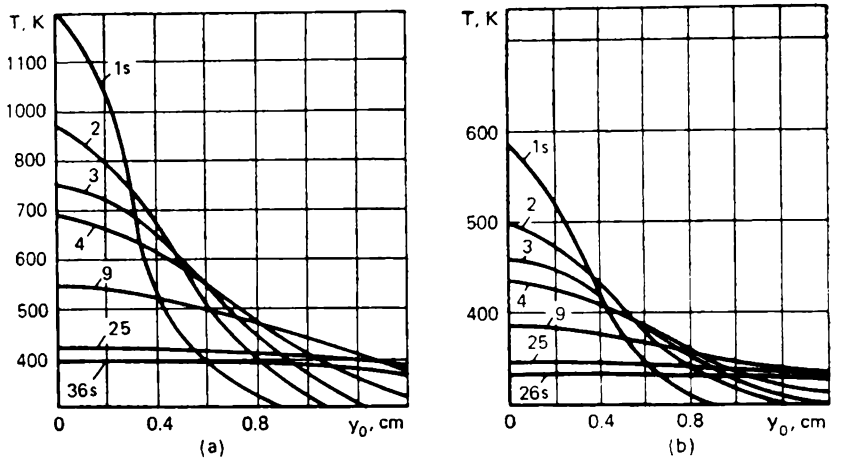

Fig. 13.12. Curves of temperature distribution over the package in the direction from its center and normal to the beam path at various moments of time after welding one side of the package: (*a*) continuous welding, $P = 300$ W; (*b*) pulse welding, $P = 85$ W

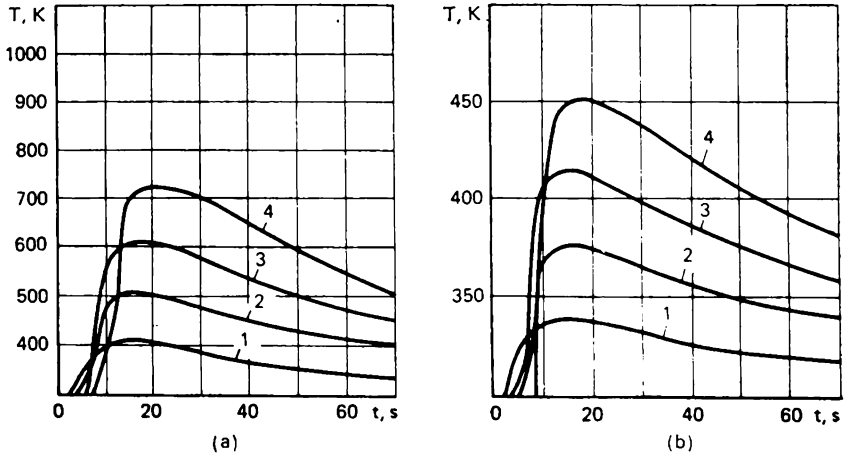

Fig. 13.13. Thermal cycling in the center of package ($y_0 = 1.2$ cm) after successive welding of one side (*1*), two sides (*2*), three sides (*3*), and four sides (*4*) of the package; (*a*) continuous welding, $P = 300$ W; (*b*) pulse welding, $P = 85$ W

Obviously, sealing operations must be made with the use of massive heat sinks which have good contact with the package. The model of heat propagation then reduces to the case of heating by a powerful fast-moving point source:

$$T(y', z, t) = [P/(2\pi\lambda v_w t)] \exp[(-y^2 + z^2)/4at] \qquad (13.3)$$

At point $y = 0.1$ cm on the package surface ($z = 0$), we have $T(0.1, 0, 1) = 110$ K after 1 s. At point y after $t = 9$ s, the temperature is $T(1, 0, 9) = 7.1$ K.

The temperature in the package center with regard to room temperature is

$$T = 4 \times 7.1 + 300 \approx 330 \text{ K}$$

To prevent overheating of IC components, the techniques of package sealing with EBW must employ heat removal arrangements (Figs. 13.13-13.18).

The choice of conditions of package sealing. The calculations of package sealing by EBW techniques are made for both "soft" and "hard" conditions of heating [9, 10, 11]. In "soft" conditions, the rate of energy delivery to the weld zone is slower than the rate of heat removal by thermal conduction. The opposite is true for "hard" conditions.

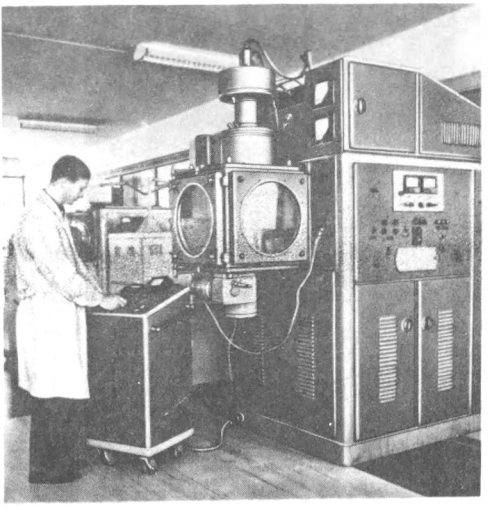

Fig. 13.14. Industrial EB welder A.306.05 for IC package sealing

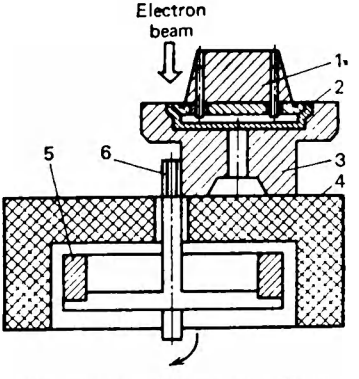

Fig. 13.15. Schematic diagram of an arrangement for EB welding of rectangular packages: *1*, heat sink; *2*, package; *3*, guide block; *4*, table; *5*, magnet; *6*, roller

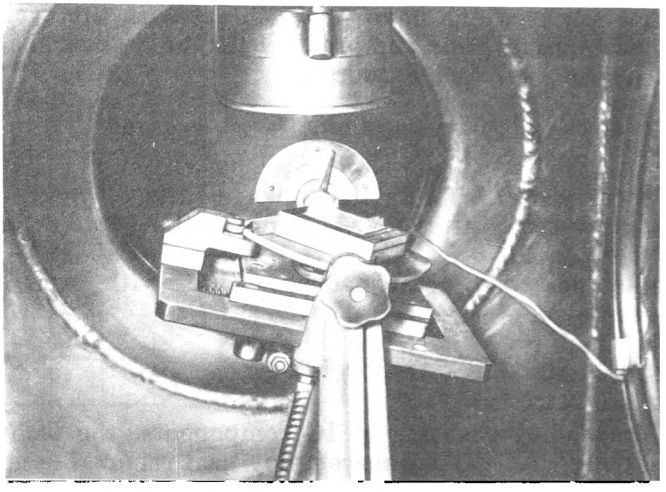

Fig. 13.16. Heat sink in the chamber of the A.306.05 setup for rectangular package sealing

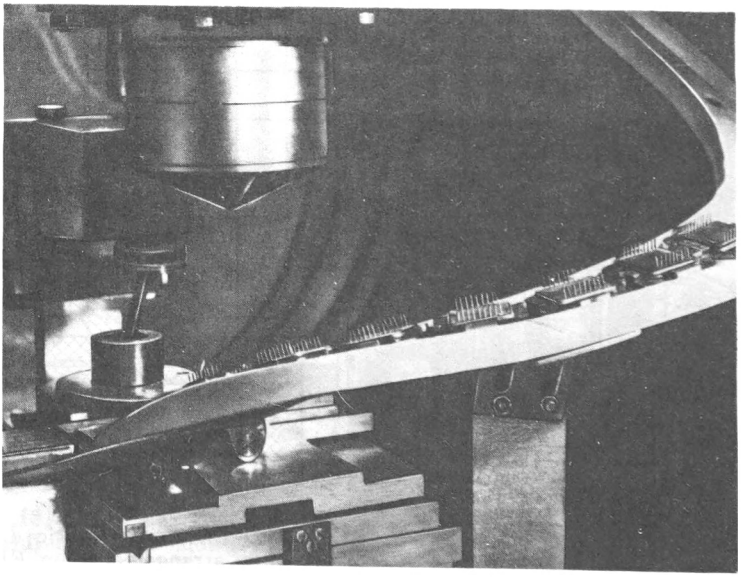

Fig. 13.17. Arrangement for batch welding of IC packages on A.306.05 and A.306.13 setups

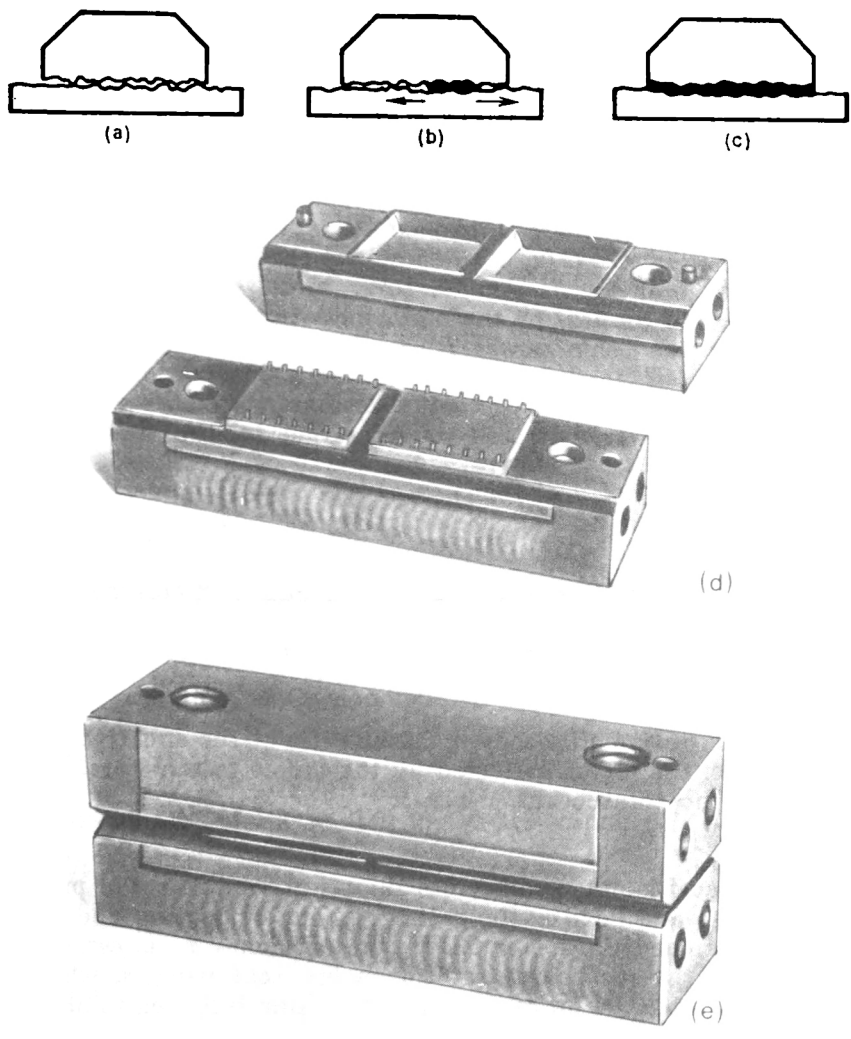

Fig. 13.18. Contact between the heat sink plate and package header with and without vacuum-degassed oil filled in-between: (*a*) contact without oil; (*b*) spread of oil in the gap; (*c*) contact produced via oil ensuring minimum thermal resistance; (*d*) and (*e*) general views of heat sinks

The choice of optimal conditions calls for defining the range of soft conditions; hard conditions are conducive to intense vaporization, which leads to splashes and burns, i.e. to a higher percentage of rejects.

Calculations and experiments have established a narrow range of the critical heat power density q_c, which divides the soft and hard conditions of heating.

The total thermal efficiency of sealing. A CEF moving along the edges of a package at a speed v_w melts through the zone of metal of a cross-sectional area A. Fusion, or weld penetration, can be regarded as the process of heating of a metal zone above the melting point T_m, to which there corresponds a total specific heat energy of phase transition, C_m (J/kg). The power of the heat source required to melt the zone of cross section A to T_m must be equal to $v_w A \rho C_m$. But because of the loss by thermal conduction, this power is always lower than the beam power $P = IV$.

The total thermal efficiency of weld penetration, η_w, is the ratio of the power needed to melt the volume of metal per unit time to the total power delivered to the target by the electron beam:

$$\eta_w = v_w A \rho C_m / P \tag{13.4}$$

where $C_m = cT_m + L_m$, and L_m is the latent heat of melting (fusion).

Weld penetration involves two processes: metal heating and fusion to or slightly above T_m.

The total efficiency η_w is therefore the product of the effective efficiency η_e of heating and thermal efficiency η_T of fusion, $\eta_w = \eta_e \eta_T$.

The effective efficiency η_e is the ratio of the effective heat power P_e, i.e. the power delivered by the source to the metal per unit time, to the total beam power

$$\eta_e = P_e / P \tag{13.5}$$

The coefficient η_e describes the effectiveness of the process of heat release and heat exchange in the zone of heating and depends on welding conditions. For EBW, the efficiency η_e is essentially a function of the coefficient of electron backscattering, s, which ranges from 0.5 to 0.05 for groups of metals from tungsten to aluminum [8]:

$$\eta_e = 1 - ns \tag{13.6}$$

where $n \approx 0.45$ to 0.50 is a factor used to account for the energy of backscattered electrons.

The thermal efficiency of penetration

$$\eta_T = v_w A \rho C_m / P_e \tag{13.7}$$

is the ratio of the power $v_w A\rho C_m$ expended on melting the metal to the effective power delivered per unit time by the heat source. The coefficient η_T determines the effectiveness of utilization of heat energy supplied by a moving heat source and depends on heat transfer in the metal due to thermal conduction.

In the conditions of electron beam and laser welding of packages, η_T ranges from 0.1 to 0.2.

Estimation of weld penetration. Consider the relation between the geometry of a fusion zone and characteristics of the electron beam creating a heat source in the target.

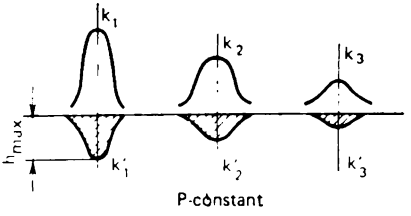

Fig. 13.19. Relation between beam parameters and fusion zone geometry

Assume the effective power of a Gaussian beam is constant, but its concentration coefficient k changes. For EBW, this is equivalent to changes in the degree of beam focusing.

As is known from experiments [8], the geometry of the fusion zone varies appreciably under these conditions, but its cross section A remains constant. The character of changes in the isothermal curve of fusion approximately follows the law of normal distribution. The geometry of the fusion zone in a way repeats the pattern of the Gaussian power distribution, but the values of concentration coefficient k' for fusion zones differ from corresponding values of k (Fig. 13.19).

The volume of the fusion zone produced during the dwell time t_p of the pulse is

$$V = h_{\max}\pi/k' \tag{13.8}$$

The volume of the melted metal per second is

$$V/t_p = h_{\max}\pi/k't_p \tag{13.9}$$

Considering that $P_e = \eta_e P$, from (13.7) we obtain the volume of melt per second:

$$v_w A = \eta_e P\eta_T/\rho C_m \tag{13.10}$$

Comparing (13.9) with (13.10) gives

$$\eta_e\eta_T P/\rho C_m = h_{\max}\pi/k't_p \tag{13.11}$$

Assuming that the width of welded package edges, $2b$, is equal to the fusion zone diameter, $d_{1/e} = 2b$, we get

$$d_{1/e} = 2/\sqrt{k'}, \quad k' = 1/b^2$$

From (13.11) with consideration for k' it follows that the penetration depth at t_p is

$$h'_{\max} = \eta_e \eta_T P t_p / \pi b^2 \rho C_m \tag{13.12}$$

For continuous welding, we can set $t_p \approx d_{1/e}/v_w = 2b/v_w$. Hence,

$$h_{\max} = \eta_e \eta_T 4P/[\pi\ (2b)\ v_w \rho C_m] \tag{13.13}$$

References

1. I. V. Zuev. *Use of pulsed electron beams for film deposition.* Proceedings of MIET. Physics and Mathematics Series, vol. 22, p. 99, 1976.
2. I. L. Roykh and L. N. Koltunova. *Protective vacuum coatings on steel.* Moscow, Mashinostroenie, 1976 (in Russian).
3. Leon S. Maissel and Reinhard Glang (eds). *Handbook of Thin Film Technology.* McGraw Hill Book Company, Vol. 1, 1970.
4. G. L. Aranovich and B. A. Vishnyakov. *Formation of thin films under electron bombardment.* Fizika i Khimiya Obrabotki Materialov, No. 1, p. 72, 1977.
5. N. I. Glushchenko, N. E. Ledenko, and A. L. Rvachev. *Formation of ohmic contacts on wide-gap III-V compound semiconductors by electric flash evaporation.* Fizika i Khimiya Obrabotki Materialov, No. 6, p. 139, 1975.
6. N. V. Grevtsev, V. D. Zolotukhin, Yu. M. Kashurnikov, et al. *On the character of vaporization of copper heated by current pulses.* Teplofizika Vysokikh Temperatur, 15: No. 2, p. 362, 1977.
7. B. A. Osadin and G. I. Shapovalov. *Thin-film deposition with the aid of pulse plasma generators.* Fizika i Khimiya Obrabotki Materialov, No. 5, p. 43, 1976.
8. N. N. Rykalin, I. V. Zuev, and A. A. Uglov. *Fundamentals of electron beam processing of materials.* Moscow, Mashinostroenie, 1978 (in Russian).
9. E. A. Zhilkov and I. V. Zuev. *Hybrid IC assembling.* Moscow, MIET, 1978 (in Russian).
10. I. V. Zuev. *Choice of the conditions of IC package sealing by EBW.* Svarochnoe Proizvodstvo, No. 10, p. 18, 1975.
11. I. V. Zuev and P. G. Zakirov. *Increasing the efficiency of microwelding and bonding of thin metal pieces in instrument engineering.* Kiev, Znanie, 1982 (in Russian).

Chapter 14

CONTROL OF ELECTRON BEAM-MATERIAL INTERACTION

14.1. ELECTRON EMISSION

Along with thermal losses, the total energy balance involved in EB-material interactions must take into consideration the losses due to the emission of inelastically and elastically scattered secondary electrons and also losses due to light radiation and X-radiation. At the melting point and at temperatures above T_m of metals, thermionic emission becomes appreciable. The analysis reveals [1, 2] that the power losses due to the emission of true secondary electrons and thermionic electrons and also due to light emission and X-radiation are negligible in comparison with the beam power. Elastically and inelastically scattered electrons account for the main fraction of losses, for example, up to 50% in tungsten. In this connection, the authors of work [3] consider the effective efficiency of EB material processing to be largely dependent on the reflectivity of materials.

There are a few methods for estimating the reflectivity R. Some authors of the works in the field under consideration hold the idea that R is a function of only the atomic number Z of an element: $R = (7Z - 80)/(14Z - 80)$ or $R = \ln(Z/6) - 0.25$. The assumption is that R only depends on the beam energy: $E/R = Z^{1/3}E^{1/2}$.

The effective efficiency is

$$\eta_e = 1 - nR \tag{14.1}$$

where $n = 0.45$ to 0.50 is the proportionality factor defining the energy distribution of backscattered electrons.

From the measurements of R it follows that the reflectivity linearly decreases with increasing EB power. The experimental data presented in Fig. 14.1 allow us to estimate the constant $\delta' = R\delta Z^{1/3} = 1.1 \times 10^{-4}$ cm from the values of characteristics listed in Table 14.1. In this table, ρ is the mass density, δ the electron penetration depth (free path), Z the atomic number, R the reflectivity, and γ the arithmetic mean deviation of δ' in percent.

The refined analysis of experimental values of R given in Table 14.2 shows that R can be found from expression $R = m/CZ^{1/3}$ with an accuracy sufficient for engineering calculations. In the above expression, m is the atomic mass, g, and C is the constant equal to

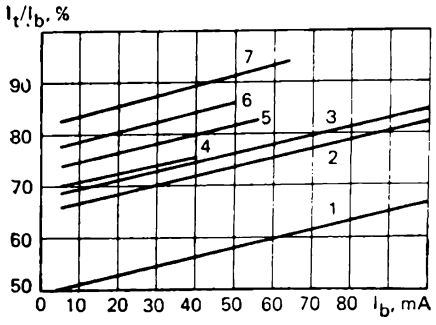

Fig. 14.1. Current I_t through the target of W (*1*), Mo (*2*), Ni and Cu (*3*), stainless steel (*4*), Zr (*5*), Ti (*6*), and Al (*7*) as a function of beam current I_b

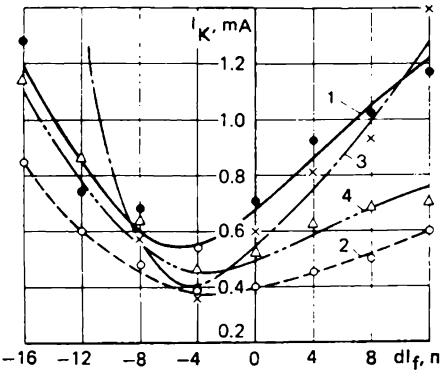

Fig. 14.2. Secondary emission current I_s as a function of the degree of focusing, dI_f, in welding stainless steel at various values of energy input per unit weld length: *1*, 6540 J/cm; *2*, 4360 J/cm; *3*, 3275 J/cm; *4*, 2180 J/cm

106×10^{-23} g and 15.5×10^{-23} g for light elements ($Z = 6$ or 7) and heavy elements ($Z = 74$ to 92) respectively.

The curve of the time-dependent current passing through the target enables us to judge the emission from the zone of interaction for one EB pulse. Depending on the power density q, this curve expands or contracts along the time axis, but retains extreme points.

At a pulse length $t \leqslant t_1$ (see Fig. 12.3), the beam can heat metal to a specified temperature $T \leqslant T_m$. When $t \leqslant (t_1 + t_2)$, melting without intense vaporization is possible; when $t \leqslant (t_1 + t_2 + t_3)$, the beam can produce a cavity to any specified depth.

TABLE 14.1. Experimental Characteristics of Some Metals at $V = 20$ kV and $I = 4$ mA

Metal	ρ, g/cm³	$\delta \times 10^4$, cm	Z	R	$\delta' = R\delta Z^{1/3}$	γ, %
Aluminum	2.7	3.1	13	0.17	1.23	15.0
Titanium	4.5	1.9	22	0.22	1.17	9.3
Zirconium	6.5	1.3	40	0.26	1.16	8.4
Stainless steel	7.9	1.0	26	0.30	0.83	16.8
Nickel	8.9	0.94	28	0.32	0.91	15.0
Copper	8.95	0.93	29	0.32	0.92	14.0
Cobalt	10.2	0.82	42	0.34	0.97	9.3
Tungsten	19.0	0.43	74	0.50	0.91	15.0

TABLE 14.2. **Relation between R and Some Characteristics of Elements**

Element	Z	$m\times10^{24}$, g	$V = 30$ kV			$V = 10$ kV			$V = 5$ kV		
			R	$\frac{m\times10^{23}}{RZ^{1/3}}$	γ, %	R	$\frac{m\times10^{23}}{RZ^{1/3}}$	γ, %	R	$\frac{m\times10^{23}}{RZ^{1/3}}$	γ, %
C	6	10.8	0.06	9.9	−11.6	0.072	8.2	−22.0	0.085	7.0	−32.0
Al	13	44.8	0.155	12.3	+9.8	0.177	10.8	+2.9	0.186	10.3	0
Si	14	48.0	0.162	12.3	+9.8	0.186	10.7	+1.9	0.197	10.1	−1.9
Ti	22	80.0	0.254	11.2	0	0.268	10.6	+1.0	0.270	10.6	+2.9
Cr	24	85.7	0.27	11.0	+1.8	0.283	10.5	0	0.285	10.4	+1.0
Fe	26	92.5	0.288	10.9	−2.7	0.296	10.6	−1.0	0.3	10.5	+1.9
Ni	28	97.4	0.308	10.4	−7.1	0.323	9.9	−5.7	0.333	9.7	−5.8
Cu	29	105	0.319	10.6	−5.3	0.339	10.0	−4.8	0.352	9.6	−6.8
Zn	30	109	0.33	10.7	−4.5	0.342	10.3	−1.9	0.352	10.0	−2.9
Ge	32	122	0.334	11.5	+2.7	0.349	11.0	+4.8	0.362	10.6	+2.9
Mo	42	160	0.385	12.0	+7.1	0.381	12.1	+15.2	0.367	12.6	+22.2
Ag	47	179	0.42	11.8	+5.3	0.420	11.8	+12.4	0.418	11.8	+14.5
W	74	306	0.501	14.6	−2.7	0.483	15.1	−2.6	0.472	15.5	−3.1
Pt	78	324	0.516	14.7	−2.0	0.503	15.0	−3.2	0.486	15.6	−2.5
Au	79	328	0.521	14.7	−2.0	0.501	15.3	−1.3	0.489	15.7	−1.9
U	92	381	0.534	15.8	+5.3	0.513	16.4	+5.8	0.495	17.0	+6.3

When the beam is continuously swept over the target surface to effect, for example, deep penetration welding, the details of the emission curve specific to one pulse become "smeared", and the curve displays either a maximum at t_2 or a minimum at t_3 depending on the penetration depth achieved. Nevertheless, in the case of the continuous EB used, various configurations of the fusion zones correspond to various portions of the emission curve.

Figure 14.2 illustrates the curves of emission current I_K passed from the fusion zone to the collector and recorded with the aid of a semicircular slit-type sensor for the case of EB welding of stainless steel. Figure 14.3 demonstrates the relation between the geometry of fusion zones and the curve of emission current.

The curve of the current passing through the target can have a W-shape apart from a V-shape [3, 4], as displayed in Fig. 14.4. If during the EB-material interaction the shape of the cavity produced is close to the cylindrical shape, the electrons emitted at various angles from the cavity bottom will fall on the cavity walls; with an increase of the cavity depth, the amount of the electrons trapped in the cavity grows. The left branch of the V-shaped curve should always be at a lower level than the right branch if the cavity depth is large. Indeed, over the initial period of interaction of the beam with a flat metal surface, the position of the left branch of the curve depends on the surface reflectivity R. At the end of interaction, when the cavity is sufficiently deep, the cavity walls trap not only thermionic electrons but also backscattered electrons, the number of

which is a function of R. For this reason, the right branch of the V-shaped curve is higher than the left branch (Fig. 14.4*a*).

If, in the process of interaction, the cavity begins to assume a conical shape (Fig. 14.4*b*), the walls of the cavity will also trap the emitted electrons. But with an increase in the taper angle and since the cavity becomes deeper, there comes a point where the electrons emitted from the bottom will freely escape the cavity without impinging on the walls. A further increase in the depth of the conical cavity will enable the walls to trap some emitted electrons, but with a lower efficiency than is the case for the cavity of Fig. 14.4*a*. Therefore, the right branch lies somewhat higher than or at the level of the left branch, and the amplitude of the central peak does not exceed the levels of the left and right branches (Fig. 14.4*c*).

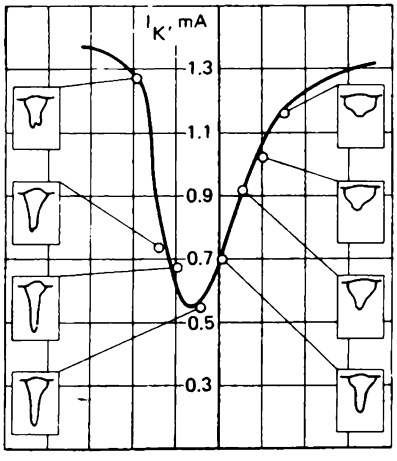

Fig. 14.3. Electron emission current I_K moving from the fusion zone to the collector as a function of dI_f and typical cross sections of fusion zones in welding at 6540 J/cm

The angular distribution of backscattered electrons largely obeys the cosine law (Fig. 14.5). It is then safe to apply the laws of molecular flows through cylindrical and conical openings (tubes) and evaluate the relation between the secondary emission current and the geometry of cavities.

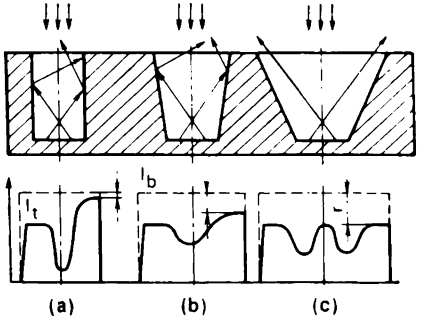

Fig. 14.4. Schemes illustrative of V-shaped and W-shaped curves of current I_t passing through the target

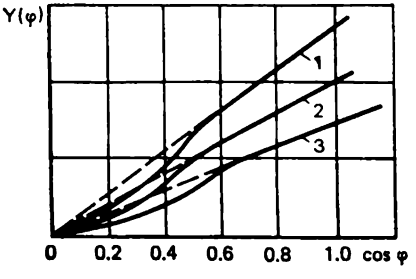

Fig. 14.5. Angular distribution Y (in arbitrary units) of electrons backscattered from the targets of gold (*1*), silver (*2*), and copper (*3*) bombarded at 30 keV

TABLE 14.3. **Probability Factor W for Passage of the Molecular Flow Through Cylindrical Tubes**

h/r	W	h/r	W	h/r	W	h/r	W
0	1	1.3	0.6139	3.2	0.4062	16	0.1367
0.1	0.9524	1.4	0.5970	3.4	0.3931	18	0.1240
0.2	0.9092	1.5	0.5810	3.6	0.3809	20	0.1135
0.3	0.8699	1.6	0.5659	3.8	0.3695	30	0.0797
0.4	0.8341	1.7	0.5518	4.0	0.3589	40	0.0613
0.5	0.8013	1.8	0.5384	5.0	0.3146	50	0.0499
0.6	0.7711	1.9	0.5226	6.0	0.2807	60	0.0420
0.7	0.7434	2.0	0.5136	7.0	0.2537	70	0.0363
0.8	0.7177	2.2	0.4914	8.0	0.2316	80	0.0319
0.9	0.6940	2.4	0.4711	9.0	0.2131	90	0.0285
1.0	0.6720	2.6	0.4527	10	0.1973	100	0.0258
1.1	0.6514	2.8	0.4359	12	0.1719	1000	0.002658
1.2	0.6320	3.0	0.4205	14	0.1523		

TABLE 14.4. **Probability Factor W for Passage of the Molecular Flow Through Conical Tubes Tapering in the Direction of Flow**

Half-angle at vertex of cone, degree	h/r						
	0.1	0.2	0.5	1.0	2.0	5.0	10.0
0	0.952399	0.909215	0.801271	0.671984	0.514231	0.310525	0.190940
1	0.954079	0.912490	0.808852	0.685401	0.536021	0.345995	0.236829
5	0.960373	0.924763	0.837261	0.735659	0.617560	0.478646	0.408600
10	0.967347	0.938350	0.868615	0.790779	0.705799	0.617242	0.580298
20	0.97865	0.96027	0.91851	0.87642	0.83704	0.80558	0.79641
30	0.98691	0.97614	0.95344	0.93338	0.91771	0.90814	0.90611
40	0.99268	0.98701	0.97619	0.96806	0.96288	0.96046	0.96008
50	0.9964	0.9939	0.9896	0.9870	0.9857	0.9852	0.9851
60	0.9986	0.9977	0.9965	0.9959	0.9957	0.9956	0.9955
70	0.9996	0.9994	0.9993	0.9992	0.9992	0.9992	0.9991
80	1.0000	1.0000	1.0000	1.0000	1.0000	1.0000	1.0000
89	1.0000	1.0000	1.0000	1.0000	1.0000	1.0000	1.0000

The calculated values of the probability factor W for the passage of a molecular flow through a tube are available in literature on the subject. Tables 14.3 and 14.4 list the values of W as a function of h/r, where h is the cavity depth and r is the cavity radius.

The rate of the molecular flow through a tube is

$$c_f = WAm \tag{14.2}$$

where A is the cross-sectional area of the tube and m the amount of the material vaporized per unit time per unit area of the bottom of the cylindrical cavity.

To estimate the emission current moving from the cavity, expression (14.2) can be written in the form

$$I_K = WRI_b \tag{14.3}$$

where W is the factor of probability that the backscattered electrons can escape the cavity, R the reflectivity, and I_b the beam current.

If we assume that the efficiency η_e of EB material heating is in the main dependent on the loss due to backscattered electrons, then we can write in view of (14.1) and (14.2) that

$$\eta_e = 1 - nWR \tag{14.4}$$

The results of experimental checks on the validity of expression (14.4) are given in Table 14.5.

TABLE 14.5. **Comparison between the Predicted and Experimental Values of η_e at Various Values of the Opening Angle α and Depth h of the Cylindrical Cavity of $r=1.5$ mm in Stainless Steel Parts**

α, degree	h, mm	h/r	W	η_e[1]
10	8.5	5.67	0.295	0.96/0.98
15	5.6	3.73	0.375	0.95/0.97
30	2.6	1.73	0.54	0.92/0.92
45	1.5	1.0	0.672	0.90/0.88
60	0.9	0.58	0.79	0.88/0.87
75	0.4	0.26	0.89	0.87/0.86

[1] The numerator and denominator give predicted and experimental values respectively.

As follows from Table 14.6, the efficiency η_e approaches 0.95-0.97 at $h/r > 2$ or at an aspect ratio of $h/b > 1$ in the case of welding, where b is the weld width.

The data of Table 14.7 attest that at a cavity taper angle of 30°, practically all electrons leave the cavity, and so the efficiency of melting decreases appreciably.

The use of probability factors W calculated for short and long cylindrical, conical, and rectangular tubes allows us to estimate the emission current and thus to control the cavity shape in pulse welding and cutting of materials.

The analysis of formula (14.4) shows that this expression does not cover a fraction of primary electrons impinging on the cavity bottom because most of these electrons are scattered back and absorbed by cavity walls.

TABLE 14.6. Effect of the Cavity Profile on Emission of Electrons from an Aluminum Sample at $R=0.17$ and $n=0.5$

h/r	W	$\eta_e = 1-nWR$
0	1	0.915
0.5	0.8013	0.932
1.0	0.6720	0.943
2.0	0.5136	0.956
3.0	0.4205	0.964
4.0	0.3589	0.970
5.0	0.3146	0.973
7.0	0.2537	0.980
10.0	0.1973	0.983

TABLE 14.7. Effect of Cavity Taper on Emission of Electrons from an Aluminum Sample at $h/r=10$

Half-angle at vertex of cone, degree	Probability factor W	η_e
5	0.4086	0.97
10	0.5803	0.95
20	0.79641	0.93
30	0.90611	0.92
40	0.96008	0.918
50	0.9851	0.916

Calculations reveal that the efficiency of heating of the weld pool as a function of the keyhole depth exhibits a maximum at a definite angle of convergence of the electron beam on the target and at a definite degree of focusing of the EB on the surface. As the keyhole depth increases, the specific energy distribution over the beam cross sections gradually smoothes out and becomes uniform. In the interaction of the EB with metals, there is a possibility of "focusing" of primary electrons by the keyhole walls.

14.2. WELD PENETRATION CONTROL

The curve of the current passing through the target and collector has a clearly defined shape in pulse welding (Fig. 14.6), which is not the case for continuous welding. In the latter case the curve becomes smoother in shape, but it retains the extremum corresponding to the maximum or minimum of thermionic current.

When the beam power density approaches a maximum critical value, q_c, the curve of current I_t passing through the target during changes in the focus current I_f displays a minimum corresponding to the intense thermionic emission (transient process). When $q > q_c$, this curve has a maximum, and the curve of emission current I_K (collector current) has a minimum. Changes in I, V, and d of the beam at $q \geqslant q_c$ leads to displacements of extreme points depending

on the current I_f or to variations of the amplitudes of the maximum and minimum currents flowing through the target and collector. The curves retain the extreme points, which feature can be put to use for control of the weld depth.

Automatic control of the maximum penetration depth must take into account the following features: (1) the nonlinear static characteristic I_t (I_f) which has a maximum defined by a quadratic function and subjected to the displacement with changes in the EB power; (2) steady coordinate drift of this characteristic with a smooth change in the beam current and voltage; (3) high level of noise in the output signal I_t; and (4) dynamic fraction P_f, which can be defined as a linear function in a first approximation.

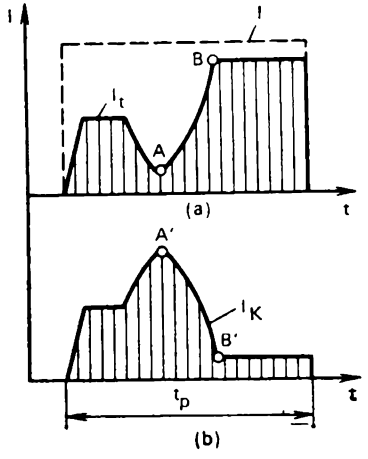

Fig. 14.6. Drawings of oscilloscope traces of current I_t through the target (*a*) and emission current I_K through the collector (*b*). The current pulse from the power source is shown by a dash line

Figure 14.7 illustrates an example of the weld penetration controller based on an analog computer in combination with an adapter comprising electronic devices and relays. Amplifier A_5 sums up two signals arriving at its input: the signal of the output voltage from a sawtooth (ramp) generator (STG) and the signal from a random signal generator (RSG). The STG enables a wide adjustment of the rate of growth of the output voltage. Integrator A_1 is used to store the value of the quality number. The signal at the output of an amplifier A_2 is proportional to the current difference of the stored and the actual voltage.

The voltage difference taken off A_2 arrives at an integrator A_3 which accumulates data. The diode circuit of A_4 provides for threshold values A and B. An excess of one threshold value over the other causes the stepping relay (SR) to operate. The contacts of SR reset the accumulating elements and enable the next storage before the system performs a subsequent step. If the compared values give a decrement, the reverse-current relay (RR) enables the reversal, the direction of further motion being retained by virtue of the flip-flop that stores the requisite bit of information. The signal of a step arrives at the control circuit of the current in the focusing coil.

Tests have revealed that the controller is stable in operation, and the suggested algorithmic method ensures good noise immunity.

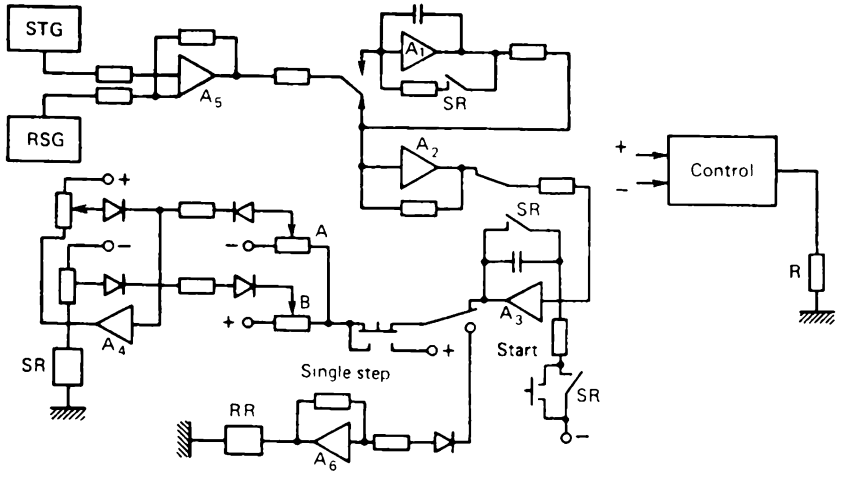

Fig. 14.7. Block diagram of weld penetration controller

The operation of the controller has been tried out at EB work stations. Welding in stainless steel and titanium at $P = 1$ to 10 kW has shown that the penetration depth deviates from a maximum value by $\pm 3\%$.

14.3. CONTROL OF EB HEATING STAGES

To identify the stages of EB material heating, we need to study the time dependence of the current moving through a sample at the invariable values of the main parameters of electron beam proces-

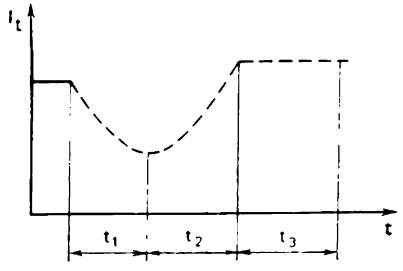

Fig. 14.8. Drawing of the oscilloscope trace of target current I_t

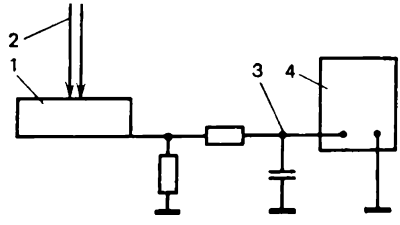

Fig. 14.9. Block diagram of the system for measuring current I_t through a target: *1*, target; *2*, electron beam; *3*, *RC* filter; *4*, oscillograph

sing [3, 5]. Workers of [3, 5] obtained these relations for W, Mo, Zr, Ti, Cu, Al, Ni, and scale-resistant steel at an accelerating voltage $V_{ac} = 20$ kV, beam current $I_b = 0$ to 250 mA, and EB interaction

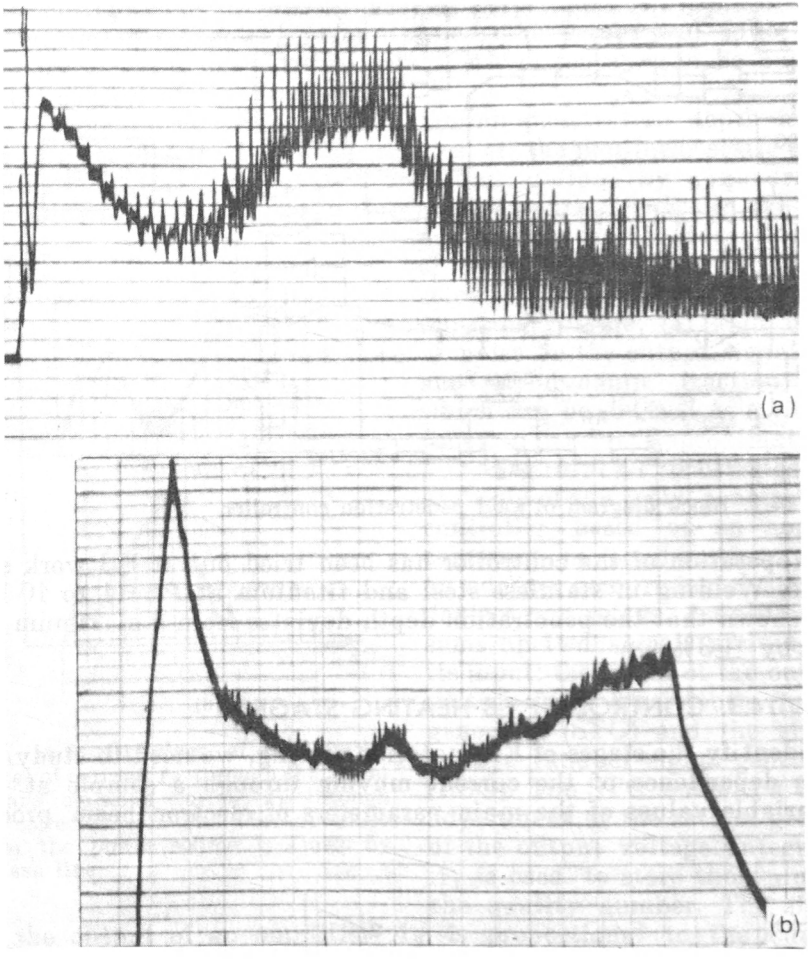

Fig. 14.10. Oscillograph record of I_t through a target: (*a*) direct recording of I_t; (*b*) recording of I_t with the use of an *RC* filter

time $t = 1$ ms to 5 s. Changes in the current I_t through a target were recorded at constant parameters of processing. The drawing of a typical oscilloscope trace of I_t is shown in Fig. 14.8. Within a large portion of the curve (dash line), the current I_t is found to be pulsating. In the time interval t_1, the ripple frequency is 50 Hz with a frequency of 300 Hz superimposed on the pulsating current; in the interval t_2, high-frequency pulsations up to 10^3 Hz are superimposed on the current of 50 Hz; in the interval t_3, the ripple frequency ran-

ges from 6 to 50 Hz. The dash line of Fig. 14.8 demonstrates changes in the mean value of pulsating current I_t.

Work [6] contains similar relations obtained for scale-resistant steel treated at $V_{ac} = 30$ kV and $I_b = 400$ mA. The current I_t pulsated at a frequency of 0.05 to 30 Hz when deep penetration welds up to 30 mm were made.

The factors that cause I_t to pulsate can be the following: pulsations of supply voltage at 50 and 300 Hz; interaction of the EB with the evaporating metal at frequencies in the order of units of a kilohertz; and vibrations of the liquid metal in the cavity at 0.05 to 50 Hz.

Figure 14.9 displays the schematic diagram of a measuring system used to investigate the relation between the character of changes in I_t and the degree of EB heating of the metal. The signal that has to come to the input of a mirror-galvanometer oscillograph

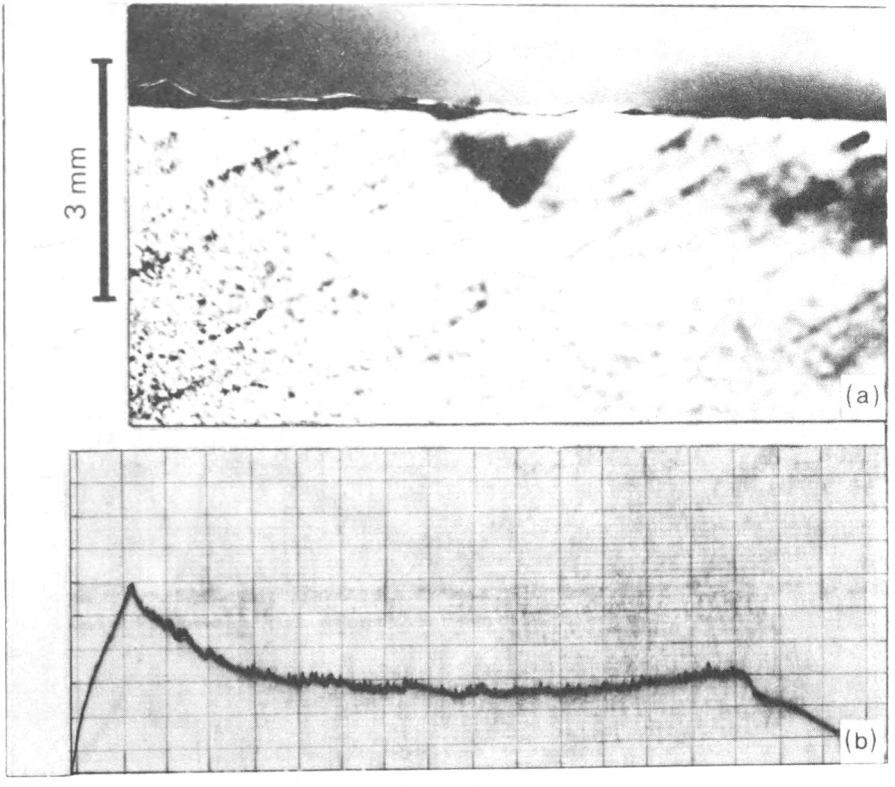

Fig. 14.11. Macrosection of the fusion region in St3 steel (*a*) and oscillograph record of current I_t in the target (*b*). Operation number I

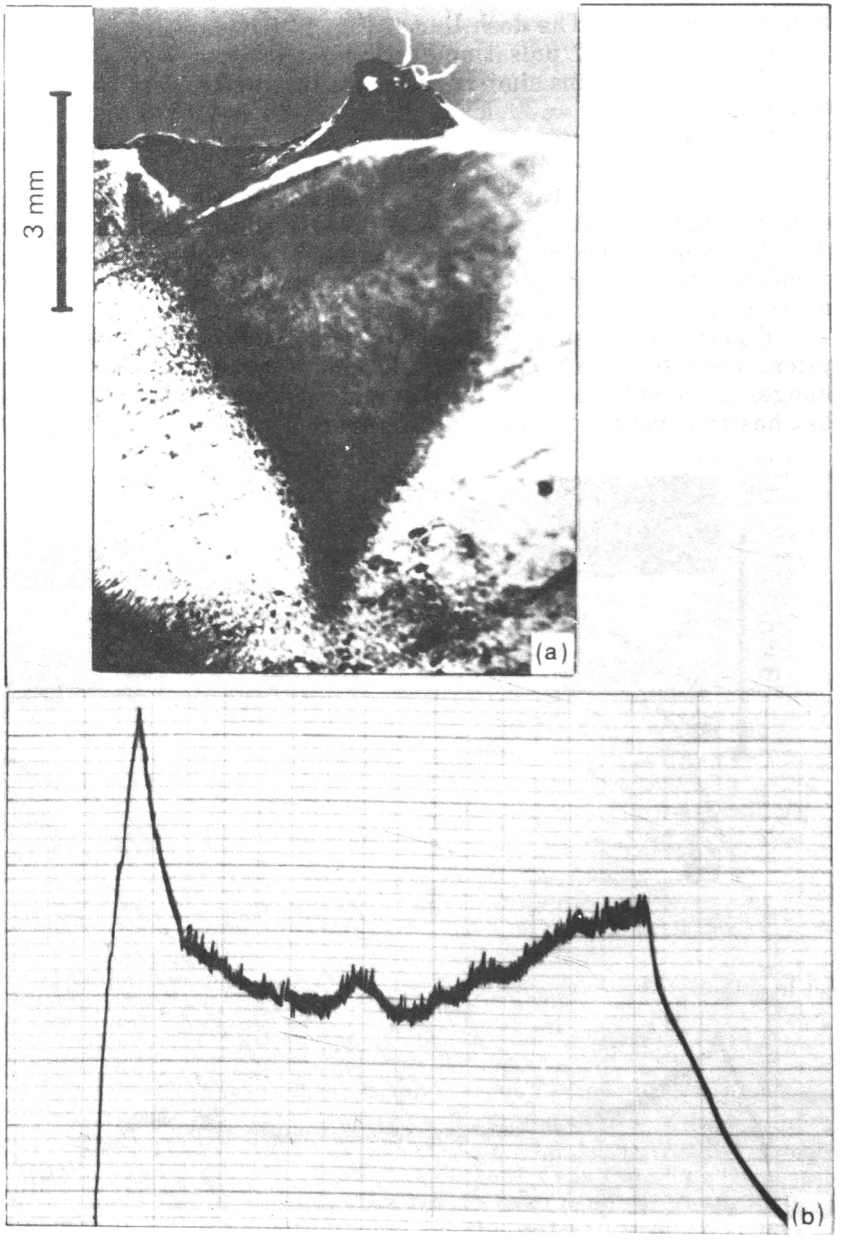

Fig. 14.12. Macrosection of the fusion region in St3 steel (*a*) and oscillograph record of current I_t in the target (*b*). Operation number II

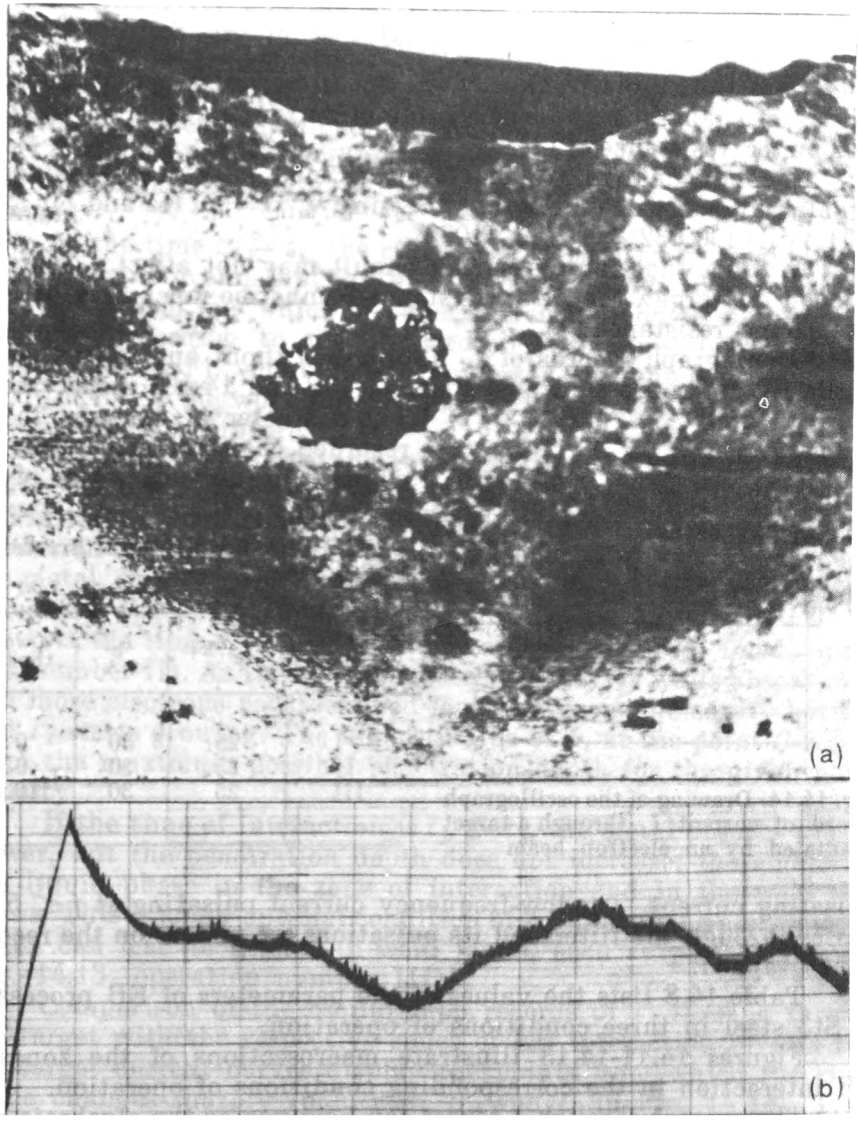

Fig. 14.13. Macrosection of the fusion region in St3 steel (*a*) and oscillograph record of current I_t (*b*). Operation number III

passes through a low-pass RC filter whose transmission band is chosen proceeding from the relations

$$2\pi f > 1/RC > 2\pi f_t \tag{14.5}$$

$$1/2\pi fC \ll R_g \tag{14.6}$$

where f is the ripple frequency, R the filter resistance, f_t the frequency of changes in the mean value of current I_t, and R_g the galvanometer resistance.

If conditions (14.5) and (14.6) are met, only a low-frequency signal arrives at the oscillograph. Setting $f_{min} = 50$ Hz and $f_{tmax} = 5$ Hz gives $0.032 < RC < 0.032$.

In order that the measuring circuit may not affect I_t passing through the target, the filter resistance R must be much greater than the ground resistance R_{gr}.

Oscillograph records of I_t obtained without and with the use of the RC filter are shown in Figs. 14.10*a* and 14.10*b* respectively. The character of changes in the recorded signal corresponds to changes in the mean value of the pulsating current. The low-frequency current pulsating at $f \leqslant 5$ Hz passes through the filter and its pulsations are visible on the records photographed.

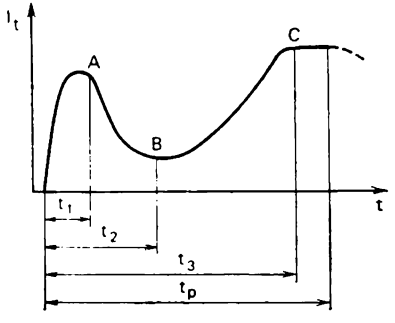

Fig. 14.14. Drawing of the oscillograph record of current I_t through a target irradiated by an electron beam

TABLE 14.8. **Conditions of Processing of St3 Steel Samples**

Operation number	V_{ac}, kV	I_b, mA	Dwell time, s
I	25	30	0.5
II	25	30	3.0
III	25	30	10.0

Table 14.8 lists the values of the parameters of EB processing of St3 steel in three conditions of operation.

Figures 14.11-14.13 illustrate macrosections of the zones of EB interaction in the corresponding conditions of operation.

The current through a target can be given as the algebraic sum of the currents:

$$I_t = I_b - (I_s + I_{th}) \tag{14.7}$$

where I_b is the beam current, I_s the total current of secondary and backscattered electrons, and I_{th} the thermionic current.

As the transient process ceases and the EB system begins to operate steadily, the current I_t remains constant up to the point A (Fig. 14.14). The limiting value of I_t over this period is governed by the reflectivity and the secondary emission ratio for secondary electrons which are in fact temperature-independent. During the time t_1 the target surface rises to a temperature approximately equal to the melting temperature. Most metals such as Al, Cu, Ti, Ni, Zr, and stainless steel, except for W and Mo, begin to melt by the moment of the time corresponding to point A. The samples of St3 steel begin to melt practically as soon as the transient process terminates.

At the time $t_2 - t_1$, the current I_t drops sharply because of intense thermionic emission. In this time interval, the current I_t obeys equation (14.7), in which I_b and I_s remain constant, while I_{th} increases according to the Richardson-Dushman relation: $T_{th} = AT^2 \exp(-\varphi/kT)$, where A is a universal constant equal to 1.2×10^6 A/m^{2}K^2, φ the work function, k the Boltzmann constant, and T the surface temperature.

The work function φ and constant A depend on the type of material and the state of the target surface. The point B on the curve of Fig. 14.14 corresponds to the onset of intense vaporization. The formation of the cavity, i.e. the propagation of the vapor front into the metal, by the moment when the time t_2 elapses does not yet take place (see Fig. 14.11, operation number I).

At the time $t_3 - t_2$, the cavity appears (see Fig. 14.11, operation number II). As its depth increases, the cavity walls absorb more and more electrons backscattered (emitted) from the cavity bottom, and I_t starts growing. The highest value of I_t at the point C results from the maximum possible penetration depth for the given power density.

If the time of interaction is $t_p > t_3$, the metal absorbs the EB power, but the penetration depth does not increase; the amount of the liquid phase in the zone of interaction and in the weld zone grows. This is a non-optimal condition of EB processing and welding, which can lead to defects in weld joints, such as gas cavities (see Fig. 14.13, operation number III).

Comparison of the oscillograph records of I_t flowing through the target with the respective zones of EB interaction reveals that the target current curves display the points from which the curve shape changes sharply (points A, B, and C in Fig. 14.14). These points are indicative of the beginning and end of the definite stages of EB heating. Determining the moments corresponding to sharp changes in the current I_t, we can single out the following stages of the process of EB-metal interaction:

(a) heating of the target to the temperature of onset of intense thermionic emission, i.e. to the melting point, over the period t_1;

(b) heating of the target to the onset of intense vaporization, over the period t_2;

(c) formation of the cavity, over the period t_3;

(d) heating in the "nonoptimal" condition, over the period $t_p - t_3$.

So, the recording and analysis of the time-dependent current flowing through the target allow us to clarify the EB heating stages, i.e. to control continuously the process of EB-material interaction.

14.4. WELD PENETRATION CONTROL BY THE ION CURRENT RIPPLE FREQUENCY

Work [7] describes the experimental relation of the ripple frequency of the vapor stream flowing from the cavity (i.e. the ripple frequency of the ion current or secondary electron current) to the penetration depth and the degree of EB focusing.

The experiments revealed that in EB welding of steels up to 30 mm thick at a power of up to 12 kW, the ion current ripple frequency (free-running frequency) varied linearly with the generalized parameter: $(hv_w/P)\, v_w/(P_0 + P)$. Here, h is the penetration depth, P the EB power, v_w the weld speed, and P_0 the threshold power at which the ion current begins to pulsate. The experimental value of P_0 was equal to 0.9 kW.

In experiments, use was made of a closed-type ion current sensor, the measuring electrode of which was at a negative potential of 200 V relative to the target and was shielded to prevent backscattered electrons from falling on it. The voltage drop across a 4-kΩ leak resistor was controlled with a capacitor charge-discharge frequency meter and a spectrum analyzer. The spectrograms were displayed on the screen of a cathode-ray tube. The results of measurement of the frequency meter were recorded. Let us now consider the results of experiments.

In welding scale-resistant steel samples, the EB defocusing at a constant energy input per unit weld length, P/v_w, causes sharp changes in the ion current ripple frequency. Changes in the average weld penetration h from 16 to 13 mm, i.e. by 21%, correspond to changes in the average ripple frequency f from 0.9 to 0.4 kHz. The frequency f varies by a factor of more than 2 with an insignificant variation of the penetration depth.

The results are similar for an aluminum-magnesium alloy. The ion current decreases in the cases of both a considerable EB defocusing and at a maximum penetration depth. In the first case, a decrease in the ion current results from a low beam power density and a slower rate of alloy vaporization; in the second case, the main factor responsible for this effect is a reduction of the cavity width

with increasing depth, which impedes the flow of electrons out of the hole. When the degree of focusing is constant, but the energy input varies, the ripple frequency drops with increasing penetration depth.

The ripple frequency-penetration depth relation is more dependent on the degree of focusing, i.e. the power density, than on the energy input. As is obvious from Table 14.9, changes in the penetration depth from 0.75 to 0.45 cm with an increase of the beam power from 2 to 7 kW cause the ripple frequency to vary from 1.4 to 0.66 kHz.

TABLE 14.9. **Weld Penetration for Scale-Resistant Steel Welded at Different Degrees of Focusing and Different Energy Input [7]**

h, cm	P, kW	v_w, cm/s	P/v_w, kJ/cm	f, kHz
0.38	1.30	1.10	1.20	2.55
0.73	2.55	1.10	2.30	1.70
0.75	2.00	0.86	2.30	1.40
1.38	4.90	1.10	4.45	0.87
1.80	7.35	1.10	6.70	0.73
2.30	7.00	0.86	8.15	0.52
2.45	7.00	0.86	8.15	0.66
3.00	10.00	0.86	11.65	0.38
2.10	7.35	1.10	6.70	0.59
2.30	11.60	1.50	7.75	0.58
1.30	4.00	0.56	7.15	0.45

In the generalized parameter given above, the cofactor hv_w/P is the ratio of the area of the weld zone melted per second to the beam power. The cofactor $v_w/(P_0 + P)$ is the quantity which is the inverse of the energy input.

The analysis of the spectrum of the ion current ripple frequency shows that the pulsations have an almost harmonic pattern at a relatively low beam power. As the beam power increases, the frequency spectrum expands and displays other harmonics. At a power density that enables a penetration depth in excess of 30 mm, the frequency spectrum turns almost completely to a noise spectrum. For control of the degree of beam focusing and the penetration depth by the free-running frequency in the case of welding metals over 30 mm thick, it is probably necessary to use more responsive sensors and more precise measuring devices.

References

1. L. V. Boriskina, A. N. Kabanov, and V. N. Yudaev. *On scattering of the electron beam during its interaction with a material.* Fizika i Khimiya Obrabotki Materialov, No. 5, p. 20, 1974.
2. M. A. Kosykh and N. K. Ilyushchenko. *Experimental studies of electron-beam keyholing*: in Electron beam welding. Moscow, MDNTP, 1974 (in Russian).
3. N. N. Rykalin, I. V. Zuev, and A. A. Uglov. *Fundamentals of electron beam processing of materials.* Moscow, Mashinostroenie, 1978 (in Russian).
4. L. S. Movsesyants. *Current through a target as a function of the EB weld depth and width*: in Electron beam welding. Moscow, MDNTP, 1974 (in Russian).
5. I. V. Zuev and V. B. Zvyagin. *Control of the EB weld depth and width in sealing IC packages*: in Welding and soldering in electronic industry and instrument making. Leningrad, LDNTP, 1980 (in Russian).
6. V. I. Zharinov. *Kinetics of formation of the EB weld joint*: in Proceedings of the 5th All-Union conference on electron beam welding. Kiev, Naukova Dumka, 1977 (in Russian).
7. K. S. Akopyants and A. V. Emchenko-Rybko. *Control of weld penetration and EB focusing by the ion current ripple frequency.* Avtomaticheskaya Svarka, No. 9, p. 28, 1981.

Part 4
LASER AND ELECTRON BEAM EQUIPMENT

Chapter 15
LASER AND ELECTRON BEAM SETUPS

15.1. LASER SETUPS

The basic parameters of an industrial laser and, hence, of the laser setup incorporating it are the energy in a pulse, pulse duration, and diameter of the focused spot on the target surface.

There are many varieties of laser setups, or work stations, but each contains basic units which are common to any type. Fig. 15.1 shows the block diagram of an industrial laser setup which includes the following common basic units [1, 2]: a laser head *1*; power supply unit *2*; unit *3* to trigger a flashtube; optical system *6* to focus the beam and view the irradiated area; and work table *7* to move a properly clamped workpiece. In a number of cases, a laser setup is made complete with a laser energy control (adjusting) unit *5*, system *8* for automatic stabilization of the energy output, and an electronic or electromechanical programming unit *9* which controls the passage of pulses to a target and the movement of the work table.

The **laser head** consists of a laser medium, resonator (resonant cavity), and optical pump system.

Examples of the laser rods used in solid-state lasers are ruby rods containing Cr^{3+} as the lasant and Al_2O_3 as the host, neodymium-glass rods where Nd^{3+} acts as the lasant and glass of various grades as the host material, Nd-YAG (yttrium-aluminum-garnet) rods, and calcium tungstate rods. The properties of these laser materials were given detailed treatment in Ch. 1. Let us note in passing that Nd-glass and Nd-YAG lasers have a lower generation threshold and can afford a higher efficiency than ruby lasers [1].

The parameters of Nd-glass and YAG lasers are less dependent on temperature than those of ruby lasers [1, 3]. This circumstance explains why the first two types are more stable in operation and allow the use of simpler methods of laser medium cooling.

As noted in work [1], the present technology offers the possibility of producing rods of high optical quality and of much larger sizes than the technique of laser crystal growth. For example, industrial lasers use 26-cm long rods 1.0-1.5 cm in diameter, which can produce pulses of a few tens of joules and have the lifetime in excess

of 10^6 shots. But a relatively low thermal conductivity of the rods in comparison with that of crystalline materials makes it difficult to remove heat from the rod during optical pumping and limits both the average laser power output and pulse repetition rate. Nd-glass lasers commonly operate at a pulse repetition rate of a few hertz, most often in the order of 1 Hz, which is sufficient for spot welding and hole drilling. But these lasers prove ineffective for use in seam welding and cutting since a low repetition rate results in insufficient weld speeds and cutting rates.

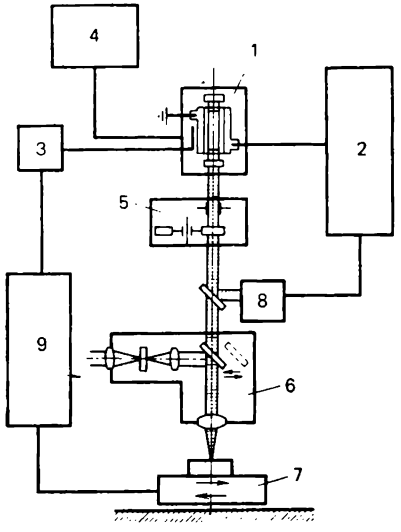

Fig. 15.1. Block diagram of a laser equipment setup: *1*, laser head; *2*, power supply source; *3*, flashtube assembly; *4*, cooling system; *5*, energy control device; *6*, optical system comprising beam focusing and viewing optics; *7*, work table; *8*, system of automatic stabilization of output energy; *9*, program unit

YAG lasers display more favorable thermal characteristics and have a much lower generation threshold. In comparison with Nd-glass rods, YAG rods exhibit a higher thermal conductivity (by a factor of ten), a lower thermal expansion coefficients, and higher mechanical strength. That is why they can stand up to appreciable thermal loads, i.e. have a high threshold for damage. It is thus possible to employ these lasers in efficient setups for seam welding and cutting at a pulse repetition rate of 10-100 Hz and an average laser power of 100 W and over [1].

The Q-switching carried out during continuous pumping with the aid of an acoustic shutter (modulator) enables the YAG laser to operate at a high repetition rate of 1 to 40 kHz with a peak power of 1 to 5 kW and an average power of 50 W. This ensures a high rate of cutting of thin films and efficient scribing of semiconductor materials [1, 4]. But the crystal YAG is much more expensive than Nd-glass, so it is more advantageous to use Nd-glass rods where a pulse repetition rate of 1 to 5 Hz is sufficient.

Flashtubes (flashlamps) and reflectors form an optical pump system defined by such parameters as the density of the radiant flux impinging from the flashtube onto the rod, uniformity of the light field within the confines of the reflector, and the lifetime of both the reflector and the flashtube.

Early lasers employed a pump source which consisted of a helical flashtube wrapped round the rod and housed inside a cylindrical diffuse reflector. In modern designs, the pump is commonly built up of a straight tube and a reflector in the form of an elliptic or circular cylinder with a reflecting mirror surface, which most effectively utilizes the radiation emitted from the tube. The focusing properties of the ellipse are used by locating the straight tube and the cylindrical laser rod on the optical axes of the elliptic cylinder. The light flux from the tube arranged at one of the focuses of the ellipse is reflected from the mirror surface and focused on the rod at the second focal point.

However, the asymmetrical structure of such a pump produces a nonuniformly distributed light field at the rod end. This results in a nonuniform energy distribution over the beam cross section and thus leads to a lower accuracy of hole drilling.

A symmetrical pump provides a more uniform energy distribution but at a sacrifice in the efficiency.

An example of the symmetrical pump with a coaxial flashtube used in a Kvant-3 laser setup is given in work [2]. The ring discharge in this tube provides a uniform irradiation of the rod housed inside the cavity of the tube. Where it is required to excite uniformly as large a volume of the laser medium as possible, mirror surfaces are replaced by diffusively reflecting surfaces with a $MgCO_3$ coating.

The most popular designs of pumps with straight flashtubes placed inside cylindrical reflectors are shown in Fig. 15.2*a*, *b*, *c*, and *d*. The flashtube and the rod are fitted adjacent to each other inside a chamber with a mirror surface. The volume of the chamber and its shape are selected experimentally [1, 2, 5]. The light-trapping efficiency of the compact-type chambers of Fig. 15.2*c* and *d* is two or three times as high as that of the chamber with a coaxial flashtube, illustrated in Fig. 15.2*e*.

The design of Fig. 15.2*f* with a spheroidal reflector and the design of Fig. 15.2*g* with a conical reflector, where the rod and the flashtube lie successively on the same axis, ensure a high symmetry of the light pump field and appreciable efficiency of utilization of the flashtube radiation.

Some industrial lasers use cylindrical or elliptic reflectors made up of glass or quartz tubes noted for the longest lifetime and high efficiency. These reflectors, illustrated in Fig. 15.2*h* and *i*, are given outer coatings of silver or magnesia [2].

The **resonator,** or **resonant cavity,** determines the temporal profile of the laser beam. The use of spherical mirrors in resonators appreciably improves the spatial and temporal profile of the beam and sometimes enables the laser to generate spikeless, smooth pulses. But a high divergence of the beam inherent in this type of resonator

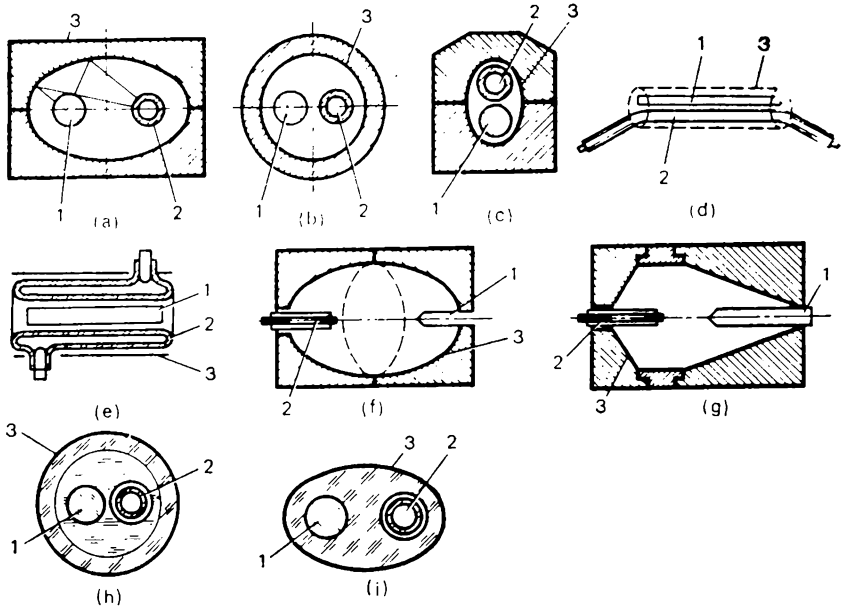

Fig. 15.2. Types of optical pump chambers for lasers: (*a*) chamber with reflector in the form of elliptic cylinder; (*b*) circular cylinder; (*c*) configuration with close coupling between linear flashtube and laser rod; (*d*) close-coupled configuration; (*e*) configuration with coaxial flashtube} wrapped round the laser rod; (*f*) ellipsoid of revolution; (*g*) biconical configuration; (*h*) configuration with tubular quartz reflector; (*i*) quartz-filled cavity; *1*, laser rod; *2*, pump flashtube; *3*, reflecting coating

limits the application of lasers with spherical mirrors in some fields, for example, where it is necessary to pierce fine holes.

The pump structure must offer the possibility of a highly parallel arrangement of mirrors, to within $\sim 10''$, and be rigid enough to retain the optimal alignment during a long period of operation. From the energy viewpoint, the spherical-mirror resonator is less critical to alignment than the parallel-mirror counterpart.

The cavity mirrors for solid-state lasers can be made integral with a laser rod by depositing silver coatings on the flat and parallel ends of the rod. The main requirement placed on cavity mirrors is that they must ensure a minimum loss of energy. In early lasers, the mirrors were thin silver coatings often deposited directly on the rod ends. The energy loss of such mirrors was 5-10% and the reflectivity did not exceed 90-95% in the visible region.

High energy losses reduce the quality factor of the cavity and rapidly degrade the mirrors, causing premature damage under radiation. For example, the coatings of silver on the ends of rods can stand

up to only a few hundred laser shots at an energy in the pulse of no more than 1 J.

Modern industrial lasers employ external mirrors with multilayer dielectric coatings formed of alternately deposited transparent layers with different refractive indexes n_1 and n_2 and optical thickness $n_1h_1 = n_2h_2 = \lambda/4$, where h_1 and h_2 are the geometric thickness of the layers respectively. For operation in the visible region, use is made of such compounds as zinc sulfide ZnS ($n_1 = 2.3$) and cryolite Na_3AlF_6 ($n_2 = 1.35$). The reflectivity R of mirrors increases with the number of layers. Semireflecting mirrors with R ranging from 30 to 50% consist of 3 to 7 dielectric layers; totally reflecting mirrors (total reflectors) with $R > 99\%$ consist of 15-17 layers, the absorptivity of which does not exceed 0.1-0.3%.

The repetitive-pulse operation of lasers at a high repetition rate leads to changes in the properties of the resonator due to thermal deformation of the rod, which becomes similar to a positive lens. The flat-mirror resonator then behaves like a spherical resonator: its Q factor for higher-order modes increases and the laser operates in a larger number of modes [2]. For this reason, the laser energy, beam divergence, and pulse duration become greater in the transient and steady-state conditions of operation, which is particularly the case for a Nd-doped laser, where heating of the rod weakly affects the spectral emission characteristics.

The easiest way of achieving the symmetry of thermal deformation, which is appreciable in a repetitively pulsed laser, is to utilize pumps in the form of a spheroid. It is felt that axicon and spherocon pumps look promising for industrial lasers because they ensure both a high light-trapping efficiency and symmetry of the light pump field [2].

Xenon flashtubes find most extensive uses as pump sources in which maxima of emission spectra lie near the absorption bands for such laser materials as ruby and Nd-glass in the visible and infrared regions.

The limiting values of the performance characteristics of xenon flashtubes most widely used in commercial laser systems are given in Tables 15.1 and 15.2 [6]. The lifetime of modern flashtubes ranges from 10^5 to 10^6 shots [2].

A feature specific to laser mediums used in gas lasers is that they exhibit a high optical homogeneity, which results in a small beam divergence, of the order of 5′ for commercially available single-mode lasers [1]. Also, electric current directly passing through the medium affords the population inversion.

To enable gas lasers to operate on a CW basis, the laser medium is mainly excited by a steady-state glow discharge which causes a time-constant current to flow through the plasma as the discharge tube electrodes are fed with a constant voltage supplied from a high-voltage rectifier via a voltage stabilizer [1].

TABLE 15.1. **Performance Characteristics of Linear Xenon Flashtubes**

Tube	Light spot size, mm	Resistance, Ω	Flashtube energy, J	Firing voltage, V	Self-firing voltage, V	Mean power, W
IFP-400	5×40	—	400	—	—	—
IFP-800	7×80	0.3	800	700	3200	1000
IFP-1000-2	7×80	—	1000	—	—	—
IFP-1200	6.3×120	0.25	1200	—	—	1000
IFP-2000	11×130	0.2	2000	1200	2600	133
IFP-5000	11×250	0.4	5000	1600	5000	170
IFP-15000	10×580	1.5	15000	2000	9000	1250

Notes: 1. In the tube designations, the transliterated Russian letters denote the following: I, pulsed lamp; F, fluorescent; and P, linear. The figures attached to the letters stand for the energy delivered in a single shot.
2. The firing voltage is a minimum voltage across the bank of capacitors, at which the discharge between the tube electrodes occurs after applying a high voltage trigger pulse from an external trigger circuit.
3. The self-firing (self-breakdown) voltage is the voltage at which the interelectrode discharge can appear without a trigger pulse.

TABLE 15.2. **Some Performance Characteristics of Flashtubes [6]**

Tube	Tube dia., mm	Interelectrode gap, mm	Laser setup	Capacitor bank value, μF	Initial voltage, kV	Limiting voltage, kV	Discharge time, ms	Pulse repetition rate, Hz	Life, number of shots (thou.)	Radiant energy, J
IFP-800	7	80	Korund	100	0.9	1.25	0.2	5	500	0.3
			Kvant-11	75	0.6	1.0	0.2	100	2500	0.2
IFP-1200	7	120	Kvant-9	800	1.3	1.7	0.7	1	100	8.0
			Kvant-9	800	0.7	1.7	0.7	1	200	2.0
IFP-5000	11	250	Kvant-10	2000	1.7	2.2	6.0	1	300	15.0

For pulsed operation to be secured, pulsed discharges must be set up by allowing the current from a high-voltage source to flow through the laser mixture for short periods of time. The population inversion is determined by the properties of the nonsteady-state plasma. The maximum pulse repetition rate, which reaches a few kilohertz, is limited only by the time lag of the processes in gas-discharge plasma [1].

The gas laser head, just like the solid-state laser head, includes a resonator with a gas-discharge tube placed between mirrors. As distinct from a laser rod where the particle concentration is as high as 10^{17}-10^{20} cm^{-3}, a gas mixture has a lower particle concentration,

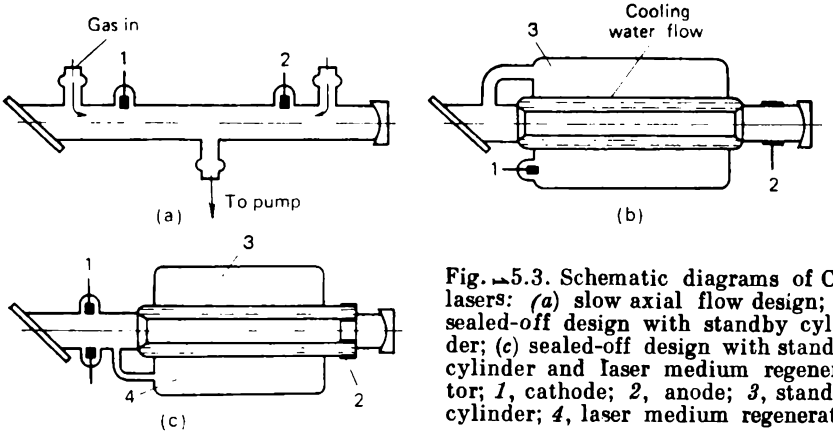

Fig. 5.3. Schematic diagrams of CO_2 lasers: *(a)* slow axial flow design; *(b)* sealed-off design with standby cylinder; *(c)* sealed-off design with standby cylinder and laser medium regenerator; *1*, cathode; *2*, anode; *3*, standby cylinder; *4*, laser medium regenerator

in the order of 10^{13}-10^{16} cm^{-3}, therefore a gas laser requires a large tube length to be able to provide high output power. Structures and configurations of gas laser heads have been discussed in [1, 4].

The laser head of a CW or pulsed gas laser is a glass or quartz tube filled with a gas and sealed or left open to allow the gas to flow through it. The tube is complete with metal electrodes fitted into it and secured in position by any of the practical methods. The mirrors can be located inside the tube or be external to it [1, 4].

The output windows positioned at Brewster's angle to the optical axis of the cavity afford a linear polarization of the beam at a minimum loss of the laser radiation.

Examples of the discharge tube configurations for CO_2 lasers produced in the USSR are shown in Fig. 15.3 [1, 2, 4, 7]. In the design of Fig. 15.3*a*, which illustrates the tube for slow axial flow CO_2 lasers of the Kardamon and Katun models, there is a need to replace the gas mixture because of the dissociation of CO_2 into O_2 and CO. The lifetime of sealed-off discharge tubes of Fig. 15.3*b* and *c* reaches a few thousand hours [1].

To obtain a higher laser power and to prolong the life of gas lasers, the gas mixture is continuously blown through the discharge tube. In this case, the output powers per meter of the discharge tube range from 30 to 70 W/m in slow axial flow lasers and reach 250 W/m in fast gas transport lasers. To achieve a large tube length in a small volume, most of the high-power axial gas flow lasers use a folded tube configuration, in which two reflectors located at an angle of 45° to the beam direction turn the beam through 180°. Similar designs of the tubes are used in Katun and Kardamon lasers [8]. In distinction to sealed-off gas lasers, the above lasers require the gas injection and gas pumping-out systems of smaller sizes. The pum-

ping-out (exhaust) system serves to maintain a vacuum in the discharge tube.

The discharge in a tube is initiated by applying a high dc or ac voltage of 10 to 20 kV to its electrodes.

The carrying structure of the Katun laser is a frame from duralumin I-beams, which rests on three supports. The frame houses the system of gas-discharge tubes in jackets for water cooling and two end prisms with mirrors [8]. The discharge tubes *1*, illustrated in Fig. 15.4*b*, are arranged in two rows, two tubes in the upper and four in the lower row. Each tube has two discharge gaps with high-voltage electrodes denoted by Roman numerals in Fig. 15.4*a*. The electrodes are connected across water ballast resistors. Two spherical mirrors, namely, a high-reflectivity mirror *3* and semireflecting mirror *4* with radii of curvature of 40 m, form a resonator.

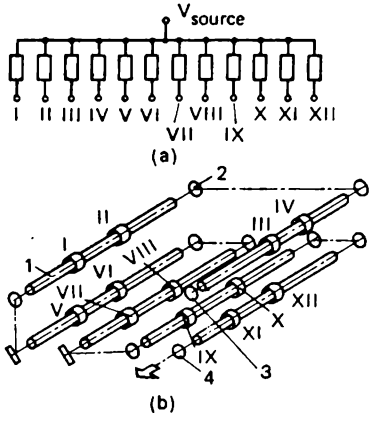

Fig. 15.4. Schematic diagrams of electrical system (*a*) and optical system of a high-power CO_2 laser

Ten flat turning mirrors *2* optically connect all the discharge tubes *1*. Mirrors *3* are made from invar and coated with silver. The material of mirror *4* is gallium arsenide. The output mirror *4* is protected against the environment by a potassium chloride window. All the mirrors are set in adjustable water-cooled cells fitted to end prisms. The cells also serve as ground electrodes for discharge tubes.

The design of the Kardamon laser is approximately the same: four discharge tubes, each about 6.5 m long, are rigidly positioned in a 53-cm diameter steel pipe and optically coupled together with six 100% reflecting superinvar mirrors with copper monoxide coatings. The mirrors are fitted in adjustable water-cooled seats. The rear total reflector is also made of superinvar; the front total reflector has a KCl substrate. The radii of curvature of these reflectors are equal to $\sim$24 m. In the central portion of each discharge tube there is a discharge-free gap.

One more type of optical cavity used in laser systems is a planoconcave resonator which consists of a flat semireflecting output mirror and a concave reflector, the radius of curvature of which should be equal to or larger than the distance between these two mirrors that comprise a hemispheric system. The substrates of reflectors are either polished, vacuum-refined, copper plates with

coatings of solid amorphous nickel or corrosion-resistant steel plates. Layers of gold deposited on the substrates can also form mirror surfaces. High-power CO_2 lasers use water-cooling systems to remove heat from mirror substrates and mirror holders. Such mirrors withstand a radiant flux density in excess of 50 kW/cm² in the CW mode of operation.

The substrates of semireflecting mirrors are made of germanium or gallium arsenide and, more rarely, of cadmium telluride or zinc selenide. The ground and polished semiconductor substrates are given thin dielectric coatings, for example, of ZnSe or ThF_4, with an optical thickness of $\sim\lambda/4$ to ensure the required transmittance. Germanium mirrors withstand a radiant flux density of 200-350 W/cm² and gallium-arsenide mirrors can endure up to 1 kW/cm² in CW operation. In high-power CO_2 lasers, the joints of semireflecting mirrors are cooled by water circulated in the cooling system.

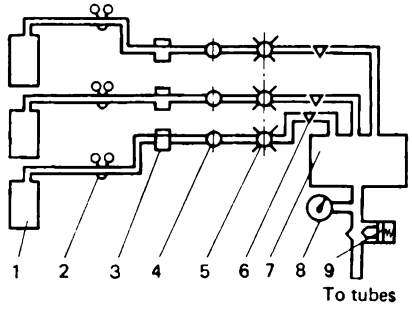

Fig. 15.5. Schematic diagram of the gas pumping system of a CO_2 laser

The gas flow system of the Katun laser is arranged in one of the three supports of the carrying structure. This system, as illustrated in Fig. 15.5, serves to provide the rated flow of the gas mixture to the discharge tubes and consists of high-pressure cylinders *1*, gas pressure regulators *2*, gas pressure stabilizers *3*, controllers *4*, cutoff valves *5*, flow regulators *6*, mixing chamber *7*, check vacuum gage *8*, and solenoid-operated valve *9* [8]. The gases CO_2, N_2, and He are fed from the cylinders *1* into the system through regulators *2* disposed in the control cabinet. The flow regulators *6* ensure a 1:1.5:10 mixture of CO_2, N_2, and He in the mixing chamber *7*. The throttle located downstream of the chamber maintains a pressure of the gas mixture in the range of 0.02 to 0.04 MPa, the pressure being controlled by the gage *8*. The gas mixture arrives at the discharge tubes via the electromagnetic valve.

The vacuum pump of the pumping-out system evacuates the gas mixture from the discharge tubes. To exclude ingress of oil vapors from the pump into the tubes, the system incorporates an oil trap and electromagnetic cutoff valve. Control over the system airtightness and the partial pressures of gases is made with the aid of a vacuum gage.

Optical systems. An optical system of an industrial laser setup consists of beam positioning optics (focusing system) intended to transmit and shape the beam and beam control optics (viewing sy-

stem) intended to guide the beam to the target and view the process of material treatment.

The light field at the focal spot differs in intensity from that ahead of the optical system, and the resultant irradiance integrated over the entire irradiated area is equal to the sum of the irradiances of all the points on this area.

The spatial characteristics of the shaped beam depend on the properties of the beam emitted from the laser rod, the position of the target relative to the focus of the optical system, and the parameters of the optical system proper.

Let us consider some optical systems currently used in laser equipment setups and also systems which may find effective use in various processes, for example, laser hole piercing and cutting. An optical system composed of refracting, reflecting, and focusing optical elements can deliver the beam to the target at any angle to the target surface, for a requisite distance from the laser head to the target, and also to the difficult-to-reach areas. The distance between the laser and the target is determined by the type of process run and the optics used. For example, in remote handling of radioactive materials, this distance can be appreciable [1].

The beam of a laser working at a wavelength in the visible or the infrared can be bent in the desired direction with the aid of a total internal reflection (TIR) prism or a cold-light mirror with a multilayer dielectric coating. Lasers emitting at 10.6 μm use gold-coated and aluminum-coated metal mirrors which have a high reflectivity and are resistant to oxidation in air.

If seam welds or cuts are to be made in the desired contours or holes to be pierced one by one along the coordinate axes, it is necessary to tackle the problem involving the motion of the beam and workpiece with respect to each other. One way of solving the problem is to move a workpiece, which it is justifiable to do if small-size parts are to be cut or welded. Another way is to scan the beam if the parts are large in size and the rates of welding or cutting must be high. The latter approach makes it possible to dispense with a number of moving mechanisms, improve the accuracy of treatment, and cut down the time required to clamp and remove the parts.

The beam can be swept in any desired contours over the target with the aid of a system of mirrors moving along the appropriate coordinate axes (Fig. 15.6*a*). Mirrors *2* and *3* and lens *4* move jointly along the X axis, but it is only the mirror *3* with the lens *4* that can travel in the Y direction. The joint motion of the corresponding elements in the X and Y directions causes the beam to shift along any desired path [1].

If short contour tracks are to be run, the beam focused spot can be shifted with the aid of the mirrors *2* and *3* as they revolve around their mutually perpendicular axes, thereby changing the

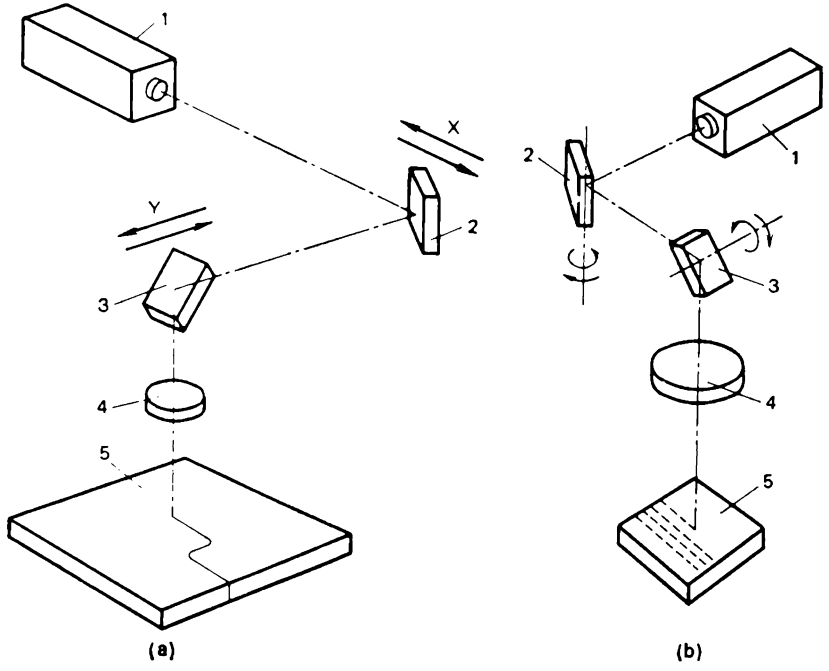

Fig. 15.6. Laser beam guiding systems used to run contour tracks on the target surface: (*a*) system with sliding mirrors; (*b*) system with rotating mirrors; *1*, laser head; *2*, *3*, moving mirrors; *4*, objective lens; *5*, target

angle of incidence of the beam relative to the optical axis of the stationary lens (Fig. 15.6*b*).

The beam can be swept over in a circle by causing the optical system that consists of a mirror and a lens to rotate about the beam axis and thus to shift the focal spot along a circular track [1]. If the radius of the circle does not exceed the radius of the field of view of the lens, the circular track can be produced by shifting the lens and rotating it about the beam axis.

Material processing in the focal plane of lenses. A number of industrial laser setups employ optical focusing systems of simple versions, such as illustrated in Fig. 15.7 [1, 2]. The radiation pattern of the beam after the focal plane depends on the paths of inner rays outgoing from the edges of the lighting spot at the end of the laser rod. The highest laser power density is in the region between the focal plane F' of the lens and the image plane S' of the aperture stop located near the output mirror of the laser.

If the system does not contain a limiting aperture, the beam waist inside the cavity should be taken as the minimum cross section

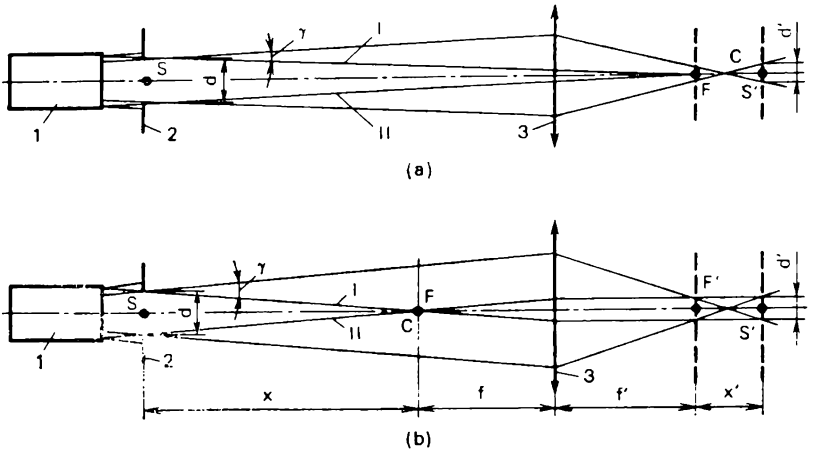

Fig. 15.7. Schematic diagram of laser beam focusing: (*a*) point *C* of intersection of rays *I* and *II* lies beyond the front focus of the lens; (*b*) point *C* of intersection of rays coincides with the front focus of the lens; *1*, laser head; *2*, aperture; *3*, focusing lens

of the beam. In symmetrical resonators, the waist is at the center of the cavity between the mirrors. In planoconcave resonators, the waist is in the plane of the flat mirror. To reduce the dimensions of laser systems, the focusing lens should be sited as close to the laser resonator as possible. The focused spot of a minimum size will then lie in the focal plane F'.

The diameter of the light spot in the focal plane is $d \approx \approx f' \tan \gamma \approx f'\gamma$, where γ is the angle of beam divergence and f' is the lens focal length.

It is possible to reduce the spot diameter by decreasing either f' or γ. But the approach to decrease the focal length f' is inadvisable since the optical system will then have a shorter working optical distance from the laser to the target and will call for protection of the focusing lens against spatter occurring during laser-material interaction. Besides, the use of short-focus lenses makes the results of material processing more strongly dependent on the alignment of the optical axes of the laser cavity and the focusing system and also leads to changes in the position of the target relative to the focal plane. A way to reduce the focused spot diameter to a few micrometers and to extend the working optical distance is to place a telescope ahead of a long-focus lens in a manner illustrated in Fig. 15.8. This type of optical system can focus the laser beam to a spot 5 μm in diameter and ensure a long working optical distance, for example, 100 mm and 70 mm in Luch-10 and Kvant-3 laser setups respectively.

The diameter of the light spot focused by this optical system is written as

$$d = \gamma f'/M$$

where M is the visible magnification of the telescope.

In some commercial laser setups, the optical systems contain elements that significantly improve the laser beam collimation, i.e. reduce the beam divergence. This type of optical system consists of two lenses, the first being a diverging (negative) lens and the second a converging (positive) lens, which form a Galilean telescope [2]. A decrease in the angle of divergence is approximately proportional to the angular magnification of the system:

$$\gamma_0 = 1/M_0 - f_1'/f_2'$$

where M_0 is the lateral magnification of the system, and f_1' and f_2' are the focal length of the converging and the diverging optical element respectively.

The optical system with converging and diverging elements also reduces spherical aberration which considerably increases the effective spot size [2].

A disadvantage of the described method of beam positioning is that the optical system can produce beam images of only circular or linear shapes on the target using spherical or cylindrical lenses respectively. But the most substantial disadvantage of the method is a relatively low accuracy of material processing because the beam spots produced lie in the image plane of the end of the laser rod, the radiation pattern from which is asymmetrical for many reasons.

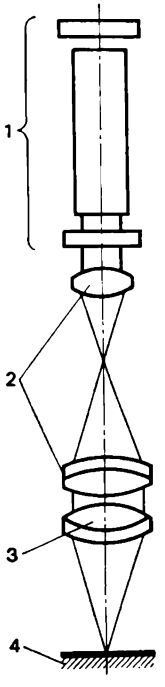

Fig. 15.8. Illustration of an optical system for an industrial laser setup with an increased laser-to-target distance: *1*, laser; *2*, telescope; *3*, focusing lens; *4*, workpiece

If a workpiece lies in the focal plane of the optical system, the irradiance distribution over the target surface becomes dependent on the angular irradiance distribution in the laser beam. The pattern of irradiance on the target surface is most often asymmetrical because of a low optical homogeneity of laser rods, imperfect systems

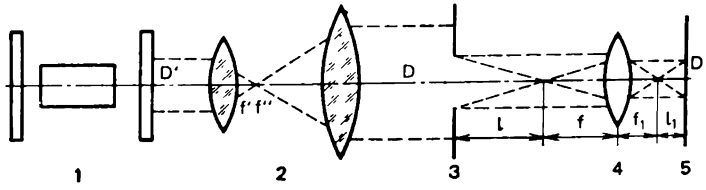

Fig. 15.9. Schematic diagram of a projection system for laser material processing: *1*, laser; *2*, telescope; *3*, mask; *4*, projection lens; *5*, workpiece

of pumping, inaccurate alignment of cavity mirrors, and other factors. The accuracy of laser machining, for example, hole piercing, can be improved with the aid of the projection method of beam guiding, which is briefly described in Ch. 7.

Since the cross section of a hole depends on the profile of the beam between the focal plane and the image plane of the laser rod end or the aperture stop, the optical system can be built up so that the point of intersection of multiple inner rays, which determine the beam profile, is coincident with the front focus of the lens, as illustrated in Fig. 15.7*b*. In this case, the light beam becomes cylindrical in shape, the length of the cylindrical section of the beam is $x' = f^2\gamma/d$, where d is the aperture diameter. The use of the optical system that produces the cylindrical beam section enables the laser setup to increase the hole depth by a factor of 1.5-2 and appreciably reduce the taper of holes [2].

The projection method for material processing. The main advantages of the projection method of beam guiding are the following: the possibility of producing a complicated pattern of the beam image on the target, which reproduces the pattern on the mask to a reduced scale; high resolution; and simultaneous treatment of work areas that are much larger in size than the focal spot. So, it is possible to form complicated patterns of printed circuits with a large component density and arrays of round or any other holes in thin films which can serve as grids, for example [2]. The method is also applicable for surface heat treatment of materials along any desired paths. The material treatment in the plane of image of the mask or the aperture stop greatly increases the reproducibility of holes since the aperture cuts off the outer edges of the beam emitted from the rod end.

The schematic diagram of a projection system of beam positioning is shown in Fig. 15.9 [4]. A lens or telescope *2* expands the beam from a laser *1* to the size of the mask and projection lens *4* translates the image of the openings in the mask onto target *5*. The choice of the type of material processing depends on the laser power density in the irradiated spots which reproduce the pattern on the mask. The telescope increases the cross section of the beam to a size in excess of the size of the mask and simultaneously reduces the laser

pulse fluence to a value which does not cause damage to the mask. The projection lens reduces the image of the pattern on the mask to the required size and ensures such a value of the fluence which is necessary for the given process.

The most important parameters of the optical system under consideration are the linear reduction β of the projection system or the projection lens, which determines the resolution of the optical system, and the linear magnification M of the telescope, which determines the total area of the surface irradiated at the same moment. Consider in more detail these parameters using the results of studies presented in [2].

The nominal reduction of the projection lens is $\beta = D_1/D_m$, where D_m is the size of the mask or the size of a portion of the pattern on the mask and D_1 the size of the corresponding image of the pattern. The system must satisfy the condition

$$\beta_{min} < \beta < \beta_{max}$$

The minimum reduction β_{min} is the value at which the beam delivers the required energy per unit area on the target without causing damage to the mask: $\beta_{min} = \sqrt{Q_m/Q_t}$, where Q_m is the threshold of the energy density (fluence, J/cm^2) at which damage to the mask begins, and Q_t is the threshold of the energy on the target for a particular type of material processing.

The limit on the maximum reduction β_{max}, or the minimum magnification which affords the minimum size of the pattern image on the target, is set by the diffraction effects in the aperture of the projection system. The maximum reduction is defined by the expression

$$\beta_{max} = \frac{\lambda f}{(D_0 - D)\, d_{min} - \lambda f}$$

Here λ is the laser wavelength, f the focal length of the projection lens, D_0 the diameter of the entrance pupil of the projection system, D the total size of the mask, and d_{min} the minimum size of the slot in the pattern on the mask.

On specifying β, we can estimate d_{min}, D, and the distance l between the mask and the front focus of the projection lens:

$$d_{min} = d'_{min}/\beta, \quad D = D_1/\beta, \text{ and } l = f/\beta.$$

Obtaining large values of reduction β calls for a considerable increase in the dimensions of the optical system. The use of collecting lenses can alleviate the problem.

The beam totally covers the mask when the telescope ensures a magnification $M \geqslant D/D'$, where D' is the beam diameter. The fluence Q must satisfy the condition

$$Q_m M^2 > Q > Q_t M^2 \beta$$

where $Q_m = QM^2$ is the fluence on the mask and $Q_t = Q\beta^2M^2$ is the fluence on the target.

If the diameter of the beam at the exit from the laser is larger than the size of the mask, it is more advantageous to use simplified optical systems, for example, without a telescope. Such systems are now used in a number of models of commercially available laser setups. If there is no need to reduce the image of the pattern on the mask and the energy density is sufficient for a particular type of material treatment, it is safe to dispense with the projection system, too, and place the mask directly on the target surface.

It is of interest to look at the optical system described in [2] for piercing unrounded holes. It consists of two telescopic arrangements. The first expands the laser beam and allows it to impinge on the mask with an orifice of a complicated shape. The second projects the orifice image on the target surface. Since the first telescope decreases the power density of the beam by expanding it, common photographic transparencies can serve as the masks.

Other optical systems. Figure 15.10 illustrates an optical system employed in several models of laser setups, namely, SU-1, UL-2, and UL-20 [2]. The focusing optics and viewing optics are independent systems. The optical viewing system is a microscope located at an angle to the optical axis of the focusing lens. The microscope can magnify an image in the range attainable by a light microscope. The tilted position of the microscope does not allow the treatment of recesses, for example, hole drilling in diamond dies and watch jewels, nor does it allow the welding of parts with a dense layout. A fraction of the field of view of the microscope proves blurred and the shape of the objects distorted in the perspective, with the result that it is impossible to carry out an accurate control and precise measurement of the holes pierced. The beam positioning optics in which the viewing system and the focusing system have a common lens are free of the above shortcomings [2]. The focusing and the

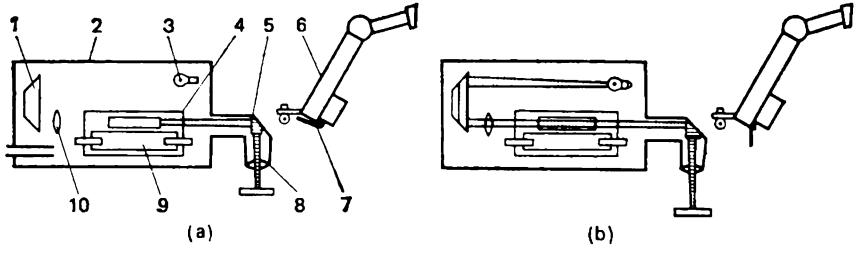

Fig. 15.10. Beam positioning and viewing systems of the SU-1 laser setup: (*a*) beam guiding to initiate welding with the blind held in position; (*b*) beam guiding to the spot of welding with the blind removed; *1*, *5*, prisms; *2*, casing; *3*, lamp; *4*, laser; *6*, microscope; *7*, blind; *8*, focusing lens; *9*, pump flashtube; 10, lens

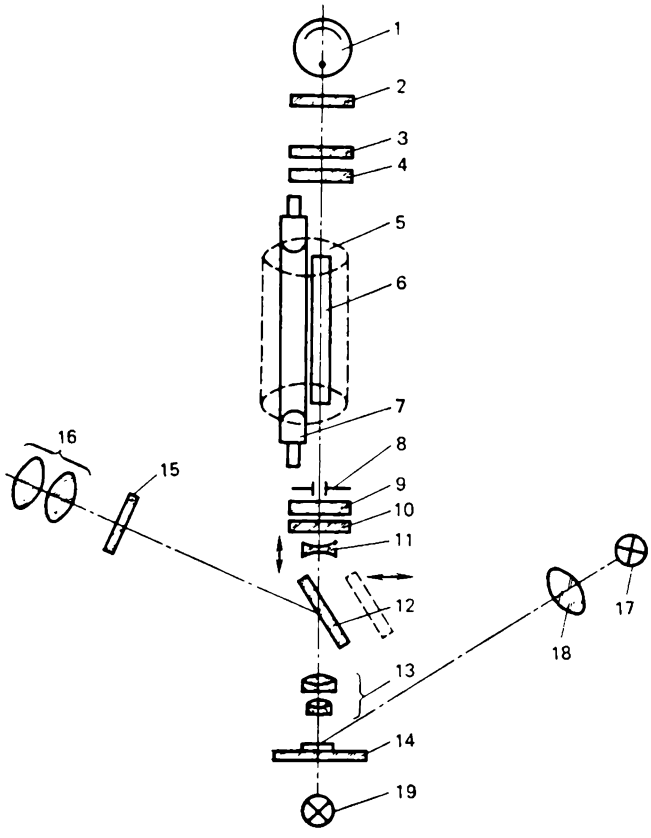

Fig. 15.11. Optical system of the K-3 laser setup: *1*, photocell; *2*, light filter; *3*, *10*, protective glass plates; *4*, 95% cavity mirror; *5*, reflector; *6*, ruby rod; *7*, pump flashtube; *8*, iris aperture; *9*, 50% cavity mirror; *11*, diverging lens; *12*, movable prism; *13*, lens column; *14*, microscope slide (object carrier); *15*, sight graticule (crosshairs); *16*, eyepiece; *17*, lighting lamp; *18*, condenser; *19*, mirror for lighting drilled holes from bottom

viewing system are built up as an integral assembly with the use of sliding (displaced) mirrors and prisms (in K-3 and K-3M laser setups) and also with the use of aperture mirrors (in a K-2 laser setup).

The optical system of the K-3 laser setup is shown in Fig. 15.11. The 95% mirror *4* and 50% mirror *9* (with a 75 × 7 mm ruby rod *6* placed in-between) form the laser cavity. The reflecting coatings of the mirrors are protected by glass plates *3* and *10*. The iris diaphragm *8* located near the laser cavity serves to control the beam energy. The

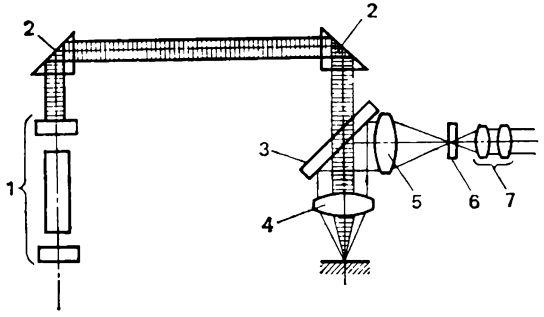

Fig. 15.12. Optical system of the K-2 laser setup: *1*, laser; *2*, prism; *3*, mirror with aperture in the reflective coating; *4*, focusing lens; *5*, lens of optical viewing system; *6*, crosshairs; *7*, eyepiece

flashtube *7* and laser rod *6* are housed in an elliptic reflector *5* with polished walls. The laser beam is focused with the aid of a diverging lens *11* and lens *13* of the microscope.

The prism *12* and eyepiece *16* of the microscope photographic attachment are used to guide the beam to the target and observe the process. When the laser is switched on, the prism is swung out of the beam path. The sight graticule *15* positioned in the focal plane of the eyepiece enables the observer to project the cross-hairs with a reference scale on the target and thus precisely locate the beam on the target surface. The lamp *17* with a condenser *18* illuminates the work area. The mirror *19* serves for lighting of the holes pierced in workpieces. The photocell *1* used for the indirect laser energy measurement detects the light flux passing through the mirror *4* with a transmittance of less than 5% and light filter *2*. In the K-3M setup, the prism *12* is replaced by a sliding mirror and the mirror *19* is changed for a lamp to light holes from the bottom.

Figure 15.12 illustrates an optical system of the K-2 laser setup [2]. A feature specific to this system is that it has a mirror with an orifice in the reflective coating to enable the joint operation of the focusing and viewing optics.

The laser setups of later generations incorporate more elaborate special-purpose optical systems. Such a system used in the Kvant-10 laser setup is illustrated in Fig. 15.13. The laser cavity consists of two spherical mirrors *1* and *2* spaced 56 cm apart, each having a radius of curvature of 1 200 cm. The beam passes through an iris aperture *4* used to adjust the beam diameter and a telescope formed by optical elements *5* and *6*. The telescope gives a 2 × magnification and thus reduces the beam divergence by one half. The diverging element *5* of the telescope can be moved along the optical axis to enable the adjustment of the beam divergence. The interference (cold) mirror *8* guides the beam to a 70 cm focal length lens *10*

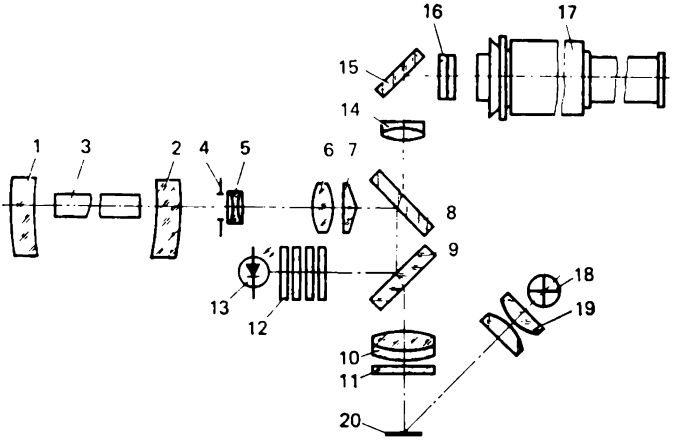

Fig. 15.13. Optical system of the Kvant-10 laser setup: *1*, *2*, cavity mirrors; *3*, laser rod; *4*, iris aperture; *5*, *6*, optical components of telescope; *7*, biprism; *8*, interference mirror; *10*, objective lens; *11*, protective glass plate; *12*, set of light filters; *13*, photodiode; *14*, viewing lens; *15*, mirror; *16*, light filter; *17*, binocular attachment; *18*, lighting lamp; *19*, condenser; *20*, target surface

which focuses it on the surface of a workpiece *20*. The glass plate *11* protects the lens against the blowoff material evaporated from the laser-welded parts.

A fraction of beam energy (about 8%) is diverted by a glass plate *9* to a photodiode *13* of the energy-level indicator. The optical viewing system intended to guide the beam and ensure the visual inspection of the weld joints consists of a lens *10*, viewing lens *14*, mirror *15*, light filters *16*, and binocular attachment *17*. The viewing system provides a total magnification of 33 power with a 3-mm diameter of the field of view. Two light sources are used to illuminate the parts being welded.

An optical system of the Kvant-9 setup appears in Fig. 15.14. The beam shaped in the laser cavity passes through a telescope composed of lenses *5* and *6* and impinges on a focusing lens *8* protected against spatter from the target *24* by a replaceable glass plate *9*. Interchangeable diaphragms of various aperture diameters can be used to adjust the beam energy. The setup is complete with two focusing lenses, the focal lengths of which are 24 and 38 mm respectively. The three-power telescope is a separate unit made as an attachment. The beam can be focused by the lens together with the attachment or without it. This attachment is used for drilling holes less than 0.1 mm in diameter.

The optical viewing system of the Kvant-9 model consists of two independent microscopes with a common eyepiece *19*. The mic-

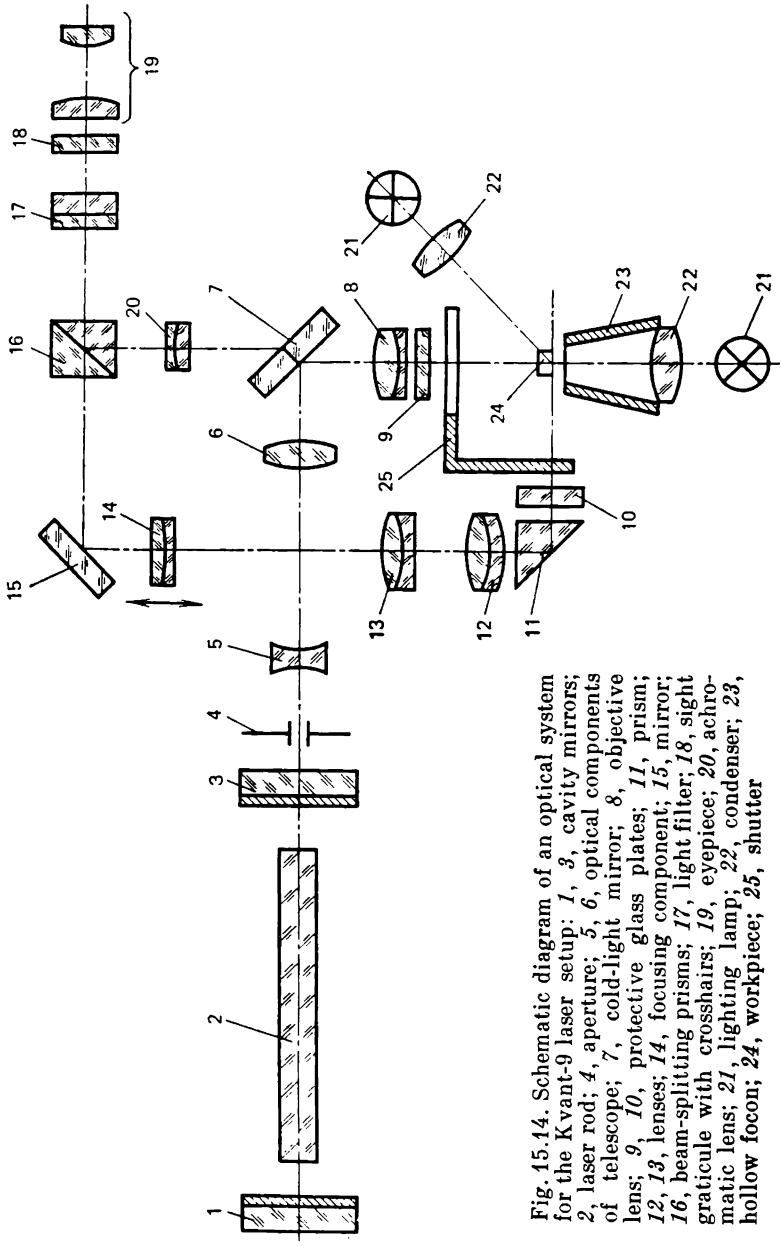

Fig. 15.14. Schematic diagram of an optical system for the Kvant-9 laser setup: *1*, *3*, cavity mirrors; *2*, laser rod; *4*, aperture; *5*, *6*, optical components of telescope; *7*, cold-light mirror; *8*, objective lens; *9*, *10*, protective glass plates; *11*, prism; *12*, *13*, lenses; *14*, focusing component; *15*, mirror; *16*, beam-splitting prisms; *17*, light filter; *18*, sight graticule with crosshairs; *19*, eyepiece; *20*, achromatic lens; *21*, lighting lamp; *22*, condenser; *23*, hollow focon; *24*, workpiece; *25*, shutter

roscope which serves to take a top view of the target and to guide the beam to the desired spot on the surface comprises a lens *8*, achromatic lens *20*, light filters *17*, cross-hairs *18*, and eyepiece *19*. The second microscope serves to take a side view of the target and comprises a glass plate *10*, swing prism *11*, lenses *12* and *13*, movable focusing element *14*, mirror *15*, and components common to both microscopes, namely, light filters *17*, cross-hairs *18*, and eyepiece *19*. To adjust the focusing system for operation with the first microscope, the optical system contains an interference mirror *7* which almost totally reflects the laser light, but is transparent to a larger portion of the visible region. The cubical beam splitter *16* enables the observer to register the fields of view of both microscopes. The microscope intended to observe the target surface gives a 62.5 × magnification and 39.2 × magnification with 24-mm and 38-mm focal length lenses respectively. The microscope intended to take a side view provides a constant 62.5× magnification. The latter microscope enables the observer to control the cross section of hole pierced in a transparent material. The use of such a system in laser setups has considerably increased the accuracy of rough drilling of holes in diamond dies and reduced tolerances for fine drilling.

Two light sources consisting of lamps *21* with condensers *22* illuminate the target. The hollow focon *23* improves the distribution of the laser light on the target surface. The shutter *25* serves to change over from one optical viewing branch to the other.

The beam positioning arrangement of the optical system used in the Kvant-9 setup is similar to the beam handling equipment used in the SLS-10-1 model. The focal length of the lens is 40 mm. Since one of the elements of the telescope is movable, it is possible to vary the beam divergence ahead of the focusing lens and thus to adjust the diameter of the focused beam [1].

In Fig. 15.15 is shown the schematic diagram of the optical system employed in the Kvant-12 laser setup [9]. After exiting from the cavity mirror *3* with a transmittance of 70%, the beam of the laser *2* impinges on the telescope composed of a short-focus element *4* and long-focus element *5*. The telescope decreases the beam divergence. The cold mirror *10* steers the beam to a focusing lens *12* with a focal length of 50 and 100 mm. This lens together with the telescope can focus the beam to a spot 0.25 to 1.0 mm in diameter. The beam diameter can be varied either in a step-by-step manner using replaceable short-focus elements or in a continuous manner by moving the long-focus element of the telescope.

The viewing system proper includes a viewing lens *6*, reversing prism *8*, and binocular attachment *9*. The shutter *7* protects the operator's eye from the radiation of the plasma plume occurring in the weld zone and from the laser light reflected from the welded parts. The shutter moves in step with laser pulses in such a manner

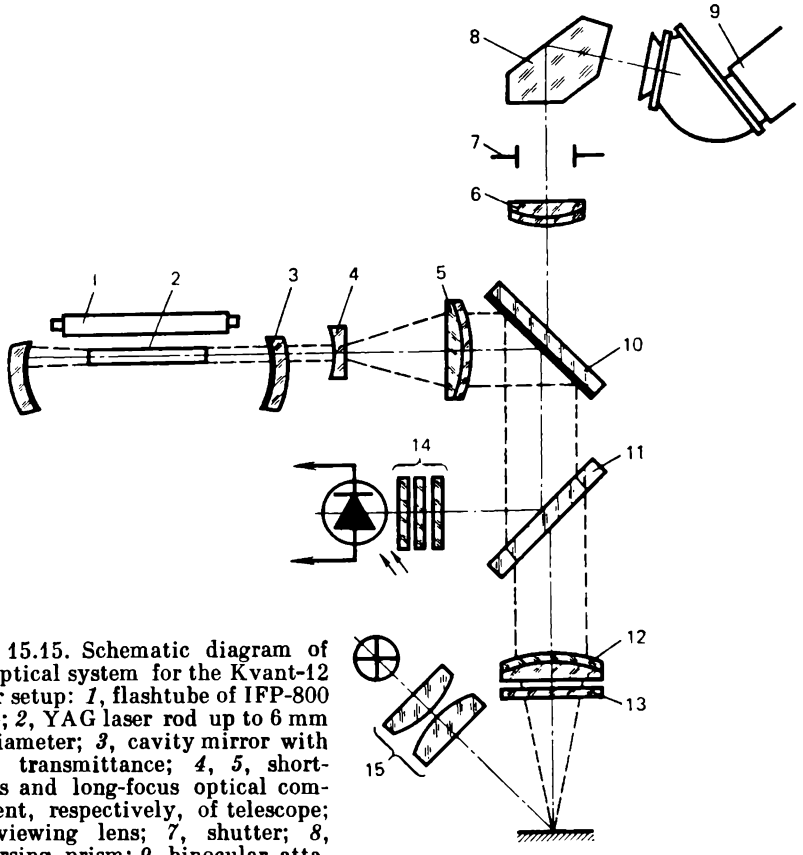

Fig. 15.15. Schematic diagram of an optical system for the Kvant-12 laser setup: *1*, flashtube of IFP-800 type; *2*, YAG laser rod up to 6 mm in diameter; *3*, cavity mirror with 70% transmittance; *4*, *5*, short-focus and long-focus optical component, respectively, of telescope; *6*, viewing lens; *7*, shutter; *8*, reversing prism; *9*, binocular attachment; *10*, cold-light mirror; *11*, glass plate; *12*, focusing lens; *13*, protective glass plate; *14*, light filters; *15*, condenser

that it shuts off the viewing system at the instant of the shot. The shutter-opening time is so chosen that the operator does not perceive changes in illumination within his field of view. The shutter enables the operator to observe continuously the process of welding.

One of the methods that permits an appreciable increase in the rate of material processing, apart from the method that relies on a high pulse repetition rate, is to distribute the beam, for example, from a YAG laser over a few work regions, as illustrated in Fig. 15.16 [1]. The scheme of Fig. 15.16*a* uses beam-splitting mirrors to distribute the beam over the targets, the number of which is only limited by the level of laser energy and energy loss in the mirrors; the splitted beam retains its initial spatial profile. The scheme of Fig. 15.16*b* relies on prisms with two or more reflecting surfaces which can differ in reflectivity. A disadvantage of this system is that the splitted

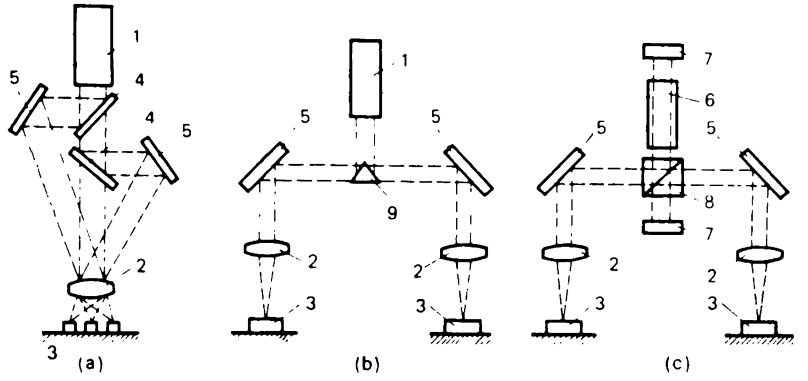

Fig. 15.16. Laser beam splitting optics for switching the split beams to several working positions: *1*, lasers; *2*, focusing lenses; *3*, workpieces; *4*, beam-splitting mirrors; *5*, turning mirrors; *6*, laser rod; *7*, totally reflecting cavity end mirrors; *8*, output beam-splitting prisms; *9*, polygonal prism (beam splitter)

beams have the shape of sectors in cross section, which adversely affect the profile of round holes. In the scheme of Fig. 15.16*c*, a cubical beam splitter placed in the laser cavity formed by two total reflectors *7* divides the beam and guides the splitted beams in opposite directions. The laser setup model K-13 employs an optical system displayed in Fig. 15.17, which splits the beam between two work

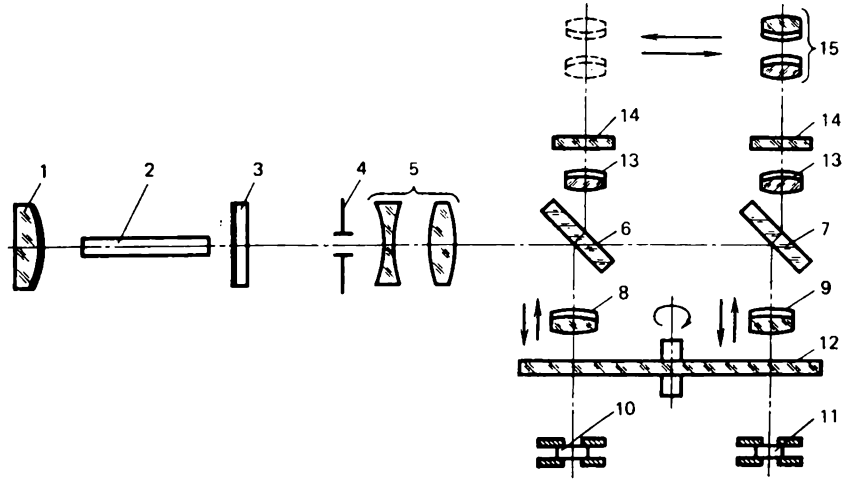

Fig. 15.17. Schematic diagram of an optical system for the K-13 laser setup: *1*, *3*, cavity mirrors; *2*, laser rod; *4*, aperture; *5*, telescopic system; *6*, beam-splitting cold-light mirror; *7*, 100% cold-light mirror; *8*, *9*, objective lenses; *10*, *11*, workpieces; *12*, revolving protective disk; *13*, achromatic lens; *14*, sight graticules with crosshairs; *15*, movable eyepiece

regions [1]. The setup delivers up to 1 J of energy in a 0.25-ms pulse to each work region at a pulse repetition rate of 3 Hz.

In AK-345 and AK-378 laser setups, a projection system is used to position the beam on the target. This system in combination with a focusing lens has determined the choice of the laser cavity, the main dimensions of the setups, and their layout [10]. The focusing lens with a 34 mm focal length provides a working optical distance of 28 mm. In the AK-345 model, the beam leaves the cavity through an aperture 2 or 3 mm across in a totally reflecting mirror, the aperture being projected on the target. In the AK-378 model, a mirror with a transmittance of 25% is used to extract the beam from the cavity, with the result that the entire end of the laser rod is projected on the target.

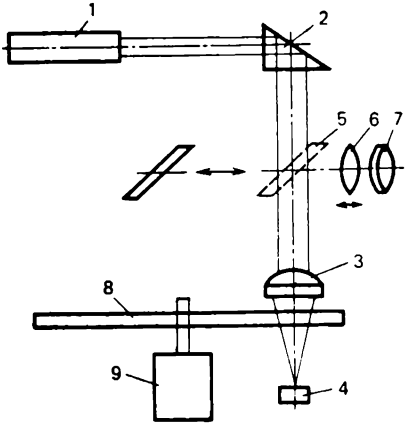

Fig. 15.18. Optical system of the AK-345 laser machine: *1*, laser head; *2*, prism; *3*, objective lens; *4*, workpiece; *5*, movable mirror; *6*, lens; *7*, eyepiece; *8*, glass plate; *9*, electric motor

In Fig. 15.18 is shown the optical system of the AK-345 model. The prism *2* deflects the horizontal beam emitted from the laser *1* at a right angle and lens *3* focuses the vertical beam on the target *4*. The lens *3*, the movable mirror *5*, and the telescope consisting of a 110 mm focal length lens *6* and eyepiece *7* constitute a viewing system with a 45× magnification. The glass plate *8* set in rotary motion by an electric motor *9* protects the lens *3* from the blowoff material. The AK-378 model is free of the deflection prism since the laser rod is sited in a vertical position.

The optical system of an experimental laser setup K-5 designed to engrave patterns on thin-film coatings is shown in Fig. 15.19*a*. The spherical mirrors form a confocal cavity and ensure a high quality factor for off-axial oscillations, thereby providing a very uniform distribution of the irradiance over the beam cross section. The telescope gives an expansion of 25×, so that it expands the beam diameter to the mask size equal to 45 cm. The projection system composed of a collecting lens and an objective lens projects the mask pattern on the target to form the image on a 1:4 scale. A25 × microscope enables the operator to accurately align the work areas on the target and images of the mask pattern projected by the optical system when the light source consisting of a lighting lamp and a condenser illuminates the target. The K-5 laser assembly can produce

thin-film patterns on a 20 by 20 mm area with a resolution of 30 lines per mm [1].

Figure 15.19*b* illustrates the optical system of the Kvant-17 laser setup, in which the laser head contains two YAG rods *1* placed in separate optical pumping chambers.

The Kvant-9 and Kvant-9M setups. These laser systems are designed to drill holes in diamonds for diamond dies and also in blanks of other materials. They are advisable for use in tool engineering, electronic industry, and instrument making [2, 9, 11].

These systems find most profitable applications as tools for rough drilling of holes in diamonds to produce diamond dies for extrusion of wire. The rate of laser drilling of holes in diamonds is 20 times and 200 times as high as that attainable in electromechanical and mechanical drilling respectively. The initial holes can be pierced by one or a few pulses. A single pulse can pierce a hole from 0.0005 to 0.04 and up to 0.1 cm in diameter and depth respectively; a series of pulses produce a hole up to 0.8 mm in diameter and up to 3 mm in depth.

These machine tools use Nd-glass lasers. The optical system which gives a 62× magnification enables the operator to control the process in two planes normal to each other. The target images register in one field of view, so it is possible to control the size and profile of holes pierced in transparent materials.

Each setup includes a work table with a laser head and optical system, a power supply source, a system of cooling the laser with distilled water, and a control system.

Technical Data

	Kvant-9	Kvant-9M
Hole diameter, mm	0.005-0.8	0.005-2.0
Hole depth, mm	up to 3	
Maximum pulse energy, J	8	
Pulse length, ms	0.5-0.7	0.5
Pulse repetition rate, ppm	6-60	6-180
Flashtube life, shots	200×10^3	

The SLS-10-1 setup. This is a laser machine intended for spot welding of various materials, including such refractory metals as molybdenum and tantalum, up to 0.4 mm thick. It finds application in the production of electronic devices and relays [2, 9].

The SLS-10-1 laser welder is notable for a high quality of joints it produces in the atmosphere of an inert gas, accurate adjustment, and good reproduction of the length and shape of pulses. The design of the setup offers the possibility of replacing the cavity elements without the readjustment. This laser welder is now available in a few modifications, which are semiautomatic special-purpose machines designed to weld the parts of instruments.

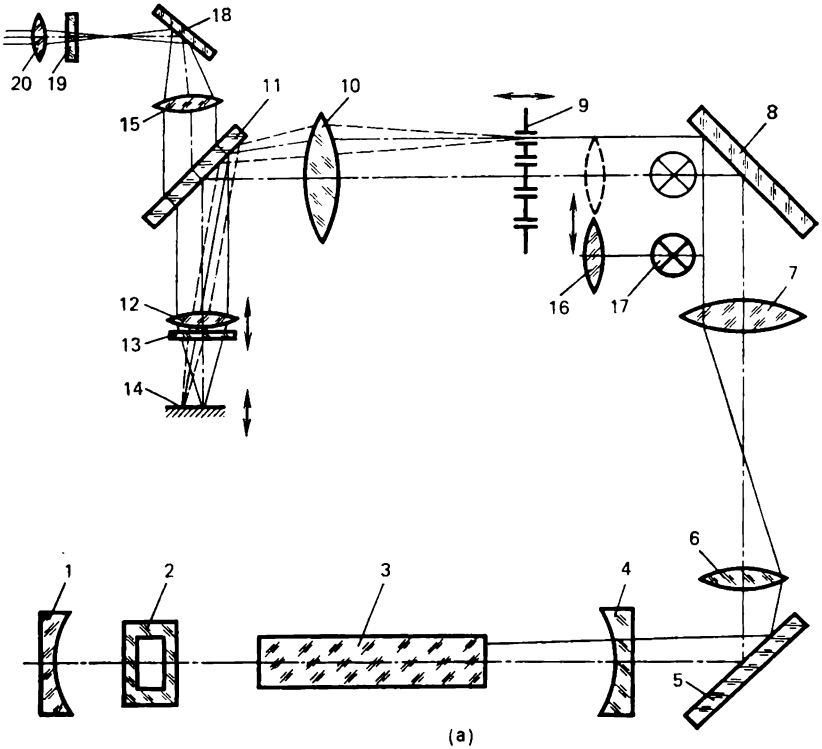

(a)

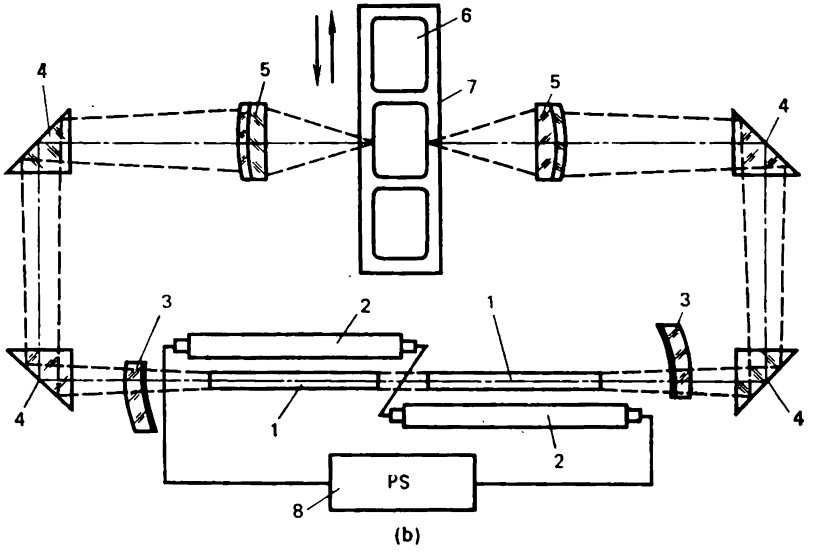

(b)

Technical Data

Laser spot diameter, mm	0.4-1.5
Pulse energy, J	up to 8
Pulse length, ms	2, 4
Pulse repetition rate, ppm	30
Supply voltage, V	220/380
Power consumption, kW	2.5
Overall dimensions, mm:	
machine	1005×820×1255
power unit	540×598×1212
Mass, kg	350

The Kvant-11 setup. This is a semi-automatic machine based on a YAG laser and intended for scribing the semiconductor wafers with active elements into chips having individual integrated circuits [9]:

Technical Data

Rate of scribing with cut 0.025 cm deep, cm/min	12.0
Maximum depth of cut, mm	0.04
Width of scorched zone, cm	0.02
Average laser power, W	20
Laser spot diameter, μm	30-300
Supply voltage, V	220/380
Power consumption, kW	2
Overall dimensions, mm	1150×700×1200
Mass, kg	200

The Kvant-10 setup. This is a spot welding machine used to join parts of various materials 0.05-0.10 cm thick in the production of electronic devices, relays, and precision instruments [2, 9, 12].

The setup is equipped with a Nd-glass pulsed laser. The optical system gives a 33 × magnification for control of the process of welding. The design allows the use of various fixtures for the pieces to be welded.

The machine is complete with a dust-exhaust chamber and can produce welds in an inert cover gas. The constructional arrangement is such that the machine can yield vacuum-tight seam welds produced

Fig. 15.19. Schematic diagrams of optical systems for the K-5 laser setup (*a*): *1*, *4*, cavity mirrors; *2*, Q-switch; *3*, laser rod; *5*, *8*, *11*, *18*, turning cold-light mirrors; *6*, *7*, optical elements of lighting telescope system; *9*, mask; *10*, collecting lens; *12*, projection lens; *13*, protective glass plate; *14*, workpiece; *15*, lens; *16*, condenser; *17*, lighting lamp; *19*, sight graticule with crosshairs; *20*, eyepiece; for the Kvant-17 laser setup (*b*): *1*, YAG laser rods; *2*, pump flashtubes; *3*, spherical mirrors of the same transmittance; *4*, total internal reflection prisms; *5*, focusing lenses; *6*, integrated circuit packages; *7*, grid-type pallet of charging device; *8*, power source (PS)

by overlapping spots at a weld rate of up to 30 mm/min. The pulse energy is stable. The distance from the focusing lens to the target surface is 60 mm.

Technical Data

Laser spot diameter, mm	0.4-1.4
Rated pulse energy, J	10
Maximum pulse energy, J	30
Pulse length, ms	4.0
Pulse repetition rate, ppm	60
Flashtube life, shots	300×10^3
Supply voltage, V	220/380
Power consumption, kW	6
Overall dimensions, mm:	
machine	$1225\times1040\times930$
power unit	$1375\times595\times595$
Mass, kg:	
machine	150
power unit	200

The Kvant-12 setup. The machine is complete with a YAG laser intended to produce seam welds between thin parts of similar and dissimilar metals and alloys with a minimum of deformation of the parts and a high rate of local heating. This laser welder finds applications in the production of electronic and semiconductor devices, instruments of fine mechanics, and eleotromagnetic miniature relays [9].

The laser head is fitted with a two-loop cooling system. The optical viewing system provides a $40\times$ and $20\times$ magnification with the use of two interchangeable lenses. Apart from the repetitively pulsed mode of operation, the laser can weld in the single-pulse mode with hand triggering.

Technical Data

Rate of welding of kovar at weld penetration of 0.3 mm, mm/min	150
Average laser power, W	30
Pulse repetition rate, Hz	up to 20
Pulse energy, J	up to 3
Pulse length, ms	1.5, 2.0, 2.5, 4.0
Laser spot diameter at the focus of optical system, mm	0.25-1.0
Supply voltage, V	220/380
Power consumption, kW	6
Overall dimensions, mm:	
machine with the laser	$1000\times950\times1230$
power unit	$595\times595\times2000$
Mass, kg:	
machine with the laser	250
power unit	350

The Kvant-16 setup. It is used for surface hardening of dies and molds made of tool steels. Laser hardening decreases the wear rate of parts by a factor of 2 to 4 as compared to that of parts subjected to conventional heat treatment. The setup can be adapted to pulse welding of metals with a weld penetration of up to 0.7 mm [9].

Technical Data

Heat Treatment	
Coverage rate, mm^2/min	50
Case depth, mm	0.1
Incident laser beam diameter, mm	2-5
Pulse energy, J	30
Welding	
Weld depth, for nickel, cm	0.07
Incident laser beam diameter, cm	0.07-0.14
Pulse energy, J	30
Pulse length, ms	4-7
Pulse repetition rate, Hz	0.1-1.0
Laser rod size, cm	1.2×26.0
Flashlamp	IFP-5000-1
Magnification of optical detection system, ×	6.2-12.5
Field of vision of optical detection system, cm	0.7-1.4
Working focal length of lens, cm	6.0
Maximum size of piece welded, cm	10.0×10.0×5.0
Supply voltage, V	220/380
Power consumption, kW	12
Overall dimensions, mm:	
machine	122.5×104.0×95.0
power unit	137.5×59.5×61.0
Mass, kg:	
machine	150
power unit	200

The Kvant-18 setup. The machine is designed for pulsed heat treatment of the working surfaces of metal parts to increase their wear resistance and also for spot welding of metals.

It can find application for heat treatment of dies, cutting and measuring tools used in the production of electronic devices and for welding parts and assemblies of electronic devices.

The Kvant-18 uses a laser head with one rectangular Nd-glass rod or four cylindrical Nd-glass rods which emit the beams of the corresponding profiles to produce rectangular or round hardened spots on the target surface. The rectangular beam scanned over the target surface can harden long rectilinear edges of tools of complicated shapes.

The optical system secures a stable position of the focal plane with respect to the surface of treatment and can smoothly vary the

beam spot size over a wide range. It is thus possible to adjust the conditions of hardening of various tools by slightly changing the size of the hot spot. The thermal conditions of the laser head remain invariable with changes in the spot size. The use of a long-focus lens offers the possibility of hardening the tools whose profile varies in height by ± 10 mm without shifting the target along the vertical axis. The optical system includes adjusting elements (semireflecting mirrors) which distribute more uniformly the laser power density over the focal spot and, hence, improve the quality of heat treatment. The Kvant-18 laser setup is a more reliable machine than the Kvant-16 and is capable of surface hardening with laser pulses of a wider range of tools and machine-tool attachments.

Technical Data

Coverage rate of hardening, mm²/min	
in argon cover gas	to 8.00
in air	to 9.00
Welding speed, spots per min	to 30
Maximum size of workpiece surface hardened or welded, mm	200×200×300
Dimensions of work zone, mm	600×600×500
Maximum penetration depth, for Ni-Co alloy, mm	1.5
Maximum depth of hardening, for high-quality carbon tool steel, mm	0.16
Incident laser beam diameter, cm	
in heat treating	0.4-1.6
in welding	0.1-0.4
Control range of pulse energy, J	8 to 130
Pulse repetition rate, Hz	no less than 0.5
Pulse length at 10% of pulse maximum level, ms	no less than 8-10
Power consumption, kW	no more than 20
Mass of setup, kg	1400
Area of work station, m²	11

The Kvant-17 setup. This is a special-purpose two-beam semiautomatic welder with a YAG laser intended for sealing metal-glass integrated-circuit packages with lead-out pins. Each side of the package can measure from 10 to 40 mm [9].

Technical Data

Throughput capacity in sealing 3.0×4.0-cm integrated-circuit packages, pack per hour	to 120
Total thickness of edges welded, mm	0.5-0.8
Energy in each pulse, J	4
Total average laser power, W	80
Pulse repetition rate, Hz	10
Pulse length, ms	1.5, 2.0, 2.5, 4.0

Supply voltage, V	220/380
Power consumption, kW	12
Overall dimensions, mm:	
welding bench	910×700×1080
power unit	595×595×2000
Mass, kg:	
welding bench	200
power unit	350

The Cristal-6 setup. This is a Nd-glass laser machine designed for milling and hole piercing in various metals and nonmetals such as ceramics, glass ceramics, ferrite, and ruby [9].

Technical Data

Diameter of hole drilled, mm	0.1-0.6
Depth of hole drilled or depth of cut, mm	to 3
Width of groove cut, mm	0.005-0.02
Treatment accuracy class	3-4
Pulse energy, J	0.5-4.0
Pulse repetition rate, Hz	0.5-20
Power consumption, kW	4.5
Overall dimensions, mm	1250×950×1300
Wear-out life of the main elements of the laser run idle without performing schedule work, millions of shots:	
flashtube	0.5
laser rod	4
cavity mirrors	20

The Cristal-7 setup. The machine employs a Nd-glass laser to pierce through holes in parts intended for use as tools to work pieces in contours on electrospark discharge machines [9].

Technical Data

Laser wavelength, μm	1.06
Pulse length, μm	150-200
Pulse energy, J	0.1-5
Pulse repetition rate, Hz	0.5-10
Diameter of hole drilled, mm	0.05-0.4
Accuracy of motion along coordinate axes, mm	±0.003
Depth of hole drilled, mm	to 4
Power consumption, kW	4.5
Overall dimensions, mm	1700×900×1500

The Cristal-8 setup. This is an automatic machine furnished with a Nd-glass laser to trim thick film resistors. The laser trimmer operates at a frequency of 20 Hz.

Technical Data

Thickness of film trimmed, μm	to 30
Width of cut, mm	0.1-0.2
Accuracy of trimming, %	±5
Machine time required to trim one resistor, s	1.5
Pulse energy, J	0.1
Pulse length, ms	0.1-0.2
Power consumption, kW	2.5
Overall dimensions, mm	2800×1100×1500
Mass, kg	400

The Cristal-10 setup. The machine operates with a nitrogen laser intended to trim film resistors of integrated circuits. The work table can move to provide motion of the beam from one circuit module to another in the range of the wafer size. The scanning system enables the beam to travel within the limits of one module [9].

Technical Data

Thickness of film cut, μm	to 1
Width of cut, μm	5-30
Speed of cutting of resistor film, mm/s	4
Area trimmed, mm	60×60
Laser wavelength, μm	0.33
Laser pulse power, kW	1-2
Pulse length, ns	10-15
Pulse repetition rate, Hz	100
Power consumption, W	500
Overall dimensions, mm	2000×600×1180

The Cristal-1A setup. The machine is designed to cut glass tubes by a CO_2 laser beam using the technique of controlled fracturing through rapid heating [9].

Technical Data

Accuracy of fracturing, mm	0.1
Nonsquareness of cut, mm	no more than 0.1
Time of cutting of tube, s:	
glass S-87-1	2-4
glass S-49-2	5-20
Tube diameter, mm	5-60
Tube wall thickness, mm	0.5-2.0
Laser power, W	25-40

The Korund setup. This is a Nd-glass laser driller, which finds wide use for rough drilling of holes in watch jewels [2, 9]. The laser drills a hole by a series of pulses 50 to 75 μs long, each delivering 0.1 to 0.5 J of energy. Multiple-pulse laser drilling rules out cracking, reduces the thickness of the scorched layer to 2 μm, and en-

sures an accuracy of holes to within 0.02 mm. The laser driller can be set for manual or automatic operation at a specified pulse frequency. The rate of automatic hole drilling is one hole per second. The setup is complete with an automatic charging device and a forced water cooling system.

Technical Data

Diameter of hole drilled, mm	0.03-0.15
Thickness of material drilled, mm	to 1.0
Pulse energy, J	to 0.5
Pulse length, μm	50-75
Pulse repetition rate, Hz	to 10
Wear-out life of the main elements of the laser run idle, without performing schedule work, millions of shots:	
flashlamp	1
laser rod	5
cavity mirrors	20
Supply voltage, V	220/380
Power consumption, kW	2.0
Overall dimensions, mm	600×1200×1400
Mass, kg	300

The AK-345 and AK-378 setups. These are laser drillers primarily used to pierce holes in ruby watch jewels.

Technical Data

	AK-345	AK-378
Diameter of hole drilled, μm	50-80	80-200
Jewel thickness, mm	0.5	0.5, 0.75
Number of pulses to pierce one hole	2	4, 6
Time required to pierce one hole, s	0.8	0.8, 1.2
Pulse energy, J	0.2, 0.5	1.5
Pulse repetition rate, Hz	2.5	5

Numerically controlled (NC) 4222 F2 machine tool [10]. The setup is a modification of the 4222 machine tool which is the base model of a few designs intended to perform specific operations such as marking and trimming of diamonds and cutting in desired contours. The base model uses a projection system for positioning the beam on the target, which enables a smooth adjustment of the laser spot in the zone of interaction. This base model is made complete with two replaceable laser heads using Nd-glass rods. The elliptic resonator houses either a 5 × 100-mm rod with an IFP-800 flashtube or a 6 × 130-mm rod with an IFP-1200 flashtube.

Structurally, the 4222 model is a T-shaped work station consisting of a column to carry the laser head with beam positioning optics and a moving *x-y* positioning work table with fixtures, which is set up on a bedplate welded to the column.

The 4222 F2 machine tool is designed to drill a large number of holes 10 to 200 μm in diameter through workpieces in order to produce the elements of gas-discharge tubes, grids, and other parts and also to cut grooves in difficult-to-reach areas. The numerical control (NC) system ensures the automatic operation of the laser and x-y positioning of the work table according to the assigned program. The table drive is built up of two step motors running in discrete steps of 10 μm. The table moves along two coordinate axes for distances of 300 and 100 mm respectively. The NC system enables the laser to pierce holes along each coordinate axis at a pitch of up to 10 mm irrespective of one discrete step. The number of pulses needed to pierce one hole ranges from 1 to 100. The hourly output of the laser driller is over 10 000 holes at a pitch of up to 1.5 mm. Provision is made to program the process of cutting in complicated contours.

The Kizil setup. The machine utilizes a Nd-glass laser to pierce fine holes in thin films and metal foil [4]. The laser operates in the pulsed mode. The Q of the cavity can be switched to extract pulses with durations of a few tens of nanoseconds.

The gas laser setups. Gas lasers can operate in the continuous-wave mode or the repetitively pulsed mode at a high repetition rate and have ten times the efficiency of solid-state lasers, so that they can work materials at appreciable rates and perform an extended range of operations. In comparison with solid-state lasers, gas lasers display a better reproducibility of the spatial and temporal profiles of the beam, beam energy, and other parameters. These lasers are in many cases fairly easy to attend, and well developed models feature high reliability and prolonged service life. Table 15.3 lists the output characteristics of some industrial gas lasers and also presents the characteristics of two solid-state lasers for comparison.

The type OKG-15 CO_2 laser operates in the pulsed mode using for the purpose a requisite power unit and a pump. It can find efficient applications as a tool to pierce holes through nonmetallic materials, to trim thick film resistors, and perform other operations [4, 7]. For example, the TILU-1 setup equipped with the OKG-15 laser is a high-efficiency laser resistor trimmer which has replaced the entire automatic resistor-trimming line consisting of 20 pulsed ruby lasers of the SU-1 type.

A nitrogen laser is convenient for use as a cutter and trimmer of thin films. An example is the nitrogen laser which operates at a wavelength of 0.33 μm and emits 0.01 to 0.1 MJ of energy in a pulse with 10-40 ns duration at a pulse repetition rate of a few hundred hertz. The short wavelength facilitates the beam focusing and the short pulse generally causes no damage to the substrate as it vaporizes lines in thin films. Besides, since the pulse repetition rate is high, the process can be run at an increased rate. Lasers of the LGI-21 and Signal-3 models are commercially available for thin-

TABLE 15.3. **Output Characteristics of Some Industrial Gas Lasers and Two Solid-State Lasers**

Laser type	Laser medium	Pulse repetition rate, Hz	Laser wave length, μm	CW power, W	Pulse energy, J	Pulse length, $\tau \times 10^4$, s	Lifetime of elements, h	Purpose
LTI-5	Nd-YAG	50	1.06	—	0.01	2	—	Experimental
LTI-4	Nd-YAG	100	1.06	—	0.1	2	—	Cutting and scribing of silicon
LG-22	CO_2-N_2-He	CW operation	10.6	40	—	—	500	Welding, cutting
LG-17	CO_2-N_2-He	CW operation	10.6	30	—	—	1000	Cutting of structural glass shapes, scribing of glass plates, trimming of resistors, production of printing plates
OKG-15	CO_2-N_2-He	CW operation	10.6	5	—	—	500, 2000	Trimming of thick film resistors
OKG-17	CO_2-N_2-He	CW operation	10.6	40	—	—	500	Trimming of thick film resistors
LG-137	CO_2-N_2-He	CW operation	10.6	15	—	—	300	Trimming of thick film resistors

Continued

Laser type	Laser medium	Pulse repetition rate, Hz	Laser wave length, μm	CW power, W	Pulse length, J	Pulse length, $\tau \times 10^4$, s	Lifetime of elements, h	Purpose
Impulls	CO_2-N_2-He	50	10.6	—	2	1	1000	Experimental
LUND-100	CO_2-N_2-He	CW operation	10.6	100	—	—	—	Experimental, general
LGI-21	N_2	100	0.3371	—	10^{-5}	1×10^{-8}	500	Processing of thin films and semiconductors
Signal-3	N_2	150	0.3371	—	10^{-4}	3×10^{-8}	1000	Processing of thin films and semiconductors
LGI-37	Ar	100-700	0.5260 0.5330 0.5397 0.5955	—	6×10^{-4}	3×10^{-7}	100	Experimental
LG-109	Ar	CW operation	0.4880	1	—	—	100	Experimental
OKG-19	He-Cd	CW operation	0.4416 0.3250	50×10^{-3} 10×10^{-3}	—	—	300	Experimental
LGI-17	He-Cd	5000	1.118 1.150 1.206	—	4×10^{-3}	8×10^{-5}	300	Experimental

film processing both in air and in vacuum, which produce a circular beam in cross section (similar nitrogen lasers available in other countries emit a rectangular beam). These lasers can be used to make trimming cuts in high-value film resistors so as to trim them to close tolerances, adjust quartz crystal vibrators for the specified frequencies, and produce gap capacitors. They are also suitable for the separation of *pn* junctions in the fabrication of semiconductor devices, formation of mesa-structures, scribing of integrated circuit silicon wafers, and precision cutting of semiconductor materials such as single crystals of indium antimonide, gallium arsenide, and germanium.

A helium-cadmium laser offers promise as a processing tool for use in photochemistry since it affords the highest quantum energy as against other lasers. A high-coherent helium-neon laser is also applicable for material processing and can be used to best advantage for thin film evaporation. It emits up to 250 W of power in a pulse at a pulse repetition rate of up to 2 000 Hz.

The LURM automatic laser setup for program-controlled single-ply cutting of nonmetallic materials. This setup is designed for applications in various branches of light industry. It can also find uses in aircraft, shipbuilding, automotive, chemical, and other industries [7]. The work station consists of a CO_2 laser of the Kardamon model with an optical system, a numeric control unit, and a two-axis system which has an automatic feeder to advance the material reeled off the roll to the proper location and a pickup device for the cut pieces. The laser cutting head is mounted on a carriage moved along the guide of a gantry by means of a rack-and-gear drive. The gantry is a platform with two posts fastened to the frame of the setup. The cutting table with an aluminum honey-comb surface runs on a rail track between the posts. The table is set in motion by means of the rack gear of the feed mechanism. The vacuum pumping system exhausts the blowoff material and thus holds down the material when it is spread on the honey-comb surface.

The accuracy of the patterns cut out from the parent sheet is 0.8-1.0 mm.

Technical Data

Type of setup	Single-position
Maximum dimensions of pieces cut out, cm:	
width	160.0
length	150.0
Linear speed of cutting, m/min	to 42
Drive of feed mechanism	Electrohydraulic, step type
Program control system	Two-axis, NC, continuous-path
Type of program unit	EM-907

Type of interpolation	Curvilinear
Working pulse frequency, Hz	2 000
Maximum frequency for a high-speed step, Hz	8 000
Data input means	Eight-track punched tape, with parity check
Laser used	CO_2 type
Laser wavelength, μm	10.6
Lasing	Continuous-wave
Output power in multimode operation, W	800
Cooling	Forced, fluid
Cooling water injection rate, l/min	no more than 5
Power consumption, kW	27.5
Three-phase supply voltage, V	380
Overall dimensions, mm	6500×3540×1860
Mass of setup, kg	2400

The industrial laser setup for program-controlled cutting of textile materials [8]. This laser cloth cutter consists of a CO_2 laser of the Katun-1 type operating at 800 W, two-axis gantry-type unit, and laser cutting table. The setup is a part of an automatic transfer line for multiple-ply cutting of textiles.

Technical Data on the Setup

Laser power, W	800
Focused spot diameter, minimum, mm	0.4
Dimensions of pattern cut, mm	6000×2000
Cutting speed, cm/min	0.6-1.0
Pressure of cut-assist gas in cutting head, MPa	0.4
Water feed rate for resonator cooling, l/min	20
Input power from three-phase 220/380-volt 50-hertz supply line, kW	30

Technical Data on Katun-1 Laser

Laser wavelength, μm	10.6
CW power, W	800
Diameter of beam on semireflecting mirror, mm	5.5
Beam divergence, rad	1×10^{-3}
Working pressure of gas mixture, Pa	1×10^{4}
Ratio of gas mixture components	1 : 1.5 : 10
Number of gas-discharge tubes	6
Number of flat turning mirrors of resonator	10
Power consumption, kW	25
Overall dimensions, mm:	
laser	6500×600×1300
power unit	600×1300×1800
gas blower enclosure	600×1300×1800
Cutting head, mm	
focal length of focusing system	200
focused spot diameter	0.04
Assist-gas pressure, MPa	to 0.5

The gaseous decomposition products formed in the course of cutting are removed through the cavities in the cutting table by means of an exhaust ventilation system. The laser cutting assembly is complete with a digital curvilinear interpolator.

The Almaz-5 gas laser cutting setup. The machine utilizes a gas laser to cut 2.5 × 3-m patterns from the parent blank of corrosion-resistant steel up to 5 mm thick at a cutting rate of 0.5-4.0 m/min with an accuracy of ±0.5 mm. The laser operates at a maximum power of 800 W. The setup utilizes a production-type electric motor drive and an NC unit. The gantry structure accommodates the drives of the cutting head, gas pipelines, and electric power supply mains.

The laser cutter affords an increased accuracy of cutting at high rates. The equipment specifications stipulate the limits of percentage deviations of cut piece sizes, which lie between ±0.3 and ±0.5 mm. Cutting to within ±0.1-0.2 mm is also practicable in definite working conditions. The maximum rate of metal cutting ranges between 10 and 15 m/min.

The equipment setup includes reflecting mirrors, a beam shutter, a cutting head, and a gas-feed piping system with solenoid-operated valves. The reflecting mirrors are fitted with a device intended to position the beam along the axes of the guides of the setup. The shutter of the electromagnetic type serves to intercept the laser beam during the cutting operation.

The cutting head has a nozzle coaxial with the beam to allow the gas to flow to the zone of cutting and an electromechanical floating arrangement to stabilize the position of the focal plane of the laser beam.

The URSP-1 laser setup for separation of glass shapes. This laser glass cutter operates on the principle of controlled fracturing along the desired path; the focused laser beam rapidly heats the glass surface and the mechanical stresses so produced lead to a localized fracture which follows along the beam path [2]. The setup uses two sealed-off continuous CO_2 lasers each emitting 25 W of power in the beam and two focusing systems each moving in one plane along the straight path of the line of fracture. Such an arrangement enables the lasers to cut in two opposite planes, for example, glass shapes in the form of a rectangular box or a channel bar with a wavy cross section and also sheet glass in the continuous process.

Technical Data

Rate of cutting, m/s	to 3.5
Maximum height of glass section, mm	60
Glass section width, mm	600
Glass thickness, mm	10
Supply voltage, V(Hz)	220 (50)
Power consumption, kW	2

Overall dimensions, mm . . . . . 3350×1410×500
Water cooling system:
pressure, MPa 1.5
flow rate, l/min . . . . . to 10

The laser engraving machine. It is built around an automatic electrogravure machine and intended for the fabrication of nonmetallic printing plates [12]. The use of the focused laser beam instead of the graver has increased the production rate approximately fivefold, improved the reproducibility and reliability of engraving plates, and prolonged their life. The laser is equipped with an electrooptic shutter based on gallium arsenide to modulate the beam intensity.

The performance characteristics of the laser engraver are the following: the screen size is 27, 34, 48, 54, 68, and 96 lines per cm; the linear speed of engraving is up to 10 m/min; and the maximum dimensions of the laser-engraved pattern are 45 by 35 cm. The overall dimensions of the machine are 163.6 × 60.0 × 130.0 cm. The intake power from a 220-V, 50-Hz supply line is 2 kW. The continuous CO_2 laser delivers 25 W of power to the focal area, the minimum diameter of which is 100 μm.

The Kvant-15 setup. The machine is complete with a YAG laser providing the output at a 1.06 μm wavelength and intended for spot and seam welding of various metals and alloys. This laser welder is similar in design to the Kvant-12 setup, but unlike the latter model, it incorporates two optical pumps which increase the laser power output and enable the laser to weld at a higher speed.

The Kvant-15 can also be adapted to cut metals and heat treat the surfaces of workpieces and tools. The performance and output characteristics of the setup are the following: the weld speed is 60 to 350 mm/min; the energy in a pulse is no less than 6.3 J; the pulse duration is 0.6-4.0 μs; the laser spot diameter is 0.5-1.3 mm; the pulse repetition rate is up to 12 Hz; and the penetration depth is up to 1 mm.

The Kvarts-2 nitrogen laser setup. The machine can be used at laboratories and shops to trim monolithic quartz crystal filters and precision crystal vibrators, so as to adjust them for the desired frequencies, and also to perform precision engraving on thin metal films [12]. The laser trimmer operates in the pulsed mode and delivers 1 000 W of power in a pulse to the target surface. The adjustable pulse repetition rate ranges from 1 to 100 Hz. The laser operates with a projection system to produce trimming cuts on the parts in the desired contours. The square mask inserted in the beam provides engraved patterns on the part, which measure 10 by 10 mm and 100 by 100 mm. The optical viewing system gives a 100 × magnification. The linear field of view is 0.075 cm. The work table can move in the horizontal plane along x and y axes and also in the vertical direction along the z axis.

The Modul setup. The machine is designed to make cuts in thick films and to trim film resistors. Its use has made it possible to increase the production rate and improve the quality of resistors, whose values are reproducible to good tolerances [12]. This laser trimmer is made complete with a repetitively pulsed CO_2 laser which emits a train of pulses with a peak power of 1 kW, a pulse duration of 150 μs, and a pulse repetition rate of 150 Hz. The intake power from the supply line is 1 kW. The setup measures 300 × 200 × × 250 cm and weighs 300 kg.

The UPR-1 CO_2 laser setup. This is an automatic laser trimmer intended to trim the resistors of thick-film integrated circuits [9]. The adjustment of coordinate axes for the onset of resistor trimming is made with the aid of a template. The production rate of the laser setup is up to 1500 resistors per hour. Trimming is accurate to within ±3% and the pattern of trimming measures 2.0 by 2.0 cm. The CO_2 laser delivers 0.05 J of energy in a pulse of 0.2 ms duration and operates at a pulse repetition rate of 35-100 Hz. The setup consumes 3 kW of power, measures 110 × 130 × 240 mm, and weighs 250 kg.

The LNR-1 CO_2 laser setup. This is an automatic machine designed for cutting wafers into resistor pieces [9]. The production rate is 1 500 resistors per hour. The rated values of the resistors range from 100 to 5×10^6 ohms. The accuracy of cutting is ±2-4%. The width of the groove cut is 0.01 to 0.03 cm. The CO_2 laser operates at 5-10 W of average power and emits 0.1-ms duration pulses at a pulse repetition rate of 300 Hz. The overall dimensions of the automatic laser cutter are 200 × 75 × 200 mm.

15.2. ELECTRON BEAM SETUPS

Setups of the ELURO type for hole drilling and microwelding. These are, as a rule, universal assemblies designed for hole drilling, cutting, and microwelding of parts used in the devices of electronics, radioelectronics, fine mechanics, etc. The features of the ELURO setup are the following [5].

1. The gun with a high accelerating voltage of 75-200 kV together with a stabilized power source produces a beam 10 to 100 μm in diameter, which has fairly stable parameters and delivers a sufficiently high power. The electron gun can operate both in the continuous and the pulsed mode.

2. Electromagnetic deflectors control the beam and move it over the target surface within a small area at a high accuracy.

3. Manipulators ensure an accurate alignment of the zone of interaction and the electron beam that impinges on the target surface and offer the possibility of program-controlled positioning of the target.

4. Electric drives of the manipulators offer a stability of the speed of target travel to within $\pm 1\%$ with variations of the supply voltage.

5. Optical viewing systems used to control the process of hole drilling or welding give a magnification of 50 to 100 diameters.

6. The vacuum in a chamber up to 0.5 m^3 reaches no more than 5×10^3 Pa. The time it takes to pump the chamber for the working vacuum is 3 to 15 min.

7. The electron gun sited on the chamber is stationary, while the target is set in motion.

Technical Data on the ELURO Setup

Anode voltage, kV	to 100
Electron beam current, mA	10
Diameter of the beam focused on the target surface, μm	10
Pulse operation:	
pulse repetition rate, kHz	1.0-3.3
pulse length, μs	2-14
Motion of the table in horizontal plane along each axis, maximum, mm	150-200
Accuracy of table positioning, μm	3-5
Beam diameter with the setup operating as a scanning microscope, μm	1
Dimensions of the surface area swept over by the beam, mm	4×4
Working pressure in the chamber, Pa	5×10^{-3}
Time to reach working pressure, min	10-15

The factors conducive to the instability of the pulsed beam and, hence, the errors in the reproducibility of the diameters of the holes drilled have been treated in work [14].

Variations of the EB current of the triode gun used in the ELURO setup result from the following factors: the instability of accelerating voltage V, grid bias voltage V_g, and modulation voltage V_m; changes in the pressure p of the residual gas in the chamber and cathode temperature T; and deviations of the geometrical parameters of the gun due to heating of the cathode unit, particularly the deviation of the dip of the filamentary cathode in the cavity of the control electrode called the grid. This dip of the filament determines the cutoff (blanking) voltage V_c of the gun. The electron beam current as a function of the above mentioned parameters can be written as

$$I = f(V, V_g, V_m, p, T, V_c)$$

Since the pressure p in the gun chamber is generally invariable, the effect of p can be neglected. The effect of temperature T can be judged from the effect of filament current I_F since at a constant

filament voltage, the cathode temperature depends on I_F. Hence,

$$I = f(V, V_g, V_m, I_F, V_c)$$

A change in the beam current, ΔI, due to variations of the accelerating voltage ΔV, is given by the expression $\Delta I = SK\,\Delta V$, where $S = dI/dV_g$ is the transconductance of the electron gun and K the grid penetration factor defined as the ratio of the grid cutoff voltage to the beam voltage, $K = V_c/V$. The modulation (drive) characteristics of the electron gun of the ELURO setup model for accelerating voltages of 50, 75, and 100 kV are shown in Fig. 15.20.

As seen from the curves, the instability of the accelerating voltage results in the shift of the modulation characteristics. The instability of the grid bias voltage leads to the shift of the quiescent point on the modulation characteristic. The effect of the instability of modulation voltage V_m is similar, as is clear from the graph of Fig. 15.20*c*. These factors cause a change in the beam current by a value of ΔI, i.e. a change in the peak amplitude of current pulses.

Figure 15.21 displays the curves of beam current I_b as a function of filament current I_F for the EB setup under consideration. The curves *1*, *2* and *3* allow us to estimate the beam current deviations ΔI_1, ΔI_2, and ΔI_3 respectively, due to variations of the filament current.

When the setup is in operation, the heater of the cathode assembly heats up the cathode components and causes them to elongate. After switching the setup, the filament elongates over an initial period of a few minutes, following which its length does not change.

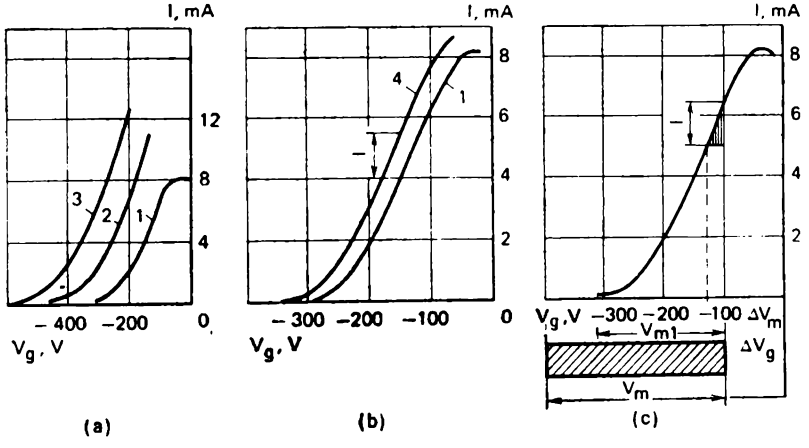

Fig. 15.20. Modulation characteristics (*a*) of the electron gun used in the ELURO setup and curves (*b*) and (*c*) illustrative of the shift of the quiescent point on modulation characteristics due to instability of electron gun parameters [14]: *1*, $V = 50$ kV; *2*, $V = 75$ kV; *3*, $V = 100$ kV; *4*, $V = 55$ kV

However, when the setup operates over a prolonged period, for example, a few hours, the grid begins to elongate under the action of heat transferred from the cathode. This leads to a continuous increase in the distance between cathode and grid and also to changes in the cutoff voltage and beam current: $\Delta I_3 = S\,\Delta V_c$, where ΔV_c is the deviation of the cutoff voltage for the electron gun. The absolute deviation ΔI_3 is a constant value since the value of the current applied to the filamentary cathode is the same in all the conditions of the setup operation. The deviation of the EB current due to changes in the filament current and grid heating shows up as the current drift and represents a systematic error.

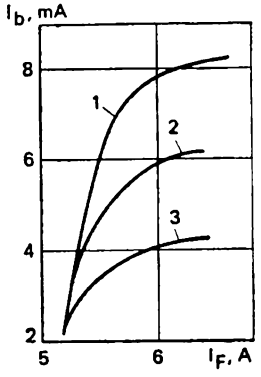

Fig. 15.21. Electron beam current I_b as a function of filament current I_F [14]

Table 15.4 lists the predicted and experimental values of the beam current deviations ΔI_1, ΔI_2, ΔI_3, resultant deviation ΔI, and deviation Δd of the diameter of the zone of interaction in 0.3-mm thick steel irradiated by the beam of the ELURO setup operating during 20 minutes and 1 hour [14]. The predicted values are the results calculated from the experimental modulation characteristics.

TABLE 15.4. **Deviations of the Beam Current and the Diameter of the Zone of Interaction in 0.3-mm Thick Steel**

Beam voltage V, kV	Beam current I, mA	Theory						Experiment		
		ΔI_1	ΔI_2	ΔI_3	ΔI	Δd, μm		ΔI, mA	Δd, μm	
						20 min	1 h		20 min	1 h
50	4	0.011	0.05	0.043	0.104	0.83	2.5	0.086	0.69	2.07
50	6	0.01	0.075	0.043	0.128	1.024	3.07	0.12	0.96	2.88
50	8	0.009	0.1	0.043	0.152	1.216	3.65	0.14	1.12	3.36
75	4	0.018	0.05	0.043	0.11	1.1	3.3	—	—	—
75	6	0.017	0.075	0.043	0.135	1.35	4.05	—	—	—
75	8	0.015	0.1	0.043	0.158	1.58	4.74	—	—	—

The main factors responsible for the deviations of the electron beam current from the nominal values in the EB setup under consideration are the instability of the source power and variations of the

cutoff potential of the electron gun due to changes in both the filament current and the dip of the filament.

The EB setups of the ELURO type can efficiently perform hole drilling or welding operations if the instability of source power is held in the range from 10^{-3} to 3×10^{-3} of the nominal value.

Setups for welding thin metal workpieces. These electron beam welders are available in three modifications, which have found extensive uses in industry. They employ commercial electron-optical systems which include electron guns as sources of electrons and focusing optics. An example of such a system is the A.852.04 model which provides an accelerating voltage of up to 25 kV and current of up to 200 mA.

The electron beam welders incorporate work tables to enable the beam to produce longitudinal or circular welds and pellets to accommodate up to 12 cylindrical parts in the chamber at a time.

The constructional arrangement of this type of EB welder allows for mechanical positioning of the electron-optical system in the chamber along with electromagnetic beam deflection.

As an example, let us consider a type LEV-80-1 welding setup developed on the basis of A.305.05 and A.306.13 electron beam welders [15].

The setup is capable of producing quality welds between parts 0.04 to 5.0 mm thick. It rules out spoilage due to burns in the case of breakdown occurring in a power source or electron-optical system. The oil-free exhaust system incorporated in the setup excludes the contamination of welded parts by hydrocarbons.

The LEV-80-1 utilizes a radically new electron-optical system which makes it possible to form an electron beam 0.1-0.2 mm in diameter without aperturing and to increase appreciably the beam power density. Control and pulse modulation of the electron beam is brought about by adjusting the anode voltage of the two-electrode gun.

The electron gun of the electron-optical system includes a quick-change filamentary cathode with its end facing the aperture in the grid. The setup is complete with a fundamentally new system of lighting of the weld zone in the chamber and a more elaborate eight-step mechanism for turning the pieces to be welded. The wobble of spindles of this mechanism does not exceed 0.01 mm.

Structurally, the laser welding work station consists of a laser welder proper and a power unit. The laser welder comprises the following main units: a welding chamber with a driving mechanism to rotate the pieces being welded and a system of lighting of the weld zone; an electron-optical system with a viewer to watch the process of welding; and an exhaust system with an automatic control unit.

Technical Data

Accelerating voltage, kV	25
Beam current, mA:	
in continuous-beam welding	0-80
in pulsed-beam welding	0-80
in single-pulse welding	0-80
Pulse length, ms	2-40
Pulse spacing, ms	5-200
Method of control of beam current	Anode voltage adjustment
Range of adjustment of anode voltage in electron emission system, kV	0-3
Size of the focused electron beam at beam current of 80 mA, mm	0.2
Inner dimensions of welding chamber, mm:	
diameter	300
length	775
Overall dimensions, mm	1100×1970×2000

Work [16] presented the results of experimental studies on the spatial structure of beams from a type A.852.26 electron-optical system employed in the LEV-80-1 setup. Figure 15.22 illustrates the experimental results (light circles) obtained with the aid of an analyzer using a probing molybdenum plate with an orifice 17 μm in diameter. The accelerating voltage of the setup was 20 kV and the beam current reached 0-100 mA. The cathode was made of lanthanium hexaboride LaB_6, which operated at 1 870 K and used the space charge to limit the emission current.

As seen from Fig. 15.22, the predicted values (full curve) agree well with the experimental values of the current density in the least cross section of the beam. The maximum deviation (6%) from the Gaussian curve only occurs at a level of $J = 0.05$ to $0.06\ J_{max}$. This type of deviation stems from the focusing system aberrations which initiate the circle of confusion.

The oscillograph records taken in different cross sections of the electron beam reveal that the Gaussian distribution also holds at a certain distance from the plane of the least diameter of the beam.

The curve of the current density distribution is plotted at a beam current I_b of 5, 10, 20, 30, 50 and 500 mA and also at a gun-to-analyzer distance l of 81, 96, 111, and 126 mm (the distance from the horizontal axis of the focusing system to the plane of the analyzer or to the target surface).

The experimental plots of the beam radius in the plane of the analyzer against the focusing current I_f of the magnetic lens are shown in Fig. 15.23. Each curve corresponds to a definite beam current and displays a clearly defined minimum. An increase in the beam current causes the minimum radius of the beam to grow. For example, at $I_b = 5$ mA the minimum radius is 0.087 mm, while at

I_b = 50 mA this radius increases to 0.2 mm. An increased beam current results in the shift of the image plane of crossover. Thus, if we focus the electron beam of a current of 5 mA to a spot of R_{min} = 0.087 mm in the plane of the analyzer and then increase the beam current to 30 mA without changing the magnetic lens current (I_f = 130 mA), then beam radius will grow to 0.28 mm in this plane. The electron beam will not be brought to a tight focus. To reach a minimum radius of 0.125 mm at I_b = 30 mA, the focusing current I_f should be increased to 132.5 mA.

The adjustment of the beam current thus leads not only to changes in the beam radius but also to the shift of the image plane of crossover along the optical axis of the system. This circumstance should be taken into account when passing from "adjusting" conditions to operating conditions.

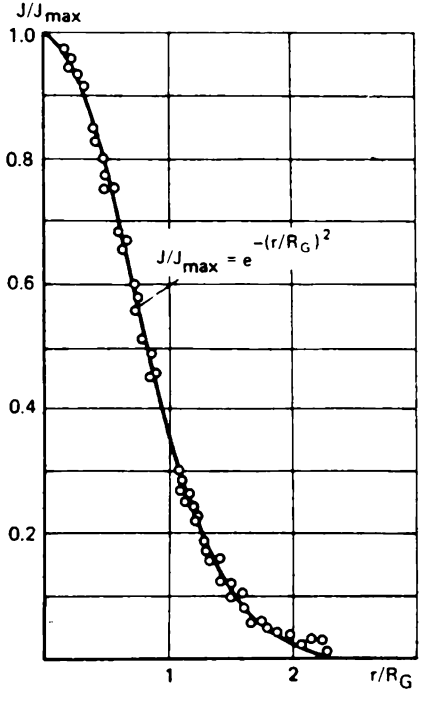

Fig. 15.22. Distribution of current density over the least cross section of the electron beam [16]

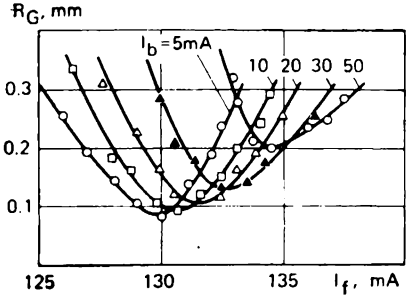

Fig. 15. 23. Gaussian radius R_G of the electron beam as a function of focusing current I_f of the magnetic lens at different values of beam current I_b and constant distance l from the gun to the analyzer (or target) [16]

The curves illustrative of the effect of the beam current on the Gaussian beam radius R_G in the plane of the least cross section of the beam are given in Fig. 15.24. The dependence of R_G on I_b is nonlinear. The radius R_G increases with the beam current. The dash curves on this figure illustrate changes in R_G at different values of the gun-to-analyzer distance l but at certain constant values of the beam current.

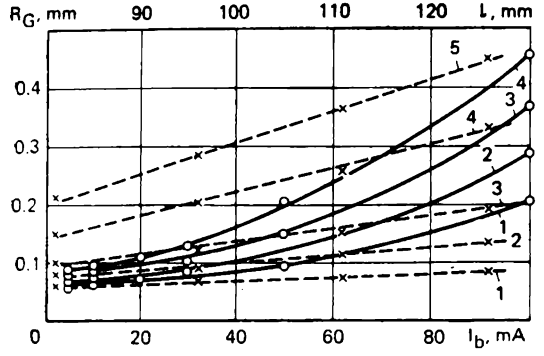

Fig. 15.24. Gaussian radius R_G of the electron beam in the plane of the least cross section as a function of beam current I_b and gun-to-analyzer distance l. Full lines are the plots of R_G against I_b at $l = 81$ mm (curve *1*), $l = 96$ mm (curve *2*), $l = 11$ mm (curve *3*), and $l = 126$ mm (curve *4*). Dash lines are the plots of R_G against l at beam currents of 5 mA (curve *1*), 30 mA (curve *2*), 50 mA (curve *3*), 80 mA (curve *4*), and 100 mA (curve *5*)

Changes both in the beam radius and in the position of the image plane of crossover with an increase in the beam current have an appreciable effect on the maximum current density J_{max}.

Figure 15.25 demonstrates the plots of the maximum current density J_{max} in the cross section of the beam and electron beam power density q against the beam current I_b. The curves display peaks whose positions depend on the value of the gun-to-analyzer distance l.

If the maximum current density in the least cross section of the beam is taken as the figure of merit of the electron-optical sy-

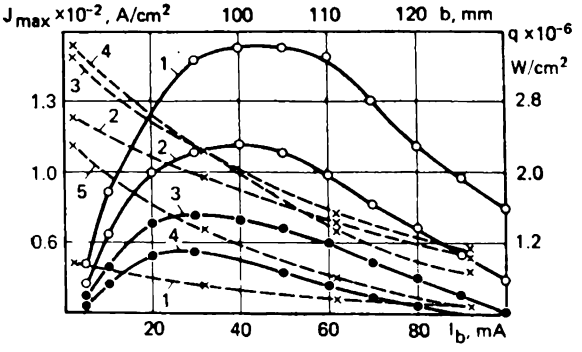

Fig. 15.25. Maximum current density J_{max} and maximum power density q versus electron beam current I_b and gun-to-target distance l. Full lines are the plots of J_{max} and q against I_b at distances l of 81, 96, 111, and 126 mm (curves *1*, *2*, *3*, and *4* respectively). Dash lines are the plots of J_{max} and q against l at I_b of 5, 20, 40, 60, and 80 mA (curves *1*, *2*, *3*, *4*, *5*, respectively)

stem, then the character of the recorded changes in J_{max} will define the optimal range of adjustment of the beam current. For the system under discussion, the optimal range of adjustment of I_b lies between 0 and 50 mA at a gun-to-target distance l of 81 mm.

The type ELU setup. There are a number of modifications of the ELU setup developed at the Research Institute of Technology and Industrial Engineering and intended for welding small, medium-size, and large pieces and assemblies [17].

The features specific to ELU modifications are that each is complete with a large vacuum chamber and includes special-purpose welding manipulators and auxiliary mechanisms.

The electron-optical system of the ELU incorporates an electron gun with a ribbon-type cathode and composite focusing optics. Power units provide an accelerating voltage of up to 60 kV and beam current of 35, 75, and 170 mA. The diameter of the electron beam spot is $\leqslant$0.6 mm. The setup is equipped with an exhaust system and oil-trapping devices.

The ELU-8 version of the setup is fitted with a sectional vacuum chamber which consists of three portions: the main chamber 1 150 mm in diameter and 1 650 mm in length; additional chamber 1 150 mm in diameter and 1 000 mm in length; and extension chamber 770 mm in diameter and 1 000 mm in length. The main and the additional chamber have ports where electron-beam welding guns are set up. Each gun is made complete with a driving mechanism to move the gun in the vertical direction with due regard for the diameters and shapes of the pieces to be welded.

The chamber is closed with a cover sliding on rollers along the guides of the frame. Interchangeable welding manipulators are mounted on the sliding cover and the electric drives of the manipulators are fitted on the frame.

In the ELU-9 setup and in a number of its modifications, the main and additional chambers and also the welding manipulators are made larger in overall dimensions. Besides, each design incorporates several ports for welding guns.

The ELU-10 setup has one vacuum chamber 2 300 mm in diameter and 4 100 mm in length and four ports for welding guns. The ELU-11 setup is a single-chamber EB welder with six ports for welding guns. The chamber is 2 850 mm in diameter and 6 000 mm in length. The ELU-12 setup is similar in design, but the length of the 2 850-mm diameter chamber is 7 200 mm.

The ELU-13 has the shape of a polygon in cross section. Its length is 10 000 mm, maximum width is 3 400 mm, and height is 5 400 mm. The drives of the welding manipulators of this setup are mounted inside the vacuum chamber.

References

1. F. F. Vododovatov, A. A. Chelny, V. P. Veyko, et al. *Lasers in industry.* Moscow, Energiya, 1985 (in Russian).
2. N. N. Rykalin, A. A. Uglov, and A. N. Kokora. *Laser machining and welding.* Moscow, Mir Publishers, 1978.
3. V. M. Vakulenko and L. P. Ivanov. *Power sources for lasers.* Moscow, Sovetskoe Radio, 1980 (in Russian).
4. V. P. Veyko and M. N. Libenson. *Laser material processing.* Lenizdat, 1973 (in Russian).
5. V. V. Bashenko. *Industrial electron beam setups.* Mashinostroenie, 1972 (in Russian).
6. I. S. Marshak, A. S. Doynikov, V. P. Zhiltsov, et al. Edited by I. S. Marshak. *Pulsed light sources.* Moscow, Energiya, 1978 (in Russian).
7. V. K. Raevich, G. A. Zaydenberg, A. N. Kokora, et al. *An automatic program-controlled laser setup for cutting out nonmetallic materials.* Kvantovaya Elektronika, 3: No. 7, p. 1543, 1976.
8. A. A. Biryukov, A. R. Molgachev, L. N. Safonov, et al. *Program-controlled cutting of textile materials.* Moscow, Legkaya Industriya, 1978 (in Russian).
9. *Laser equipment.* Elektronnaya Promyshlennost, No. 1, p. 69, 1976.
10. E. D. Vaks, A. M. Epikhin, V. A. Krushenok, et al. *Laser technology in instrument making and fine mechanics*: in Works of ENIMS in the field of laser hole drilling and cutting. 3d Series, Moscow, Mashinostroenie, 1980 (in Russian).
11. V. S. Bogoyavlenskiy, V. P. Ivanov, and A. A. Chelny. *Quantum electronics at the exhibition "Machine Engineering-721".* Elektronnaya Promyshlennost, No. 5, p. 96, 1972.
12. K. I. Krylov, V. T. Prokopenko, and A. S. Mitrofanov. *Application of lasers to machine building and instrument making.* Leningrad, Mashinostroenie, 1978 (in Russian).
13. A. V. Tikhomirov, M. V. Evdokushin, Yu. V. Kurlovich, et al. *Laser technology in instrument making and fine mechanic.* Moscow, Mashinostroenie, 1980 (in Russian).
14. A. N. Kabanov, M. A. Kalinin, L. I. Podgornova, et al. *The effect of beam current instability on the parameters of electron beam processing of material.* Fizika i Khimiya Obrabotki Materialov, No. 6, p. 26, 1970.
15. A. F. Khudyshev. *A new industrial prototype of the electron beam welder*: in Electron Beam Welding. Moscow, MDNTP, 1978 (in Russian).
16. K. E. Karashokov, N. T. Ostroverkhov, and V. K. Popov. *Experimental studies of spatial and temporal profiles of the electron beam.* Fisika i Khimiya Obrabotki Materialov, No. 2, p. 9, 1971.
17. A. I. Chvertko, O. K. Nazarenko, A. M. Svyatskiy, et al. *Electron beam welding equipment.* Kiev, Naukova dumka, 1973 (in Russian).

INDEX

Aberration, spherical, 61-65, 75, 545
Ablation problems, 159-165
Absorption, 12-17, 27
  flash, 224
  photoelectric, 211
  resonance, 13
  spontaneous, 13
Absorption coefficient, 68, 211-229, 280
  gas, 27
  glass, 22,23
  plasma, 223
Absorption cross section, 29
Absorption depth, 204
Absorption efficiency, 169
Absorption spectrum, 17
Absorptivity, 100, 149, 189, 197, 271, 272
  metal, 360
  optical material, 70
  temperature dependence, 147
Accelerating voltage, 74, 75, 90, 107, 504
Activator, 15
Alloying, 306-313
Alloying elements, 310
  methods of coating, 310-312
  redistribution, 341
Amorphization, 320-324
Analysis, laser-treated material, 321-324
  electron probe X-ray, 339
  heat transfer, 362
  laser cutting, 391, 393
  spectrum, 339
  X-ray, 344, 352
Angle of convergence, 368, 369
Angle of divergence, 55, 56, 59
Annealing, 278
Aspect ratio, 168, 186, 368, 406, 477
Austenizing, 297

Back pressure, 168, 178, 195, 452
Backscattering,
  electron, 109
Beam collimation, 53
Beam directionality, 53
Beam divergence,
  diffraction-limited, 53
  dye laser, 30
Bessel function, 134, 144, 183
Bethe law, 110
Biot criterion, 121
Biot's variational formalism, 163
Blowoff material, 209, 451
Boltzmann constant, 35, 75
Boltzmann equation, 207
Bouguer law, 122
Breakdown,
  cold gas, 244
  laser-induced, 244
  nitrogen, 251
  time, 251, 252
Bubble, 199-205
  diameter, 201
  fluctuation, 205
  growth, 199, 453
  growth rate, 204
  lifetime, 200-205

Capillary waves,
  attenuation factor, 192
Carbide synthesis, 267
Carbon distribution, 340, 341
  in laser interaction zone, 389
Cauchy problem, 181
Cavity formation,
  kinetics, 490-495
Chebychev-Hermite polynomials, 80
Chelates, 26, 27
Circular ripple waves, 190, 192
Cladding, 314-316, 324
Coherence,
  function, 52
  length, 52
  spatial, 51-53
  temporal, 51-53
  time, 52
Coherent radiation, 52
Coherent source,
  extended diffraction-limited, 55
Collision frequency 248-251
Collisions, 31, 197
  in atomic gas, 248
Compression wave, 453
Concentration coefficient, 101, 179
  current density, 80, 90-93
Condensation rate, 420
Cooling rate, 141, 283
Cover gases, 325, 344
Coverage rate, 334
  laser heat treatment, 334, 335
Current density distribution, 77-93
  electron beam, 77-81
    Gaussian, 77-93
Cuts, 396
  depth, 395-399
  dimensions, 396
  profiles, 397
  width, 395
Cutting, 386-402

Damage threshold, 70, 534, 547
Deep penetration,
melting, 182, 367-369
power density for, 187
welding, 358, 413, 417
Depth,
cut, 395-399
focus, 61, 62
hardening, 133, 280, 331
heat distribution, 281
melting, 133
total diffusion, 107
Deflectors, 338
Detonation wave, 212
Diffraction, 10, 62
Diffraction limited spot, 61
Diffraction limited value, 32, 55
Diketones, 26
Discharge current, 33
Discharge tubes,
folded, 539
sealed-off, 539
water-cooled, 33
Disintegration, 194
thermal model, 195
Distribution functions,
E-beam current, 83
Dwell time, 99, 186, 194, 195
Dyes, 29

E-beam
accelerating voltage, 74, 90, 107, 504
actigmatism, 89
cavity formation, 490-495
cross section, 93
current, 74, 578-580
current density, 74-89
cutting, 456
diameter, 75, 88
distribution functions, 83
evaporators, 507
film deposition, 501-503
fluence, 547
focusing, 469, 470
heating control, 523
hole drilling, 451, 456-467
aspect ratio, 462
brittle material, 466
metal, 461
pulsed, 461
rate, 458, 462
material removal, 458-461
efficiency, 460
melting, 463
parameters, 74-77, 81
positioning, 548
power density, 74
spatial-temporal characteristics, 105
voltage,
effect on weld depth, 484-487
welding, 469, 503
deep penetration, 469, 481
IC package, 503-514
methods, 487
parameters, 477, 478
wire bonding, 503, 504
E-beam interaction,
control, 515
with silicon, 462, 463
with solids, 451-468
E-beam setups, 573-581
drilling, 573
welding, 573, 577, 581
Einstein coefficients, 12, 13
Electromagnetic wave spectrum, 9
Electron beam, see E-beam
Electron gun,
characteristics, 575, 576
Electron scattering, 211
Emission, 12, 515-521
electron, 358, 515
fluorescent, 17
ion, 358
luminescent, 23
resonance, 12
secondary, 493, 515
spectrum, 30, 51
spontaneous, 12-17, 25
stimulated (coherent), 12-17
thermionic, 359, 493
Energy,
electron, 11
rotational, 11
vibrational, 11
Energy density, 56
Energy levels, 10
dyes, 30
liquids, 25
Energy spectrum, 11, 28
Euler's function, 119

Flash absorption, 224
Flashtubes, 534
characteristics, 538
coaxial, 535, 536
lifetime, 537
straight, 535, 536
xenon, 537
Fluence, 547
Fluorescence, 12-26
emission, 57
coherent, 16
spontaneous, 16

Fluorescence,
lifetime, 29
yield, 27
Fluorides, 21
Flushing process, 424, 425
Focal position,
E-beam, 454, 455
L-beam, 367
in cutting, 397
in drilling, 431-433
Focal spot size, 368
Focusing, 55, 469, 470
Focusing current,
E-beam, 74, 88
Focusing systems, 541-558
Fourier analysis, 116
Fourier criterion, 121, 122
Fraunhofer zone, 54, 55
Free oscillation, 236, 496-500
Freezing rate, 192
Fresnel zone, 54, 55
Fringe count, 18
Fusion front, 219
propagation rate, 342
Fusion zone, 168, 368, 474, 475
profiles, 176, 177, 470, 471

Gain, laser medium, 49, 57
Galilean telescope, 60, 64
Garnets, characteristics, 20
Gas breakdown, 239-252
optical, 234
threshold, 234
Gas pumping system,
CO_2 laser, 541
Gauss law, 114
Gaussian beam, 55
Gaussian distribution, 100
Glasses, 21-24
Green function method, 116

Hardened tracks, 327-331
Hardened zones, 332
Hardening, 277-325
in cover gas, 325
physical principles, 279
shock, 279
transformation, 278, 279
Heat affected zone, 91, 134, 138, 190, 194, 235
Heat balance equations, 175
Heat density distribution, 113, 114
Heat saturation coefficient, 134, 136
Heat penetration depth, 280, 281
Heat power density,
calculation, 122-133
critical (threshold), 137-139
Heat sink, 145
Heat sources, 100, 101
circular, 143
constant, 144, 155
fast, 137
Gaussian, 124-136, 180
moving, 134, 157, 363
linear, 173
plane, 105, 134
point, 170, 171
stationary, 115, 123, 170, 182
surface, 136, 182
volume, 105-133
Heat source problems, 115
Heat transfer, 128, 177
Heat transfer coefficient, 99, 124, 128, 145
Heat transfer equations, 116-132, 194
Heat transfer problems 280
linear, 115-133
nonlinear, 145
three-dimensional, 149, 270
unidimensional, 155
Heat treatment, 233, 277
methods, 278
physical principles, 279
Heating,
finite thickness plate, 124, 134
rate, 141-144, 157, 282
semi-infinite body, 122, 128, 135, 270
surface, 128
Hole drilling, 386-450
effect of pulse length, 428
parameters, 428
Hole profiles, 185, 431, 432
Hot spot radius,
calculation, 129

IC package sealing,
conditions, 506-509
methods 505
temperature calculation for, 506-509
thermal efficiency, 512
Interaction, 234, 286-297
E-beam, 112, 113, 145, 451
L-beam, 145
with Blowoff material, 209-230
with iron, 286-297
with iron-carbon alloys, 286-297
pulse laser, 286-297
thermal, 233
thermochemical, 233
Interaction time (see dwell time), 201

Interaction zone,
diameter, 240
E-beam-material, 112
hydrodynamic processes in, 168-189
L-beam-material, 92, 194
models, 109, 194
shielding, 234
thermal processes in, 98
Interface,
gas-liquid, 202
liquid-solid, 177
vapor-liquid, 218
Interference, 10
Inverse Bremsstrahlung, 211, 223
Inverse population, 31
Isothermal transformations,
in carbon steel, 334
Iterative process, 154

Kerf width, 392, 395-399
laser power effect on, 397, 398
Keyhole, 185-187, 361, 365
dwell time, 185, 365
Keyhole modeling, 185, 404-406, 417
Keyholing, 184, 362-367, 404-406, 469, 490
Knudsen layer, 197, 206

Laplace formula, 191
Laplace transforms, 116
Lasant, 15
requirements for, 16
Lasers,
chemical, 48-50
electron-transition, 49
vibrational transition, 49
CW, 33-35, 63
efficiency, 24, 28
energy levels, 10, 30
excitation threshold, 21
gas, 31-34, 567
argon, 10, 33, 35
CO, 41
CO_2, 10
electroionization, 41
fast gas transport, 37, 539
mirrors for, 71
optical materials for, 67
slow axial flow, 539
TEA, 38-40
vibration-rotation, 36
helium-neon, 10, 31, 35
ion, 33
medium for, 31-35
metal vapor, 34
molecular, 34-41
gas-discharge, 32, 35
gas-dynamic, 43
chemically pumped, 47
electrically excited, 47
electroarodynamic, 47, 48
heat-pumped, 44-47
liquid, 24-26
dye, characteristics, 30
materials for, 24-26
solid-state, 15
gallium arsenide, 10
materials for, 14, 15
Nd-glass, 10
ruby, 10
YAG, 20, 63
normal pulse (free-running), 286
quasi-continuous, 104
power density, 24
pulsed, 33-35, 286
spiking, 103, 193
wavelengths, 10
Laser
alloying, 306-313
continuous, 307
of iron, 308, 309
pulsed, 307
of steel, 308
amorphization, 320-324
cladding materials for, 314-316, 324
cutting, 386-402
gas assist, 387-389, 395
of nonmetals, 395
gas pressure conditions, 395
parameters, 398
rate, 388, 390, 396
specific energy for, 394
drilling, 280, 419-450
critical power density for, 419, 420
deep hole, 439
effect of pulse length on, 428
fine, 447
multiple-shot, 423-443
normal pulse, 434
precision, 441
process, 425-428
single-shot, 423, 445
split pulse, 449
glazing, 324
hardening, 286-354
examples, 351
of dies, 352
multimode, 331
in nitrogen, 343
normal pulse, 339, 340
by pulse overlapping, 325-329

Laser
heat treatment, 286-309
coverage rate, 335
examples, 350
features, 324
of iron, 286-305
of iron alloys, 286-305
requirements, 324
keyholing, 367, 406
preheating, 348
shock hardening, 317
welding, 358
continuous, 358, 363, 371
deep penetration, 358, 413, 417
pulse, 358, 362, 371
seam, 371, 402-416
technology, 370
Laser action, 9-14
Laser-as isted machining (LAM), 347
Laser beam (L-beam), 55-61, 100
collimation, 60
defocusing, 331
divergence, 59-61, 545
focused spot, 60, 61
focusing, 55-59, 396
Gaussian, 55-63
geometry, 64
patterns, 56
power density, 100, 101
radius, 58, 59
waist, 58
Laser beam guiding systems, 337, 543, 544
Laser cloth cutters, 391, 395, 570
Laser cutting machines, 569-573
Laser-drilled holes,
aspect. ratio, 439
depth, 440
dimensions, 430, 437, 443
large diameter, 443
profiles, 431, 432, 440
quality, 435
reproducibility, 436, 437, 447
surface finish, 434
Laser drillers, 557, 563-566
Laser efficiency, 24
CW, 35
dye, 30
pulsed, 35
Laser engraving machines, 572
Laser gain, 49, 57
Laser heads, 533, 534
Laser heat treating setups, 561-566
Laser-induced plasma, 217-224
Laser-induced spark, 214, 234
Laser-material interaction, 286
in argon, 239
CW, 297
effect of gases on, 242
in helium, 241
at high pressure, 234-239
in nitrogen, 235
Q-switched, 316
Laser materials, 14-35
active, 15
amorphous, 21
crystalline, 16
host, 15
liquid, 24
optical, 67-72
Laser medium excitation, 31
Laser medium gain, 49
Laser milling machines, 563
Laser optical systems, 336, 337
Laser operation,
continuous, 225-228
free-running (normal pulse), 102, 103
quasisteady-state, 225
spiking, 225-228
steady-state, 225
Laser polarization,
effect on cutting, 401
Laser power density, 100, 101, 197
critical, 205
Laser pulses, 102
free running (normal), 103
giant, 104, 105
Laser radiation, 9-32
characteristics, 51
effect on corrosion resistance, 346
focusing, 55
as heat source, 9-15
spatial-temporal characteristics, 100
Laser scribing machines, 559
Laser setups, 533-572
Laser-supported absorption (LSA) wave, 227, 233
Laser-supported detonation (LSD) wave, 253
Laser trimmers, 563-573
Laser weld joints, 374
designs, 375, 379
quality, 377
Laser welders, 557-572
Latent heat of melting, 472
Latent heat of vaporization, 362, 456
L-beam, see laser beam
Lenses, 62-66
focusing, 65,66
Lens beam expender, 64
Lens focal length, 56, 59
Liquid phase, 189-192

Lorentzian lineshape, 14
Luminescence, 15-30
  long-time, 29, 30
  short-time, 29, 30
Luminescence spectrum, 29
Luminescent quantum yield, 25
Low-threshold gas breakdown, 224

Mass transfer, 203, 246
  processes, 339
Material blowof , 201, 371, 373
Material removal, laser-induced, 419
  by vaporization, 420
Materials for laser, 15, 67-72
Maxwell distribution, 35, 207
Maxwell velocity distribution function, 182
Measurement methods,
  probing beam, 94-96
  rotating-probe, 76
  stationary-probe, 90
  thin-film probe, 92
Mediums for gas lasers, 31
Melt
  depth, 89, 365, 366, 465-467
    calculation, 132, 133
  flushing, 200, 374
    mechanisms, 202, 424, 451
  formation, 169
  solidification, 190
  surface deformation, 178-184
  temperature, 137, 175
  velocity potential, 190
  zone, 464, 465
    profile, 465-467
Melting, 358, 463
  efficiency, 369
Methods of producing beam image,
  contact, 335
  contouring, 335, 336
  projection, 335, 336, 546
Microhardness, L-beam induced, 238, 289
  armco-iron, 297
  steel, 299, 301
Mirrors, 71, 537, 558
Modes,
  cylindrical, 57
  Gaussian, 58
  longitudinal, 57
  rectangular, 57
  TEM, 56-64
Mode locking, 102
Models,
  Einstein, 183
  electron beam-solid interaction, 496, 498
  electron energy distribution, 106-109
  free-oscillation system, 497
  heat sink, 143
  laser cutting, 391
  melting process, 174
  point heat source, 130
  semi-infinite body, 130-132, 144, 362
  surface vaporization, 194-207
  temperature field, 130
  three-dimensional, 123
  unidimensional, 117-123,138,139, 195
  uniform irradiance, 285
  vacuum vaporization, 205-209
Molten pool, 168
  crystallization, 189
  radius, 172, 173
Monochromaticity, 51
Monte Carlo method, 108, 207

Nitride synthesis,
  laser-induced, 263, 265
Nitriding, 345, 346
  analysis, 345
  pulsed laser, 345
  Q-switched laser, 345
Nonlinearity conditions, 146
Normal distribution law, 180

Optical constants
  temperature dependence, 158
Optical breakdown, 214, 236, 237, 246, 248
  mechanisms, 244
  nitrogen, 251
Optical materials, 67
  characteristics, 68
Optical properties, 272, 273, 280
Optical pumps, 534-536
Optical systems, 60-66, 533
  Cassegrain, 66
  for laser drilling, 447
Optical thickness, 215
Oscillations, self-sustained, 236 476-500
Oscillation threshold, 27
Output power,
  argon laser, 33
  fast flow CO_2 laser, 38
  frequency spectrum, 57
Overheating, 201
Overlapping patterns, 327-328, 330
Oxidation, laser-induced, 269
  effect on optical properties, 272
  isothermal, 269
Oxides, 16-21

Parameters,
gas dynamic, 213
metal, 208
Patterns of hardened tracks, 327-333
Penetration depth, 89, 175, 205, 365-376, 484-487
electron, 106, 113
laser beam, 122
Percussion, laser-induced, 438, 441
Perturbation decay time, 192
Phase boundary, 171
Phase transformation, 281
temperature, 285
Phosphorescence, 26
Photoelectric effect, 359
Pierce method, 85
Planck's constant, 9, 221
Plasma
density, 256-259
dynamics,
at high nitrogen pressure, 252-259
effects, 217-219, 227, 233
energy
time dependence, 229-231
formation, 217-224
in nitrogen, 235
frequency, 237
ignition threshold, 217
opaque, 235, 243, 252, 266
optical breakdown, 237
oscillation, 236
pressure, 256-259
temperature, 256-259
velocity, 257
Plasmatron, 39, 48
Point heat source, 170, 171
Polarization, 54, 401
Population inversion, 26, 31
in chemical laser, 48
in gas-dynamic laser, 44
Power density, 24, 56, 63, 74, 75, 100
critical (threshold), 131, 187, 189, 234, 275, 364, 419, 420
heat, 90, 122, 131
spectral, 51
Power density distribution, 54, 100
normal (Gaussian), 101, 182
radial, 156,
spatial, 100
uniform, 101
Precipitation hardening, 289
Problems,
gas-kinetic, 198
vacuum vaporization, 205
Pulse
decoupling time, 202
fluence, 322, 324
interaction, giant, 316-319
length, dye laser, 30
repetition rate, dye laser, 30
welding, 358-365, 377
Pumping, 27, 43, 44

Q-factor, 25
Q-switching, 102
Quasi-continuous operation, 102
Quenching, 280, 320
melt, 320

Radiation,
coherent, 13
fluorescent, 14
intensity, 55
interaction with substances, 12
penetration, 204
plane-polarized, 54
spontaneous emission, 11
stimulated emission, 11
Radiation units, 10
Rare-earth elements, 25, 26
oxides, 20
Rayleigh rate, 204
Rayleigh zone, 55
Reactive (back) pressure, 168, 178-183, 195
Recoil force, 367
Recoil momentum, 202, 421
Reduction,
CO_2 laser-induced, 260
in gases, 260-263
metal, 260-263
Reflecting objectives, 65, 66
Reflectivity, 54, 100, 221
metal, 280, 359-361
Reflectors,
cylindrical, 535
double-mirror Cassegrain, 368
elliptic, 535
spheroidal, 535
Reflective index, 19, 65
Resonators, 534, 535
flat-mirror, 537
planoconcave, 540
spherical, 537
Ripple frequency,
ion current, 530
Ruby, 16, 17
damage threshold, 19
Ruby rods, 28

Scanners, 338
Scanning systems, 337, 338

Scattering, 113
angle, 111
backward, 109
Rutherford elastic, 110
Scribing, 386, 391
Semi-infinite body, 130, 131
Shielding, 215-225, 255
target surface, 209, 240
Shock hardening, 278, 317
Shock wave, 222, 254, 255-258
effects, 316
formation, 318
Mach, 225, 226
pressure, 317, 318
supersonic, 257
Spatial distribution,
heat power density, 114
Spatial intensity profiles,
laser beam, 331
Spatial patterns, 56, 57, 331
transverse-mode, 57
Spatial-temporal characteristics
E-beam, 105
L-beam, 100-105
Specific heat, 145
melting, 170
vaporization, 140, 175
Specific mass removal, 242
Spectral width, 51
Spherical aberration, 61-65, 75
Spiking operation, 102, 103, 193
Spot (pulse) overlap ratio, 327, 353, 380, 457
Stefan-Boltzmann constant, 129
Stefan problem, 145, 159, 171
Stimulated emission, 12-16, 24
gas laser, 33
liquid laser, 24-30
Successive approximation,
method, 149, 150
Surface hardening, 233, 277, 286
depth, 282
Surface hardness, L-beam induced,
in nirogen, 239
Surface vaporization, 194-198
Synthesis, laser-induced, 260-268
inorganic material,
in gases, 263-268

Target shielding, 235, 240
plasma, 243
Temperature distribution, 226, 280, 365
Temperature field, 130, 136, 228
Temperature gradient,
distribution, 282
Thermal conductivity, 17, 145
Thermal constants,
temperature dependence, 152, 157, 158
Thermal diffusion depth, 343
Thermal diffusivity, 99, 140, 153
Thermal emission, electron, 245
Thermal processes, 98, 451
calculation, 363
in E-beam-solid interaction, 490
in interaction zone, 217
in laser welding, 358-370
Thermochemical processes, 233, 269-274
Threshold energy, 26
Threshold density, 24, 189
energy, 24
power, 366, 420
Transforms, 146-155
Transitions, 31, 32
intercombination, 26
probability, 12
stimulated, 13
Transmissitivity,
optical material, 68, 69
Transverse modes, 56, 57
cylindrical, 57, 58
rectangular, 57, 58
Trimming, 387

Ultrasonic vibrations, 358

Vacuum film deposition, 501
Vapor back pressure, 452
Vapor, expansion,
in vacuum, 205
Vapor flow,
backward, 206
mass rate, 206
Vapor front, 196
speed, 197, 420
Vapor heating,
laser radiation, 209
Vapor supersaturation, 215
Vaporization, 194-218, 451
explosive, 202
diffusive, 218
specific (latent) heat, 140, 195, 198
surface, 194-198, 203
models, 194-198
problems, 197-198
rate, 196, 420
thermal theory, 194-198
threshold, 215
temperature, 219, 139, 197
vacuum, 205
volumetric, 198-203, 452

Velocity distribution,
Maxwellian, 206
particle, 205
Viewing systems, 541, 548
Volume specific heat 473
Volumetric expansion coefficient, 177

Wavelengths of radiation, 9, 10
Welds,
aspect ratio, 406
butt, 382, 378, 381
designs, 379
dimensions, 472
parameters, 472
types, 375
Weld
efficiency, 361, 368, 408, 463
penetration, 364-376, 403, 475, 482, 513
control, 521-531
speed (rate), 369, 370, 405
zone, 130
temperature field, 130
Welding, 358-418
CW laser, 371, 402-407
with cover gas, 406-408
E-beam, 469-488
dissimilar metals, 381
examples, 384-386
groove, 380
laser pulse parameters for, 372
at low pressure, 416
overlapping pulse, 380
pulse, 371
similar metals, 381

YAG crystals, 20

TO THE READER

Mir Publishers would be grateful for your comments on the content, translation and design of the book. We would also be pleased to receive any other suggestions you may wish to make.

Our address is: USSR, 129820, Moscow I-110, GSP, Pervy Rizhsky Pereulok, 2, Mir Publishers.

The handbook contains information on the basic thermophysical and hydrodynamic processes involved in the treatment o materials by laser and electron beams and also describes the methods of calculation of thermal processes. The coverage includes heat treatment, filr and coat forming, metal welding and cutting, and the equipment used for the purpose. The handbook is intended for workers in mechanical engineering.